T. G. Sitharam
S. V. Dinesh
Ravi Jakka   *Editors*

Soil Dynamics

Select Proceedings of 7th ICRAGEE 2020

Springer

Lecture Notes in Civil Engineering

Volume 119

Lecture Notes in Civil Engineering (LNCE) publishes the latest developments in Civil Engineering - quickly, informally and in top quality. Though original research reported in proceedings and post-proceedings represents the core of LNCE, edited volumes of exceptionally high quality and interest may also be considered for publication. Volumes published in LNCE embrace all aspects and subfields of, as well as new challenges in, Civil Engineering. Topics in the series include:

- Construction and Structural Mechanics
- Building Materials
- Concrete, Steel and Timber Structures
- Geotechnical Engineering
- Earthquake Engineering
- Coastal Engineering
- Ocean and Offshore Engineering; Ships and Floating Structures
- Hydraulics, Hydrology and Water Resources Engineering
- Environmental Engineering and Sustainability
- Structural Health and Monitoring
- Surveying and Geographical Information Systems
- Indoor Environments
- Transportation and Traffic
- Risk Analysis
- Safety and Security

To submit a proposal or request further information, please contact the appropriate Springer Editor:

– Pierpaolo Riva at pierpaolo.riva@springer.com (Europe and Americas);
– Swati Meherishi at swati.meherishi@springer.com (Asia - except China, and Australia, New Zealand);
– Wayne Hu at wayne.hu@springer.com (China).

All books in the series now indexed by Scopus and EI Compendex database!

More information about this series at http://www.springer.com/series/15087

T. G. Sitharam · S. V. Dinesh · Ravi Jakka
Editors

Soil Dynamics

Select Proceedings of 7th ICRAGEE 2020

Editors
T. G. Sitharam
Indian Institute of Technology Guwahati
Guwahati, Assam, India

S. V. Dinesh
Department of Civil Engineering
Siddaganga Institute of Technology
Tumakuru, Karnataka, India

Ravi Jakka
Department of Earthquake Engineering
Indian Institute of Technology Roorkee
Roorkee, Uttarakhand, India

Preface

Soil dynamics is an important component of earthquake engineering that deals with the response of soil to dynamic loads. This book volume contains latest research papers on field and laboratory testing of soils for the estimation of dynamic soil properties, soil liquefaction, and soil–structure interaction under dynamic loading selected from the proceedings of 7th International Conference on Recent Advances in Geotechnical Earthquake Engineering and Soil Dynamics, 2021.

We thank all the staff of Springer for their full support and cooperation at all the stages of the publication of this book. We do hope that this book will be beneficial to students, researchers, and professionals working in the field of earthquake hazards. The comments and suggestions from the readers and users of this book are most welcome.

We thank and acknowledge the service of following reviewers for their valuable time and efforts.

Guwahati, India   T. G. Sitharam
Tumakuru, India   S. V. Dinesh
Roorkee, India   Ravi Jakka

Acknowledgements

Contents

About the Editors

Prof. T. G. Sitharam is currently the Director of Indian Institute of Technology Guwahati, India. He is also KSIIDC Chair Professor in the area of Energy and Mechanical Sciences and Senior Professor at the Department of Civil Engineering, Indian Institute of Science, Bengaluru (IISc). He was the founder Chairman of the Center for Infrastructure, Sustainable Transport and Urban Planning (CiSTUP) at IISc, and is presently the Chairman of the AICTE South Western Zonal Committee, Regional office at Bengaluru and President of the Indian Society for Earthquake Technology (ISET). Prof Sitharam is the founder President of the International Association for Coastal Reservoir Research (IACRR). He has been a Visiting Professor at Yamaguchi University, Japan; University of Waterloo, Canada; University of Dolhousie, Halifax, Canada; and ISM Dhanbad, Jharkhand, and was a Research Scientist at the Center for Earth Sciences and Engineering, University of Texas at Austin, Texas, USA until 1994.

Prof. S. V. Dinesh is currently working as Professor in the Department of Civil Engineering at Siddaganga Institute of Technology (SIT), Tumkur. He completed his postdoc research from Yamaguchi University, Japan under NPEE fellowship from MHRD, Government of India. He is the recipient of Institution of Engineers fellowship. He is life member of many professional Societies. His areas of interest in research is in Geotechnical engineering, Geotechnical earthquake engineering and Pavement geotechnics. He has guided 7 doctoral students and 60 M.Tech. thesis. He has more than 100 publications in reputed journals and conferences. As a geotechnical consultant, he has advised and acted as consultant covering a wide range of civil and geotechnical structures for the past two decades.

Prof. Ravi Jakka is working as Associate Professor in the Department of Earth-quake Engineering, Indian Institute of Technology, Roorkee. He is also currently serving as Secretary, Indian Society of Earthquake Technology (ISET). He has graduated in Civil Engineering from Andhra University Engineering College in the year 2001. He has obtained masters and doctorate degrees from IIT Delhi in the years 2003 and 2007 respectively. His areas of interest are Dynamic Site Characterization, Soil Liquefaction, Seismic Slope Stability of Dams, Landslides, Foundations & Seismic Hazard Assessment. He has published over 100 articles in reputed international journals and conferences. He has supervised over 35 Masters Dissertations and 6 Ph.D. thesis, while he is currently guiding 10 Ph.D. thesis. He has received prestigious DAAD and National Doctoral fellowships. He has obtained University Gold Medal from Andhra University. He also received 'Young Geotechnical Engineer Best Paper Award' from Indian Geotechnical Society. He was instrumental in the development of Earthquake Early Warning System for northern India, a prestigious national project. He is also the Organizing Secretary to 7th International Conference on Recent Advances in Geotechnical Earthquake Engineering.

Dynamic Soil Properties of Enzymatic Cement-Stabilised Clay

Check for updates

Geethu Thomas and **Kodi Rangaswamy**

Abstract The usage of nontraditional additives in the field of ground improvement of cohesive soils became imperative because some of them can lessen the deleterious effect on the environment. Enzymes extracted from natural sources are useful in modifying the soil-strength and stiffness. Degradation of shear modulus and accumulation of pore water pressure under dynamic soil conditions need to be considered before constructing any structures with weak sub-strata, exceptionally soft clay. The present study aims at improving the dynamic soil properties of soft clay by stabilising with a bio-enzyme. A series of cyclic triaxial tests were conducted to analyse the effect on various features like shear modulus, damping ratio, pore pressure ratio, etc., with the various cyclic shear strains (%). The degradation of shear modulus and accumulation of pore water pressure decrease with an increase in shear strain amplitude in untreated clay soil samples. A similar but improved trend was observed in the treated soils with the optimum bio-enzyme dosage and 1% cement. From the results, it can be concluded that the enzymatic cement-stabilised clay responds to the earthquake and other similar dynamic soil conditions than the natural soft clay. This technique can be used in the field of geotechnical earthquake engineering, which can reduce the ground amplification in soil-strata encountered with soft clay.

Keywords Dynamic soil properties · Soil stabilisation · Bio-enzyme

1 Introduction

Soil layer properties can significantly influence the ground response during seismic motion. A soil layer can amplify or de-amplify the seismic wave depending on the local site conditions. A prior seismic evaluation of a site is essential to reduce the consequences during such situations [1]. The determination of dynamic soil properties is a prerequisite for the evaluation of a site response during an earthquake or similar circumstances with dynamic loading conditions. Shear modulus and damping

G. Thomas (✉) · K. Rangaswamy
Department of Civil Engineering, National Institute of Technology, Calicut, India
e-mail: toms88geethu@gmail.com

ratio are sensitive to strain, which varies with the depth and magnitude of ground response. Stiffness and damping characteristics of soil are significant for all levels of strain conditions such as low, intermediate and high strain levels. The loading rate, number of loading cycles and volume change characteristics can also influence the shear strength of cyclically loaded soils at high strain levels [2]. Truthfully, the loading rate has a minor effect on shear strength of soils, whereas higher loading cycles can significantly reduce shear strength of the both cohesionless and cohesive soils. Comparatively smaller specimens are prepared for the laboratory tests which possibly represent the in situ soil with a larger volume. The choice of a particular laboratory test among the various other laboratory tests may be based on the suitability of that test to resolve the current problem of interest. Cyclic triaxial tests (for large strain cases 10^{-3} and higher) and resonant column tests (for low strain cases $10^{-6} \sim 10^{-5}$) are commonly used laboratory tests for finding the dynamic properties of the soils. Cyclic triaxial test results are reliable and helpful to understand the soil response under dynamic loading conditions even if the testing conditions do not truly represent the site conditions [3]. Vucetic and Dobry [5] compiled 16 publications around the globe to prepare a design chart based on the factors affecting the dynamic response of cohesive soils. Shear modulus degradation and damping ratio variation with cyclic shear strain are prepared, which can be applied to the various soil conditions based on the plasticity characteristics and over-consolidation ratio. The key factors that influence the dynamic soil properties of a cohesive soil are confining pressure, void ratio, geologic age, cementation, over-consolidation, plasticity index, cyclic strain, strain rate (frequency of loading) and the number of cycles among which void ratio is relevant in the case of cohesionless soils[4].

Soft clay due to its low bearing capacity and high compressibility makes the construction complicated even under static loading. During an earthquake, the ground moves randomly in all directions, and there is static as well as dynamic loading. The pulsating stresses can consume the stiffness of the soils dramatically; it is termed as stiffness degradation of soil. Relatively high plastic clays exhibit a significant rate of stiffness degradation and low damping ratio compared to that of low plastic clays. An amplified ground motion can be expected in high plastic clays which behave almost linearly to the seismic motion [5].

Soft soil is improved for its properties during static loading and successfully implemented in several field conditions. The soil stabilisation is changing the trend of using traditional additives (cement, lime, fly ash, etc.) with partially or entirely replaced by non-traditional additives like enzymes, nanoparticles or combination of both traditional and non-traditional additives. Soil stabilised with cement and other additives is found to be effective in improving the dynamic soil response under earthquake loading conditions. The necessity of getting more knowledge about the effect of soil stabilisation in dynamic soil properties is very demanding in the current scenario of increasing urbanisation and lack of free spaces for the construction.

The present study is aimed at introducing a combination of an enzyme with the organic origin and a small amount of cement for the improvement of soft clay. The optimum dosage which gives maximum strength is chosen for the cyclic triaxial tests. The process of finding the optimum dosages and the mechanism behind the strength

improvement is published in Thomas and Rangaswamy [6], which is briefly quoted in the following sessions. The addition of cement causes strength improvement of soil but to minimise the effect on the environment, its dosage is limited to 1% by dry weight of soil in the present study. The advantages of using a bio-enzyme are many; some are listed as follows: (1) non-toxic, (2) derived from natural materials, (3) economical, (4) easy to use, (5) requires very less quantity to get the desired strength improvement since the bacteria would not get disintegrated even after many reactions and (6) eco-friendly.

2   Experimental Program

All tests for the present study were conducted in Geotechnical Engineering Laboratory, at NIT, Calicut. Soil samples were collected from a boring site at Ernakulam, Kerala. The sample belongs to clay with high compressibility according to the A-line chart given by Indian Standard Soil Classification System. The basic properties of the soil under consideration are listed in Table 1. The effect of stabilisation under static loading condition is studied on soil samples prepared with 1% Portland Pozzolana cement (manufactured by Ramco Cements Pvt Ltd., India), and the optimum dosage of Terrazyme (0.06 ml/kg of soil) was found out from a series of unconfined compressive strength tests and Atterberg limit tests [6].

Table 1   Properties of soil collected from Ernakulam, Kerala

Properties	Value
Specific gravity	2.50
Liquid limit	91%
Plasticity index	58
Clay	46%
Soil Classification (ISSCS)	CH
Unconfined compressive strength	28 kPa

Table 2   Unconfined compressive strength of enzymatic soil–cement

Combinations	Terrazyme dosage, ml/kg	Unconfined compressive strength (kPa) in 28 days
VS	0	28.00
VS + C1	0	88.54
VS + C1 + TD1	0.04	113.01
VS + C1 + TD2	0.06	127.14
VS + C1 + TD3	0.08	118.98
VS + C1 + TD4	0.10	114.78

Table 2 shows the details of the dosages added to the soil for the present study for getting the optimum dosage of the bio-enzyme. The unconfined compressive strength got increased with increase in Terrazyme dosage (denoted as TD), but after dosage 2 (TD2) the strength started decreasing. This reduction happens due to the slippage of soil particles in the presence of excess calcium silicate hydrate (C-S–H) gel produced during the pozzolanic reaction. The plasticity index of the untreated soil was around 58, which reduced to 16.5 due to the enzymatic cement treatment in 28 days of curing.

2.1 Cyclic Triaxial Testing Details

The preparation of the soil samples for the cyclic triaxial testing is already discussed in the previous section. The samples are saturated up to Skempton's pore pressure parameter B around 0.97 by sequentially increasing the back pressure and confining pressure. After the saturation process, the sample is allowed to consolidate under corresponding effective confining pressure (150 kPa in this work) and then sheared under cyclic loading. Table 3 shows the list of parameters considered in the present study. Consolidated undrained (CU) cyclic triaxial tests in the strain-controlled mode were conducted on untreated and treated (enzymatic soil–cement) soil.

Shear strain can be expressed as $\gamma = (1 + \upsilon) \times \varepsilon$.

where ε = axial strain and υ = Poisson's ratio (taken as 0.5 as in incompressible material, if the soil is below water table and saturated).

A hysteresis curve is plotted between the cyclic shear stress and cyclic shear strain to determine the shear modulus and damping ratio of the desired cycle number. It is observed that the shear modulus of the soil sample decreases with the increase in the number of cycles of loading (Refer to Fig. 1). The closed loops of hysteresis curves agree with the theory by Hardin and Drnevich [7] since the over-consolidation ratio (OCR) of the soil is 1. The reduction in shear modulus of the soil sample is represented by the stepping down of the hysteresis loop in higher cycle numbers. Due to the effect of stabilisation, the reduction in stiffness becomes slower as compared

Table 3 Details of cyclic triaxial test for the present study

Parameter	Value/ details
Test mode	Strain controlled
Effective confining pressure	150 kPa
Loading frequency	1 Hz
Cyclic shear strain	0.15, 1.125 and 2.7%
Additive dosage	1% cement + Terrazyme (0.06 ml/kg)
Number of cycles	1, 10, 100
Curing period	28 days
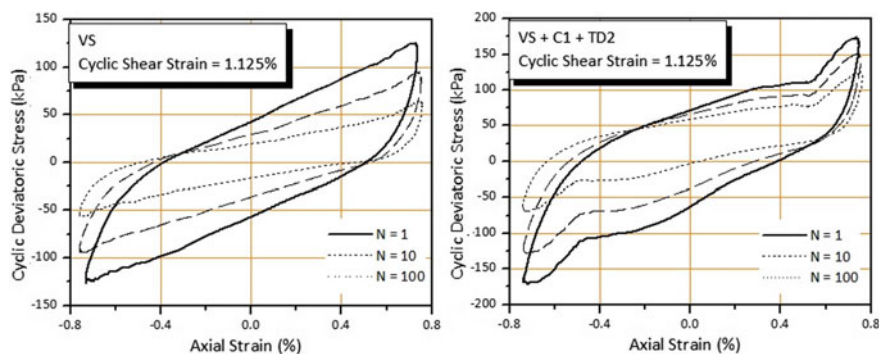
Fig. 1 A typical plot of degradation of shear modulus with the number of cycles

to the untreated soil. The larger area of the hysteresis loop indicates that the energy dissipation is more. Energy dissipation is more at the initial number of cycles; this is why the area of the loop becomes smaller as the number of cycles increases. The increase in the stiffness of treated soil is observable from the changes in the hysteresis curves.

3 Results and Discussion

3.1 Effect on Shear Modulus

The cyclic shear modulus of the untreated and treated soil increases with the decrease in cyclic shear strain amplitude. The addition of bio-enzyme into the soil increased the shear modulus of the soft clay (Refer to Fig. 2). Similar behaviour of shear modulus was observed in cohesive soils by Subramaniam and Banerjee [8] when cement is added. Figure 3 shows the variation of shear modulus with the number of cycles before and after enzymatic treatment in soil–cement.

As previously mentioned, the untreated soil is high plastic clay with a plasticity index of 58 and the treated soil modified to a plasticity index of 16.5. In Fig. 3, the degradation rate with the number of loading cycles of untreated soil with high plasticity index (PI) is slower than that of treated soil with lower PI. This change shows well agreement with the statement published in the article by Vucetic and Dobry [5], which is valid for normally consolidated clays. The influence of PI on ground response has been studied by Vucetic and Dobry (1991). A response spectrum of 35-m-deep clay deposit is presented in the same work which evidences that soils with high PI showed a peak ground acceleration in the range of 0.45–0.65 g (at structure time period T around 2 s), whereas the response spectrum of low plastic clay never exceeds 0.15 g. A similar reduction in ground amplification during a
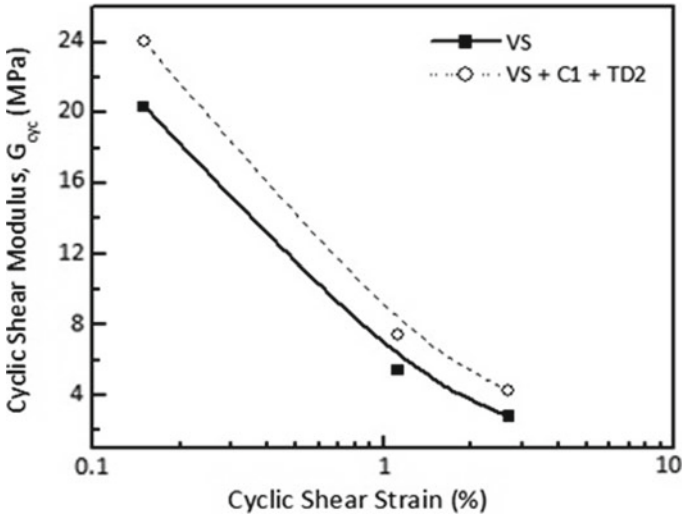
Fig. 2 Variation of cyclic shear modulus with cyclic shear strain

Fig. 3 Shear modulus
variation with number of
cycles for untreated and
treated soil samples
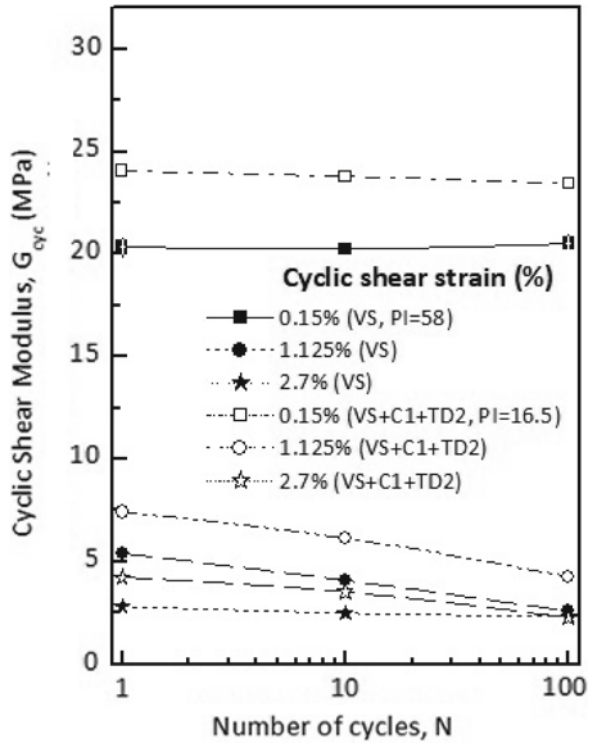
Fig. 4 Effect of stabilisation on material damping ratio
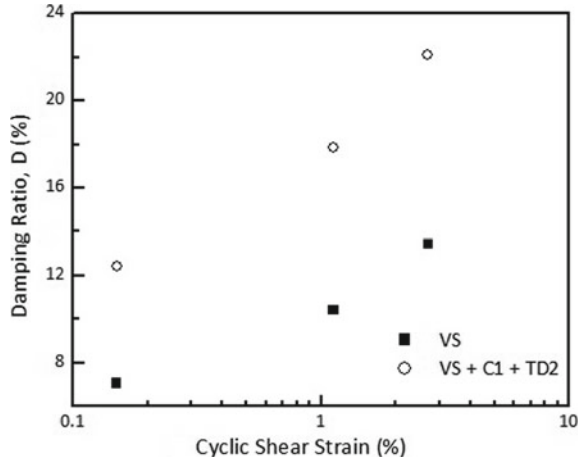
seismic activity can be expected in the present study on the treated soils with lower PI.

3.2 Effect on Damping Ratio

The effect of enzymatic cement treatment in soft soil based on the change in damping ratio is displayed in Fig. 4. In the present study, the damping ratio is calculated for the first cycle. Damping ratio increases with an increase in cyclic shear strain applied to the soil sample. The damping ratio of the treated soil is more compared to that of untreated soil. An increase in the area of the hysteresis loop is observed in Fig. 1, which indicates the increase in energy absorption capacity of treated soil. The increment in damping ratio represents the soil resistance towards the seismic activity due to the addition of bio-enzyme in the cemented soil. The damping ratio of stabilised soil increased 1.7 times (average) that of untreated soil. The stress dissipation and energy absorption are more in treated soil due to particle densification, pore volume reduction and better bonding between the cemented particles. The improved damping characteristics of treated soil can help the soil to reduce the expected ground amplification in the soft clay deposit [5].

3.3 Effect on Pore Pressure Ratio

The pore pressure ratio (PPR) increases with the number of cycles and then reaches a steady value; beyond that value, the pore pressure ratio remains almost constant even when the number of cycles increases (Fig. 5). The number of loading cycles
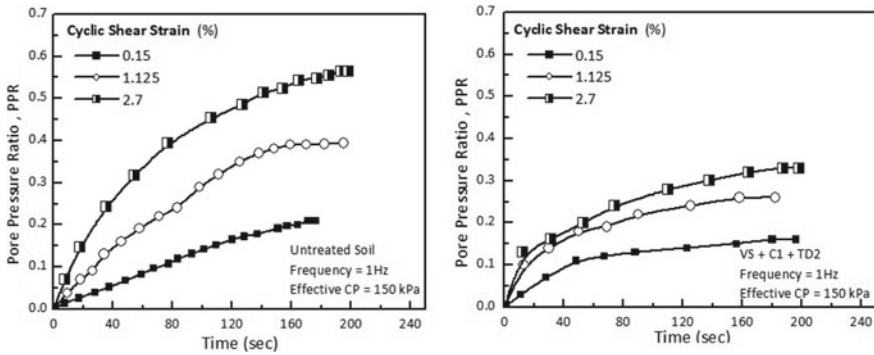
Fig. 5 Effect of stabilisation on PPR of soil

required for becoming the pore pressure ratio a constant value is lesser in lower strain amplitudes [8]. The enzymatic stabilised soil exhibited comparatively lower pore pressure ratio than that of untreated soil. The reduction in PPR of treated soil implies that the enzymatic cement stabilisation is effective in reducing the pore volume of soil matrix and thereby reducing the pore pressure build up in the saturated soil during cyclic loading. The reduced value of pore pressure ratio shows that the soil can respond well to the dynamic loading conditions due to the chemical and physical changes happened in the soil structure because of the enzymatic cement inclusion.

4 Stabilising Mechanism of Enzymatic Cement—Soil

Terrazyme is an organic-fermented product which is a highly concentrated liquid-based enzyme derived from vegetable extracts. In early days, it has used for agricultural purposes since it can improve the cultivation and the plastic characteristics of the soil. Terrazyme without the presence of cement/ lime might not be able to exhibit a significant change in the soil properties even though it can slightly contribute to the consistency limits as well as unconfined compressive strength [9]. The presence of optimum cement dosage accelerates the rate of bio-enzyme reaction, thereby the strength and stiffness of the soil are improved. The adsorbed water layer is surrounding the clay particles reform to a thinner layer because of the dissociation of water molecules due to the addition of Terrazyme dosage [6]. The reduction of free water trapped in between the particle interfaces occurs, which thereby brings the clay flakes to come closer and exhibit better bond strength. Pore volume reduction, reduced affinity to moisture, effective densification of the soil matrix and reduced plasticity index are the main attractive benefits of using Terrazyme along with a small quantity of cement. In the presence of ample moisture content, cement and terrazyme react with clay mineral to produce calcium silicate hydrate (C-S–H) gel

which is responsible for the strength improvement and better bonding between the particles.

Bio-clogging and bio-cementation are the main two processes that happen inside the enzymatic soil mixture [10]. In the presence of microbial action, pore spaces get clogged by the resulting gel, which reduces the pore spaces between the clay flakes; this is known as bio-clogging. Bio-cementation is the process of improving the bond strength by the cementation action in the presence of bacteria. In the initial stage, the rate of reaction is faster, which then comes to a uniform manner after some time. The microbial action, along with the minute particle movement, occurs in the soil–cement–enzyme matrix in which the particle from catalysis has high energy initially, and it slows down once the energy declines.

5   Conclusions

This study examined the impact of stabilisation with optimum dosages of Terrazyme in the presence of 1% of cement on dynamic soil properties of soft clay with the aid of cyclic triaxial testing apparatus. The results of this study can be summarised as follows:

- Energy dissipation is observed as more in the initial number of cycles; this is why the loop area in the hysteresis curve becomes smaller as the cycle proceeds.
- The cyclic shear modulus of the untreated and treated soil increases with the decrease in cyclic shear strain amplitude. The addition of bio-enzyme into the soil increased the shear modulus of the soft clay.
- Untreated soil with high plasticity index behaves more linearly to the cyclic strain response than treated soil with lower plasticity. A reduced rate of degradation of shear modulus with the number of cycles is observed at a high plasticity index.
- Damping ratio increases with an increase in cyclic shear strain applied to the soil sample.
- The increment in damping ratio represents the resistance towards the seismic activity due to the addition of bio-enzyme in the cemented soil. The damping ratio of stabilised soil increased 1.7 times (average) that of untreated soil.
- The stress dissipation and energy absorption are more in treated soil due to particle densification, pore volume reduction and better bonding between the cemented particles.
- The pore pressure ratio increases with the number of cycles and then reaches a steady value; beyond that value, the pore pressure ratio remains almost constant even when the number of cycles increases. The enzymatic stabilised soil exhibited comparatively lower pore pressure ratio than that of untreated soil. The reduction in PPR of treated soil implies that the enzymatic cement stabilisation is effective in reducing the pore volume of soil matrix and thereby reducing the pore pressure build up in the saturated soil during cyclic loading.

It can be summarised that the inclusion of enzymatic cement in the soft soil can be successfully applied to the field cases where static and dynamic loading conditions are expected. The enzymatic cement–soil can respond well to the static as well as dynamic loading.

References

1. Semblat JF, Kham M, Parara E, Bard PY, Pitilakis K, Makra K, Raptakis D (2005) Seismic wave amplification: basin geometry vs soil layering. Soil Dyn Earthq Eng 25(7–10):529–538
2. Kramer SL (2007) Geotechnical earthquake engineering. First Impression. Pearson Education Inc., India
3. Vijayasri T, Patra N, Raychowdhury P (2016) Cyclic behavior and liquefaction potential of Renusagar Pond Ash reinforced with geotextiles. J Mater Civ Engg 28(11):4016125–1–10
4. Seed, HB, Idriss I (1970) Soil moduli and damping factors for dynamic response analysis. Rep. No. EERC 70–10, Fundam. Soil Mech. Elsvier
5. Vucetic M, Dobry R (1991) Effect of soil plasticity on cyclic response. J Geotech Eng 117(1):89–107
6. Thomas G, Rangaswamy, K (2019) Strength behavior of enzymatic cement treated clay. Int J Geotech Eng 1–14. https://doi.org/10.1080/19386362.2019.1622854
7. Hardin BO, Drnevich VP (1972) Shear modulus and damping in soils: design equations and curves. J Soil Mech Found Div 98(7):667–692
8. Subramaniam P, Banerjee S (2014) Factors affecting shear modulus deg- radation of cement treated clay. Soil Dyn Earthq Eng 65:181–188
9. Eujine GN, Chandrakaran S, Sankar N (2017) Accelerated subgrade stabilization using enzymatic lime technique. J Mater Civ Eng ASCE 29(9):1–7
10. Yue-jun LI, Liang LI, Han-cheng DAN (2011) Study on application of TerraZyme in road base course of road. Appl Mech Mater 97–98:1098–1108

Effect of Fines Content on Dynamic Properties of Sand Using Bender Element

Sandip Shivaji Bhutale and R. S. Dalvi

Abstract Shear wave propagation in the soil is a physical phenomenon and has been used widely for monitoring as well as for assessing the seismic property in geotechnical engineering. Shear wave velocity (V_s) and small-strain shear modulus (G_{max}) are the key parameters in defining material response to various dynamic loadings. Generally, sand is weak in dynamic loading and also contains few non-plastic fines up to a certain extent. Thus, to have a better fundamental understanding of the deformation behaviour of sand fines mixtures, a bender element tests have been performed. From the bender element tests, it was concluded that G_{max} is significantly dependent on relative density which is a function of void ratio, fines content and confining pressure. It was also observed that the value of shear wave velocity and shear modulus depends upon saturation. Dry specimen comparatively gives a higher values of shear wave velocity and shear modulus than a saturated specimen. It was also observed that up to certain fines content, the maximum and minimum void ratio decreased and after that, there was an increase in maximum and minimum void ratio. Based on regression analysis technique a modified model for evaluation method of small strain shear modulus (G_{max}) of sand-fines mixture was proposed and verified using equation proposed by Seed and Idriss (1970). Test results indicated that the modified equation accounting for the influence of fines content can predict the G_{max} of sand-fines mixture satisfactorily. From the experimental results, it was concluded that fines content plays an essential role in shear wave velocity and small strain shear modulus.

Keywords Bender element · Shear wave velocity · Small strain shear modulus · Clean sand · Limiting fines content

S. S. Bhutale (✉)
Geotechnical Engineering, College of Engineering Pune, Pune, India
e-mail: sanshivraje@gmail.com

R. S. Dalvi
Civil Engineering Department, College of Engineering Pune, Pune, India

1 Introduction

The small strain shear modulus, G_{max} ($G_{max} = \rho V_s^2$, ρ: density of soil) and shear-wave velocity (V_s), are the fundamental parameters of the soil dynamic, which plays an important role in the soil deformation prediction, liquefaction evaluation, analysis of the seismic response and other geotechnical problems. The soil properties which are needed in the analysis and design of structure subjected to dynamic loading are modulus of elasticity (E), small strain shear modulus (G), Poisson's ratio (μ) and dynamic elastic constants, such as coefficient of elastic uniform compression C_u, coefficient of uniform shear C_τ, coefficient of elastic non-uniform compression C_ϕ and coefficient of elastic non-uniform shear C_ψ. The measurement of dynamic soil properties is a critical task in the solution of geotechnical engineering problems. A wide variety of field and laboratory techniques are available each with different advantages and limitations with respect to different problems. Many are oriented toward measurement of low-strain properties and many other toward properties mobilized at larger strains. In the case of laboratory testing to calculate low strain soil dynamic properties there is two commonly used method one is bender element test and another one is a resonant column test. Out of these two, bender element tests are simplest, easy to handle as compare to resonant column tests. Taking this advantage for the present work bender element was used to determine the dynamic properties of soil. Usually, natural sandy soil contains not only a sand particle but also the fines content (FC) in the mixture can be represented in percentage by mass. It was found that FC has significant effects on the mechanical response of the mixture of sand and fines. Choo and Burns (2015) studied the effect of grain size and FC on the sandy soil using bender element tests. It was found that the shear wave velocity (V_s) decreased with the increase of FC at particular relative density and the shear wave velocity of the sandy soil with various FC was almost same when the skeleton void ratio was uniform. To measure the shear wave velocity the experimental arrangement and detail given by Melissa et al. [1]. According to Melissa et al. bender element (BE) testing has appeared as one promising way to obtain shear modulus at small strains. A voltage signal is applied to a piezoceramic element, which transmits a small shearing movement over one end of the cylindrical soil specimen. This disturbance travels along with the specimen until the other end where a similar element receives the mechanical perturbation and generates a voltage. The signal travels a distance between elements (L_{TT}) and the time difference between the emitted and received signals represents the time of the propagation of the signal. These measurements enable one to compute the shear wave velocity (V_S) and the small strain shear modulus (G_{max}) of a specimen with a known soil mass density (ρ). The shear wave velocity is measured by using Eqs. 1 and 2.

$$V_s = L_{TT}(tt - t_c) \tag{1}$$

$$G_{max} = (V_s)^2 \tag{2}$$

where, L_{TT} = tip-to-tip distance between the bender elements [2] (Viggiani and Atkinson 1995); tt = time difference between the initiation of the source wave and the arrival of the shear wave; and t_c = system calibration time obtained when L_{TT} is zero. Shear waves generated in soils during the BE tests induce very small strains, less than 10^{-3}% which is within the elastic zone for nearly all soils. Shear wave travel time was calculated as the difference between the start of the transmitted signal and the start of the first major positively polarized up rise minus the system calibration time, t_c. In many cases, the received wave displayed a slight negative dip before the first major peak, representing near field effects, which generally occur when L_{TT} is less than twice the wavelength of the shear wave, and which were more pronounced for shorter and softer specimens. Thus, received waves were interpreted by projecting a horizontal reference line from the initial flat portion of the received wave and the intersection of this line and the received wave was used as the arrival time as shown in Fig. 1.

In present work bender element tests were performed on clean sand and sand with FC. The effect of FC on dynamic properties of sand with different relative densities and confining pressure was studied. Furthermore, the correlation between shear wave velocity and small strain shear modulus with void ratio was established. The results were verified with the help of Seed and Idriss (1970) equation.
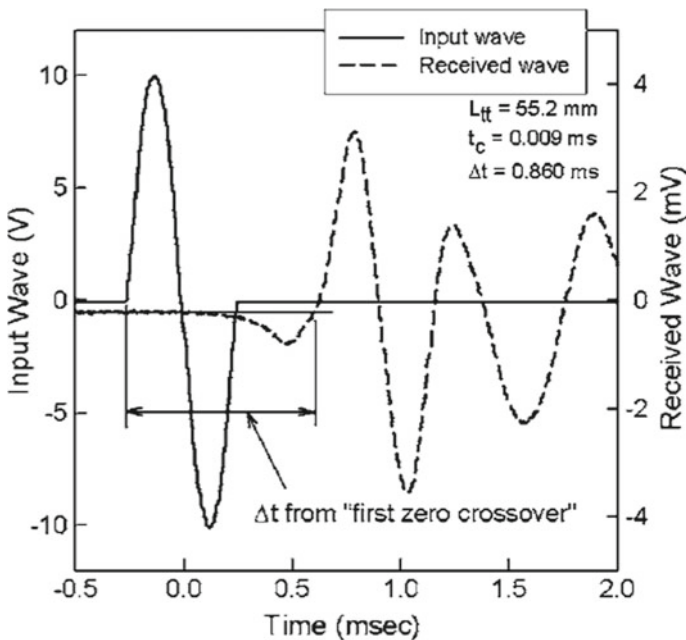
Fig. 1 Estimation of time of elapse between transmitting and receiving wave on oscilloscope (Fam et al. 1995)

2 Testing of Specimens

In the laboratory experiment clean sand is used as base sand and quarry dust was used as fines. The oven dried sand was separated through the IS sieve of 0.075 mm size. The particle of the size larger than 0.075 mm was chosen as sand, whereas the quarry dust which was pass through the IS sieve of 0.075 mm size was taken as fines. The grain size distribution curves for sand and sand with different FC are shown in Fig. 2.

Table 1 Shows the index properties of sand and fines of testing material, based on index properties the material classified as poorly graded sand and inorganic silt.

Figure 3 shows the effect of FC on minimum and maximum void ratio. As the FC increases from 0% to limiting fines content the maximum void ratio and the minimum void ratio of sand goes on decreasing, after exceeding the limiting fines content the value of both maximum and minimum void ratio of sand increases.
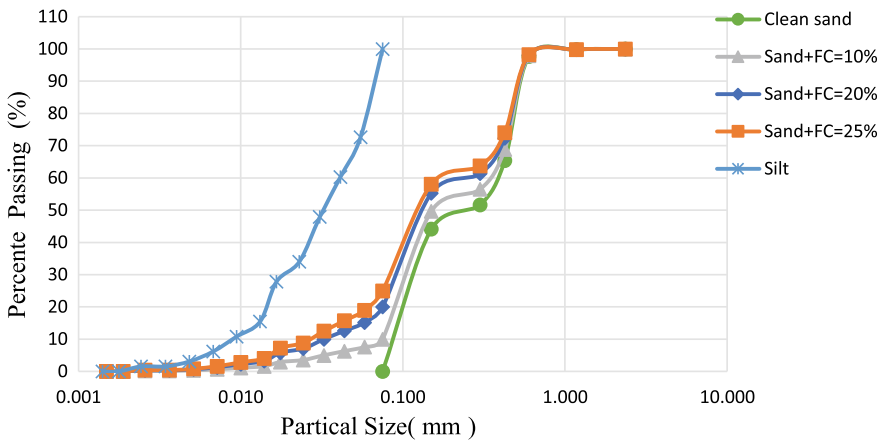
Fig. 2 Grain size distribution curves of the clean sand and different FC

Table 1 Index properties of sand and fines

Property	Symbol	Unit	Sand	Fine
Average particle size	D_{50}	mm	0.27	0.033
Effective particle size	D_{10}	mm	0.088	0.009
Uniformity coefficient	C_u		4.4	4.7
Coefficient of curvature	C_c		0.4	0.9
Specific gravity	G		2.67	2.83
Maximum void ratio	e_{max}		0.70	1.60
Minimum void ratio	e_{min}		0.45	0.74
Classification			SP	ML
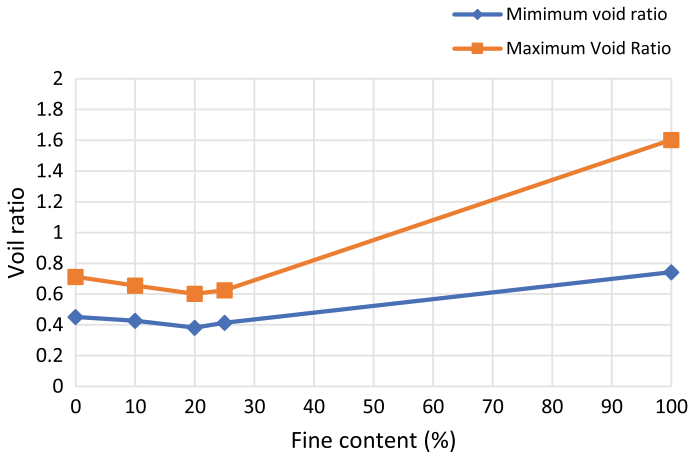
Fig. 3 Maximum and minimum void ratio of the mixtures with different fines content

3 Sample Preparation and Tests

All specimens were prepared by the saturated tamping method [3] in conjunction with the under-compaction technique. This method was chosen because it could produce a very wide range of void ratio and has the advantage of controlling the void ratio and quick saturation. Initially the quantity of water was taken which is equal to 90% of water required for fully saturation of sample. The water required for fully saturation was calculated from theoretical relationship between degree of saturation(S), void ratio(e), water content (w) and specific gravity(G) which is given as Se = Gw. After adding of water, the sample was thoroughly mixed and divided in five equal parts. The sample was filled in five equal layers and tamping was done to achieve required relative density. The specimen was saturated via the back-pressure saturation method. The pore pressure coefficient B was measured after saturation. The specimen was considered as saturated when Skempton's parameter B was larger than 0.95. The specimen was tested under isotropic condition at required confining pressure.

4 Results and Discussion

The tests were conducted by means of the bender element with piezoceramic bender elements installed at bottom and top of the triaxial cell. The set of equipment is as shown in Fig. 4. The sine wave was generated by means of function generator. The generated wave amplified and passed through soil sample which is placed in triaxial cell with embedded bender element through transmitting sensor. This transmitting wave passed through sample and it received at another end by means of
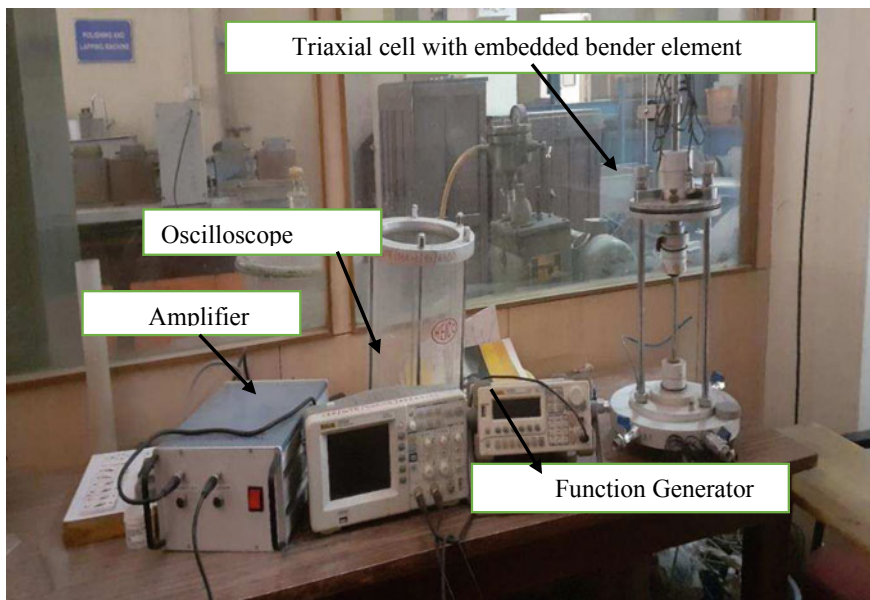
Fig. 4 Existing bender element test set up in Geotechnical engineering laboratory, Civil Engg. Department, College of Engineering Pune

receiving sensor. These transmitting and receiving wave were displays on oscilloscope. The time of elapse between transmitting and receiving wave are directly measured on oscilloscopes. The frequency and amplitude were taken as 2 kHz and 20 V respectively. The small strain shear modulus was computed using the Eq. 3.

$$G_{max} = \rho V_s^2 \tag{3}$$

Where, G_{max} is small strain shear modulus , ρ is mass density in kg/m^3 and V_s is shear wave velocity in m/s which was calculated by using Eq. 2.

$$V_s = \frac{Tiptotipdistance(L)ofsample}{Timeoftravel} \tag{4}$$

The shear wave velocity was calculated using the difference between the transmitting time and the first arrival time of S-wave.

5 Effect of Fines Content on Shear Wave Velocity (V_s) and Small Strain Shear Modulus (G_{max})

The shear wave velocity (V_s) and small strain shear modulus (G_{max}) were evaluated under the saturated condition for different relative density and confining pressure. The V_s and G_{max} obtained from the bender element test were plotted against fines content with different confining pressure as shown in Figs. 5a, b, 6a, b and 7a, b. From the graph, it is clear that the value of V_s and G_{max} increase with an increase in FC up to the value of limiting fines content (LFC). Then further increase in FC results in the decrease the value of V_s and G_{max}. This could be due to the limiting FC of sand. At this stage the voids of the sand filled by the fines due to which soil skeleton becomes stronger hence value of V_s and G_{max} increases. Further addition of fines in sand causes destruction in soil skeleton and fines start dominating instead

(a)

(b)
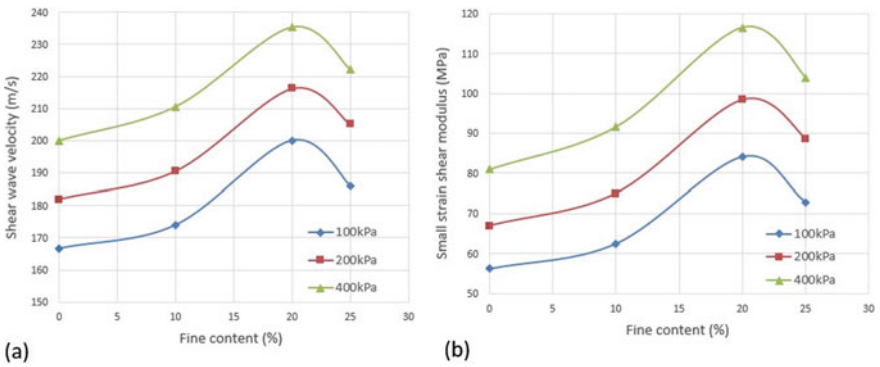
Fig. 5 Variation of **a** shear wave velocity. **b** Small strain shear modulus with fines content at RD = 30%

(a)

(b)
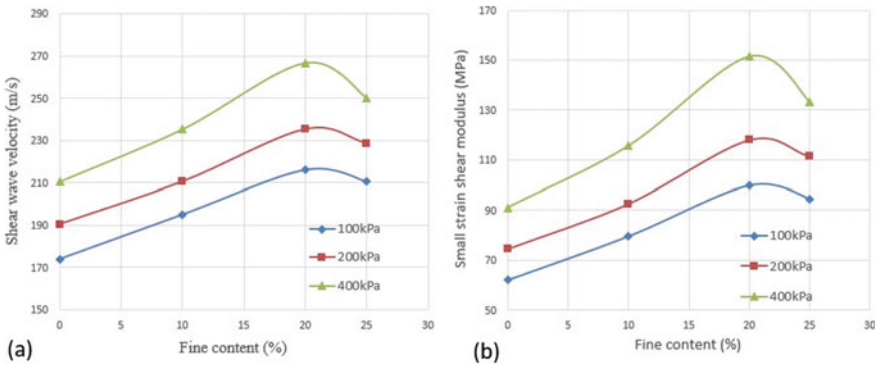
Fig. 6 Variation of **a** shear wave velocity. **b** Small strain shear modulus with fines content at RD = 45%
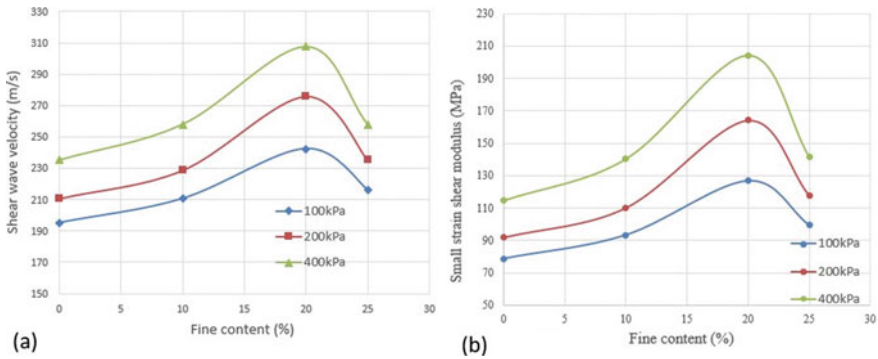
Fig. 7 Variation of **a** shear wave velocity. **b** Small strain shear modulus with fines content at RD = 60%

of sand which results in weakening of the soil skeleton and V_s and G_{max} goes on decreasing.

6 Effect of Confining Pressure and Relative Density on V_s and G_{max}

Figures 5a, 6a and 7a show effect of fines content on shear wave velocity and Figs. 5b, 6b and 7b demonstrate effect of fines content on small strain shear modulus for 30, 45 and 60% relative densities. It is observed that V_s and G_{max} were higher for higher relative density irrespective of confining pressure. As the value of relative density increases the V_s and G_{max} goes on increasing for given the confining pressure. As the relative density increases the compactness of soil skeleton increases which results in the increase of stiffness of soil skeleton, hence V_s and G_{max} is higher for greater relative density at given confining pressure.

7 Correlation of V_s and G_{max} with Void Ratio

From the above discussion, it is clear that the value of V_s and G_{max} depends on confining pressure and void ratio. It means V_s and G_{max} directly depends on void ratio, hence there must be some correlation of V_s and G_{max} with void ratio. In this study, correlation of both the V_s and G_{max} power function was preferred as it has the least constant and simple for derivation. In the present study data obtain from the performed test was used for regression analysis. As per test recorded data there are twelve sample points hence the equation valid for this range of data. The obtained power function is in the form of.

$$F(x) = Ax^{-n} \tag{5}$$

Where, x is a representative of void ratio (**e**).

A and **n** are constant.

The trend of variation of regression analysis for present study as shown in Figs. 8 and 9. The value of these constant depends on confining pressure as '*A*' and '*n*' are the representative of confining pressure. These values are independent on the value of void ratio. These equations are valid only when the value of the range of $0.45 \le e \ge 0.63$. This could be due to test data was limited to these range of soil skeleton.

The correlation equations for V_s and G_{max} and regression coefficient for different confining pressure are shown in Table 2.
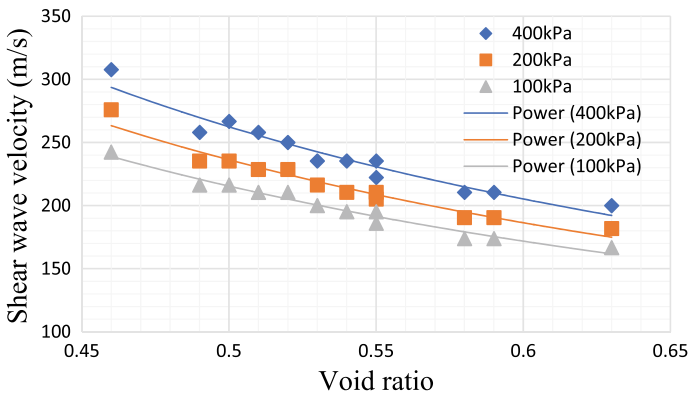
Fig. 8 Variation trend of shear wave velocity with the void ratio
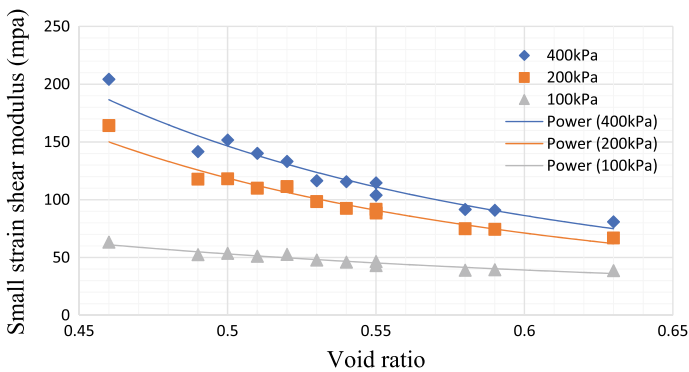
Fig. 9 Variation trend of small strain shear modulus with the void ratio

Table 2 The correlation equation and regression coefficient for different confining pressure

CP (kPa)	Correlation V_s (m/s). G_{max} (MPa)		$R^2 V_s$. G_{max}	
100	$V_s = 91.17e^{-1.24}$	$G_{max} = 15.35e^{-2.68}$	0.967	0.97
200	$V_s = 95.92e^{-1.30}$	$G_{max} = 16.98e^{-2.80}$	0.96	0.96
400	$V_s = 103.1e^{-1.34}$	$G_{max} = 17.62e^{-2.90}$	0.94	0.95
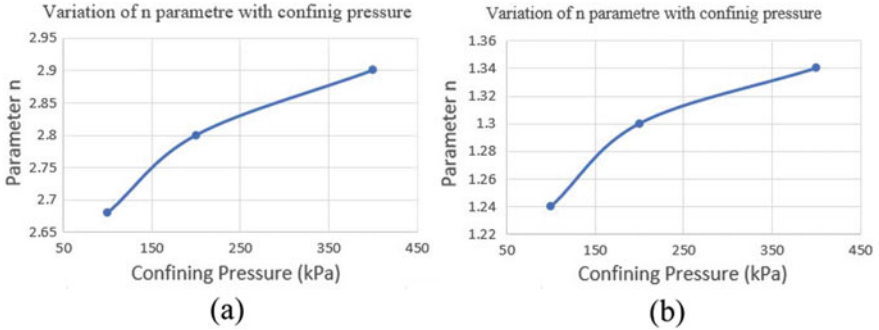
Fig.10 Variation of **a** shear wave velocity parameter 'n' **b** small strain shear modulus 'n' parameter with confining pressure

8 Effect of Confining Pressure on Parameter a and N

The estimated values of constant parameter 'n' of V_s and G_{max} are plotted against confining pressure as shown in Fig. 10a, b. This graphical variation gives an idea about the effect of confining pressure on the parameter 'n' for V_s and G_{max}. From Figs. 10a, b it is clear that the power parameter 'n' follows same trend in shear wave velocity as well as small strain shear modulus. As the confining pressure increases value of n increases at the same time regression coefficient goes on decreasing. From this relation it is clear that the value of parameter 'n' only depends on the confining pressure.

9 Validation of Results

The values of shear modulus evaluated from experimental results were compared with the values calculated by using empirical formula given by Seed and Idriss (1970).

$$G_{max} = 218.8 K_{2(max)} (\sigma_0)^{0.5} \tag{6}$$

Where, $K_{2(max)}$ is constant depends on relative density of soil which is given in Table.3 and σ_0 is confining pressure in kPa. This relation depends on the value of

Table.3 Comparison between analytical and experimental values at dry condition

Relative Density	Confining pressure (kPa)	K_{2max}	G_{max} (Analytical) (MPa)	G_{max} (Experimental) (MPa)	Percentage of variation (%)
30	100	34	74.40	62.36	16
	200	34	105.21	90.68	13.81
	400	34	148.79	133.71	10.13

relative density of soil and valid for clean sand at dry condition. The experimental, analytical values and percentage variation were calculated and shown in of Table.3. It is found that the analytical values are slightly greater than that of experimental values under dry condition.

10   Conclusion

The bender element tests were conducted to measure shear wave velocity and small strain shear modulus (G_{max})of the sand-fines mixtures. The key factors are studied, including effect of fines content, confining pressure, relative density, void ratio and saturation. A new correlation of shear wave velocity and shear modulus with void ratio for sand fines mixture is obtained.

Based on the experimental work carried out in the present study, the following conclusions are drawn.

- For sand fines mixture, the value of shear wave velocity (V_s) and small strain shear modulus (G_{max}) increases with increase in fines content up to the limiting fines content. Further addition of fines results in decrease in the value of shear wave velocity and small strain shear modulus.
- The correlation of shear wave velocity and small strain shear modulus with void ratio is established.
- The value of shear wave velocity and small strain shear modulus of the mixtures with various fines content increases with the increase of confining pressure.
- The shear wave velocity and small strain shear modulus of the sand fines mixtures decreases as the void ratio increases for the given confining pressure.

References

1. Melissa M, DeGroot DJ, Sheahan TC (2007) Nondestructive sample quality assessment of a soft clay using shear wave velocity. J Geotech Geoenviron Eng 133(4):424–432
2. Dyvik R, Madshus C (1985) Laboratory measurements of G_{max} using bender elements: advances in the art of testing soils under cyclic conditions. ASCE, New York, pp 186–196

3. Yan-Guo Z, Yun-Min C (2007) Laboratory investigation on assessing liquefaction resistance of sandy soils by shear wave velocity. J. Geotech Geoenviron Eng 133(8):959–972
4. Charles, Erin (2007) Determination of shear-wave velocities and shear moduli of completely decomposed tuff. J Geotech Geoenviron Eng 133(6):630–640
5. Dash HK, Sitharam TG (2011) Undrained monotonic response of sand–silt mixtures: effect of nonplastic fines. Geomech Geoeng Int J 6(1):47–58
6. Harikumar M, Sankar N, Chandrakaran S (2014) An alternate method of saturating sand specimens in triaxial tests. Int J Eng Res Tech (IJERT) ISSN: 2278–018
7. Antonio J, Carraro H, Monica Prezzi AM, Rodrigo, S (2009) Shear strength and stiffness of sands containing plastic or nonplastic fines. J Geotech Environ Eng ASCE 1090–0241, 135:9(1167)
8. Jaya V, Dodagoudar GR, Boominathan A (2012) Modulus reduction and damping curves for sand of south-east coast of India. J Earthquake Tsunami 6(1250016): 19
9. Yoo J-K, Park D, Baxter CDP (2018) Estimation of drained shear strength of granular soil from shear wave velocity and confining stress. J Geotech Geoenviron Eng. https://doi.org/10.1061/(ASCE)GT.1943-5606.0001876
10. Lee J-S, Carlos Santamarina J (2005) Bender elements: performance and signal interpretation. J Geotech Geoenviron Eng 131(9):1063–1070
11. Lade PV, Liggio CD, Yamamuro JA (1998) Effects of nonplastic fines on minimum and maximum void ratios of sand Geotech Test J, ASTM 21 (4):336–347
12. Zuon Lu, Baudet BA (2015) Determination of the transitional fines content of sand-nonplastic fines mixtures. Soils Found 55(1):213–219
13. Fam MA, Santamarina JC (1995) Study of geoprocesses with complementary wave measurements in an oedometer. Geotech Test J, 19(4):307–314
14. Viggiani G, Atkinson JH (1995) Stiffness of fine-grained soil at very small strains Géotechnique, 45(2) (1995), pp 249–265
15. Seed HB, Idriss IM (1990) Soil moduli and damping factors for dynamic response analyses, Report EERC 70–10, Earthq Eng Res Cent, Univer-sity of California, Berkeley

Dynamic Pore Pressure Responses of Sand–Rubber Tire Shred Mixtures from Cyclic Simple Shear and Cyclic Triaxial Tests

B. R. Madhusudhan ⓘ**, A. Boominathan** ⓘ**, and S. Banerjee** ⓘ

Abstract The cyclic simple shear tests best represent the in situ seismic stress conditions. However, cyclic triaxial tests are more popularly used. Also, the sand–rubber tire shred mixtures have recently gained research importance for their potential and possibility to act as seismic base isolation materials of buildings. The past studies could be found which deal with the dynamic properties such as the shear modulus and damping ratio of the sand–rubber tire shred mixtures. However, from the perspective of seismic isolation, it is necessary to study the pore pressure behavior of these mixtures. In view of the above, in the present study, the strain-controlled cyclic simple shear and cyclic triaxial tests are carried out on the weighed proportions of rubber tire shreds mixed with sand. The measured pore pressure responses from the both the cyclic tests are compared. It is found that the excess pore pressures generated in the cyclic triaxial testing are significantly higher than those developed during cyclic simple shear testing.

Keywords Cyclic simple shear · Cyclic triaxial · Sand–rubber mixtures · Pore pressures · Seismic isolation

B. R. Madhusudhan (✉)
Centre for Industrial Consultancy and Sponsored Research Geotechnical Engineering Division, Department of Civil Engineering, Indian Institute of Technology Madras, Chennai, TN 600036, India
e-mail: madhusudhanbr.iitm@gmail.com

A. Boominathan · S. Banerjee
Geotechnical Engineering Division, Department of Civil Engineering, Indian Institute of Technology Madras, Chennai, TN 600036, India
e-mail: boomi@iitm.ac.in

S. Banerjee
e-mail: subhadeep@iitm.ac.in
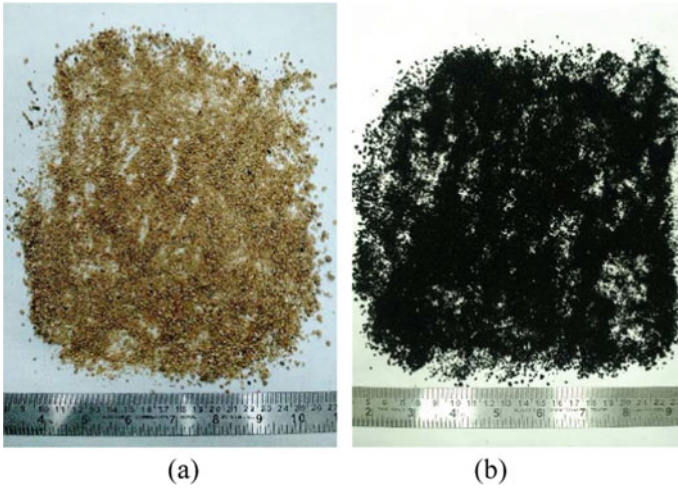
Fig. 1 Materials used for testing **a** pure sand **b** pure rubber tire shreds

1 Introduction

The recent researches show that the sand–rubber tire shred mixtures have gained research prominence due to their favorable properties for various geotechnical applications [1–9]. Among various applications, the suitability of the mixtures for the seismic base isolation of low-rise buildings is a notable one. The past studies of the authors [10–17] provide comprehensive laboratory studies enumerating various geotechnical properties which indicate the suitability of sand–rubber tire shred mixtures for seismic base isolation of low-rise buildings. However, the pore pressure responses of these mixtures were not reported and hence demand attention.

The cyclic triaxial tests are most commonly used tests to determine the dynamic response of soils. However, the cyclic simple shear tests are considered as the best representative tests to simulate in situ seismic conditions on a laboratory specimen.

The present study deals with the sand–rubber tire shred mixture specimens subjected to both cyclic triaxial and cyclic simple shear testing. This paper deals with the comparison of the pore pressure responses of the mixtures during both the types of testing.

Table 1 Material properties

Item	G_s	D_{10} (mm)	C_u	C_c	$\gamma_{d\max}$ (kN/m^3)	$\gamma_{d\min}$ (kN/m^3)
Sand	2.68	0.22	3.18	0.80	17.6	15.3
Rubber tire shreds	1.14	0.35	3.57	1.12	5.2	2.8

2 Materials and Test Methodology

2.1 Materials

Uniformly graded river sand (Fig. 1a) used for construction of buildings is selected for testing. The steel wires present in the rubber tires were completely removed and further shredded in the shredding machine to obtain rubber shreds. These rubber shreds were further sieved through sieve no. 10 to obtain particles of fine size (less than 2 mm) (Fig. 1b). The properties of sand and rubber tire shreds are summarized in Table 1.

3 Test Methodology and Program

The testing was carried out on pure sand (0%), pure rubber tire shreds (100%) and sand–rubber tire shred mixtures with 10, 30, and 50% rubber content by weight. The size of the specimen adopted was 70 mm diameter and 28 mm height for cyclic simple shear testing and 50 mm diameter and 100 mm height for cyclic triaxial testing. The specimens were prepared dry deposition and tamping method by filling the split mold. Each layer was given sufficient numbers of tamping to achieve a dense specimen. VJ Tech, UK, make cyclic simple shear apparatus and Wykeham Farrance, UK, make cyclic triaxial apparatus available at Soil Dynamics and Earthquake Engineering Laboratory, IIT Madras, was used for testing. The cyclic simple shear apparatus is shown in Fig. 2. The typical unreinforced specimens set up for cyclic simple shear testing and cyclic triaxial testing are shown in Fig. 3a, b, respectively.

The specimens prepared were saturated till Skempton's pore pressure coefficient (B-Value) greater than 0.95 was achieved. Then, consolidation was done under an effective confining pressure of 100 kPa. The strain-controlled cyclic triaxial and cyclic simple shear tests were carried out on the prepared specimens at 0.1, 1.0 and 5.0 Hz frequencies at a confining pressure of 100 kPa. The specimens were subjected to 50 numbers of loading cycles. It is to be noted that in cyclic triaxial tests, the cyclic loading is applied in the vertical direction whereas it is horizontal cyclic shearing in cyclic simple shear tests.
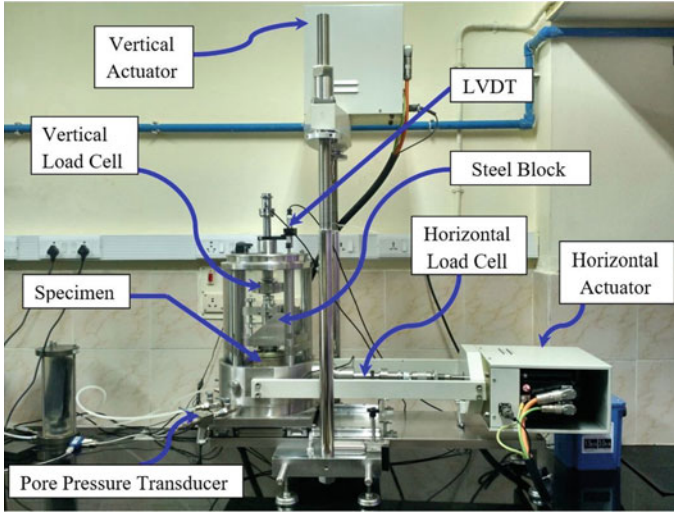
Fig. 2 Cyclic simple shear apparatus
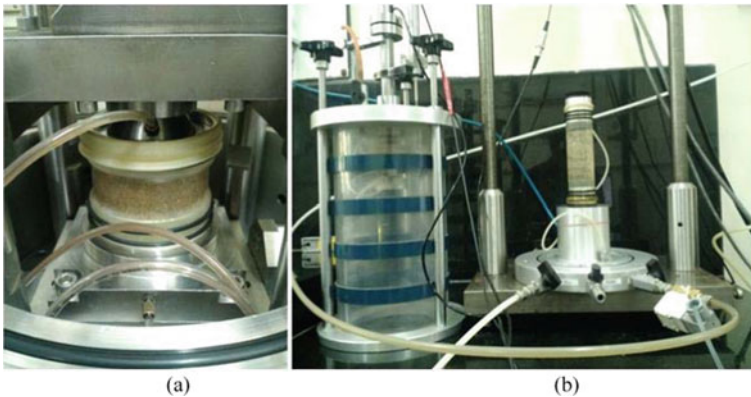
Fig. 3 Typical specimen setup for **a** cyclic simple shear test **b** cyclic triaxial test

4 Results and Discussion

In the present study, the pore pressure response is analyzed in terms of the pore pressure ratio (r_u). In the case of cyclic simple shear tests, the pore pressure ratio is obtained from the measured excess pore water pressure normalized by the initial total vertical stress, whereas in the case of cyclic triaxial tests, the pore pressure ratio is obtained by normalizing the measured excess pore water pressure with the initial effective confining stress. The pore pressure ratio as a function of the number of loading cycles obtained from cyclic simple shear tests (CSS) and cyclic triaxial

(CTX) tests carried out on sand–rubber tire shred mixtures at a frequency of 0.1 Hz at a confining stress of 100 kPa are plotted in Fig. 4.

From Fig. 4, it can be observed that at 0.1 Hz frequency level, the cyclic triaxial shear tests on sand–rubber tire shred mixtures result in positive excess pore pressures. With increase in the rubber content, although reduction is observed in the developed excess pore pressures, they remain positive throughout. On the contrary, the negative excess pore pressures develop during cyclic simple shear tests irrespective of the rubber content although some positive excess pore pressures develop initially for lower rubber contents.
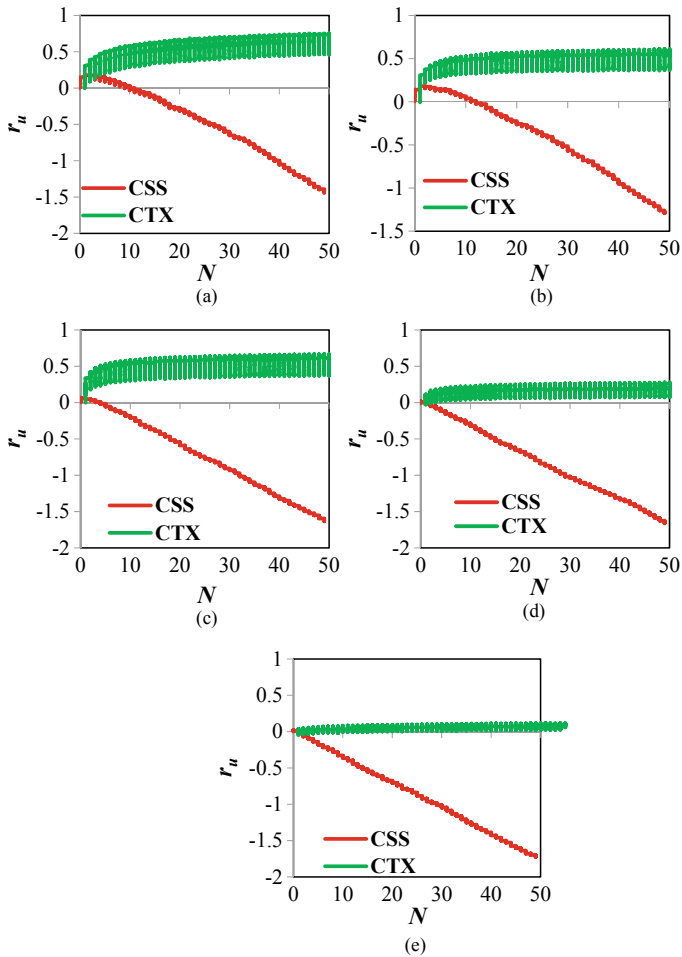
Fig. 4 Variation of pore pressure ratio of the mixtures with the number of loading cycles from CSS and CTX tests (0.1 Hz frequency, 100 kPa confining stress) for rubber contents **a** 0% **b** 10% **c** 30% **d** 50% **e** 100%
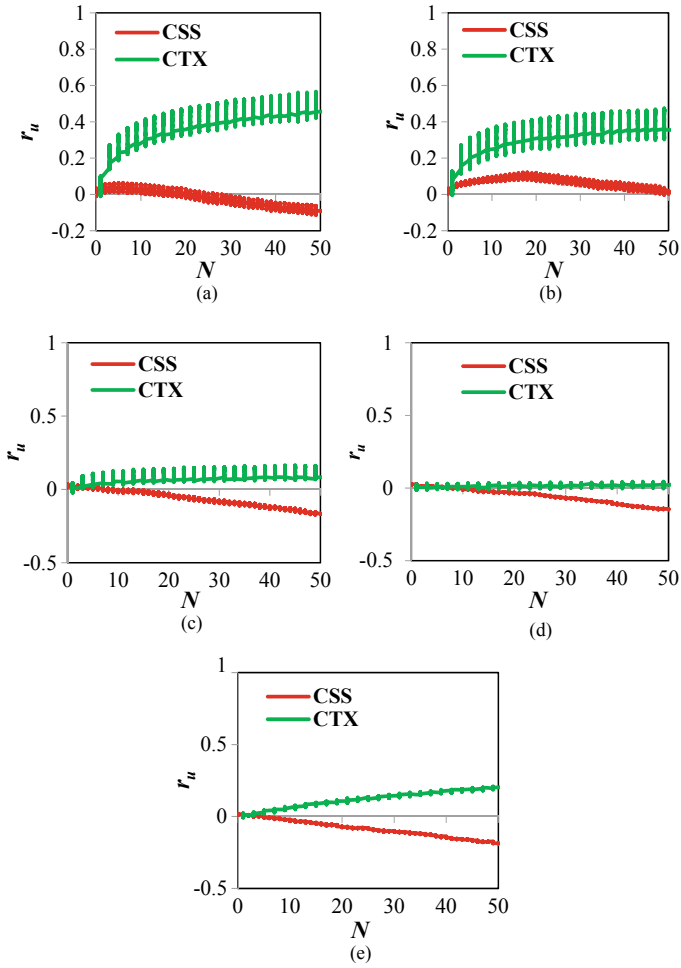
Fig. 5 Variation of pore pressure ratio of the mixtures with the number of loading cycles from CSS and CTX tests (1 Hz frequency, 0.15% shear strain, 100 kPa confining stress) for rubber contents **a** 0% **b** 10% **c** 30% **d** 50% **e** 100%

The pore pressure ratio as a function of the number of loading cycles obtained from cyclic simple shear tests and cyclic triaxial tests carried out on sand–rubber tire shred mixtures at a frequency of 1 Hz at a confining stress of 100 kPa and at various shear strain levels are plotted in Figs. 5, 6, 7 and 8. From the figures, it can be observed that the cyclic triaxial tests on sand–rubber tire shred mixtures (which had resulted in positive excess pore pressures at 0.1 Hz frequency) also exhibit positive excess pore pressures at 1 Hz frequency level but at low shear strain levels. However, this gradually changes, and the excess pore pressures become negative with increase in shear strain at 1 Hz frequency.
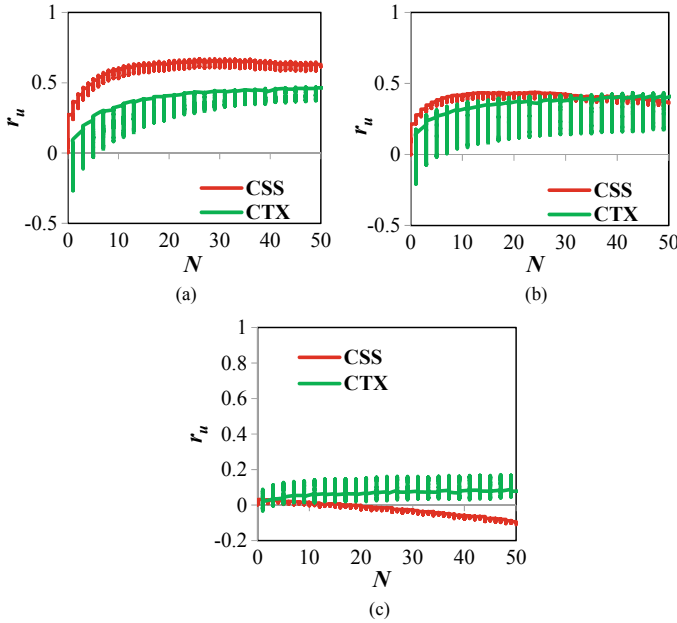
Fig. 6 Variation of pore pressure ratio of the mixtures with the number of loading cycles from CSS and CTX tests (1 Hz frequency, 0.75% shear strain and 100 kPa confining stress) for rubber contents **a** 0% **b** 10% **c** 50%

In the case of cyclic simple shear tests on sand–rubber tire shred mixtures (the negative excess pore pressures had been observed at 0.1 Hz frequency), the developed excess pore pressure becomes less negative and similarly is also observed to become slightly positive particularly for lower rubber contents.

The variation of pore pressure ratio as a function of the number of loading cycles obtained from cyclic simple shear tests and cyclic triaxial tests carried out on sand–rubber tire shred mixtures at a frequency of 5 Hz at a confining stress of 100 kPa are plotted in Fig. 9. From Fig. 9, it can be observed that at 0.1 Hz frequency level, the cyclic triaxial tests on sand–rubber tire shred mixtures result in negative excess pore pressures.

On the contrary, the positive excess pore pressures develop during cyclic simple shear tests irrespective of the rubber content although reduction of the positive excess pore pressures is observed with the increase in the rubber content. The observed excess pore pressure responses of sand–rubber tire shred mixtures from both cyclic simple shear and cyclic triaxial tests at 5 Hz frequency are opposite to the observed excess pore pressure response at 0.1 Hz frequency level.

The differences in the pore pressure responses observed during the cyclic simple shear tests and the cyclic triaxial tests could be attributed to the differences in nature of loading. In the case of cyclic triaxial tests, the cyclic loading is in the vertical direction, whereas the direction of cyclic loading is horizontal during cyclic simple
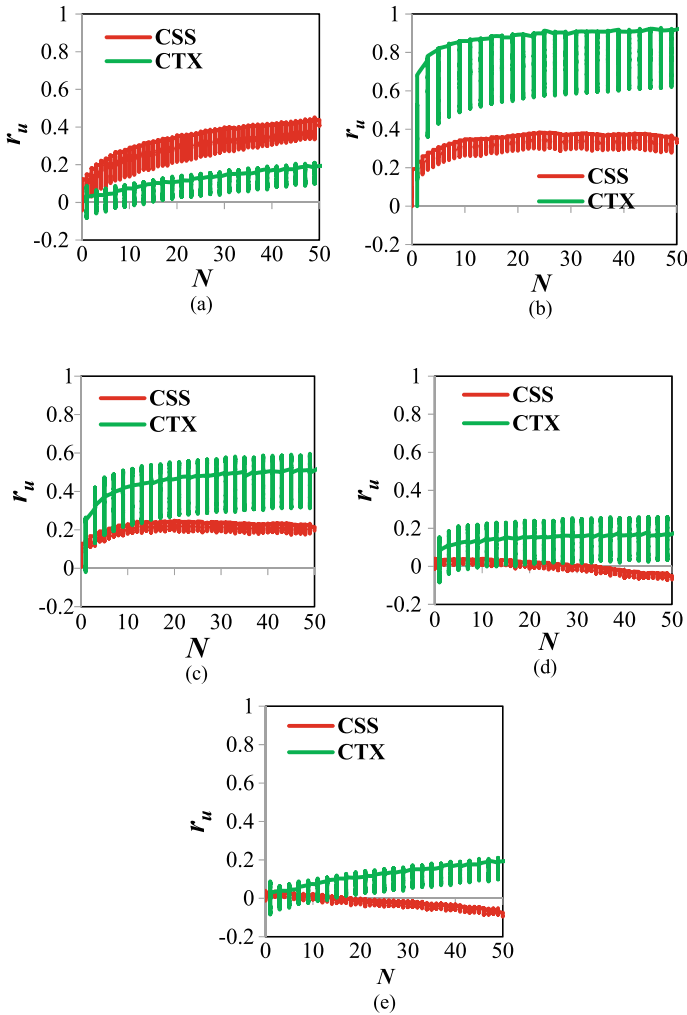
Fig. 7 Variation of pore pressure ratio of the mixtures with the number of loading cycles from CSS and CTX tests (1 Hz frequency, 1.5% shear strain and 100 kPa confining stress) for rubber contents **a** 0% **b** 10% **c** 30% **d** 50% **e** 100%

shear tests. Significant differences in the dynamic shear modulus from both the types of cyclic tests were also found in the past study [14]. The reason was reported to be the difference in the sizes of the specimen used despite the testing conditions remaining the same. Although the shape of the specimen is cylindrical in both the cyclic tests, the oblong nature of the cyclic triaxial specimen supplemented with the direction of loading results in differences in modulus determined.

In the present study, since the measured pore pressures obtained are different in both the types of cyclic tests, similar afore-mentioned reasons could be postulated.
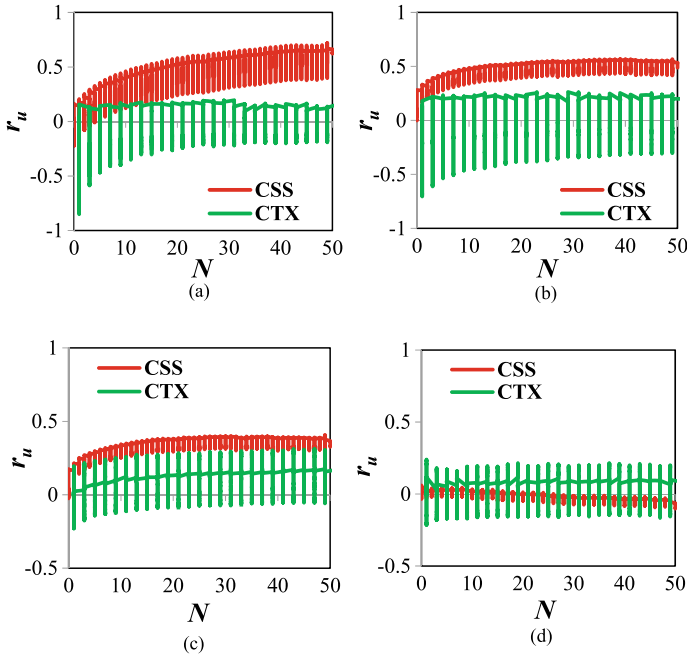
Fig. 8 Variation of pore pressure ratio of the mixtures with the number of loading cycles from CSS and CTX tests (1 Hz frequency, 3% shear strain and 100 kPa confining stress) for rubber contents **a** 0% **b** 10% **c** 30% **d** 100%

However, further studies are necessary in this direction on different types of soils under different conditions to explore and reason the observed behavior.

5 Conclusions

In the present study, the strain-controlled cyclic simple shear tests and cyclic triaxial tests are carried out on gravimetric mixtures of sand and rubber tire shreds. The pore pressure responses of the mixtures are measured and analyzed in terms of the pore pressure ratio. The following are the conclusions drawn from the present study.

The frequency of cyclic loading has a significant influence on the developed excess pore pressures. At lower frequency levels (0.1 Hz), the positive pore pressures are observed from cyclic triaxial tests, whereas negative pore pressures develop when the mixtures are subjected to cyclic simple shear loading. This gradually changes with increase in frequency level. This observation flips at the higher frequency loading (5 Hz) where the negative pore pressures are recorded during cyclic triaxial tests whereas positive pore pressures are observed during cyclic simple shear tests.
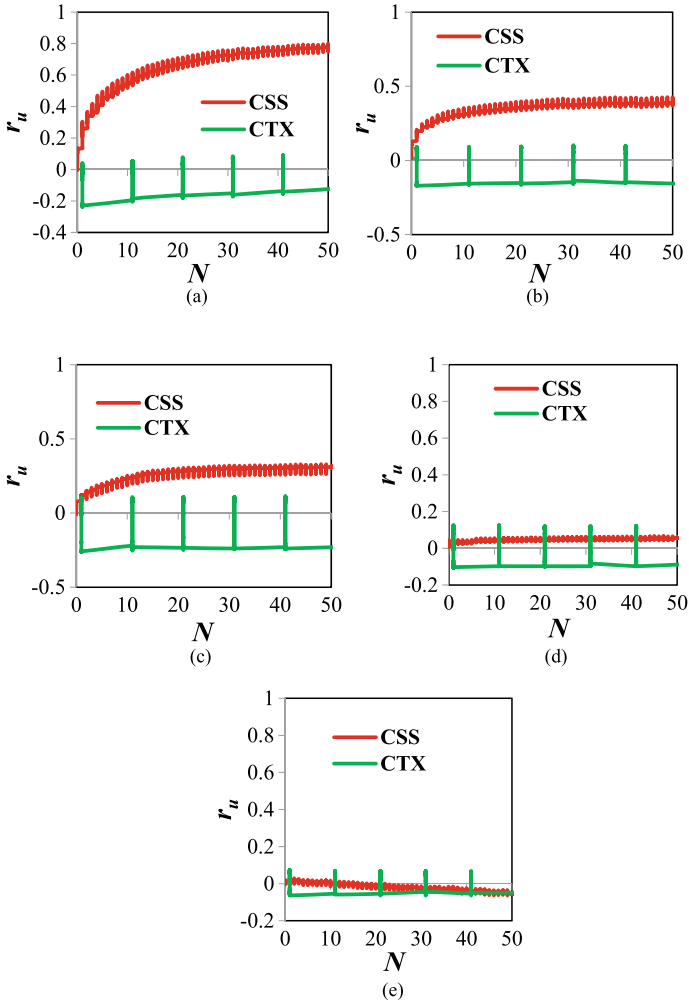
Fig. 9 Variation of pore pressure ratio of the mixtures with the number of loading cycles from CSS and CTX tests (5 Hz frequency, 100 kPa confining stress) for rubber contents **a** 0% **b** 10% **c** 30% **d** 50% **e** 100%

Lower shear strain levels during cyclic loading result in lower values of pore pressures and vice versa.

The effect of rubber content is to reduce the developed pore pressures during cyclic loading. Hence, this characteristic of the sand–rubber tire shred mixtures is favorable for their application as seismic base isolation of buildings.

The differences in the pore pressure responses observed during the cyclic simple shear tests and the cyclic triaxial tests could be attributed to the difference in the loading direction and also to the specimen sizes. Further studies on other types of

soils are necessary to determine the reasons for the differences observed in the present study.

References

1. Humphrey DN, Sandford TC, Cribbs MM, Manion WP (1993) Shear strength and compressibility of tire chips for use as retaining wall backfill. In Transportation research Record 1422, National Research Council, Transportation Research Board, Washington, D.C., pp 29–35
2. Ahmed I, Lovell CW (1993) Rubber soils as light weight geomaterials. In Transportation research rec. no. 1422, Transportation Research Board, Washington, D.C.
3. Edil TB, Bosscher PJ (1994) Engineering properties of tire chips and soil mixtures. Geotech Test J 17(4):453–464
4. Poh PSH, Broms BB (1995) Slope stabilization using old rubber tires and geotextiles. J Perform Construc Fac 9(1):76–80
5. Foose GJ, Benson CH, Bosscher PJ (1996) Sand reinforced with shredded waste tires. J Geotech Geoenviron Eng 122(9):760–767
6. Bosscher PJ, Edil TB, Kuraoka S (1997) Design of highway embankments using tire chips. J Geotech Geoenviron Eng. https://doi.org/10.1061/(ASCE)1090-0241(1997)123:4(295),295-304
7. Tweedie JJ, Humphrey DN, Sandford TC (1998) Tire shreds as lightweight retaining wall backfill: active conditions. J Geotech Geoenviron Eng 124(11):1061–1070
8. Lee JH, Salgado R, Bernall A, Lovell CW (1999) Shredded tires and rubber-sand as lightweight backfill. J Geotech Geoenviron Eng. https://doi.org/10.1061/(ASCE)1090-0241(1999)125:2(132),132-141
9. Rowe RK, McIsaac R (2005) Clogging of tire shreds and gravel permeated with landfill leachate. J Geotech Geoenviron Eng 131(6):682–693
10. Madhusudhan BR, Boominathan A, Banerjee S (2017) Static and large-strain dynamic properties of sand-rubber tire shred mixtures. J Mater Civil Eng. https://doi.org/10.1061/(ASCE)MT.1943-5533.0002016
11. Madhusudhan BR, Boominathan A, Banerjee S (2018) Comparison of cyclic triaxial test results on sand-rubber tire shred mixtures with dynamic simple shear test results. ASCE GSP 293. https://doi.org/10.1061/9780784481486.014
12. Madhusudhan BR, Boominathan A, Banerjee S (2019a) Factors affecting strength and stiffness of dry sand-rubber tire shred mixtures. Geotech Geol Eng 37(4):2763–2780. https://doi.org/10.1007/s10706-018-00792-y
13. Madhusudhan BR, Boominathan A, Banerjee S (2019b) Engineering properties of sand-rubber tire shred mixtures. Int J Geotech Eng https://doi.org/10.1080/19386362.2019.1617479
14. Madhusudhan BR, Boominathan A, Banerjee S (2020) Effect of specimen size on the dynamic properties of river sand and rubber tire shreds from cyclic triaxial and cyclic simple shear tests. In Geotechnical characterization and modelling, lecture notes in Civil Engineering, Springer Nature. vol 85., https://doi.org/10.1007/978-981-15-6086-6_37
15. Madhusudhan BR, Boominathan A, Banerjee S (2020) Cyclic simple shear response of sand–rubber tire chip mixtures. Int J Geomech, 20(9), https://doi.org/10.1061/(ASCE)GM.1943-5622.0001761
16. Madhusudhan BR, Boominathan A, Banerjee S (2019) Properties of Sand–Rubber Tyre Shreds Mixtures for Seismic Isolation Applications. In Soil Dynamics and Earthquake Geotechnical Engineering. Lecture Notes in Civil Engineering, vol 15. Springer, Singapore. https://doi.org/10.1007/978-981-13-0562-7_29
17. Madhusudhan BR, Boominathan A, Banerjee S (2019) 1g model tests on buildings founded on sand-rubber tire shreds mixture. In Earthquake Geotechnical Engineering for Protection and Development of Environment and Constructions. Proceedings of the 7th International

Calibration Exercise of Fixed-Free Resonant Column Apparatus

Ninad Sanjeev Shinde and **Jyant Kumar**

Abstract In this paper, the conventional calibration exercise for resonant column apparatus has been re-examined and some recommendations were provided to improve the accuracy of the test results. During the testing, specimen is assumed to be fixed at bottom and dynamic torsional vibrations are applied at the top using drive system consisting of four magnets. Due to complicated geometry of the drive system, its mass polar moment of inertia (J_d) is found to be difficult to estimate. So, calibration exercise is performed to determine J_d. In this present study, calibration rods of aluminum of known stiffness were used. The diameter of each aluminum rod was varied from 8 to 15 mm and keeping the constant height of 100 mm. The study revealed that the mass polar moment of inertia of the resonant column system is frequency dependent. Also, the solid cylindrical sand specimens were tested using resonant column tests and bender elements tests with varying confining pressure and relative density.

Keywords Resonant column · Dynamic properties · Shear modulus

1 Introduction

It appears that first resonant column tests were introduced to the rock testing during 1930 by Japanese engineers and later around early 1970 it became widely popular to the dynamic testing of the soils [1–5]. The resonant column tests are primarily used to calculate small strain dynamic properties of soils such as modulus and damping. Conventionally, the resonant column tests were conducted on the solid cylindrical and hollow cylindrical specimens of length to diameter ratio of ≈2. Typically, the resonant column apparatus is used in the fixed-free configuration. In which the specimen is subjected to torsional vibrations in the fixed free configuration, where base of the specimen is assumed to be fixed and top is subjected to torsional vibrations. Considering these boundary conditions and using the one-dimensional theory of

N. S. Shinde (✉) · J. Kumar
Civil Engineering Department, Indian Institute of Science, Bangalore, India
e-mail: shindes@iisc.ac.in

wave propagation, the shear wave velocity can be computed by following expression [6],

$$\frac{J_s}{J_d + J_0} = \frac{\omega_n L}{V_s} \tan \frac{\omega_n L}{V_s}$$ (1)

where (i) L is the height of the specimen, (ii) J_0 and J_s refer to the mass polar moment of inertia of the top cap and cylindrical specimen about its longitudinal axis, respectively, (iii) J_d is the mass polar moment of inertia of the drive mechanism, and (iv) ω_n indicates the circular frequency at resonance corresponding to the fundamental mode. Accordingly, by relating V_s and the mass density (ρ) of soil specimen, the shear modulus (G) is determined by using the following expression:

$$G = \rho V_s^2$$ (2)

A calibration exercise has to be conducted as per ASTM D4015 [7] using metal calibration bars of known stiffness to determine the magnitude of J_d. It is assumed that during the loading, only the specimen vibrates, and all other parts of the apparatus are presumed to be rigid and rigidly connected. But in practice, while testing very stiff specimen, the apparatus is found to be vibrating along with the specimen. This causes the J_d to shoot up abruptly and consequently, lowering the V_s substantially up to 32.2%, which is found to be inaccurate by testing the metal specimen of known stiffness [8, 9]. Hardin et al. [10] reported that at very high $f_n > 170$ Hz, the coupling between specimen and end platens no longer remains rigid, thus the magnitudes of both G and damping ratios (D) were found to be erroneous. Drnevich [3] advised to find out upper limit of the resonant column apparatus prior to the testing, to avoid inaccurate output.

Thus, accurate estimation of J_d is vital for determining stiffness of the given specimen. This paper gives crucial insights into the conventional calibration exercise for resonant column apparatus and provides some necessary recommendations to improve the accuracy of results using the resonant column apparatus.

2   Basic Features of Resonant Column Apparatus

The resonant column apparatus used in the present study is supplied by GDS Instruments, Hampshire, UK. A schematic illustration of resonant column system is presented in the Fig. 1 consisting of different parts of the system. The specimen is assumed to be fixed at bottom and subjected to torsional vibrations at the top of the specimen using the drive mechanism. The drive mechanism consists of four magnets and a pair of coils surrounding each magnet. The torsional vibrations of varying magnitude are applied by changing the input voltage. The current flowing to the coils generates an electromagnetic force in each coil in the same direction, so that
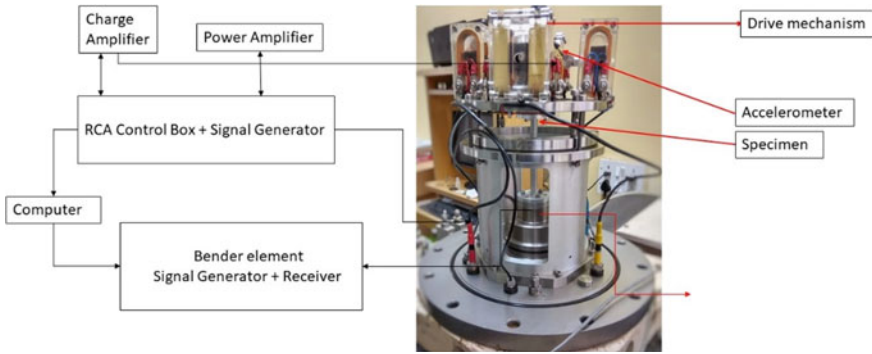
Fig. 1 A schematic of resonant column apparatus and its components

torque is applied at the top of the specimen. A bandwidth of frequency is selected corresponding to each input voltage and the amplitude of the vibrations is recorded for each frequency. A frequency, for which amplitude recorded to be maximum, is termed as the resonant frequency. An accelerometer is attached at the top of the specimen to measure the vibrations. The strain magnitude, recorded using piezoelectric transducer, corresponding to the peak amplitude is calculated using the expression given by Kumar and Shinde [11] having same boundary conditions and transducer gain value. The strain range obtained in the present study is in the range of 0.0001% to 0.01%. The triaxial cell has a capacity of 1 MPa.

3 Calibration Exercise and Validation

In Eq. (1), the estimation of magnitude of the J_s and J_0 is straightforward due to their simple geometry. On the other hand, the magnitude of J_d is difficult to estimate because of its complex geometry. ASTM-D4015 [7] have suggested to conduct calibration exercise using metal specimen of known stiffness. So, in order to estimate J_d, the calibration exercise was conducted using metal specimen of aluminum and mild steel. The height of each specimen was kept constant at 100 mm and the diameters of aluminum specimen were 8, 10, 12, and 15 mm, whereas the diameters of the mild steel specimen were 8, 10, and 12 mm. Four additional circular weights of 125 g were placed at the top of the specimen, to obtain range of resonant frequency for the same stiffness of the metal specimen. Figure 2 shows the calibration bars and additional circular weights.

At first, resonant frequency was obtained for the given input voltage and corresponding peak amplitude is recorded. For aluminum specimens, the resonant frequencies were found to be varying from 26.2 to 89.8 Hz. For mild steel specimens, the resonant frequencies were found to be varying from 44.2 to 101.5 Hz. The circular resonant frequency (ω_n) can be related to torsional stiffness (K_T) and J_s by using the
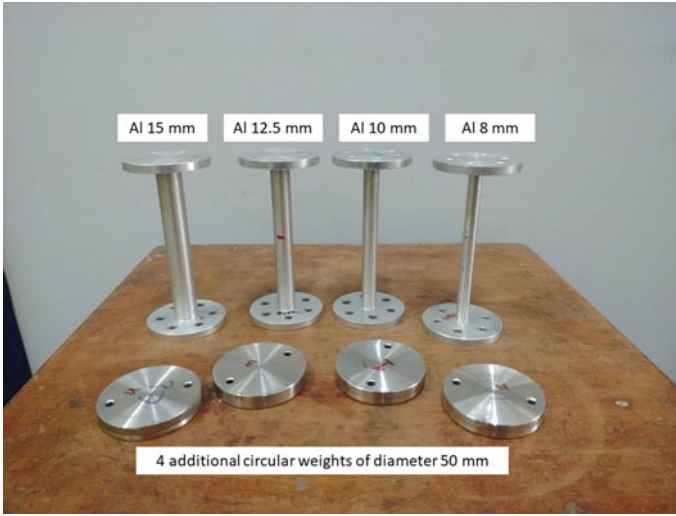
Fig. 2 Calibration bars of aluminum of varying diameters and four additional circular weights

following equation [12]:

$$\omega_n = \sqrt{\frac{K_T}{J_0 + J_d + \frac{J_s}{3}}} \tag{3}$$

It can be noted from the above expression that the resonant frequency is found to be increasing with the increase in diameter of the bar. By plotting $J_{as} = J_s/3 + J_0$ against $1/\omega_n^2$, the negative intercept on the J_{as} axis provides the value of J_d for each bar. Figure 3 indicates the variation of J_{as} against $1/\omega_n^2$.

Generally, the average of J_d for all the bar is used in the calculations for V_s as per Eq. (1). For same stiffness of the bars and same drive system the J_d has to be the same as per theory. Figure 4 shows the plot between J_d against resonant frequency (f_n), which clearly indicates that the magnitudes of J_d for different diameter of the calibration bars is increasing with the increase in the diameter of the bar (i.e., increase in the resonant frequency).

From Fig. 4, it was found that J_d is frequency dependent, this may be because of imperfect fixity of the base of the specimen. So, to calculate J_d corresponding to the different resonant frequencies, the third-order polynomial equation best fitted for the present calibration bar data is given below

$$J_d = 1 \times 10^{-9} f_n^3 + 2 \times 10^{-7} f_n^2 + 6 \times 10^{-6} f_n + 0.0036 \tag{4}$$

where f_n is the resonant frequency in Hz.

A set of resonant column experiments on the soil specimen were conducted to examine the proposed formulae and its effects on the values of corresponding shear

Fig. 3 Variation of J_{as} against $1/\omega_n^2$ for aluminum specimen of varying diameter

(a)
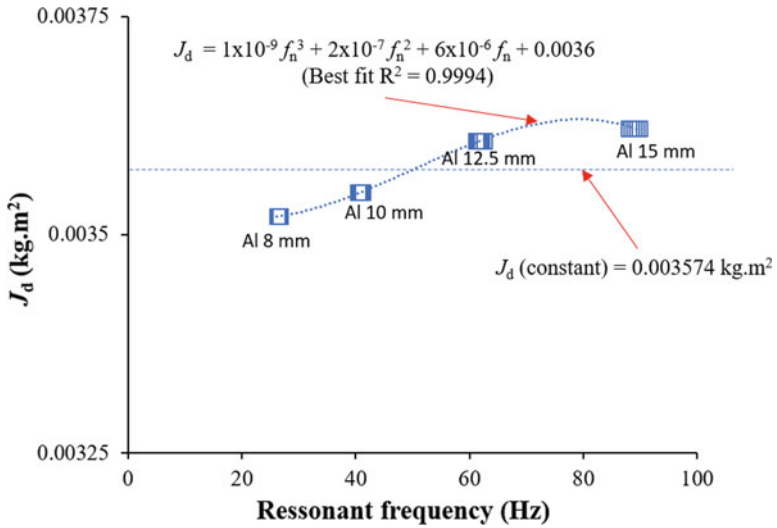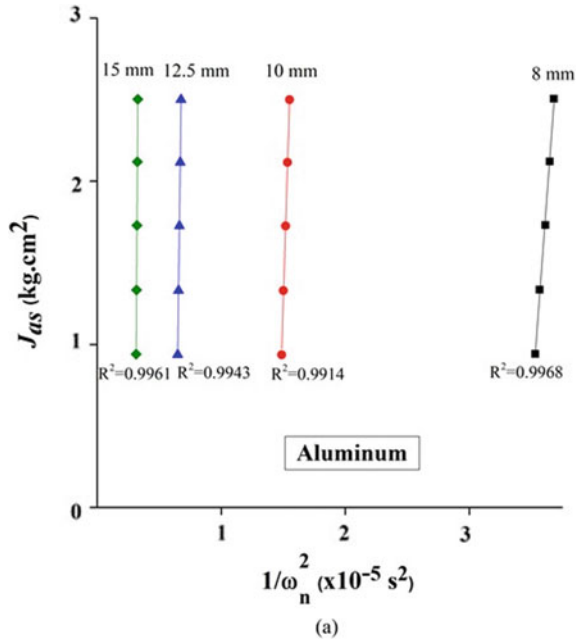
Fig. 4 Variation of J_d with resonant frequency

modulus. Calibration bars covered wide range of frequencies as mentioned above. Cauvery sand was used in the present study. The testing program and material specifications for this sand are presented in Table 1.

The solid cylindrical specimens of sand were prepared by using dry-pluviation technique. The specimen dimensions were 50 mm diameter and 100 mm height. The specimens were subjected to isotropic confining pressures of 100, 300, 500, and 700 kPa. The relative density of the specimen used in the present study was 80%. The resonant frequencies obtained from the torsion tests were used to determine shear modulus using Eq. (2) and the corresponding shear strain levels were also determined. The average value of the J_d is used for the calculations. In the present study, the average value of J_d was found to be 0.003574 kg-m^2 [7]. The variation of the shear modulus against the shear strain is plotted in Fig. 5.

Table 1 Material properties and testing program for sand

Basic properties sand	Testing program	
	Relative density(%)	Confining pressure(kPa)
Specific gravity (G_s) = 2.67	79.5–81.2%	100, 300, 500, 700
Degree of roundness = Angular		
Coefficient of uniformity (C_u) = 3.16		
Coefficient of curvature (C_c) = 0.66		
ρ_{dmax}(kg/m^3) = 1358.9 kg/m^3		
ρ_{dmin}(kg/m^3) = 1698.7 kg/m^3		
D_{10} = 0.21		
D_{30} = 0.31		
D_{60} = 0.68		
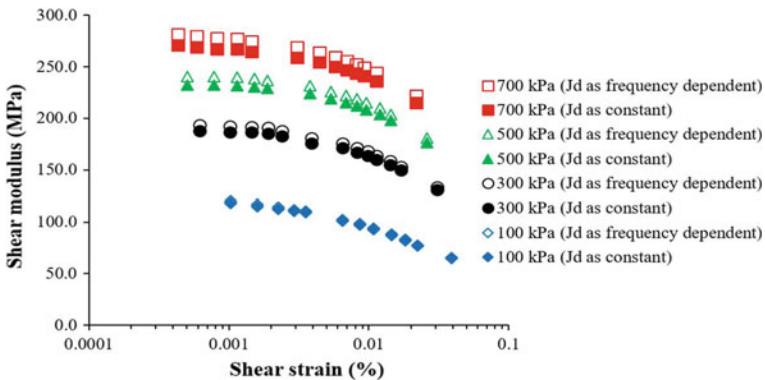
Fig. 5 Variation of shear modulus vs shear strain for J_d as a constant and J_d as a frequency dependent

Fig. 6 Comparison of shear modulus calculated from resonant column and bender elements
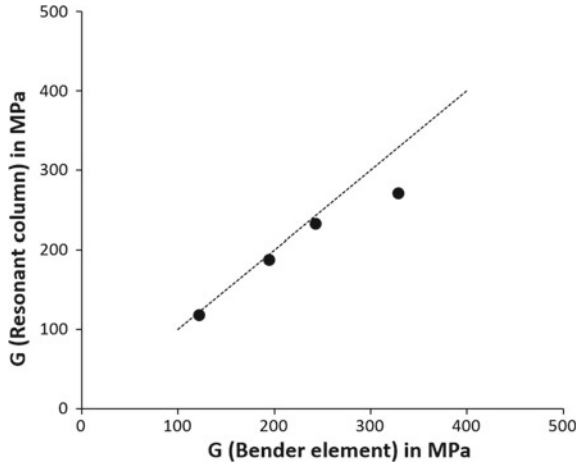
It can be noted that as the confining pressure increases the specimen stiffness increases and the consequence, the resonant frequency, and corresponding shear modulus were found to be increased. As the resonant frequencies increased beyond 85 Hz, the apparatus limitations such as base fixity and basic assumption of only specimen is vibrating, were observed to be violated in the study carried out by Kumar and Shinde [11]. Because of this, the authors have reported that the shear wave velocity is found to be decreasing as stiffer specimen is used. Similar observations were made in the study conducted by Kumar and Clayton [8]. Using Eq. (4), shear modulus is calculated considering J_d as frequency dependent. It can be seen from Fig. 5 that the shear modulus values are found to be on higher side and this effect is more as the confining pressure increases (i.e., for stiff specimen).

Bender element tests were also conducted on the same specimen. As the strain levels in bender element tests are found to be on lower side as compared to resonant column tests, the shear modulus from bender elements is usually on the higher side. The values of shear modulus obtained by considering J_d as frequency dependent and the shear modulus calculated using bender element tests were compared in Fig. 6. The values were found to be consistent with the bender element tests and validate the reliability of calibration exercise.

4 Conclusion

It is recommended that calibrations exercise should be performed if the apparatus is used for long time. For testing specimen of higher stiffness or specimens of resonant frequencies greater than 85 Hz, it is recommended that apparatus limits should be established. It can be noted that accurate estimation of mass polar moment of inertia (J_d) is crucial in determining shear modulus of the specimen. The J_d is found to be

frequency dependent. Hence, it is recommended that the J_d should be first determined over the range of frequencies for which soil or rock specimen to be tested. Then using the best fit curve, the J_d should be estimated for each resonant frequency and should be used to determine shear modulus of given specimen. The shear modulus values calculated from this exercise are found to be on higher side for stiffer specimens.

References

1. Drnevich VP, Hardin BO, Shippy DJ (1978) Modulus and damping of soils by the resonant-column method. Dynamic Geotechnical Testing, ASTM STP654. In Silver ML, Tiedemann D, eds ASTM International, West Conshohocken, PA, pp 91–125
2. Chung RM, Yokel FY, Drnevich VP (1984) Evaluation of dynamic properties of sands by resonant column testing. Geotech Test J 7(2):60–69
3. Drnevich VP (1978) Resonant column testing problems and solutions. Dynamic Geotechnical Testing, ASTM STP654. In Silver, MS, Tiedemann D (eds) ASTM International West Conshohocken, PA, pp 384–398
4. Sasanakul I, Bay J (2010) Calibration of equipment damping in a resonant column and torsional shear testing device. Geotech Test J 33(5):363–374
5. Li H, He H, Senetakis K (2018) Calibration exercise of a hardin-type resonant column. Géotechnique 68(2):171–176
6. Richart FE Jr, Hall JR Jr, Woods RD (1970) Vibrations of soils and foundations. Prentice Hall, Upper Saddle River, NJ
7. ASTM D4015–15 (2015) Standard test methods for modulus and damping of soils by resonant-column method. In ASTM International, West Conshohocken, PA. https://doi.org/10.1520/D4015-15E01
8. Kumar J, Clayton CRI (2007) Effect of specimen torsional stiffness on resonant column test results. Can Geotech J 44(2):221–230
9. Clayton CRI, Priest JA, Bui M, Zervos A, Kim SG (2009) The Stokoe resonant column apparatus: effects of stiffness, mass and specimen fixity. Géotechnique. 59(5):429–437
10. Hardin K, Drnevich VP, Wang J, Sams CE (1994) Resonant column testing at pressures up to 3.5 MPa (500 psi). In Ebelhar R, Drnevich V, Kutter B (eds) Dynamic geotechnical testing II, West Conshohocken, PA, ASTM International, pp 222–233
11. Kumar J, Shinde NS (2019) Shear moduli of metal specimens using resonant column tests. J Test Eval 48(6)
12. Timoshenko S (1937) Vibration problems in engineering, 2nd edn. D. Van Nostrand Company, New York

Investigation of Dynamic Response of Rubber Tire Chips for Geotechnical Applications

Adyasha Swayamsiddha Amanta and **Satyanarayana Murty Dasaka**

Abstract With increasing vehicular traffic on the roads, the production of rubber is steeply increased over the years. Consequently, more and more scrapped rubber tires are discarded every year, and most of them are ended up in municipal landfills. As a remedy to this, researchers are trying to use these wastes in better ways, such as filling material in earthen embankments, rather than letting them get dumped in landfills. This study aims to investigate the effect of dynamic loads on the performance of rubber tire chips, a scrap tire derivative, in its saturated state. For the study, a series of strain-controlled cyclic triaxial tests were performed. The parameters like cyclic strain amplitude (0.075, 0.1125, 0.15, 0.1875, 0.225, 0.2625, and 0.3%) and confining pressure (50, 75, and 100 kPa) were selected as variables. The rubber tire chips with average dimension of 12 mm x 20 mm were considered for the study. The dynamic properties obtained are compared with that of the Indian standard sand. The number of loading cycles for initiation of liquefaction is used to compare the liquefaction potential of the rubber tire chips with that of the standard sand. The cyclic tests showed that the tire chips do not liquefy for large number of loading cycles. The tire chips showed very high damping ratios in comparison with sand but are considerably low in their shear modulus.

Keywords Tire chips · Cyclic triaxial apparatus · Dynamic response

1 Introduction

The liquefaction phenomenon is known long back, but it drew attention after the devastating 1964 Alaska and Niigata earthquakes [20]. After 1964, many studies had been reported to counteract liquefaction. The methods, like densification, solidification, deep mixing, desaturation, drainage, chemical grouting, etc., are proposed to counteract liquefaction. Liquefaction is a phenomenon generally seen in the loose saturated granular soils. This is a state where the soil loses all its shear strength and

A. S. Amanta (✉) · S. M. Dasaka
Indian Institute of Technology Bombay, Mumbai 400076, India
e-mail: adyasha@iitb.ac.in

starts behaving like a viscous liquid. Due to the loss of strength, the liquefied soil can no longer support any structure standing on it. The effect of liquefaction is very fatal in the constructed facilities. Liquefaction was reported to claim many lives and properties in the past. Damages due to this can be reduced by increasing the shear strength and stiffness of the soil. In element tests under undrained conditions, when the excess pore water pressure generated becomes almost equal to the initial effective stress, a soil is said to be liquefied. Generally, in cyclic triaxial test, the liquefaction potential of any material is measured in terms of number of loading cycles to reach initial liquefaction, i.e., the loading cycle at which the excess pore pressure ratio value becomes unity.

With the increasing loads on the roads in the form of heavy traffic, the loads on landfills are also increasing in the form of scrap tires. They are vulnerable to fire in the landfills. In a day-to-day life, a huge number of scrap tires are discarded in the landfills daily, hence, many researchers are trying to give a better destiny to these tires rather than dumping them in the landfills. ASTM D6270 (2008) specifies three different categories of the scrap tire types used for the application of civil engineering works. They are tire crumbs (length less than 10 mm), tire chips (length in between 10 and 50 mm), and tire shreds (the length is greater than 50 mm). Use of scrap tire derivatives has been reported for different civil engineering applications, such as, in highway embankments [6], lightweight backfill materials [2, 7, 12, 14, 16, 18], soil reinforcement [1, 9, 11], drainage material [8, 15], for ground improvement [13], vibration reduction [10, 11, 17, 19], to name a few.

This paper focuses on the dynamic response of scrap tire chips. The study of the dynamic behavior was carried out using cyclic triaxial apparatus, and it is compared to that of the Indian standard sand (Grade II).

2 Materials, Experimental Program, and Methodology

2.1 Material Used

Scrap tire chips used in this study are cut from the scrap tires. The tire chips used are 20 mm long with 12×12 mm cross section in average. Figure 1 shows the scrap tire chips used. The tire chips have a specific gravity of 1.136, which fits fine with the average value of 1.01–1.27 specified in ASTM D6270 [5]. The maximum and minimum dry unit weights of the tire chips were found to be 5.32kN/m^3 and 5.17kN/m^3, respectively.

As discussed in the previous section, Indian standard sand, Grade II, was used in the study. It is poorly graded sand, with a mean diameter of 0.57 mm and specific gravity of 2.62. The maximum and minimum dry unit weights of the sand are 17.04 and 14.18 kN/m^3, respectively.

Fig. 1 Tire chips used in the study

2.2 Experimental Program and Methodology

A computer-controlled cyclic triaxial apparatus was used to perform the undrained cyclic triaxial tests on fully saturated scrap tire chips and sand samples. The program consisted of a number of strain-controlled undrained tests considering confining pressure and strain amplitudes as variables. The tests were carried out at three different confining pressures of 50, 75, and 100 kPa. The strain amplitudes considered in the study were 0.075, 0.1125, 0.15, 0.1875, 0.225, 0.2625, and 0.3%. The desired strain amplitudes were applied in the form of sinusoidal waves at a frequency of 1 Hz on both saturated tire chips and sands samples, individually.

For the study, sample of 100 mm diameter and 200 mm height was tested. Both the sand and the tire chips samples were prepared with a relative density of 60%. The dynamic response of the samples was studied as per the ASTM D5311 [4] and ASTM D3999 [3]. The dry samples were prepared by dry pluviation method and were mounted on the pedestal using vacuum method. Then the samples were saturated by back pressure method maintaining an effective confining pressure of 15–20 kPa till the B value exceeds 0.95. The saturation stage was then followed by the consolidation stage. After consolidation, the samples were subjected to the sinusoidal cyclic loading. The data acquisition system connected to the apparatus was capable of continuous monitoring and logging of the data during the tests.

3 Results and Discussion

The typical results of cyclic triaxial tests are shown in Figs. 2 and 3 for scrap tire chips and sands, respectively. The figures show results of the experiments conducted at 0.15% strain amplitude, 50 kPa confining pressure, and 1 Hz frequency. These figures present response of deviatoric stress, excess pore pressure, strain amplitude,
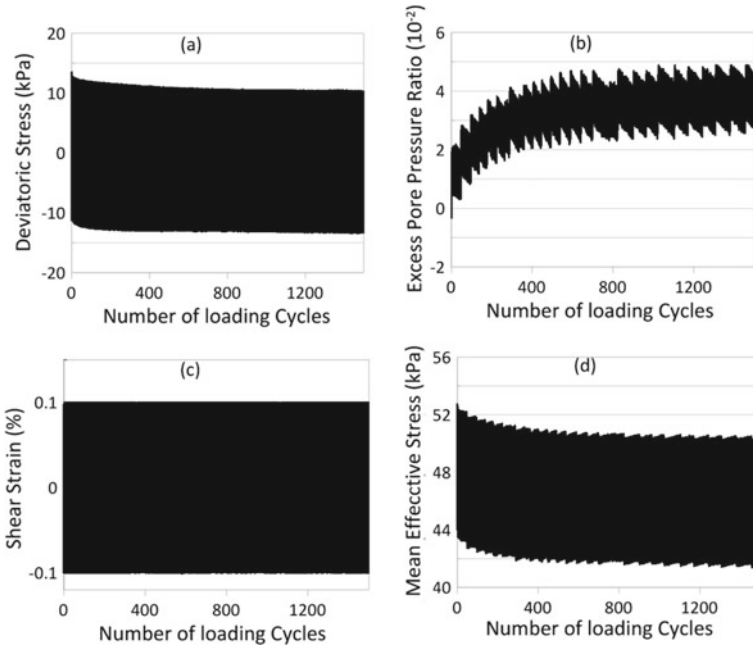
Fig. 2 Typical cyclic triaxial test results of tire chips
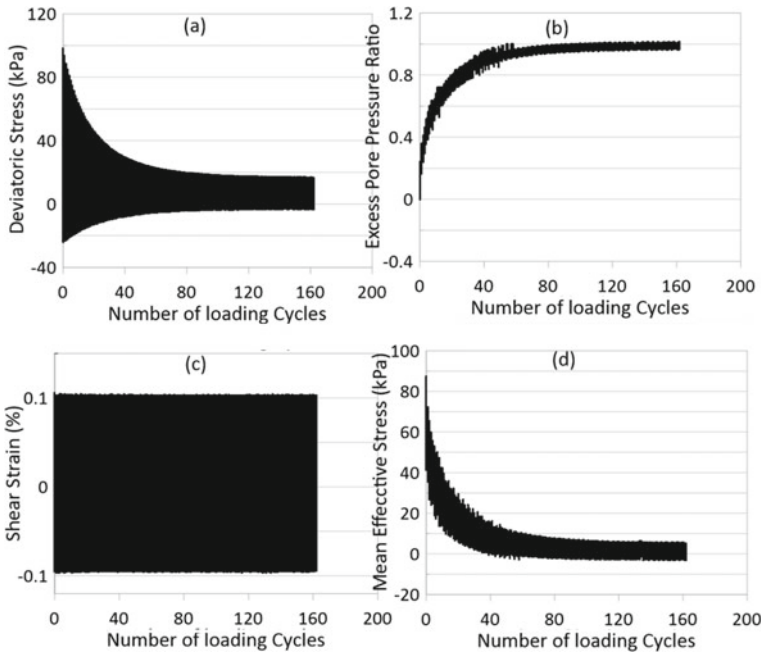
Fig. 3 Typical cyclic triaxial test results of sand

and mean effective stresses with the number of loading cycles. It can be clearly seen that both the materials behave in similar way to the external loads.

The deviatoric stress and the mean effective stress showed a decrease with the increasing number of loading cycles. This behavior is very clear in case of fully saturated sand, whereas in the tire chips as the stiffness degradation is not very fast, this behavior is not very remarkable. The magnitude of maximum deviatoric stress was 10.58 kPa for the initial cycle and was 10.29 kPa at the end of 1500 cycles for the saturated tire chips sample, whereas the initial maximum deviatoric stress of fully saturated sand sample was much higher, i.e., 98 kPa for the initial cycle and it degraded to almost zero in just 70 cycles, under similar conditions. In the same way, the magnitude of maximum mean effective stress decreased from 52.57 to 50.17 kPa in 1500 cycles for rubber tire chips, whereas for sand sample the value decreased from a value of 87 kPa to about zero in just 70 cycles. It can be said that the degradation of stiffness is much faster in case of sand as compared to tire chips.

The liquefaction potential of a sample is defined in terms of excess pore pressure ratio (R_u), i.e., the ratio of the excess pore pressure generated to the initial effective stress in the sample. When this R_u value reaches one, the sample is said to be liquefied. The number of loading cycles at which this R_u value reaches one is taken as the measure of the liquefaction potential of a sample, i.e., the more is the number of cycles the more is the resistance toward liquefaction. Figures 2b and 3b present the variation of excess pore pressure ratio with the number of loading cycles for tire chips and sand, respectively. It can be seen that the excess pore pressure ratio increases with the increasing loading cycles. The R_u hardly reached a value of around 0.048 even after 1500 number of loading cycles for samples tire chips, whereas the sand sample liquefied in 70 loading cycles.

The liquefaction response of the tire chips for all the different combinations of confining pressures and strain amplitudes is presented in Fig. 4. The saturated tire chips were subjected to 1500 number of loading cycles in all the cases. Even after 1500 number of loading cycles none of the cases was observed to be liquefied. Even with the highest strain amplitude and minimum confining pressure R_u reached only a value of 0.09. This indicates that the tire chips show high resistance towards liquefaction.

3.1 Dynamic Properties

The dynamic properties of the materials were calculated from the hysteresis loop obtained from the test, i.e., the deviatoric stress versus strain graph. Figures 5 and 6 present the variation of shear modulus and damping ratio of both materials at the third cycle of the hysteresis loop. The plot also shows the effect of the confining pressure and strain amplitudes on these dynamic properties.

Figure 5 clearly shows that the shear modulus, that represents the stiffness of the soil, highly depends on the confining pressure and the strain amplitude applied. The stiffness of the soil is high for higher confining pressure, whereas it shows a lower
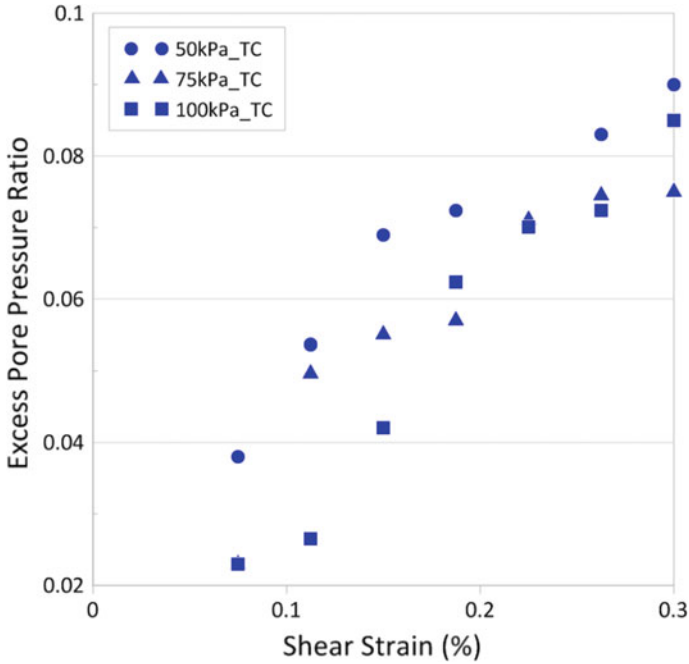
Fig. 4 Excess pore pressure ratio with shear strain (TC-tire chips)

value at higher strain amplitudes. Similar behavior is observed for both the materials considered.

The shear modulus of sand is found to be very high in comparison with that of tire chips. The maximum value of the shear modulus, under the different cases considered in the study, was 8 kPa for minimum strain amplitude, i.e., 0.075% and highest confining pressure, i.e., 100 kPa. Under similar conditions, the shear modulus for sand was around 56 kPa, which is 7 times that of tire chips. The minimum value of shear modulus for sand, under the different conditions considered, was 7 kPa for highest strain amplitude and lowest confining pressure considered. The corresponding shear modulus for tire chips was about 3 kPa.

Similarly, Fig. 6 indicates the dependence of damping ratio on the confining pressure and strain amplitude. The damping ratio value showed a decrease with increasing confining pressure, whereas it increases with the strain amplitude.

The damping ratio of sand is found to be very low in comparison with that of tire chips. The maximum value of the damping ratio found, among the different cases considered for the study, was 0.6, for maximum strain amplitude, i.e., 0.3% and minimum confining pressure, i.e., 50 kPa. Under similar conditions, the damping ratio for sand was around 0.26 which is even less than half of that of tire chips. The minimum value of damping ratio for sand, under the different conditions considered, was 0.23 for lowest strain amplitude and highest confining pressure considered. The corresponding damping ratio for tire chips was about 0.12.
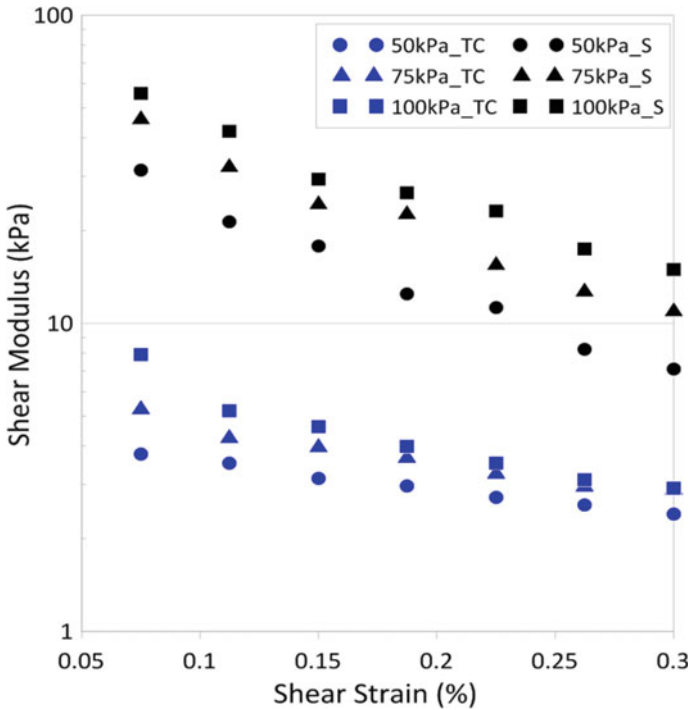
Fig. 5 Variation of shear modulus with shear strain (S-sand and TC-tire chips)

From the above discussions, it can be concluded that the tire chips are very good at the damping but have a very low shear modulus, whereas the sand exhibits lower damping ratio and high shear modulus.

In view of higher damping, tire chips are better than sand, and in terms of shear modulus, sand is better than tire chips. However, as discussed in the earlier section, bulk utilization of tire derived materials reduces burden on the environment, and further studies in this direction are warranted to understand the behavior of tire chips-sand mixtures as a practical solution to liquefaction mitigation.

4   Conclusions

This study investigated the dynamic properties of the rubber tire chips and also compared the properties with that of the Indian standard sand (Grade II). The cyclic triaxial apparatus was employed for the testing. Strain-controlled cyclic triaxial tests were carried out considering strain amplitudes and confining pressure as variables. Important conclusions drawn from the study are as follows:
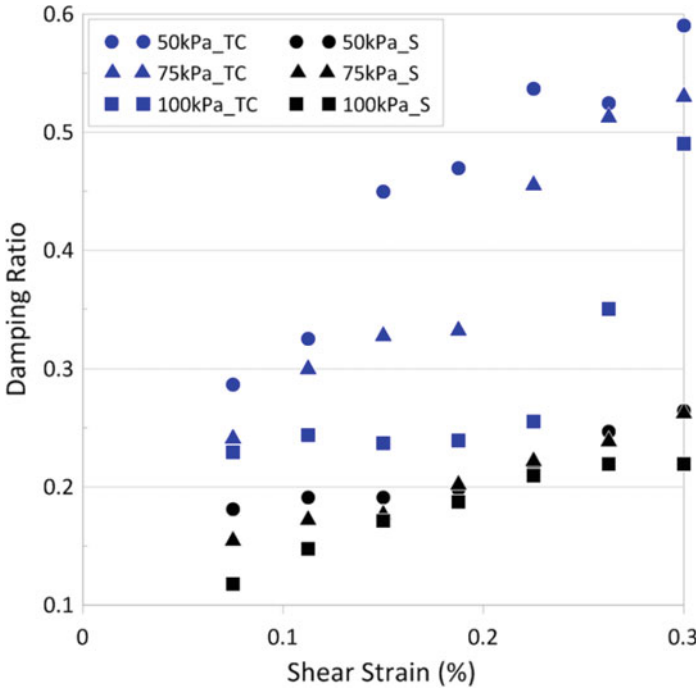
Fig. 6 Variation of damping ratio with shear strain (S-sand and TC-tire chips)

- The tire chips have very high damping ratio but very low shear modulus in comparison with that of the sand.
- Tire chips are very resistant towards liquefaction and even after 1500 number of loading cycles the material samples made of tire chips did not liquefy.
- For both the materials, the trend of observed behavior is almost identical. The deviatoric stress and mean effective stress decreased and the pore water pressure increased with the increasing loading cycles.

References

1. Abdrabbo FM, Abouseeda HM, Gaaver KE, El-Marassi MA (2005) Behavior of strip footings resting on sand reinforced with tire-chips. Slopes and retaining structures under seismic and static conditions, pp 1–14
2. Abiuchou T, Tawfiq K, Edil TB, Benson CH (2004) Behavior of a soil-tire shreds backfill for modular block-wall. Recycl Mater Geotech ASCE 162–172
3. ASTM D3999–91 (1996) Standard test methods for the determination of the modulus and damping properties of soils using the Cycilc Triaxial Apparatus. Reproduced
4. ASTM D5311–92 (1992) Standard test method for load controlled cyclic triaxial strength of soil

5. ASTMD6270–17 (2017) Standard practice for use of scrap tires in civil engineering applications
6. Bosscher PJ, Edil TB, Kuraoka S (1997) Design of highway embankments using tire chips. Geotechnical and Geo-Environ Eng ASCE 123(4):295–304
7. Cecich V, Gonzales L, Hoisaeter A, Williams J, Reddy K (1996) Use of shredded tires as lightweight backfill material for retaining structures. Waste Manage Res 14:433–451
8. Edil TB, Park JK, Kim JY (2004) Effectiveness of scrap tire chips as sorptive drainage material. J Environ Eng ASCE 130(7):824–831
9. Foose GJ, Benson CH, Bosscher PJ (1996) Sand Reinforced with Shredded Waste Tires. J Geotech Eng ASCE 122(9):760–767
10. Hazarika H, Kohama E, Sugano T (2008) Underwater shake table tests on waterfront structures protected with tire chips cushion. J Geotech Geoenviron Eng ASCE 134(12):1706–1719
11. Hazarika H, Yasuhara K, Kikuchi Y, Karmokar AK, Mitarai Y (2010) Multifaceted potentials of tire-derived three dimensional geosynthetics in geotechnical applications and their evaluation. Geotext Geomembr 28(3):303–315
12. Lee JH, Salgado R, Bernal A, Lovell CW (1999) Shredded tires and rubber-sand as lightweight backfill. Geotech Geo-Environ Eng ASCE 125(2):132–141
13. Mashiri MS, Vinod JS, Sheikh MN (2016) Liquefaction potential and dynamic properties of sand-tyre chip (STCh) mixtures. Geotech Test J ASTM 39(1):69–79
14. Masad E, Taha R, Ho C, Papagiannakis T (1996) Engineering properties of tire/soil mixtures as a lightweight fill material. Geotechnical Testing Journal, ASTM 19(3):297–304
15. Reddy KR, Stark TD, Marella A (2010) Beneficial use of shredded tires as drainage material in cover systems for abandoned landfills. Practice Periodical of Hazardous Toxic Radioactive Waste Management ASCE 14(1):47–60
16. Shrestha S, Ravichandran N, Raveendra M, Attenhofer JA (2016) Design and analysis of retaining wall backfilled with shredded tire and subjected to earthquake shaking. Soil Dyn Earthq Eng 90:227–239
17. Tsang HH (2008) Seismic isolation by rubber–soil mixtures for developing countries. Earthquake Eng Struct Dynam 37(2):283–303
18. Tweedie JJ, Humphrey DN, Sandford TC (1998) Tire shreds as lightweight retaining wall backfill: active conditions. Geotech Geo-Environ Eng ASCE 124(11):1061–1070
19. Wolfe SL, Humphrey DN, Wetzel EA (2004) Development of tire shred underlayment to reduce ground borne vibration from LRT track. Geotechnical engineering for transportation projects, ASCE, pp 750–759
20. Yasuda S (2007) Methods for remediation of existing structures against liquefaction. In Proceedings of the 4th international conference on earthquake geotechnical engineering, keynote lecture

Implications of On-Sample LVDTs in Cyclic Triaxial Test to Measure Small-Strain Shear Modulus

Shiv Shankar Kumar, A. Murali Krishna, and Arindam Dey

Abstract To evaluate the importance of small-strain shear modulus in geotechnical engineering applications, different techniques such as bender element, resonant column apparatus and on-sample LVDTs are being used by the researchers. This paper presents the results obtained from resonant column tests, bender element tests and on-sample LVDT for sandy soil, to emphasise the significance of on-sample LVDT for the measurements of small-strain properties, in contrast to the resonant column and bender element tests. Results indicated that the on-sample LVDT is successful and useful for the evaluation of dynamic soil properties at small strain.

Keywords Small strain · Cyclic triaxial test · On-sample LVDT · Shear modulus degradation curve

1 Introduction

The small-strain shear modulus (i.e. maximum shear modulus, G_{max}) of the soil is an important dynamic parameter for many geotechnical engineering applications, including seismic soil structure interaction and ground response analysis. The very small-strain stiffness, associated with shear strains $(\gamma) \leq 1 \times 10^{-6}$, is a fundamental property of all types of geotechnical materials including clays, silts, sands, gravels and rocks, subjected to static and dynamic loading at drained or undrained loading conditions. In this strain range, soils exhibit mostly elastic and recoverable behaviour. Therefore, in the recent years several techniques involving the application of bender elements, resonant column apparatus and on-sample transducers are developed to determine G_{max}.

S. Shankar Kumar
Department of Civil Engineering, National Institute of Technology, Patna 800005, India

A. Murali Krishna
Department of Civil Engineering, IIT Tirupati, Tirupati, Andhra Pradesh 517506, India

A. Dey (✉)
Department of Civil Engineering, IIT Guwahati, Assam 781039, India
e-mail: arindam.dey@iitg.ac.in

The importance of the measurements of small strains and corresponding G_{max}, using resonant column tests and its use in earthquake geotechnical engineering, is already discussed by several researchers [1, 2, 3, 4]. It was reported that the value of G_{max} depends on the several parameters such as void ratio, confining stress, soil structure, degree of saturation, temperature and stress history. Researchers have also used on-sample linear variable differential transducers (LVDTs) and various other instrumentations during triaxial testing to measure local small strains and corresponding G_{max}. Based on the literature survey reported by Kumar et al. [5], it can be stated that the both resonant column tests and on-sample transducers provide the dynamic soil properties over a wide strain range, i.e. from 0.0001–0.1% and 3×10^{-3}-10%, respectively. Both resonant column tests and on-sample transducers can effectively measure the small strain in the order of $10^{-4}\%$ and $3 \times 10^{-3}\%$, respectively. However, very few studies (e.g. Gookin et al. [6]) provided the comprehensive analysis to measure the small strains using on-sample LVDTs in contrast to the resonant column tests. This paper presents the combined results obtained from resonant column tests, bender element and on-sample transducers for same soil, to emphasise the importance of on-sample transducers for the measurements of small strains and the corresponding properties.

2 Experimental Investigation

Brahmaputra sand (BS) obtained from Guwahati region (Assam, India) is used for the study. Particle size of BS (Fig. 1) was determined by conducting dry sieve analysis
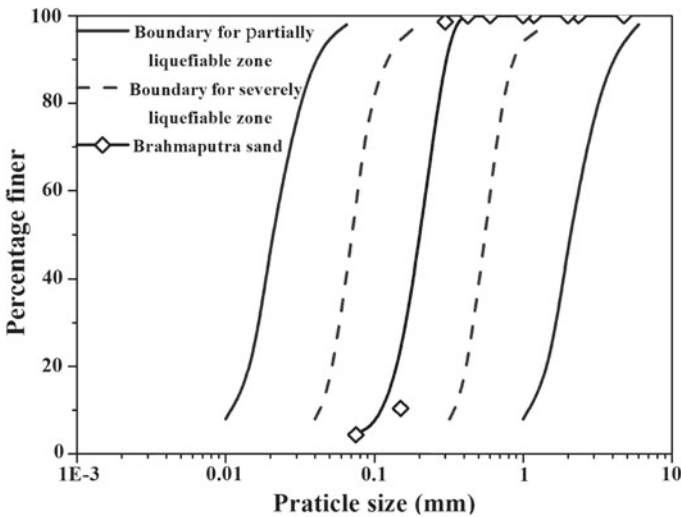
Fig. 1 Particle size distribution of Brahmaputra sand

Table 1 Physical properties of collected Brahmaputra sand (BS)

Unit weight (kN/m³)		Specific gravity	D_{10} (mm)	C_u	C_c
γ_{max}	γ_{min}				
16.84	13.85	2.7	0.13	1.47	1.09

and the same was classified as poorly graded sand (SP). As per the criterion provided by Tsuchida [7], the soil belongs to the category of severely liquefiable soils. Table 1 lists the index properties of the soil such as minimum and maximum dry unit weight, specific gravity, coefficient of curvature (C_c) and uniformity coefficient (C_u).

An automated pneumatic-controlled cyclic triaxial apparatus, also facilitating monotonic tests, was used for the experimental investigations, as shown in Fig. 2. It consists of a 100 kN capacity loading frame fitted with an actuator (±15 mm displacement range) operating over a frequency range of 0.01–10 Hz, a triaxial cell having (2000 kPa capacity), and an air compressor having a maximum capacity of 800 kPa. During monotonic compression shear, the shearing was done with upward movement of base pedestal, while actuator remained immobile. The instrumentations available with the apparatus are: linear variable differential transducers (LVDT) of measuring displacement 30 mm; one submersible load cell of capacity 25 kN; three pressure transducers of 1000 kPa capacity to measure cell pressure, back pressure and pore water pressure; and one volume change measuring device. The testing is controlled by a compact dynamic controller (CDC) unit, which conveys the instructions provided by software and record the data by data logger.

Dry pluviation technique was adopted to prepare the cylindrical specimens of BS of 70 mm diameter and 140 mm height. A nominal vacuum pressure of 15–20 kPa
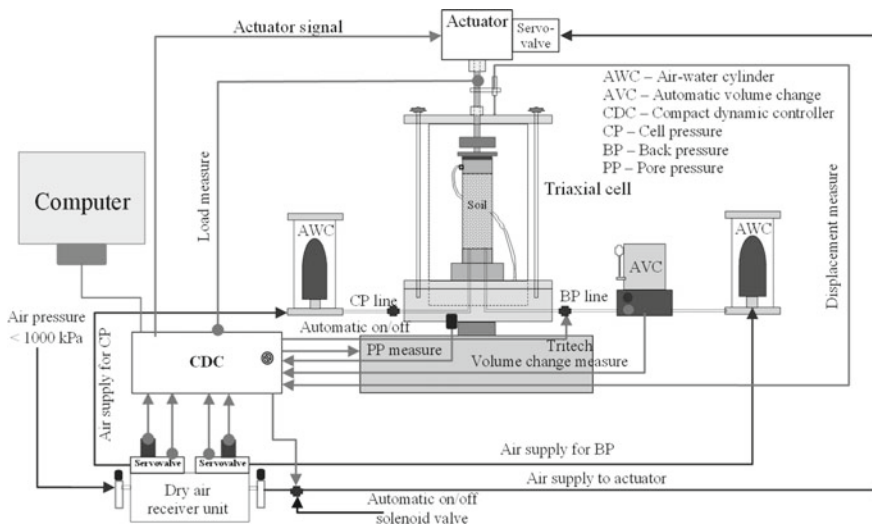
Fig. 2 Layout of cyclic triaxial test set-up

was used to maintain the verticality of the specimen (as per Ishihara et al. [8]). In order to achieve a quick saturation, carbon dioxide was flushed through the specimen for 10–15 min, with a pressure lesser than the applied cell pressure (CP), followed by flushing with de-aired water. To attain the saturation, CP and back pressure (BP) were then gradually increased in stages, while maintaining an almost constant differential pressure of 10 kPa, and checking the pore pressure parameter (B) after each CP increment. At a BP of 200 kPa, the B-value was obtained to be greater than 0.96 and then saturation process was terminated. The test specimens were consolidated to the targeted effective stress levels before the application of monotonic loading.

The local axial strain developed in the specimen during the triaxial test specimen was measured using two linear variable displacement transducers (LVDTs), oriented vertically at the middle of the specimen as shown in Fig. 3. Each transducer was fixed on the specimens with two mounting blocks, which displaces relative to one another as the specimen deforms. The mounting block was fixed on the soil specimens with rubber band of the same stiffness as of membrane. The displacement recorded by transducers, required to calculate the local axial strain, uses the initial distance between mounting blocks, i.e. the gauge length, rather than the initial specimen length.
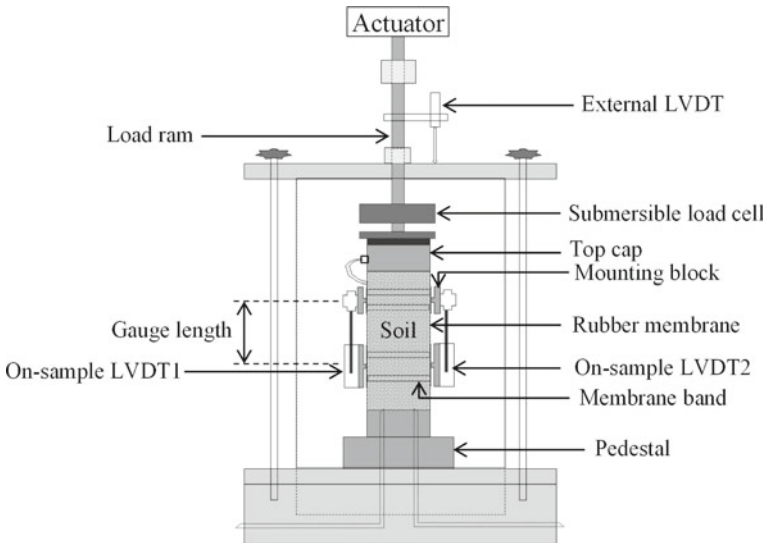
Fig. 3 Schematic diagram of the use of on-sample LVDTs

3 Results and Discussions

3.1 Results Based on Resonant Column Tests

To evaluate its dynamic properties at low strain levels, Dammala et al. [4] carried out the resonant column tests on dry Brahmaputra sand (BS) specimens at different relative densities (D_r) and confining pressures (σ_c) ranging from 30 to 70% and 50 to 600 kPa, respectively. The data shown by shaded region in Fig. 4 present the variations in G/G_{max} over the shear strain range 0.0001–0.1%. The dynamic property obtained at this complete test strain range may not be suitably used for partially or fully saturated soils; owing to the increase in pore water pressures (PWP) beyond a shear strain (γ) of 0.01% that significantly affects the volumetric changes and strength degradation. This limiting value of shear strain ($\gamma = 0.01\%$) is reported as a volumetric threshold shear strain (γ_{tv}) below which no significant pore water pressure is generated in the saturated cohesionless specimen [9, 10]. For clean dry sand, the values of γ_{tv} were found to be in the range of 0.02–0.03% (Silver and Seed 1971). Therefore, as the tests were done on dry sands, the use of Dammala et al. [4] data for shear strain range from 0.01–0.1% may not be judicious for the saturated sandy soil, as it does not cater the PWP increase that would occur in the saturated conditions. However, the consideration of dynamic properties of soil up to γ_{tv} (i.e. $\gamma = 0.01\%$) will not violate the assumption that the dynamic properties of dry and saturated cohesionless soil up to 0.01% are nearly same. Recently, Maheshwari and Kirar [11] have conducted resonant column tests on sandy soil specimens, collected from different depths during standard penetration tests, and having water content (w_c) ranging from 6 to 30%. Jafarian et al. (2018) also conducted resonant column tests on saturated sand for the estimation of strain-dependent dynamic properties. Both the above data are presented in Fig. 4. Based on the results, it can be stated that water content present in the specimen significantly (more than 50%) affects the low strain dynamic properties. The obtained tests data are then compared with proposed range of the variation of G/G_{max} for sands by Seed and Idriss [1], and the same is highlighted in Fig. 4. It can be clearly observed that, in comparison with the Seed and Idriss [1] model, Dammala et al. [4] overestimate the modulus degradation (as it was for dry sands), whereas Maheshwari and Kirar [11] show good agreement with the Seed and Idriss [1] model (both tests are for saturated sands), thereby reinforcing the dependency of dynamic properties on water content.

3.2 Results Based on On-Sample LVDTs

The present study includes the outcomes of cyclic triaxial tests conducted on saturated BS to evaluate the dynamic properties of saturated BS over a wide strain range based on locally mobilised shear strains. To measure the local strains, on-sample LVDTs

M:\Scanning\Springer\Bwf\505623_1_En\Chapter6\
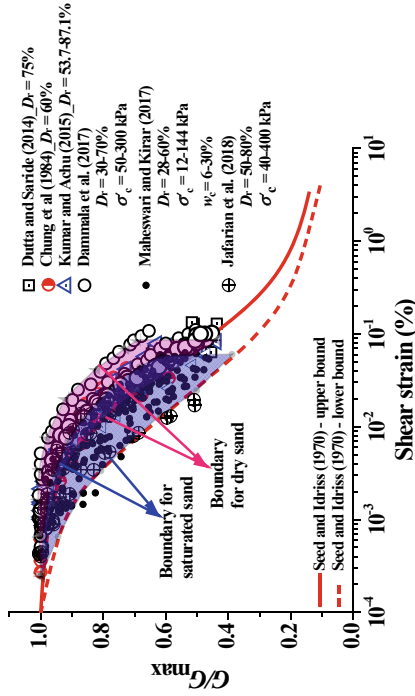
Fig. 4 Modulus reduction curve based on resonant column tests
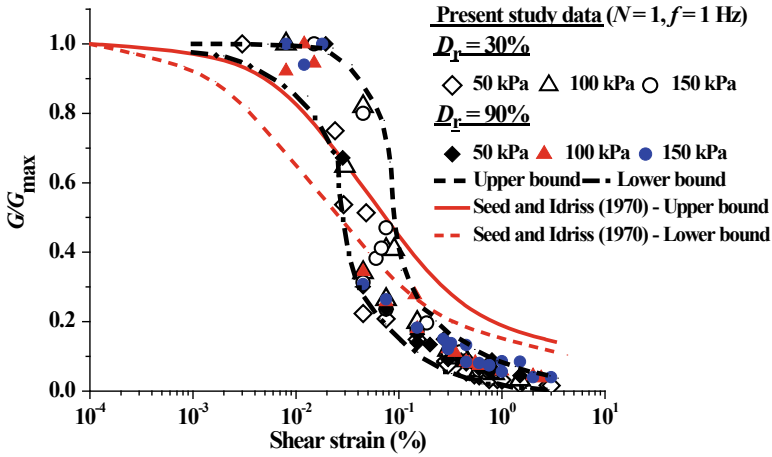
Fig. 5 Modulus reduction curve based on on-sample LVDTs in cyclic triaxial tests

were used on the BS specimens. Guided by the technical specification of the on-sample LVDT, the instrument is capable pf measuring low as well as high strains. Figure 5 represents the modulus reduction curve (represented by strain-dependent G/G_{max}) based on the on-sample LVDT measurements.

The maximum shear modulus (G_{max}), estimated from the on-sample LVDT measurements, was used to normalise G (i.e. the secant modulus obtained from local strain measurements) (Kumar et al. 2018). The application of on-sample LVDT at the mid-height of the sample aids in the measurement of local strains, which remains nearly unaffected by the boundary conditions imposed by the top and bottom caps of the triaxial cell. Hence, this measurement is more realistic than the global information obtained from a conventionally placed LVDT outside the sample. Based on the results beyond a shear strain of 0.01%, it can be stated apart from obtaining the shear modulus at low strains (less than 0.01%), the on-sample LVDTs can be effectively used even to obtain the same at high strain range (greater than 0.01%). Thus, these findings highlight the importance of the use of on-sample LVDT for the measurement of local strains which can be used to obtain the dynamic response of cohesionless soil over a wide range of strain (10^{-4}–4%, as shown in Fig. 5).

3.3 Results Based on Bender Element Tests

Maheshwari and Kirar [11] have used bender element (BE) in triaxial test to evaluate the maximum shear modulus (G_{max}) of fine sandy soil, which had a similar particle size gradation as that of BS. Figure 6 depicts the G/G_{max} value reported by Maheshwari and Kirar [11] using BE tests. For shear strain greater than 0.03%, it is seen that G/G_{max} values (where G_{max} evaluated using BE) obtained by Maheshwari
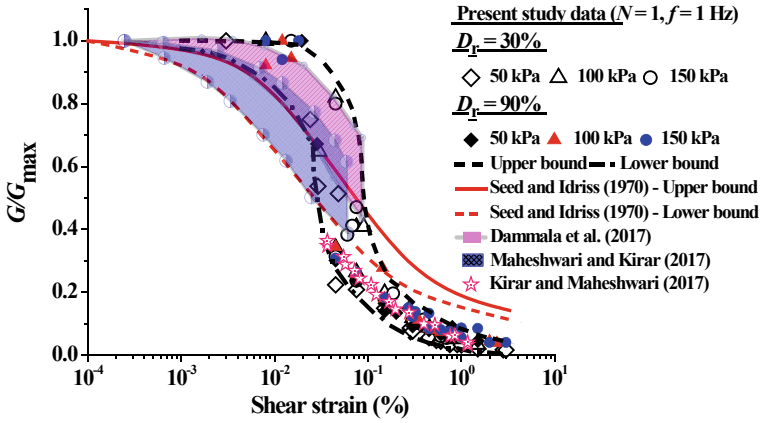
Fig. 6 Combined plots of modulus reduction based on resonant column tests, bender element tests and on-sample LVDTs along with Seed and Idriss [1] proposed curve

and Kirar [11] show good agreement with the G/G_{max} values (where G_{max} evaluated using on-sample LVDT) obtained in the present study. Therefore, the inclusion of BE test data (see Fig. 6) also reflects the significance of using on-sample LVDT for the measurement of G_{max}.

3.4 Combined Results from Resonant Column Tests and On-Sample LVDTs

Figure 6 presents the combined results obtained from resonant column tests, bender element tests and triaxial tests using on-sample LVDTs. It can be seen that G/G_{max} obtained, for strain range less than 0.01%, from all the instruments are in close agreement from each other, which reinforces the effective usage of the on-sample LVDT for measuring small strains. On-sample LVDTs are found equally capable to measure the high strain properties, for strain range greater than 0.03%. Therefore, it can be stated that the on-sample transducers, with its capability of measuring local strains, can be efficiently used to evaluate the small-strain dynamic properties of a soil specimen, as well as its high strain range properties through cyclic triaxial testing.

4   Final Remarks and Conclusions

The following are the final remarks and conclusions from the present study:Resonant column tests and bender element tests provide only the low strain dynamic soil properties, whereas the application of on-sample LVDT in triaxial test aids in determining both low-strain and high-strain dynamic soil properties a single test specimen. Since the conventional tests require multiple specimens for testing various ranges of strain, it is difficult to maintain the uniformity of such soil specimens. The application of on-sample LVDT aids in overcoming this difficulty.Low strain dynamic properties are significantly affected by water content (w_c) present in the soil specimens.The results obtained from the resonant column tests, bender element tests and on-sample LVDT in triaxial test, indicated that the on-sample LVDT is equally capable to measure the dynamic properties of soils for small strain.

References

1. Seed HB, Idriss IM (1970) Soil moduli and damping factors for dynamic response analysis, Rep. No. EERC 70–10, Earthquake Engineering Research Center, Berkeley, California
2. Vucetic M, Dobry R (1991) Effect of soil plasticity on cyclic response. J Geotech Eng ASCE 117(1):89–107
3. Dutta TT, Saride S (2014) Dynamic properties of clean sand from resonant column studies. In Proceedings of Indian geotechnical conference, IGC-2014, Kakinada, India
4. Dammala PK, Krishna AM, Bhattacharya S, Nikitas G, Rouholamin M (2017) Dynamic soil properties for seismic ground response studies in Northeastern India. Soil Dyn Earthq Eng 100:357–370
5. Kumar SS, Krishna AM, Dey A (2019) Local strain measurements in triaxial tests using on-sample transducers. In Geotechnical characterisation and geoenvironmental engineering, Springer, Singapore, pp 93–101
6. Gookin W, Riemer M, Boulanger R, Bray J (1996) Development of cyclic triaxial apparatus with broad frequency and strain ranges. Transp Res Rec J Transp Res Board 1548:1–8
7. Tsuchida H (1970) Prediction and counter measure against the liquefaction in sand deposits. In Proceeding of the seminar in the Port and Harbour Research Institute, Ministry of Transport, pp 1–33
8. Ishihara K, Silver LM, Kitagawa H (1978) Cyclic strength of unsaturated sands obtained by large diameter sampling. Soils Found 18:61–76
9. Vucetic M (1994) Cyclic threshold shear strains in soils. J Geotech Eng 120(12):2208–2228
10. Hashash YMA, Musgrove MI, Harmon JA, Groholsk DR, Phillips CA, Park D (2015) DEEPSOIL 6.1, User Manual
11. Maheshwari BK, Kirar B (2017) Dynamic properties of soils at low strains in Roorkee region using resonant column tests. Int J Geotec Eng 1–12. https://doi.org/10.1080/19386362.2017.1365474

Use of Biosensors for Assessing Soil Stabilization with MICP—A Review

M. S. Varnitha, Bharathi Ganesh, Sureka Naagesh, B. V. Manjunatha, and H. N. Ramesh

Abstract Soil stabilization is a process of mixing of the parent soil with other soil, cement, lime, bituminous products, and silicates to improve shear strength and swell shrink behavior of the native soil. Bio-enzymes used for chemical soil stabilization are chemical, organic, and liquid concentrated substances. Microbially induced calcium carbonate precipitation (MICP) consists of producing calcium carbonate by hydrolyzing urea carried out by several microorganisms. Naturally, the deposition of $CaCO_3$ in the void spaces leads to clogging of voids in the material. Hence, MICP treatment is becoming more popular, safe, and sustainable method in the field of soil stabilization and also for rehabilitation of historical monuments, ancient masonry, and concrete structures. Hence, monitoring the biological process is essential as it strongly depends on environmental conditions and dosages of both bacteria and food present. A urease quantification using magnetic biosensor is an emerging efficient tool for this purpose. This review presents the effectiveness of the microbially induced calcium precipitation (MICP) as a stabilization method. Literature on laboratory studies on plant-derived urease induced carbonate precipitation is scanty. There

M. S. Varnitha (✉)
Nitte Meenakshi Institute of Technology, Bengaluru, India
e-mail: varnitha.ms@gmail.com

B. Ganesh
Nitte Meenakshi Institute of Technology, Bengaluru, India
e-mail: bharathi.ganesh@nmit.ac.in

S. Naagesh
BMSCE, Bengaluru, India
e-mail: rs.civ@bmsce.ac.in

B. V. Manjunatha
Department of Civil Engineering, DSCE, Bengaluru, India
e-mail: manjunathmbv@gmail.com

H. N. Ramesh
UVCE, Bangalore University, Bengaluru, India
e-mail: rheddur@yahoo.com

M. S. Varnitha
KSSEM, Bengaluru, India

is a scope for more exploratory works at laboratory scale to assess the effectiveness of the carbonate precipitation via plant-derived urease for industrial/field applications. The major challenges in this area for field applications include assessment of subsurface soil condition and their interaction with the available fluids and minerals, groundwater flow and available minerals Therefore, it is necessary to investigate the durability and reversibility of the carbonate precipitation process under economical point of view.

1 Introduction

With the rapid change in the global urbanization and industrialization, there is an unpredicted growth in the population and intense development in developing countries like India. Urbanization in India is neither unique nor exclusive but is similar to a worldwide phenomenon [1]. The population dynamics is changing fast with 55% of the world's population lives in urban areas, a proportion that is expected to increase to 68% by 2050; future increases in the size of the world's urban population are expected to be highly concentrated in just a few countries. The future expected increase in urban population dynamics results in huge demand for housing and infrastructure projects and also commuting facilities, requiring enormous area of land for construction, irrespective of its suitability. Hence, it is required to use the land available for construction activities enhancing the engineering properties of the soil.

Some area where soil is of not expected quality needs to be stabilized prior to the construction activities. Researchers have found remedial methods to improve the engineering properties of soil. For stabilization of soil chemical or mechanical methods is the most effective technique to alter the engineering properties and bearing capacity of the soil [2, 3] to meet required specifications. Other common methods are controlled compaction, proportioning, and/or the addition of suitable admixture or stabilizers. It is a well-known fact that engineering properties of the soil can be enhanced by physical, chemical, biological, or combined methods. Stabilization can improve the shear strength and expansion or contraction behavior of the native soil and making it suitable for the purpose of construction of clay liners, soil subgrade, etc.

Some of the waste products from cultivations and industries are utilized for soil stabilization. On the one hand, there is a large requirement of land to cater to the increased population, and on the other hand, there is a huge generation of wastes from many industries, including construction industry [1]. Due to shortage of naturally available materials, there is a need for such a waste material which is not hazardous to environmental, enhances the sustainability of construction, in terms of availability, quality, and economy [4]. Handling the requirement of huge quantity of construction

materials and managing/disposing of the waste generated from construction is the key for successful urban planning without depending on depleting natural resources. There comes the major role for handling waste generated for useful applications [5].

Synthetic chemical stabilizers available are hazardous to environment due to the higher costs and CO_2 emission released during the cement production. Due to these drawbacks, new stabilizers such as bio-enzymes have emerged as an innovative technique. Bio-enzymes are chemical, organic, and liquid concentrated substances which are used to improve the stability of soil sub-base of pavement applications. An organic catalyst which speeds up the chemical reaction is called the bio-enzyme [6]. A number of such enzymes were used for improving the strength and durability characteristics of soil. Recent development of bio-enzymes is emerging as an effective measure which is safe and effective [6]. Such a chemical reaction is slow and enzymes are not the part of the end product. Hence, bio-enzymes are widely used for soil stabilization.

Bio-enzymes are integral parts of microbial geo-technology, a branch of geotechnical engineering that deals with the application of microbiological methods to improve the physical properties of soil to make it suitable for construction activities addressing the need of environmental factors. Microbial geo-technology is further explored which gives rise to two applications, namely bio-clogging [2] and bio-stabilization. Bio-clogging is a process of production of pore-filling materials through microbial means which reduces the porosity and hydraulic conductivity of soil whereas bio-stabilization is the process of in situ production of binding materials through microbial processes which increases shear strength of soil [5].

Microbially induced calcium carbonate precipitate (MICP) is a process of producing calcium carbonate by hydrolyzing urea, with the help of several microorganisms. Treatment of cracks in stones, concrete constructions, producing water proofing paints, and cementation of soils is few applications of MICP [7].

Cases showing good results of MICP treatment are increasing, particularly in case of rehabilitation of historical monuments and mortar/concrete structures. However, monitoring the biological process is essential to assess the effectiveness of the process as MICP strongly depends on environmental conditions and dosages of both bacteria and food present. Adequate tools are necessary for monitoring the progress of MICP in field applications [8]. A urease quantification magnetic biosensor is the most recent emerging sensor, used as an efficient tool for this purpose.

The present paper brings-in the traditional and non-traditional materials for soil stabilization, mechanism of soil stabilization, enzymes and types available, bio-enzymes, bacteria, cultivation of MICP, types of bacteria, principle and working of bio-sensors, essential features of bio-sensors for assessing soil stabilization/engineering properties of soil, followed by rational conclusions.

2   Materials and Methodology

2.1   *Cement*

The soil stabilized with cement is known as soil cement. Chemical reaction between cement and soil leads to cementation of the particles. Cement stabilization is more suitable for coarse grained soils. Generally ordinary portland cement is used for stabilization. High early-strength cement can also be used which is more effective while it is required to speed up the construction. The amount of cement required for this purpose varies from 5 to 15% by weight of the soil. The amount of cement added depends on the fineness of the soil also. These percentages of cement required for stabilization are found out by performing compressive strength and durability tests. It has been observed that more strength and stability is developed if the fine-grained soil are compacted in wet condition with optimum water content and the coarse grained soil on the dry side of the optimum water content. Lime, calcium chloride, and fly ash are also added as additives [9].

2.2   *Lime*

Lime is an effective material in treating plastic clayey soils and can be used alone or in the combination with cement, bitumen, or fly ash. Addition of lime to the soil reduces plasticity index in highly plastic soil. Generally, there is an increase in optimum water content and decrease in maximum dry density when lime is used showing increase in strength and durability of soil. Generally, 2 to 8% of lime is required for coarse grained soil and 5 to 10% for plastic soils whereas amount of admixtures like fly ash may vary from 8 to 20% of the soil by weight [10].

2.2.1   Non-traditional stabilizers

Non-traditional additives are classified into seven groups: ionic, enzymes, lignosulfonates, salts, petroleum resins, polymers, and tree resins [9, 11, 12].

Ionic stabilizers. Ionic stabilizers have gained popularity because of their requirement in small quantities for effective stabilization. Ionic stabilizers change the concentration of electrolyte in the pore fluid which results in cation exchange, leading to flocculation of the clay minerals. The process is of adsorption of ions, ionic reactions with soil constituents and ion exchange alter the molecular structure of the soil [6]. These reactions reduce the surface charge of the soil particles, resulting in loss of double-layer water and allowing for close packing or even flocculation of the soil particles as illustrated with pictorial representation (Fig. 1). Ionic stabilizers are suitable only for fine-grained soils, silts, and clays.
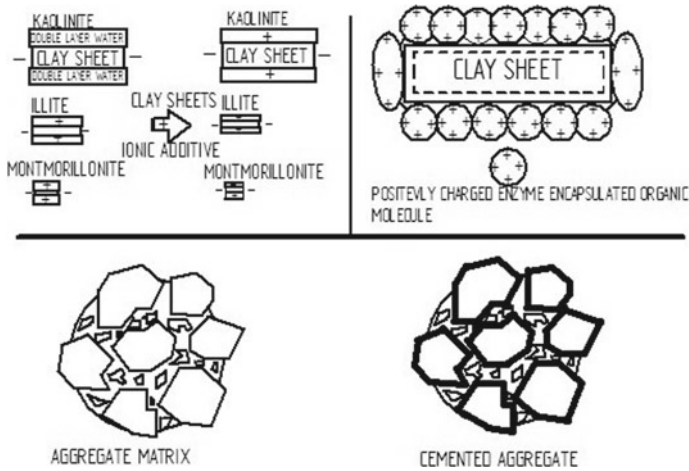
Fig. 1 Stabilization mechanisms [7]

Enzymes. Enzymes only facilitates the reaction and will not be consumed during the reaction [6]. Mobility of an enzyme is essential for it to reach a reaction site. Enzymes are catalysts used in small dosages and enzymes are actively present in the soil until the reaction is complete. Enzymes are also soil specific, they are suitable for the clay materials particularly high-plasticity clays with some organic content which have an affinity for water [6]. Best examples are silts and granular soils which cannot be stabilized with enzyme products.

Polymer stabilizers. The polymer stabilizer bonds with soil particles physically which gives rise to the emulsion. When water evaporates from emulsion it leaves a soil–polymer matrix. Physical properties and capacity of polymer to coat the soil particles decide the improvement in the strength of soil. Polymer emulsions are suitable for granular materials. Due to reduced mixing efficiency polymer emulsions are less suitable for fine-grained soils. They have excellent tensile and flexural strength [9, 13].

2.3   Different Types of Bio-enzymes

Renolith. The usage of Renolith improves the strength of soil during cement stabilization process and provides sufficient flexibility of standard cement stabilized pavements. A specific dosage of water is added while using the Renolith during mixing. It is an in-situ process and is applicable to a wide range of soil from fine sands to high plasticity clays. The stabilization carried out with a bio-enzyme mixed with soil or cement and water, an exothermic chemical reaction takes place which helps provide a densified layer of soil–polymer mixer [7].

Perma-Zyme. Perma-zyme acts as a catalyst during enzymatic reaction during which the active reaction sites are formed due to large molecular structures. These active reaction sites assist molecular bonding and interaction. It increases compaction and optimizes the natural properties of soil [14].

Terra Zyme. An organic compound Terra Zyme is a natural catalyst. It is extracted from vegetables and can be effectively used in soil to improve the strength, performance, higher resistance toward deformation and load bearing capacity of soils [15]. It is diluted with water of specified dosage before the application. These are suitable for fine-grained soils (e.g., clay) [16].

3 Calcium Carbonate Precipitates

Urease enzymes from the microbes when hydrolyzed produce calcium carbonate precipitate called microbially induced calcium carbonate precipitate (MICP). Urea, obtained from mammals and decomposition of uric acid excreted by birds, is used as fertilizers [2, 15]. As urea content increases in soil it gives rise to contamination and produce harmful algae. One mole of ammonia and carbonic acid is produced by a spontaneous hydrolysis process during the microbial urease activity when one mole of urea gets converted to one mole of ammonia and one mole of carbonate, which is expressed in chemical equations as follows[2].

$$CO (NH_2)_2 + H2O \rightarrow NH_2COOH + NH_3CO (NH_2)_2$$
$$+ H2O \rightarrow NH_2COOH + NH_3 \tag{1}$$

$$NH_2COOH + H_2O \rightarrow NH_3 + H2CO_3NH_2COOH + H_2O \rightarrow NH_3 + H2CO_3 \tag{2}$$
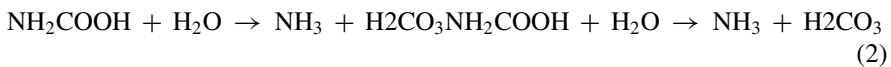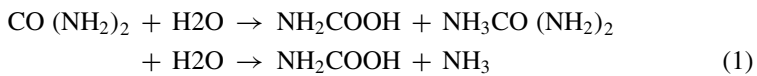
This product equilibrates in water to form bicarbonate, produce one mole of ammonia and hydroxide which results in pH increase.

$$NH_2COOH + H_2O \rightarrow NH_3 + H2CO_3NH_2COOH + H_2O \rightarrow NH_3 + H2CO_3 \tag{3}$$

$$NH_3 + H2O \rightarrow OH^{--} + NH_4^+NH_3 + H2O \rightarrow OH^{--} + NH_4^+ \tag{4}$$

$$Ca^{+2} + CO_3^{2-} \rightarrow CaCO_3Ca^{+2} + CO_3^{2-} \rightarrow CaCO_3 \tag{5}$$
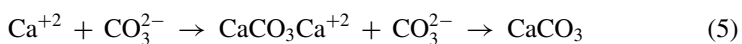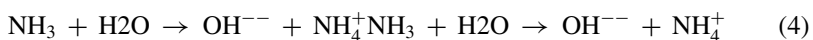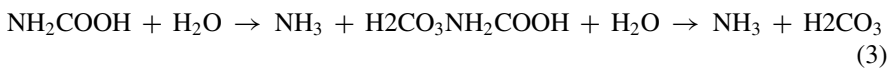
Carbonic acid increases CO_2 conversion which in turn increases carbonate production. Bicarbonate and ammonium ion are accumulated in cell due to hydrolysis of urea. The process of bicarbonate production is pH dependent which occurs under alkaline conditions. An alkaline environment in which calcium and calcium

carbonates are present abundantly facilitates $CaCO_3$ precipitation outside the cell. The above calcium carbonate precipitation can occur in three different ways: by microorganisms, by plant, or/and by sewage sludge.

3.1 Microorganisms

Microbially induced calcium carbonate precipitates can be produced by the following three types of microorganisms: (i) photosynthetic microorganisms; (ii) sulfate reducing bacteria; (iii) microorganisms involved in nitrogen cycle [2, 9, 17].

Bacteria. The bio-mineralization is a process of formation of cementation of minerals carried out by the bacterium, an organism present in nature as natural calcium source which produce calcium carbonate precipitate. This metabolic process carried out by bacteria, (e.g., urea hydrolysis, denitrification, sulfate reduction, Iron reduction) produces carbonic anhydrase enzymes, which have the ability to produce calcium carbonate precipitates. The majority of research is focused on urease-producing microorganisms. Non-ureolytic bacteria are helpful in MICP production in mixed culture, as they provide the nucleation site for calcium carbonate precipitation [2, 18].

Microalgae. Microalgae can be utilized as a reaction site for MICP. There will be an increase in pH value, when microalgae consume CO_2 producing calcium carbonate as carbonates [2, 4, 19].

The quantification of the enzyme is reflected by the quantity of calcium carbonate that precipitates and also it ensures the continuity of bio-cementation process. The operation of sensor is based on a competitive-binding affinity (Fig. 2). Urease is firstly immobilized over the magnetic sensor. In parallel, antibodies are labeled with nanoparticles. These antibodies will either recognize or bind to the urease present in the sample or will bind to the immobilized urease over the sensor. The antibodies that bound to the immobilized urease stand over the sensor after washing and the magnetic beads will create a fringe field further detected by the sensor when applying an external magnetic field. Quantification of urease present in the sample is inversely proportional to the signal obtained from the sensor: Maximum signal is found when

Fig. 2 Schematic of a typical urea biosensor [20]
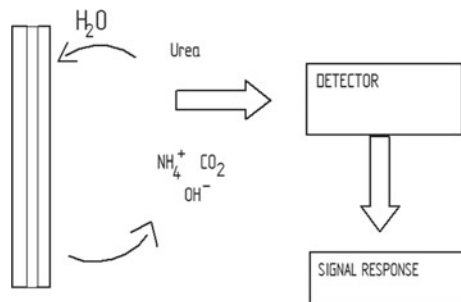
there is no urease in the solution and vice versa, i.e., lack of signal indicates the maximum quantity of urease in the sample.

4 Biosensors

An analytical device that combines biological materials (e.g.,—enzymes, nucleic acids (DNA and RNA), microorganisms, whole cells, antibodies, cell receptors, or biologically derived materials) in contact with a physico-chemical transducer as analyzer is known as bio-sensor [21]. The bio-sensors may be electrochemical, thermometric, optical, piezoelectric, or magnetic based on the type of signals it analyzes in which transducer converts bio-chemical signal into a quantifiable signal of required/respective type [4].

Enzymatic biosensors utilize the bio-specificity of an enzymatic reaction. The bio-sensing element of a urea biosensor is urease which is most commonly used. Enzymatic urea biosensors utilize biochemical reactions. In other words, analyte (urea) and enzyme (urease) result in a product (ammonium ion) that can be detected and quantified using a (amperometric/potentiometric/optical thermal/piezoelectric) transducer [4, 20].

5 Conclusion

This review presents the use of microbially induced calcium carbonate precipitation as an effective ecofriendly solution for soil stabilization. In conclusion, diversified application of creolizes-driven MICP for a wide variety of engineered treatments including modification of construction materials, cementing porous media, hydraulic control, and remediating environmental contaminants is presented. The assessment of subsurface soil condition including soil type, pH, mineralogy and their interaction with the available fluids and minerals, groundwater flow and available minerals and most favorable conditions for application of MICP are the major challenges in this method of using MICP for soil stabilization. This problem can be eliminated using a properly designed bio-sensor which may help in predicting the specification for some of the variable parameters of soil for effective utilization of MICP for improvement in engineering properties of soil. The potential use of bio-minerals has brought a new revolution in various engineering field applications creating lot of scope to explore more in this field to make the process more environmentally safe, cost effective, and to develop as a convenient technology from laboratory to field scales.

Other areas needed to be explored are economic feasibility and reduction in unwanted by-products like ammonia production during hydrolysis of urea, use of biosensor for assessment of durability, longevity and reversibility of the carbonate precipitation process, economy associated with this process.

Laboratory experiments should be carried out in abundance to determine the effectiveness of the carbonate precipitation via plant-derived urease for industrial/field applications.

References

1. Prathima G, Bharathi G, Nagaraj KP (2017) Optimum use of alternate material for aggregates—an approach for waste management in urban areas for sustainability, urbanisation challenges in emerging economics. In ASCE-INDIA conference 2017, proceedings and Online ASCE Publication, IIT Delhi. https://doi.org/10.1061/9780784482025.023, **Published online:** 13 Dec 2018

2. Manjunath KV, Himanshu S, Manish K, Prem K, Rakesh K (2012) Stabilization of black cotton soil using ground granulated blast furnace slag. In Proceedings of international conference on advances in architecture and civil engineering (AARCV)

3. Ramesh HN, Sagar SR (2015) Effect of drying on the strength properties of terrazyme treated expansive and non-expansive soils, In 50th Indian geotechnical conference, Pune, India

4. Singh A, Garg P (2015) Evaluation of renolith as a subgrade stabilizer, 50th Indian geotechnical conference. Pune, Maharashtra, India

5. Behiry AEAEM (2013) A review of aggregate selection used for rigid pavements under traffic and environmental conditions. Adv Res in Eng J 1(2)

6. Venkatasubramanian C, Dhinakaran G (2011) Effect of Bio-Enzymatic Soil stabilization on unconfined compressive strength and California bearing ratio. J Eng Appl Sci 6(5):295–298

7. Cheng L, Shahin MA (2016) Urease active bioslurry: a novel soil improvement approach based on microbially induced carbonate precipitation" Can. Geotech J 53:1376–1385

8. Hui Xu, Zheng H, Wang J-N, Ding X-Q, Chen P (2016) Laboratory method of microbial induced solidification/stabilization for municipal solid waste incineration fly ash. MethodsX 6:1036–1043

9. Tingle JS, Kent Newman J, Larson SL, Weiss CA, Rushing JF (2007) Stabilization mechanisms of nontraditional additives, transportation research board of the national academies, Washington, D.C., pp 59–67

10. Umar M (2016) KhairulAnuarKassim, and Kenny Tiong Ping Chieti: biological process of soil improvement in civil engineering: a review. J Rock Mech Geotech Eng 8:767–774

11. Naagesh S, Gangadhara S (2010) Swelling properties of bio-enzyme treated expansive soil. Int J Eng Stud ISSN 0975- 6469 vol 2(2) Davanagere, Karnataka, India

12. Rani D, Kawasaki S (2016) Effective use of plant-derived urease in the field of geoenvironmental/geotechnical engineering. J Civil Environ Engg 6(1)

13. Jayalekshmi S, Reddy MA (2014) Studies on polymer based chemical treated clay soil**,** National Institute of Technology, Tiruchirappalli-620015 India

14. Rajoria V, Kaur S (2014) Soil stabilization using polymer stabilizer, Department of Civil Engineering, Maulana Azad National Institute of Technology, Bhopal-462051, India

15. DeJonga JT, Mortensenb BM, Martinezb BC, Nelsonc DC (2010) Bio-mediated soil improvement. Ecol Eng 36:197–210

16. Ravi Shankar AU, Rai HK, Mithanthaya R (2013) Bio-enzyme stabilized lateritic soil as a highway material, Indian Roads Congress J 18

17. Dhawan G, Sumana G, Malhotra BD (2009) Recent developments in urea biosensors. Biochem Eng J (2009)

18. DeJong JT, Fritzges MB, Nüsslein K (2006) Microbially induced cementation to control sand response to undrained shear. J Geotech Geoenviron Eng 132(11):1381–1392

19. Kavazanjian E, Karatas I (2006) Microbiological improvement of the physical properties of soil, international conference on case histories in geotechnical engineering

20. Dhawan G, Sumana G, Malhotra BD (2009) Recent developments in urea biosensors. Biochem Eng J 44:42–52
21. Cardoso SMF (2015) Development of a urease quantification biosensor to monitor biocementation processes in soils

Geotechnical Properties of Lunar Soil Simulantions

T. Prabu , **I. Venugopal, and K. Muthukkumaran**

Abstract Understanding the behavior of lunar regolith is important for designing the in-situ test equipment and building structures on the moon for the futuristic moon colonization. The Apollo missions brought back a small quantity of lunar soil to earth to assess the geotechnical properties of the lunar soil. However, it is essential to develop a lunar soil simulant (LSS) that is inexpensive and produced in large quantities to fulfill the extended research on lunar regolith. This paper presents the physical properties like specific gravity, particle size distribution, relative densities, etc., of a newly developed lunar soil simulant (LSS) for Chandrayaan missions. The triaxial test was conducted on the LSS at different confining pressures to discuss the influence of confining pressure on the stress–strain behavior of the LSS. The cyclic triaxial test was performed to find the dynamic properties like shear modulus, damping ratio, bulk modulus, and Poisson's ratio of the LSS. The results were compared with the lunar soil Apollo 16 and simulants like GRC-3 and JSC-1A. The results evidence that the new LSS has similar properties of the lunar soil and can be used for future extended research about the lunar regolith.

Keywords Lunar soil simulant · Cyclic triaxial · Moonquake

1 Introduction

The establishment of base operations on the moon leads to the preparation and implementation of further exploration of the solar system. The surface mobility, scientific instrument, and communities also must address the lunar materials as well. The various engineering and material science studies that are necessary for these endeavors will mostly address the lunar regolith. There is an obvious and important

T. Prabu (✉) · K. Muthukkumaran
Department of Civil Engineering, National Institute of Technology, Tiruchirapalli, Tamil Nadu, India
e-mail: tp.civilnitt@gmail.com

I. Venugopal
C&MG LEOS, U R Rao Satellite Centre, Indian Space Research Organization, Bangalore, India

need for simulants of the lunar regolith/soil with which these investigations can proceed. Many factors must be considered in making lunar simulants for various ISRU projects. Also, the complete characterization of lunar soil simulant (LSS) is very much important for lunar mission projects and enables the prediction of actual wheel-soil interactions hence, for the optimal design of the automobile industry as well. Also, it is necessary to find the dynamic properties of the LSS to understand the behavior of the LSS under the moonquake. This paper explains the geotechnical properties of the newly developed lunar soil simulant, which is compared with the Apollo-16 lunar soil and other lunar stimulants like GRC-3 [18], JSC-1 [26], and NAO-1 [22], etc. The cyclic triaxial test was performed to simulate the moonquake conditions and to find the dynamic properties like shear modulus, bulk modulus, damping ratio, and Poisson's ratio of the LSS.

2   Sample Preparation

Most of the lunar regolith/soil contains a lot of glass produced by a micrometeorite, and the rocks are made up of feldspar and anorthosite minerals. Such similar anorthosite rock belts were identified at Sittampundi (Fig. 1), Salem, Tamilnadu.
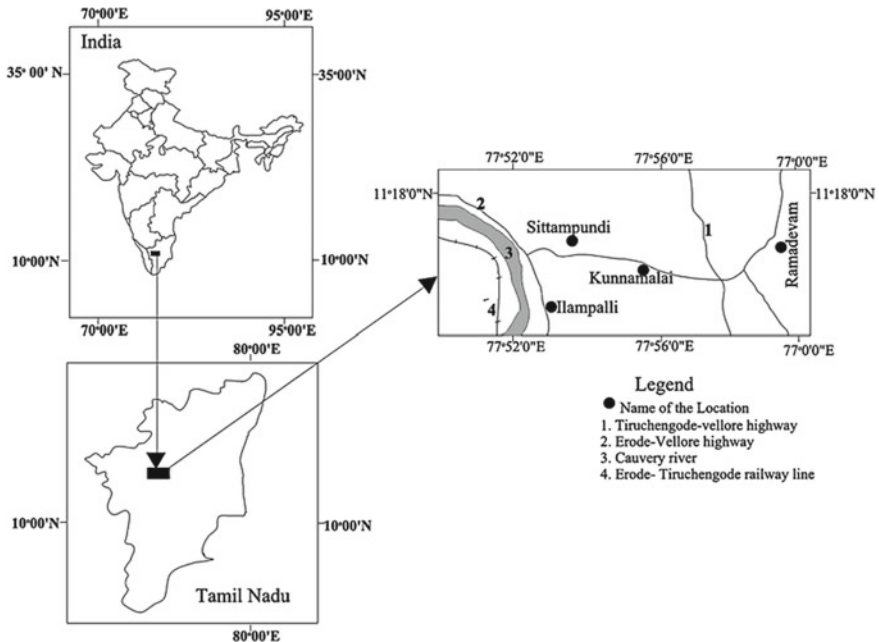
Fig. 1 Location map of the Sittampundi Anorthosite Complex (Google image)

Table 1 Comparison of chemical composition of Apollo-16 lunar soil and lunar simulants

Elements	Apollo-16 lunar soil	Sittampundi samples	TJ-1	NAO-1	FJS-1	JSC-1
SiO_2	44.75	45.52	47.70	44.67	49.14	47.71
TiO_2	0.05	0.04	2.00	0.03	1.91	1.59
Al_2O_3	35.65	29.82	16.20	36.15	16.23	15.02
Cr_2O_3	ND	ND	ND	0.01	ND	ND
FeO	ND	ND	ND	0.11	8.3	7.35
Fe_2O_3	0.64	0.80	10.75	ND	4.77	3.44
MgO	0.13	0.02	0.15	0.02	0.19	0.18
MnO	0.55	2.44	5.04	0.01	3.84	9.01
CaO	16.4	17.61	8.21	18.3	9.13	10.42
Na_2O	1.5	1.67	4.92	0.62	2.75	2.7
K_2O	0.77	0.01	2.29	0.01	1.01	0.82
P_2O_5	0.00	0.02	0.58	0.0	0.44	0.66
BaO	ND	ND	0.06	ND	ND	ND
NiO	ND	ND	ND	0.04	ND	ND
SrO	ND	ND	0.09	ND	ND	ND
LOI	ND	1.16	0.92	ND	0.43	0.11
Total	99.99	99.11	98.90	100.00	98.14	99.65

The rock samples were collected from the site to find the mineralogy and chemical composition. The chemical composition and mineralogy of the samples were determined by using energy dispersive X-ray analysis (EDX) and X-ray diffraction (XRD) analysis conducted on a few samples. The results confirm that the samples were matching the mineralogy and chemical composition of the Apollo-16 lunar soil and other lunar stimulants like TJ-1 [20], NAO-1 [22], FJS-1 [21], and JSC-1 [26]. The comparative results of chemical composition are given in Table 1. The rock samples were pulverized into different grain sizes, and various trial mixes were made with different proportions to obtain a similar gradation of Apollo-16 lunar soil.

3 Tests on Samples

The geotechnical and dynamic properties of the lunar soil stimulant (LSS) were determined based on the procedures and methods given in the ASTM/IS standards [1–15]. A list of tests conducted on the LSS is given in Table 2. The tests were repeated multiple times to ensure the reliability of the results.

Table 2 Geotechnical properties of the LSS

ASTM standard	Geotechnical properties	Values
D421	Specific gravity, G_s	2.70
D6913	Fines, %	40–48
ASTM D2487	Soil classification (USCS)	Silty sand
D4914	Bulk density, ρ (g/cm^3)	1.50
D4253-e1 and D4254	Relative density, %	63
	Maximum density, ρ_{max} (g/cm^3)	1.75
	Minimum density, ρ_{min} (g/cm^3)	1.18
	Maximum void ratio, e_{max}	1.24
	Minimum void ratio, e_{min}	0.56
D698-e2 and D1557-e1	Maximum dry density, ρ_{dmax} (g/cm^3)	1.45
	Optimum moisture content, %	12.77
D3080/IS2720 and D2850	Cohesion stress, c (kPa)	0.456
	Angle of internal friction, ϕ (°)	38°
D2435	Compression index, C_c	0.036
	Swelling index, C_s	0.001

3.1 Geotechnical Properties

The geotechnical properties of the LSS were determined in order to assess the geomechanical properties for designing the in-situ exploration equipment and formulating the foundation design criteria for lunar structures. The determined geotechnical properties of the LSS are given in Table 2.

Dynamic Properties

The dynamic properties like shear modulus, damping ratio, bulk modulus, Poisson's ratio of the LSS were determined by conducting the cyclic triaxial test and bender element test.

Cyclic triaxial test

In order to simulate the moonquake intensity at the laboratory level, the cyclic triaxial test was preferred. The dynamic properties of the LSS were assessed by conducting the triaxial test at varying frequencies and different confining pressures. The LSS samples were prepared at its measured bulk density and tested as per the method which is given in the ASTM D2435 standards. The prepared samples were tested

at frequencies of 0.5 Hz, 1 Hz, 1.5 Hz, and 2 Hz, at different confining pressures ranging from 0.5 to 2 kPa. The sample preparation for the cyclic triaxial test, its confinement chamber with applied confining pressure, and the loading assembly are shown in Fig. 2a–c.

Bender Element test

The shear modulus of the LSS has been determined by conducting the cyclic triaxial test. In order to find the maximum shear modulus of the LSS, the bender element test was performed as per the standards mentioned in the ASTM WK23118. Using the measured shear wave velocity from the bender element test, the maximum shear modulus was calculated. Figure 3 shows the bender element test.

4 Results and Discussions

The grain size influences the Shear strength [17, 24, 25, 27] and wheel-soil interaction properties [19, 23, 29, 31, 32] of the soil and rover respectively. So, the grain size distribution of the LSS was considered as the most important parameter and analyzed in detail. Although the newly developed LSS matches the grain size distribution of the Apollo-16 lunar soil, this study focused on comparing the same with other lunar high land simulants such as NAO-1 [22], NT-LHT-2M [33], and KLS-1 [30]. The gradation of the LSS was most similar to the other high land simulants and also closer to the Apollo-16 lunar soil limits. The specific gravity and bulk density of the LSS were measured and compared with the same lunar high land simulants and Apollo-16 lunar soil. The measured specific gravity value of LSS is 2.70, which is comparably lower than the Apollo soil, but closer to some other lunar simulants like TJ-1 [20], GRC-3 [18], and DNA-1A [24]. The measured bulk density of the LSS also falls within the range of lunar soils given by Mitchel et al. (1972b) and Carrier et al. (1991)

   The shear strength of lunar soils is a significant factor influencing their engineering properties, e.g., ultimate bearing capacity, slope stability, and trafficability [16]. LSS also subjected to measure the shear strength parameters angle of internal friction and cohesion. Direct shear tests were chosen to measure the shear strength of LSS for the sake of convenience and economy. However, the triaxial compression tests also carried out to measure the shear strength properties. From the test results, the internal friction angle ϕ and cohesion c of the dried LSS are 38° and 0.456 kPa, respectively. They have been obtained by the fitted linear regression line of the peak shear stress at normal pressures of 50, 100, 150, and 200 kPa. From the compressibility test results, it is observed that the LSS is low compressible and minimal swelling in nature. The shear modulus of the LSS with respect to different applied confining pressure and also different frequencies is in the range of 3000–6000 kPa. The corresponding damping ration of the LSS is in the range of 14–25%. The maximum shear modulus of the LSS was measured by using the bender element test which is given in Table 3. A typical shear wave curve obtained from bender element test is shown in Fig. 4.

Fig. 2 Triaxial test of LSS-ISAC-1. **a** Sample preparation, **b** confining chamber with sample, **c** loading assembly of triaxial test

Fig. 3 Bender element test setup

Table 3 Bender element test
results

Confining pressure (kPa)	Time	Shear wave velocity (m/s)	Shear modulus (G_{max}) (kPa)
0	1.73 ms	41.61	2682
50	1.01 ms	71.28	7872
100	910 μs	79.12	9699
150	860 μs	83.72	10,860
200	780 μs	92.30	13,200
250	750 μs	96	14,279
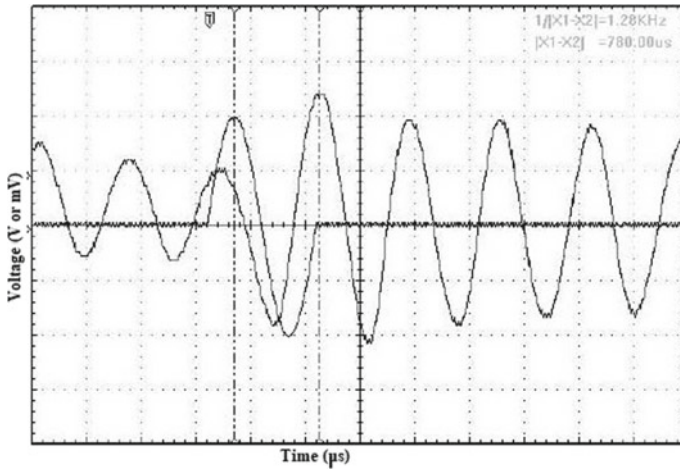
Fig. 4 A typical shear wave curve obtained from bender element test

5   Conclusion

Understanding the physical and chemical properties of the lunar regolith is very much important for the futuristic moon colonization, lunar explorations, and other lunar missions. However, the available lunar returned samples are very much less and far too small to be used for macroscale research programs. Therefore, a new lunar soil simulant (LSS) was developed by the Indian Space Research Organization, India, in large quantities for the extended research about the lunar surface and lunar highlands.

The chemical and physical (geotechnical engineering) properties of LSS were verified to represent the real characteristics of Apollo-16 lunar soil. The index/physical properties of the LSS were examined by conducting a series of laboratory tests and summarized in Table 3. The shear strength properties of LSS were evaluated via direct shear and triaxial tests within the context of Mohr–Coulomb failure criteria. The peak internal friction angle of LSS is high and increases with density, with negligible cohesion. The measured peak friction angle was 38° on average, and interparticle cohesion was 0.456 kPa. Standard laboratory oedometer apparatus testing yielded a compression index of (C_c) 0.036 and a swelling index of (C_s) 0.001 for LSS.

The dynamic properties of the LSS were assessed by conducting the cyclic triaxial test, which is used to simulate the moonquake conditions at the laboratory level. Based on the results, the geotechnical properties of the new LSS were cumulatively matching with the Apollo-16 lunar soil and some other lunar simulants. Hence, the LSS can be used for the extended research on the lunar regolith.

References

1. ASTM (2016) Standard test methods for density of soil and rock in place by the sand replacement method in a test pit. ASTM D4914, West Conshohocken
2. ASTM (2016) Standard test methods for maximum index density and unit weight of soils using a vibratory table. ASTM D4253-e1, West Conshohocken
3. ASTM (2016) Standard test methods for minimum index density and unit weight of soils and calculation of relative density. ASTM D4254, West Conshohocken
4. ASTM (2017) Standard test methods for particle-size distribution (gradation) of soils using sieve analysis. ASTM D6913, West Conshohocken
5. ASTM (2017) Standard test method for particle-size distribution (gradation) of fine-grained soils using the sedimentation (hydrometer) analysis. ASTM D7928, West Conshohocken
6. ASTM (2017) Standard practice for classification of soils for engineering purposes (unified soil classification system). ASTM D2487, West Conshohocken
7. ASTM (20174) Standard test methods for liquid limit, plastic limit, and plasticity index of soils. ASTM D4318-e1, West Conshohocken
8. ASTM (2015) Standard test method for unconsolidated-undrained triaxial compression test on cohesive soils. ASTM D2850, West Conshohocken
9. ASTM (2012) Standard test methods for laboratory compaction characteristics of soil using standard effort (12 400 ft-lbf/ft^3 (600 kN-m/m^3)). ASTM D698-e2, West Conshohocken
10. ASTM (2011) Standard test method for direct shear test of soils under consolidated drained conditions. D3080, West Conshohocken
11. ASTM (2011) Standard test methods for one-dimensional consolidation properties of soils using incremental loading. ASTM D2435, West Conshohocken
12. ASTM (2012) Standard test methods for laboratory compaction characteristics of soil using modified effort (56,000 ft-lbf/ft^3 (2,700 kN-m/m^3)). ASTM D1557-e1, West Conshohocken
13. ASTM (2014) Standard test method for repetitive static plate load tests of soils and flexible pavement components, for use in evaluation and design of airport and highway pavements. D1195/D1195(M)-09, West Conshohocken
14. ASTM (2014) Standard test methods for specific gravity of soil solids by water pycnometer. ASTM D421, West Conshohocken
15. ASTM (2013) Standard test methods for cyclic triaxial test of soils. ASTM D5311-M13, West Conshohocken
16. Carrier WD, III, Olhoeft GR, Mendell W (1991) Physical properties of the lunar soil. In: Heiken G, Vaniman D, French B (eds) Lunar sourcebook: a user's guide to the Moon. Cambridge, University Press, New York, pp 475–594
17. Florez E, Roslyakov S, Iskander S, Baamer M, Iskander M (2015) Geotechnical properties of BP-1 lunar regolith simulant. J Aerosp Eng 28(5):04014124
18. He C, Zeng X, Wilkinson A (2013) Geotechnical properties of GRC-3 lunar simulant. J Aerosp Eng 26(3):528–534
19. Ishigami G, Miwa A, Nagatani K, Kazuya Y (2007) Terramechanics-based model for steering maneuver of planetary exploration rovers on loose soil. J Field Robot 24:233–250
20. Jiang MJ, Li LQ, Liu F, Sun YG (2012) Properties of TJ-1 lunar soil simulant. J Aerosp Eng 25(3):463–469

21. Kanamori H, Udagawa S, Yoshida T, Matsumoto S, Takagi K (1998) Properties of lunar soil simulant manufactured in Japan. In: Space 98 Proceeding of 6th international conference and exposition on engineering, construction, and operations in space. ASCE, Reston, VA, pp 462–468
22. Li YQ, Liu JZ, Yue ZY (2009) NAO-1: Lunar highland soil simulant developed in China. J Aerosp Eng 22(1):53–57
23. Liu J, Gao H, Deng Z (2009) Mechanical analysis of a drum-type wheel rolling on loose sandy soil. J Harbin Eng Univ 30:1029–1034
24. Marzulli V, Cafaro F (2019) Geotechnical properties of uncompacted DNA-1A lunar simulant. J Aerosp Eng 32(2):04018153
25. Matsushima T, Ishikawa T (2014) Particle grading effect on mechanical properties of lunar soil simulant FJS-1. Earth Space. https://doi.org/10.1061/9780784479179.008
26. McKay DS, Carter JL, Boles WW, Allen CC, Allton JH (1991) JSC-1: a new lunar soil simulant. Eng Constr Oper Space IV(2):857–866
27. Mitchell JK, Houston WN (1974) Apollo soil mechanics experiment S-200. Final Report, NASA Contract NAS 9-11266. Space Sciences Laboratory Series 15, Issue 7, University of California, Berkeley
28. Mitchell JK, Houston WN, Scott RF, Costes NC, Carrier WD, Bromwell LG (1972b) Mechanical properties of lunar soil-Density, porosity, cohesion, and angle of internal friction. In: Lunar Science Conference. MIT Press, Houston, pp 3235–3253
29. Oravec HA (2009) Understanding the mechanical behavior of lunar soils for the study of vehicle mobility. Ph.D. thesis, Case Western Reserve University, Cleveland
30. Ryu BH, Wang CC, Chang I (2018) Development and Geotechnical engineering properties of KLS-1 lunar simulant. J Aerosp Eng 31(1):04017083
31. Tao J, Wang L, Wu F (2006) Mechanical analysis of wheel-soil interaction of lunar rover. Mach Des Manuf 12:56–57
32. Yu X, Fang L, Liu J (2012) interaction mechanical analysis between the lunar rover wheel-leg foot and lunar soil. In: International workshop on information and electronics engineering (IWIEE). Procedia Eng 29:58–63
33. Zeng X, He C, Wilkinson A (2010) Geotechnical properties of NT-LHT-2M lunar highland simulant. J Aerosp Eng. https://doi.org/10.1061/(ASCE)AS.1943-5525.0000026,213-218

Dynamic Characterization of Sand of Indo-Bangla Border for Seismic Design

Rajat Debnath, Rajib Saha, and Sumanta Haldar

Abstract Agartala, the capital city of northeastern state Tripura, is growing fast in terms of infrastructural facilities and population due to its global importance by acting as a business corridor for southeast Asian countries through Bangladesh. This region was categorized as Indo-Bangla sedimentary basin which is also identified as a seismically active zone since the number of active faults. Likewise, Chittagong fault has passed near to this region. The present study is an attempt to perform dynamic characterization by performing dynamic laboratory tests on the Holocene age sandy soil collected from different depth as well as varying locations of Agartala. Bender element (BE) tests are carried out on the remolded soil samples. Hence, the present study will offer different dynamic characteristics of sand, which will be helpful to carry out local site effect studies and especially for prediction of severity of liquefaction of this area.

Keywords Sandy soil · Bender element · Shear wave velocity

1 Introduction

Sandy soil of Holocene age was collected from Indo-Bangla seismic region (Fig. 1a, b) to evaluate the liquefaction behavior of soil by evaluating various dynamic parameters by conducting non-destructive (NDT) bender element (BE) test. Though wide variety of results are available on tests conducted on various types of soil ([1, 2], [14],[15],[16]), however, limited work has been carried out on the soil available in the Indo-Bangla region, since the local geology plays a pivotal role in determining the characteristics, nature, and type of soil. Exploratory borehole (BH) was conducted at the site to evaluate the subsoil profile, since the region falls under a highly active

R. Debnath · R. Saha (✉)
Civil Engineering Department, NIT Agartala, Tripura 799046, India
e-mail: rajib.iitbbsr@gmail.com

S. Haldar
School of Infrastructure, IIT Bhubaneswar, Odisha 752050, India
e-mail: sumanta@iitbbs.ac.in
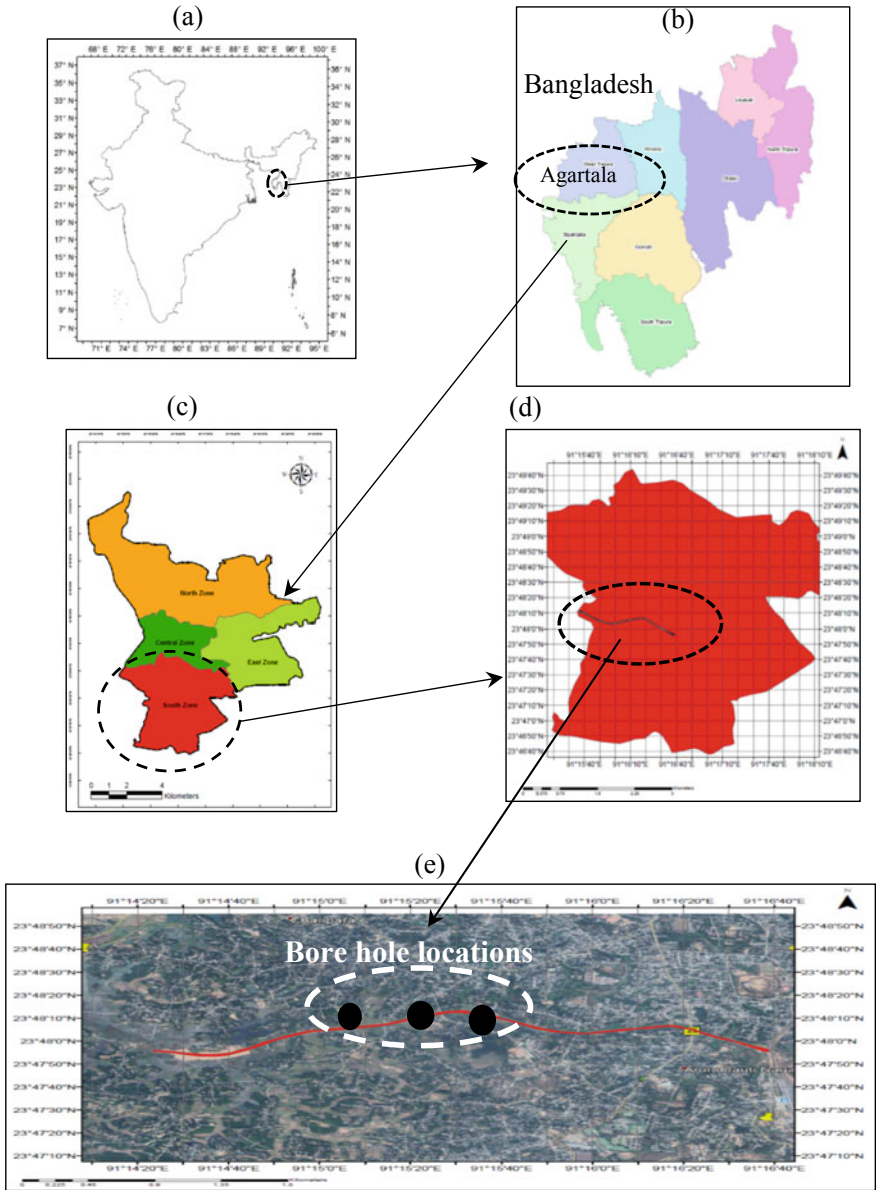
Fig. 1 **a** India map, **b** Tripura map, **c** Agartala map, **d** location of site, **e** location of bore holes for sample collection

seismic region, hence detailed investigation of soil is highly essential for evaluating the response of soil at different frequencies and for evaluating important dynamic properties such as V_s and G_{max}.

Disturbed soil (DS) samples collected from site falling within the coordinates 91° 15′ 0″ E to 91° 15′ 40″ E and 23° 48′ 0″ N to 23° 48′ 20″ N as shown in Fig. 1c were undergone laboratory investigation to ascertain both static and dynamic parameters which would play a vital role in assessing the dynamic behavior of soil and thus these characteristics would play a vital role in assessing the response of soil during liquefaction. Since the region falls under seismic region V, this study would help in assessing the behavior of soil under dynamic loads.

2   Seismological Overview of Indo-Bangla Region

Indo-Bangla region, falling with the northeastern state of Tripura, as shown in Fig. 1a is one of the most active and the region is densely populated and Agartala city which falls within this region with the coordinates (23.75°–23.90° N and 91.25°–91.35° E), as shown in Fig. 1, falls under highest zone V as per the seismic zoning map of Bureau of Indian Standards (BIS 2002). Sylhet trough of Indo-Bangla region being a tectonically complex province comprising of Mesozoic and Cenozoic age sedimentary rock. Sylhet trough is being developed by the movement of Shillong massif in the north, westward propagation of Indo-Burman mobile belt. Sedimentary sequence encountered in the formation is divided into following lithostratigraphic units, from oldest to youngest comprising of Bhuban (1194 m) and Bokabil (798 m), which are formations of Surma group (Miocene age), followed by Tipam sandstone (646 m) and Girujan clay (411 m) which are of Tipam group of Mio-Pliocene age followed by youngest formation of Duptila of Plio-Pleistocene age.)

Disturbed samples of sand were collected from this region from locations as shown in Fig. 1c. Several EQs have occurred in the past, [20], due to these faults thus making this region one of the most seismically vulnerable regions of the world. Some major EQs which have occurred due to the faults are 1869 Cachar EQ ($M_w = 7.5$) due to plate boundary-2 fault of moment magnitude, 1885 Bengal EQ ($M_w = 7.0$) due to Modhupur fault, 1897 Great Indian EQ ($M_w = 8.1$) due to Dauki fault, and 1918 Srimangal EQ ($Mw = 7.6$) due to plate boundary-2 fault are some of the major EQs which have occurred in this region. Any important structure which is built in this region, especially lifeline structures, detailed dynamic laboratory investigation needs to be conducted to prevent the structure from any future damage and the present study focuses on evaluating dynamic parameters that would enable in assessing the response of the collected samples.

3   Laboratory Investigation

3.1   Sample Preparation

Disturbed samples obtained from field by subsoil investigation by standard penetration test (*SPT*) as shown in Fig. 2a, three borings were conducted at the site, and the locations of three boreholes are shown in Fig. 1e, and experimental investigations were conducted on the samples collected to determine physical and engineering parameters of soil. In order to determine shear strength parameters of sandy soil specimens collected as shown in Fig. 2c, soil specimens were prepared in the laboratory by tamping method in three layers at the required relative density for the consolidated undrained (*CU*) triaxial test. For evaluating dynamic parameters by BE method, samples were prepared in cylindrical moulds at the required relative density by tamping method at a height (*H*) to diameter (*D*) ratio of 1:2, as shown in Fig. 2c.

3.2   Evaluation of Static Parameters

Water content of the soil was determined by oven drying the sandy soil at 105 °C as shown in Table 1, to determine the grain size sieve analysis were performed to evaluate the type of sandy soil as shown in Fig. 3a, as per IS:2720 (Part 4), from the results obtained from sieve analysis it showed that the soil samples contained sand percentage ranging from 95 to 98%, and the sands obtained were well graded in nature, coefficient of uniformity (C_u), and coefficient of curvature (C_c) along with other physical properties are shown in Table 1.

Shear strength parameters were measured along with the rate of change of pore water pressure (PWP), variation of PWP versus shearing strain at varying confining pressure (CP) are shown in Fig. 3b.

3.3   Evaluation of Dynamic Parameters

V_s of soil was evaluated by performing BE test, as shown in Fig. 4. Cylindrical samples were prepared by the tamping method keeping *H/D* as 1:2. Piezoelectric BE elements were used for determining V_s, at strains in the range of 10^{-6}, which is well within the elasticity of most of the soils, since its first usage [3–5]. BE are mounted at the top and bottom of a triaxial apparatus as shown in Fig. 2e and the signals are being transmitted through these piezoceramic BE. The length traveled by the signal is the height of the soil sample, which is being referred to as length of travel time (L_{tt}) and the corresponding time required to travel that length which is recorded in the digital oscilloscope, which in turn helps in evaluating the shear
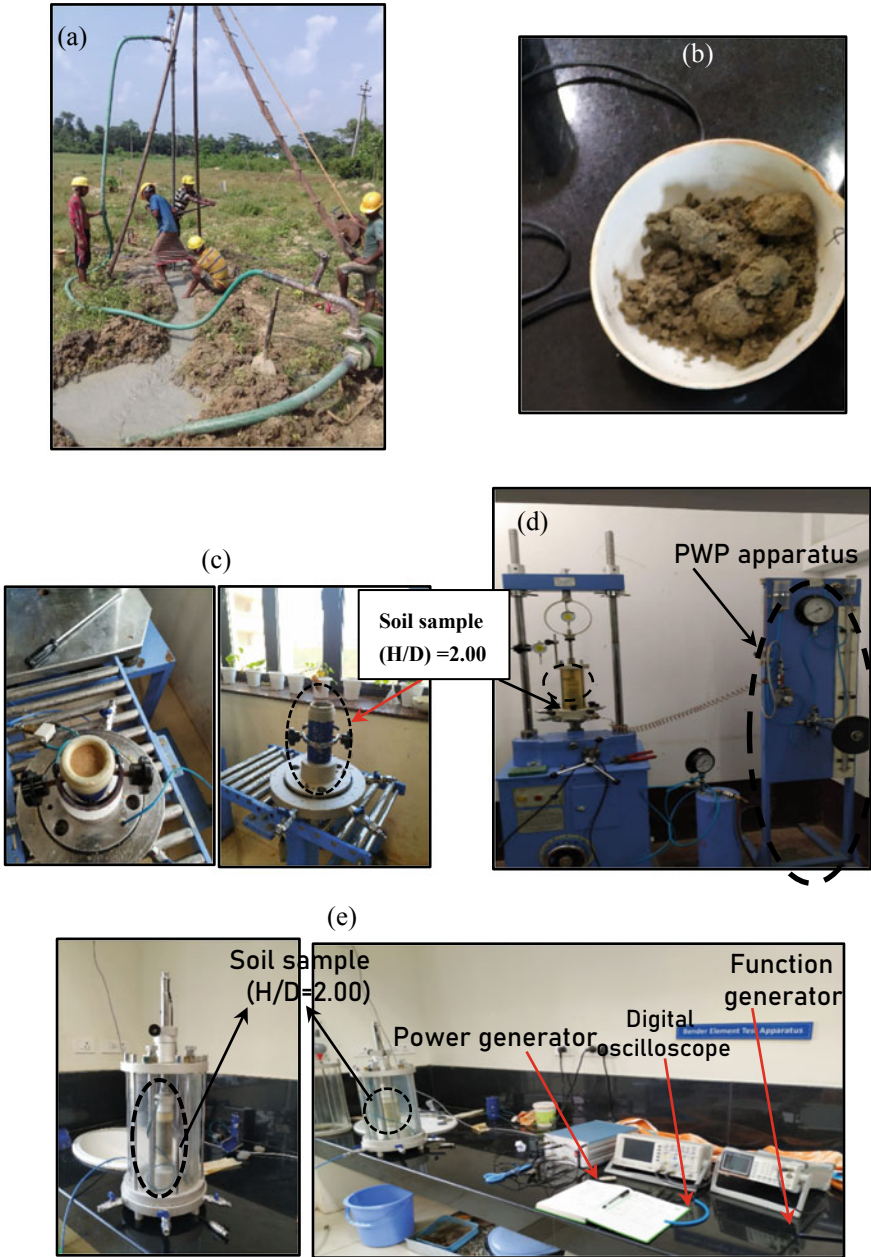
Fig. 2 a Collection of samples from site. **b** Disturbed sand samples. **c** Samples prepared by tamping method. **d** Triaxial CU test. **e** Bender element test

Table 1 Index properties of cohesionless soil

Soil type	Specific gravity, G_s	Coefficient of uniformity, C_u	Coefficient of curvature, C_c	USCS classification
LS-1	2.66	7.23	2.01	SM
LS-2	2.67	8.11	1.66	SM
LS-3	2.68	6.23	1.45	SM
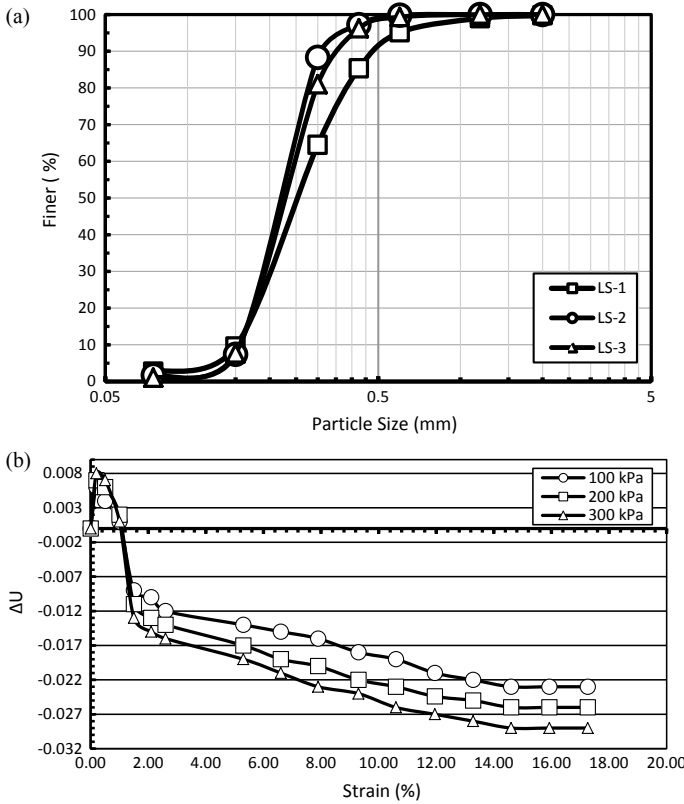
Fig. 3 a Grain size analysis of soil. **b** Rate of change of *PWP* with varying CP

wave velocity of the soil, at varying *CP* and input frequency (f_{in}), ([1, 6–8], [17]). BE producing shear wave is followed by transmission of compression wave and reflected shear wave, being referred to as near field effect. Such near field effect creates difficulty in accurate measurement of the shear wave arrival whose effect can be minimized by enhancing the input frequency ([9], [18]). Keeping near field effects into consideration the present study was conducted at frequency ranging from 0.5 to 5 kHz, where the graphs indicated that with the simultaneous increase of input
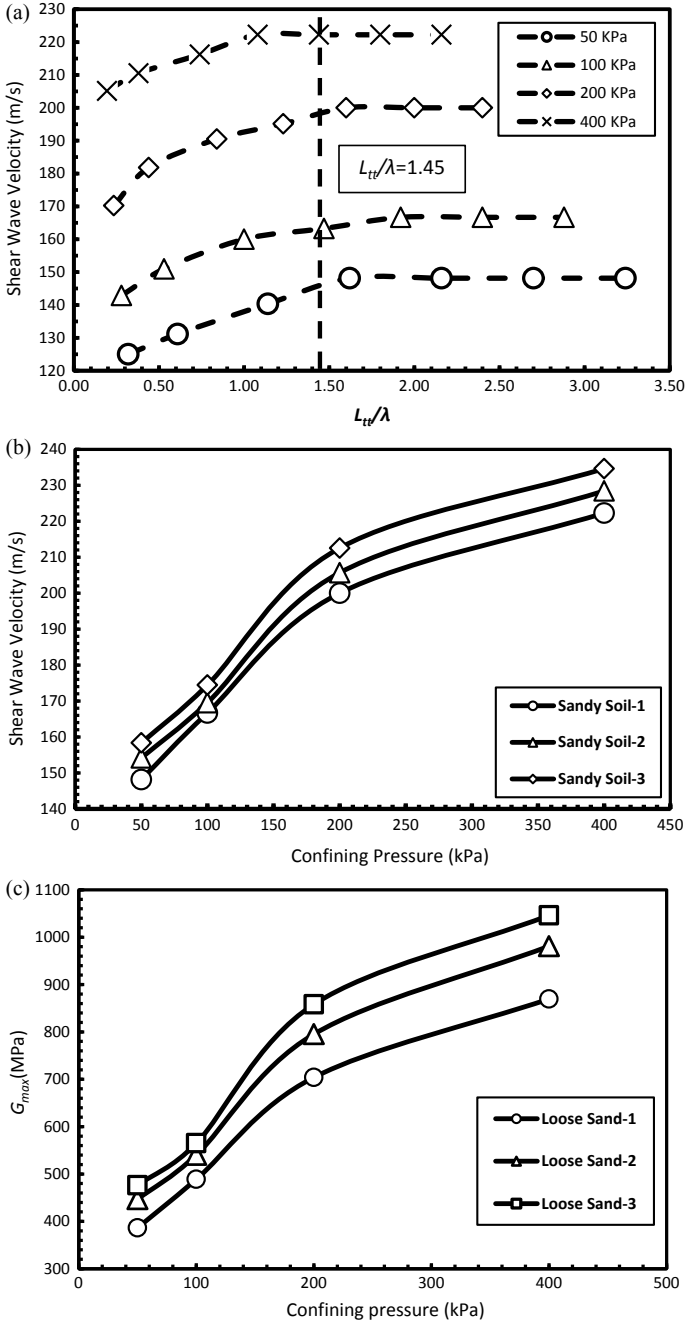
Fig. 4 **a** Sample graphs of L_{tt}/λ for sandy soil. **b** Variation of V_s with CP. **c** Variation of G_{max} with CP

frequency, effects of near field effects are being reduced in evaluating the L_{tt}/λ ratio, which also helps in evaluating V_s by minimizing the near field effect.

4   Results and Discussion

4.1   Wavepath Length to Input Frequency

The ratio of wavelength path (L_{tt}) to that of wavelength (λ) determines the convergence of V_s to a point and constant value is obtained which can be taken into consideration to reduce near field effects. Near field effect gets reduced along with the increase of input frequency and thus L_{tt}/λ plays a vital role in this regard. Various researchers have pointed out various L_{tt}/λ ratio ranging from 1.60 to 8.00 [1, 8, 10– 12]. The dependence on L_{tt}/λ ratio is due to the variation in the values of shear wave velocity and the point at which all the values converge can be taken as the V_s of the respective soil. Values obtained from the graph varied from 1.60 to 1.80 for three sand samples as shown in Fig. 4.

4.2   Shear Wave Velocity

Sand samples were taken into consideration for the present study for the determination of shear wave velocity at input frequencies ranging from 0.50 to 5.00 kHz at confining pressure of 50, 100, 200, and 400 kPa. The reconstituted sample is prepared in case of sandy soil by tamping method, where the soil was tamped to the desired relative density of 0.40, compacting it in three layers. The height and diameter ratio of all the samples were kept at 2.00. From the tests conducted the V_s varied from LS, as shown in Fig. 5.

4.3   Comparison of Field V_s and Experimental V_s

Standard penetration (SPT) tests were conducted in the field to determine the N value, various correlations are provided by various researchers to derive V_s in the field correlating with N value, and graphs of N value along with their corresponding V_s are shown in Table 3. V_s were also determined in the laboratory by BE test, by attaining the similar effective stress under in situ conditions up to a depth of 5.00 m, from where the disturbed sand samples were collected for the sandy samples. V_s were obtained from N value by adopting the correlation proposed by [19] and were compared with the V_s obtained in the laboratory which also validated the V_s values, obtained by the BE test. The values obtained after correlation from the field with the

$$G_{max} = \frac{A \times (P_a)^{1-m}(\sigma_C')}{(0.3 + 0.7e^2)}$$

Fig. 5 Empirical equation of G_{max}

Fitting parameters
A=2905.10
m=0.4041
R²=0.901
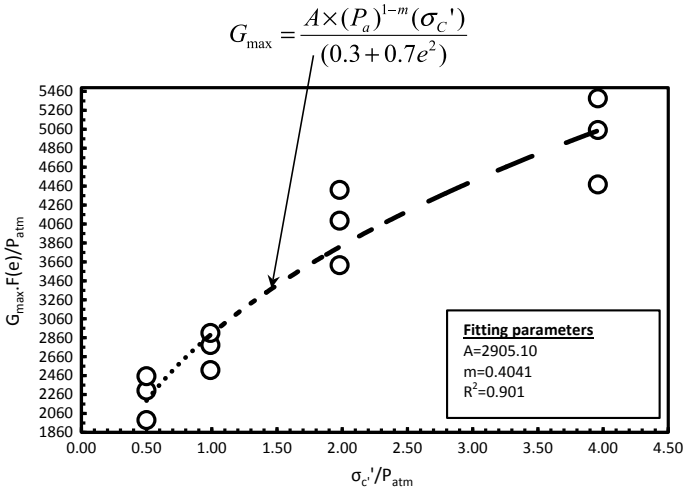
values obtained in the laboratory are shown in Table 2. The correlation proposed by Dikmen which was used for the present study was,

$$V_s = 73N^{0.33}, \text{ for cohesionless soil} \tag{1}$$

Table 2 Shear strength parameters of sandy soil

Nature of soil	Corrected N value	Cohesion, C (T/m²)	Angle of internal friction (°)	γ_{sat} (T/m³)	Void ratio (e_o)
LS-1	11	0	25	1.83	0.52
LS-2	12	0	26	1.85	0.57
LS-3	14	0	28	1.94	0.64

Table 3 Comparison of field V_s (SPT Test) and laboratory (BE test)V_s

Soil type	In situ N value	V_s obtained from correlation with SPT value (m/s)	V_s obtained from BE test (m/s)
LS-1	10	156.07	166.00
LS -2	11	161.06	168.00
LS -3	13	170.18	174.00

4.4   Maximum Shear Modulus

$G_{\max}$ was evaluated from V_s of soil from the elastic wave equation as shown in Eq. 1. $G_{\max}$*plays a vital role in GRA* of soil and plays a vital role in assessing the response of soil to dynamic loads. $G_{\max}$ values were evaluated for LS which varies along with the variation of CP, which are shown in Fig. 4c.

$$G_{\max} = \rho V_s \tag{2}$$

where
ρ = density of soil specimen.

4.5   Empirical Equation of G_{max}

Evaluation of $G_{\max}$ with the help of an empirical equation has been proposed by various researchers and several forms of $G_{\max}$ equations are stated in Bai et al. (2011), Dammala et al. [13]. $G_{\max}$ equations are mainly based on the function of void ratio, atmospheric pressure, and effective stresses. $G_{\max}$ equations formulated by Hardin are one of the most widely adopted formulations by various researchers for its dimensional consistency and can be applied to the soil with varying void ratio. The general form of the equation is stated as.

$$G_{\max} = \frac{A \times (P_a)^{1-m}\left(\sigma'_c\right)}{(0.3 + 0.7e^2)} \tag{3}$$

where $G_{\max}$ is maximum shear modulus (MPa), A is a constant term depended on soil, P_a is standard atmospheric pressure, σ'_c, confining pressure acting on soil specimen, e is the void ratio, m is stress depending factor. In the present study, sandy samples were taken into consideration, and BE tests were performed on the samples at varying confining pressure which was undergone regression analysis to determine the fitting parameters based on Eq. (2). Figure 5 shows the regression analysis of three sandy soil varieties and the various constant parameters such as A, m and with their coefficient of correlation, R^2.

5   Summary and Conclusions

S wave velocities with the help of BE incorporated in a triaxial cell were measured simultaneously at varying confining pressure and input frequencies on three sand samples, which were collected from the Indo-Bangladesh border. Various dynamic parameters were evaluated which can play a vital role in ground response analysis

(*GRA*) of various lifeline structures which is to be constructed at the proposed study area. Various dynamic parameters which are being evaluated are stated below:

(a) Near field effect in case of BE possesses a substantial problem in the determination of actual values, which however can be minimized by increasing the input frequency. For the present study, L_{tt}/λ ratio was obtained for sandy soil whose values ranged from 1.45 to 1.80.
(b) V_s of all the four varieties of soils are evaluated at varying confining pressures and the obtained V_s values were validated with the V_s obtained in the field, by correlation with *SPT-N* value and the results obtained were quite reasonable, which validated the V_s obtained in the laboratory with that of the field.
(c) G_{max} and analytical expressions of G_{max} were evaluated for four soil types which varied from soil to soil, and these values can be utilized for *GRA* of the structure.

References

1. Arulnathan R, Boulanger RW, Riemer MF (1998) Analysis of bender element tests. J Geotech Test J 21(2):120–131
2. Wang Y, Yan W, Lo KF (2007) Laboratory and in-situ measurement of attenuation in soil. In: Viana da Fonseca A, Mayne P (eds) Proceedings of 2nd conference on geotechnical and geophysical site characterization, vol 2. Porto, Mill press, Rotterdam, pp 1883–1889
3. Shirley DJ (1978) An improved shear wave transducer. J Acoust Soc Am 63(5):1643–1645
4. Shirley DJ, Hampton LD (1978) Shear wave measurements in laboratory sediments. J Acoust Soc Am 63(2):607–613
5. Jovičić V, Coop MR, Simić M (1996) Objective criteria for determining Gmax from bender element tests. J Geotechn 46(2):357–362
6. Dyvik R, Madshus C (1985) Lab measurements of Gmax using bender element. In: Proceedings of ASCE convention on advances in the art of testing soils under cyclic conditions, pp 186–196
7. Pennington D, Nash D, Lings M (1997) Anisotropy of G0 shear stiffness in Gault clay. J Geotechn 47(3):391–398
8. Arroyo M, Wood DM, Greening PD (2003) Source near-field effects and pulse tests in soil samples. J. Geotechn 53(3):337–345
9. Lee JS, Santamarina J (2005) Bender elements: performance and signal interpretation. J Geotech Geoenviron Eng 131(9):1063–1070
10. Brignoli EGM, Gotti M, Stokoe KH II (1996) Measurement of shear waves in laboratory specimens by means of piezoelectric transducers. J Geotech Test J 19(4):384–397
11. Brocanelli D, Rinaldi V (1998) Measurement of low-strain material damping and wave velocity with bender elements in the frequency domain. J Can Geotech J 35(6):1032–1040
12. Sánchez-Salinero I, Roesset JM, Stokoe KH (1987) Analytical studies of body wave propagation and attenuation. Rep. No. GR 86–15, University of Texas at Austin, Austin
13. Dammala PK, Krishna AM, Bhattacharya S et al (2017) Dynamic soil properties for seismic ground response studies in Northeastern India. J Soil Dyn Earthq Eng 100(1):357–370
14. Leong EC, Yeo SH, Rahardjo H (2005) Measuring shear wave velocity using bender elements. Geotech Test J 28(5):488–498
15. Devi RD, Sahu RB, Mukherjee S (2015) Shear strength of organic clay in Kolkata Region. Indian Geotech J 45(1):25–34
16. Gu X, Yang J, Huang M (2013) Laboratory measurements of small strain properties of dry sands by bender element. Soils Found 53(5):735–745

17. Fioravante V, Capoferri R (2001) On the use of multi-directional piezoelectric transducers in triaxial testing. Geotech Test J 24(3):243–255
18. Lings ML, Greening PD (2001) A novel bender/extender element for soil testing. Géotechnique 51 (8):713–717
19. Dikmen Ü (2009) Statistical correlations of shear wave velocity and penetration resistance for soils. J Geophys Eng 6(1):61–72
20. Saha R, Debnath R, Dash S, Haldar S (2020) Engineering Reconnaissance Following the Magnitude 5.7 Tripura Earthquake on January 3, (2017). J Perform Construct Facilit 34:504–510
21. Bai L (2011) Preloading effects on dynamic sand behavior by resonant column tests. Doctoral thesis, Technischen Universität Berlin

Effect of Matric Suction and CSR on Dynamic Response of Expansive Soil

Naman Kantesaria and Ajanta Sachan

Abstract The unsaturated shear behaviour of soil is governed by the presence of negative pore water pressure or matric suction (u_a-u_w). Based on the distribution of solid, water and air phases, the soil–water characteristics curve (SWCC) is divided into three zones such as (1) boundary effect zone, (2) transition zone and (3) residual suction zone. The dynamic shear behaviour of soil in these three zones is entirely different due to their particular suction characteristics. However, this aspect of expansive soil has not been explored yet. Expansive soil has a very wide range of suction variation from 0 to 10,00,000 kPa. Hence, the aim of the current study is to evaluate the dynamic response of Nagpur expansive soil subjected to variation of matric suction and cyclic stress ratio (CSR). A series of stress-controlled cyclic simple shear (CSS) tests were carried out on the compacted specimens of Nagpur expansive soil at varying CSR (0.1, 0.3, and 0.5) and degree of saturation (30, 50, 70, and 95%). SWCC of Nagpur soil was determined through the filter paper method, and the saturation values for CSS tests were chosen to cover all the three zones of SWCC. Shear modulus was found to increase with the increase in matric suction until residual suction zone arrived. However, it decreased with further increase in matric suction. Rate and magnitude of stiffness degradation were observed to reduce with the decrease in CSR for complete matric suction range of Nagpur expansive soil. Dissipated cumulative strain energy and cumulative cyclic shear strain were maximum for lowest matric suction specimens for all CSRs.

Keywords Unsaturated expansive soil · Dynamic behaviour · Soil–water characteristic curve (SWCC) · Shear modulus · Damping ratio

N. Kantesaria (✉) · A. Sachan
Civil Engineering Department, Indian Institute of Technology Gandhinagar, Gandhinagar, India
e-mail: naman.kantesaria@iitgn.ac.in

A. Sachan
e-mail: ajanta@iitgn.ac.in

1   Introduction

The arid and semi-arid regions of the world have natural hydraulic datum at a very large depth. The soils above the natural hydraulic datum remain unsaturated, and their mechanical behaviour is diverse with conventional soil mechanics. This behaviour is due to the presence of negative pore water pressure or matric suction (u_a-u_w), generated through capillarity and surface tension. In the past, several researchers [1–5] studied the various methods of matric suction measurement, development of soil–water characteristics curve and relation of these properties to monotonic shear strength parameters (c and φ). However, very limited research has been done to study the influence of suction on dynamic behaviour of unsaturated soils. Understanding of unsaturated dynamic shear behaviour of soil is extremely important for the design and analysis of several geotechnical structures. Chin et al. [6] investigated the cyclic behaviour of unsaturated silt under suction-controlled simple shear condition with maximum suction range of 200 kPa. They found increase in shear modulus and reduction in damping ratio with increase in matric suction. Hosseini et al. [7] performed suction-controlled triaxial tests to study the monotonic, cyclic and post-cyclic behaviour of low plasticity clay (CL) under the maximum applied suction of 90 kPa. Shear strength and shear modulus were found to increase with the increase in confining pressure and initial suction. Le and Ghayoomi [8] conducted a series of suction-controlled cyclic simple shear tests to investigate strain-dependent dynamic properties of unsaturated sands. They applied maximum of 10 kPa matric suction and concluded that the volumetric strain generation is partially saturated sand was lower than that of saturated sand. Pandya and Sachan [9] conducted a series of cyclic triaxial tests on unsaturated specimens of Ahmedabad cohesive soil to investigate the effect of matric suction and initial static loading. They found significant improvement in shear modulus with matric suction and initial static loading. These previous studies were mainly focused on the cohesionless to low plasticity cohesive soils under extremely low suction range. However, geotechnical engineers often come across the high plasticity expansive soil during the construction of earthen dams, road-railway embankments, levees, canals, building foundations, etc. These soils have very wide range of matric suction ranging from 0 to 1,000,000 kPa [2]. Hence, it becomes very important to understand the dynamic behaviour of these soils under wide range of matric suction and loading conditions.

The objective of the current study is to evaluate the dynamic behaviour of Nagpur expansive soil under the influence of different initial matric suctions and cyclic stress ratios (CSRs). A series of stress-controlled cyclic simple tests were performed on the Nagpur soil at four different degrees of saturations (30, 50, 70 and 95%) and three different CSR values (0.1, 0.3 and 0.5). The attempt was made to explain the dynamic response of Nagpur soil with distinct characteristics of SWCC.

2 Material Properties and Specimen Preparation

Soil used in the current study was collected from left bank canal of Gosikhurd dam, Nagpur (India). The grain size distribution of Nagpur soil indicated the presence of 6% sand, 34% silt and 60% clay. The liquid limit, plastic limit and specific gravity were obtained as 77%, 28.5% and 2.74%, respectively. The soil was classified as clay with high plasticity (CH type) according to Indian standard soil classification system. The differential free swell index (DFSI) of Nagpur soil was determined as 123% and that indicated the soil to be highly expansive soil [10]. The compacted specimens for both the filter paper tests and cyclic simple shear (CSS) tests were prepared by moist tamping method [11, 12] at constant dry density of 1.34 g/cc. The 75 mm diameter and 25 mm height specimens for filter paper tests were prepared at different water contents ranging from 11.4 to 36.2% (S_r = 30 to 95%). However, the water content (w) of the CSS specimens was varied as 11.4%, 19.0%, 26.6% and 36.2% to achieve the required degree of saturation (S_r) of 30%, 50%, 70% and 95%, respectively. The diameter and height of CSS specimens were kept as 70 mm and 20 mm, respectively.

3 Experimental Programme

3.1 Filter Paper Test (Matric Suction)

Matric suction of Nagpur expansive soil was determined by conducting in-contact filter paper tests as per ASTM D5298-10 [11]. An oven-dried Whatman 42 (ashless) filter paper of 55 mm diameter was sandwiched between two 60 mm diameter filter paper to prevent centre filter paper from soil contamination. This stake of filter papers was then carefully placed between two prepared soil specimens of equal dry density and water content. The proper contact between the soil specimens and filter papers was assured by sealing this assembly through electric tap from side and top. These prepared samples were then put inside the temperature-controlled incubator for seven days to acquire equilibrium. The temperature during seven-day equilibrium period was maintained as constant 20 °C. After seven days, the middle filter paper was carefully removed and its water content was determined accurately with weighing it using balance precision of 0.0001 g. The soil suction was then determined through the calibration curve given in ASTM code for Whatman 42 filter paper. To ensure repeatability, matric suction of each soil specimen was measured twice.

3.2 Cyclic Simple Shear Test

The cyclic simple shear (CSS) tests were carried out in the Norwegian Geotechnical Institute (NGI)-type cyclic simple shear set-up as per ASTM D6528-17 [12]. The prepared specimen was transferred in the CSS mould having pin-typed base plate. The mould contains several small thickness Teflon rings with very low friction to allow the specimen to shear in any possible weak plane. The 100 kPa normal pressure is then applied and allowed specimen to undergo compression in $K0$ condition. The stress-controlled shearing was then applied at three different cyclic stress ratios (CSRs) of 0.1, 0.3 and 0.5, at a constant loading frequency of 1 Hz. The CSR is defined as Eq. (1).

$$\text{CSR} = \frac{\text{Shear Stress}}{\text{Normal Stress}} = \frac{\tau}{\sigma_N} \tag{1}$$

The detailed experimental programme with test number is mentioned in Table 1. The specimen height was kept constant during the process of shearing by controlling axial displacement as constant with the accuracy of 0.5μ (0.0025%). Each specimen (except $T9$ and $T12$) was subjected to 1000 cycles of uniform sinusoidal dynamic loading.

Table 1 Dynamic shear strength parameters of unsaturated Nagpur expansive soil

Test series	Test number	CSR	S_r	u_a-u_w (kPa)	G (kPa)	D (%)	Cumulative ΔW (kJ/m³)	Cumulative γ_{cy} (%)
S1	T1	0.1	30	19,062	14,178	27	11	0.07
	T2		50	4279	14,013	27	12	0.07
	T3		70	1548	11,865	28	14	0.09
	T4		95	48	8739	29	22	0.13
S2	T5	0.3	30	19,062	10,197	29	152	0.31
	T6		50	4279	12,668	27	122	0.25
	T7		70	1548	8996	29	210	0.43
	T8		95	48	3056	33	1377	2.89
S3	T9	0.5	30	19,062	6751	35	112	13.99
	T10		50	4279	9279	28	9	0.57
	T11		70	1548	8614	31	10	0.59
	T12		95	48	922	43	418	23.53

Fig. 1 Soil–water
characteristic curve (SWCC)
of Nagpur expansive soil
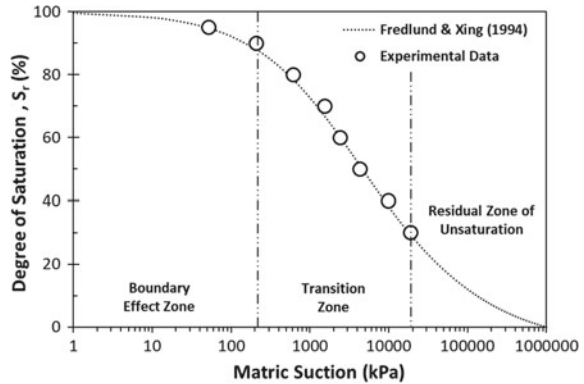
4   Results and Discussions

4.1   Soil–Water Characteristics Curve (SWCC)

The soil–water characteristics curve (SWCC) of Nagpur expansive soil determined
through filter paper tests is plotted in Fig. 1. The SWCC gives the relation between
soil moisture and matric suction. In the present study, SWCC was expressed in terms
of degree of saturation (S_r) and matric suction (u_a-u_w). To cover the entire range
of matric suction, the mathematical fit given by Fredlund and Xing [13] was used
and shown as dotted line in Fig. 1. The air-entry value (AEV) and residual degree
of saturation (S_r)$_r$ were estimated as 210 kPa (at S_r = 88%) and 30%, respectively
[2]. The residual suction value at (S_r)$_r$ = 30% was found to be 19,062 kPa. Based
on these values, the SWCC was divided into three zones: (1) boundary effect zone
(S_r > 88%), (2) transition zone (30% < S_r < 88%) and (3) residual suction zone (S_r
< 30%). These three zones are basically characterized by their distinct moisture–
suction relationship, and they had significant effect on shear behaviour of soil [2, 14,
15]. Hence, the saturation values were selected in such a way that it covered all the
three zones of SWCC for CSS tests on compacted Nagpur soil.

4.2   Hysteresis Behaviour and Cyclic Shear Strain Accumulation

Cyclic stress–strain behaviour as hysteresis response for series $S1$, $S2$ and $S3$ is shown
in Fig. 2a–c, respectively. Each figure shows the variation in hysteresis loops for first
10 loading cycles, as a function of initial matric suction and CSR. At lower CSR of 0.1
(series S1), the inclination of loops decreased with increase in initial matric suction.
The highest angle (rotation angle) between hysteresis loop and horizontal axis was
observed for specimen with highest matric suction ($T1$). For higher CSR in series
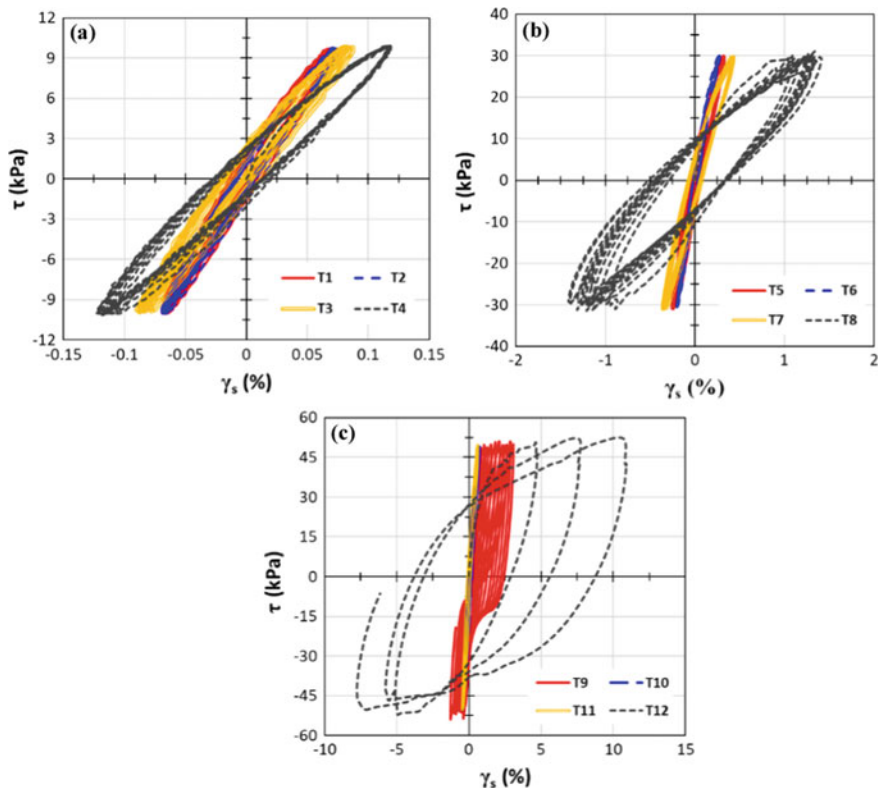
Fig. 2 Hysteresis shear response of Nagpur soil. **a** Series $S1$, **b** series $S2$, **c** series $S3$

$S2$ and $S3$, the rotation angle of hysteresis response was found to be increased with increase in initial matric suction up to $S_r = 50\%$ $\{(u_a\text{-}u_w) = 4279 \text{ kPa}\}$. However, rotation angle again decreased for $S_r = 30\%$ specimen. The expansion of loops with each repeated loading cycles was observed to be profound for higher CSRs due to large degradation of soil structure at higher applied load. However, the specimens whose initial matric suction lied in the transition zone range did not show significant degradation or expansion in hysteresis behaviour at all CSR levels. The loops were almost symmetric with respect to shear strain for series $S1$, and it indicated that the large component of total strain generation remained elastic. However, the development and accumulation of plastic strain component might shift the hysteresis loops in one direction significantly for the specimens of 0.3 and 0.5 CSRs.

The accumulated cyclic shear strain (γ_{cy}) with number of loading cycles is shown in Fig. 3a–c for series $S1$, $S2$, and $S3$, respectively. The maximum accumulated strain and its relation to initial matric suction for all CSR are presented in Fig. 3d and Table 1. For all the three series, highest accumulated shear strain at any number of loading cycle was found in the specimens with lowest initial matric suction$\{(u_a\text{-}u_w) = 48 \text{ kPa}\}$. Matric suction added additional force to hold the particles together
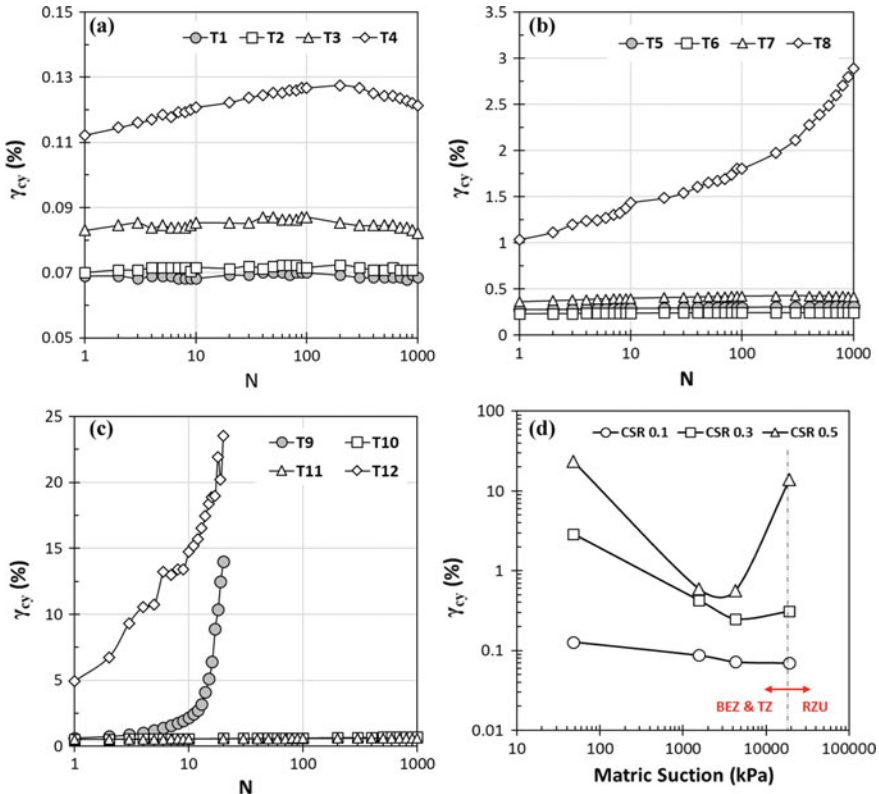
Fig. 3 Effect of initial matric suction and CSR on cumulative strain response of Nagpur soil. **a** Series S1, **b** series S2, **c** series S3, **d** summarized curve

and it reduced the particle deformation. However, at very high suctions greater than residual suction value, the net contribution of suction might reduce the load carrying capacity of soil and displayed excessive deformation. This could be due to the uneven and localized distribution of matric suction and loss of capillary necks within the soil mass at very low water content [14, 16, 17]. This phenomenon was observed for the compacted specimens of $T5$ and $T9$ at higher CSR of 0.3 and 0.5, respectively (Fig. 3d). However, for low load application as in the case of CSR 0.1, the clay buttress phenomena in $T1$ specimen might have prevented the excessive deformation and increased the stiffness [18]. The limiting shear strain ($\gamma_s > 10\%$) was adopted as failure criteria in the present study. Only two specimens, $T9$ and $T12$, reached the shear strain of 10% and failed at 4 and 18 loading cycle (N), respectively. All other specimens completed the 1000 loading cycles with gradually increased shear strain (Fig. 3).

4.3   Dynamic Parameters

Shear modulus (G) at different numbers of loading cycles was evaluated as per Eq. (2).

$$G = \frac{\tau_1 + \tau_2}{\gamma_1 + \gamma_2} \tag{2}$$

where τ_1 and τ_2 are maximum and minimum shear stresses at each loading cycle; γ_1 and γ_2 are shear strain corresponding to τ_1 and τ_2, respectively. The calculated shear modulus for each loading cycle is plotted in Fig. 4a–c for series $S1$, $S2$ and $S3$, respectively. Shear modulus (G) was found to increase significantly with increase in initial matric suction till it reached the residual suction value (Table 1). Thereafter, the value of shear modulus for $T5$ and $T9$ specimen decreased with further increase in matric suction. Highest shear modulus (G) of 14,178 kPa was found for $T1$ specimen at lowest CSR of 0.1. As CSR increased from 0.1 to 0.5, the soil structure exhibited
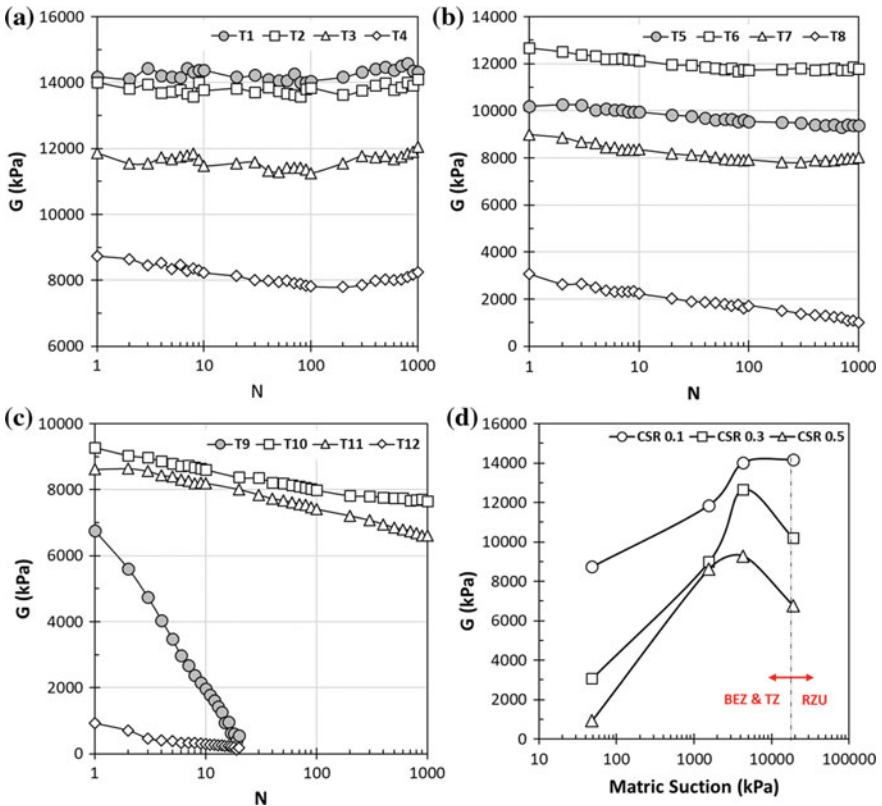
Fig. 4 Effect of initial matric suction and CSR on shear modulus of Nagpur soil. **a** Series $S1$, **b** series $S2$, **c** series $S3$, **d** summarized curve

higher shear stress leading to higher degradation in particle structure. Hence, the shear modulus of $S1$ was observed to be higher as compared to $S3$ and $S5$. The degradation in shear modulus with number of loading cycles was evident in series $S5$ due to higher plastic strain accumulation with each cycle of loading. The maximum decrease in 'G' value was observed to be 92 and 80% for T5 and T9 specimens, respectively, with repeated loading cycles. The shear modulus variation with initial matric suction for each CSR is presented in Fig. 4d.

Damping ratio (D) is the ratio of dissipated strain energy to applied elastic strain energy, and it was estimated based on the equation suggested by Sitharam et al. [19]. Estimated damping ratio as a function of loading cycles and matric suction is shown in Fig. 5. The damping ratio was found to increase with decrease in matric suction for series $S1$ (Fig. 5a). However, due to high plastic deformation and capillary neck breaks, the damping ratio for $T5$ and $T9$ specimen again increased as matric suction reached to the residual state. Highest damping of 43% was obtained for $T12$ specimen under 0.5 CSR loading (Table 1). Matric suction holds the particles together, and it
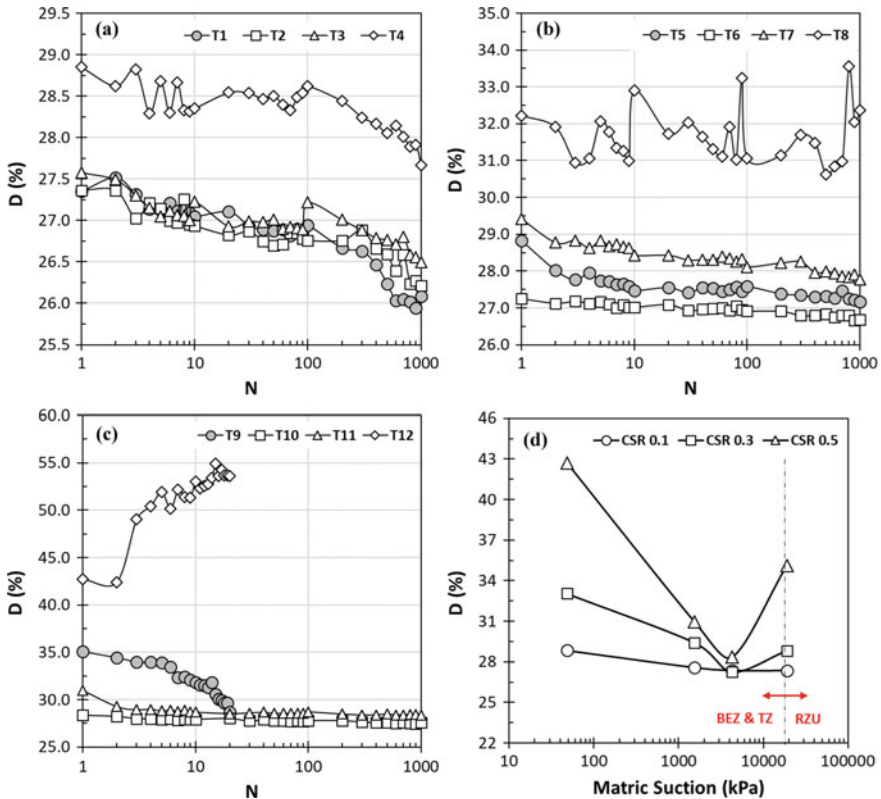
Fig. 5 Effect of initial matric suction and CSR on damping ratio of Nagpur soil. **a** Series $S1$, **b** series $S2$, **c** series $S3$, **d** summarized curve

eventually resisted the particle structure degradation leading to the decreased strain energy dissipation. The increase in CSR exhibited the significant increase in damping at all the matric suction levels. Increase in applied load led to higher particle bond breakage and that resulted in higher damping. Damping ratio was observed to reduce gradually with the number of repeated loading cycles for all the CSR and matric suction values.

4.4 Cyclic Stiffness Degradation

Stiffness degradation during cyclic loading can be characterized by calculating cyclic degradation index ($\delta*$). Mortezaie and Vucetic [20] and Thian and Lee [21] suggested Eq. (3) to calculate the $\delta*$ in stress-controlled loading conditions:

$$\delta* = \frac{G_N}{G_1} \tag{3}$$

where G_N is secant shear modulus at any Nth cycle and G_1 is the secant shear modulus of first cycle. The $\delta*$ variation with number of loading cycles is shown in Fig. 6a–c for series $S1$, $S2$ and $S3$, respectively. Lower degradation index specified higher stiffness degradation and increase in irreversible strain with repeated loading cycles [21]. The lowest values of $\delta*$ were found for two failed specimens of $T9$ and $T12$. The specimens ($T2$, $T3$, $T6$, $T7$, $T10$ and $T11$) that had initial suction in transition zone displayed very less stiffness degradation and that remained consistent for all CSR values. The significant stiffness degradation was observed for the specimens ($T4$, $T8$ and $T12$) with lowest matric suction due to the lack of additional bonding force. The increase in applied load (CSR) also lowered the $\delta*$ values and degradation of stiffness at faster rate. Except CSR 0.1, the reduction in $\delta*$ values with number of cycles was observed to follow the linear relationship.

4.5 Cumulative Energy Dissipation

Dynamic instability of soil mass can also be accessed through cumulative strain energy dissipation concept. Voznesensky and Nordal [22] proposed a procedure to determine the cumulative energy dissipation (ΔW) per unit volume of soil mass during cyclic loading. The same procedure was adopted in the present study to evaluate the energy dissipation response, and it is presented in Fig. 7a–c for series $S1$, $S2$ and $S3$, respectively. The total dissipated energy at the end of shearing stage for all the specimens is listed in Table 1. The total cumulated strain energy was found to increase significantly with decrease in initial suction value till residual state. In $S3$ series, the dissipated cumulated energy at the end of shearing for $T12$ specimen was found to be 46% higher than $T10$ specimen. This difference was
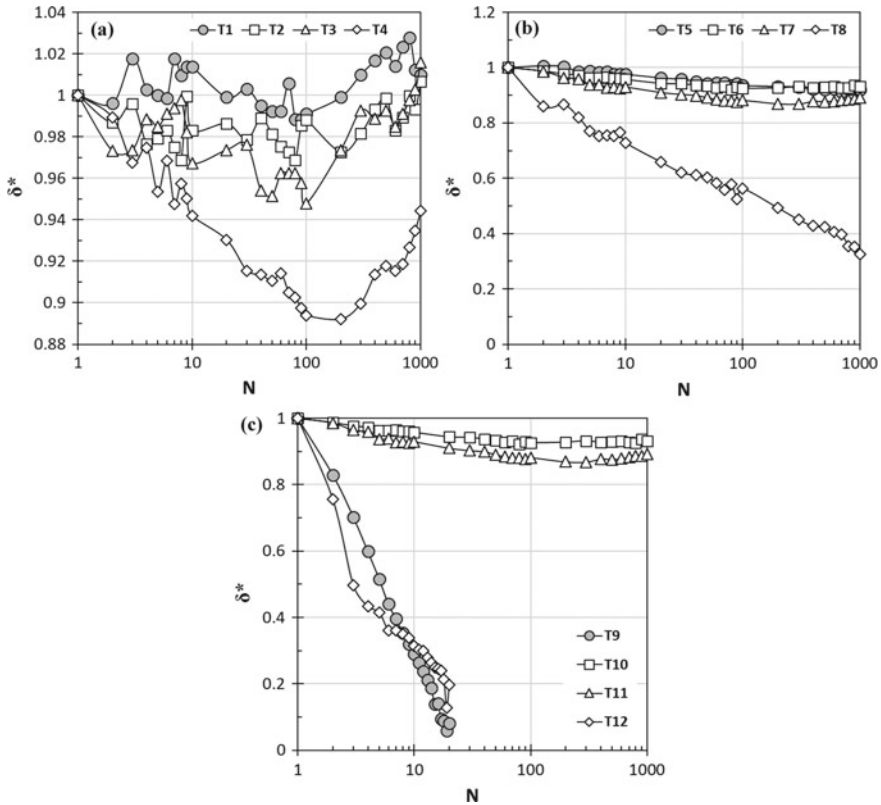
Fig. 6 Effect of initial matric suction and CSR on stiffness degradation response of Nagpur soil. **a** Series $S1$, **b** series $S2$, **c** series $S3$

reduced as 11 and 2% for series $S2$ and $S1$, respectively (Table 1). The strain energy dissipation per loading cycle was observed to increase with repeated loading cycles and CSR. The load repetition in soil mass degraded the particle structure and that caused irreversible strain accumulation. Due to this, the higher energy was dissipated during each successive loading cycle and the stress–strain loops expanded. However, the increase in dissipated energy with loading cycle in specimens of CSR 0.1 was found insignificant, and it is specified that the major strain component remained elastic in nature (Fig. 7a).

5 Conclusions

A series of stress-controlled cyclic simple shear tests were conducted on the unsaturated specimens of compacted Nagpur expansive soil to evaluate the effect of initial
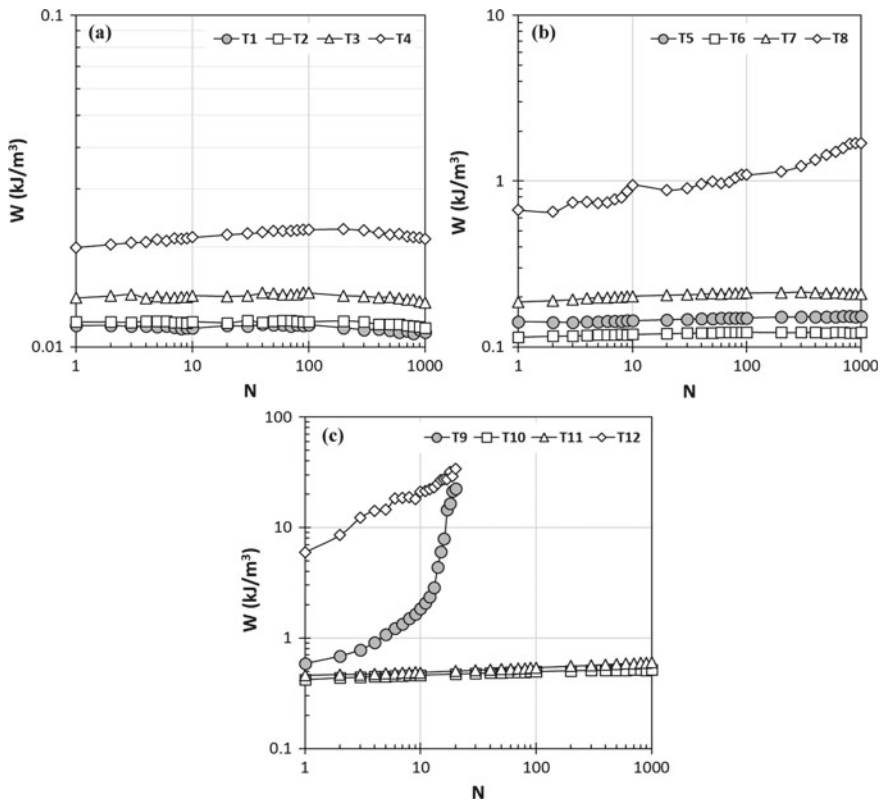
Fig. 7 Effect of initial matric suction and CSR on energy dissipation response of Nagpur soil. **a** Series $S1$, **b** series $S2$, **c** series $S3$

matric suction and CSR on dynamic behaviour of soil. The results were analysed in terms of hysteresis response, shear strain accumulation (γ_{cy}), shear modulus (G), damping ratio (D), cyclic degradation index (δ^*) and cumulative strain energy dissipation (ΔW). The major conclusions of the present study are as follows:

- Hysteresis shear response of soil was significantly governed by initial matric suction state and applied CSR. The inclination of hysteresis loop and shear modulus (G) was observed to increase with increase in CSR and decrease in initial matric suction till residual suction state. In residual suction zone, the compacted soil behaviour changed and displayed the reverse trend for higher applied loading of CSR 0.3 and 0.5.

- Reduction in matric suction caused higher accumulation of shear strain (γ_{cy}) with faster rate.

- Damping ratio (D) was decreased with increase in initial suction during boundary effect zone and transition zone. However, reverse trend was observed in residual suction zone. The increase in CSR led to higher damping ratio at all suction values.

- The amplitude and rate of stiffness degradation ($\delta*$) were found to be higher for lower initial matric suction. The degradation in stiffness was found to increase with the increase in CSR (0.1–0.5).
- The strain energy dissipation was increased with repeated loading cycles. The cumulated dissipated energy (ΔW) at the end of shearing was observed to be the maximum at lowest matric suction.
- The specimens in residual suction zone displayed higher strength and stiffness to dynamic loading at smaller CSR. However, the sudden drop in stiffness was observed when CSR was increased up to a certain value.

References

1. Fredlund DG, Morgenstern NR, Widger RA (1978) The shear strength of unsaturated soils. Can Geotech J 15(3):313–321
2. Fredlund DG, Rahardjo H (1993) Soil mechanics for unsaturated soils. Wiley, New York
3. Rahardjo H, Lim TT, Chang MF, Fredlund DG (1995) Shear-strength characteristics of a residual soil. Can Geotech J 32(1):60–77
4. Tripathy S, Tadza MYM, Thomas HR (2014) Soil-water characteristic curves of clays. Can Geotech J 51(8):869–883
5. Fredlund DG, Vanapalli SK (2002) Shear strength of unsaturated soils. Methods Soil Anal Part 4:329–361
6. Chin KB, Leong EC, Rahardjo H (2009) Cyclic behaviour of unsaturated silt in suction-controlled simple shear apparatus. In: Unsaturated soils, two volume set: experimental studies in unsaturated soils and expansive soils, vol 1, Theoretical and numerical advances in unsaturated soil mechanics, vol 2, p 65
7. Hosseini SMR, Naeini SA, Hassanlourad M (2017) Monotonic, cyclic and post-cyclic behaviour of an unsaturated clayey soil. Int J Geotech Eng 11(3):225–235
8. Le KN, Ghayoomi M (2017) Cyclic direct simple shear test to measure strain-dependent dynamic properties of unsaturated sand. Geotech Test J 40(3):381–395
9. Pandya S, Sachan A (2018) Effect of matric suction and initial static loading on dynamic behaviour of unsaturated cohesive soil. Int J Geotech Eng 12(5):438–448
10. IS: 2911(PART-III) (1980) Indian standard code of practice for design and construction of under-reamed piles, BIS
11. ASTM D5298-10 (2010) Standard test method for measurement of soil potential (suction) using filter paper. ASTM International, West Conshohocken, 2003. https://doi.org/10.1520/D5298-10
12. ASTM D6528-17 (2017) Standard test method for consolidated undrained direct simple shear testing of fine grain soils
13. Fredlund DG, Xing A (1994) Equations for the soil-water characteristic curve. Can Geotech J 31(4):521–532
14. Vanapalli SK, Fredlund DG, Pufahl DE, Clifton AW (1996) Model for the prediction of shear strength with respect to soil suction. Can Geotech J 33(3):379–392
15. Vanapalli SK, Fredlund DG (2000) Comparison of different procedures to predict unsaturated soil shear strength. In Advances in unsaturated geotechnics, pp 195–209
16. Cho GC, Santamarina JC (2001) Unsaturated particulate materials—particle-level studies. J Geotech Geoenviron Eng 127(1):84–96
17. Vesga LF (2009) Direct tensile-shear test (DTS) on unsaturated kaolinite clay. Geotech Test J 32(5):397–409
18. Santamarina JC, Klein KA, Fam MA (2001) Soils and waves. Wiley, New York

19. Sitharam TG, Govindaraju L, Sridharan A (2004) Dynamic properties and liquefaction potential of soils. Curr Sci 87(10)
20. Mortezaie AR, Vucetic M (2013) Effect of frequency and vertical stress on cyclic degradation and pore water pressure in clay in the NGI simple shear device. J Geotechn Geoenviron Eng 139(10):1727–1737
21. Thian SY, Lee CY (2017) Cyclic stress-controlled tests on offshore clay. J Rock Mech Geotech Eng 9(2):376–381
22. Voznesensky EA, Nordal S (1999) Dynamic instability of clays: an energy approach. Soil Dyn Earthquake Eng 18(2):125–133

Effect of Relative Compaction on Dynamic Behaviour of Low Plasticity Cohesive Soil

Adarsh Singh Thakur, Naman Kantesaria, and Ajanta Sachan

Abstract Relative density is commonly used to quantify the looseness or denseness of the in situ soil. However, its determination is not possible in the case of cohesive soils. Hence, relative compaction is used as a governing parameter to represent the different states of natural in situ conditions in cohesive soils. Relative compaction is defined as the ratio of field dry density to the maximum dry density determined by the standard Proctor test. The amount and rate of strength and stiffness degradation of soil under dynamic loading depend largely on their compaction state. The aim of the current study is to evaluate the effect of relative compaction on the dynamic behaviour of low plasticity cohesive soil collected from Chobari Dam, Gujarat. A series of two-way displacement-controlled cyclic triaxial tests and 1D consolidation (oedometer) tests were performed on the specimens of Chobari Dam soil. The specimens were prepared at different relative compactions of 65, 70, 75, 80, 85, 90 and 100%. The hysteresis behaviour of Chobari Dam soil was evaluated based on the variation in shear modulus (G), damping ratio (D) and cyclic stiffness degradation index (δ). Shear modulus was found to increase with the increase in relative compaction, while cyclic stiffness degradation was observed to decrease as relative compaction decreased to 80%. The variation in cyclic stiffness degradation was observed to be insignificant for relative compaction below 80%. Rate of degradation of damping ratio was observed to be reduced with the decrease in relative compaction.

Keywords Relative compaction · Dynamic behaviour · Low plasticity soil · Shear modulus · Damping ratio

A. Singh Thakur (✉) · N. Kantesaria · A. Sachan
Civil Engineering Department, Indian Institute of Technology Gandhinagar, Gandhinagar, India
e-mail: adarsh.thakur@iitgn.ac.in

N. Kantesaria
e-mail: naman.kantesaria@iitgn.ac.in

A. Sachan
e-mail: ajanta@iitgn.ac.in

1   Introduction

The soils in natural conditions are found in states ranging from loosest to densest. Relative density is a commonly used parameter to quantify the density state of cohesionless soil. However, its determination in cohesive soil is difficult due to particle floc formation. Hence, relative compaction is adopted in the present study to quantify the various in situ density states of cohesive soil. Relative compaction (RC) is defined as the ratio of in situ or compacted density of soil to the maximum dry density (MDD) obtained by the standard Proctor test. The dynamic properties of soil including shear modulus, damping ratio and stiffness degradation largely depend on the compaction state of the soil. The assessment of these properties of soil under cyclic loading conditions is essential for the stability analysis of geotechnical structures. In the past, several authors [5, 6, 11, 14, 10, 18–20, 22] investigated the effect of relative density, fine content, soil properties and stress history on dynamic parameters of cohesionless soil. Wang et al. [23] studied the cyclic and post-cyclic behaviour of low plasticity silt and the impact of additional clay content in it. They reported that with increasing clay content, the soil displayed cyclic softening behaviour rather than flow liquefaction. Soralump and Prasomsri [21] studied the cyclic degradation, cyclic pore water pressure generation and volumetric cyclic threshold shear strain on 12 compacted clay specimens. They found a lower generation of pore water pressure in compacted clays than other types of soils at corresponding cyclic shear strain amplitude. Eseller-Bayat et al. [8] studied the combined effect of relative density, plasticity index (PI), fine content and cyclic stress ratio (CSR) on the liquefaction susceptibility of sand. They found that the higher PI and higher relative density reduced the liquefaction potential of sandy soil. Kumar et al. [16] conducted a series of cyclic triaxial tests on low plasticity cohesive soil with two different initial dry densities and water content. Shear modulus reduction and damping ratio were found to be unaffected by initial dry density and water content. Pandya and Sachan [17] investigated the effect of initial void ratio on dynamic response of saturated high plasticity cohesive soil through cyclic triaxial tests. They found a substantial increase in cyclic stiffness of soil with initial densification. The soil used in the present research is a CL-ML type of soil. Boulanger and Idriss [4] illustrated that the soil having properties similar to the tested soil displayed intermediate transitional response between the well-defined 'sand-like behaviour' and 'clay-like behaviour'. However, very limited research has been done to evaluate this transitional behaviour of such soils. Hence, the current research is focused on evaluating the effect of relative compaction on the hysteresis response, stiffness degradation and dynamic properties of saturated low plasticity cohesive soil (CL-ML type) subjected to cyclic loading. A series of strain-controlled cyclic triaxial and oedometer tests were performed on the Chobari dam soil at different relative compaction values (65, 70, 75, 80, 85, 90 and 100%).

Table 1 Compressibility and dynamic parameters of Chobari dam soil

Relative compaction (%)	Initial dry density (g/cc)	Initial void ratio	C_c	r_u	G (MPa)	D (%)	t
65	1.3	1.07	0.182	0.67	10.8	44.2	0.08
70	1.4	0.93	0.164	0.72	12.0	42.2	0.18
75	1.5	0.8	0.156	0.73	11.7	43.8	0.21
80	1.6	0.69	0.150	0.65	13.1	44.4	0.22
85	1.7	0.59	0.132	0.66	13.6	42.0	0.19
90	1.8	0.5	0.072	0.71	16.5	40.3	0.17
100	1.99	0.38	0.054	0.55	21.5	39.2	0.17

2 Material Properties and Specimen Preparation

In the current study, soil was collected from the Chobari Dam, Kutch, Gujarat (India). Grain size distribution tests exhibited the following composition: 48% sand, 42% silt and 10% clay. The specific gravity, liquid limit and plastic limit were obtained to be 2.7%, 23% and 16%, respectively. The soil was classified as CL-ML, as per the Indian Standard Soil Classification System (ISSCS). Standard Proctor test of Chobari soil exhibited the optimum moisture content (OMC) and maximum dry density (MDD) to be 11.6% and 1.99 g/cc, respectively. The specimens at different relative compaction values (65, 70, 75, 80, 85, 90 and 100%) were prepared using moist tamping method, as per ASTM D4767-04 [2]. The corresponding void ratio and initial dry density with respect to relative compaction values of Chobari dam soil are listed in Table 1. The specimens for cyclic triaxial tests (50 mm diameter and 100 mm height) were prepared in three-piece aluminium mould. Six vertical filter strips of 10 mm width were attached with soil specimen to accelerate the process of saturation and consolidation. For oedometer tests, the specimens of 60 mm diameter and 20 mm height were prepared in consolidation ring.

3 Experimental Programme

In the present study, a series of 1D consolidation and two-way strain-controlled cyclic triaxial tests were performed on soil specimens at different relative compactions. In 1D consolidation test, seating load of 5 kPa was applied for 24 h and vertical stresses of 10, 20, 50, 100, 200, 400 and 800 kPa were applied sequentially at an interval of 24 h [15]. Two-way strain-controlled cyclic triaxial tests were performed at an axial strain amplitude of 0.1% and frequency of 1 Hz under the confining pressure of 100 kPa [1]. Submersible load cell of capacity 10 kN, LVDT with the capacity of ±10 mm and 1000 kPa capacity triaxial cell were used in cyclic triaxial setup. The specimens were saturated using two-step process. In first step, water flushing was conducted

and then forced saturation was applied. Both the processes were performed under the effective confining pressure of 20 kPa. Skempton's pore pressure parameter (B) was checked after every increment and was assured to be 0.95 before consolidation to acquire complete saturation. The back pressure till saturation was kept constant as 510 kPa for all the relative compaction specimens to maintain the uniformity. The isotropic consolidation was performed at 100 kPa of effective confining pressure. Strain-controlled cyclic loading in the form of sinusoidal waves was then applied and continued till 250 cycles to study the dynamic behaviour of low plasticity cohesive soil under undrained conditions.

4   Results and Discussions

4.1   Effect of Relative Compaction on Compressibility Behaviour of Chobari Soil

The results of 1D consolidation test at different relative compactions indicated the reduction in compression index (C_c) with the decrease in void ratio (Table 1). The C_c values were reduced from 0.182 to 0.054 with increasing relative compaction values from 65 to 100% (Fig. 1). Analogous response was observed for void ratio versus log (σ') curve, as shown in Fig. 2. The decrease in area of consolidation curve was observed with increasing initial dry density of specimens, which exhibited the reduction in the magnitude of settlement with advancement in closer packing of particles.
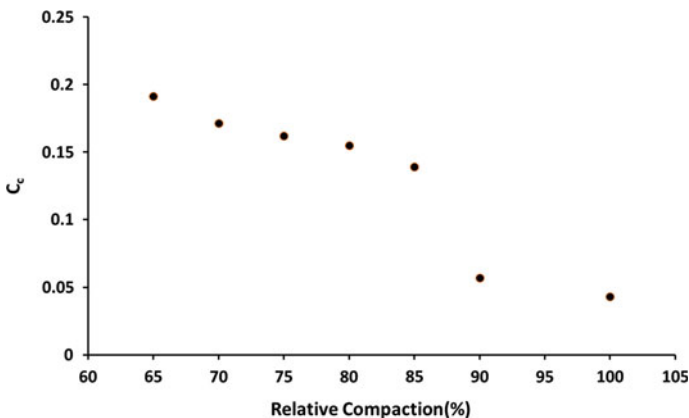
Fig. 1   Variation of compression index (C_c) with different relative compactions
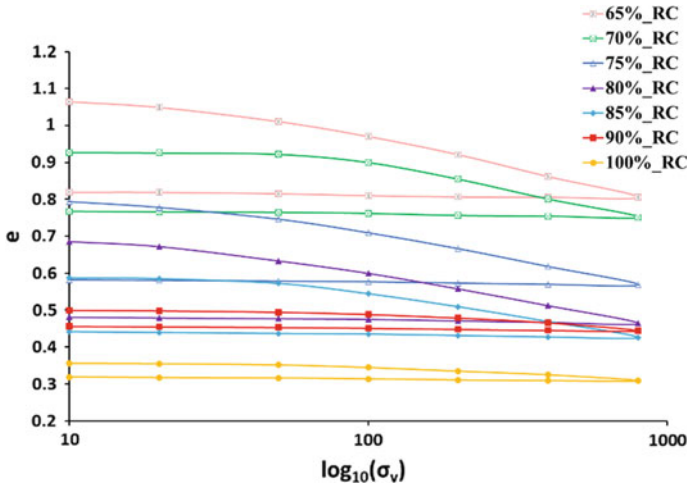
Fig. 2 Consolidation curves of Chobari soil at different relative compactions

4.2 Effect of Relative Compaction on Dynamic Behaviour of Chobari Soil

Hysteresis Response and Pore Pressure Evolution

The hysteresis response of Chobari dam soil at different relative compactions is shown in Fig. 3. All the cyclic triaxial tests were performed up to 250 loading cycles, but only 10 hysteresis loops (10 loading cycles) were shown to analyse the effect
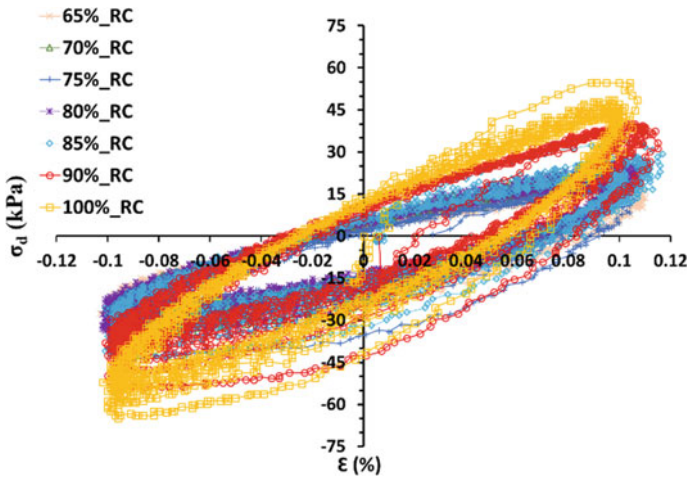
Fig. 3 Hysteresis behaviour of Chobari soil at different relative compactions
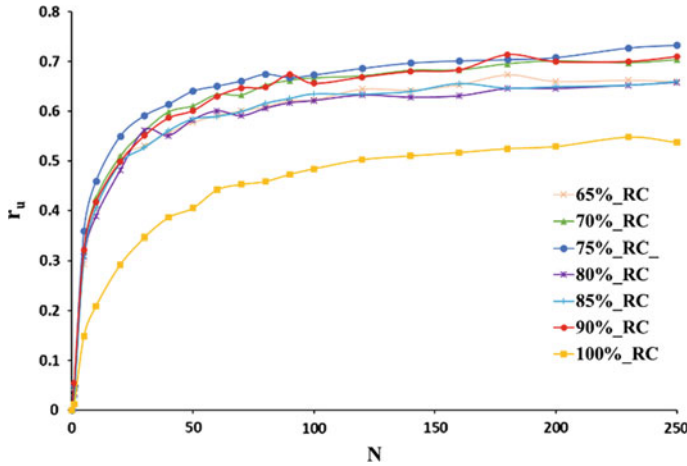
Fig. 4 Pore water pressure ratio (r_u) of Chobari soil at different relative compactions

of relative compaction on dynamic behaviour of Chobari soil. It was observed that the hysteresis loop of each cyclic triaxial test progressed downward as the number of cycles increased, which depicted the stiffness degradation of soil. The inclination of hysteresis loop with horizontal axis (rotation angle) increased with the increase in relative compaction of soil. The increased densification and lower void ratio at higher relative compaction were observed due to better contact forces among soil particles, which led to higher load carrying capacity of dense specimens (higher relative compaction) at same strain levels as compared to others. Figure 4 presents the pore water pressure response in terms of r_u, which is the ratio of pore water pressure generated to the pre-shear effective confining pressure. The pore water pressure generated for 100% relative compaction was observed to be lower than other relative compaction due to the closed particle packing and less available void space to compress the particles further. Other than 100% RC, the specimens showed negligible variation in r_u value and displayed similar trend. The r_u value was observed to increase with number of loading cycles significantly till 100 cycles for all the specimens. The response got stabilized after 100 loading cycles for all the specimens with different relative compactions. The maximum r_u value for different relative compactions is presented in Table 1.

Dynamic Properties

Dynamic properties such as shear modulus (G) and damping ratio (D) were obtained at 1, 2, 3, 4, 5, 10, 20, 40, 60, 80, 100, 120, 140, 160, 180, 200, 230 and 250 loading cycles. Shear modulus of soil was calculated from dynamic Young's modulus (E_{dyn}) and Poisson's ratio as per the suggestions of Fahoum et al. [9] and Delfosse-Ribay et al. [7]. Equation (1) was used to evaluate the dynamic Young's modulus.

$$E_{dyn} = \frac{\sigma_{d1} + \sigma_{d2}}{\varepsilon_{d1} + \varepsilon_{d2}} \tag{1}$$

where σ_{d1} = maximum cyclic deviatoric stress and σ_{d2} = minimum cyclic deviatoric stress as shown in Fig. 5; ε_{d1} and ε_{d2} = axial strains corresponding to σ_{d1} and σ_{d2}, respectively. Shear modulus (G) was determined using Eq. (2):

$$G = \frac{E_{dyn}}{2(1 + \mu)} \tag{2}$$

Poisson's ratio (μ) was taken as 0.5 for saturated undrained conditions. Damping ratio (D) was defined as the amount of energy dissipated due to cyclic loading [17] and it was obtained using Eq. (3):

$$D(\%) = \frac{\text{Area of hysterisis loop}}{2\pi (\text{Area of} \Delta aob + \text{Area of} \Delta cod)} \times 100 \tag{3}$$

Area of hysteresis loop represented the dissipated strain energy, and area enclosed by Δaob and Δcod represented the applied elastic strain energy. The calculated values of shear modulus (G) and damping ratio (D) from above equations with number of loading cycles are shown in Figs. 6 and 7, respectively.

Shear modulus of Chobari dam soil was observed to decrease with the increase in loading cycles due to the large plastic deformation at higher number of cycles, generated by breakdown of inter-particle structure and bond. Shear modulus was also observed to be increased from 10.8 to 21.5 MPa with rise in relative compaction from
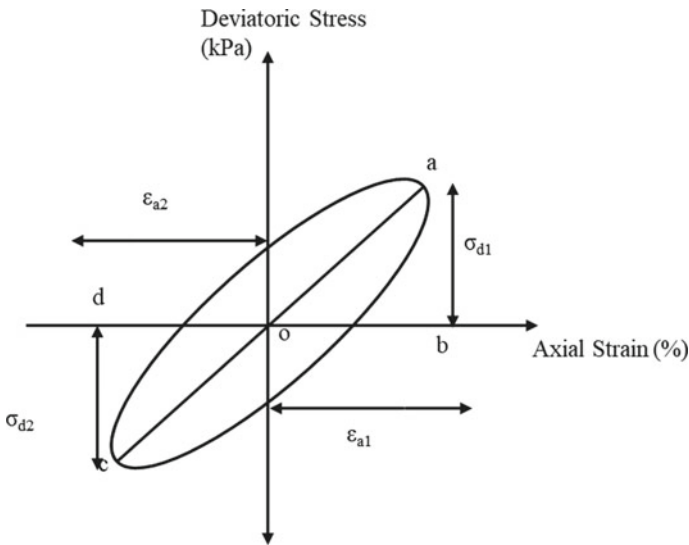
Fig. 5 Typical hysteresis loop for cyclic loading
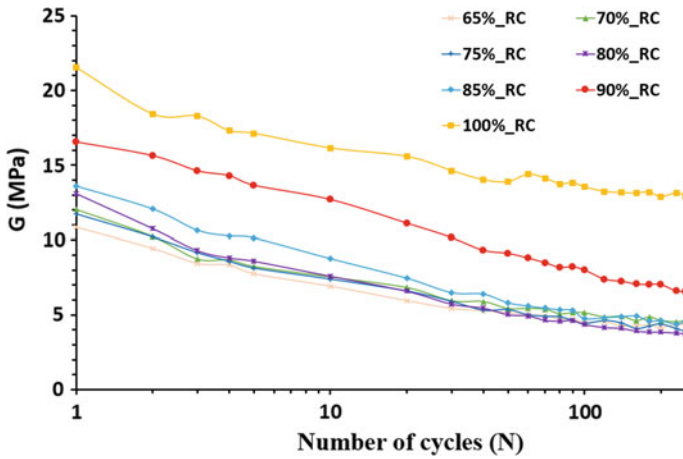
Fig. 6 Variation in shear modulus (G) of Chobari soil at different relative compactions
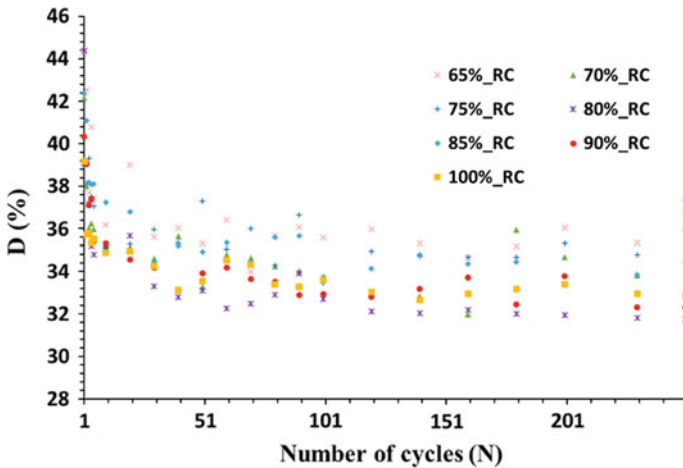
Fig. 7 Variation in damping of Chobari soil at different relative compactions

65 to 100%. The large particle contact points and stronger bonds were responsible for higher shear modulus values for higher relative compaction specimens. The preliminary degradation of shear modulus was observed to be quick due to the particle deterioration in the preliminary cycles, and further, the decay rate was stabilized.

The values of shear modulus and damping at first cycle of dynamic triaxial test are shown in Table 1. The variation in the value of damping ratio for first cycle was observed to be insignificant till 80% relative compaction (RC), which later decreased rapidly for 100% RC (densest packing). This behaviour could be due to the restriction in the movement of particles in denser packing. The lowest damping ratio of 39.2%

was observed for 100% RC in the first cycle. Damping ratio decreased significantly in first few cycles giving analogous results with the shear modulus in preliminary cycles.

Cyclic Stiffness Degradation Index

Influence of load repetition on shear modulus of soil was determined by evaluating cyclic degradation index (δ). Cyclic degradation index (δ) represents the intensity of stiffness degradation of saturated soil under cyclic loading conditions. Cyclic degradation index (δ) is defined as the ratio of shear modulus at Nth cycle (G_N) to that of the first cycle (G_1), as mentioned in Eq. (4) described by Kramer [15] and Boulanger et al. [3]:

$$\delta = \frac{G_N}{G_1} \tag{4}$$

Cyclic degradation index (δ) decreased as the RC increased from 100 to 80%, which was further observed to be increased again as RC decreased to 65% (Fig. 8). The decrease in δ was obtained to be significant from 100 to 80% RC. However, the reverse increment in δ was not prominent from 80% RC to 65% RC specimens. The cyclic degradation index was observed to be lowest for densest specimen (100% RC). Cyclic degradation parameter (t) is an another important parameter which indicates the rate of stiffness degradation. It was calculated as per Eq. (5) proposed by Idriss et al. [12]. The slope of δ-log N lines defines the degradation parameter (t).

$$t = -\frac{\log(\delta)}{\log(N)} \tag{5}$$
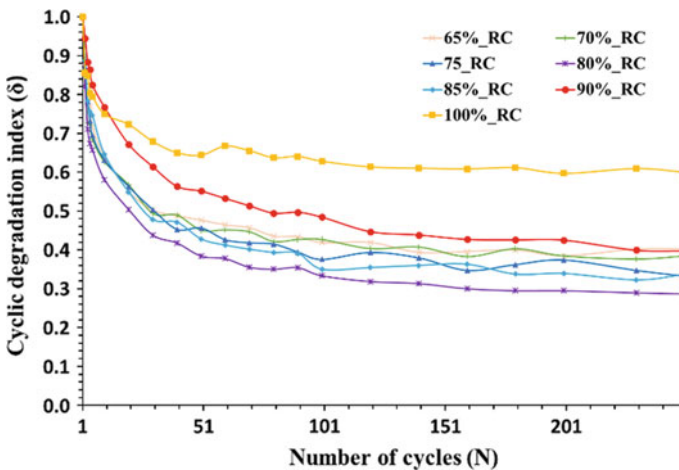
Fig. 8 Variation in cyclic degradation index of Chobari soil at different relative compactions

where δ = cyclic degradation index, and N = number of cycles. The cyclic degradation parameter (t) was evaluated for each loading cycle and an average value for all the cycles was determined (Table 1). The cyclic degradation parameter (t) was obtained to be increased from minimum of 0.08 to maximum of 0.22 for RC values varying from 100 to 80%. This indicated that the rate of stiffness degradation for dense specimen was less as compared to that of loose specimens. The reason could be the deferred particle structure breakdown and plastic deformation in dense specimens as compared to loose specimens.

5   Conclusions

A series of cyclic triaxial tests and 1D consolidation tests were performed to evaluate the effect of relative compaction (RC) on compressibility and dynamic behaviour of Chobari soil. The results were analysed in terms of compressibility index (C_c), shear modulus (G), damping ratio (D), cyclic degradation index (δ) and cyclic degradation parameter (t). The major conclusions of the present study are as follows:

- Compression index (C_c) significantly reduced with increasing RC.
- Hysteresis loops were observed to be shifted in upward direction and attained higher rotation angle as relative compaction increased. Pore pressure evolution increased with increase in RC during cyclic loading.
- Maximum shear modulus was obtained for 100% RC specimen and it decreased continuously with reduction in RC. Damping ratio was found to be reduced with increase in RC.
- The amplitude and rate of stiffness degradation of dense specimens (i.e. RC = 85, 90 and 100%) were observed to be lower as compared to loose specimens. After 80% RC, the soil behaviour reversed and cyclic degradation parameter (t) was found to be decreased to 65% RC.

References

1. ASTM D3999/D3999M-11e1 (2018) Standard test methods for the determination of the modulus and damping properties of soils using the cyclic triaxial apparatus
2. ASTM D4767-04 (2018) Standard test method for consolidated undrained triaxial compression test for cohesive soils
3. Boulanger RW, Arulnathan R, Harder LF Jr, Torres RA, Driller MW (1998) Dynamic properties of Sherman Island peat. J Geotech Geoenviron Eng 124(1):12–20. https://doi.org/10.1061/(ASCE)1090-0241(1998)124:1(12)
4. Boulanger RW, Idriss IM (2006) Liquefaction susceptibility criteria for silts and clays. J Geotechn Geoenviron Eng 132(11):1413–1426
5. Carraro JAH, Bandini P, Salgado R (2003) Liquefaction resistance of clean and nonplastic silty sands based on cone penetration resistance. J Geotechn Geoenviron Eng 129(11):965–976

6. Choo H, Burns S (2014) Effect of overconsolidation ratio on dynamic properties of binary mixtures of silica particles. Soil Dyn and Earthquake Eng 60:44–50. https://doi.org/10.1016/j.soildyn.2014.01.015

7. Delfosse-Ribay E, Djeran-Maigre I, Cabrillac R, Gouvenot D (2004) Shear modulus and damping ratio of grouted sand. Soil Dyn Earthquake Eng 24(6):461–471. https://doi.org/10.1016/j.soildyn.2004.02.004

8. Eseller-Bayat EE, Monkul MM, Akin Ö, Yenigun S (2019) The coupled influence of relative density, CSR, plasticity and content of fines on cyclic liquefaction resistance of sands. J Earthquake Eng 23(6):909–929. https://doi.org/10.1080/13632469.2017.1342297

9. Fahoum K, Aggour MS, Amini F (1996) Dynamic properties of cohesive soils treated with lime. J Geotech Eng 122(5):382–389

10. Gu C, Gu Z, Cai Y, Wang J, Ling D (2017) Dynamic modulus characteristics of saturated clays under variable confining pressure. Can Geotech J 54(5):729–735. https://doi.org/10.1139/cgj-2016-0441

11. Hussain M, Sachan A (2019) Effect of loading conditions and stress history on cyclic behavior of Kutch soil. Geomech Geoeng 1–19. https://doi.org/10.1080/17486025.2019.1635716

12. Idriss IM, Dobry RM, Doyle EH, Singh RD (1976). Behavior of soft clays under earthquake loading conditions. In: Offshore technology conference. offshore technology conference, Jan 1976. https://doi.org/10.4043/2671-MS

13. IS 2720 Part 15 (1986) Determination of consolidation properties. Bureau of Indian Standards, New Delhi, India

14. Ishihara K, Takatsu H (1979) Effects of overconsolidation and K0 conditions on the liquefaction characteristics of sands. Soils Found 19(4):59–68

15. Kramer SL (1996) Geotechnical earthquake engineering. International series in Civil engineering and engineering mechanics. Prentice Hall, New Jersey

16. Kumar SS, Krishna AM, Dey A (2018) Dynamic properties and liquefaction behaviour of cohesive soil in northeast India under staged cyclic loading. J Rock Mech Geotechn Eng 10(5):958–967

17. Pandya S, Sachan A (2019) Experimental studies on effect of load repetition on dynamic characteristics of saturated Ahmedabad cohesive soil. Int J Civil Eng 17(6):781–792

18. Polito CP, Martin II JR (2001) Effects of non-plastic fines on the liquefaction resistance of sands. J Geotechn Eng Div 127:408–415. https://doi.org/10.1061/(ASCE)1090-0241(2001)127:5(408)

19. Seed HB, Wong RT, Idriss IM, Tokimatsu K (1986) Moduli and damping factors for dynamic analyses of cohesionless soils. J Geotech Eng 112(11):1016–1032. https://doi.org/10.1061/(ASCE)0733-9410(1986)112:11(1016)

20. Shankar Kumar S, Murali Krishna A, Dey A (2014) Parameters influencing dynamic soil properties: a review treatise. Int J Innov Res Sci 3(4):47–60

21. Soralump S, Prasomsri J (2016) Cyclic pore water pressure generation and stiffness degradation in compacted clays. J Geotechn Geoenviron Eng 142(1):1–13

22. Tokimatsu K, Yoshimi Y (1984) Criteria of soil liquefaction with SPT and fines content. In: The Proceedings of the 8th world conference on earthquake engineering, San Francisco

23. Wang S, Luna R, Zhao H (2015) Cyclic and post-cyclic shear behavior of low-plasticity silt with varying clay content. Soil Dyn. Earthquake Eng. 75:112–120

Stress–Strain Behavior of Non-liquefied Soil and Liquefied Soil

Arup Bhattacharjee, Begum Emte Ajom, and Partha Pratim Baruah

Abstract The development of high pore pressure in loose soil during the earthquake often liquefies the soil. Liquefied soils have the potential to undergo extremely large deformation. These large deformations are associated with strains that are induced in the liquefied ground. Therefore, it is necessary to know the behavior of the soil during as well as after the liquefaction to estimate large displacements of ground or the settlement of structures due to liquefaction. Finite element models can be used to depict the behavior of the liquefied soil. In this paper, the stress–strain relationships of soil undergoing liquefaction have been studied by simulating a finite element model in OpenSees. A multi-layered single soil column is modeled in 2D and is subjected to a considered bedrock motion. A bridge site in Golaghat district of Assam (India) has been selected for this study. The required input parameters for the analysis are obtained by carrying out standard penetration test (SPT) and laboratory tests of the soil samples collected from the particular site. From the analysis, it has been found that most of the layers of the soil column get liquefied under that particular input motion. Thus, the stress–strain relationships of each layer have been presented and are compared to distinguish the behavior of liquefied and non-liquefied soil layers.

Keywords Hysteresis curve · Liquefaction · OpenSees · Stress–strain relationship

1 Introduction

Liquefaction had been studied extensively by researchers all around the world right after two main significant earthquakes, the 1964 Niigata earthquake and 1964 Alaska

A. Bhattacharjee (✉) · B. E. Ajom · P. P. Baruah
Department of Civil Engineering, Jorhat Engineering College, Jorhat, Assam, India
e-mail: bhatta_arup@yahoo.com

B. E. Ajom
e-mail: begumemte@gmail.com

P. P. Baruah
e-mail: parthabaruah39@gmail.com

earthquake. Liquefied soils have the potential to undergo extremely large deformations. For example, during the 1964 Niigata earthquake and 1983 Nihonkai-Chubu earthquakes, liquefaction-induced ground displacement reached several meters [1]. These large displacements are associated with strains that are induced in the liquefied ground on the order of several percent or even larger, as have been observed in model tests by various researchers [2–4]. In this paper, an attempt has been made to study the stress–strain relations by developing a finite element model in an open-source finite element program, OpenSees. The stress–strain relation at a selected bridge site on a liquefiable soil is being presented and compared with that of virgin soil of same location.

2   Modeling of Soil Profile

An existing RCC bridge over River Dhansiri on NH-37 located in Golaghat District of Assam (India) built and opened for traffic in the year 1964 is considered for this study. The bridge is supported by six numbers of piers and abutments on well foundation. The depth of each well foundation is 24 m. The standard penetration test has been carried out in the study area to collect the geotechnical data. The unit weights, shear wave velocities, etc., obtained from field and laboratory tests are used as input parameters for the soil model. It is found that the soil stratigraphy of the bridge site consists of sandy layers over 24 m of depth with a clay layer at a depth of 5 m from the surface. The relative densities are obtained using the correlation between SPT N values and relative density for sandy soils [5]. The bridge site comprises of medium to loose sand deposits with the ground water table at the surface. The shear wave velocity is estimated using the correlation with N values for all types of soil [6]. The bore log of the geotechnical investigation showing different soil properties is shown in Table 1.

Using the data obtained from the field investigation and laboratory tests, liquefaction analyses are carried out in Open System for Earthquake Engineering Simulations (OpenSees) finite-element analysis software framework.

A multi-layered single column of soil is modeled in 2D and is subjected to an earthquake excitation at the base. The soil is modeled using nine node quadrilateral elements and the materials used are Pressure Dependent Multi Yield02 material for sand and Pressure Independent Multi Yield material for clay. Nine nodded quadrilateral elements are able to track displacements of solid, pore-water pressure in the fluid. Four corner nodes of the element have three degrees of freedom (DoF), three translational, and one pore pressure (shown in red in Fig. 1). The interior nodes have two translational DoF (shown in blue in Fig. 1). To represent underlain bedrock condition, a higher value of density and shear wave velocity, 2500 kg/m^3 and 700 m/s, respectively, is assigned to nodes at the bottom of soil column. The Lysmer–Kuhlemeyer dashpot [7] is incorporated at the base of the soil column using the viscous uniaxial material and a zero-length element. The dashpot material model is dashpot coefficient. The dashpot coefficient is the product of the mass density and shear wave

Table 1 Typical soil borehole and laboratory tests data for the bridge site

Depth (m)	Soil type	Relative density, D_r (%)	SPT-N values	Saturated soil mass density, ρ_{sat} (kg/m³)	Shear wave velocity, V_s (m/s)	Friction angle, ϕ (°)	Cohesion, c (kPa)
1	Medium sand	53	8	1640	178.8	33.5	–
2	Medium sand	42	6	1500	164.0	32	–
3	Medium sand	64	13	1810	206.9	35	–
4	Loose sand	23	2	1440	117.8	31	–
5	Clay	–	3	2690	133.1	0	37
6	Medium sand	52	7	1640	171.8	33.5	–
7	Medium sand	46	10	1570	191.2	33.5	–
8	Medium sand	53	8	1590	178.8	33.5	–
9	Medium sand	49	15	1630	216.1	33.5	–
10	Loose sand	28	6	1320	164.0	31	–
11	Medium sand	36	6	1460	164.0	32	–
12	Medium sand	45	10	1610	191.3	32	–
13	Medium sand	37	8	1520	178.8	32	–
14	Medium sand	41	9	1550	185.3	32	–
15	Medium sand	41	10	1540	191.3	32	–
16	Medium sand	46	18	1580	228.3	33.5	–
17	Medium sand	46	16	1600	220.3	33.5	–
18	Loose sand	35	10	1460	191.3	31	–
19	Medium sand	40	10	1520	191.3	32	–
20	Medium sand	41	14	1600	211.7	32	–

Table 1 (continued)

Depth (m)	Soil type	Relative density, D_r (%)	SPT-N values	Saturated soil mass density, ρ_{sat} (kg/m^3)	Shear wave velocity, V_s (m/s)	Friction angle, ϕ (°)	Cohesion, c (kPa)
21	Medium sand	60	25	1910	252.0	35	–
22	Medium sand	57	24	1610	248.9	35	–
23	Medium sand	52	25	1590	252.0	33.5	–
24	Medium sand	56	29	1820	263.5	35	–
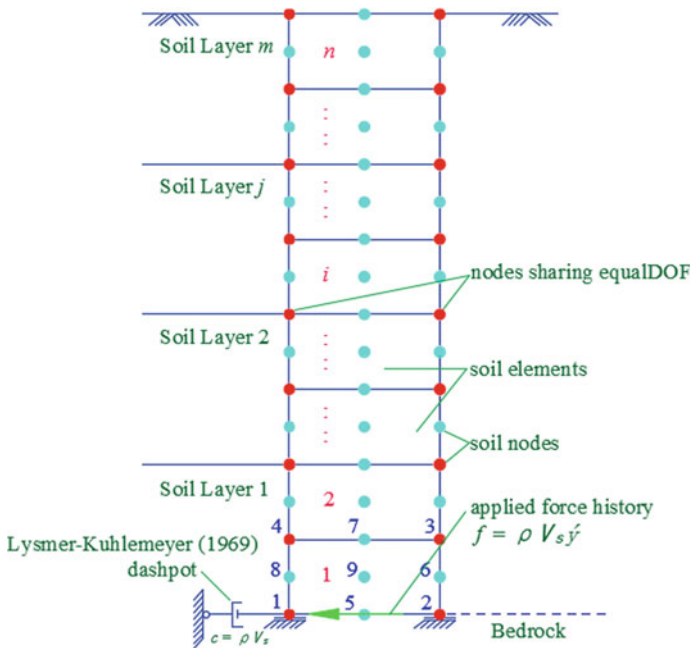
Fig. 1 FEM model of soil layer

velocity of the underlying layer with the area of the base of the soil column [8]. The input soil parameters are summarized in Table 2.

To perform a 1D free-field analysis, periodic boundary conditions are assumed. In OpenSees, periodic boundary conditions are achieved by setting a multi-point constraint between nodes at the same depth from the surface. This multi-point constraint controls the constrained nodes to have the same horizontal and vertical displacements at either end of the soil column.

Table 2 Parameter values for the soil material models

Depth (m)	Shear modulus, G (kPa)	Bulk modulus, B (kPa)	Phase transformation angle, $\phi_{PT}(°)$	Non-negative constants				Void ratio, e
				Contact1	Contact3	Dilate1	Dilate3	
1	52,429.88	233,000	25.5	0.045	0.15	0.06	0.15	0.7
2	40,344	220,000	26	0.067	0.23	0.06	0.27	0.77
3	77,481.77	240,000	26	0.028	0.05	0.1	0.05	0.65
4	19,982.65	160,000	31	0.087	0.18	0	0	0.85
5	47,654.99	300,000	–	–	–	–	–	–
6	48,404.99	233,000	25.5	0.045	0.15	0.06	0.15	0.7
7	57,395.18	233,000	25.5	0.045	0.15	0.06	0.15	0.7
8	50,831.41	233,000	25.5	0.045	0.15	0.06	0.15	0.7
9	76,119.71	233,000	25.5	0.045	0.15	0.06	0.15	0.7
10	35,502.72	160,000	31	0.087	0.18	0	0.18	0.85
11	39,268.16	220,000	26	0.067	0.23	0.06	0.23	0.77
12	58,919.06	220,000	26	0.067	0.23	0.06	0.23	0.77
13	48,593.55	220,000	26	0.067	0.23	0.06	0.23	0.77
14	53,220.94	220,000	26	0.067	0.23	0.06	0.23	0.77
15	56,357.36	220,000	26	0.067	0.23	0.06	0.23	0.77
16	82,351.01	233,000	25.5	0.045	0.15	0.06	0.15	0.7
17	77,651.34	233,000	25.5	0.045	0.15	0.06	0.15	0.7
18	53,429.71	160,000	31	0.087	0.18	0	0.18	0.85
19	55,625.45	220,000	26	0.067	0.23	0.06	0.23	0.77
20	71,707.02	220,000	26	0.067	0.23	0.06	0.23	0.77
21	121,292.6	240,000	26	0.028	0.05	0.1	0.05	0.65
22	99,741.45	240,000	26	0.028	0.05	0.1	0.05	0.65
23	100,971.4	233,000	25.5	0.045	0.15	0.06	0.15	0.7
24	126,366.7	240,000	26	0.028	0.05	0.1	0.05	0.65

After the free-field analysis, seismic analysis of the bridge foundation is carried out. The well foundation is modeled using the nonlinear beam-column element [9], which is based on the non-iterative (or iterative) force formulation, and considers the spread of plasticity along the element. The well foundation is modeled as fiber section. The uniaxial materials used for modeling the concrete and the reinforcing steel are designated in OpenSees as Concrete02 [10] and Steel02 [11], respectively. The input material properties of well foundation are summarized in Table 3. The soil column is connected to the well foundation with zero-length nonlinear springs which represent the flexibility of the soil–foundation interface.

Three types of soil–interface springs are used to model the soil–foundation interface: lateral resistance (p-y), skin friction (t-z), and end bearing resistance (q-z). Each spring is defined by an ultimate resistance (p_{ult}, t_{ult}, and q_{ult}) and the displacement

Table 3 Calculated p-y, t-z, and q-z soil–interface spring value

Depth (m)	p_{ult} (kN)	y_{50} (m)	t_{ult}/q_{ult} (kN)	z_{50} (m)
0	0	0.00351	241.340	0.002295
1	46.2346	0.00418	241.340	0.002295
2	115.323	0.01389	192.727	0.002753
3	247.705	0.00542	316.041	0.002187
4	241.611	0.00672	86.1930	0.003364
5	228.938	0.00509	258.579	0.004583
6	491.177	0.00910	229.848	0.002286
7	751.223	0.01193	201.117	0.002497
8	949.747	0.02860	241.340	0.002300
9	1008.44	0.01620	201.117	0.002244
10	983.870	0.01422	114.924	0.003193
11	1275.03	0.01675	143.655	0.002625
12	1639.42	0.01975	160.893	0.002047
13	1789.00	0.01989	155.147	0.002705
14	1977.58	0.01570	189.624	0.002783
15	2795.82	0.02072	189.624	0.002772
16	3228.32	0.04864	201.117	0.002427
17	3640.12	0.03096	201.117	0.002475
18	3695.69	0.02968	143.655	0.002784
19	5445.58	0.02589	195.370	0.004583
20	3893.54	0.01759	189.624	0.002767
21	7158.26	0.03791	287.310	0.002241
22	4930.47	0.02025	28,142.99	0.034000

at which 50% of the ultimate resistance is mobilized (i.e., y_{50} for p-y and z_{50} for the t-z springs) [12]. The values of p_{ult}, t_{ult}, q_{ult} and the corresponding y_{50} and z_{50} are summarized in Table 3. The schematic of the finite element model developed in OpenSees with the various well, spring, and soil components is illustrated in Fig. 2. The stages of simulation of well foundation in liquefied soil are explained at [13].

The Loma Prieta earthquake (1989) motion recorded at station Gilroy No. 1 EW pertaining to PGA 0.47 g has been selected for the study, and the acceleration time history is shown in Fig. 3.

3 Strain Variations in Liquefied Soil

The pore pressure ratios (computed as the ratio of excess pore pressure to initial effective vertical stress) obtained from four corner nodes of each element with depth
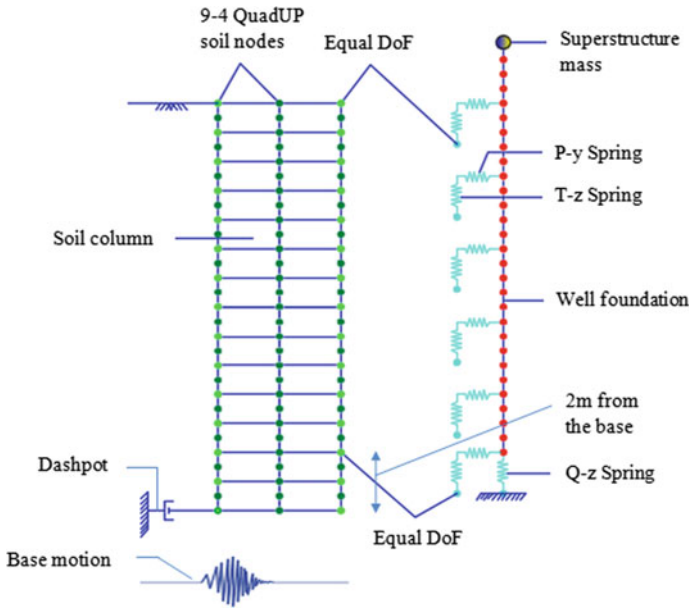
Fig. 2 Schematic representing the finite element model for soil–foundation system
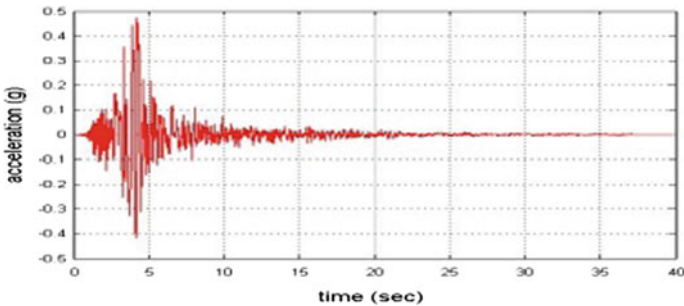
Fig. 3 Acceleration time history of Loma Prieta earthquake, 1989

of the soil layers are shown in Fig. 4a. The pore pressure ratios from 6 to 20 m depth are equal to 1, indicating zone of liquefaction.

The variation of maximum strain with depth is shown in Fig. 4b. The strain percentages are more from 6 to 20 m depth indicating the liquefaction of soil. The layers comprising of loose sand (i.e., at 10 and 18 m depth) are subjected to more strain than any other layer. The maximum strain variation with depth is determined for soil coupled with well foundation and is shown in Fig. 4c. No such significant variation of strains is observed for soil model and soil coupled with well foundation. The liquefaction of soil is not affected by the well foundation of the bridge constructed long back.
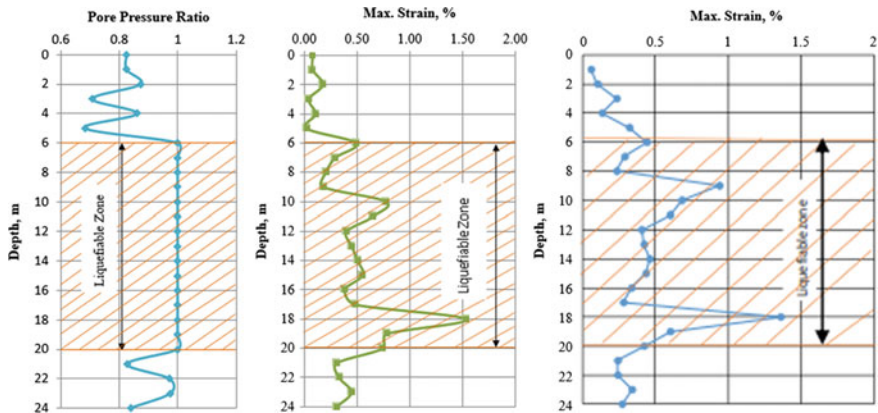
Fig. 4 **a** Variation of pore pressure ratio with depth, **b** variation of maximum strain of soil, **c** variation of maximum strain of soil coupled with well foundation

Figure 5 shows stress–strain variation of soil. The stress–strain curves are plotted in two different colors to distinguish between the liquefied layers and non-liquefied layers. Stress–strain curves for liquefied layers are in red and non-liquefied in blue. The stress–strain plot of non-liquefied soil, i.e., 3, 4, and 5 m, is closed having similar hysteresis loop with low value of strain. It is also true for bottom non-liquefied soil layers, i.e., 21, 23, and 24 m. The hysteresis loops are also formed in liquefied zone, but the amounts of strains produced are much higher than that of non-liquefied zone. The hysteresis loops of liquefied soil, i.e., 13, 14, and 15 m depth, are flatter with almost zero stress with large amount of strain.

Figure 6 shows the stress–strain variation of soil (in red color) and liquefied soil coupled with well foundation (in blue color) for soil at 13, 14, and 15 m. The hysteresis loop of soil is flatter with almost zero stress and large strain. There is no such significant variation of strain of soil, and soil coupled with well foundation is observed. There is not much alteration of stress–strain behavior of liquefied soil and liquefied soil with well foundation.

4   Conclusions

This paper highlights stress–strain variation of soil during liquefaction. The strain in the liquefied layer is much higher than that of non-liquefied layer. The stress–strain hysteresis of liquefied layers of soil is flatter indicating more strain with negligible stress during liquefaction, while that of non-liquefied layers is low strain with higher amount of stress. The well foundations do not have much effect on liquefaction of soil. The strain levels during liquefaction are almost similar to that of liquefied soil without well foundation.
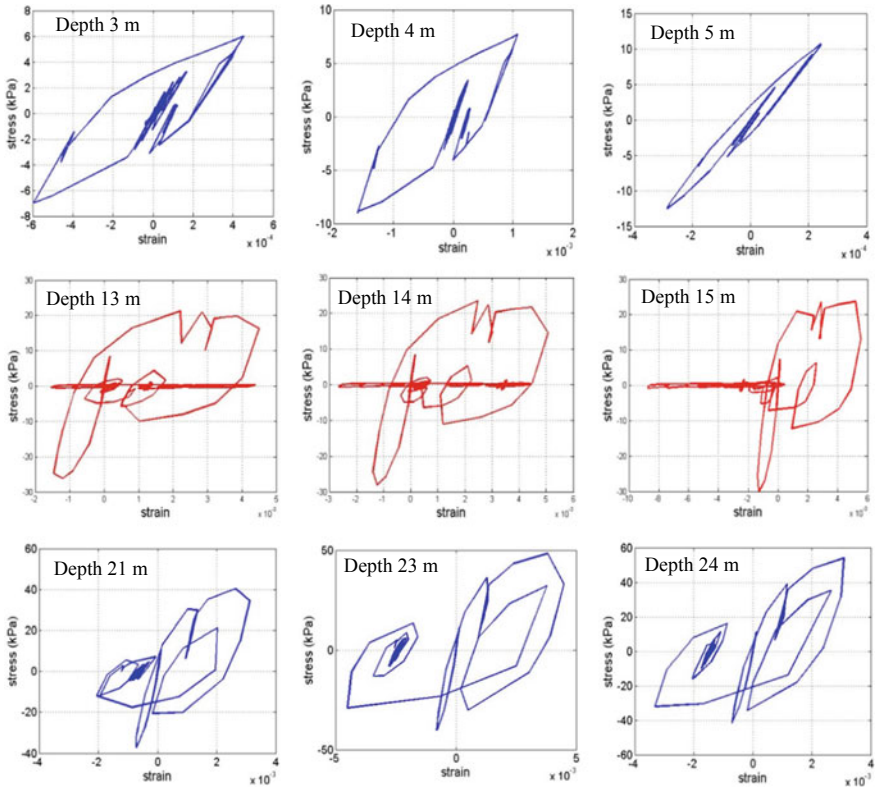
Fig. 5 Stress–strain variation of non-liquefied and liquefied soil
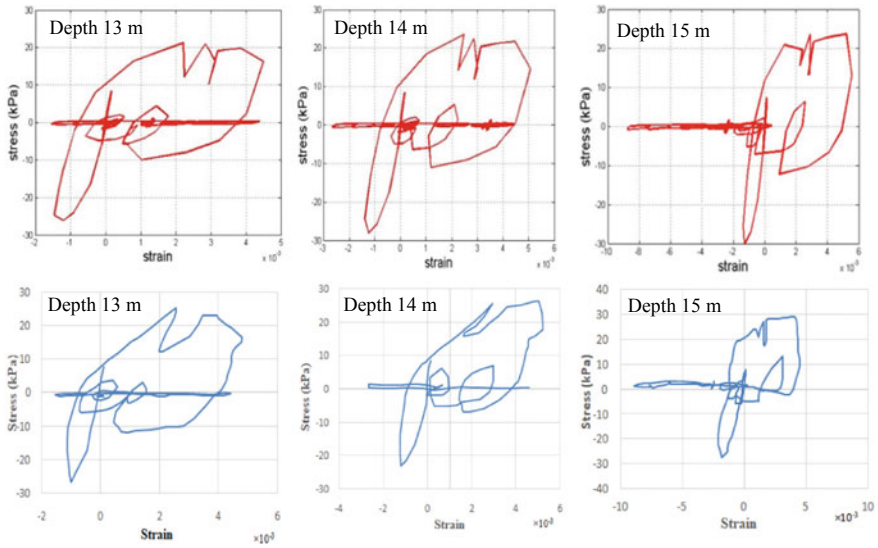
Fig. 6 Stress–strain variation of liquefied soil (in red color) and liquefied soil coupled with well foundation (in blue color)

References

1. Hamada M, O'Rourke TD, Yoshida N (1993) Liquefaction-induced large ground displacement. In: Performance of ground and soil structures during earthquakes, 13th ICSMFE, pp 93–108
2. Yasuda S, Nagase H, Kiku H, Uchida Y (1992) The mechanism and a simplified procedure for the analysis of permanent ground displacement due to liquefaction. Soils Found 32(1):149–160
3. Sasaki Y, Towhata I, Tokida K, Yamada K, Matsumoto H, Tamari Y, Saya S (1992) Mechanism of permanent displacement of ground caused by seismic liquefaction. Soils Found 32(3):79–96
4. Koseki J, Matsuo O, Koga Y (1997) Uplift behavior of underground structures caused by liquefaction of surrounding soil during earthquake. Soils Found 37(1):97–108
5. Cubrinovski M, Ishihara K (1999) Empirical correlation between SPT *N*-value and relative density for sandy soils. Jpn Geotechn Soc 39(5):61–71
6. Maheswari RU, Boominathan A, Dodagoudar GR (2008) Development of empirical correlation between shear wave velocity and standard penetration resistance in soils of Chennai city. In: The 14th world conference on earthquake Engineering, Beijing, China
7. Lysmer J, Kuhlemeyer AM (1969) Finite dynamic model for infinite media. J Eng Mech Div ASCE 95:859–877
8. Joyner WB, Chen ATF (1975) Calculation of nonlinear ground response in earthquakes. Bull Seismol Soc Am 65(5):1315–1336
9. Neuenhofer A, Filippou FC (1999) Geometrically nonlinear flexibility-based frame finite element, vol 124, p 704, 1998. J StructEng 125(1):116–126
10. YassinMHM (1994) Nonlinear analysis of prestressed concrete structures under monotonic and cycling loads. Ph.D. Thesis, University of California, Berkeley, California
11. Filippou FC, Bertero VV, Popov EP (1983) Effects of bond deterioration on hysteretic behavior of reinforced concrete joints. Earthquake Engineering Research Center, Berkeley
12. Boulanger RW, Curras CJ, Kutter BL, Wilson DW, Abghari A (1999) Seismic soil-pile-structure interaction experiments and analyses. J Geotechn Geoenviron Eng 125(9):750–759

13. Ajom BE, Bhattacharjee A (2018) Seismic re-qualification of Caisson supported Dhansiri River Bridge, tunneling in soft ground, ground conditioning and modification techniques—part of sustainable civil infrastructure. Springer Book Series, pp 187–203. https://doi.org/10.1007/978-3-319-95783-8_16

Dynamic Properties of Sand Reinforced with Recycled High Impact Polystyrene (HIPS)

Surya Muthukumar, Jagath Bhogadi, Saisudheerreddy Bogathi, Aaseesh Kunappareddy, Reena Jesuraj, Vinay Babu, Priyadarshini Vijayakumar, and Nivetha Jagadeesan

Abstract This study focuses on the improvement of dynamic properties of sand with the addition of recycled high impact polystyrene (HIPS) which is an e-waste. It is a cost-effective plastic material processed from tough polystyrene resins which have high impact resistance and dimensional stability. It has a wide application in the manufacturing of low-strength structural components, machined prototypes and computer components. Hence, it results in a large amount of e-waste after disposal. Due to its toughness and impact resistance, it can be used along with sand to improve its strength parameters. The effect on static and dynamic strength of sand for various proportions of recycled HIPS is studied. Dynamic properties like the coefficient of uniform and nonuniform elastic compression and shear values are the input parameters to predict the ground response. Those parameters were identified from the laboratory tests. The bearing capacity of reinforced and unreinforced sand was obtained from plate load tests. The cyclic plate load tests were done, and it is found that there is an increase in the values of the coefficient of uniform elastic compression and shear modulus. The dynamic properties for reinforced and unreinforced sand were obtained, analyzed, and compared.

Keywords Dynamic properties · High impact polystyrene (HIPS) · Shear modulus · Reinforced sand · Cyclic plate load

1 Introduction

Geotechnical structures subjected to dynamic stresses produced by earthquake, machine vibration or vehicular load require dynamic analysis to assess their responses and to mitigate the risks [1]. Machine foundation should withstand static and dynamic loads. The foundation will be designed heavy in comparison with the self-weight of the machine to withstand the dynamic load. The dynamic load with small magnitude

S. Muthukumar (✉) · J. Bhogadi · S. Bogathi · A. Kunappareddy · R. Jesuraj · V. Babu · P. Vijayakumar · N. Jagadeesan
Department of Civil Engineering, Amrita School of Engineering, Amrita Vishwa Vidyapeetham, Coimbatore, India
e-mail: m_surya@cb.amrita.edu

that acts repeatedly over a large period of time causes continuous deformation of the supporting soil. To withstand this effect, the soil should behave elastically [11]. To minimize the deformation, soil is reinforced by several methods.

Geosynthetic reinforced soil used for construction of footings over soft soil, slope stabilization and road construction provide ease in construction, reduction in cost and improved performance [10]. EPS beads, shredded tire waste, rubber chips and crumbs can be used along with the fill material as soil reinforcement [4, 5]. These lightweight fill materials have a wide range of applications as it reduces the overburden and lateral earth pressure. It reduces the effect of the driving forces and increases the stability of slopes and thus acts as a seismic buffer to relieve the seismic forces [5]. Soil under pavement will be subjected to cyclic loading due to the vehicle passes. The soil is mixed with granular rubbers that showed a reduction in the plastic deformations and an increase in the resilient displacements [10]. Cohesive soil treated with lime showed an improved dynamic property. Increase in lime content increases the shear modulus and decreases the damping [2].

Due to the rapid growth in the development of technology, the development of e-waste has increased in multiple folds. More than 30 million tons of e-wastes are produced every year in India. It is then collected and recycled by some companies. It consists of chemical components such as lead, mercury and beryllium and plastics such as polystyrene. An attempt has been made to enhance the dynamic property of soil by adding polystyrene. It has a complex structure which can absorb the seismic energy. High impact polystyrene (HIPS) which is an e-waste is a polymeric matrix mostly in pellet form [7]. It is a non-biodegradable plastic waste which can withstand high temperature and take up high impact loads [6]. It has very low density and high compressibility and possesses good flexural and rupture strength in shear [5]. HIPS increases the energy dissipation capacity. In concrete, the inclusion of HIPS as partial replacement of fine aggregate showed reduction in bulk density and dynamic modulus of elasticity [13].

The analysis of soil engineering problem involving dynamic loads requires the identification of two significant parameters, the shear modulus and the damping ratio [2]. Dynamic properties of soil depend on parameters like void ratio, confining pressure, plasticity, strain amplitude and morphology [3]. Tire rubber and synthetic fibers are found to increase the damping ratio [1]. Scrap tire, rubber fibers, polyethylene and polypropylene fibers are used in soil to improve the dynamic behavior of soil [1]. The inclusion of geogrid reinforcement in soil decreases the total settlement and the coefficient of elastic uniform compression [9].

Dynamic soil properties such as coefficient of elastic uniform compression, shear and nonuniform compression, shear can be calculated from the applied load and the elastic rebound of the soil [12]. C_u is the important parameter in the design of machine foundation which is assessed by the cyclic load test [11].

Coefficient of elastic uniform compression, $C_u = P/S_e$.

The correlations of the dynamic properties [12] were given as

Coefficient of elastic uniform shear, $C_\tau = C_u/1.75$.

Coefficient of elastic nonuniform compression, $C_\varphi = 3.46\ C_\tau$.

Coefficient of elastic nonuniform shear, $C_\psi = 1.5\ C_\tau$.

The main objective of this research is to investigate the improvement of strength parameters and dynamic behavior of sand due to the inclusion of HIPS. The behavior of sand HIPS mixture under the cyclic loads is studied. The experimental program consists of plate load and cyclic plate load test.

2 Materials

2.1 Hips

High impact polystyrene was procured from Coimbatore as shown in Fig. 1. It is an e-waste and available in plenty. It is a low-cost tough plastic that is easy to thermoform and fabricate. HIPS is often specified for low-strength structural application. It is used where foundations and structures are prone to higher vibrations. It can also be used in different proportions for various materials in backfills, foundations, footpaths, roads, etc. The general physical properties of HIPS [7] are listed in Table 1.

Fig. 1 High impact polystyrene

Table 1 Properties of HIPS

Properties	Value
Tensile strength (kg/ cm^2)	310
Tensile elongation at break (%)	40
Specific gravity	1.04
Heat distortion temperature °C	85

2.2 Sand

The fine aggregate used in this study is river sand and classified as poorly graded sand (SP) from the graph shown in Fig. 2. The various properties of the sand are identified by laboratory tests which are listed in Table 2.
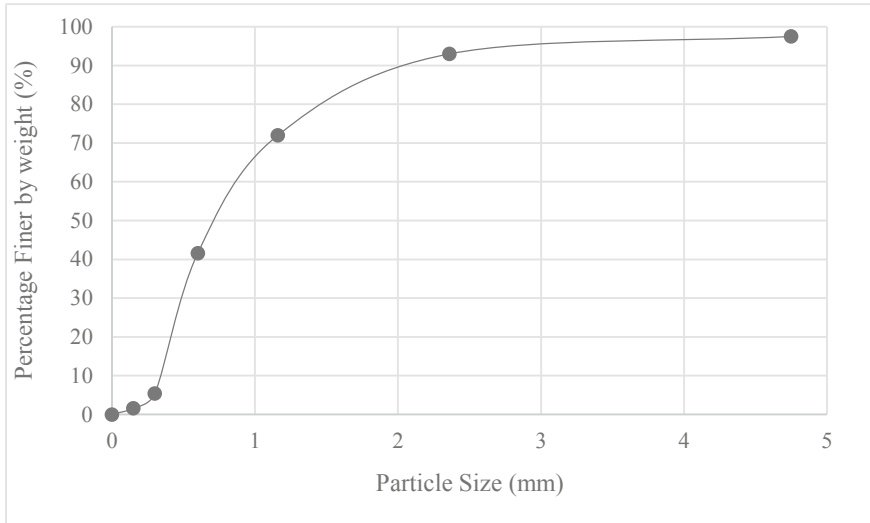
Fig. 2 Grain size distribution of soil

Table 2 Properties of sand

Properties	Value
Specific gravity	2.62
Effective size (mm), D_{10}	0.35
Uniformity coefficient C_u	2.457
Coefficient of curvature C_c	0.830
Soil classification	Poorly graded sand (SP)
Bulk density (kN/m^3)	1.51
Angle of internal friction, φ (°)	38

3 Laboratory Tests

3.1 Relative Density

Relative density test is carried out on a 100×100 cm vibrating table. A standard with guide sleeves is filled with sand and is assembled on the vibrating table. Surcharge weight is applied on the sand, and the vibrating table is set to vibrate at 3600 rpm for 8 min. The sand gets compacted, and the volume has decreased. With known new volume and weight, relative density of the sand can be calculated.

3.2 Direct Shear Tests

The shear strength of the sand sample is tested using direct shear test according to IS 2720 Part 8-1972. A shear box of 60 mm × 60 mm in plan and 40 mm in depth is used in the tests. The soil sample is taken in the targeted relative density, and the volume is calculated. The known volume of sand is mixed with the HIPS in various percentages. The mixture is poured from a constant height in layers and compacted using square base tamping rod until it fills the shear box fully. The box is placed in the apparatus and displacement is applied at the rate of 1.20 mm/min. The shearing force, horizontal and vertical displacements were measured until failure. The sample is sheared till failure is reached or till a lateral movement of 20% of the length is obtained. Then, the angle of internal friction is found out.

3.3 Plate Load Test

The laboratory model footing tests are conducted on the tank assembled with the loading frame. The tank of size 500 mm × 500 mm × 500 mm is made up of thick steel plates and Perspex sheet on the front side. The square steel footing used in this study is of dimensions 100 mm side and 10 mm thickness. The size of the testing tank should be greater than or equal to five times the size of the footing plate [8].

The load is applied directly with a constant rate of loading, and the respective settlement is obtained. The bearing capacity is calculated by observing the load applied when the maximum 50 mm settlement occurs.

3.4 Cyclic Plate Load Test

The test is performed as per IS 5249-1992. The laboratory model footing tests are conducted on the tank assembled with the loading frame. The cyclic loading is applied

at a constant rate from 0 to a value of load, and settlement occurred is noted. Later unloading will be done for which the rebound settlement is noted. From the cyclic plate load test, the elastic settlement of the footing for unreinforced and reinforced sand is found to be linearly varying with the applied load.

4 Laboratory Model Tests

4.1 Testing Procedure

To evaluate the optimum content of HIPS in sand, a series of direct shear tests are conducted. The optimum percentage is mixed with sand to identify the bearing capacity and coefficient of elastic uniform compression under the cyclic loading.

The load is applied by a hydraulic jack imposed by a manually operated pump on the model test tank. The settlement of the footing plate was measured through two linear dial gauges at the diagonal ends.

Laboratory model footing tests were conducted to find the cyclic load resistance of the reinforced sand with HIPS. The reinforced sand bed was prepared by rainfall method to maintain the relative density to 70%. The cyclic plate load test was conducted on the prepared sand bed with and without HIPS. The load is applied in cyclic method to obtain the elastic settlement. A predetermined vertical load increment is applied until the settlement becomes negligible. The settlement is measured using dial gauges. The applied load is released to zero, and the elastic rebound settlement of the footing plate is recorded. The test is continued for many cycles of loads until the sand bed shows large settlement values.

From the applied pressure settlement curve, the elastic rebound value is calculated for each cycle using the equation [9],

$$\text{Elastic settlement } S_e = S - S_r$$

where
S—total settlement.
S_r—residual settlement.

5 Results

5.1 Improvement in the Angle of Internal Friction

The angle of internal friction increases with addition of high impact polystyrene. The HIPS is added in sand in 2, 5, 6, 7 and 8% by weight. Initially, the angle of internal friction increases up to 5% which is the optimum content and then reduces as shown
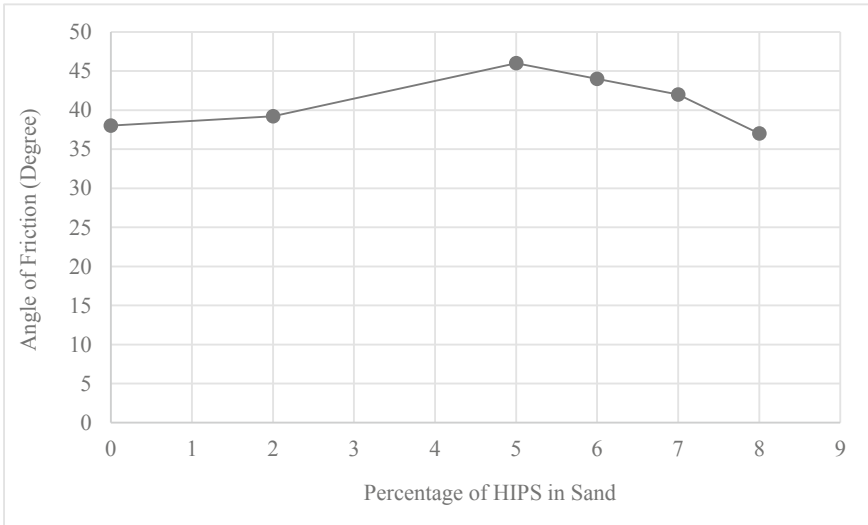
Fig. 3 Variation of the angle of friction at different percentages of HIPS

in graph (Fig. 3). So in the direct shear test, the optimum percentage to be considered is 5% and the angle of internal friction was found to be 46°.

5.2 Improvement in Bearing Capacity

The incorporation of HIPS at optimum content of 5% in soil has shown an improvement between the applied pressure and settlement behavior of soil. The results of the plate load tests are discussed. The bearing capacity of the unreinforced soil is found to be 185 kN/m^2 as shown in graph (Fig. 4). The improved bearing capacity after the inclusion of HIPS is found as 240 kN/m^2 as shown in graph (Fig. 5).

5.3 Improvement in Dynamic Property of Sand with HIPS

Cyclic plate load test is performed on the unreinforced sand to calculate the coefficient of elastic uniform compression. From the known bearing capacity value, the load is divided and applied into certain values and releases to zero to measure the elastic settlement. The cyclic plate load test is conducted until the settlement of the soil reaches 50 mm as shown in Fig. 6.

A graph is drawn between the applied pressure and elastic settlement as shown in Fig. 7. The slope of the line which corresponds to the coefficient of elastic uniform compression is found as 1.33×10^5 kN/m^3.
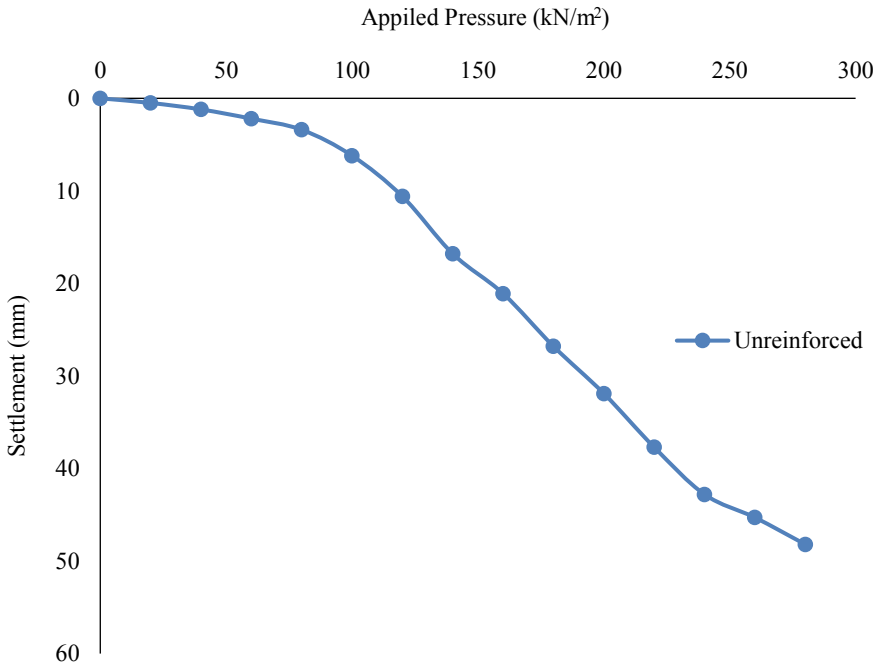
Fig. 4 Variation of settlement with applied pressure on the unreinforced sand
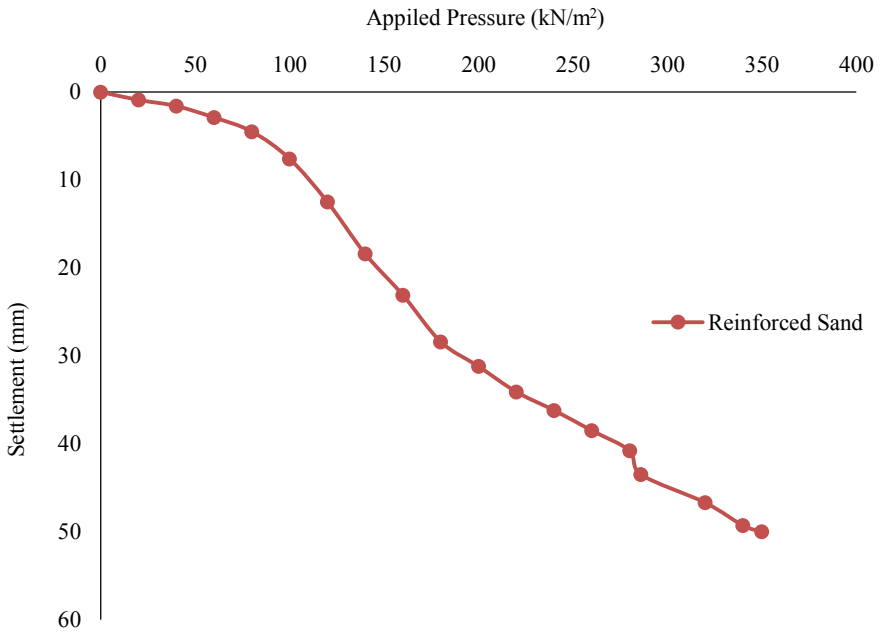
Fig. 5 Variation of settlement with applied pressure on the reinforced sand
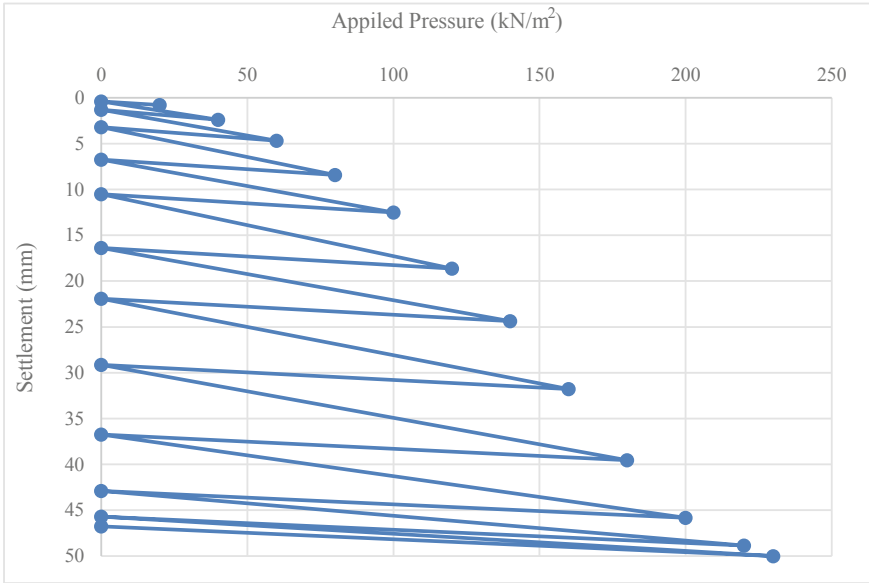
Fig. 6 Cyclic plate load test on the unreinforced sand
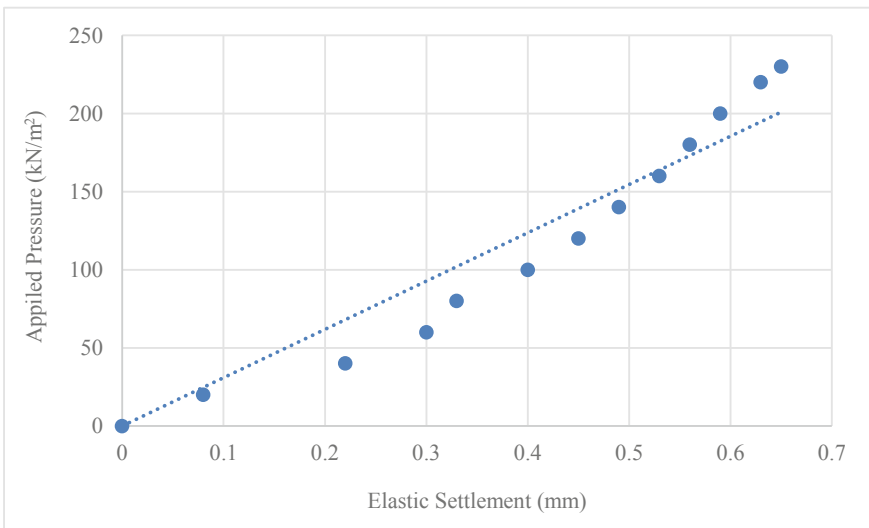
Fig. 7 Variation of applied pressure with elastic settlement on the unreinforced sand

The cyclic plate load test is repeated for the sand mixed with optimum percentage of HIPS and filled at 70% relative density by height of fall method in the model tank. From the cyclic plate load test, a graph is drawn between the applied pressure and settlement as shown in Fig. 8. The elastic settlement is calculated for each load value and graph is drawn between elastic settlement and applied pressure as shown in Fig. 9. The slope of the line which corresponds to the coefficient of elastic uniform compression of the reinforced sand with HIPS is found as 2.35×10^5 kN/m^3.

It can be clearly seen that the coefficient of elastic uniform compression increased significantly with the inclusion of HIPS. The addition of 5% of HIPS in sand showed an increase in the bearing capacity; above that, the improvement was insignificant due to the reduction in the frictional resistance. The inclusion of HIPS improves the internal frictional resistance only up to the optimum value. The increase in density of soil also influences the C_u as reported by Vantamuri et al. [12]. Slope of that line is higher for the reinforced than the unreinforced. The damping capacity is higher for the reinforced sand [9].

The improved bearing capacity and dynamic properties are due to the particle heterogeneity that allows the tensile strength to be carried between the soil particles and HIPS.

The sand–HIPS mixture absorbs more energy than the unreinforced sand. Hence, it reduces the settlement and reduction of stresses in static and dynamic state; the percentage improvement in the dynamic properties is shown in Table 3.

6 Conclusions

A series of laboratory tests were conducted to identify the optimum percentage of HIPS in sand for the improvement of shear strength and its effect on the enhancement of its dynamic properties. The inclusion of HIPS in sand has a significant impact on its static and dynamic properties.

The following conclusions are drawn from the study:

HIPS is replaced in various proportions (2, 5, 6, 7, 8%) with sand. The angle of internal friction is found to be 38° for unreinforced sand, and the maximum angle of internal friction is 46° for a replacement of 5%.

An improvement of 29.73% in the bearing capacity is observed when an optimum percentage of HIPS is added in the sand.

For the 5% replacement of HIPS in sand, the coefficient of elastic uniform compression has increased to 76.69%.

The overall improvement of the dynamic property of the sand reinforced with HIPS is found to be 76%.
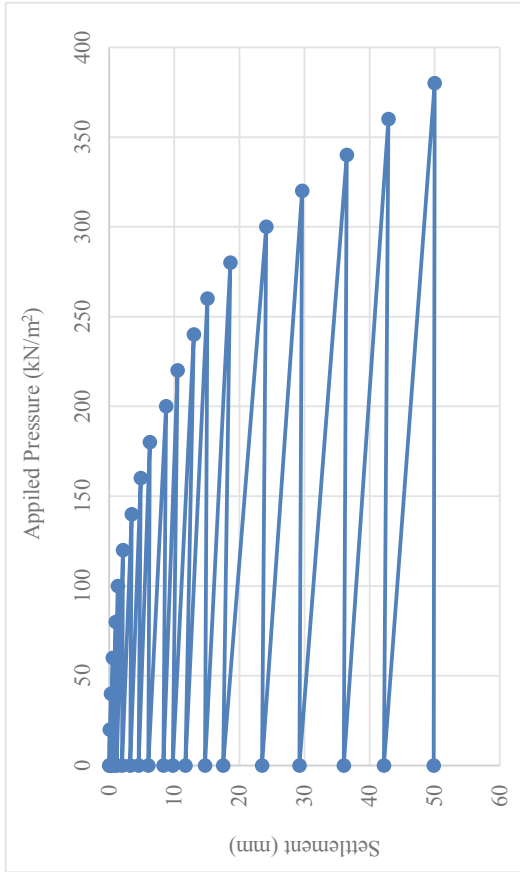
Fig. 8 Cyclic plate load test on the unreinforced sand
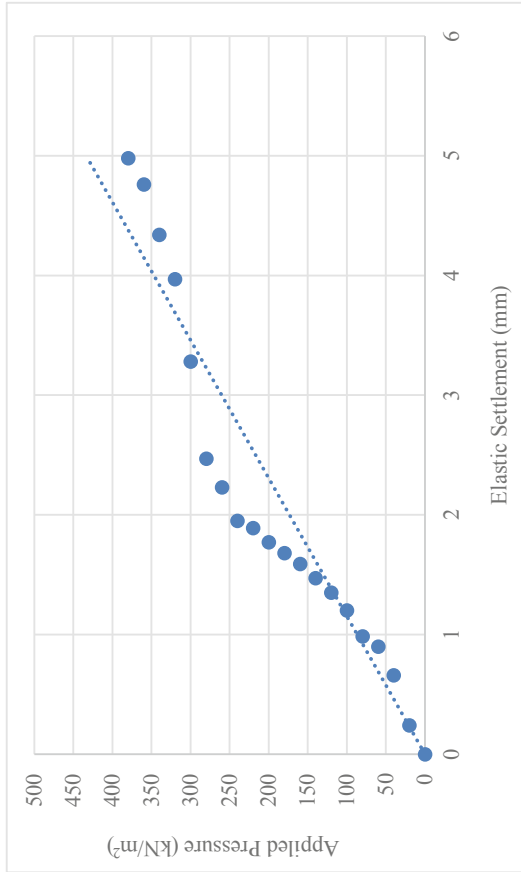
Fig. 9 Variation of applied pressure with elastic settlement on the reinforced sand

Table 3 Dynamic properties of unreinforced and reinforced sand

Properties	Unreinforced sand (kN/m^3)	Reinforced sand (kN/m^3)	Percentage improvement (%)
Coefficient of elastic uniform compression	1.33×10^5	2.35×10^5	76.69
Coefficient of elastic uniform shear	0.76×10^5	1.34×10^5	76.31
Coefficient of elastic nonuniform compression	2.63×10^5	4.64×10^5	76.42
Coefficient of elastic nonuniform shear	1.14×10^5	2.01×10^5	76.31

References

1. Akbulut S, Arasan S, Kalkan E (2007) Modification of clayey soils using scrap tire rubber and synthetic fibers. Appl Clay Sci 38:23–32. https://doi.org/10.1016/j.clay.2007.02.001
2. Amini F, Fahoum K, Aggour MS (1996) Dynamic properties of cohesive soils treated with lime. J Geotechn Eng 122:382–389
3. Dinesh BGSSV (2017) Dynamic properties of sand—fines mixtures. Geotech Geol Eng. https://doi.org/10.1007/s10706-017-0247-3
4. Eldesouky HM, Morsy MM, Mansour MF (2015) Fiber-reinforced sand strength and dilation characteristics. AIN SHAMS Eng J. https://doi.org/10.1016/j.asej.2015.06.003
5. Karimpour-fard M, Chenari RJ (2015) Shear strength characteristics of sand mixed with Eps beads using large direct shear strength characteristics of sand mixed with Eps beads using large direct shear apparatus. Electron J Geotechn Eng 20(8):2205–2220
6. Muthukumar S, Bavithran OKC, Nandagopal AR, Snehashree T (2017) stability study on eco-friendly flexible pavement using e-waste and Hips. Int J Civil Eng Technol 8:956–965
7. Oumer AN, Bachtiar D (2014) Modeling and experimental validation of tensile properties of sugar palm fiber reinforced high impact polystyrene composites. Fibers Polym 15:334–339. https://doi.org/10.1007/s12221-014-0334-5
8. Ramesh HN, A VKH (2013) Effect of static and cyclic loading on behavior of fiber reinforced sand. IOSR J Eng (IOSRJEN) 3:56–63
9. Saran S, Lavania BVK, Sharma RK (1995) Cycle plate load tests on reinforced sand
10. Tafreshi SNM, Khalaj O, Dawson AR, Transportation N, Centre E Repeated loading of soil containing granulated rubber and multiple geocell layers. 1–38
11. Tafreshi SNM, Zarei SE, Soltanpour Y (2008) Cyclic loading on foundation to evaluate the coefficient of elastic uniform compression of sand, pp 3–10
12. Vantamuri SN (2015) Performance of cyclic loading on circular footing, pp 515–519
13. Wang R, Meyer C (2012) Cement & concrete composites performance of cement mortar made with recycled high impact polystyrene. Cem Concr Compos 34:975–981. https://doi.org/10.1016/j.cemconcomp.2012.06.014

A Comparative Case Study on Various Admixtures Used for Soil Stabilization

Ankush Baranwal, Ajay Yadav, and Sneha Gupta

Abstract Soil stabilization is a technique in which we alter the soil to enhance the properties by using thermal, electrical, mechanical and chemical processes. However, the thermal and electrical processes of soil stabilization are rarely used. Nowadays, the chemical process of soil stabilization is in much use. In this, some known admixtures like rice husk, plastic waste, vetiver grass, fly ash, lime, etc., are used that change the physical and chemical properties of soil and make it more suitable for which the same is done. This review paper discusses the importance and scope of recent trends in soil stabilization. This paper also seeks to investigate various existing methods of soil stabilization and also presents a comparative case study of soil stabilization techniques using rice husk, fly ash and vetiver grass. The reviewer has examined the most suitable admixture among these and henceforth provided excellent quality of stabilized soil. Research and findings of this paper based on experiments like Atterberg limit, Proctor compaction test, California Bearing Ratio (C.B.R.) test, unconfined compressive strength test shear strength, etc., will help engineers to choose the best method to stabilize soil for various construction purposes. It is investigated that fly ash is the best admixture for soil stabilization under the consideration of cost optimization. Also, soil stabilization of black cotton soil with rice husk is best for the rice-producing region where rice hush ash (R.H.A.) is available at a low cost.

Keywords Soil stabilization · Fly husk · Rice husk · Vetiver grass

A. Baranwal · A. Yadav (✉) · S. Gupta
Madan Mohan Malaviya University of Technology, Gorakhpur, India
e-mail: ajay06950@gmail.com

A. Baranwal
e-mail: abmmmutgkp1999@gmail.com

S. Gupta
e-mail: sgce@mmmut.ac.in

1 Introduction

Soil is the essential requirement for building any structure like highway construction, the foundation of a multi-storey building and tower, etc. There are many types of soil present in our surrounding but in that more area is covered with BC soil (black cotton soil or expansive soil) which shows swelling and shrinkage characteristics due to variation in moisture content because of the presence of montmorillonite group in much quantity which makes the soil unstable, and for that, soil to stabilized. The stability, serviceability and economy of the structure considerably influence with the characteristics of the subsoil of the project site. Among the various soil types present in our surrounding, some are called problematic soil, which does not allow to sustain any structure on it due to low bearing capacity, high swelling and shrinkage property, minimum durability, etc. [1]. It was found that almost 21% of the Indian landmass is occupied with BC soil or expansive soil, which is not suitable for such purpose [2].

The complete process involving the transformation of these problematic soil into problem-free soil is termed as soil stabilization, and the stabilizer or admixture by which this gets to achieve is known as a stabilizing agent (Table 1).

This study is organized as follows: Sect. 2, soil stabilization; Sect. 3, components of soil stabilization; Sect. 4, review.

Table 1 State-wise distribution of black soils in India. *Source* [3]
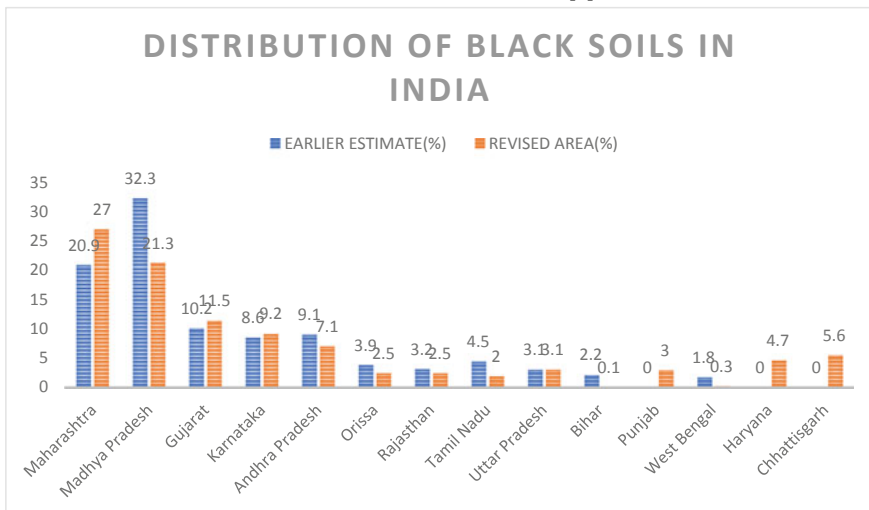
2 Soil Stabilization

Soil stabilization is a technique in which we alter the soil to enhance their physical and chemical properties by using some known admixtures like rice husk, plastic wastes, vetiver grass, to make it more suitable for construction purposes. By enhancing the properties of soil like boost up in strength and bearing capacity to control the free swelling and shrinkage characteristics caused by water content variation, increment in resistance to erosion and to reduce the pavement thickness in road construction [1]. The soil stabilization can be derived from thermal, electrical, mechanical and chemical processes in which the thermal and electrical processes of soil stabilization are rarely used [4]. It can be done in mainly two ways:

```
                    SOIL STABILIZATION

      Mechanical                            Chemical
       Process                               Process
```

- It is particularly effective for cohesionless soil and mechanical energy will responsible for the rearrangement of particle and it's interlocking [5].
- In this soil, stabilization can be done through the physical process by changing the corporeal nature of native soil either by inducing vibration or compaction.
- This can be done by reinforcing the soil, by compaction and by mechanical remediation [6].

NOTE: Mechanical stabilization is not the main aim of this review and will not be further discussed but somehow, we restrict our discussion up to soil reinforcement.

- In this, soil stabilization can be done by adding stabilizing agents (cementaneous material) or admixture. Hence, chemical reactions take place between Virgin soil and stabilizing agent aftermath change its behaviour i.e. from problematic to problem free.
- It can be achieved with the help of admixtures like fly ash, Portland cement, Rich husk Ash (RHA), lime, Plastic waste, shredded tyre, glass dust and bitumen emulsion.

NOTE: Chemical stabilization is the main purpose of this review and however, under this, we restrict our discussion to two named admixtures i.e. fly ash and rice husk. So, this paper completely revolves around these two and one vetiver grasses from mechanical stabilization and will discuss further.

Nowadays, to tackle the problem of expansive or black cotton soil, chemical stabilization is more used, and in this, instead of mechanical stabilization due to number of reasons, some are noted below:

- Eco-friendly: Unsafe disposal will cause breathing problem and diseases like asthma.
- Economical: The admixtures used for stabilization are mainly by-products and produced in abundant quantity; that is, it is not too costly.
- Performance: Its performance is also better than mechanical process.
- Availability: It is easily available.

3 Components of Soil Stabilization

The components of soil stabilization include the native soil or virgin soil and stabilizing agent (binder) which have cementaneous property, and after mixing with virgin soil, it able to enhance the engineering properties of the same and thus make able to use at construction site.

3.1 Soil

Soils are formed by weathering of rocks that may be physical weathering or may be chemical weathering. The soil types formed by physical weathering are gravel, sand and silt. And the soil type formed by chemical weathering is clayey soil. Often soft soil (clayey soil and organic soil) is undertaken for stabilization to achieve desirable engineering properties.

Clay is the material whose particle size is less than 2 micron, which swells on absorbing water into it and shrinks on removal of water. Mineralogical properties are main the reason for this behaviour. Kaolinite, illite and montmorillonite are the three main clay minerals, and among the three, kaolinitic clays are considered to be more stable, montmorillonite soils are more expansive/swelling in nature, and illitic clays fall in between. BC soil contains montmorillonite in very large amount which governs its property of swelling and shrinkage. Depending on its application in civil engineering, different ways of stabilization are employed to give it more strength (Fig. 1; Table 2).

Fig. 1 Black cotton soil. *Source* [7]

Table 2 Distribution of clay minerals and expansive soil properties. *Source* [6]
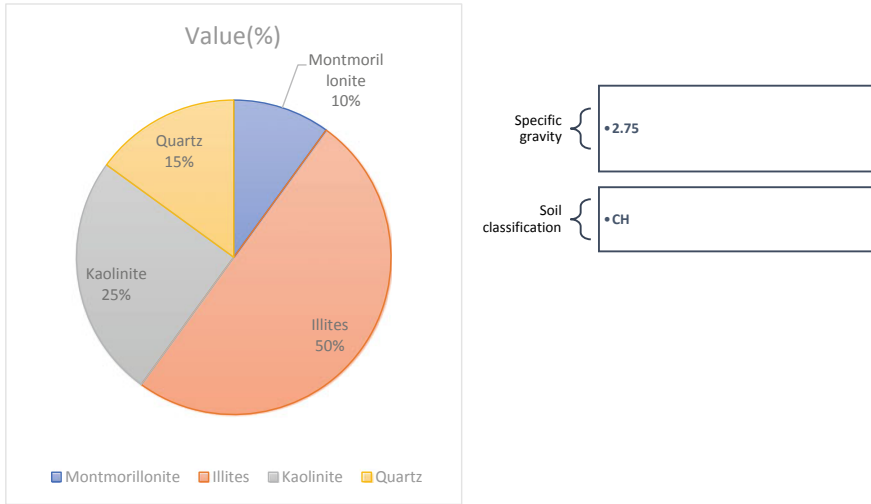
3.2 Fly Ash

Fly ash is a waste material collected from the burning of coal in thermal power plant. Fly ash is silt-size non-cohesive material which consists of alumina, silica and iron whose specific gravity is lesser than normal soil. It is produced in huge amount due to the presence of a large number of thermal power plants across the world. It is used in many engineering construction applications. Fly ash is economical and environmentally friendly, and improper disposal of fly ash causes breathing problems and diseases like asthma [8] (Fig. 2; Table 3).

Fig. 2 Fly ash. *Source* [10]

Table 3 Chemical composition of Class C and Class F fly ashes. *Source* [9]
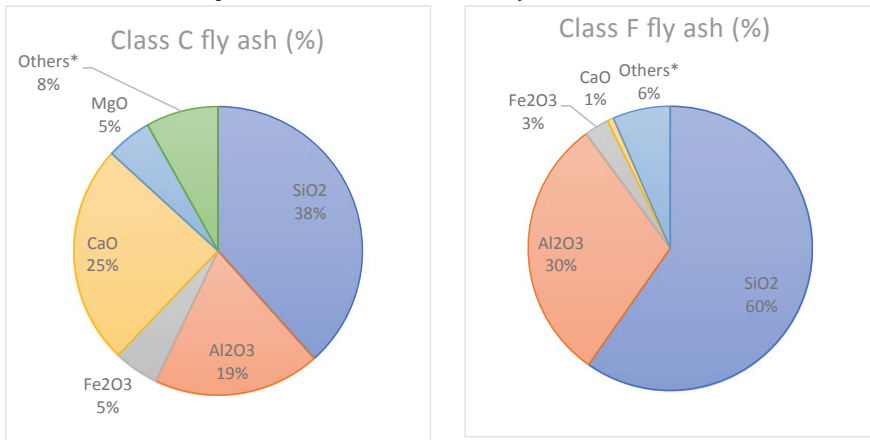
3.3 Rice Hush Ash

Rice husk is very worthless and a by-product of rice mill. Almost 60 million tons of rice husk are produced in India. The husk is not acceptable for the animal as a meal because of negligible digestible protein content. So, this is used as fuel in thermal power plants to produce electricity. After that, 20% of the initial mass of husk gets converted into rice husk ash (RHA) which means 12 million tons, which is a huge quantity. To value this residue is an alternative to its final attitude with environmental usefulness. Rice husk ash has no cementing property alone but when gets combined with some other binders like hydrated lime possesses cementacious property [11, 12] (Fig. 3; Table 4).

Fig. 3 Rich husk ash.
Source [14]

Table 4 Chemical composition and physical properties of rice husk ash. *Source* [13]

Chemical composition of Rich Husk Ash

3%

5%

92%

■ Silicon dioxide (SiO2) % ■ Other dioxide (%) ■ Loss of ignition (%)

| Specific Gravity | • 2.32 |
| Colour | • Whitish grey |
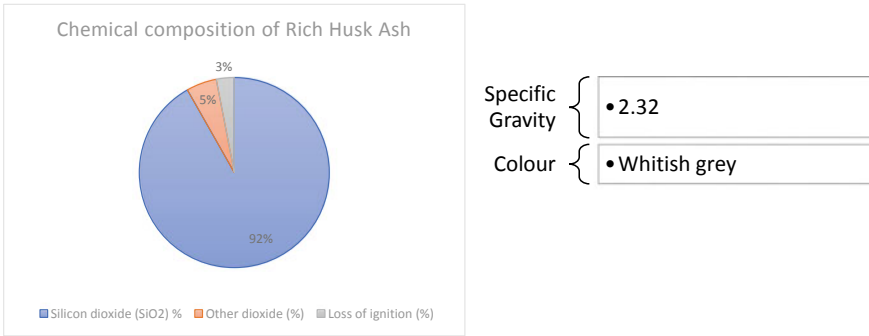
3.4 Vetiver Grass

Vetiver is a perennial bunchgrass of the family "Poaceae", native to India. It is found in large amount along the roadside and grows on their own. Stabilization due to this in soil is kind of mechanical stabilization. This vegetation material not only reduces soil erosion and runoff but also controls the moisture fluctuations in soil and change the other parameters of soil provide slope stability to ground [15] (Fig. 4).

4 Review

In this section, researchers reviewed various papers on soil stabilization using fly ash, rice husk ash and vetiver grass.

Fig. 4 Vetiver grass. *Source* [16]

4.1 Fly Ash

Expansive soil has intense moisture variations because of the montmorillonite group which absorbs water and is a reason in damaging the lightweight structure. On fly ash addition in varying % in expensive soil, the unconfined compressive strength and OMC increase to enhance the engineering properties of soil and make more suitable to use in construction works. Liquid limit and plastic limit also increased on the addition of fly ash in varying %. However, liquid limit shows little variation as compared to the plastic limit [17]. The plasticity index, as well as the free swell index is reduced because of the increase in the plastic limit [18].

Fly ash has two classes, one is class C and the other is class F; nearly about 24% and 9% of CaO are present in C and F class fly ashes, respectively. When fly ash is mixed with native soil along with some water, it shows cementing property without adding any activators such as lime and cement; it happens due to the presence of CaO in considerable amount which makes the soil more stable [5].

Moving to the dynamic properties of soil, it was observed that shear modulus of treated soil (with fly ash) will increase where the damping ratio of the same will decrease. It was also seen that if we increased the curing period, then the time-dependent and pozzolanic properties come into action which makes the soil more rigid [18].

When we add lime in addition to fly ash, it provides much cementing property and gets more rigid on drying. As the increase in the amount of lime and fly ash, there is a noticeable reduction in maximum dry density, free swell and swelling capacity under 50 kPa pressure, and a complementary increase in the percentage of coarse particles, OMC and CBR values [6]. The use of fly ash in soil stabilization not only leads to better chances in the engineering properties of the soil but is also the best answer for safe disposal of fly ash [19].

4.2 Rice Husk Ash

It was noticed that RHA used in stabilization needs some activators like lime, cement, etc., and in this, more water is required to compact the soil due to the absorption of water by RHA [20, 21].

It is observed that the addition of rice husk ash with lime in the soil increases its UCS; it is due to the formation of a pozzolanic reaction that bonds the grains together, and this reaction is formed when low reactive RHA reacts with lime. The increase in UCS is up to an optimum value and beyond that, the UCS starts decreasing. And the higher value of UCS can be achieved by adding a larger amount of RHA and the least amount of lime in it. In countries where RHA is produced in larger quantities, the improper disposal of RHA causes environmental impingement; proper disposal of RHA reduces the environmental pollution and disposal cost; and it is also conserved as a non-renewable resource [11].

When residual soil is treated with rice husk ash and ordinary Portland cement, it reduces the plasticity of residual soil. The unconfined compressive strength (UCS) of cement-stabilized soil increases with the increment in husk ash; to achieve a given strength, the cement is mixed in lesser amount with RHA. When cement content increases, the MDD slightly decreases and OMC increases steeply. The CBR value increases up to an optimum amount, and beyond that, the CBR value starts decreasing [22].

When clayey soil stabilized with the combination of cement kiln dust (CKD) and RHA at varying dosages, it is observed that the properties of stabilized soils were improved. The improvement depends on the type and amount of stabilizer, stabilizer combinations, and age. CKD-stabilized soil shows self-cementing property, and it also shows higher strength, elastic modulus, CBR, water resistance, shrinkage values and lower water absorption sorptivity as compared to the RHA-stabilized soil. The combination of CKD and RHA produces better improvement in properties and also shows higher CBR value (>80%) which can be used for making low-cost houses, and it also promotes sustainable development in the construction of highway subgrade, building foundation, etc. [23].

4.3 Vetiver Grass

It is observed that the addition of roots of vetiver grass as a root matrix in the soil increases the OMC and an increase in the UCS was almost double. The water gets absorbed in the root which increases the weight of root mass, thereby increasing the shear strength, stability and OMC. The permeability of the soil decreases with the growth of vetiver root content in the soil; this indicates that the soil becomes denser. The vetiver roots get degraded after a period of time and converted into humus and provide more stability to the soil [15].

5 Conclusion

The black cotton soil or expansive soil is much seriously concerned in construction; due to these anomalous behaviours and damages to the structure, the purpose of this study was to investigate the usage of admixture in stabilizing the expansive soil. The following conclusion is studied from the review:

1. Fly ash stabilization enhances the geotechnical properties of soil, shear modulus will get increased, while liquid limit, plasticity index, free swell index and damping ratio get reduced.
2. On increasing the curing period, the treated soil (with fly ash) will get more rigid.

3. A small amount of lime in addition to fly ash makes a considerable increase in OMC and CBR and an apparent decrease in the MDD and free swell index due to the function of cationic exchange.
4. The addition of rice husk ash with lime increases the UCS due to the formation of pozzolanic reaction, and the increase is up to an optimum value; beyond that, UCS starts decreasing.
5. The addition of RHA with ordinary Portland cement decreases the plasticity and MDD of the soil but increases the UCS and OMC. The CBR value also increases up to an optimum amount; beyond that, it decreases.
6. Soil stabilized with CKD and RHA shows improvement in the properties. CKD-stabilized soil shows self-cementing property and also shows higher strength, elastic modulus, CBR, water resistance, shrinkage values and lower water absorption sorptivity
7. Vetiver grass as a root matrix increases the shear strength, stability and OMC of vetiver soil. After degradation, the vetiver roots are converted into humus and provide more stability to the soil.
8. Chemical stabilization is better than mechanical stabilization.
9. The fly ash is better stabilizer than rice husk ash.

References

1. Karthik S, Ashok Kumar E, Gowtham P, Elango G, Gokul D, Thangaraj S (2014) Soil stabilization by using fly ash. IOSR Journal of Mechanical and Civil Engineering. 10:20–26. https://doi.org/10.9790/16841062026
2. Bhuvaneshwari S, Gandhi SR. Stabilization of expansive soils using fly ash. In: fly ash utilization programme (FAUP), Delhi, India
3. Chandran P, Ray S, Mandal C, Mandal D, Prasad J, Sarkar D, Tiwary P, Patil N, Reddy GPO, Lokhande M, Wadhai K, Dongare V, Sidhu G, Sahoo A, Nair K, Singh S, Pal D, Bhattacharyya T (2012) Revision of black soil map of india for sustainable crop production
4. National Academies of Sciences, Engineering, and Medicine (2009) Recommended practice for stabilization of subgrade soils and base materials. The National Academies Press, Washington, DC. https://doi.org/10.17226/22999.
5. Makusa PG (2012) Soil stablization methods and materials. Luleå University of Technology, Sweden. https://www.diva-portal.org/smash/get/diva2:997144/FULLTEXT01.pdf
6. Ji-ru Z, Xing CJ (2002) Wuhan Univ Technol-Mat Sci Ed 17:73. https://doi.org/10.1007/BF02838423
7. https://forum.byjus.com/the-soil-which-is-formed-due-to-weathering-of-lava-rock-is-called
8. Ji-ru Z, Xing C (2002) Stabilization of expansive soil by lime and fly ash. J Wuhan Univ Technol Sci. Ed. 17:73–77. https://doi.org/10.1007/BF02838423
9. Bentz D, Ferraris C (2010) Rheology and setting of high volume fly ash mixtures. Cement Concr Compos 32:265–270. https://doi.org/10.1016/j.cemconcomp.2010.01.008

10. https://www.flexicon.com/Materials-Handled/Fly-Ash.html
11. Behak L (2017) Soil stabilization with rice husk ash. https://doi.org/10.5772/66311
12. Basha EA, Hashim R, Mahmud HB, Muntohar A (2005) Stabilization of residual soil with rice husk ash and cement. Constr Build Mater 19(448):453. https://doi.org/10.1016/j.conbuildmat.2004.08.001
13. Rahman MA (1987) Effects of cement-rice husk ash mixture on geotechnical properties of lateritic soils: Japanese society of soil mechanics and foundation engineering. Soil Found 27(2):61–65 (1987)
14. https://gharpedia.com/blog/rice-husk-ash-in-concrete-pros-cons/
15. Gopinath R, Ganapathy G, Saravanan S, Vijayan V, Muthukumar S, Muthuseenivasan M, Muthuraj V, Prabu V (2015). Experimental studies on soil stabilization using vetiver root as reinforcement. 10
16. https://www.molokaiseedcompany.com/product/sunshine-vetiver-grass/
17. Yashwantsinh Z (2013) Stabilization of expansive soil using fly ash
18. Dutta TT, Saride S (2016) Dynamic properties of moderately expansive soil stabilized with Class C fly ash. https://doi.org/10.1061/9780784480144.094.Retrieved from 19 Jan 2020
19. Udhayashankar D, Harari SCP (2012) Stabilization of black cotton soils using fly ash, hubballidharwad municipal corporation area, Karnataka, India. GJRE 12:2
20. Gudeta AD, Patel AV (12AD) A critical review on soil stabilization using different industrial wastes and admixtures. Int Res J Eng Technol (IRJET) 4(12):1674–1678
21. Yadu L, Tripathi R, Singh D (2020) Comparison of fly ash and rice husk ash stabilized black cotton soil
22. Basha EA, Hashim R, Mahmud HB, Muntohar A (2005) Stabilization of residual soil with rice husk ash and cement. Constr Build Mater 19:448–453. https://doi.org/10.1016/j.conbuildmat.2004.08.001
23. Hossain K (2011) Stabilized Soils Incorporating Combinations of rice husk ash and cement kiln dust. J Mater Civ Eng 23:1320–1327. https://doi.org/10.1061/(ASCE)MT.1943-5533.0000310

Seismic Performance of Cohesionless Soil Underneath Gravity Dam

Asad H. Aldefae [iD]**, Mohammed S. Shamkhi, and Thulfiqar Kh. Alhachami**

Abstract Earthquake is one of the worst disasters that any geotechnical designer must keep in their mind during the design steps of any infrastructure. In this paper, seismic performance (i.e., the dynamic response) of foundation (the soil underneath gravity dam) is investigated under sinusoidal wave. Three main shaking table models (1-g) of concrete gravity dam built on a cohesionless soil are tested under 0.7 g sine waveform. The first test contained a concrete dam model which built on dry sand (empty case), the second is constructed in case of fully saturated cohesionless soil (empty also), whereas the last one, the dam is filled with water (i.e., at the upstream). The principles of physical modeling in geotechnics are used in both model construction of the concrete dam and the model preparation. The results of the shaking tests showed that the dynamic response (i.e., the measured acceleration) at different depths and positions for the soil particularly at the upstream side is strongly influenced by the water height at the upstream (i.e., *H*) with less effect in case of dry soil foundation underneath an empty dam, while it is so clear in case of the saturated foundation for empty dam. The response for the soil underneath the dam model is very safe because of the heavyweight of the dam model, and this was very important finding as this area may contain construction of some significant structural parts such as the blanket of the dam or cutoffs. The pore water pressure governed also during the shaking led to liquefaction under the dam model.

Keywords Cohesionless soil · Dynamic response · Shaking table

1 Introduction

Concrete gravity dam is one of the most complex infrastructure projects, which is constructed and designed in such a way that its own weight resists the external forces. Its behavior under earthquake excitation has become a major concern for researchers because any design error will lead to severe economic problems and significant loss

A. H. Aldefae (✉) · M. S. Shamkhi · T. Kh. Alhachami
College of Engineering, University of Wasit, Wasit, Iraq
e-mail: asadaldefae@uowasit.edu.iq

of life and equipment. Thus, seismic analysis of dams in seismic active areas is very important for predicting dam responses to ground motion. There are many studies that address the seismic performance and the dynamic performance of soil layers underneath the gravity dam, concerning spreading, amplification and attenuation in seismic waves [1]. Because of the difficult and complex circumstances surrounding the physical modeling process problem, little experimental works were conducted in the development of soil strata behavior under concrete dams. Reference [2] presented an experimental study on seismic behavior analysis of soil under concrete dam using two accelerometers. The results have been shown that the variations of acceleration in the dam with empty reservoir are smaller than the variations of acceleration in model with full reservoir.

Reference [3] investigated the optimal design of gravity dam and the response of the soil underneath it when it is exposed to seismic excitations using cohesionless soil with $D_r = 60$ and 80% using four accelerometers. The results show that the acceleration variations differ on the soil layers due to earthquake shaking, depending on the position of the sensors, and they are very low on the ground due to absorption of the impact wave of acceleration by the saturated soil particles.

The aim of this study is to investigate the seismic performance and the dynamic response of cohesionless soil (medium dense state) underneath gravity dam. Two experimental tests were conducted: (1) dam built on dry and saturated cohesionless soil (empty model) and (2) dam with full reservoir water using an earthquake simulator device, with 0.92 g input motion.

2   Physical Modeling and Design of the Model

The physical modeling in the hydraulic structures and water management project studies may be classified into linear and nonlinear. A linear model simulates the behavior of its prototype structure in the linearly elastic response range only. The tensile and compressive strengths of the materials (i.e., concrete) with associated failure strains do not have to be scaled. The nonlinear model should simulate the response of its prototype through failure. Consequently, the stress–strain relation of the model material should be appropriately scaled from those of the prototype material. In order to construct a physical model, a process of physical modeling based on idealizations and simplifications regarding the behavior model of the concrete dam should be involved. Substantially, the physical model is represented by a scaled structure with the same shape as the real structure.

In order to get logical and realistic results to be obtained from physical model to the prototype, mechanical characteristics and geometrical dimensions should be in certain ratios. If these ratios are achieved with ideal test conditions, the behavior of the prototype under dynamic loadings can be recognized using the physical quantities measured on model and the similitude ratios. Due to the difficulty of achieving these ideal conditions, the physical model will include some simplifications with respect to the prototype behavior model [4]. In this study, a small scale of concrete dam was

Fig. 1 Geometric of dam model
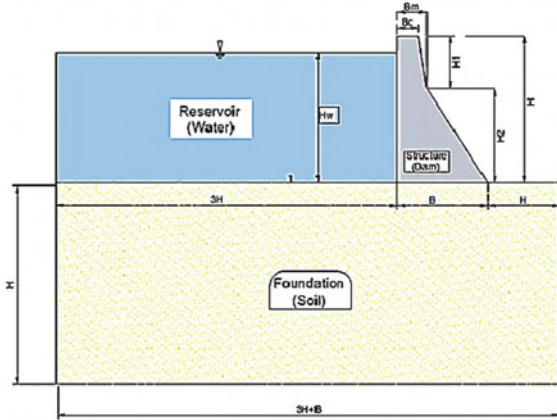
Table 1 Table captions should be placed above the tables

Dimensions (cm)	Variables
40	H
27	B
36	H_w
14	H_1
26	H_2
6	B_c
8	B_m

used with certain dimensions, which simulates existing dams in reality proportional to the size of shacking table machine as shown in Fig. 1 and Table 1.

3 Soil–Structure Interaction

When the soil–structure system imperiled to an earthquake excitation, the soil–structure interaction (SSI) influences the response of the structure. Generally, the dynamic response intensity of a structure depends on the soil–foundation system, the characteristics of the ground motion and the dynamic properties of the structure. The state of deformation (i.e., accelerations, velocities particle and displacements) in the supporting soil is different from that in the free [5].

When the structure is stiff and massive (i.e., gravity dam), the SSI plays a critical role in the dynamic response of the structure. On the other hand, the effect of SSI is negligible in case of the soil is very dense and rigid and if the structure is flexible, such as moment-resisting frames supported on stiff soil [6]. Commonly, the SSI has two main effects on structural response: (1) The SSI system has an increasing

number of degrees of freedom and thus modification of dynamic characteristics, and (2) a large part of the vibration energy of a SSI system can be dissipated either by radiation waves, emitted from the vibrating foundation–structure system back into the soil, or by hysteretic material damping in the soil [7]. Finally, SSI effects can lead to an increased structural response in specific seismic and soil environments, depending on the design response spectrum for the site.

4   Foundation Properties

The foundation of the physical model was cohesionless soil (i.e., sand) with a golden yellow appearance. The specifications of this sand are similar to the HST95 silica sand. First, the sand was dried in the oven for 24 h. After that, it was sieved in #10 in order to prevent the passage of large particles. The prepared sand was poorly graded sand with clay (SP-SC) according to USCS. The fundamental physical properties were identified in the laboratory in order to make a comparison with the properties of HST95 silica sand and HST50 Ottawa sand as shown in Fig. 2 which were commonly used in the University of Dundee [1, 8]. The physical properties of the sand used as well as the properties of both HST95 and HST50 silica sand and Ottawa sand are shown in Table 2 and Fig. 2.

In the physical model process, the soil specimen must be reconstituted to its natural state. Same procedure that was presented in the model preparation is followed by Humaish et al. [9]. As a result, the air pluviation technique was used to get the same specifications, density characteristics and the behavior of cohesionless soils that will be used as a foundation for the dam model. This technique is distinguished easily during the instruments installation, easy of model preparation and can achieve uniform soil layers (Fig. 3).

In this study, the relative density of $D_r = 55\%$ (i.e., medium dense soil) was used, based on 1.1 m container height and 3.5 mm slot size. This density was compared with both [1, 10] as shown in Fig. 4.

Fig. 2 Grain size distribution of used sand
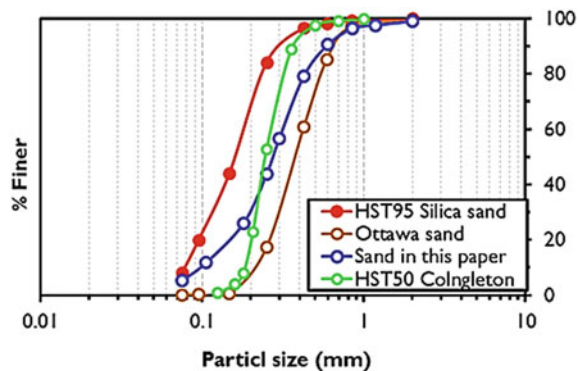
Table 2 Physical properties of used sand

The property	This sand	HST95 silica sand	Ottawa sand
Specific gravity, G_y	2.67	2.63	2.64
Shape	Rounded	Rounded	Rounded
Mean particle size, D_{50}	0.28	0.15	0.32
Coefficient of uniformity, C_u	2.85	1.9	1.68
Coefficient of gradation, C_z	1.32	0.95	1.08
Minimum dry unit weight, $\gamma_{d\,min}\left(\frac{kN}{m^3}\right)$	14.8	14.7	14.9
Maximum dry unit weight, $\gamma_{d\,max}\left(\frac{kN}{m^3}\right)$	19.1	19.2	19.5

Fig. 3 Mechanical air pluviator machine
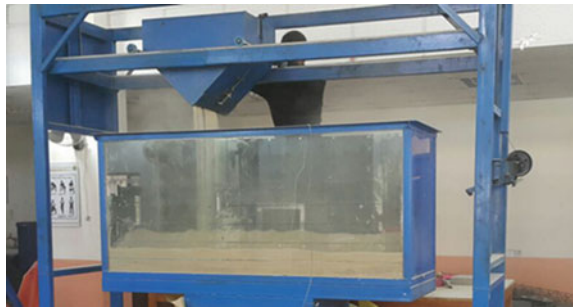
Fig. 4 Slot size correlation with relative density
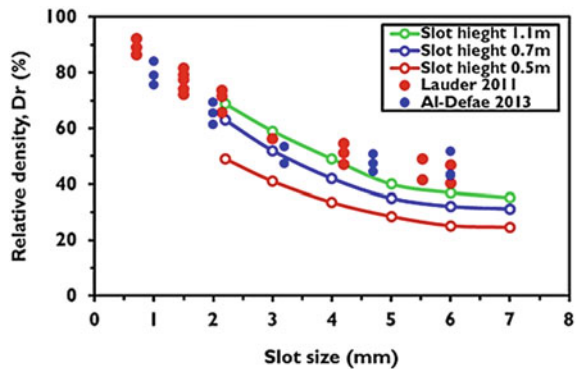
5 The Input Motion

The dynamic response of the model was carried out by applying a specific strong input motion which has peak ground acceleration up to 0.86 g with 10 s duration. Figure 5 describes the input motion in time and frequency domain with 1.6 Hz predominant frequency.
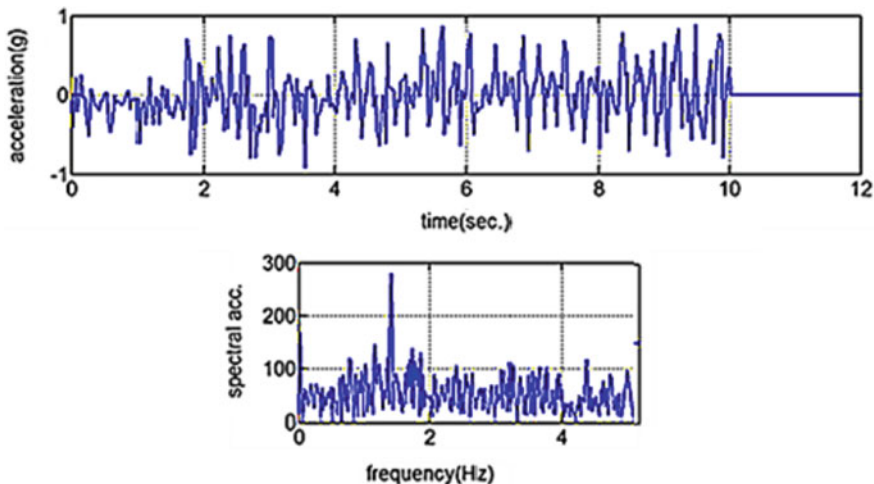
Fig. 5 Input motion in; **a** time domain and **b** frequency domain

Three types of tests were performed: (1) in case of the empty reservoir (dry cohesionless soil), (2) in case of the empty reservoir (saturated cohesionless soil) and (3) dam filled with water as shown in Figs. 6, 7 and 8. The acceleration reading was determined using ACC-ADXL78, which is characterized by: (1) small size, available in a 5 mm × 5 mm × 2 mm dimensions, and this gives maneuvering in using in the soil layers; (2) low power consumption (1.3 mA); and (3) high linearity (0.2% of full scale).
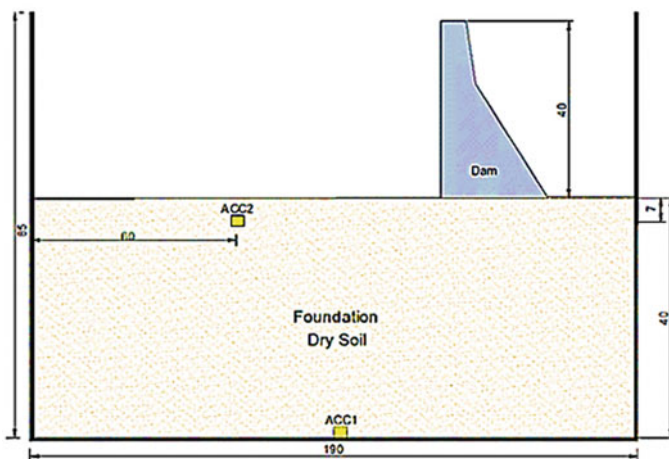
Fig. 6 Shaking table model layout with instruments, all dimensions in cm (in case of empty reservoir and dry soil)
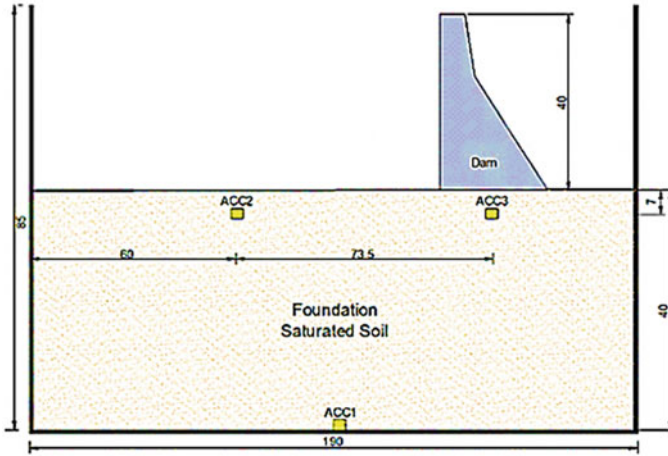
Fig. 7 Shaking table model layout with instruments, all dimensions in cm (in case of empty reservoir and saturated soil)
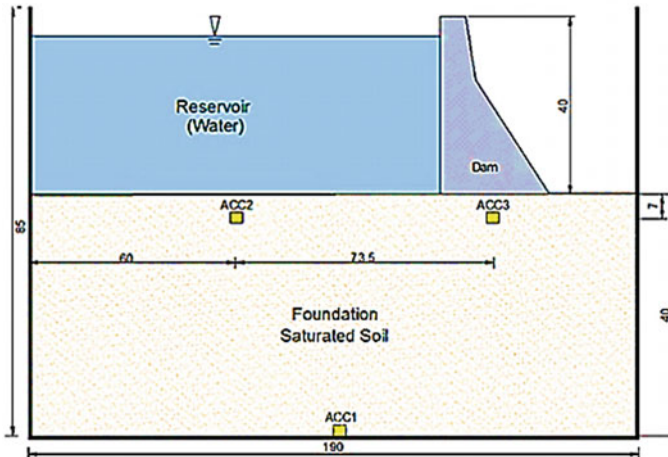
Fig. 8 Shaking table model layout with instruments, all dimensions in cm (in case filled with water)

6 Results and Discussion

6.1 Acceleration Response and Spectral Acceleration (Test 1)

The dynamic response of the dam foundation system is estimated from the measured acceleration for the soil layers. Figure 9 shows how the soil layers behave under
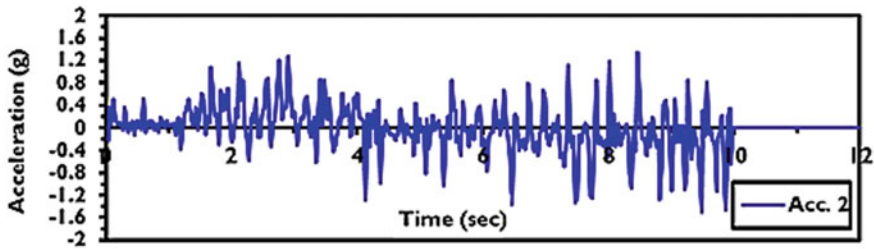
Fig. 9 Acceleration response of the dam foundation system
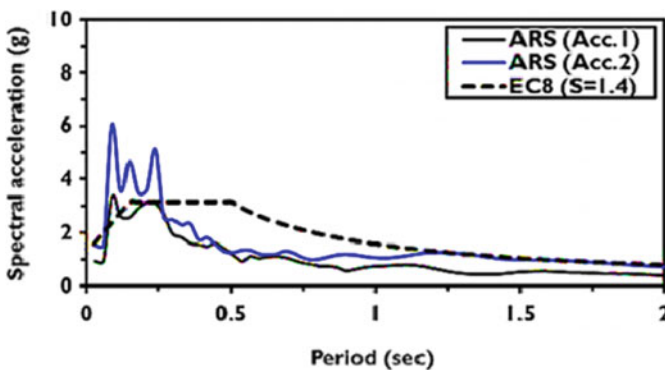
Fig. 10 Effect of shaking on the acceleration response spectra (5% structural damping)

dynamic motion. The response for the dam foundation (Acc. 2) was about 1.53, and this value gave an amplification factor which is equal to 1.66. The results were consistent with the fact that the seismic motion was amplified as it moved from the rock bed to the surface of the earth [1, 11].

The acceleration response spectra performed depending on the elastic design response spectrum from Euro code 8 [12] and design of structures for earthquake resistance (Part 1: General rules, seismic actions and rules for buildings) as shown in Fig. 10. The spectral acceleration is greatly affected by the magnitude of the acceleration, and there is an amplitude ranging from $T = 0.1$ to $T = 0.35$. Also, the spectral design for EC depends on the natural period (i.e., the amplification factor (S) increases to 1.7) during the low period interval ($T = 0.15$ s) and reducing back after ($T = 0.15$ s).

6.2 Acceleration Response and Spectral Acceleration (Test 2)

The acceleration measurement when the soil is fully saturated is shown in Fig. 11, which varies from the dry soil (i.e., Test 1). There is a reduction in the reading of
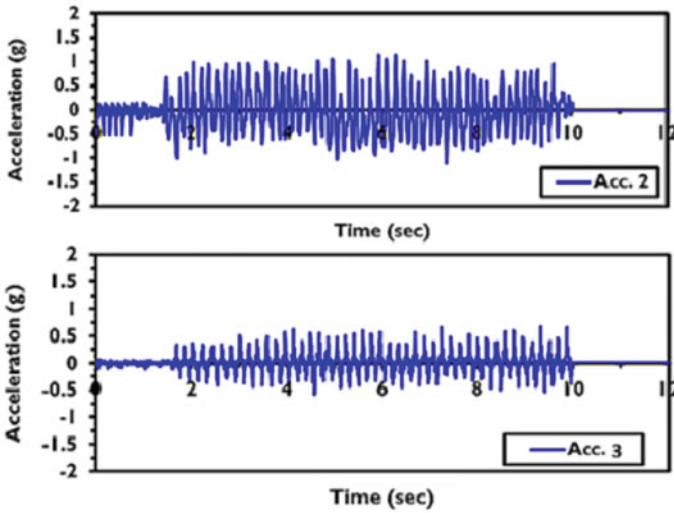
Fig. 11 Time acceleration of Test 2

Acc.2 (which is equal to 1.05 g) which is contrary with the amplification observed in the dry model.

There is attenuation occurring due to saturated soil particles that absorb the acceleration wave. Also, it was observed that the acceleration reading of the acceleration sensor below the dam model (Acc.3) was a low value ($g = 0.5$) which is equivalent to about 45% of the amplitude of the input motion (i.e., $g = 0.82$).

The significant attenuation occurred due to the heavyweight of the concrete dam model, which prevents the soil layers underneath the dam from amplification compared with ACC2. The acceleration response spectrum for the empty saturated model is shown in Fig. 12. The effective period that must be taken into account in saturated soil is varied from 0.2 s (5 Hz) and 0.04 s (25 Hz). Also, it can be seen that the response of the accelerometer which is located close to the dam foundation (i.e.,

Fig. 12 Acceleration response spectra for Test 2 (empty saturated dam model)
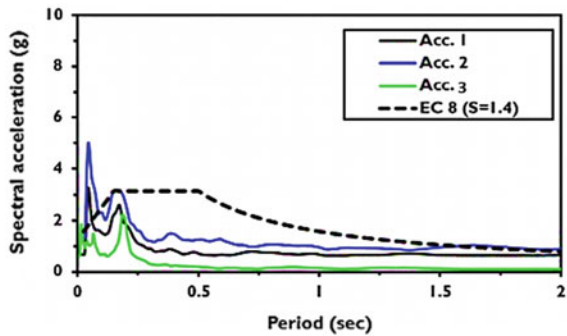
Acc.3) has not been much exited. This is due to the periodic stress resulting from the shaking in the position where the heavyweight of the dam has limited the amplification in the seismic waves. The dynamic response for saturated cohesionless soil has been less effective than the response in dry cohesionless soil for two substantial causes: (1) The saturated soil has large density compared with dry soil state and (2) the periodic stress–strain behavior for the voids ratio that filled with water has been less exciting to shaking compared with voids filled with air.

6.3   Acceleration Response and Spectral Acceleration (Test 3)

Figure 13 demonstrates the acceleration measurement in case of full reservoir. A green line is added to the graph (i.e., Acc.2) that illustrates the average values for the acceleration reading. A prominent attenuation was observed for the acceleration measured by Acc.2, due to the weight of the water at the upstream which prevents the wave from spreading, making a big amplitude cyclic motion at this zone. Also, the dynamic response of Acc.3 (underneath the dam model) is similar to Test 2, and this is because of the heavyweight of the model itself.

The acceleration response spectrum for Test 3 is plotted in Fig. 14, which is different from last two tests. It can be concluded that the ARS (i.e., elastic response
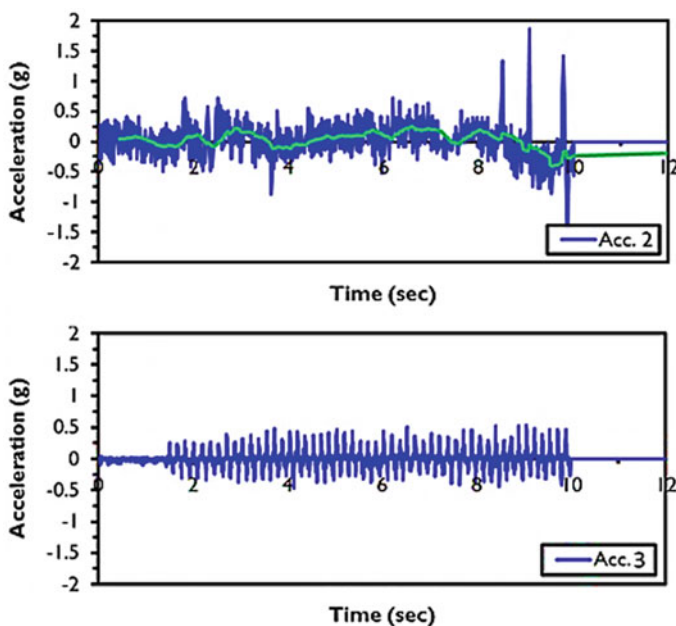
Fig. 13 Time domain for the measured acceleration (Test 3)

Fig. 14 Spectral acceleration for Test 3 (filled with water dam model)
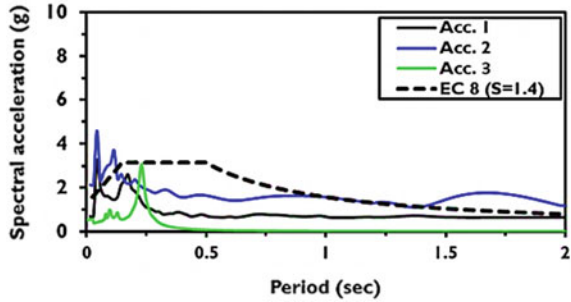
spectrum) exceeds the limitations of the EC8 for a very low period (i.e., less than 0.15 s) and at high period (i.e., 1.2 s), which indicates that the frequency ranges above 7 Hz and below 0.8 Hz. In addition, the dynamic response of the Acc.4 is still beneath predicted with the limits of the EC8.

7 Conclusions

This paper conducted an experimental work on the seismic performance and the dynamic response of the foundation underneath a concrete gravity dam using the earthquake simulator device. The main conclusions may be summarized as follows:

1. The reading of Acc.2 and Acc.3 was amplified due to site amplification. On the other hand, the amplification of the motion begins from the bedrock to the ground surface.
2. The saturated soil particles are either absorbed or damped in the seismic wave. This was clearly observed by reading the sensor Acc.2 in the saturated dam model (Test 1) compared with dry model (Test 2).
3. There is noticeable attenuation in the reading of acceleration sensor Acc.3 in both Test 2 and Test 3. This was occurring due to the heavy load of the dam model, causing a constraint of the seismic wave.
4. Finally, the response to the soil underneath the dam model is very safe because of the heavyweight of the dam model. This is a very important finding as this area may contain the construction of some significant structural parts such as the blanket of the dam or cutoffs.

References

1. Al-Defae AH, Caucis K, Knappett JA (2013) Aftershocks and the whole-life seismic performance of granular slopes. Géotechnique 63(14):1230–1244

2. Resatalab S, Attarnejad R, Ghalandarzadeh A (2013) Experimental investigation on interaction of concrete gravity dam-reservoir-foundation on shaking table. Tech J Eng Appl Sci TJEAS 1756–1762

3. Al-qaisi AZ, Omran HA, Al-Shukur AK (2016) Optimal design of concrete gravity dams on random soil. Ph.D. thesis, Building and Construction Engineering Department, College of Engineering, University of Technology, Baghdad, Iraq

4. Rosca B (2008) Physical model method for seismic study of concrete dams. Buletinul Institutului Politehnic Din Iasi 4(3):57–76

5. Johnson IJ, Alamo CA Earthquake engineering hand book, chapter 10: soil structure interaction. CRC Press LLC

6. Elnashai S, Amr (2015) Fundamentals of earthquake engineering, 2nd edn. Wiley, USA

7. Pitilakis D, Dietz M, Wood DM, Clouteau D, Modaressi A (2008) Numerical simulation of dynamic soil-structure interaction in shacking table test. Soil Dyn Earthquake Eng 28(6):453–467

8. Al-Baghdadi TA, Brown MJ, Knappett JA, Aldefae AH (2017) Effects of vertical loading on lateral screw pile performance. Proc Inst Civil Eng: Geotech Eng J 170(GE3):259–272

9. Humaish AH, Shamkhi MS, Al-Hachami THKH (2018) Seismic performance of concrete dam-reservoir system. Int J Eng Technol 4(20):4873–4879

10. Bertalot D, Brennan AJ, Villalobos FA (2013) Influence of bearing pressure on liquefaction-induced settlement of shallow foundations. Géotechnique 63(5):391–399

11. Brennan AJ, Madabhushi SPJ (2009) Amplification of seismic accelerations at slope crests. Can Geotech J 45(5):585–594

12. Standard B (2005) Eurocode 8: Design of structures for earthquake resistance. Part, 1, 1998-1

Liquefaction Resistance of Desaturated and Partly Saturated Clean Sand

Dhanaji Chavan ⓘ**, T. G. Sitharam** ⓘ**, and P. Anbazhagan** ⓘ

Abstract Induced desaturation has been emerging as a new liquefaction mitigation technique. Laboratory study carried out, so far, on induced desaturation has mainly focused on shaking table and centrifuge studies. In the present study, triaxial specimens of saturated clean sand have been desaturated by injecting air/CO_2 into it and stress-controlled undrained cyclic triaxial tests have been conducted on such samples. Few tests have been conducted on partly saturated samples as well. It is observed that the presence of air in the sample increases the liquefaction resistance of the sand. Further, desaturation affected not only liquefaction resistance but also dilative and contractive tendency of the soil. Slope of the phase transformation line on compression side initially increased and then decreased with reduction in degree of saturation whereas slope of phase transformation line on extension side initially decreased and then increased with reduction in the degree of saturation. In most of the cases, slope of the phase transformation line on extension side is found to be smaller than that on compression side.

Keywords Initial liquefaction · Desaturation · Phase transformation line

1 Introduction

Saturated loose sand when subjected to earthquake loading generates large pore water pressure and finally loses its strength and stiffness. This phenomenon is called as liquefaction [1]. Over the last few decades, various techniques such as explosive compaction, deep dynamic compaction and deep soil mixing have been invented to mitigate the liquefaction [2]. Induced desaturation is emerging as a new liquefaction mitigation technique over the last few years. In this technique, liquefaction susceptible saturated loose sand is desaturated by adopting one of the following techniques: (1) air injection; (2) microbial desaturation; (3) water electrolysis; (4) sand compaction pile; (5) use of sodium perborate; [3–6].

D. Chavan (✉) · T. G. Sitharam · P. Anbazhagan
Indian Institute of Science, Bangalore 560012, India
e-mail: dschavan83@gmail.com

Laboratory study carried out, so far, on induced desaturation has mainly focused on shaking table and centrifuge studies. No research has been carried out so far on air-injected desaturated triaxial specimens. Purpose of this study is: (1) to desaturate saturated triaxial specimen by CO_2 injection/air injection; (2) to assess change in liquefaction resistance on desaturation; (3) to study the effect of desaturation on contractive and dilative tendency of sample. In the present study, stress-controlled undrained cyclic triaxial tests have been conducted on CO_2 desaturated, air desaturated and partly saturated clean sandy soil.

2 Material and Methodology

2.1 *Material*

Original sand was collected from bed of Sabarmati River near IIT Gandhinagar campus, Gujarat, India. This is the area which severely suffered from 2001 Bhuj earthquake. Collected sand was passed through 2 mm IS Sieve. In the present study, sand passing through 2 mm IS Sieve and retained on 75 micron IS Sieve has been used. Gradation curve for this sand is shown in Fig. 1 and its rest of the index properties are given in Table 1. As per IS soil classification system soil comes to be poorly graded fine sand.
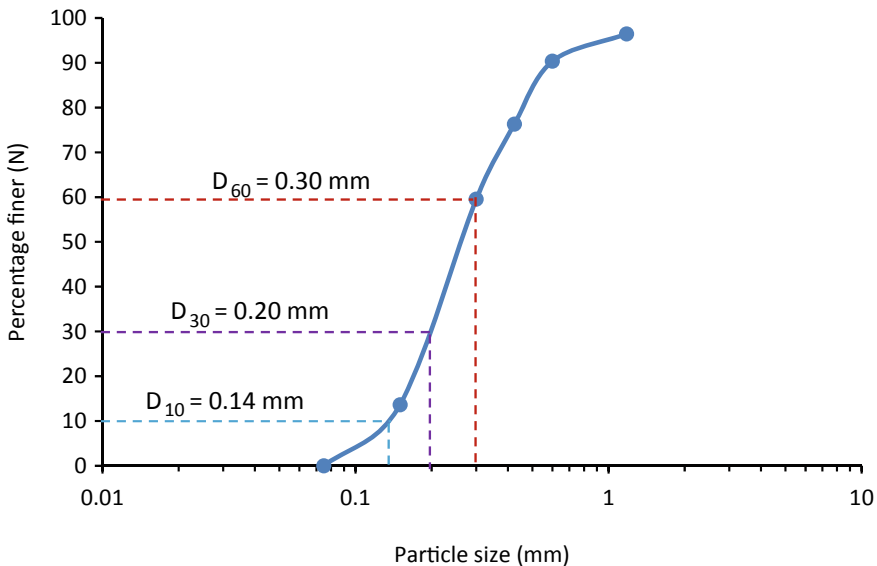
Fig. 1 Gradation curve of sand

Table 1 Index properties of the sand

G	e_{max}	e_{min}	ρ_{max} (gm/cc)	ρ_{min} (gm/cc)	D_{50} (mm)	C_u	C_c
2.65	0.84	0.45	1.83	1.44	0.27	2.14	0.95

2.2 Methodology

2.2.1 Sample Preparation

Sample was prepared by dry deposition method. Oven dry sand mass was deposited in the split mould in five layers with zero drop height. At the end of last layer little tamping and side tapping was done. Before removing split mould vacuum of 20 kPa was applied to the sample so that it can stand on its own even after removal of mould.

2.2.2 Saturation

Once sample was prepared as mentioned in above section, CO_2 gas was passed though the sample under vacuum of 20 kPa for 10 min. Then cell pressure of 20 kPa was applied and vacuum was released and again CO_2 gas was percolated through sample for another 20 min. This was followed by percolation of 1000 ml of distilled water. From several trials, it was found that this resulted into degree of saturation as high as 99%. From practical point of view, sample with degree of saturation of 99% can be considered as a fully saturated sample [7]

2.2.3 Desaturation

Once it was ensured that sample was saturated; it was desaturated by injecting/CO_2 from the bottom of the sample. The triaxial setup before and during desaturation is shown in Figs. 2 and 3. The detailed procedure adopted during desaturation is given in Fig. 4.

It should be noted that saturation and desaturation steps are not applicable to partly saturated samples. In case of partly saturated samples, once dry sample was prepared as mentioned in the "sample preparation" section, quantity of water in the range of 200–800 ml was passed through the specimen. Depending upon the quantity of water passed, different degrees of saturation were achieved. Both for desaturated and partly saturated sample, degree of saturation of the sample was computed from B parameter, using the following equation.

$$B = \frac{1}{1 + nK_s\left[S/K_w + (1 - S)/u_a\right]} \tag{1}$$
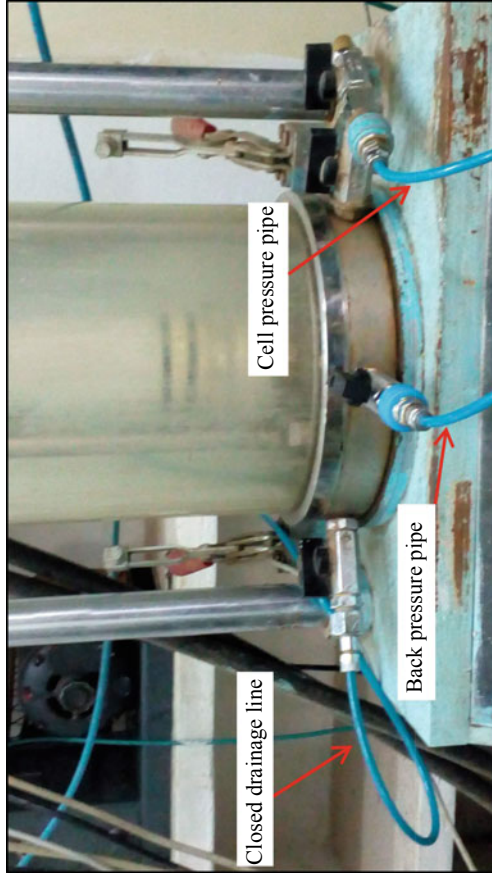
Fig. 2 Triaxial cell set up before desaturation
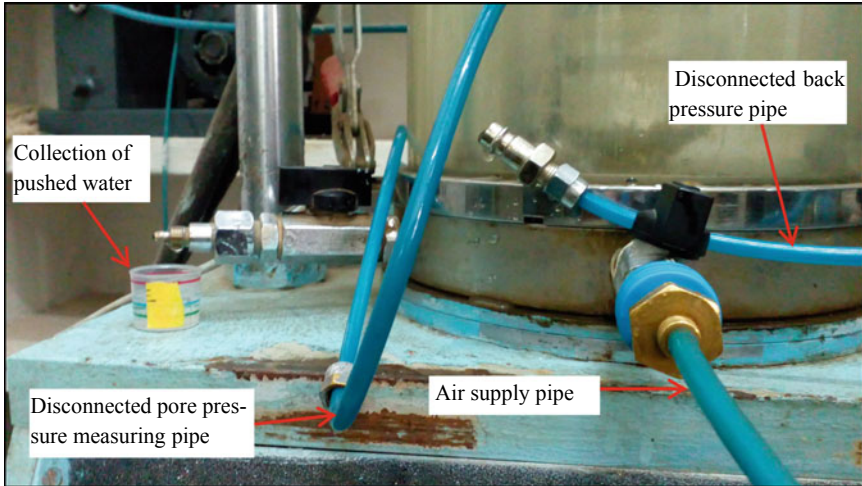
Fig. 3 Triaxial cell set up during desaturation
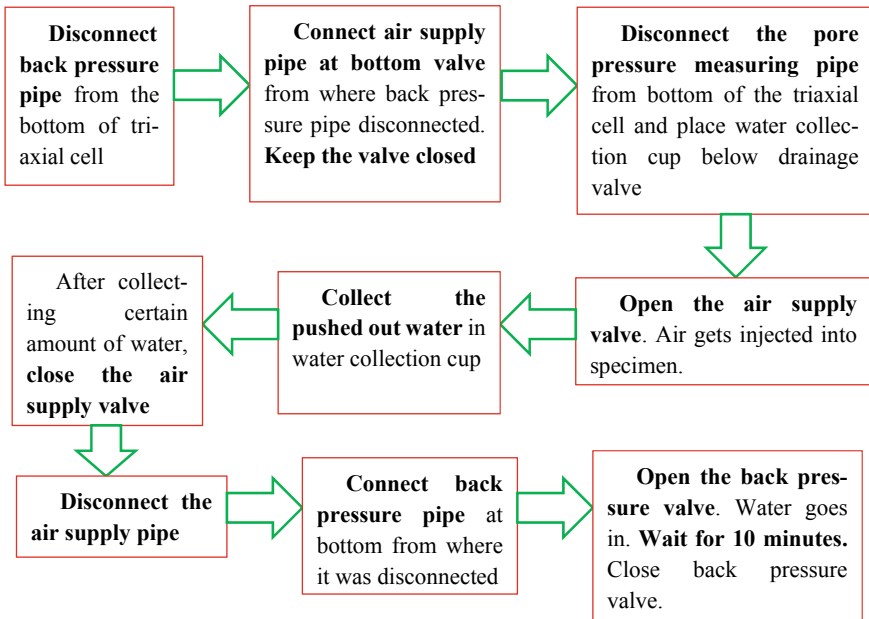
Fig. 4 Flow chart explaining steps adopted during desaturation

where, n is the porosity of the sample, S is the degree of saturation, K_s and K_w are the bulk modulus of soil skeleton and water, respectively and u_a is the absolute pore fluid pressure.

2.2.4 Application of Cyclic Loading

Back pressure valve was closed and pore pressure measuring device was connected at the drainage valve. Then, sinusoidal cyclic deviatoric stress was applied at the frequency of 0.1 Hz. Tests were conducted on samples of relative density (D_r) of 30, 40 and 60% at CSR of 0.175, 0.250 and 0.400.

3 Results and Discussion

3.1 Degree of Saturation and Initial Liquefaction

Cyclic tests were conducted on CO_2 desaturated, air desaturated and partly saturated samples. It was observed that number of cycles required for initial liquefaction (N_i) increased with decrease in degree of saturation. The trend was observed to be exponential for all three cases as shown in Fig. 5. Further, it was observed that CO_2 desaturated samples took least number of cycles and partly saturated samples took the most number of cycles for given degree of saturation to reach the initial liquefaction. Possible reason could be dissolution of injected CO_2 into the pore water during
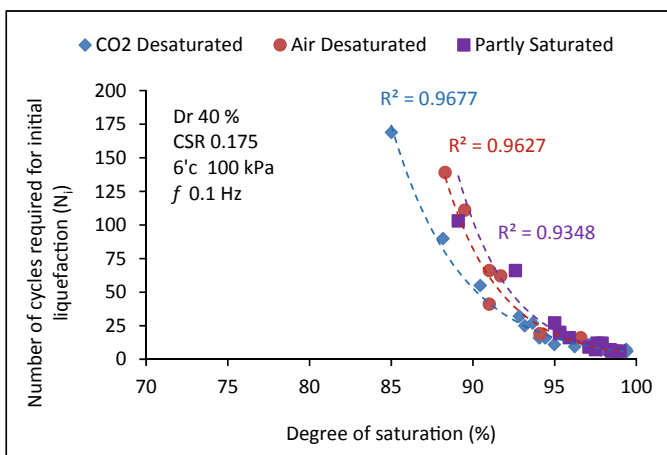
Fig. 5 Number of cycles required for initial liquefaction versus degree of saturation

the cyclic loading. The liquefaction resistance of air desaturated and partly saturated samples is very close to each other.

3.2 Effect of Desaturation on Stress Ratio at Phase Transformation

When saturated sand, dense of critical state, is subjected to undrained loading, initially it contracts and then dilates. Contraction results into increase in the pore pressure while dilation results into decrease into the pore pressure. This state results into elbow in effective stress path as shown in Fig. 6. Locus of all such point results into a straight line called as phase transformation line. It is a well-established fact that stress ratio at the phase transformation depends on void ratio and effective confining pressure. Stress ratio is the ratio of deviatoric stress and effective mean stress.

In the present study, it is investigated whether the presence of air in the voids, along with water, has any influence on the stress ratio at the phase transformation. Some of the effective stress paths are shown in Fig. 6. In this figure, *CSL* stands for critical state line, *PTLc* and *PTLe* stand for phase transformation line on compression side and phase transformation line on extension side, respectively. From the Fig. 6a, it is observed that, for given case, phase transformation line on compression side coincides with critical state line. Thus, the stress ratio for the *PTLc* equals the stress ratio for CSL, which is equal to 1.25. Further, stress ratio for *PTLe* is observed to be −0.75. For the case shown in Fig. 6b, phase transformation line on compression side is distinct from the corresponding CSL. Stress ratio for *PTLc* and *PTLe* is found to be 0.72 and −0.55 respectively. From Fig. 6, it is clear that slope of *PTLe* is less than that of *PTLc*.

Stress ratio at different degrees of saturation for various relative densities and cyclic shear stress ratio (CSR) is shown in Fig. 7. It is observed from Fig. 7a that stress ratio on compression side initially increases with decrease in degree of saturation and then decreases. On the other hand, stress ratio initially decreases and then increases with reduction in degree of saturation, during extension stage of loading as seen in Fig. 7b. Further, stress ratio for relative density of 60% is observed to be less than that for relative density of 30% and 40%, during compression stage of loading. On the other hand, during extension stage of loading, stress ratio for relative density of 60% is observed to be greater than that for relative density of 30 and 40% as seen Fig. 7b.

4 Conclusion

There is increase in the liquefaction resistance on desaturation. The trend is observed to be exponential. Further, the CO_2 desaturated samples took the least cycles while

Fig. 6 Effective stress paths showing effect of air desaturation on phase transformation

a)

b)
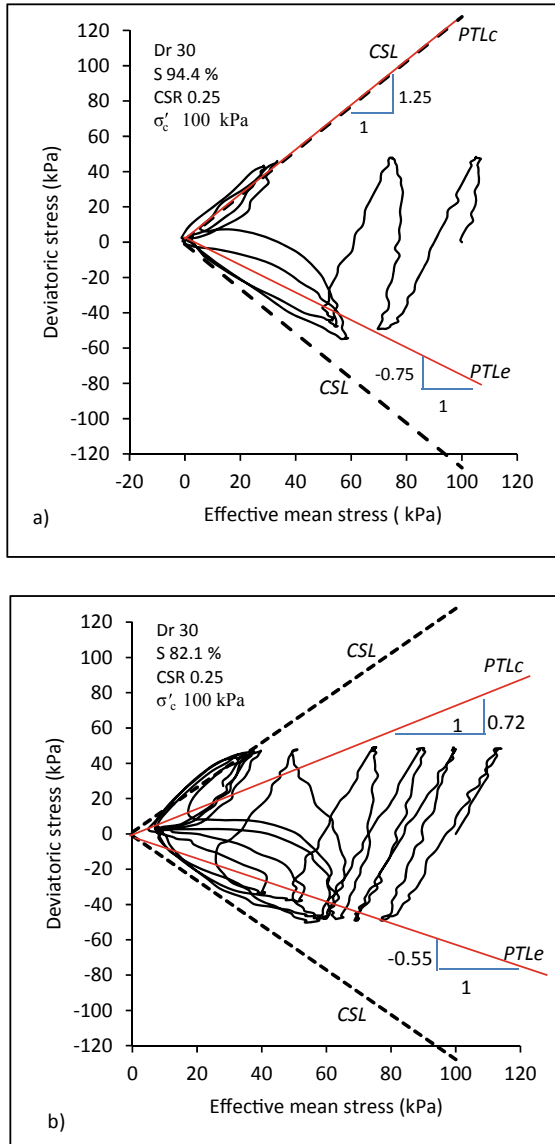
partly saturated sample took most cycles for given degree of saturation to reach the initial liquefaction. Desaturation affected contractive and dilative tendency of the sample as well. It was observed that stress ratio (i.e. slope) of the phase transformation line on compression side initially increases and then decreases with desaturation. On the other hand, slope of phase transformation line on extension side initially decreases and then increases with desaturation. Further, stress ratio for phase transformation line on extension side is found to be less than that for phase transformation line on
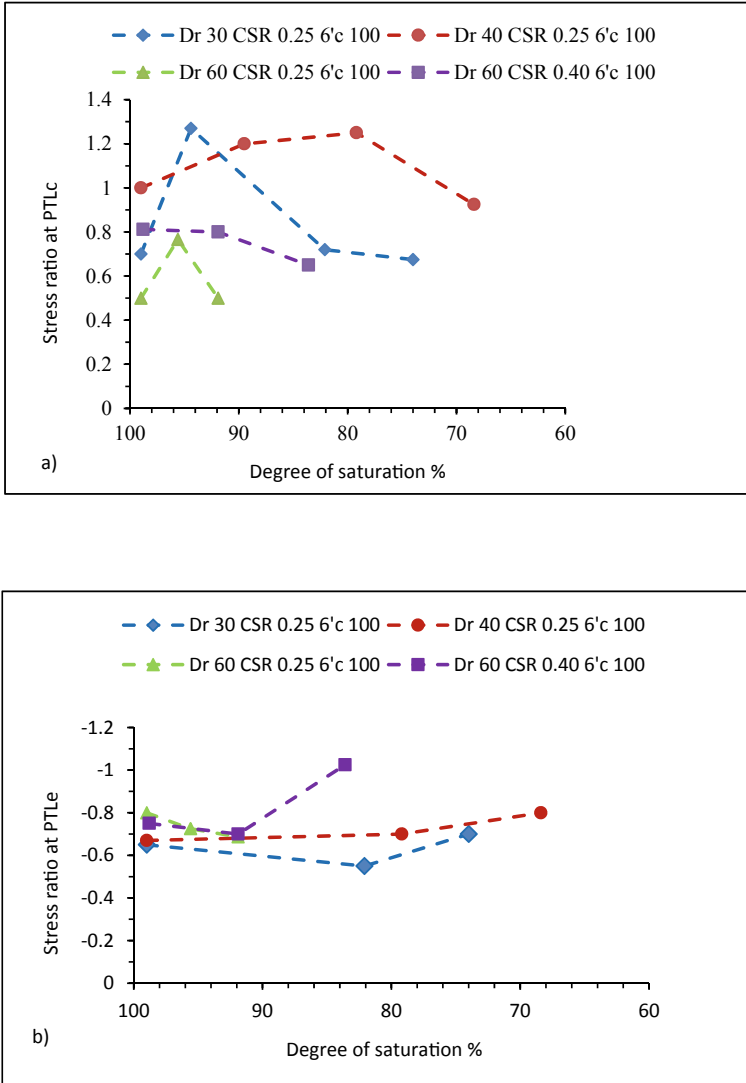
Fig. 7 Variation of stress ratio at phase transformation with degree of saturation

compression side. Comparison of stress ratio during compression shows that denser samples have smaller stress ratio while case is reverse during extension. Further study is required to have more deep insight of effect of desaturation on dilative—contractive tendency during undrained cyclic loading.

References

1. Kramer, S.L.: Geotechnical earthquake engineering. Pearson (1996)
2. Idriss, I.M., Boulanger, R..: Soil liquefaction during earthquakes. EERI (2008)
3. Okamura M, Takebayashi M, Nishida K, Fujii N, Jinguji M, Imasato T, Yasuhara H, Nakagawa E (2011) In-situ desaturation test by air injection and its evaluation through field monitoring and multiphase flow simulation. J Geotech Geoenviron Eng 137:643–652. https://doi.org/10.1061/(ASCE)GT.1943-5606.0000483
4. Yegian MK, Eseller-Bayat E, Alshawabkeh A, Ali S (2007) Induced-partial saturation for liquefaction mitigation: experimental investigation. J Geotech Geoenviron Eng. 133:372–380. https://doi.org/10.1061/(ASCE)1090-0241(2007)133:4(372)
5. Okamura M, Ishihara M, Oshita T (2003) Liquefaction resistance of sand deposit improved with sand compaction piles. Soils Found 43:175–187
6. He J, Chu J, Ivanov V (2013) Mitigation of liquefaction of saturated sand using biogas. Géotechnique. 63:267–275. https://doi.org/10.1680/geot.SIP13.P.004
7. Black D, Lee K (1973) Saturating laboratory samples by back pressure. J Soil Mech Found Div 99:75–95

Liquefaction Behavior of Low to Medium Plasticity Sand-Fines Mixtures

Muttana S. Balreddy, S. V. Dinesh, and T. G. Sitharam

Abstract During earthquake, soil deposits are subjected to cyclic loading. Under undrained conditions, cyclic shear stress causes transient disturbance and gives rise to an increase in excess pore water pressure leading to loss of shear strength in saturated soil deposits, there will be excessive strains with continued loss of shear strength resulting in liquefaction. Researchers have identified a significant number of cases where ground failure took place during earthquake in soil deposits containing fines leading to considerable damage to buildings. Some studies show a decrease in liquefaction resistance and others show an increase in liquefaction resistance with an increase in fines content in soil deposit. There is no clarity regarding the effect of fines. In view of this, an experimental investigation has been carried out to evaluate the liquefaction potential of sand-clay mixtures. A series of undrained stress-controlled cyclic triaxial shear tests were performed on reconstituted samples obtained from Cauvery River sand and sand mixtures containing different percentages of plastic fines up to 30%. This paper reports the results of stress-controlled cyclic triaxial shear tests under undrained conditions at 100 kPa confining pressure at a frequency of 0.1 Hz. The results show that the cyclic strength decrease with an increase in fines content upto 20% beyond which it increases. In the present investigation, the limiting fines content is 20%. The results of CRR were analyzed in terms of relative density, fines content, and plasticity characteristics. The results indicate that flow liquefaction depends on the acceleration (CSR) and initial state (void ratio).

Keywords Fines content · Liquefaction · Cyclic resistance ratio

M. S. Balreddy (✉) · S. V. Dinesh
Department of Civil Engineering, Siddaganga Institute of Technology, Tumakuru 572103, India
e-mail: msb@sit.ac.in

S. V. Dinesh
e-mail: dineshsv2004@gmail.com

T. G. Sitharam
Indian Institute of Technology, Guwahati 781039, India
e-mail: proftgs@gmail.com

1   Introduction

Among the seismic hazards, soil liquefaction is a major threat to human life, infrastructure, and environment. Many historical earthquakes have noticed the phenomena of soil liquefaction, some of them are 1964 Niigata, Japan, 1964 Alaska, USA and 2001 Bhuj, India. The most important step towards mitigating liquefaction hazard is by evaluating liquefaction potential of soil accurately. Although loose saturated cohesionless soils are most susceptible to loss of strength, there are studies and evidences suggesting that soils containing fines are also prone to liquefaction during earthquakes. The presence of a certain amount of fines in sand was generally considered to increase the resistance but a detailed literature review of laboratory and field investigations has clearly highlighted the conflicting evidence of the effect of fines on the liquefaction behavior of sand-fines mixtures. The situation is, however, more complicated for low-plasticity silts and clays that are near the transition zone between "sand-like" and "clay-like" behavior.

The factors affecting and the mechanism associated with the liquefaction potential of sands have been reasonably understood. Many natural and artificial soils contain combinations of fine-grained (i.e., clay and silt) and coarse-grained (i.e., sand and gravel) soils. Such soils are called intermediate or mixed soils or mixtures, in which clay contents are present in different percentages. The literature review indicates that the presence of clay fines affects the liquefaction behavior. There are studies that suggest that sand-clay mixtures are non-liquefiable when clay fines are <20% and in some cases they are liquefiable when clay fines are >15%. Some studies have indicated decrease in liquefaction resistance with an increase in plasticity and vice-versa [2, 6, 7, 10]. Some studies have reported decrease of CRR till limiting fines content. Some researchers reported that increase in plasticity reduces the liquefaction resistance of silty soils [8]. There is wide variation in the recommendations on the limiting boundaries of liquid limit and PI values on the Atterberg's limit chart for liquefaction susceptibility. Literature suggests flow liquefaction for sand-fines mixtures till PI = 7 and cyclic mobility when PI > 7 [5]. This is based on plasticity of mixtures without any reference to the level of shaking as reflected by cyclic stress ratio and initial state (relative density). Hence, it is necessary to study the liquefaction behavior of sand-fines mixtures under cyclic loading to understand the above issues related to flow liquefaction dependence on plasticity characteristics, relative density, cyclic stress ratio. The present paper reports the effect of plasticity characteristics, relative densities, and CSR on the flow liquefaction of low to medium plasticity sand-fines mixtures.

2   Materials and Experimental Methods

To understand the effect of fines on liquefaction resistance, sand and fines were used in the present investigation. Sand was procured from the Cauvery River bed, Karnataka,
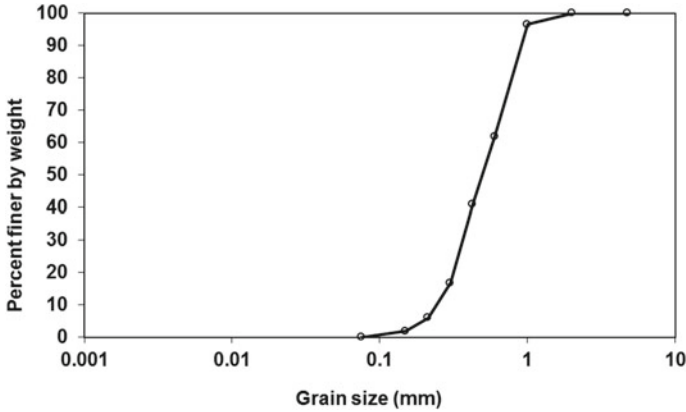
Fig. 1 Grain size distribution curves of Cauvery River clean sand (S)

India. Clayey sand was procured from locally available sources in Tumakuru region, Karnataka, India. Figure 1 shows grain size curve of clean Cauvery river sand (S). The grain size curve of sand lies within the boundaries of most liquefiable soils as proposed by Tsuchida [9]. This clearly indicates that sand under undrained conditions would liquefy during an earthquake. The specific gravity (G_s) of sand is 2.62, coefficient of curvature (C_c) is 0.9, coefficient of uniformity (C_u) is 2.4, maximum void ratio (e_{max}) is 0.99, and minimum void ratio (e_{min}) is 0.72. From the above data according to IS classification, the sand is classified as poorly graded sand (SP).

Clayey sand is available at shallow depths of 1.5–15 m from the ground level in the southern parts of Karnataka. It is white-yellowish in color. The fines ($<75\ \mu$) extracted from the clayey sand soil are designated as *F*. The specific gravity (*G*) is 2.65. The soil composition consists of gravel 01%, sand 53%, silt 28%, and clay 18%. The liquid limit is 46, plastic limit is 27, and the plasticity index is 19. The fines chosen are plastic in nature. From the above data according to IS classification, the soil is Clayey Sand (SC).

In order to study the influence of fines in the sand on liquefaction resistance, fines were separated from clayey sand and mixed with clean Cauvery River sand (S) to prepare sand-fines mixtures. The details of sand-fines mixtures prepared are shown in Table 1. The fines fraction of size less than 0.075 mm was separated from clayey sand and used as fines in the experimental program. These clay fines were mixed with the clean Cauvery River sand (S) in various proportions ranging from 0 to 30%. The three sand-fines mixtures considered are SF10, SF20, and SF30. The index properties of sand-clay mixtures refer Balreddy et al. [3]. With the addition of fines to sand, the sand-fines mixtures changes to non-plastic sand-silt mixture at 10%, sand-clay or sand-silt of low plasticity at 20% fines and sand-clay of medium plasticity at 30% of fines.

Table 1 Details of liquefaction susceptibility for soil mixtures

Soil mixtures	Fines content (%)	Liquid limit (%)	Plasticity index	Relative density (%)	CSR	CRR	Residual pore pressure ratio	Sample failure by Flow Liquefaction (FL)/Cyclic Mobility (CM)
SF00	0	0	0	50	0.15	0.162	1.0	FL
SF10	10	22	0		0.145	0.13	1.0	FL
SF20	20	26	6		0.144	0.11	1.0	FL
SF30	30	32	17		0.15	0.125	1.0	FL
SF10	10	22	0	70	0.168	0.17	1.0	FL
SF20	20	26	6		0.17	0.14	0.95	CM
SF30	30	32	17		0.165	0.155	0.92	CM

2.1 Sample Preparation

For achieving the loosest possible density, triaxial test specimens of 50 mm diameter and height 100 mm were prepared by dry deposition method. Required quantity of sand and fines were weighed. Sand and fines were divided into 10 equal parts. Each of the sand and fines portions was mixed thoroughly to have a uniform mixture. These mixture portions were filled in a membrane lined to the split mold attached to the bottom platen of the triaxial cell by using a spout of 12 mm diameter at the bottom. The spout was slowly raised along the axis of symmetry of the specimen, such that the soil was not allowed to have any drop height. The sand-fines slide down slowly. The mold was gently tapped with a wooden mallet to achieve the required density for each layer. Then the sample was subjected to low-pressure vacuum and carbon-di-oxide gas was passed for one hour. After this, de-aired distilled water was passed through the soil sample at a very small head. The specimens were saturated by applying a back pressure of 100 kPa and saturation time was maintained till the Skempton's pore pressure coefficient 'B' value exceeds 0.95.

An effective confining pressure of 100 kPa was applied and specimens were isotropically consolidated till the end of Casagrande's primary consolidation. The reduction in the void ratio before and after consolidation is found to be in the range of 0.027–0.066. An increase in the relative density after consolidation by 5–10% was observed compared to the initial relative density. In this way, the samples were prepared at relative densities of 50, 60, 70, and 80%.

2.2 Stress-Controlled Tests

In the present work in order to simulate the stress conditions existing during earthquakes, the cyclic triaxial test facility was used to conduct stress-controlled undrained cyclic triaxial shear test. The tests were performed at 100 kPa confining pressure and frequency of 0.1 Hz. ASTM: D 5311-92 (Reapproved 1996 [1]) was followed for conducting tests.

The load, deformation, cell pressure, pore water pressure data were obtained by a computer-controlled data acquisition system. In each loading cycle, 128 data points were captured. Tests were continued till an excess pore pressure is equal to confining pressure or 5% double amplitude axial strain is reached. For more details regarding the full experimental program and cyclic stress ratio amplitudes applied during the tests see Balreddy et al. [3].

3 Results and Discussion

Figure 2 shows the results of cyclic triaxial test under stress-controlled conditions on a sample of sand (SF00) having a void ratio of 0.855 ($D_r = 50\%$) at 100 kPa confining pressure at a loading frequency 0.1 Hz.

Figure 2a shows the plot of axial strain versus number of cycles. Beyond 5 cycles, the rate of development of axial strain is faster. The sample shows a large amount of axial strain on the extension side when compared to the compression side. The sample is considered to be failed when the double amplitude axial strain is 5% or when 100% excess pore water pressure develops. In this case, the sample has failed at 6th cycle.

Figure 2b shows the plot of residual pore pressure ratio versus cycle ratio. The residual pore water pressure buildup is increasing uniformly till cycle ratio of 0.7 beyond which it develops at a faster rate and attains a value of 1. The sample failed by flow liquefaction. The residual pore water pressure is responsible for the reduction in effective stress and strength loss.

Figure 2c shows the plot of double amplitude axial strain versus number of cycles. It is observed from the plot that the double amplitude axial strain is constant till 4th cycle. Beyond 4th cycle, there is a sudden buildup of axial strain. Failure is observed at 6th cycle where the double amplitude axial strain value reaches more than 5%.

Figure 2d shows the plot of deviator stress versus effective mean stress. It is observed that in the beginning the sample is subjected to low axial strain and remains constant till 4th cycle. After 4th cycle, the loop widens and enlarges with large deformation on the extension side.

Figure 3 shows the plot of cyclic resistance ratio (CRR) versus fines content at varying void ratio. The cyclic strength is more for the clean sand. For details of cyclic strength of SF00 and SF10 refer Balreddy et al. [3]. The results show that the cyclic strength decrease with an increase in fines content upto 20% beyond which it
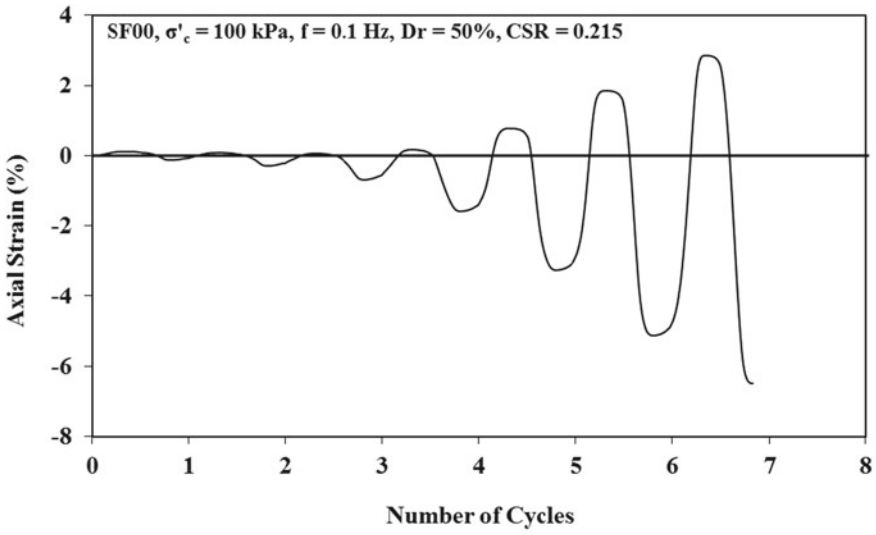
a)   Axial strain versus number of cycles
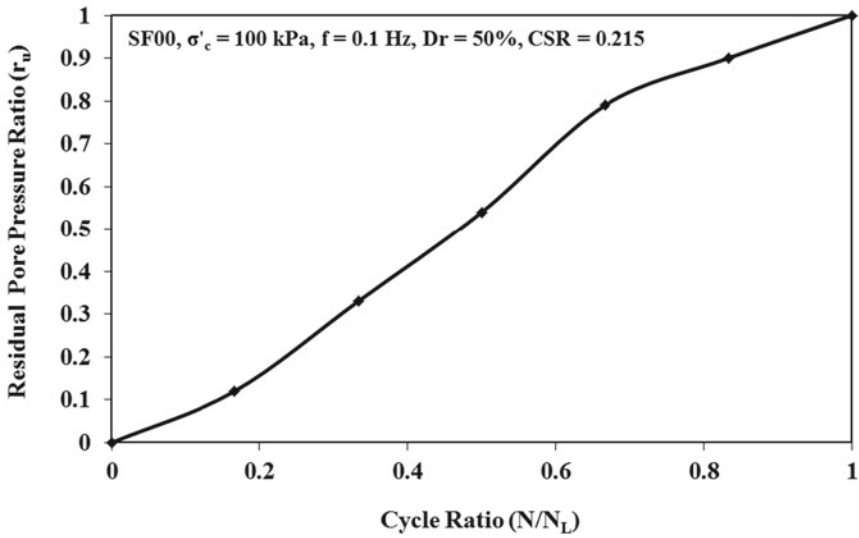
b)   esidual pore pressure ratio versus cycle ratio

Fig. 2 Typical cyclic triaxial test results of sand (SF00) sample having $e = 0.855$
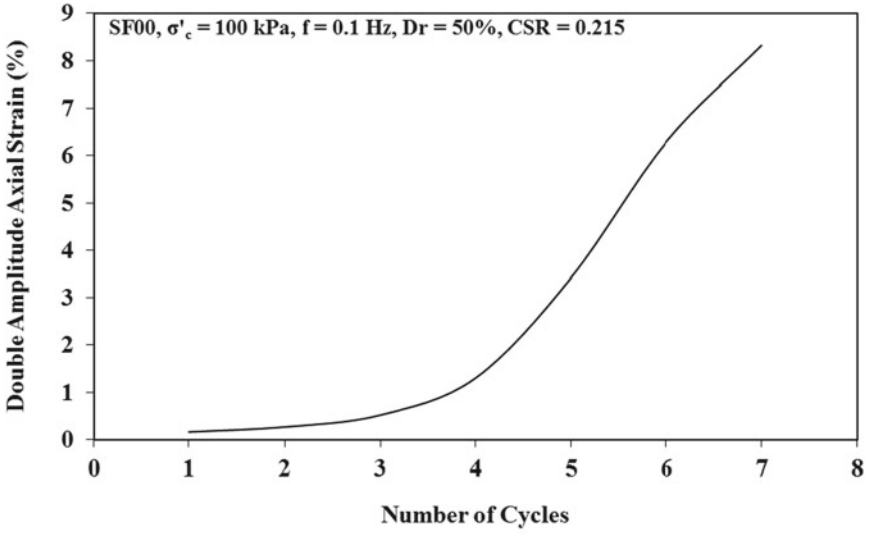
c)   Double amplitude axial strain versus number of cycles
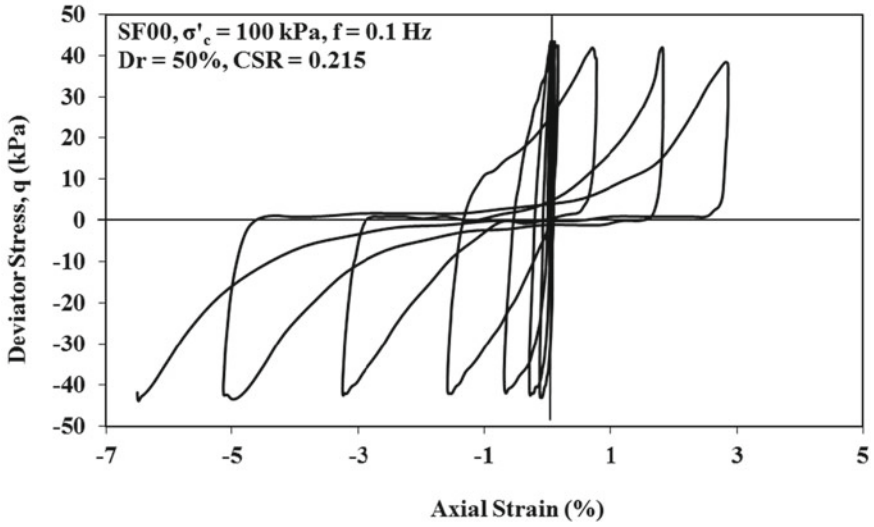
d)   Deviator stress versus Effective mean stress

Fig. 2 (continued)
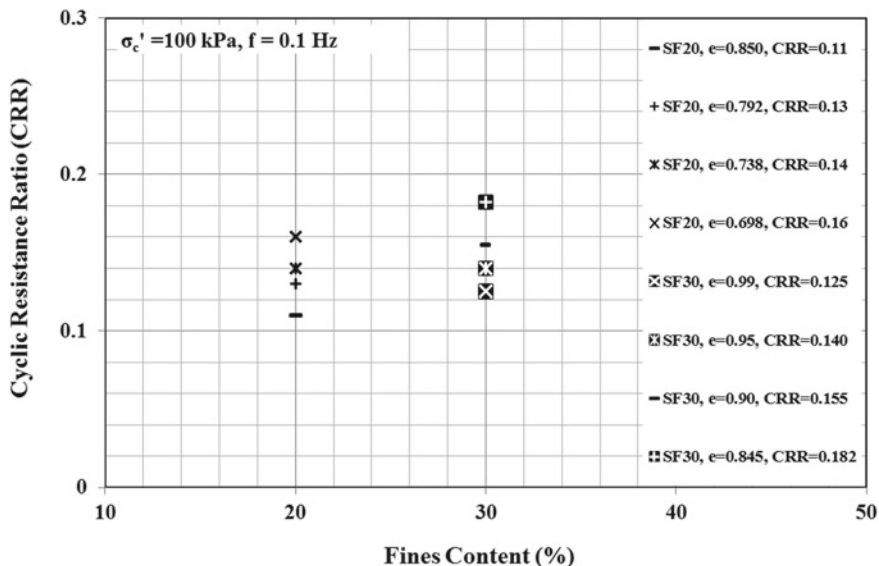
Fig. 3 Cyclic resistance ratio (CRR) versus fines content

increases. In the present investigation, the limiting fines content is 20%. Upto 20% fines content, the voids in the sand specimen will not be completely filled by fines. This results in a decrease in friction as the fines in the voids facilitate sliding. There will be a rearrangement of particles leading to increased compressive tendency which results in buildup of a large amount of excess pore water pressure and suppression of dilation thereby; there will be a reduction in strength. Cyclic strength of sand-fines mixtures at this stage is minimum due to the combined effect lubrication effect between sand and fines and suppression of dilation. Further, cyclic strength increases with the increase in the fines content beyond 20% fines content. This increase of cyclic strength is due to the fact that the fines matrix will control the behavior and sand-fines mixture shows clay-like behavior.

Table 1 shows the details of liquefaction susceptibility for soil mixtures. Sand-fines mixtures with $D_r = 50\%$ (loose state) and 70% (dense state) containing 10% fines have failed by flow liquefaction. However, dense sand-fines mixtures with 20 and 30% fines content at $D_r = 70\%$ with PI between 6 and 17 fail by cyclic mobility when the CSR > CRR. These samples exhibit clay-like behavior. The pore pressure buildup is faster with an increase in PI in loosely compacted specimens ($D_r = 50\%$) when compared to dense specimens ($D_r = 70\%$) and these samples have failed by flow liquefaction and with these sand-like behavior is observed.

Figure 4 shows the plot of cyclic resistance ratio (CRR) versus fines content at constant void ratio. It is observed that at any given void ratio, the cyclic resistance ratio decreases with an increase in fines content till limiting fines content (LFC = 20%). This indicates that the fines in the voids facilitate sliding producing soft contacts. At any given constant void ratio, CRR is minimum at limiting fines content.
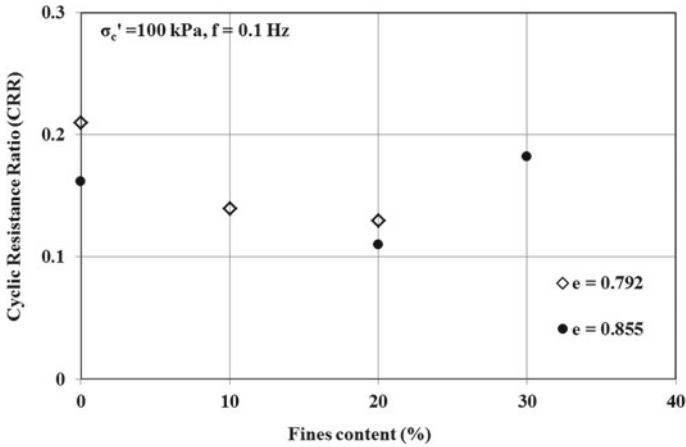
Fig. 4 Cyclic resistance ratio versus fines content at constant void ratio

The reduction in CRR is of the order 65–68% of the base sand strength (Balreddy et al. [3]).

Figure 5 shows the plot of cyclic resistance ratio versus sand skeleton void ratio for sand and sand-fines mixtures. It is observed that CRR decreases with an increase in sand skeleton void ratio. Beyond the limiting fines content of 20%, CRR increases due to the plasticity effect. For a given fines content, CRR decreases with an increase
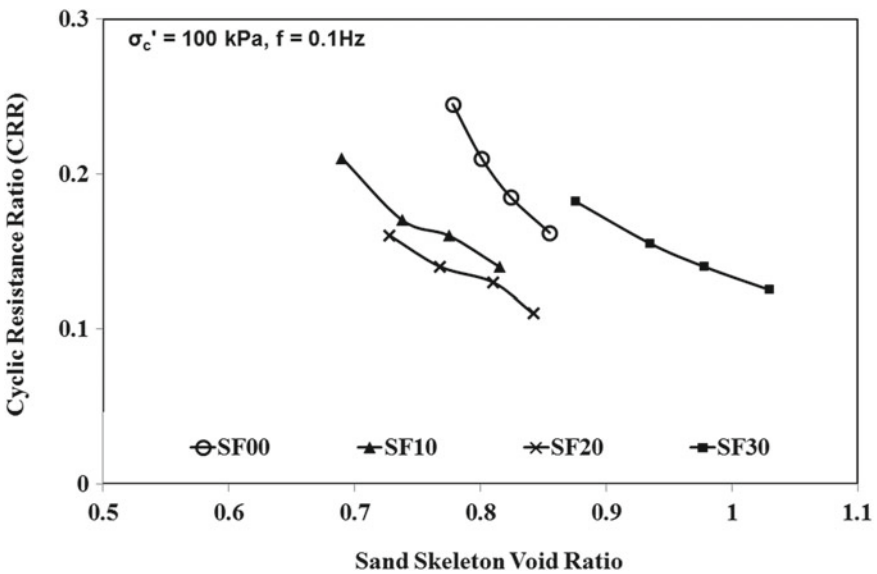
Fig. 5 Cyclic resistance ratio (CRR) versus sand skeleton void ratio
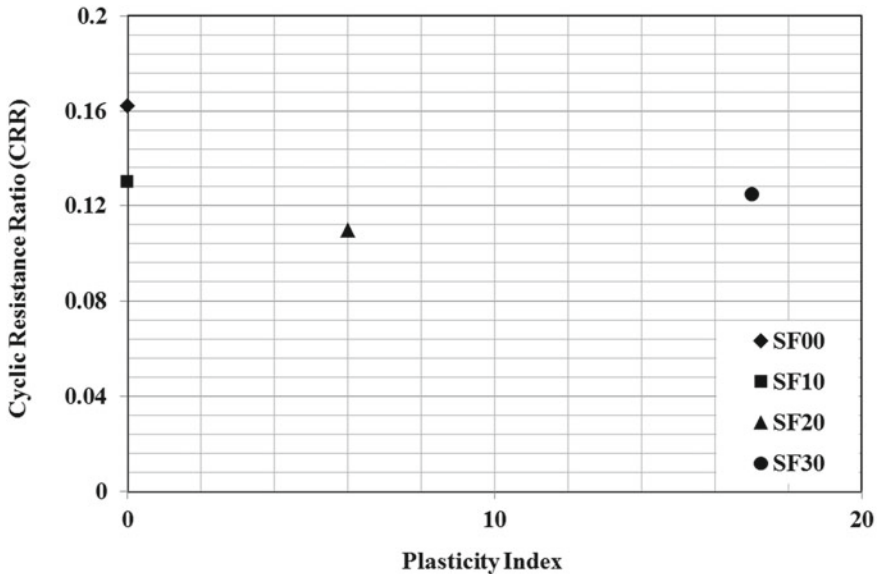
Fig. 6 Cyclic resistance ratio (CRR) versus plasticity index

in sand skeleton void ratio, also when fines content is less than limiting fines content for 10 and 20%. There is a decreasing trend with increase in sand skeleton void ratio. In general, the CRR ranges from 0.21 to 0.125 for all fines content considered in this study.

Figure 6 shows the plot of cyclic resistance ratio (CRR) versus plasticity index for the sand-fines mixtures. It is observed that clean sand has higher CRR value compared to sand-fines mixtures. Addition of fines beyond the limiting fines content, CRR increases marginally with an increase in plasticity index more studies are necessary. It is observed that when PI is less than or equal to 6, the sand-fines mixtures indicate silt like behavior characterized by flow liquefaction. When PI > 6, sand-fines mixtures indicate clay-like behavior characterized by cyclic mobility.

4 Conclusions

Based on the analysis of the results of the cyclic behavior of sand-fines mixtures, the following conclusions are drawn.

1. Addition of low plastic fines (PI = 6–17) decreases the CRR till limiting fines content of 20% beyond which it increases. The decrease of CRR due to fines content is in the range of 65–68% compared to base sand.
2. Addition of low plasticity fines beyond the limiting fines content shows a marginal increase in CRR with an increase in plasticity index.

3. Sand-fines mixtures under loose and medium dense condition ($D_r < 70\%$) fail by flow liquefaction exhibiting sand-like behavior.
4. Medium plasticity sand-fines mixtures under dense conditions ($D_r \geq 70\%$) with fines in excess of limiting fines content fail by cyclic mobility exhibiting clay-like behavior and these results are in agreement with Bayat et al. [4].

References

1. ASTM Designation: D 5311–92 (1996) Standard test method for load controlled cyclic triaxial strength of soil. In: Annual book of ASTM standards, vol 04.08
2. Balreddy MS, Dinesh SV, Sitharam T (2016) G: Influence of sand and low plasticity clay mixtures on the liquefaction and postliquefaction behavior. Jpn Geotech Soc Spec Publ 2(21):806–810
3. Balreddy MS, Dinesh SV, Sitharam TG (2019) Effect of fines on pore pressure development during cyclic loading. In: Adimoolam B, Banerjee S (eds) Soil dynamics and earthquake geotechnical engineering. Lecture Notes in Civil Engineering, vol 15. Springer, Singapore, pp 83–90
4. Bayat M, Bayat E, Aminpour H, Salarpour A (2014) Shear strength and pore-water pressure characteristics of sandy soil mixed with plastic fine. Arab J Geosci 7(3):1049–1057 (2014)
5. Boulanger RW, Idriss IM (2004) Evaluating the potential for liquefaction or cyclic failure of silts and clays. Report UCD/CGM-04/01. University of California, Davis, California
6. Gratchev IB, Sassa K, Fukuoka H (2006) How reliable is the plasticity index for estimating the liquefaction potential of clayey sands. J Geotech Geoenviron Eng ASCE 132(1):124–127
7. Ishihara K, Koseki J (1989) Discussion of cyclic shear strength of fines-containing sands. In: Earthquake geotechnical engineering, 12th international conference on soil mechanics and foundation engineering, Rio de Janeiro, pp 101–106
8. Maheshkumar G (2012) Effect of fines on the cyclic response of sandy soil. Ph.D. thesis submitted to Visvesvaraya Technological University, Belgaum
9. Tsuchida H (1970) Prediction and countermeasure against liquefaction in sand deposits. Abstract of the seminar in the Port and Harbor Research Institute, pp 3.1–3.33
10. Yasuda S, Wakamatsu K, Nagase H (1994) Liquefaction of artificially filled silty sands. Ground failure under seismic conditions. Geotechnical Special Publication No. 44, ASCE, pp 91–104

Influence of Density on the Static Liquefaction Characteristics of a Sandy Kutch Soil

R. Bhamidipati , **M. Hussain** , **and A. Sachan**

Abstract Loose sands and very loose silty sands are most susceptible to static liquefaction among all the soil types. The undrained response of granular soils is controlled by several factors including material and stress states. Loose granular soils under undrained conditions develop solid–fluid instability due to the generation of excess pore water pressure consequently leading to static liquefaction. The increased pore pressure indicates loss in effective confining pressure thereby resulting in reduced mobilized shear stress. In the recent past, a number of incidents of static liquefaction have occurred in dams across the world, causing extensive damage to life and property. In this study, the effect of relative density on the static liquefaction characteristics including undrained brittleness, collapse potential, and liquefaction potential has been explored, for a soil from the Kutch region of India. This region was severely affected by the devastating earthquake of 2001. To carry out the study, isotropically consolidated undrained compression triaxial tests were performed with frictional end rigid boundary conditions. The liquefaction resistance was observed to decrease with the increase in void ratio; however, pore pressure ratios greater than 0.85 were exhibited at void ratio corresponding to the relative density of 80% signifying intense strain softening. The samples showed an increasing trend in peak shear stress with increasing relative density. Also, the various liquefaction indices decreased with relative density, particularly above 60%. The study showed that the soil under study had a high tendency for static liquefaction.

Keywords Static liquefaction · Relative density · Pore pressure

R. Bhamidipati (✉)
Department of Civil Engineering, C V Raman College of Engineering, Bhubaneswar 752054, India
e-mail: jones.kgp@gmail.com

M. Hussain · A. Sachan
Department of Civil Engineering, Indian Institute of Technology Gandhinagar, Palaj 382355, India

1   Introduction

Sandy soils that occur in various parts of the world can be characterized by certain unique engineering and physical properties. The mechanical behavior of sands is largely guided by factors like stress state, void ratio, fines content, and boundary conditions. Loose-saturated granular soils are known to exhibit a phenomenon known as liquefaction, wherein, saturated sands lose their strength due to the application of undrained loading. The loss in strength is due to the building up of excess pore water pressures, generated due to shear loading. This creates a solid–fluid instability. Static liquefaction is a special type of liquefaction which occurs when a saturated granular soil mass loses most of its shear strength under monotonic loading. Whereas cyclic liquefaction is initiated mostly by earthquake loading, static liquefaction can also be triggered by sources such as blasting, driving of piles, railway and traffic vibrations, etc. (Kramer [1]). The failure of Calaveras dam in California (1918), Fort Peck dam on the Missouri river in Montana (1938), and the Merriespruit tailings dam failure in South Africa (1994) are just some examples of catastrophic events brought about by static liquefaction phenomenon. For many geotechnical engineering problems pertaining to saturated sandy soils, the estimation of liquefaction potential of the soils is very important, particularly so if the soil occurs in a seismically active region. The liquefaction characteristics of sandy soils have been studied by several researchers (Lade and Yamamuro [2], Papadopoulous and Tika [3], Salgado et al. [4], Yamamuro et al. [5]). It was also found that loose silty-sandy soils were most likely to be liquefiable in the event of monotonic loading (Yamamuro and Lade [6]). The dynamic properties of some soil samples collected near the Bhuj area were studied by Sitharam et al. [7] and Ravishankar et al. [8].

For this study, sandy soil near the Fatehgarh dam in the Kutch region of Gujarat was used. Kutch is one of the most seismically active regions in India, and it was struck by many massive earthquakes in the recent geological past (1819, 1956, and 2001). Fatehgarh dam region was one of the regions severely affected by the 2001 Bhuj earthquake and the associated liquefaction induced damages. Several thousand square kilometers of soils in the Kutch region experienced liquefaction due to this earthquake.

The basic properties of the soil are summarized in Table 1. Figure 1 shows the grain size distribution of the soil. The soil had a fines content of 15%, with a clay content of 4%. In this paper, the effect of relative density on the static liquefaction characteristics of the Fatehgarh dam soil was explored under undrained triaxial conditions. Relative

Table 1 Properties of the soil

G_s	2.65
% Fines	16%
% Clay	4%
e_{max}	0.59
e_{min}	0.29
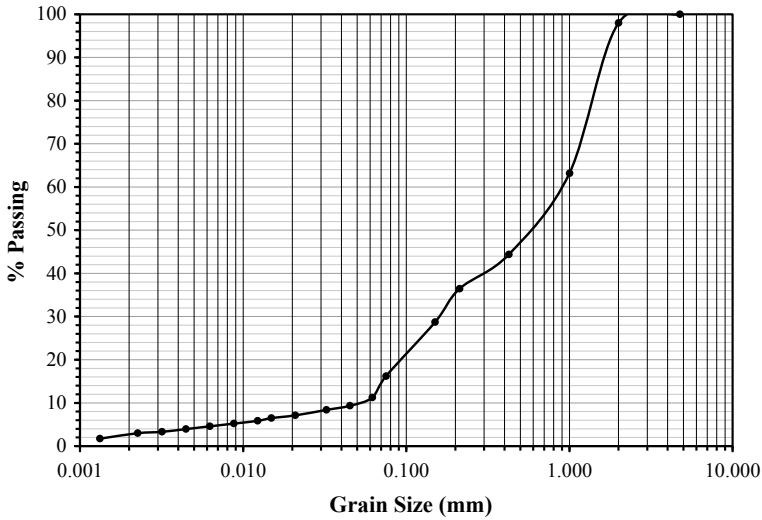
Fig. 1 Grain size distribution of the Fatehgarh dam soil

density of the soil is the single parameter that has most influence on the undrained soil response and hence on liquefaction characteristics. The liquefaction behavior of the Fatehgarh dam soil was evaluated using parameters such as Undrained Brittleness Index (I_B), Collapse Potential (CP), and Liquefaction Potential (L_P). Each of these parameters and the testing methodology adopted in the current study are explained in the following sections.

2 Methodology

The void ratios for the soil under consideration were initially calculated at relative densities of 20, 40, 60, 80, and 100% using the provisions of IS 2720-Part 14. Five specimens were prepared with different initial relative densities ranging from 20 to 100%. The void ratios corresponding to the different relative densities are presented in Table 2. Isotopically consolidated undrained compression (CIUC) triaxial tests were conducted on these samples. The samples were of 100 mm length and 50 mm diameter (maintaining an aspect ratio of 2) and were prepared using moist tamping method at an initial moisture content of 6%. After assembling the moist tamped specimens on the base pedestal in the pressure cell, carbon-dioxide at a low pressure of about 5 kPa was passed through the samples for around 30 min at a confining pressure of 20 kPa. After this, water flushing was conducted by pushing a volume of de-aired water from the base of the cell equivalent to at least two times the volume of the specimen. After the water-flushing stage, the cell and back pressures were gradually increased in steps of 40 kPa. The process was continued until a Skempton's pore—pressure

Table 2 Relative density and void ratios of samples before and after consolidation

Relative density (%)	e_o (before consolidation)	e_f (after consolidation)
20	0.53	0.49
40	0.47	0.45
60	0.41	0.40
80	0.36	0.35
100	0.29	0.29

parameter 'B' was at least 0.95 The desired saturation levels corresponding the 'B' value of 0.95 were obtained at a back pressure of 270 kPa.

After the saturation stage, the saturated specimens were subjected to isotropic consolidation at a confining pressure of 100 kPa. Consolidation was assumed to be complete when the rate of volume change was less than 5 mm^3 over a period of 5 min. The relative density values and void ratios of the specimens after consolidation are presented in Table 2. After consolidation stage, the specimens were subjected to undrained shearing at a deformation rate of 0.1 mm/min. All the tests were performed at an effective confining stress of 100 kPa owing to the fact that static liquefaction is a low-pressure phenomena Shear loading was continued until there was no change in load for a period of 5 min or an axial strain of 20% was reached, which ever was attained earlier. The vertical displacement, variations in deviator stress, and excess pore pressure were recorded throughout the duration of the test. These parameters were used to compute the effective stress parameters, q and p' of the soil specimen.

The static liquefaction characteristics of a soil specimen were determined from the experimental data using the following indices:

Liquefaction Potential (L_p) (Casagrande [9]): It is quantified in terms of variation in the effective minor principal stress during shearing with respect to the final effective minor principal stress and calculated by the following expression:

$$L_p = (s'_{3i} - s'_{3f})/s'_{3f} \tag{1}$$

where s'_{3i} and s'_{3f} are the initial and final effective minor principal stresses respectively.

Collapse potential (CP) (Thevanayagam et al. [10]): It describes the amount of reduction in mean effective confining stress, p', due to building up of excess pore pressure during shearing. It is calculated using the expression:

$$CP = (p'_i - p'_{ss})/p'_i \tag{2}$$

where p'_i and p'_{ss} are the mean effective pressures at the beginning of shearing and at steady state, respectively. CP is very close to unity for soils with a high tendency for liquefaction. For samples that show dilation right from the start of shear loading, CP is taken as zero.

Undrained Brittleness Index (I_B) (Bishop [11]): It describes the reduction in deviatoric stress, q, after the peak deviatoric stress, q_{peak}, is attained. I_B is calculated as shown:

$$I_B = (S_{uy} - S_{ul})/S_{uy} \qquad (3)$$

where S_{uy} (yield) is the same as q_{peak} and S_{ul} is the minimum deviatoric stress after the initial peak. Its values range between 0 and 1 for soils showing strain hardening response and 1 for soils exhibiting complete liquefaction. All the above-mentioned liquefaction indices are expected to show a strong positive correlation as they quantify the same phenomena of static liquefaction.

3 Results

For each specimen, the variation in deviator stress was plotted against axial strain (Fig. 2). The test results showed an increasing trend in peak deviatoric stresses with increase in relative density. The values increased from 29 kPa at a relative density of 20% to 334 kPa at a relative density of 100%. This observation is consistent with the study of Illinois River Sand and Toyoura sand specimens reported by Sadrekarimi [12]. The increase was very significant at relative density values of more than 60%. It is interesting that the specimens exhibited strain softening over the entire range of explored relative densities. Figure 3 shows the development of excess pore pressure during shearing. It was seen that from D_r% of 20% to 60%, the increase in EPP was almost close to 95% of the confining stress (100 kPa). The value decreased slightly to about 83 kPa at 80% D_r showing a shift in response and an increasing dilative undrained behavior. At D_r of 100%, the specimen initially showed a dilative
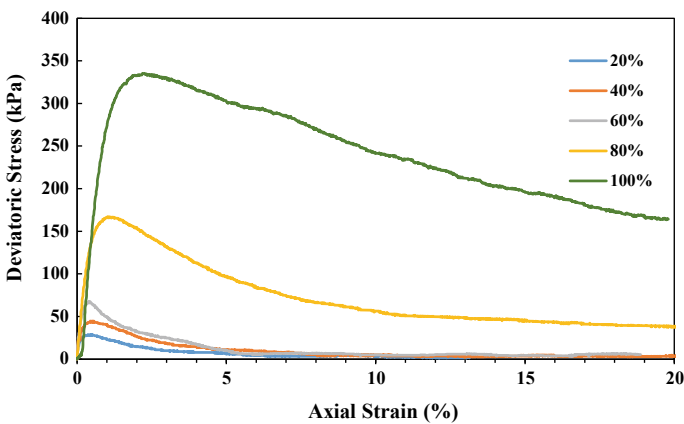
Fig. 2 Plot of deviatoric stress versus axial strain at different relative densities
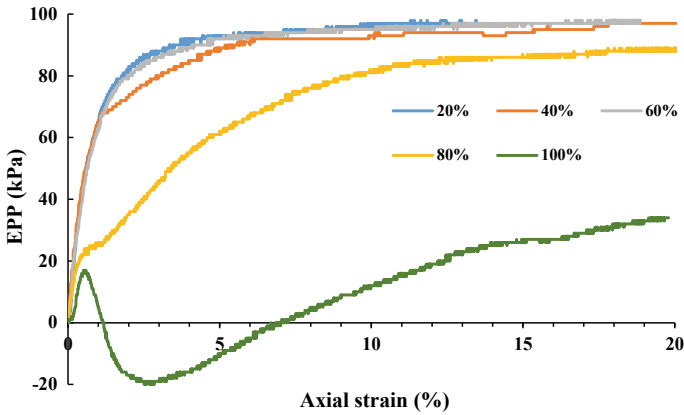
Fig. 3 Excess pore pressure versus axial strain %

response with the EPP increasing and attaining negative values between 1 and 7% axial strains. The excess pore water pressure response of the specimens captured the signature observed in the stress–strain response.

The effective stress paths for the five tests were plotted using the q–p' plane (Fig. 3). Under drained loading conditions, the variation of mean effective stress (p') depends on the initial material and stress states of the soil sample. For samples with D_r up to 60%, a decrease in p' was observed during the undrained shearing. For specimens with D_r of 70 and 100%, p' initially increased and then decreased. The increase in p' was highest for the specimen with D_r of 100%. Likewise, deviatoric stress (q) decreased for all the samples after attaining a peak value. The decrease in q increased with the decreasing relative density, an indication of increasing static liquefaction. For specimens with D_r of 20–60%, the effective stress path descended to the stress origin. This showed large susceptibility to static liquefaction for these soil samples. However, the specimens with D_r of 80 and 100% showed a lower tendency for static liquefaction. The sample with a D_r of 100% exhibited the highest resistance to liquefaction instead showed dilation during the earlier stages of shear loading. The stress path of this specimen showed an increasing trend during shearing. Even at the end of shearing, the effective stress values were higher than the initial value of 100 kPa (Fig. 4).

Liquefaction Indices including, CP and L_p, were then computed for these test specimens. Undrained stress–strain responses of the soil were used to calculate Undrained Brittleness Index (I_B). The values ranged from 0.93 to 0.51, for the different relative densities. For D_r ranging between 20 and 60%, the variation in IB was in a narrow range of 0.88 to 0.93. The values dropped to 0.76 at D_r of 80% and 0.51 at D_r of 100%. The relationship between I_B and D_r% for the samples is shown in Fig. 5.

Collapse Potential (CP) was calculated from the reduction in the mean effective stress for each test specimen during the undrained shearing. In this study, the CP values ranged from 0.975 at 20% D_r to 0.750 at D_r of 80%. For the specimen with
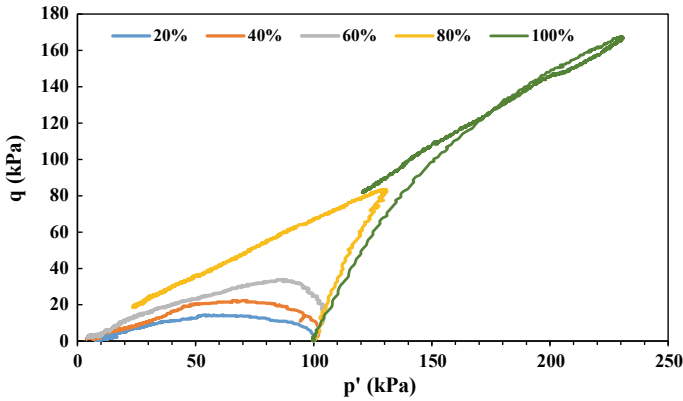
Fig. 4 Effective stress paths at different relative densities
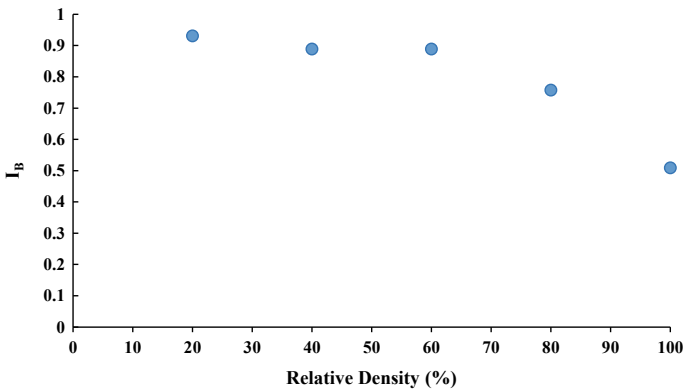
Fig. 5 Plot showing variation in I_B at different relative densities

D_r of 100%, because the p'_{ss} was observed to be higher than p'_i., CP was calculated as zero. For specimens with D_r of 20–60%, it was found that relative density had a little influence on the Collapse Potential.

Liquefaction Potential (L_p) was evaluated from the variations in the effective minor principal stress of each test specimen during the undrained shearing. The shear-induced excess pore pressure is responsible for changes in the effective minor principal stress (σ_i^3). In this case, the variation in L_p was observed to be in the range of 0.97 at D_r of 20–0.66% at D_r of 100%. As in the case of CP, the samples with relative density in the range of 20–60% showed little variation in L_p with relative density was evaluated to be 0.88 at D_r of 80% and 0.66 at D_r of 100% (Figs. 6 and 7).
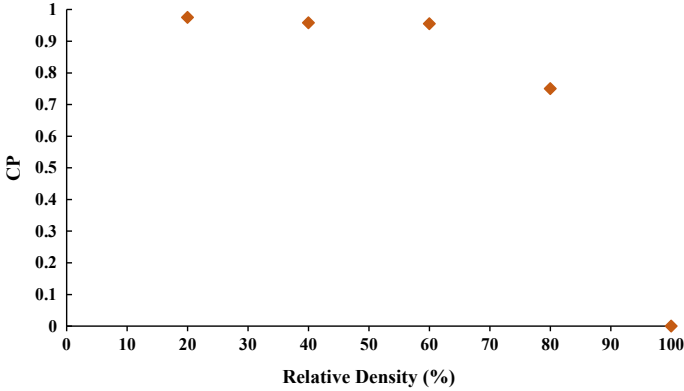
Fig. 6 Plot showing variation in CP at different relative densities
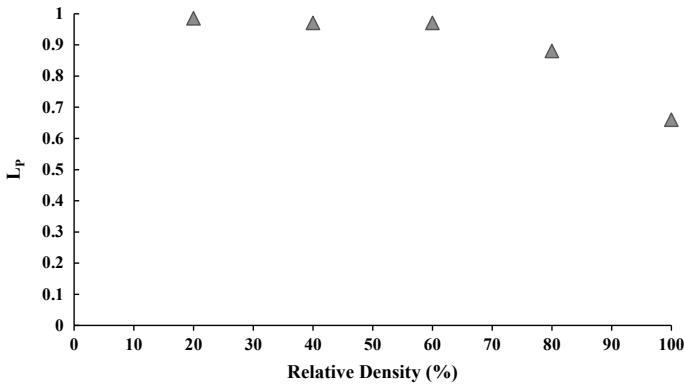
Fig. 7 Plot showing variation in L_P at different relative densities

4 Conclusion

Isotropically consolidated undrained compression triaxial tests were conducted on a Sandy Kutch soil to evaluate the liquefaction characteristics at different relative densities. The undrained response of five specimens was studied at a relative density ranging from 20 to 100%. The peak deviatoric stresses of the specimens increased with relative density. The test results showed that at relative densities of 20–60%, the sandy soil specimens showed intense strain softening and a large susceptibility to static liquefaction. In this density range, I_B, CP, and L_P were are all comparable and close to 0.9 or above. The soil specimens displayed a contractive response during shearing which was captured by all the liquefaction indices. At relative densities of 80% and above the soil specimens exhibited an increasing dilative behavior. The liquefaction indices decreased significantly, indicating an increasing resistance

toward static liquefaction. It should however be noted that even at a relative density of 100%, the specimens still showed some loss of strength, though much lesser than the looser states. This reveals the inherent tendency of the soil, under investigation, to undergo static liquefaction.

The analysis of the test results from the study showed that the Fatehgarh dam soil under investigation has a high susceptibility to liquefaction over a wide range of densities. The current study was however limited to the effect of relative density on static liquefaction characteristics of the soil, but practically liquefaction is also influenced by other factors such as fines content and plasticity index of the soils. A study of all these parameters is necessary to conduct any risk analysis associated with static liquefaction for Kutch soils.

References

1. Kramer SL (1996) Geotechnical earthquake engineering. Prentice Hall, Upper Saddle River, NJ
2. Lade PV, Yamamuro JA (1997) Effects of nonplastic fines on static liquefaction of sands. Can Geotech J 34(6):918-928
3. Papadopolou AI, Tika TM (2016) The effect of fines plasticity on monotonic undrained shear strength and liquefaction resistance of sands. Soil Dyn Earthquake Eng 88:191–206
4. Salgado R, Bandini P, Karim A (2000) Shear strength and stiffness of silty sand. J Geotech Geoenviron Eng 126(5):451–462
5. Yamamuro JA, Wood FM, Lade PV (2008) Effect of depositional method on the microstructure of silty sand. Can Geotech J 45(11):1538–1555
6. Yamamuro JA, Lade PV (1998) Steady-state concepts and static liquefaction of silty sands. J Geotech Geoenviron Eng 124(9):868–877
7. Sitaharam TG, Govindaraju L, Murthy BS (2004) Evaluation of liquefaction potential and dynamic properties of Silty Sand using cyclic triaxial testing. Geotech Testing J ASTM 27(5):423–429
8. Ravishankar BV, Sitharam TG, Govindaraju L (2005) Dynamic properties of Ahmedabad sands at large strains. In: Proceedings: Indian geotechnical conference-2005, Ahmedabad
9. Casagrande A (1976) Liquefaction and cyclic deformation of sands—A critical review. Harvard Soil Mechanics Series, Harvard University, Cambridge, Massachusetts, p 88
10. Thevanayagam S, Shenthan T, Mohan S, Liang J (2002) Undrained fragility of clean sands, silty sands and sandy silts. J Geotech Geoenviron Eng 128(10):849–859
11. Bishop AW (1971) Shear strength parameters for undisturbed and remolded soil specimens. In: The proceedings of Roscoe memorial symposium. Cambridge University, Cambridge, Mass., pp 3–58
12. Sadrekarimi A (2014) Static liquefaction-triggering analysis considering soil dilatancy. Soils Found 54(5):955–966

Addressing Influence of Prefabricated Vertical Drains in Liquefaction Resistance Under Multiple Shaking Events

Gowtham Padmanabhan and Ganesh Kumar Shanmugam

Abstract Soil liquefaction and its associated ground failures during earthquake is one of the major potential hazards in recent years. The important aspect of geotechnical earthquake engineering is to mitigate liquefaction and its associated effects for assuring the safety of foundations. To mitigate liquefaction, there are different ground improvement techniques available and installation of prefabricated vertical drains is one such recently developed improvement technique which involves installation of PVDs for dissipating pore water pressures. The present study aims to evaluate the efficiency of prefabricated vertical drains reinforced ground subjected to repeated acceleration loading conditions. Shaking table tests were performed on poorly graded sand with varying ground density conditions subjected to repeated incremental acceleration loading with and without PVD system. For experimental investigations, ground having 600 mm depth was prepared with 40 and 60% relative density. Prefabricated vertical drains were then installed at triangular pattern having *c/c* spacing of 200 mm. Then the ground was subjected to repeated incremental acceleration loading of 0.1, 0.2, 0.3, and 0.4 g with 5 Hz frequency. In repeated shaking events, subsequent acceleration loading was applied only after complete dissipation of generated pore water pressure from previous loading. The effect of pore pressure response, liquefaction resistance, and improvement in soil density with and without prefabricated vertical drains was continuously monitored and estimated. The efficiency of PVD improved ground subjected to repeated acceleration loading was assessed and the results were presented.

Keywords Liquefaction · Ground improvement techniques · Prefabricated vertical drains · Repeated acceleration loading

G. Padmanabhan (✉)
Department of Earthquake Engineering, IIT Roorkee, Roorkee, Uttarakhand, India
e-mail: gowtham@eq.iitr.ac.in

G. K. Shanmugam
Geotechnical Engineering Division, CSIR-CBRI Roorkee, Roorkee, Uttarakhand, India
e-mail: ganeshkumar@cbri.res.in

1 Introduction

Soil liquefaction and its associated ground failures during earthquake is one of the major hazards in recent years. To improve liquefaction resistance, ground improvement techniques such as stone columns, sand compaction piles, prefabricated vertical drains (PVDs), and permeation grouting have been used successfully and reported. Use of PVD for improving liquefaction resistance is recently getting importance due to its ease in installation and its draining characteristics. Installation of prefabricated vertical drains in sands induces improvement in density and drainage characteristics. This resulted in settlement reduction and increases the rate of dissipation of excess pore pressures [1, 10]. Even though, installation of PVD improves liquefaction resistance reasonably, studies relating to their performance evaluation under repeated acceleration loading conditions were limited. The present study aims to evaluate the efficiency of PVD reinforced ground subjected to repeated incremental acceleration loading conditions using uni-axial shaking table tests.

The liquefaction potential of sands has been evaluated by many researchers in the past through reduced scale models in centrifuge modeling and 1-g shaking table tests [2, 3, 8, 12, 13, 15]. The liquefaction studies on a shaking table tests prepared with large saturated samples offer many advantages when compared to other small-scale laboratory experiments and be highly helpful for evaluating liquefaction potential of sands [11]. Especially, the effect of drainage conditions on the liquefaction induced deformations was studied using the shaking table tests [7]. Even though studies on PVD for improving liquefaction resistance were available, studies relating to their performance evaluation under repeated dynamic conditions (i.e., same ground subjected to repeated acceleration of higher intensity or lower within limited time) were limited.

To validate incidence of earthquake is difficult due to its complexity. The frequency and return period of the earthquake cannot be predicted. The recent continuous ground-shaking events due to earthquake and its associated foreshock/aftershock movements observed in New Zealand, 2010–2011; Japan, 2011; Nepal, 2015; Kumamoto, 2016; Indonesia, 2018 and Canada, 2019 suggested that there is a possibility for multiple seismic events that can occur at a particular location. Considering the above multiple shaking events, repeated incremental acceleration loading conditions were selected in this study [4]. The experiments were conducted in liquefiable soil using 1-g shaking table tests with and without prefabricated vertical drains. The performance of PVD improved ground subjected to repeated acceleration loading was assessed and presented.

2 Testing and Methodology

The shaking table tests are performed on poorly graded sand collected from solani river bed, near Roorkee. The index properties of the sand are given in Table 1. The

Table 1 Index properties of the solani sand

S. no.	Property/characteristic		Value
1	Soil type		Poorly graded sand
2	Specific gravity of grains (G)		2.67
3	Uniformity coefficient (C_u)		2.63
4	Coefficient of curvature (C_c)		1.14
5	Grain size	D_{50}	0.23 mm
		D_{10}	0.09 mm
6	Maximum void ratio (e_{max})		0.87
7	Minimum void ratio (e_{min})		0.64
8	Relative density considered (D_r)		40%
			60%
9	Void ratio (e) for $D_r = 40\%$		0.80
10	Dry unit weight for $D_r = 40\%$		14.5 kN/m^3
11	Void ratio (e) for $D_r = 60\%$		0.76
12	Dry unit weight for $D_r = 60\%$		14.88 kN/m^3

obtained grain size distribution curve is falling within the range of gradation for liquefiable sand [14] indicating that the soil is more susceptible to liquefaction. The solani river sand is classified as poorly graded sand (SP) according to Indian standard [5, 6].

The liquefaction experiments are carried out on a uni-axial shaking table available at CSIR-CBRI, Roorkee having a payload capacity of three tons. The uni-shaking table can produce one-dimensional harmonic excitation at varying amplitudes (0.05–1 g) under dynamic load frequencies (0–10 Hz). A transparent acrylic model container of size 1400 × 1000 × 1000 mm was used for the studies. The tank was mounted and connected with the shaking table and then preparation of sand deposit was carried out. The amplitude acceleration and dynamic load frequency can be fixed depending on experimental test conditions. Using glass tube piezometers, the pore water pressure was measured. The piezometers were installed at 200 and 400 mm from the bottom of the tank. The prepared sand bed was shown in Fig. 1.

The occurrence of continuous ground shaking due to earthquake and associated aftershock movements developed necessity in understanding the behavior of liquefiable ground subjected to repeated shaking events. To simulate repeated earthquake events, application of incremental sequential acceleration loading in sinusoidal waveform having acceleration 0.1, 0.2, 0.3, and 0.4 g at 5 Hz constant frequency was selected and applied. The acceleration amplitudes are selected in such a way that it representing medium to severe earthquake condition.

To evaluate liquefaction resistance of the prepared model ground at 40% and 60% relative density; next acceleration loading was applied only after complete dissipation of generated excess pore water pressure from previous loading. Using glass tube piezometers, the generated excess pore water pressure and time take for dissipation of pore water pressure was estimated. Then next incremental sequential

Fig. 1 Prepared sand bed for the desired relative density

loading was applied following the same procedure as mentioned above. Before and after acceleration loading, generated excess pore water pressure and variation in relative density of the soil bed were estimated.

2.1 Prefabricated Vertical Drains

A prefabricated vertical drain is a special type of geo-composites, composed of plastic core covered with thin layer of geotextile. The vertical drains are available in the form of roll with 100 mm in width and 4 mm thickness. The commercially available vertical drains will have a maximum length up to 30 m. Vertical drains are installed to the required depth with the help of specially designed installation rig. When the vertical drain is reached to the desired depth, the installation rig is to be withdrawn. As the installation rig is pushed downward and upon its removal once the drain is in place, it disturbs the soil surrounding the drain producing shear strains and displacement that decrease its hydraulic conductivity [9]. With all other testing procedure and methodology remains the same. The prepared sand bed is installed with the 10 numbers of prefabricated vertical drains with 200 mm center to center spacing in the triangular pattern as shown in Fig. 2.

Fig. 2 Installation of prefabricated vertical drains in triangular pattern

3   Results and Discussions

3.1   *Effect of Pore Water Pressure*

In this section, effect of excess pore water pressure under sequential incremental loading for both untreated and treated conditions was discussed. As mentioned in previous section, the sequential amplitude acceleration loading was applied to the prepared soil bed incrementally, i.e., 0.1, 0.2, 0.3, and 0.4 g at 5 Hz frequency only after achieving complete dissipation of generated excess pore water pressure from previous loading.

Vertical drains perform much better than untreated ground in resisting the generation of pore water pressure. No pore water pressure was generated at 0.1 g acceleration loading for 40% density ground. Similarly, at 60% density, no excess pore water pressure was generated up to 0.2 g acceleration loading. Thus, installation of PVD effectively minimizes generation of pore water pressure. However, under repeated loading and due to soil densification due to repeated shaking generation of pore water pressure was absorbed for the PVD reinforced ground. It can be seen that the generation of excess pore water pressure is maximum at the bottom than at top location in all the testing conditions. This may be due to the initial mean effective stress at bottom is higher than effective vertical stress at top. The overburden pressure is also found to be higher at the bottom and lower at the top piezometer.

When compared to reinforced ground, the unreinforced ground liquefies rapidly even at 0.1 g acceleration whereas PVD performs effectively at 0.1 g with no liquefaction occurrence for 40% relative density and the same result has been observed for 0.1 and 0.2 g amplitude accelerations for 60% relative density. Though vertical drains are fully successful in resisting the generation of pore water pressure, some traces of ground softening are observed during the earthquake shaking. Comparatively, the generation of pore water pressure found to be minimum than unreinforced ground and vertical drains effectively mitigating liquefaction. From Figs. 3, 4, 5, 6 and 7, it is found that, both the unreinforced ground and reinforced ground subjected to incremental continuous acceleration, the generation of pore water pressure is found to higher in unreinforced ground.

The generation of excess pore water pressure in both unreinforced and reinforced ground subjected to repeated loading suggesting that, even though improvement in density occurred due to continuous shaking, still there is a possibility for liquefaction under high-intensity earthquakes. However, the generated pore water pressure was found to be lesser for PVD improved system. Installation of PVD minimizes generation of pore water pressure during initial acceleration loading, however at higher
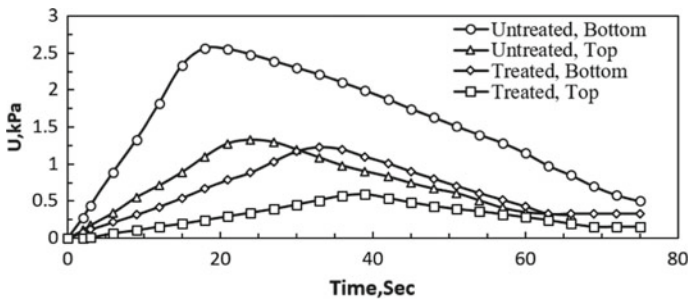
Fig. 3 Variation of excess pore water pressure with time for 0.2 g acceleration for 40% relative density for both treated and untreated conditions
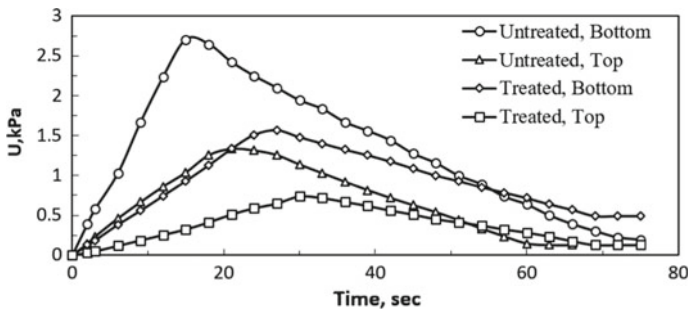
Fig. 4 Variation of excess pore water pressure with time for 0.3 g acceleration for 40% relative density for both treated and untreated conditions
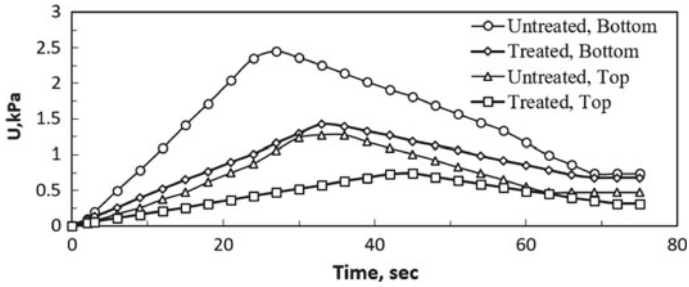
Fig. 5 Variation of excess pore water pressure with time for 0.4 g acceleration for 40% relative density for both treated and untreated conditions
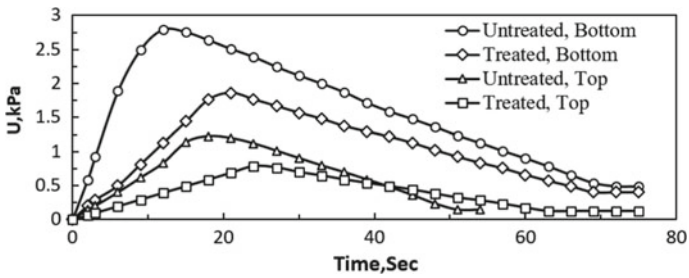
Fig. 6 Variation of excess pore water pressure with time for 0.3 g acceleration for 60% relative density for both treated and untreated conditions
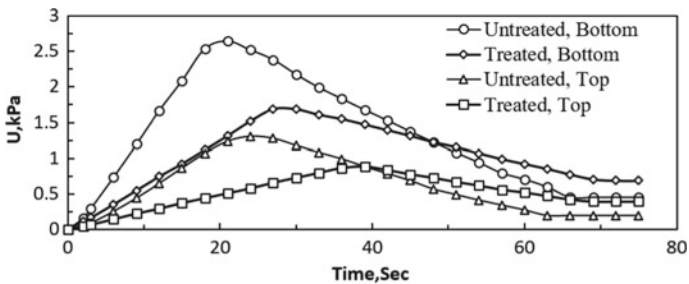
Fig. 7 Variation of excess pore water pressure with time for 0.4 g acceleration for 60% relative density for both treated and untreated conditions

acceleration, i.e., 0.3 and 0.4 g the generation of pore water pressure found to be increase but still the system performs better compared to unreinforced ground.

3.2   Effect of Relative Density

In this section, effect of relative density under sequential incremental loading for both untreated and treated conditions was discussed.

To compare soil compression with generated excess pore water pressure and pore pressure ratio under undrained conditions, the effect of relative density under incremental acceleration loading conditions is discussed in this section as shown in Figs. 8 and 9. The variation in density before and after application of incremental sequential acceleration loading was evaluated using digital static cone penetrometer. For 40% relative density, variation in relative density of the sand deposit attained is found to be 20%, 15%, 8%, and 2% greater for 0.1 g, 0.2 g, 0.3 g, and 0.4 g amplitude accelerations respectively for treated soil deposits when compared to untreated soil deposits. For 60% relative density, variation in relative density of the sand deposit attained is found to be 10%, 8%, 6%, and 3% greater for 0.1 g, 0.2 g, 0.3 g, and 0.4 g amplitude accelerations respectively for treated soil deposits when compared to untreated soil deposits. The improvement in density suggesting that, ground bed subjected to repeated acceleration loading experiencing improvement in density. Under undrained conditions, the improvement in density induces generation of pore water pressure initiating liquefaction. Comparatively, PVD installed ground offer
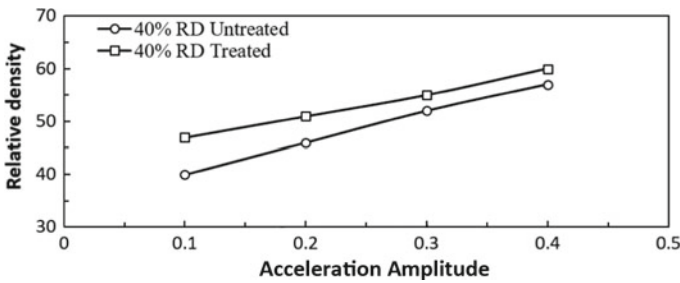
Fig. 8 Variation in relative density for 40% relative density for varying accelerations and ground conditions
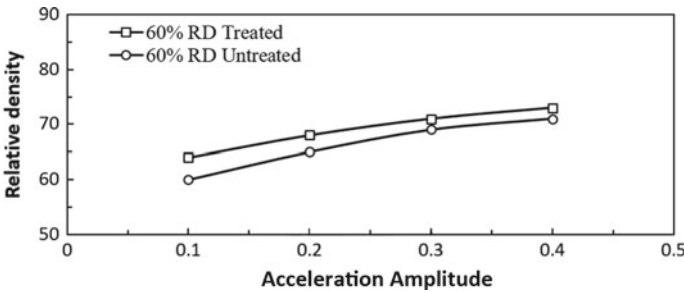
Fig. 9 Variation in relative density for 60% relative density for varying accelerations and ground conditions

effective drainage characteristics and minimize generation of pore water pressure and due to combined densification and drainage effects no liquefaction was absorbed at 0.1 at 40% and 0.1, 0.2 g at 60% density conditions. At higher acceleration loading, generation of pore water pressure was absorbed suggesting that, area replacement ratio should be selected properly such that, the performance of the system can be improved further thereby improving the liquefaction resistance against liquefaction. The variation of excess pore water pressure due to increased relative density was shown in Figs. 3, 4, 5, 6 and 7 for both treated and untreated sand deposits.

4 Conclusions

- Installation of prefabricated vertical drains minimizes generation of excess pore water pressure and also improves rate of excess pore pressure dissipation compared to untreated sand deposits even under repeated shaking events.
- Installation of PVD to liquefiable soils improves the stiffness of the soil which minimizes foundation settlement. The stiffness of the saturated sand deposit is observed through the increased relative density in treated sand deposits compared to untreated sand deposits.
- Drainage characteristics in PVD system found to be very effective in mitigating the liquefaction. Installation of prefabricated vertical drains increases relative density and reduced compressibility.
- The installation of vertical drains is found to be very effective at 0.1 g amplitude accelerations for 40 and 60% relative density and up to 0.2 g acceleration loading for 60% relative density. Under higher acceleration loading, generation of pore water pressure was absorbed. However, comparatively, ground bed with PVD shows lesser generation of pore water pressure than untreated ground.
- Selection of suitable ground improvement technique in liquefiable soils plays a major role in improving safety of major infrastructure facilities.

References

1. Balaji P, Dashti S, Liel A (2018) Influence of prefabricated vertical drains on the seismic performance of structures founded on liquefiable soils. J Geotech Geoenviron Eng ASCE 144(10):04018070
2. Dobry R, Ladd RS, Yokel FY, Chung RM, Powell D (1982) Prediction of pore water pressure buildup and liquefaction of sands during earthquakes by the cyclic strain method, vol 138. National Bureau of Standards, Gaithersburg
3. Ha IS, Olson SM, Seo MW, Kim MM (2011) Evaluation of reliquefaction resistance using shaking table tests. Soil Dyn Earthq Eng 31(4):682–691
4. https://www.usgs.gov/news/magnitude-78-earthquake-nepal-aftershocks
5. IS 2720 (Part 4) (1985) Methods of test for soils–grain size analysis

6. IS 2720 (Part 14) (2006) Methods of test for soils–determination of density index for cohesionless soils
7. Kokusho T (1999) Water film in liquefied sand and its effect on lateral spread. J Geotech Geoenviron Eng 125(10):817–826
8. Maheshwari BK, Singh HP, Saran S (2012) Effects of reinforcement on liquefaction resistance of Solani sand. J Geotech Geoenviron Eng 138(7):831–840
9. Rixner JJ, Kraemer SR, Smith AD (1986) Prefabricated vertical drains. Technical report, vol I. Engineering Guidelines, Federal Highway Administration Report FHWA/RD-86/168
10. Rollins KM, Goughnour RR, Anderson JKS, Wade SF (2004) Liquefaction hazard mitigation by prefabricated vertical drains. In: International conference on case histories in geotechnical engineering, vol 4
11. Seed HB, Idriss IM (1971) Simplified procedure for evaluating soil liquefaction potential. J Geotech Eng Div ASCE 97(9):1249–1273
12. Singh H, Maheshwari B, Saran S, Paul D (2010) Improvement in liquefaction resistance of pond ash using stone-sand columns. Int J Geotech Eng 4(1):23–30
13. Varghese RM, Latha GM (2014) Shaking table tests to investigate the influence of various factors on the liquefaction resistance of sands. Nat Hazards 73(3):1337–1351
14. Xenaki VC, Athanasopoulos GA (2003) Liquefaction resistance of sand–silt mixtures: an experimental investigation of the effect of fines. Soil Dyn Earthq Eng 23(3):1–12
15. Ye B, Ye G, Zhang F, Yashima A (2007) Experiment and numerical simulation of repeated liquefaction-consolidation of sand. Soils Found 47(3):547–558

Effect of Stress Reversal in Cyclic Instability: A DEM Study

Rohini Kolapalli, Md. Mizanur Rahman ⬤, Md. Rajibul Karim ⬤, and Hoang Bao Khoi Nguyen ⬤

Abstract Cyclic Instability, *CI* is one of the most catastrophic disasters that occur in geotechnical engineering under cyclic loading conditions. This can arise in many forms and is dependent on cyclic loading pattern. To investigate these failure patterns, a series of undrained cyclic triaxial discrete element method, DEM simulations were performed on loose state of granular materials by employing different loading patterns such as stress reversal, *SR* and non-stress reversal, *NSR* conditions. The amplitude of cyclic deviatoric stress, q_{cyc} was chosen in such a way that *SR/NSR* conditions occur. Resistance to liquefaction could either increase or decrease depending on the type of loading pattern and failure behaviour. Therefore, the effect of loading pattern on cyclic liquefaction behaviour was evaluated with DEM simulations on an assembly of spherical particles. In addition to macro-study, this study will help in capturing micromechanical parameters such as coordination number *CN* and fabric *F* under different loading patterns.

Keywords Cyclic stress reversal · Loading pattern · Fabric · Coordination number

1 Introduction

Liquefaction has gained significant research interest after the Niigata and Alaska earthquakes in 1964 where wide spread soil liquefaction was observed. Since then

R. Kolapalli (✉) · Md. R. Karim · H. B. K. Nguyen
Unisa STEM, University of South Australia, Mawson Lakes, SA 5095, Australia
e-mail: Rohini.Kolapalli@mymail.unisa.edu.au

Md. R. Karim
e-mail: Rajibul.Karim@unisa.edu.au

H. B. K. Nguyen
e-mail: Khoi.Nguyen@unisa.edu.au

Md. M. Rahman
Geotechnical Engineering, Unisa STEM, University of South Australia, Mawson Lakes, SA 5095, Australia
e-mail: Mizanur.Rahman@unisa.edu.au

liquefaction phenomenon and respective devastating effects were brought to the attention of engineers and seismologists. Hyodo et al. [1] noticed that the loose specimens under *SR* conditions exhibit flow liquefaction, *FL* while residual deformation failure, *RDF* was observed under *NSR* conditions. Yang and Sze [2] observed that failure modes of specimens prepared from moist tamping method always exhibited *FL* under both *SR* and *NSR* conditions. Vaid and Chern [3] noticed a sudden development of strain, ε_d accumulation and pore water pressure, Δu generation during cyclic shearing which was referred as point of onset of flow deformation. Hyodo et al. [4] discovered that the flow deformation during cyclic loading was associated with strain-softening behaviour observed in monotonic tests.

However, most of these studies related to liquefaction susceptibility have been limited to controlled laboratory tests on reconstituted specimens. Therefore, current study adopts an alternative approach, discrete element method, DEM where it is quite capable in reproducing similar soil for exploring the effect of loading pattern on undrained behaviour of granular materials under cyclic loading. Therefore, the primary objective of this study is to explore the significance of loading pattern on failure mechanism and liquefaction resistance on loose state of the material.

2 Discrete Element Method, DEM

DEM, initially proposed by Cundall and Strack [5], has been widely used to predict the behaviour of granular materials. Sitharam [6] conducted 2D DEM simulations for exploring the microstructure evolution of granular materials during undrained cyclic loading considering different influential factors such as constant stress and strain amplitudes. Kuhn et al. [7] conducted undrained cyclic shearing simulations by considering seismic shearing pulses with non-uniform amplitudes. Huang et al. [8] explored the effect of confining pressure, p'_0 and cyclic deviatoric stress, q_{cyc} on undrained cyclic behaviour of saturated granular materials using DEM. Recently Huang et al. [9] demonstrated DEM's ability in capturing the flow deformation of sands sheared under both monotonic and cyclic undrained loading conditions.

DEM allows user to capture the micromechanical quantities (e.g. fabric, particle contacts) of granular materials, which affects the overall observed behaviour. Coordination number, *CN* and Fabric, *F* were the two parameters that allowed us to capture the micromechanical quantities of granular material which affected the behaviour of sand under cyclic triaxial loading conditions. Rothenburg and Bathurst [10] defined $CN = (C \times 2)/N$; where C is the total number of contacts and N is number of particles in the specimen. *CN* is often correlated to stability of a soil specimen. Fabric is another micromechanical parameter where structural anisotropy can be captured. Satake [11] first proposed the following equation for the structural anisotropy

$$F = F_{ij} \frac{1}{N} \sum_{k=1}^{N} n_i^k n_j^k \qquad (1)$$

where n^k is the direction of the kth contact and N is the number of contacts in the specimen. In the current study, von Mises Fabric, F_{vM} was used for measuring the scalar quantity which is equal to $(3F_{J2D})^{\frac{1}{2}}$, where F_{J2D} is the invariant of the second invariant of the deviaotric fabric tensor and is given below.

$$F_{J2D} = \frac{1}{6}\left[(F_{11} - F_{22})^2 + (F_{11} - F_{33})^2 + (F_{22} - F_{33})^2\right] + F_{12}^2 + F_{13}^2 + F_{23}^2 \quad (2)$$

where F_{11}, F_{22} and F_{33} are the fabric in the principal directions and F_{12}, F_{13} and F_{23} are the fabric in the shear directoins.

3 DEM Model

Linear contact model is implemented in the current cyclic triaxial simulations in order to reduce the complexity and computational demand. Nguyen et al. [12] suggested a set of DEM parameters for linear contact model for warranting the numerical stability of the simulations. The same set of model parameters were used in the current study. Hence the particles are assigned a normal contact stiffness of 10^8 N/m, ratio of tangential to normal contact stiffness of 1.0, coefficient of friction at particle contacts of 0.50. Following other studies [13, 14], the particle density was scaled up to 9.76×10^8 kg/m^3 to reduce computational effort. As this DEM study considered periodic boundary so it resembles the laboratory condition.

4 Assembly Generation

OVAL, an open-source program, is used for DEM simulations. The numerical program in OVAL which was implemented by Kuhn [15] and has been used in some other studies of granular material [16–18]. In this study, three-dimensional cyclic undrained loading simulations were performed on assemblages of spherical particles [15]. Initially, the particles were generated using a random number generator function with respect to the desired particle size distribution, PSD as depicted in Fig. 1. These particles were then randomly distributed over a pre-defined space without any overlaps. Then the assembly was compressed to the initial confining stress of $p' \approx 20$ kPa using servo control mechanism. The specimen at this state was 13.7 mm × 13.7 mm × 13.7 mm consisting of 2744 spherical particles. An example of the assembly of particles is shown in Fig. 1.

It should be noted that the shapes of triaxial specimens in the laboratory were cylindrical and DEM assemblies were cubic. It is expected that under ideal conditions, these should exhibit identical behaviour. The main purpose of the current study is to capture the qualitative behaviour.

Fig. 1 Grain size distribution
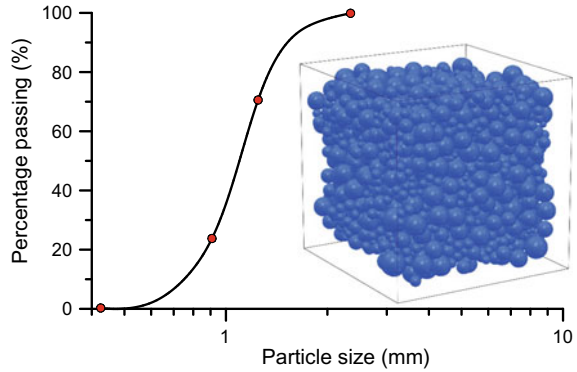
5 Testing Program

Four similar soil specimens were generated by compressing the generated assembly to a desired e_0 of 0.658 and confining stress, p'_0 of 91 kPa. Testing program includes two forms of cyclic loading: one-way cyclic loading in compression, *OWC*, two-way cyclic loading, *TWC*. In order to examine the impact of *SR*, different amplitude of cyclic deviatoric stress, q_{cyc} were chosen in such a way that *SR/NSR* conditions occur. where subscript "0" denotes the state after consolidation. In addition, monotonic triaxial DEM simulation was also conducted and the test results are compared with cyclic loading.

5.1 Results

The cyclic shearing behaviour of granular materials under *SR* and *NSR* has significant influence on the failure mechanism, pore water pressure Δu generation, strain ε_d accumulation. In addition to this, these simulations also explored the effect of loading pattern on cyclic instability (*CI*) at micro-level through coordination number, *CN* and Fabric, *F*.

One-Way Cyclic Loading, OWC. Specimen (C_01) with an $e_0 = 0.658$, $p'_0 = 91$ kPa, is sheared under one-way cyclic loading *OWC* with a q_{cyc} of 40 kPa in compression where there is *NSR*. As a result, the specimen exhibited a typical response of loose sand which is traditionally termed as residual deformation failure, *RDF*. During this failure effective stress, p' decreased with the increase in the number of loading cycles, N gradually, without abrupt loss of p' Fig. 2a. Δu increased with the increase in N and eventually reached residual pore water pressure, Δu_{res} which is approximately equal to p'_0. There was no significant amount of ε_d noticed during early stage of shearing Fig. 2b, d. Later ε_d kicks off which is defined as onset of flow and eventually large deformation has occurred. Limited flow observed in the
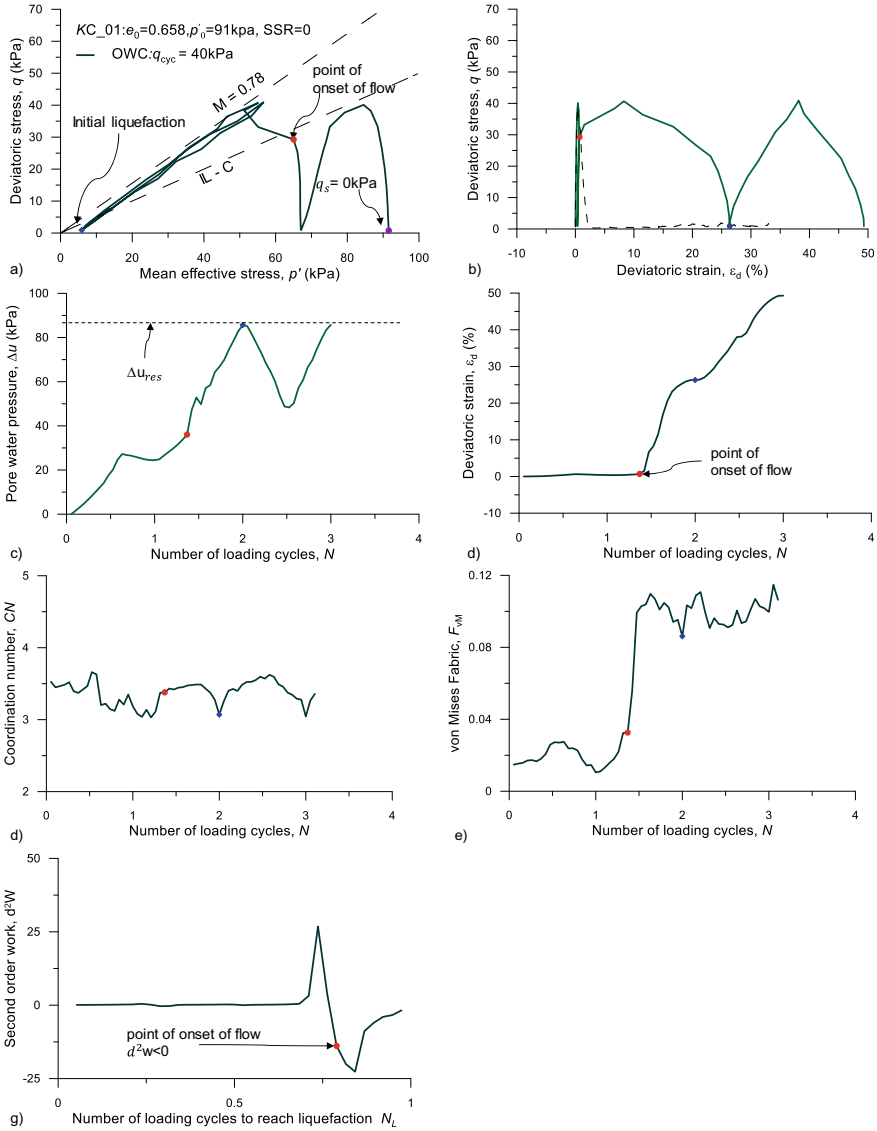
Fig. 2 Undrained behaviour of one-way cyclic loading on compression $e_0 = 0.658$, $p'_0 = 91$ kPa: **a** $q - p'$ path **b** $q - \varepsilon_d$ **c** $\Delta u - N$ **d** $\varepsilon_d - N$ **e** CN-N **f** F_{vM}-N and **g** d^2W-N_L spaces

current simulations is similar to limited liquefaction [19]. Instability line, *IL* is a line formed by joining the peak point of the undrained monotonic effective stress path, *ESP* (M_01) and the origin of the stress space as depicted in Fig. 2a. When the cyclic *ESP* approaches the *IL*, an increased leftward shift of *ESP* is noticed, which is associated with accumulation of Δu as depicted in Fig. 2b, d. This emphasizes

link between monotonic and cyclic loading. In the last few cycles, *ESP* moved up and down along the straight path through the origin of $q - p'$ space, i.e. denoted as M line which is obtained from monotonic tests (M_01) see Fig. 2a. It seems to be safer to consider the point of onset of flow which is around 1.5th loading cycle for defining liquefaction resistance when compared to pore water pressure criteria which is at around 2nd loading cycle.

CN decreases gradually with cyclic shearing till it reaches point of onset of flow. But later as there is no abrupt loss of effective stress hence *CN* fluctuates with the increase in loading cycles (Fig. 2e). F_{vM} changed gradually with the increase in the number of loading cycles and it increases abruptly at around 1.5th loading cycle which can be defined as point of onset of flow at micro-level. Soon after this cycle a significant rise in F_{vM} is noticed (see Fig. 2f).

Hill proposed second-order work [20] for evaluating the stability of granular materials, i.e. a granular material is stable only when $d^2W > 0$. This is referred as Hill's condition of instability and has been found effective for defining the instability of sands subjected to constant shear stress loading conditions in both laboratory tests [21] and DEM simulations [22]. Figure 2g demonstrates defining onset of flow by using hill's condition of instability. d^2W is small and positive before reaching the point of onset of flow. Later $d^2W < 0$ representing the point of onset of flow (Fig. 2g), which indicates a high unstable state.

Two-Way Cyclic Loading, TWC. Specimen C_02 and C_03 with same $e_0 = 0.658$ and $p'_0 = 91$ kPa when subjected to TWC with two different amplitudes of cyclic deviatoric stress, $q_{cyc} = 20$ kPa and 40 kPa respectively where SR occurs. Due to the presence of SR conditions, two specimens (C_02 and C_03) manifested limited flow flowed by cyclic mobility, LF $\rightarrow$ CM. This behaviour is referred as a hybrid failure mode where LF and CM are observed together. LF is noticed at around 1st and 12th loading cycle for $q_{cyc} = 40$ kPa and 20 kPa respectively (Fig. 2a). But later which is followed by cyclic mobility where p' transiently reaches zero effective stress but with an abrupt accumulation of large ε_d (Fig. 3a, b, d). At this point, an increase in leftward shift of cyclic ESP is noticed where Δu started to build up suddenly and eventually reached Δu_{res} which has led to transient softening and the same is presented in Fig. 3c. This CI can be triggered from the IL obtained from the monotonic tests (M_01). Cyclic ESP crosses the IL on compression side and hence failed on compression side, when sheared under $q_{cyc} = 20$ kPa and cyclic ESP crosses the IL on extension side and hence failed on extension side, when sheared under $q_{cyc} = 40$ kPa as depicted in Fig. 3a, b.

CN and F_{vM} evolved during cyclic shearing helped us in evaluating the point of onset of flow (Fig. 3e, f). At this point, contact density decreased substantially leading to decrease in effective stress. As a result, loss of average coordination number (see Fig. 3e) occurs and hence effective stress decreases causing Δu to increase.

Hill's condition of instability was also evaluated for its suitability in defining the point of onset of flow for $LF \rightarrow CM$. d^2W is very small and positive till it reaches the point of onset of flow. $d^2W < 0$ at the point of onset of flow see Fig. 3g. A significant change of F_{vM} was noticed at around 1st and 13th loading cycle for a $q_{cyc} = 40$
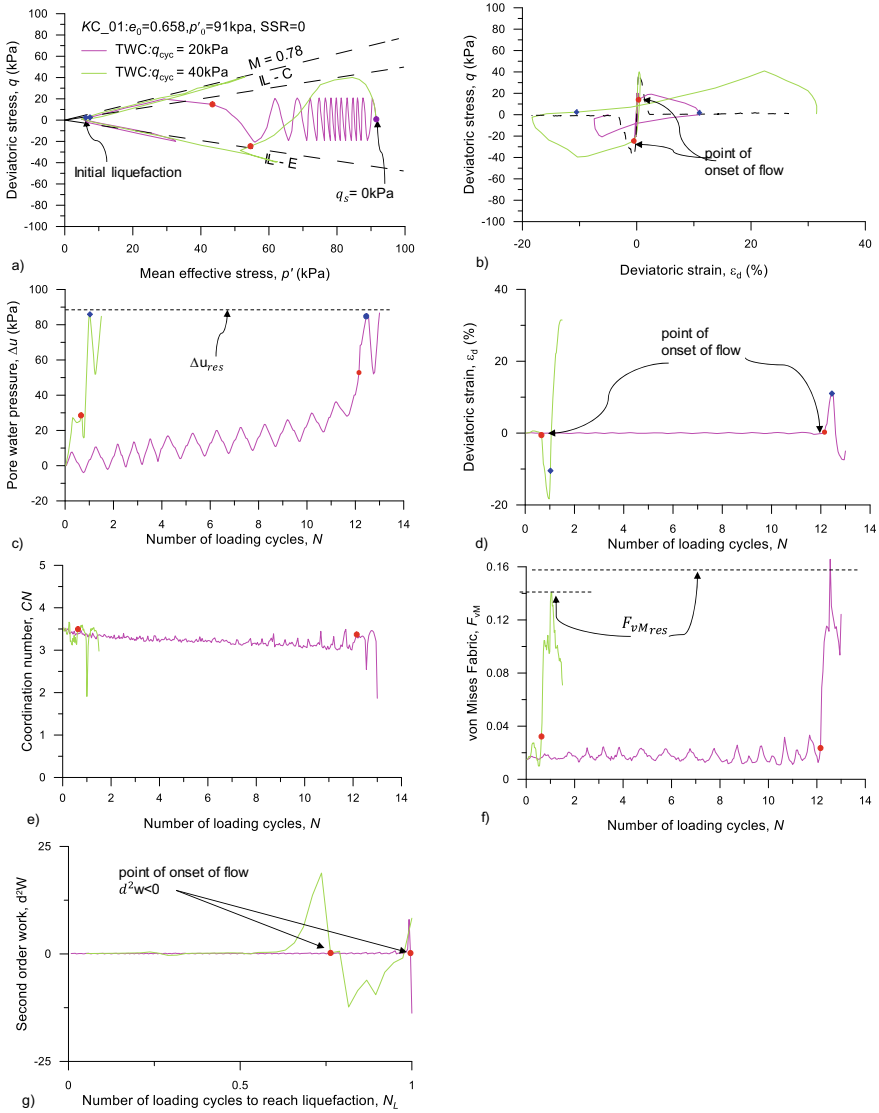
Fig. 3 Undrained behaviour of TWC on $e_0 = 0.658$, $p'_0 = 91$ kPa: **a** $q - p'$ path **b** $q - \varepsilon_d$ **c** $\Delta u - N$ **d** $\varepsilon_d - N$ **e** CN-N **f** $F_{vM} - N$ and **g** $d^2W - N_L$ spaces

kPa and 20 kPa, respectively, which had led to abrupt increase in Δu, triggering point of onset of flow is clearly observed at micro-level through F_{vM} and CN. A significant increase in F_{vM} is noticed immediately after the point of onset of flow where a significant drop in CN is noticed indicating unstable state of the specimen (Fig. 3e, f), respectively.

6 Conclusion

This study aims at exploring the effect of stress reversal on cyclic instability at micro and macro-level. The following were the significant findings from the current study.

(1) Effect of loading pattern altered the failure mechanism. Specimen when subjected to one-way cyclic loading, *OWC* exhibited residual deformation failure (*RDF*) whereas under two-way cyclic loading, *TWC* (presence of *SR*) demonstrated limited flow followed by cyclic mobility, $LF \rightarrow CM$.

(2) Failure on the compression side occurs when cyclic *ESP* intersects monotonic compression stress path prior to monotonic extension path and vice versa. Hence there exists a link between monotonic and cyclic loading.

(3) Instability line on compression and extension side which is obtained from monotonic tests formed a boundary for defining the failure plane for specimen under cyclic loading conditions. This highlights the link between monotonic and cyclic loading.

(4) Specimen with *OWC* where there is *NSR* reached its initial liquefaction point at 2nd loading cycle whereas specimen with *TWC* in the presence of *SR* with same q_{cyc} reached initial liquefaction point in 1st loading cycle. This explains specimen subjected to *SR* has less liquefaction resistance when compared with that of *NSR*.

(5) Hill's condition of instability found to be suitable for analysing point of onset of flow for both *RDF* and $LF \rightarrow CM$.

References

1. Hyodo M et al (1991) Undrained cyclic shear strength and residual shear strain of saturated sand by cyclic triaxial tests. Soils Found 31(3):60–76
2. Yang J, Sze HY (2011) Cyclic behaviour and resistance of saturated sand under non-symmetrical loading conditions. Géotechnique 61(1):59–73
3. Vaid YP, Chern JC (1983) Effect of static shear on resistance to liquefaction. Soils Found 23(1):47–60
4. Hyodo H et al (1994) Undrained cyclic and monotonic triaxial behaviour of saturated loose sand. Soils Found 34(1):19–32
5. Cundall PA, Strack ODL (1979) A discrete numerical model for granular assemblies. Géotechnique 29(1):47–65
6. Sitharam TG (2003) Discrete element modelling of cyclic behaviour of granular materials. Geotech Geol Eng 21(4):297–329
7. Kuhn M et al (2014) Investigation of cyclic liquefaction with discrete element simulations. J Geotech Geoenviron Eng 140(12):04014075
8. Huang X et al (2017) Exploring the undrained cyclic behaviour of sand using DEM. In: Li X, Feng Y, Mustoe G (eds) Proceedings of the 7th international conference on discrete element methods. Springer Singapore, Singapore, pp 757–765
9. Huang X et al (2018) DEM analysis of the onset of flow deformation of sands: linking monotonic and cyclic undrained behaviours. Acta Geotech 13(5):13

10. Rothenburg L, Bathurst RJ (1989) Analytical study of induced anisotropy in idealized granular materials. Géotechnique 39(4):601–614
11. Satake M (1982) Fabric tensor in granular materials. In: Vermeer PA, Luger HJ (eds) Proceedings of the IUTAM symposium on deformations and failure of granular materials. Delft, The Netherlands, pp 63–68
12. Nguyen H, Rahman MM, Cameron D (2015) Undrained behavior of sand by DEM study. IFCEE 2015, GSP 256. ASCE, San Antonio, USA, pp 182–191
13. Thornton C (2000) Numerical simulations of deviatoric shear deformation of granular media. Géotechnique 50(1):43–53
14. Ng T (2006) Input parameters of discrete element methods. J Eng Mech 132(7):723–729
15. Kuhn MR (2006) Oval and OvalPlot: programs for analyzing dense particle assemblies with the discrete element method. Department of Civil Engineering, University of Portland, Portland, OR, USA.
16. Nguyen HBK, Rahman MM, Fourie AB (2018) Characteristic behaviour of drained and undrained triaxial tests: a DEM study. J Geotech Geoenviron Eng (in press)
17. Rahman MM, Nguyen HBK, Rabbi ATMZ (2018) The effect of consolidation on undrained behaviour of granular materials: experiment and DEM simulation. Geotech Res 5(3):1–19
18. Nguyen HBK, Rahman MM, Fourie AB (2017) Undrained behaviour of granular material and the role of fabric in isotropic and K0 consolidations: DEM approach. Géotechnique 67(2):153–167
19. Vaid YP, Chern JC, Tumi H (1985) Confining pressure, grain angularity and liquefaction. J Geotech Eng ASCE 111(10):1229–1235
20. Hill R (1958) A general theory of uniqueness and stability in elastic-plastic solid. J Mech Phys Solids 6(3):14
21. Chu J et al (2012) Instability of loose sand under drained conditions. J Geotech Geoenviron Eng 138(2):207–216
22. Perez JCL et al (2016) Exploring the micro-mechanics of triaxial instability in granular materials. Géotechnique 1–16

Examination and Appraisal of Liquefaction Vulnerability Between Idriss–Boulanger Method and Andrus–Stokoe Method

Manali Patel ⓘ**, Tejas Thaker** ⓘ**, and Chandresh Solanki** ⓘ

Abstract The occurrence of pore pressure build-up due to earthquake subsequent with the harm of soil strength is known as liquefaction. The outcome of soil liquefaction on existing structures can be extremely disastrous. Buildings foundations rested directly on sand are prone to liquefy easily and hence lose the support, which upshots in severe and uneven settlement of the structure causing structural damage. Liquefaction potential is a term to specify whether the soil will liquefy or not. As per Bureau of Indian Standards, Ahmedabad region falls under moderate zone of earthquake hence there is a prodigious need of consideration of liquefaction potential. Around 1200 bore log data were collected from several laboratories like KCT consultancy, Ahmedabad Municipal Corporation, Anandjiwala laboratory, and Geotech Soil Testing laboratory. The soil layers of the Ahmedabad city are frequently loose alluvial soil and clayey sand which are more susceptible to liquefaction. The aim of present study is to relate the liquefaction potential by consuming two field test methods that are SPT-N value and shear wave velocity (V_s). The core objective behind the current study is to link and evaluate the liquefaction potential for Ahmedabad region and to map the liquefaction severity for the region on the basis of these two methods. Consuming these subsurface statistics, quantifiable valuation of liquefaction potential has been attempted and different hazard maps have been produced at different depths.

Keywords Pore pressure · Liquefaction · Earthquake · SPT-N value · Shear wave velocity

1 Introduction

Liquefaction was defined in the simplified method [12] to a phenomenon in which a cohesionless soil loses its strength during an earthquake and acquires a degree of

M. Patel (✉) · C. Solanki
S V National Institute of Technology, Surat, Gujarat, India
e-mail: davemanali99@gmail.com

T. Thaker
Pandit Deendayal Petroleum University, Gandhinagar, Gujarat, India

mobility sufficient to permit movements ranging from several feet to several thousand feet. The city Ahmedabad falls under seismic zone III as per Bureau of Indian Standard 1893 [8]. Although the river Sabarmati in the Ahmedabad city is non-perennial, it flows with a constant flow of water due to the construction of Sabarmati Riverfront. Therefore, there are more chances of ground water table to come up. Moreover, the city contains poorly graded sand and silty sand in the major areas which are prone to soil liquefaction. Due to the present seismicity in the city, this study is aimed to evaluate liquefaction potential and to develop the liquefaction hazard maps for the region.

2   Theoretical Study

Seed and Idriss [12] have made very first attempt to investigate the soil liquefaction potential. Afterward, many scientists [11, 13–15, 19] have updated the procedure for determining soil liquefaction potential. To study the relationship between Liquefaction Resistance and Shear Wave Velocity (V_s), many studies have been carried out by several researchers [2, 3, 9, 10, 16] based on several field tests, analytical study [4, 17] and also the laboratory experiments [5, 6, 18]. At the small strain level, the shear wave velocity which is the basic engineering property of any soil in the ground response analysis is related to the shear modulus. By using the geophysical tests, soil profiles can be generated without disturbing the soil. Thus, these non-destructive tests have grabbed more attention for the evaluation of liquefaction resistance.

3   Methodology

The quantitative assessment of liquefaction potential was studied using two approaches, namely Idriss and Boulanger [7] method and Andrus and Stokoe [1] method. In the present study, for the Ahmedabad region the magnitude of earthquake is considered as 7.7 and subsequent surface peak ground acceleration is taken as 0.16 g [8].

3.1   SPT-N Approach

Idriss and Boulanger [7] studied the several field-based procedures to assess the liquefaction potential for soils like sand during earthquakes. They reviewed the original simplified procedure proposed by Seed and Idriss [12] and found that cyclic shear stresses (*CSR*) are the essential component in the liquefaction hazard analysis. Further, in addition to CSR they have incorporated various new components and proposed a new factor cyclic resistance ratio (*CRR*) based on clean sand condition

using corrected $(N_1)_{60}$ values. Using these two parameters, factor of safety against liquefaction was calculated as FOS = CRR/CSR. Finally, the liquefaction hazard assessment was plotted using ArcGIS.

3.2 Shear Wave Velocity Approach

The shear wave velocity approach was originally proposed by Andrus–Stokoe in 1997 and subsequently Andrus has updated this approach in 1999 and 2000 [1, 3]. In the revised procedure, they have corrected the penetration resistance for overburden stress and so revised the shear wave velocity relations. Further, *CRR* was evaluated using revised shear wave velocity relations proposed by Andrus and Stokoe [1]. Finally, factor of safety was calculated and plotted using revised *CRR* and *CSR*.

In both the methods, the liquefaction was predicted by applying conditions as FOS ≤ 1 or FOS > 1. The factor of safety was evaluated for different depths as 0–3 m, 3–6 m, 6–10 m, and 10–15 m and liquefaction severity maps were generated. The suitability and limitations of both the methods have been listed in Table 1.

Table 1 Suitability and limitations of Idriss and Boulanger [7] method and Andrus–Stokoe [1] method

S. no.	Idriss and Boulanger [7] method	Andrus–Stokoe [1] method
1	This method uses the correlations to find the shear wave velocity and hence it is cheaper as it requires routine SPT tests which are less expensive. Even it is easy to collect borlog data from geotechnical consultancies. Hence this method is economic and beneficial to all	This method requires the field testing like SASW and MASW which uses the costly equipment. Hence it is the drawback for many who can not afford such costly equipment
2	Through this method, the detailed soil classification can be achieved as it uses the borlog data along with SPT values	Through this method, only stiffness of soil can be achieved and hence soil can be identified only in terms of stiff, medium, soft, etc.
3	Through this method, the actual shear wave velocity values can not be achieved as it is obtained through the correlations	Through this method, the actual shear wave velocity values can be achieved as it is obtained directly through filed tests like SASW and MASW
4	NA	The major drawback of this method is that the field testing like SASW and MASW demands many site-specific requirements which make site selection more difficult

4   Results and Discussions

For the liquefaction hazard calculations, the moment magnitude (M_w) and the surface peak ground acceleration (PGA) values are the major input parameters. The extreme earthquake of magnitude (M_w 7.7) was occurred at Bhuj city of Gujarat state in the year 2001. Thus, in the present study, the moment magnitude (M_w) is taken as 7.7. Since the study region lies in the seismic zone III [8], the value of peak ground acceleration is considered as 0.16 g.

As per the soil reports collected from the various consultancies, the water table found to be at shallow (up to 5 m) depths (Fig. 1). Looking to the scenario of water table present in the city, there is a great need for the assessment of liquefaction potential at least up to 15 m depth.

The Factor of Safety against liquefaction for Ahmedabad region has been evaluated by two approaches as follows: (I) Andrus and Stokoe [1] method which is based on Shear Wave Velocity and (II) Idriss and Boulanger [7] method which is based on SPT-N value.

The locations like Kankaria, Ghodasar and Amraivadi in the central region and Motera, Naranpura in the west region are likely to be liquefied at 0–3 m depth as per the Andrus and Stokoe [1] method (Fig. 2) whereas in SPT-N-based Idriss and Boulanger [7] method (Fig. 3), these areas are not susceptible to liquefaction.
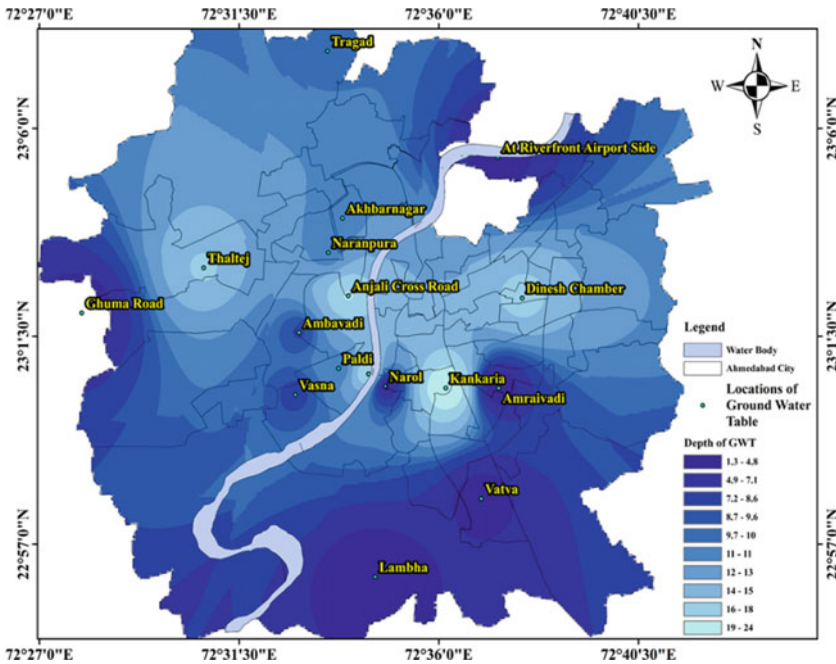
Fig. 1 Ground water contour map of Ahmedabad region
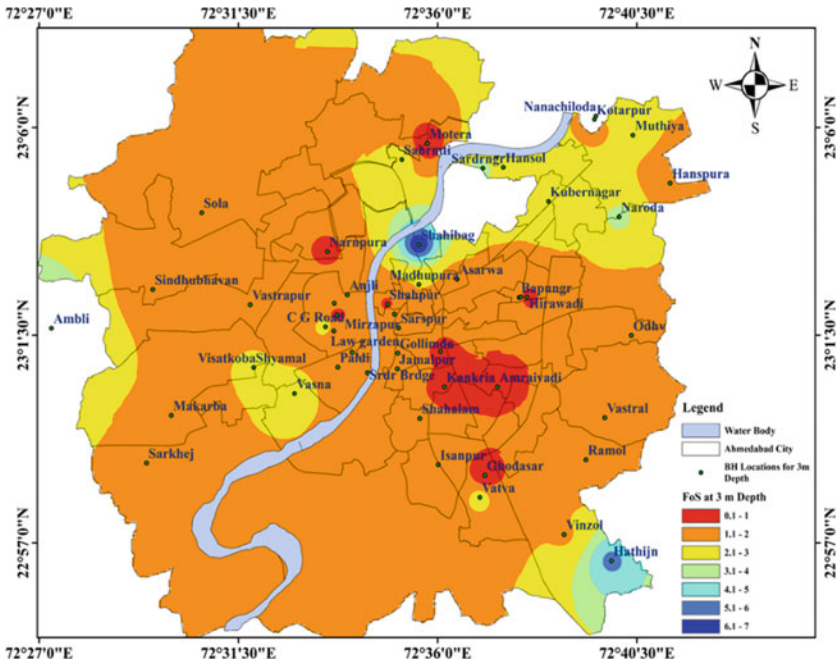
Fig. 2 Factor of safety distribution at 0–3 m depth by Andrus and Stokoe [1] method

From Figs. 4 and 5, it observed that in the central and east regions locations like Saraspur, Relief Road, Madhupura, Ghodasar, Nehrunagar, Vastral, etc. are likely to be liquefied at 3–6 m depth based on shear wave velocity method while as per SPT-N method, these areas are not likely to be liquefied.

As illustrated in Figs. 6 and 7, it can be noted that the areas in the central, east, and west regions are considered to be severe for liquefaction at 6–10 m depth from Shear Andrus and Stokoe [1] method whereas the Vatva and Sola locations in the east and west regions are likely to be liquefied as per Idriss and Boulanger [7] method.

For 15 m depth, the severity of liquefaction can be seen mainly in the central region as per Andrus and Stokoe [1] method (Fig. 8) whereas the central region can be found safe as per Idriss and Boulanger [7] method (Fig. 9).

5   Conclusions

In the present study, the liquefaction potential for the Ahmedabad city was assessed using SPT-N value and shear wave velocity (V_s) proposed by Idriss and Boulanger [7] and Andrus and Stokoe [1], respectively. From these two methods, it can be stated that Sardar Bridge, Paldi, Mirzapur in the central part, Vasna, Shyamal in the western-central part, Kankaria, Amraivadi, Odhav, Vastral, etc. in the east and
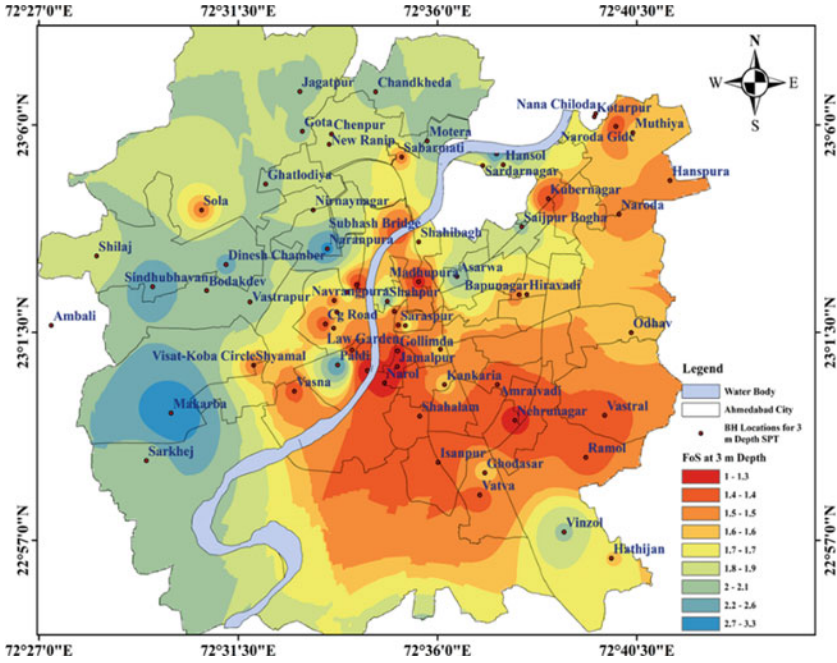
Fig. 3 Factor of safety distribution at 0–3 m depth by Idriss and Boulanger [7] method

Subhash Bridge, Madhupura, and Naroda GIDC in the north regions of the city
are likely to be liquefied on account of liquefied layers present at shallow depths
whereas Bodakdev, Visat-Koba Circle, Makarba and Sarkhej in the western region
and Dinesh Chamber, Saijpur Boga, Nikol in the north-east parts are having no risk
from liquefaction due to clayey layers at shallow depths. Therefore, the liquefaction
severity maps generated in the present study can be useful in the urban planning and
reducing risk from liquefaction through appropriate mitigation.
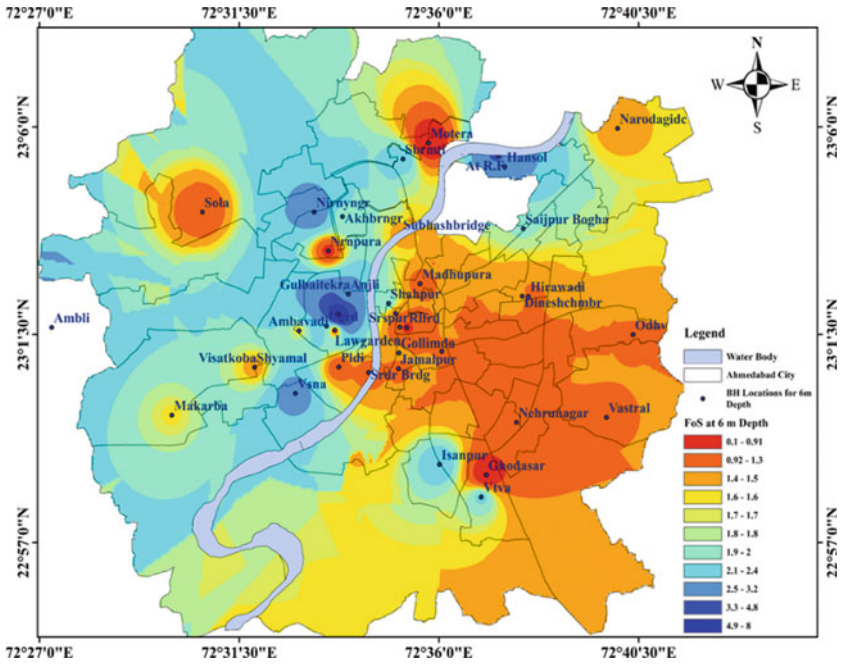
Fig. 4 Factor of safety distribution at 3–6 m depth by Andrus and Stokoe [1] method
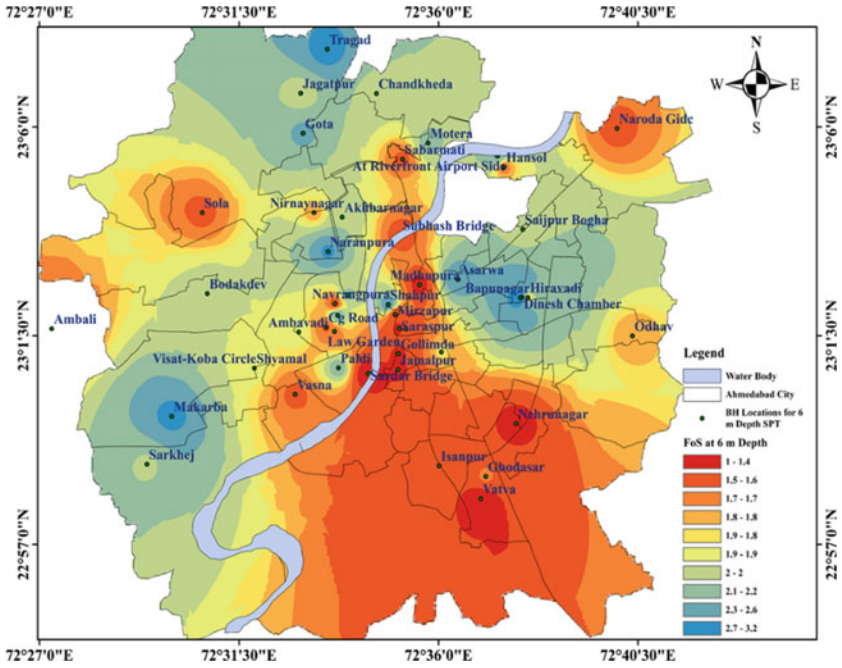
Fig. 5 Factor of safety distribution at 3–6 m depth by Idriss and Boulanger [7] method
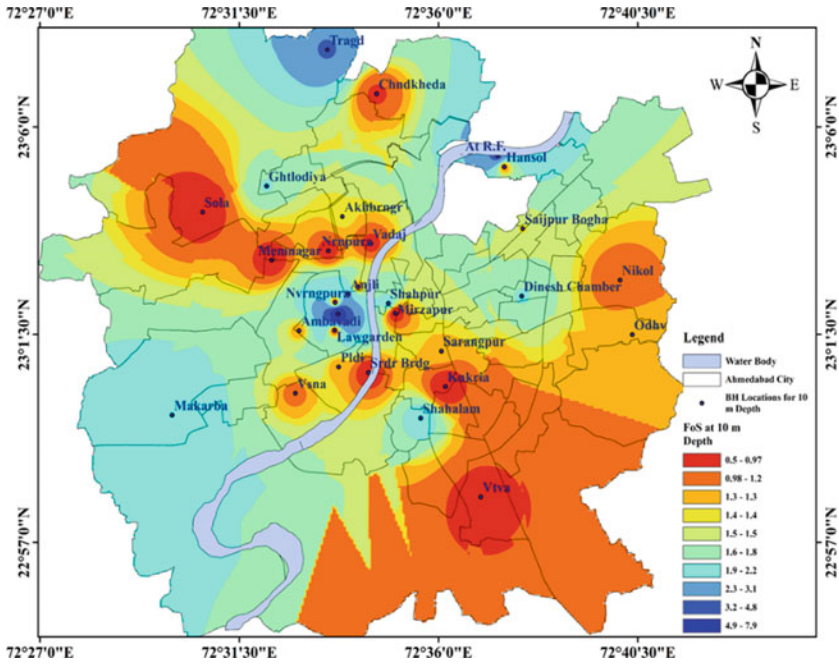
Fig. 6 Factor of safety distribution at 6–10 m depth by Andrus and Stokoe [1] method
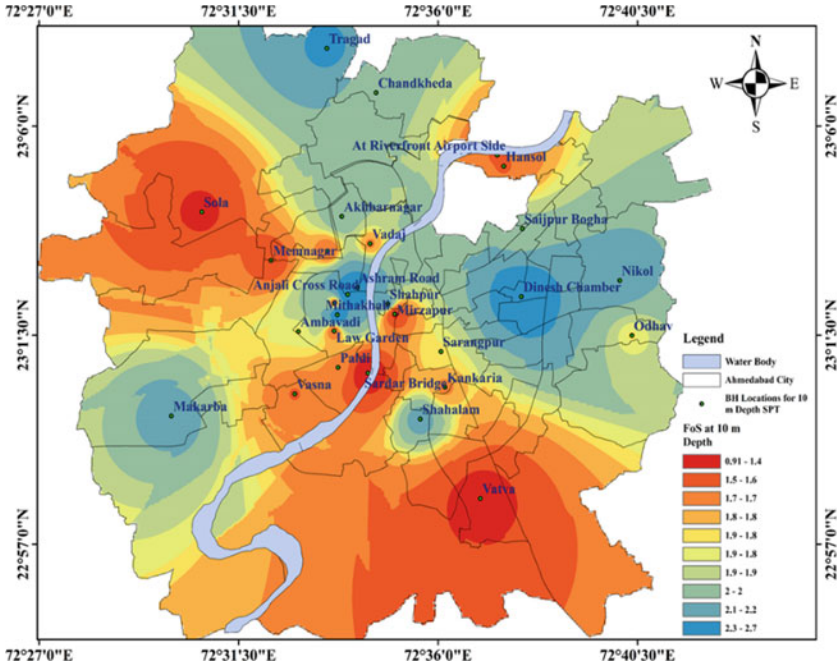
Fig. 7 Factor of safety distribution at 6–10 m depth by Idriss and Boulanger [7] method
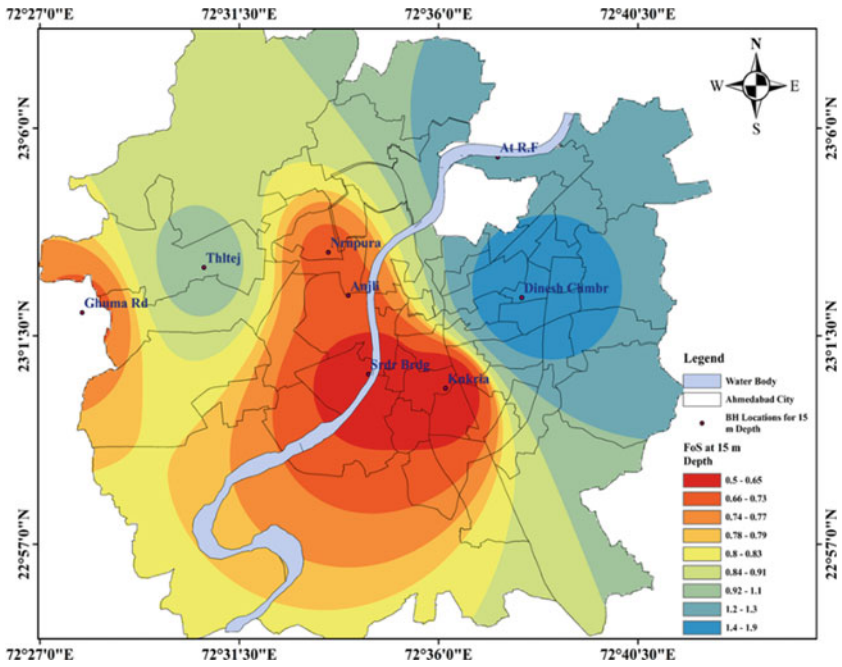
Fig. 8 Factor of safety distribution at 10–15 m depth by Andrus and Stokoe [1] method
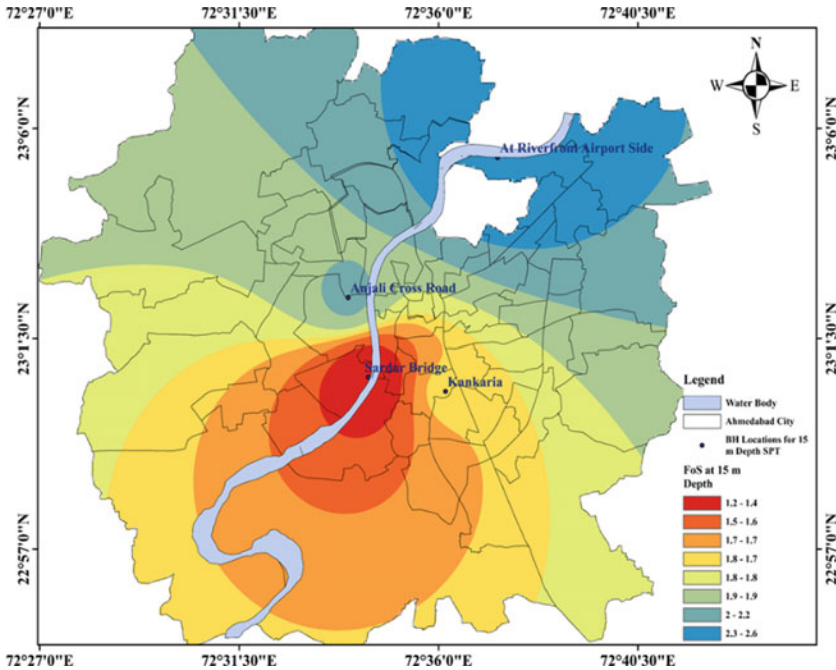
Fig. 9 Factor of safety distribution at 10–15 m depth by Idriss and Boulanger [7] method

References

1. Andrus RD, Stokoe KH II (2000) Liquefaction resistance based on shear wave velocity. J Geotech Eng Div ASCE 126(11):1015–1025
2. Andrus RD, Stokoe KH II (1997) Liquefaction resistance of soils from shear wave velocity. In: Proceedings of the NCEER workshop on evaluation of liquefaction resistance of soils, pp 98–128
3. Andrus RD, Stokoe KH II, Chung RM (1999) Draft guidelines for evaluating liquefaction resistance using shear wave velocity measurements and simplified procedures, NISTIR 6277. National Institute of Standards and Technology, Gaithersburg, MD
4. Bieschwale JG, Stokoe KH II (1984) Analytical evaluation of liquefaction potential of sands subjected to the 1981 Westmordland earthquake. Geotechnical engineering report GR-84-15. The University of Texas at Austin
5. De Alba P, Baldwin K, Janoo V, Roe G, Celikkol B (1984) Elastic-wave velocities and liquefaction potential. Geotech Test J 7(2):77087
6. Dobry R, Stokoe KH II, Ladd RS, Youd TL (1981) Liquefaction susceptibility from S-wave velocity. In: Proceedings of the ASCE national convention, in situ tests to evaluate liquefaction susceptibility. ASCE, New York
7. Idriss IM, Boulanger RW (2010) SPT-based liquefaction triggering procedures. Center for Geotechnical Modeling, University of California, USA
8. IS 1893 (2016) Indian Standard criteria for earthquake resistant design of structures, part-1 general provisions for buildings. Bureau of Indian Standards, New Delhi
9. Kayen RE, Mitchell JK, Seed RB, Lodge A, Nishio S, Coutinho R (1992) Evaluation of SPT, CPT and shear wave based methods for liquefaction potential assessment using Loma Prieta

data. In: Proceedings of 4th Japan-US workshop on earthquake resistant design of lifeline facilities and countermeasures for soil liquefaction, Hamada, pp 177–204

10. Robertson PK, Woeler DJ, Finn WDL (1992) Seismic cone penetration test for evaluating liquefaction potential under cyclic loading. J Can Geotech Eng 29:686–695

11. Seed HB, Idriss IM (1982) Ground motions and soil liquefaction during earthquakes. In: Earthquake engineering monograph, vol 134

12. Seed HB, Idriss IM (1971) Simplified procedure for evaluating soil liquefaction potential. J Soil Mech Found (ASCE97) (SM9) 1249–1273. ASCE, USA

13. Seed HB, Idriss IM, Arango I (1983) Evaluation of liquefaction potential using field performance data. J Geotech Eng ASCE 109(3):458–482

14. Seed HB, Tokimatsu K, Harder LF, Chung RM (1985) Influence of SPT procedures in soil liquefaction resistance evaluations. J Geotech Eng Div ASCE 111(12):1425–1445

15. Seed HB (1979) Soil liquefaction and cyclic mobility evaluation for level ground during earthquakes. J Geotech Eng ASCE 105:201–221

16. Stokoe KH II, Nazarian S (1985) Use of rayleigh waves in liquefaction studies. In: Woods RD (ed) Measurement and use of shear wave velocity for evaluating dynamic soil properties. ASCE, New York, pp 1–17

17. Stokoe KH II, Roesset JM, Bieschwale JG, Aound M (1988) Liquefaction potential of sands from shear wave velocity. In: Proceedings of the 9th world conference on earthquake engineering, vol III. Tokyo, Japan, pp 213–218

18. Tokimatsu K, Tuchida A (1990) Correlation between liquefaction resistance and shear wave velocity. Soils Found 30(2):33–42

19. Youd TL, Noble SK (1997) Liquefaction criteria based on statistical and probabilistic analyses. In: Proceedings of the NCEER workshop on evaluation of liquefaction resistance of soils. Technical report NCEER-97-0022. Multidisciplinary Center for Earthquake Engineering Research, Buffalo, New York, pp 201–215

Effect of Gradation and Stress Ratio on Liquefaction Response of Ennore Sand

Homit Singh Pal, Majid Hussain, Aparna Shrivastava, and Ajanta Sachan

Abstract Liquefaction behavior of soil is governed by several factors such as grain size, fines content, relative density, the magnitude of shear stress or strain, and loading conditions. Cyclic stress ratio (CSR) is one of the most important parameters that govern the liquefaction potential of sands during seismic events. The present experimental study investigates the effect of cyclic stress ratio on the liquefaction response of cohesionless soil. Five different types of specimens (S_1–S_5) were prepared including well-graded and poorly graded sands having definite proportions of three commercially available grades of Ennore sand. Grain size distribution (GSD) parameters such as coefficient of uniformity (C_u) and co-efficient of curvature (C_c) were also determined for all the five specimens. A series of stress-controlled cyclic simple shear tests were performed on these specimens prepared at 60% relative density over a wide range of CSR (0.1, 0.075, 0.05, and 0.03). The criteria for the liquefaction initiation in the present study was chosen as $r_u = 1.0$; where $r_u =$ excess pore water pressure ratio. The number of cycles to liquefaction was observed to increase with the reduction in CSR value for all five specimens. Well-graded specimen (S_4) exhibited more resistance toward liquefaction than uniformly graded specimens (S_1, S_2, S_3, and S_5) at same CSR values. The shear modulus (G) of all the specimens was observed to decrease with the reduction in mean particle diameter (D_{50}) for all CSR values.

Keywords Cyclic stress ratio · Liquefaction · Cyclic simple shear · Ennore sand

H. S. Pal · M. Hussain · A. Shrivastava (✉) · A. Sachan
Civil Engineering, Indian Institute of Technology Gandhinagar, Gandhinagar, India
e-mail: aparna.shrivastava@iitgn.ac.in

H. S. Pal
e-mail: homit.singh@btech2014.iitgn.ac.in

M. Hussain
e-mail: majid.hussain@iitgn.ac.in

A. Sachan
e-mail: ajanta@iitgn.ac.in

1 Introduction

Liquefaction is defined as the complete loss of shear strength during earthquake shaking due to development of excess pore water pressure equivalent to confining pressure. Factors affecting liquefaction characteristics include gradation, fines content, void ratio, type of fines, plasticity index, etc. Liquefaction characteristics have been evaluated by several researchers in the past. Pitman et al. [10] reported reduced strain softening with increasing percentage of fines. Carraro et al. [2] performed cyclic triaxial tests on Ottawa sand with non-plastic silt content varying from 0 to 15%. Jiaer et al. [8] studied the liquefaction triggering criteria in detail. Liquefaction susceptibility of sand-silt mixture and fine to coarse sand was investigated by performing monotonic and cyclic triaxial tests [1, 3]. Dinesh et al. [4] explored the liquefaction potential of Sabarmati sand by performing stress-controlled cyclic triaxial tests at various relative densities. Kwa and Airey [9] investigated the effect of fines on liquefaction behavior of well-graded soils by performing monotonic and cyclic triaxial tests. Zhang et al. [11] studied the liquefaction assessment criteria by performing cyclic triaxial tests on loose and dense quaternary silt under different CSR values. Some findings show an increase of liquefaction resistance with increasing fines content. Doygun et al. [5] investigated the effect of fines content and grain size of silica sand by performing monotonic and cyclic direct simple shear tests. Eseller-Bayat et al. [6] investigated the coupled effect of relative density, fines content, CSR and fines plasticity by performing stress-controlled cyclic simple shear tests on sand with silt or clay. Hussain and Sachan [7] explored the dynamic behavior of Kutch soils (Gujarat, India) under cyclic triaxial and cyclic simple shear conditions. However, combined effect of loading conditions (CSR) and gradation on liquefaction response is yet to be understood in detail. Therefore, the present study focuses on the effect of gradation of Ennore sand on liquefaction characteristics at various CSR values. The tests were conducted at stress-controlled cyclic simple shear conditions.

2 Material Properties

In the present study, Ennore sand of three different grades (S_1, S_2, and S_3) was used. Ennore sand is Indian Standard Sand used for assessing the quality of mineral mixtures like cement, lime in the construction industry. Well-graded (S_4) and poorly graded (S_5) samples of Ennore sand were prepared by mixing appropriate proportion of the three standard grades I, II, and III (S_1, S_2, S_3). Grain size distribution of five samples (S_1, S_2, S_3, S_4 and S_5) is shown in Fig. 1. The particle size of S_1, S_2, and S_3 varied from 2 mm–1 mm, 1 mm–500 µm, and 500 µm–90 µm, respectively. S_4 consisted of S_1, S_2, and S_3 in the proportion of 100: 90: 80. S_5 comprised of S_1, S_2, and S_3 in the proportion of 100:10:80. The physical properties of the five specimens such as mean particle diameter (D50), maximum void ratio (e_{max}), minimum void ratio (e_{min}), void ratio of specimens tested (e), coefficient of curvature (C_c), and
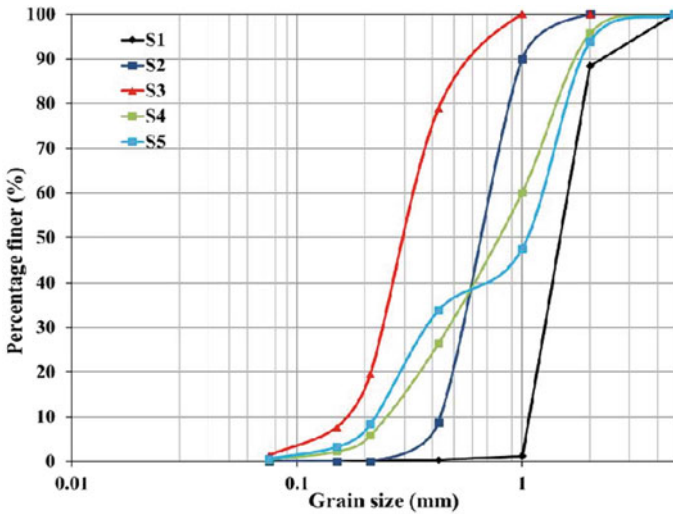
Fig. 1 Grain size distribution of Ennore sand samples with different gradation

Table 1 Physical characteristics of Ennore sand of different gradation

Sample	D_{50}	e_{max}	e_{min}	e	C_u	C_c
S_1	1.5	0.46	0.38	0.412	1.45	1.11
S_2	0.65	0.47	0.39	0.422	1.64	0.95
S_3	0.29	0.5	0.36	0.416	1.94	1.03
S_4	0.8	0.39	0.3	0.336	6.67	1.41
S_5	1.1	0.36	0.28	0.312	5.65	0.45

coefficient of uniformity (C_u) are presented in Table 1. The specific gravity of the Ennore sand was found to be 2.64 and was assumed to be same for all the specimens.

3 Specimen Preparation and Experimental Program

The present study was conducted by performing cyclic simple shear tests on Electro-mechanically Dynamic Cyclic Simple Shear (EMDCSS) system. The cyclic simple shear (CSS) setup is facilitated with three load cells of capacity 5 kN with a resolution of 0.1 N, two axial and one horizontal LVDTs with a resolution of the order of 0.1 μm. The setup is capable of applying combinations of shear forces in the horizontal direction and axial force in the vertical direction on the soil specimen. CSS tests were performed on soil specimens of 70 mm diameter and 20 mm height. The specimens were prepared by tamping dry soil mass equivalent to 60% relative density on a base pedestal in an assembly of Teflon coated low friction steel rings surrounding a

stretched latex membrane. The assembly was held tightly by a pair of clamps fixed to the base pedestal, which in turn minimized the disturbance. Specimen along with the base pedestal and the confining rings was mounted on the EMDCSS system. The specimens were saturated by percolating de-aired water from the bottom of the specimen at a seating pressure of 5 kPa. The saturated specimens were then subjected to consolidation by applying vertical stress of 100 kPa. The rigid Teflon-coated low friction confining rings ensure that the specimens were subjected to $K0$-consolidation. After consolidation, the specimens were subjected to stress-controlled cyclic loading at four different CSR, i.e., 0.1, 0.075, 0.05, and 0.03 at a frequency of 0.1 Hz.

4   Results and Discussions

A total of 20 cyclic simple shear tests were performed on different grades of Ennore sand specimens (S_1, S_2, S_3, S_4, and S_5) prepared at 60% relative density to investigate the effect of gradation and CSR on the dynamic response. Effect of particle size on the cyclic response of well-graded (S_4) and poorly graded sample (S_5) which were prepared by mixing appropriate proportions of commercially available different grades of Ennore sand was explored. The tests were performed by varying CSR values from 0.1, 0.075, 0.05, and 0.03. CSR was defined as the ratio of cyclic shear stress to that of initial normal stress (100 kPa). The state of liquefaction was reached as the pore water pressure ratio (r_u) attained value equal to 1.

4.1   Effect of Gradation on Hysteresis Response and Pore Pressure Response of Ennore Sand at Various CSR Values

The hysteresis response of Ennore sand with varying GSD at various CSR values is shown in Fig. 2. At CSR $= 0.1$ and 0.075, rapid and large deformation was observed. The total plastic strain accumulation was observed to be higher for S_3 as compared to S_1. This behavior could be attributed to the increased percentage of fine sands in S_3 which would provide easier horizontal shear displacements as compared to S_1. Specimen S_1 with coarse sand exhibited higher frictional resistance due to efficient inter-locking. The hysteresis loop for S_3 was observed to be wider compared to that of S_1 and S_2. Therefore, S_3 indicated higher energy dissipation as compared to S_2 and S_1. However, well-graded specimen (S_4) indicated less accumulation of strain as compared to S_2 and S_3. The behavior exhibited by S_4 was observed due to the better mobilization of shear stress owing to the compact configuration of the well-graded specimen. This configuration could be attributed to the voids being filled by finer sand particles ($e = 0.336$), which could provide added frictional resistance to the
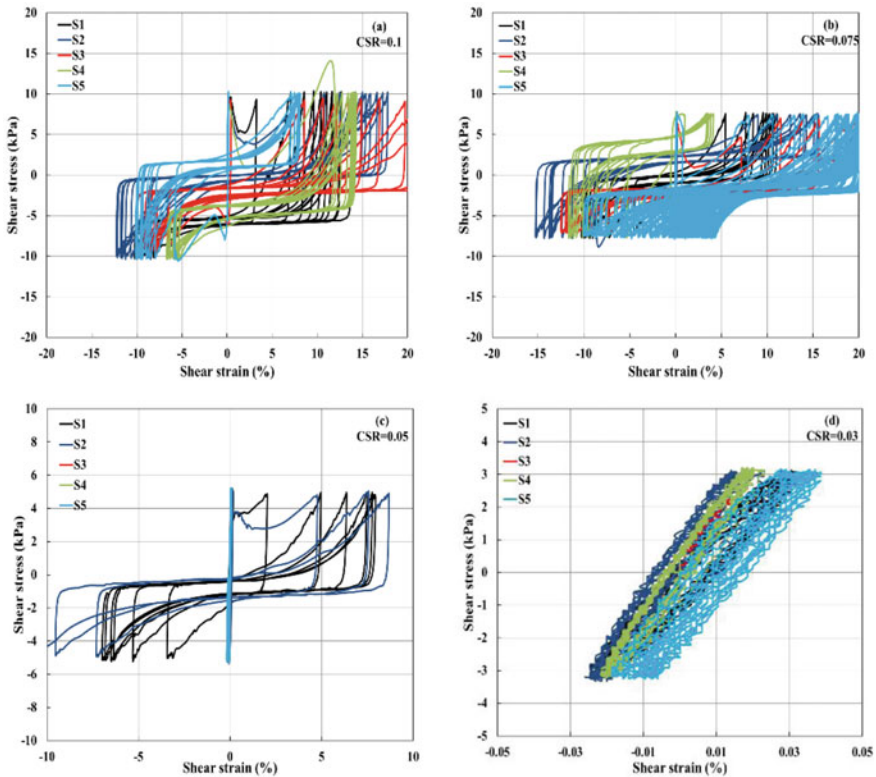
Fig. 2 Effect of gradation on hysteresis response of Ennore sand at different loading conditions. **a** CSR = 0.1, **b** CSR = 0.075, **c** CSR = 0.05, **d** CSR = 0.03

specimen under cyclic loading. The added cyclic resistance was revealed in the form of lower cyclic strains. The poorly graded specimen (S_5) showed lesser shear strain as compared to S_1. At lower CSR value 0.05, the total strain accumulation for S_1 and S_2 was 9%, however for the specimen S_3, S_4, and S_5 the strain accumulation was low almost insignificant as compared to S_1 and S_2. Further, at CSR of 0.03 specimens exhibited very low shear strains.

Figure 3 shows the pore pressure response of Ennore sand specimens with different gradation at various CSR values. It is evident that at higher level of shaking, i.e., CSR = 0.1 and 0.075, the behavior was almost similar for all the specimens, S_1–S_5. All the specimens attained liquefaction within two cycles when subjected to CSR of 0.1 and 0.075. However, at CSR = 0.05 and 0.03, the number of cycles to liquefaction increased with increasing in the fine sand content of the specimens. At CSR = 0.05, number of cycles to liquefaction was determined to be 5 and 12 for S_1 and S_3, respectively. The increased liquefaction resistance could be attributed to the large number of grain to grain contact in case of S_3 due to large number of finer sand particles. At CSR value of 0.03, the number of cycles to liquefaction of Ennore sand

Fig. 3 Effect of gradation on pore pressure response of Ennore sand at different loading conditions. **a** CSR = 0.1, **b** CSR = 0.075, **c** CSR = 0.05, **d** CSR = 0.03

was observed to be 54 and 145 for specimens S_1 and S_4, respectively. At this CSR value, well-graded specimen S_4 exhibited highest liquefaction resistance due to the compact particle structure resulting from the wide range of particle sizes.

4.2 Effect of CSR on Hysteresis Response and Pore Pressure Response of Ennore Sand with Different Gradation

Effect of CSR on hysteresis response of Ennore sand with varying gradation is represented in Fig. 4. For S_1, the total irreversible strain accumulation (14%) was obtained to be higher as the CSR increased. The rate of accumulation of cyclic strains was found to be higher at higher CSR values. The area of hysteresis loop could be observed to be greater for the higher CSR values as compared to that at lower CSR values indicating a relatively elastic response for specimens subjected to lower CSR values. The total strain accumulation was determined to be 17% and 26% at CSR = 0.1 for S_2 and S_3, respectively, which was higher as compared to S_1 at the same
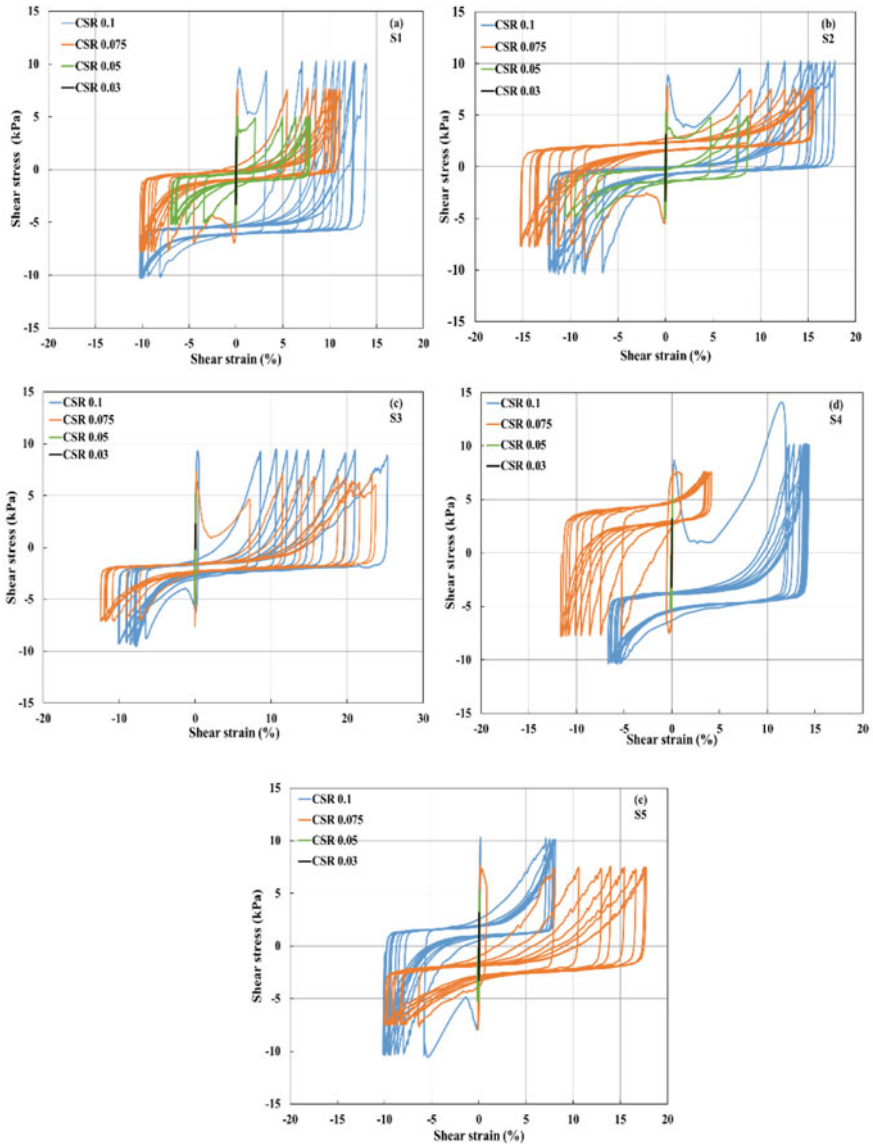
Fig. 4 Effect of CSR on hysteresis response of Ennore sand with different gradation. **a** S_1, **b** S_2, **c** S_3, **d** S_4, **e** S_5

CSR. Large accumulation of cyclic strain could be attributed to the higher initial shear load causing the distortion of the soil structure subsequently leading to higher total accumulated strain in all the specimens (S_1, S_2, S_3, S_4, and S_5). For well-graded sand (S_4), the plastic strain accumulation was pronounced for CSR = 0.1 and 0.075 as compared to lower CSR values (0.05 and 0.03). At higher CSR, the change in particle orientation within the soil skeleton made the soil more susceptible to shear deformation and subsequently led to initial liquefaction.

Effect of CSR on accumulated pore pressure with number of loading cycles for different gradations of Ennore sand is presented in Fig. 5. It is evident that the CSR values lower than 0.075 the specimens exhibited significantly lower pore pressure as compared to that at the higher CSR.

However, for well-graded specimens S_4, the excess pore pressure generated was observed to be lower and slower as compared to poorly graded specimen (S_5) and standard grade specimens (S_1, S_2, and S_3). For specimen S_4, more than 100 cycles were required to reach pore pressure ratio equal to 1.

4.3 Effect of Gradation on Number of Cycles to Liquefaction

In the current study, liquefaction criteria were defined when the pore water pressure ratio (r_u) became 1. The number of loading cycles to liquefaction for different gradations of Ennore sand specimens at different Cyclic Stress Ratio (CSR) is shown in Fig. 6. At higher CSR value (0.1), the behavior of all the sand specimens (S_1–S_5) was observed to be similar. However, at other CSR values of 0.075, 0.05, and 0.03, the cyclic strength was found to be increased as the particle size was distributed over a wider range. At CSR = 0.03, the number of cycles to liquefaction for S_1 and S_4 was observed to be 64 and 145, respectively, indicating significant increase in liquefaction resistance. The higher percentage of fine sand increased the liquefaction resistance. Therefore, specimen S_4 and S_5 which have mixed proportions of different size particles liquefied at higher number of loading cycles as compared to the coarser specimens S_1, S_2, and S_3 having uniform gradation, i.e., the particles of same size. The fine sand particles have tendency to occupy the voids between the larger sand particles which subsequently provides more frictional resistance to the soil mass and resulted into higher cyclic strength subsequently higher liquefaction resistance.

4.4 Dynamic Properties

Dynamic properties were obtained from the hysteresis response of Ennore sand [7]. Figure 7 shows the variation of cyclic degradation index (δ) with number of cycles for various Ennore sand specimens. The cyclic degradation index (δ) is defined as the ratio of the shear modulus at Nth cycle to that of 1st cycle. The value of δ decreased with increasing number of loading cycles. At CSR value of 0.1, variation of δ with
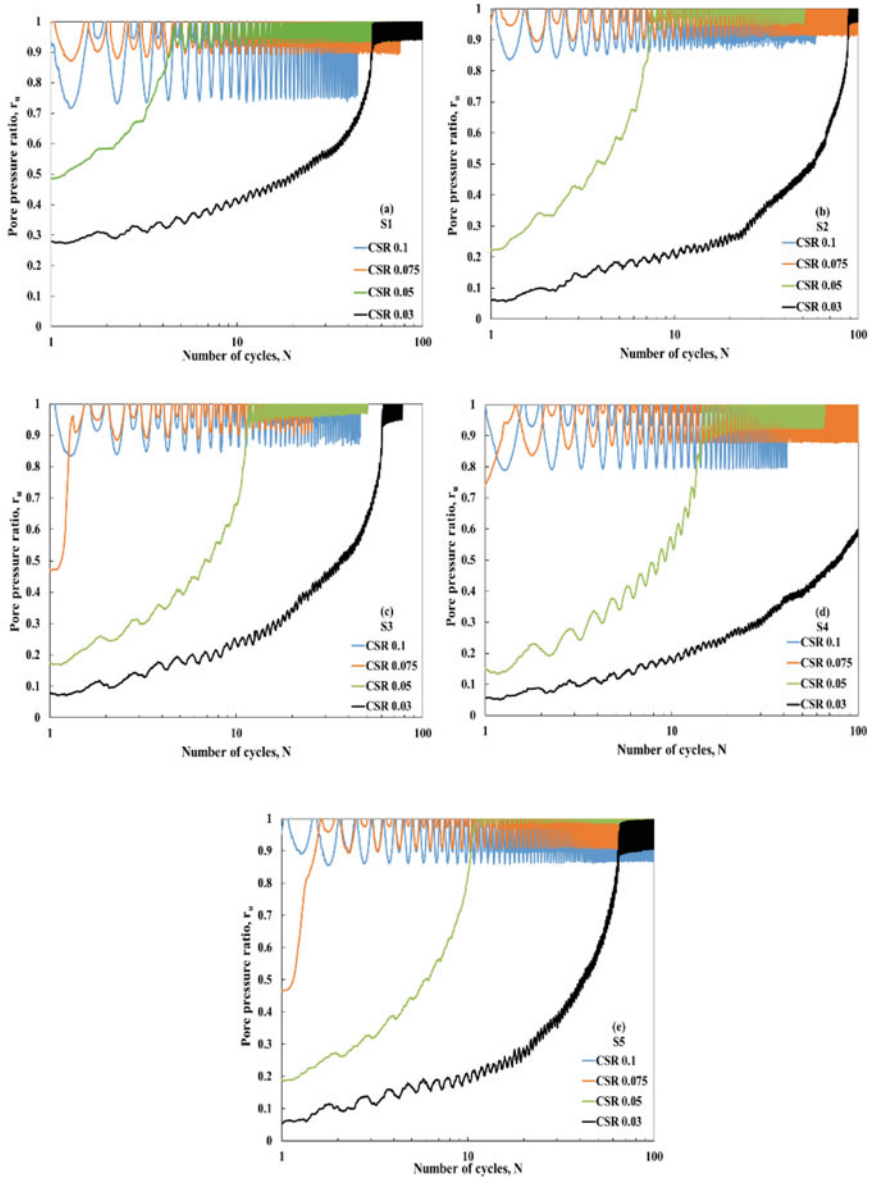
Fig. 5 Effect of CSR on pore pressure response of Ennore sand with different gradation. **a** S_1, **b** S_2, **c** S_3, **d** S_4, **e** S_5

Fig. 6 Effect of particle gradation on liquefaction response of Ennore sand
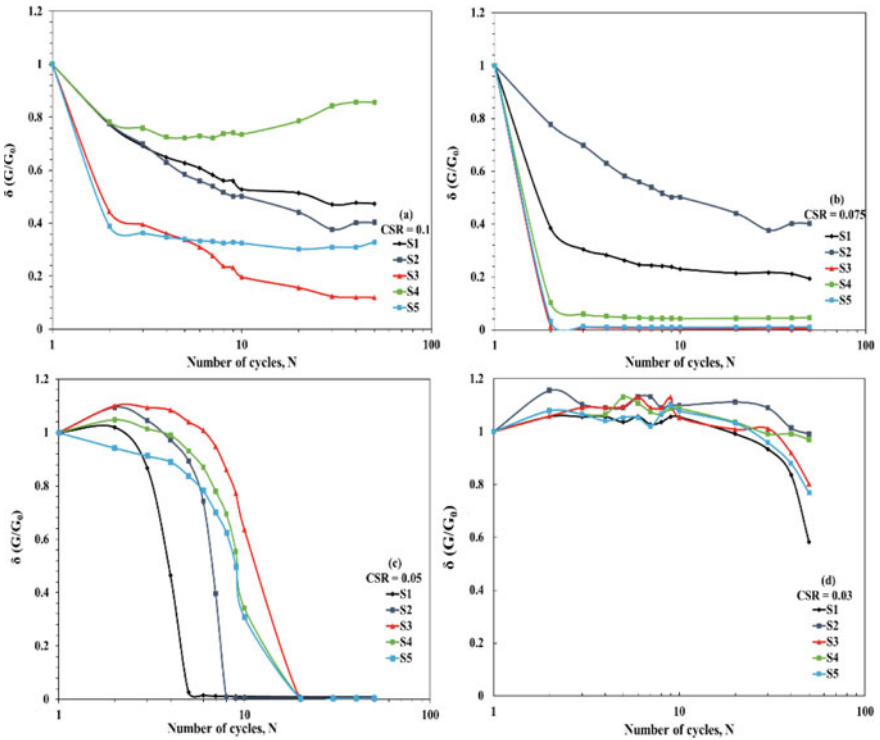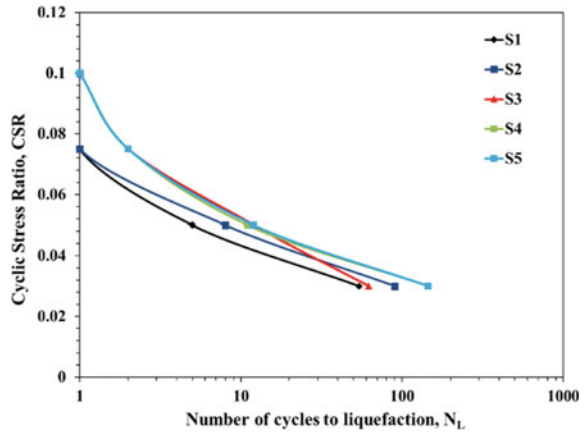
Fig. 7 Effect of gradation on cyclic degradation index of Ennore sand at different loading conditions. **a** CSR = 0.1, **b** CSR = 0.075, **c** CSR = 0.05, **d** CSR = 0.03

the number of cycles is not actually representing the true because and it is evident from the hysteresis response of all the specimens. The specimens at CSR value of 0.1 attained liquefaction within the first cycle resulting into large strain in the first cycle itself. In the subsequent cycles, the strain level was not significantly different than that of the first cycle. Hence, the values of δ evaluated were not representing a true picture and actually underestimate the degradation of cyclic shear modulus. However at CSR = 0.075 and 0.05, the rate of modulus degradation was found to be higher with increased percentage of finer sand fraction as compared to that at that CSR value of 0.03. Specimen S_3 exhibited rapid degradation of δ as compared to S_1 and could be attributed to the higher shear displacements of finer sand fraction. At CSR = 0.03, the rate of modulus degradation was observed to be nearly similar for all the specimens (S_1–S_5). This behavior could be attributed to the negligible shear displacements with loading cycles observed in the hysteresis response. For all CSR values, the shear modulus decreased with the increase in fine sand content due to weaker inter-particle contacts between fine sand particles.

Figure 8 shows the variation of damping ratio (D) with number of loading cycles for different gradations of Ennore. Damping ratio signifies the dissipation of energy
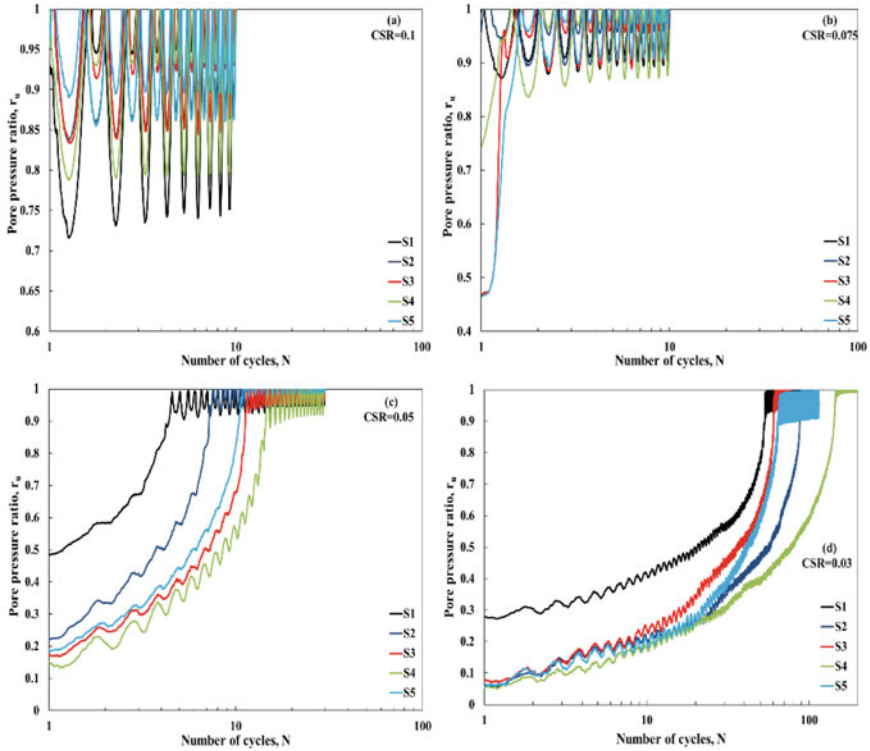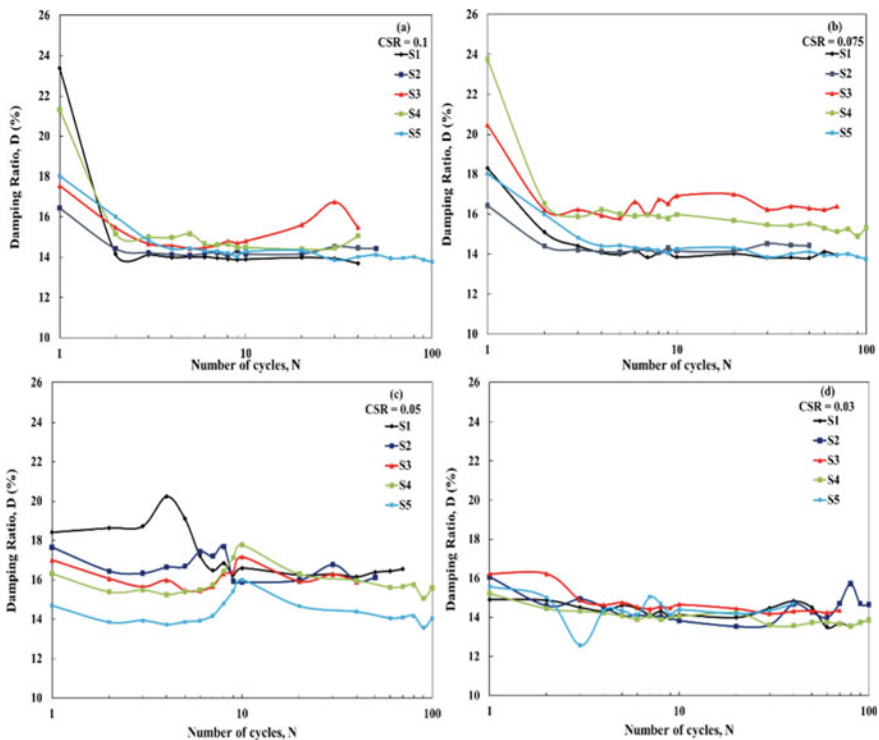

Fig. 8 Effect of gradation on damping ratio of Ennore sand at different loading conditions. **a** CSR = 0.1, **b** CSR = 0.075, **c** CSR = 0.05, **d** CSR = 0.03

under cyclic loading condition. At CSR = 0.1, 0.075, the damping was highly pronounced till 2nd cycle, whereas it became almost constant for all the Ennore sand specimens (S_1–S_5). This was because of higher plastic strain accumulation till 2nd cycle, after which there was not much strain accumulation as the specimens liquefied by the second cycle at higher CSR values. At lower CSR = 0.05 and 0.03, the damping ratio variation for specimens S_1–S_5 was found to be 2% till 100 loading cycles. This was due to the lesser shear deformation with increase in loading cycles at lower CSR values, which resulted into overlapped hysteresis loops. The signature of the variation of δ and D with the number of cycles could be related to hysteresis and pore pressure response of the specimens.

5 Results and Discussions

In the present study, liquefaction behavior of different gradation of Ennore sand was explored at various CSR values under stress-controlled cyclic simple shear condition. The following conclusion could be drawn from the study:

1. At higher CSR values of 0.1 and 0.075, the total plastic strain accumulation was observed to be higher for S_3 as compared to S_1. At higher CSR value, the total irreversible strain accumulation (14%) in S_1 was obtained to be higher as compared to lower CSR values.
2. At higher level of shaking, i.e., CSR = 0.1 and 0.075, pore pressure response was almost similar for all the specimens (S_1–S_5). All the specimens exhibited liquefaction within two loading cycles at CSR values of 0.1 and 0.075. However, at CSR = 0.05 and 0.03, the number of loading cycles to liquefaction increased with the increasing fine sand content.
3. At CSR = 0.1, 0.075, and 0.05, the rate of modulus degradation was found to be higher with increasing percentage of finer sand fraction. At CSR = 0.03, the rate of modulus degradation was similar for all the Ennore sand specimens (S_1–S_5).
4. At CSR = 0.1, and 0.075, the damping was highly pronounced till 2nd cycles whereas it became almost constant for all the Ennore sand specimens (S_1–S_5). At lower CSR = 0.05 and 0.03, the variation in damping ratio for specimens S_1–S_5 was determined to be 2% up to 100 loading cycles.

References

1. Belkhatir M, Arab A, Schanz T, Missoum H, Della N (2011) Laboratory study on the liquefaction resistance of sand-silt mixtures: effect of grading characteristics. Granular Matter 13(5):599–609
2. Carraro JAH, Bandini P, Salgado R (2003) Liquefaction resistance of clean and nonplastic silty sands based on cone penetration resistance. J Geotech Geoenviron Eng 129(11):965–976

3. Choobbasti AJ, Ghalandarzadeh A, Esmaeili M (2014) Experimental study of the grading characteristic effect on the liquefaction resistance of various graded sands and gravelly sands. Arab J Geosci 7(7):2739–2748
4. Dinesh SV, Kumar GM, Balreddy MS, Swamy BC (2011) Liquefaction potential of Sabarmati-river sand. ISET J Earthq Technol Pap 516:2–4
5. Doygun O, Brandes HG, Roy TT (2019) Effect of gradation and non-plastic fines on monotonic and cyclic simple shear strength of silica sand. Geotech Geol Eng 1–20
6. Eseller-Bayat EE, Monkul MM, Akin Ö, Yenigun S (2019) The coupled influence of relative density, CSR, plasticity and content of fines on cyclic liquefaction resistance of sands. J Earthquake Eng 23(6):909–929
7. Hussain M, Sachan A (2019) Dynamic behaviour of Kutch soils under cyclic triaxial and cyclic simple shear testing conditions. Int J Geotech Eng 1–17
8. Jiaer WU, Kammerer AM, Riemer MF, Seed RB, Pestana JM (2004) Laboratory study of liquefaction triggering criteria. In: 13th world conference on earthquake engineering. Vancouver, BC, Canada, Paper (no. 2580), Aug 2004
9. Kwa KA, Airey DW (2017) Effects of fines on liquefaction behaviour in well-graded materials. Can Geotech J 54(10):1460–1471
10. Pitman TD, Robertson PK, Sego DC (1994) Influence of fines on the col-lapse of loose sands. Can Geotech J 31(5):728–739
11. Zhang CL, Jiang GL, Su LJ, Liu WM, Zhou GD (2018) Effect of dry density on the liquefaction behaviour of quaternary silt. J Mt Sci 15(7):1597–1614

Pore Pressure Response of Natural Soils Under Various Testing Conditions

Majid Hussain and **Ajanta Sachan**

Abstract Soil behavior under undrained conditions is governed by several factors, including soil density, fines content, plasticity index and loading conditions among many others. Constitutive behavior of soil being pressure-dependent, the undrained response of soils is dictated by the development of excess pore water pressure during the applied loading. In this study, the pore pressure response of the natural Kutch soils under monotonic compression triaxial (TX), cyclic triaxial (CTX), and cyclic simple shear (CSS) conditions was investigated at their in-situ density. The explored soils vary greatly in terms of gradation, fines content, and nature of fines. The development of excess pore water pressure was compared under the three loading conditions and was analyzed in the context of fines content and plasticity index of the soils. The excess pore pressure ratio at peak stress for TX was found to be lower than that during the first cycle for both the CTX and CSS. However, at critical state, the excess pore pressure ratio for TX was higher than that during the 5th cycle for CTX and CSS. Under cyclic conditions, for a given number of cycles, the excess pore water pressure ratio under CSS conditions was always higher than that under the CTX conditions, signifying overestimation of liquefaction resistance as evaluated from the CTX tests. With an increase in the fines content and plasticity index, excess pore water pressure was observed to decrease under all the three loading conditions.

Keywords Pore pressure · Triaxial · Cyclic triaxial · Cyclic simple shear · Fines content · Plasticity index · Kutch region

1 Introduction

Soil behavior under undrained conditions is governed by several factors, including soil density, fines content, plasticity index and loading conditions among many others [7, 8]. While density is the single most parameter affecting the response of cohesionless soils, plasticity index plays a dominant role in governing the response of

M. Hussain (✉) · A. Sachan
Indian Institute of Technology Gandhinagar, Palaj, Gandhinagar 382355, India
e-mail: majid.hussain@alumni.iitgn.ac.in

cohesive soils. Constitutive behavior of soil being pressure-dependent, the response of soils is dictated by the magnitude and rate of volume changes and development of excess pore water pressure under drained and undrained loading conditions. Under undrained conditions, the findings available in the literature reveal that the development of excess pore water pressure occurs only if the applied strains are higher than a certain threshold [2]. Excess pore pressure is generated due to irreversible changes in the microstructure of the soil at shear strains higher than the threshold value. The shear-induced excess pore water pressure leads to a reduction in effective stress and hence the reduced load-carrying capacity. The nature of the excess pore water pressure development is dependent on the current material and stress states of the soil mass. It could be contractive or dilative for loose and dense soils, respectively. For loose sandy soils, the development of excess pore water pressure might be nearly equal to the initial effective confining pressure. This extreme condition subsequently leads to a state of liquefaction, a state in which the soils have nearly zero shear strength. The state of liquefaction can be reached under both the monotonic and cyclic loading leading to static and cyclic liquefaction, respectively. A number of researchers have explored the undrained response of geomaterials with focus on shear strength characteristics including liquefaction a well as cyclic degradation. Both the liquefaction and the degree of cyclic degradation are governed by the magnitude and rate of development of excess pore water pressure. Whereas cohesive soils experience lower and slower pore pressure generation, cohesionless soils display large and rapid development of the excess pore water pressure. The soils in the Kutch region, due to predominantly cohesioneless nature, have experienced large-scale liquefaction during past earthquakes including the 2001 Bhuj earthquake. However, only a few studies have been devoted to exploring the engineering behavior of the soils, particularly under undrained conditions. In other related studies by the authors, the undrained response under monotonic and cyclic conditions was explored [3, 4]. However, the pore pressure response of the soils under both the monotonic and cyclic conditions remains to be explored. In this study, the pore pressure response of Kutch soils under different loading conditions is studied.

Undrained behavior of 30 natural soils collected from 10 locations of the Kutch region in Gujarat, India is explored under monotonic triaxial (TX), cyclic triaxial (CTX), and cyclic simple shear (CSS) conditions. The soils explored consisted mainly of silty-sand and clayey-sand. In this study, excess pore pressure response of the saturated specimens under TX, CTX, and CSS testing conditions was evaluated as a function of fines content (FC), plasticity index (PI), and grain size index (I_{GS}). I_{GS} for soil was evaluated as the ratio of area under particle size distribution curve to the area encompassed between 0.001 and 75 mm, extreme soil particle size [1].

2 Materials and Methods

2.1 Material Properties

In the present study disturbed representative soil samples were collected from 10 locations from low lying Kutch region of Gujarat, India. A total of 32 samples were collected by mechanical auger boring at depths ranging from 0.5 to 2.5 m. Hussain and Sachan [3] provide a detailed account of the geotechnical properties of the soils explored in the study. The soils had properties including dry density, water content, particle size distribution, fines content, and plasticity varying over a wide range. The basic geotechnical properties of the soils are presented in Table 1 [6]. While the dry density of the Kutch soils varied from 13.37 to 17.71 kN/m^3, the fines content varied from 11 to 83%. The plasticity index of the Kutch soils explored in the current study varied from being non-plastic to 22.9%. Out of the 30 soils 16 were classified as silty-sands, 9 as clayey-sands, 3 low plasticity clay, 1 high plasticity clay, and 1 as low plasticity silt.

2.2 Testing Equipment and Specimen Preparation

The excess pore pressure response of the soils in the current study was investigated under undrained triaxial, cyclic triaxial, and cyclic simple shear conditions. Moist tamping technique was adopted for the specimen preparation at in-situ density for all the three conditions [3, 4]. The specimens for TX and CTX were saturated by back pressure saturation whereas for CSS conditions de-aired water under the influence of gravity was percolated from the bottom of the specimen. However, the specimen size was different in the case of CSS as compared to that of the TX and CTX tests (Fig. 1). In the case of CSS tests, cyclic behavior of solid cylindrical specimens of diameter 70 mm and height 20 mm was explored whereas in TX and CTX the specimen size was 50 mm in diameter and 100 mm in height. Figure 1 shows the comparison of the specimen size used in the investigation of Kutch soils in the current study. The schematic shows the relative specimen size and loading configuration for the TX, CTX, and CSS conditions. For all the three conditions deformation controlled loading was applied. For TX tests, monotonic loading was applied at a deformation rate of 0.1 mm per minute. For CTX and CSS tests, the consolidated specimens were subjected to cyclic loading of shear strain amplitude of 0.6% at a frequency of 0.1 Hz. While the direction of loading for CTX was along the longitudinal axis, for CSS the direction of loading was horizontal.

Table 1 Geotechnical properties of soils of Kutch region

Soil name	Depth (m)	γ_{di} (kN/m³)	w_c (%)	G_S	GSD				Atterberg limits			Soil class
					G (%)	S (%)	M (%)	C (%)	LL (%)	PL (%)	PI (%)	
Chang Dam			23° 27.591′ N	2.67	70° 24.408′ E							
S1 (L1)	0.5	15.00	19	2.67	6	78	11	5	–	–	–	SM
S2 (L2)	0.5	15.69	10	2.66	0	82	15	3	16	NP	NP	SM
S3 (L2)	1.5	15.70	14	2.68	5	76	17	2	20	NP	NP	SM
Kharoi			23° 28.367′ N		70° 23.330′ E							
S4	0.5	16.01	4	2.67	0	82	13	5	16	NP	NP	SM
S5	1.5	16.90	3	2.67	5	84	9	2	14	NP	NP	SP-SM
S6	2.5	16.00	2	2.67	1	86	11	2	13	NP	NP	SM
Suvai Dam			23° 36.428′ N		70° 29.821′ E							
S7	0.5	17.03	5	2.67	0	72	21	7	15	NP	NP	SM
S8	1	14.37	5	2.66	2	74	19	5	15	NP	NP	SM
S9	1.5	13.55	11	2.66	1	82	14	3	15	NP	NP	SM
Fatehgarh Dam			23° 41.369′ N		70° 48.057′ E							
S10	0.5	17.17	18	2.72	0	1	62	37	54	19	35	CH
S11	1.5	15.53	14	2.67	1	54	42	3	19	NP	NP	SM
S12	2.5	15.45	20	2.69	0	78	21	1	16	NP	NP	SM
Chobari			23° 30.722′ N		70° 20.881′ E							
S13	0.5	17.51	13	2.70	0	56	42	2	24	14	10	SC
S14	1.5	16.96	18	2.71	0	51	42	7	26	15	11	SC
S15	2.5	17.57	36	2.70	0	59	37	4	25	16	9	SC

(continued)

Table 1 (continued)

Soil name	Depth (m)	γ_{di} (kN/m³)	w_c (%)	G_S	GSD				Atterberg limits			Soil class
					G (%)	S (%)	M (%)	C (%)	LL (%)	PL (%)	PI (%)	
Khadir			23° 50.82′ N		70° 14.39′ E							
S16	0.5	15.94	3	2.66	2	79	17	2	17	NP	NP	SM
S17	1.5	16.82	2	2.66	1	74	22	3	16	NP	NP	SM
S18	2.5	16.96	1	2.66	2	88	9	1	14	NP	NP	SP-SM
Tappar Dam			23° 15.017′ N		70° 07.586′ E							
S19	0.5	17.36	13	2.67	0	58	24	18	34	11	23	SC
S20	1.5	16.39	17	2.66	5	66	14	15	31	10	21	SC
S21	2.5	17.67	23	2.68	4	72	14	10	22	10	12	SC
Budharmora			23° 20.634′ N		70° 11.501′ E							
S22	0.5	17.71	6	2.68	2	69	21	8	23	15	8	SC
S23	1.5	14.27	15	2.71	1	34	46	19	44	16	28	CL
S24	2.5	12.26	22	2.70	2	18	57	23	66	27	39	CH
Banniari			23° 24.299′ N		70° 09.910′ E							
S25	0.5	13.37	6	2.74	0	17	81	2	26	NP	NP	ML
S26	1.5	14.59	24	2.75	0	5	68	27	47	19	28	CL
S27	2	16.26	12	2.68	0	68	26	6	25	12	13	SC
S28	2.5	17.60	11	2.69	1	78	13	8	28	12	16	SC
Shivlakha Dam			23° 24.659′ N		70° 35.128′ E							
S29	0.5	14.43	2	2.69	0	71	25	4	17	NP	NP	SM

(continued)

Table 1 (continued)

Soil name	Depth (m)	γ_{di} (kN/m³)	w_c (%)	G_S	GSD				Atterberg limits			Soil class
					G (%)	S (%)	M (%)	C (%)	LL (%)	PL (%)	PI (%)	
S30	1.5	14.88	4	2.70	1	88	9	2	17	NP	NP	SP-SM
S31	2	16.37	9	2.69	1	74	18	7	15	NP	NP	SM
S32	2.5	13.40	20	2.68	0	28	50	22	39	16	23	CL
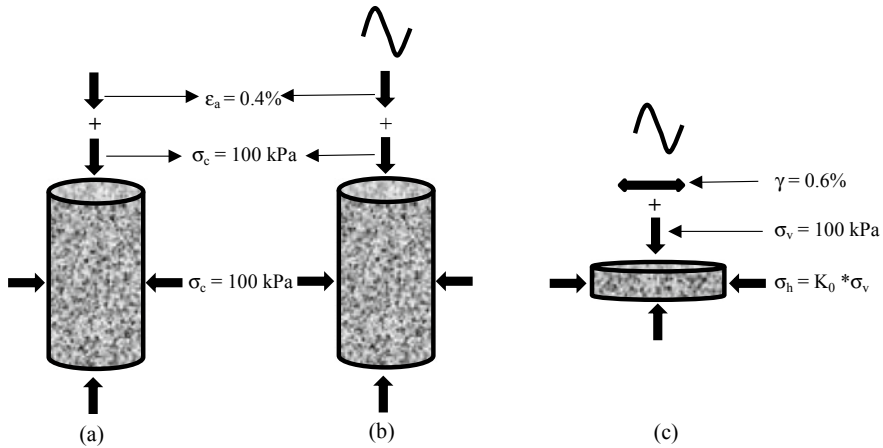
Fig. 1 Specimen size and loading configuration for various boundary conditions **a** TX, **b** CTX and **c** CSS

3 Results and Discussion

3.1 Results

Figure 2 shows the relationship of excess pore pressure ratio (r_u) with FC for the specimens of Kutch soils under the conditions of TX, CTX and CSS. Pore pressure response under monotonic compression loading at peak deviatoric stress could be observed to be lower as compared to that of cyclic loading during the first cycle (Fig. 2a). The r_u values at peak deviatoric stress for TX conditions ranged from 0.15 to 0.57 with an average value of 0.43. For CTX and CSS conditions, r_u values during the first cycle were evaluated to be ranging from 0.04 to 0.80 and 0.16 to 0.91, respectively. The corresponding average values for CTX and CSS conditions were found to be 0.53 and 0.65 respectively. The r_u values were observed to decrease with increase in the FC. It is evident from Fig. 2 that the pore pressure generation is higher during cyclic loading as compared to that during the monotonic loading. Further, the magnitude and rate of pore pressure generation were observed to be higher under CSS conditions as compared to those during CTX conditions. Specimens with lower fines content exhibited higher r_u values (Fig. 2). For a given FC it was observed that specimens with non-plastic fines displayed higher and rapid development of excess pore pressure. Figure 2b shows the relationship of r_u values with the FC for TX, CTX, and CSS conditions at the critical state and 5th cycle, respectively. It is evident from Fig. 2b that the critical state pore pressure for TX conditions is higher as compared to that at the 5th cycle for CTX and CSS conditions. For cyclic conditions, the difference between the r_u values at the 5th cycle was lower compared to that in the first cycle. However, r_u values were still higher for CSS conditions. The lower difference between the two could be attributed to the lower liquefaction resistance
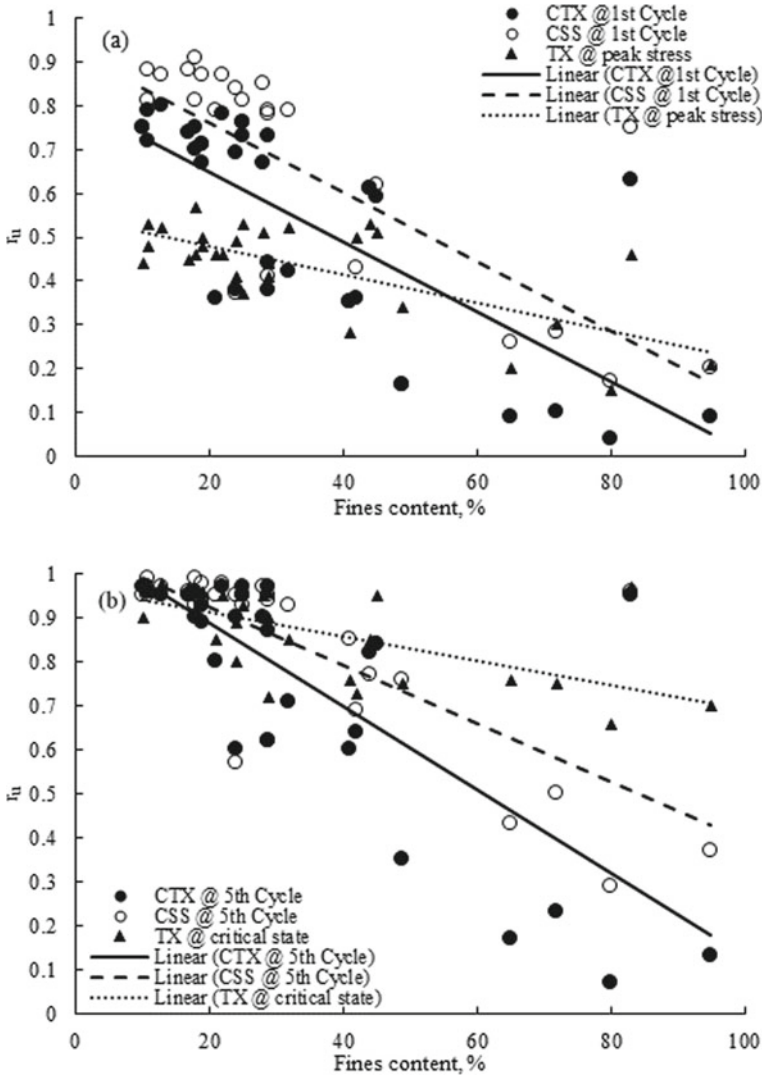
Fig. 2 Variation of pore pressure ratio with fines content under various boundary conditions. **a** Peak @ TX and 1st cycle @ CTX and CSS. **b** Critical state @ TX and 5th cycle @ CTX and CSS

where the sandy specimens liquefied within 5 cycles of cyclic loading. The pore pressure values under TX, CTX, and CSS conditions for Kutch soils are presented in Table 2. Among the cohesionless (silty-sand) specimens, r_u values were strongly influenced by the FC as compared to cohesive soils (clayey-sand) (Table 2). Figure 3 shows the relationship of excess pore pressure ratio with the PI for the specimens of Kutch soils under TX, CTX, and CSS conditions. The r_u values are same as in Fig. 2, however, the values on the x-axis reveal a reduction of pore pressure ratio

Table 2 Excess pore water pressure ratio under TX, CTX and CSS conditions for Kutch soils

| Soil name | FC (%) | PI (%) | Excess pore water pressure ratio, r_u | | | | | |
| | | | TX | | CTX | | CSS | |
			Peak	Critical state	1st cycle	5th cycle	1st cycle	5th cycle
S2	18	NP	0.46	0.96	0.75	0.96	0.91	0.99
S3	19	NP	0.48	0.96	0.67	0.89	0.87	0.98
S4	18	NP	0.57	0.92	0.70	0.90	0.81	0.93
S5	11	NP	0.53	0.96	0.79	0.96	0.81	0.95
S6	13	NP	0.52	0.98	0.80	0.95	0.87	0.97
S7	28	NP	0.51	0.95	0.67	0.90	0.85	0.97
S8	24	NP	0.49	0.89	0.69	0.90	0.84	0.95
S9	17	NP	0.45	0.97	0.74	0.95	0.88	0.96
S11	45	NP	0.51	0.95	0.59	0.84	0.62	0.84
S12	22	NP	0.46	0.95	0.78	0.97	0.87	0.98
S13	44	10.0	0.53	0.85	0.61	0.82	0.61	0.77
S14	49	11.4	0.34	0.75	0.16	0.35	0.16	0.76
S15	41	8.4	0.28	0.76	0.35	0.60	0.35	0.85
S16	19	NP	0.5	0.96	0.71	0.93	0.71	0.94
S17	25	NP	0.53	0.93	0.76	0.97	0.76	0.93
S18	10	NP	0.44	0.90	0.75	0.97	0.75	0.95
S19	42	22.9	0.5	0.73	0.36	0.64	0.43	0.69
S20	29	21.3	0.41	0.72	0.38	0.62	0.41	0.62
S21	24	11.7	0.41	0.80	0.38	0.60	0.37	0.57
S22	29	8.6	0.44	0.90	0.44	0.87	0.78	0.94
S23	65	28.6	0.2	0.76	0.09	0.17	0.26	0.43
S24	80	38.9	0.15	0.66	0.04	0.07	0.17	0.29
S25	83	NP	0.46	0.97	0.63	0.95	0.75	0.96
S26	95	28.6	0.21	0.70	0.09	0.13	0.20	0.37
S27	32	13.0	0.52	0.85	0.42	0.71	0.79	0.93
S28	21	16.3	0.46	0.85	0.36	0.80	0.79	0.95
S29	29	NP	0.44	0.96	0.73	0.97	0.79	0.95
S30	11	NP	0.48	0.98	0.72	0.96	0.88	0.99
S31	25	NP	0.37	0.96	0.73	0.95	0.81	0.95
S32	72	23.5	0.3	0.75	0.10	0.23	0.28	0.50

Fig. 3 Variation of pore pressure ratio with plasticity index under various boundary conditions. **a** Peak @ TX and 1st cycle @ CTX and CSS. **b** Critical state @ TX and 5th cycle @ CTX and CSS

with increasing PI. The variation of pore pressure with PI for all the three conditions (TX, CTX, and CSS) shows that the soils with non-plastic fines (PI = 0) exhibit large pore pressure values as compared to soils with some plasticity. The pore pressure at peak deviatoric stress and critical state for TX conditions and at the 1st and 5th cycles for CTX and CSS decreased rapidly with PI for cohesive soils. Figure 3b displays that the non-plastic soils developed r_u values higher than 0.89 and 0.85 for monotonic and cyclic loading, respectively.

Figure 4 illustrates the relationship between the pore pressure ratio and grain size index (I_{GS}) for Kutch soils. Grain size index is a direct measure of the range of particle size distribution and is higher for well-graded soils as compared to the poorly graded soils. For a given I_{GS} value the development of pore pressure was higher under monotonic compression loading as compared to the cyclic loading. Since by the definition of I_{GS}, it does not distinguish much about clean base sand and pure clay,

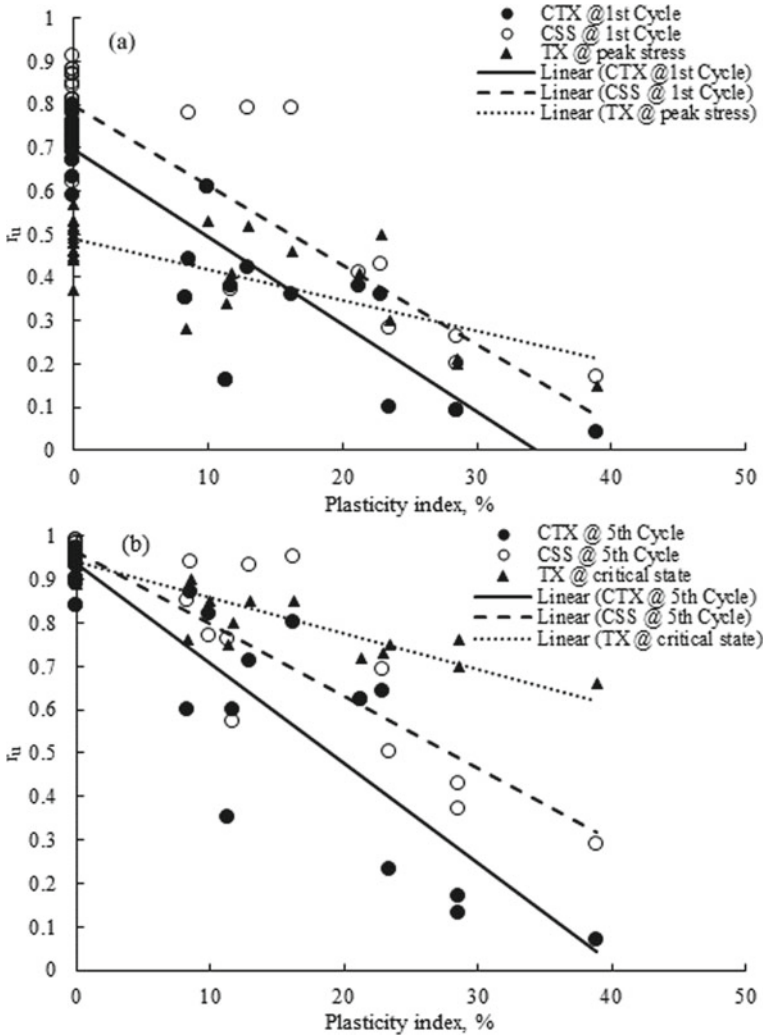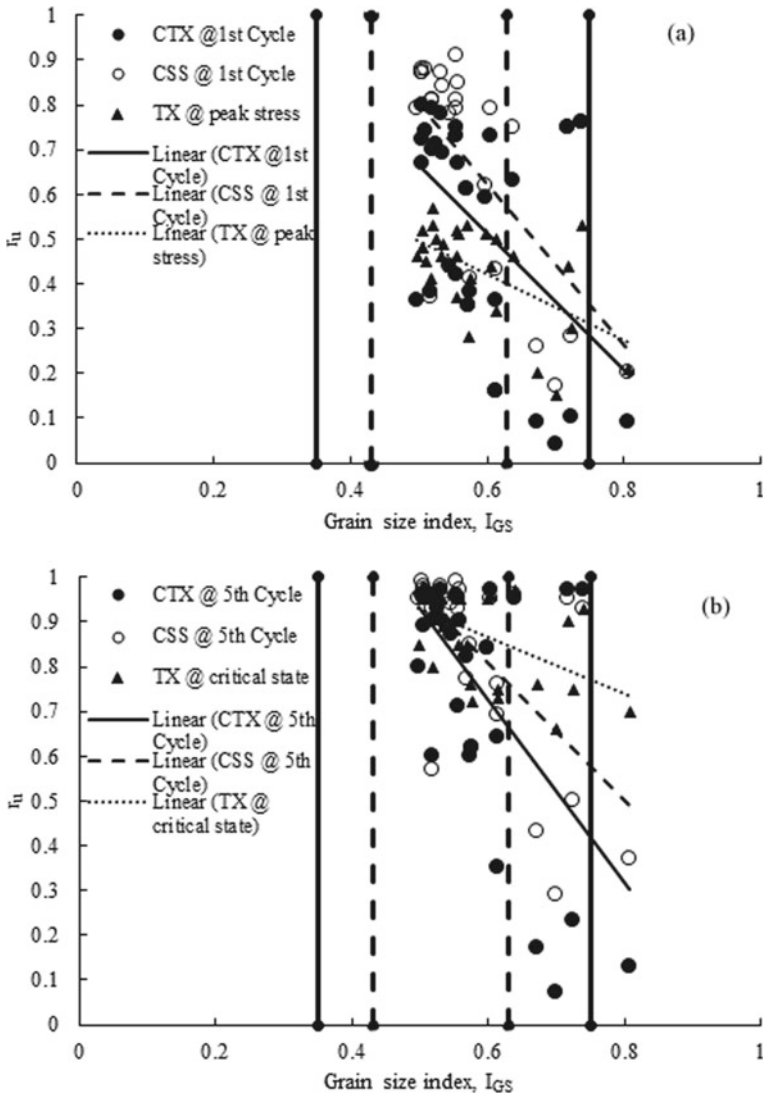Fig. 4 Variation of pore pressure ratio with grain size index under various boundary conditions. a Peak @ TX and 1st cycle @ CTX and CSS. b Critical state @ TX and 5th cycle @ CTX and CSS

the data points lying low in Fig. 4b are those of cohesive Kutch specimens. The r_u values for Kutch soil specimens are lying between the bold and dashed vertical lines which indicate the boundary for the potential liquefiable and most liquefiable soils, respectively, it is therefore evident that the Kutch specimens due to their nature of grain size distribution are highly prone to high pore pressure generation and hence susceptible to liquefaction both the static and cyclic liquefaction.

3.2 Discussion

The test results indicated that irrespective of the loading condition large excess pore pressures were generated under undrained conditions for the Kutch soils. Such r_u values are indicative of a large reduction in shear strength, which in extreme conditions leads to static and cyclic liquefaction under monotonic and cyclic loading, respectively. Owing to the generation of large excess pore pressures, cohesionless soils from the Kutch region are highly susceptible to both the static and cyclic liquefaction whereas cohesive soils are prone to large degradation in shear strength under both the monotonic and cyclic loading. The detailed account of the static and cyclic liquefaction characteristics of the Kutch soils under different loading conditions can be found elsewhere, [3–5]. The pore pressure response as presented in Figs. 2–4 and Table 2 reveals that for cohesionless soils, FC controls the magnitude and rate of pore pressure generation whereas for cohesive soils it is the plasticity index that governs the soil response. Hussain and Sachan [3, 5] describe in detail the mechanism and effect of both FC and PI on the undrained behavior of Kutch soils.

4   Conclusions

Pore pressure response of natural Kutch soils from ten locations including five dams under different loading conditions including TX, CTX, and CSS was explored in the current study. The analysis of the test results revealed the following.

(a) Irrespective of the loading conditions Kutch soils exhibited very high pore pressure response indicting large reduction in strength under both the monotonic and cyclic loading subsequently leading to static and cyclic liquefaction.
(b) Fines content plays a decisive role in governing the pore pressure response in cohesionless soils whereas in cohesive soils it is the plasticity index that dictates the soil response.
(c) Under cyclic conditions, CSS results in higher pore pressure generation as compared to that of CTX by a factor of approximately 1.3.
(d) The rate and magnitude of pore pressure generated decreased with both the fines content and plasticity index.

References

1. Erguler ZA (2016) A quantitative method of describing grain size distribution of soils and some examples for its applications. Bull Eng Geol Env 75(2):807–819
2. Hsu CC, Vucetic M (2004) Volumetric threshold shear strain for cyclic settlement. J Geotech Geoenviron Eng 130(1):58–70
3. Hussain M, Sachan A (2019) Static liquefaction and effective stress path response of Kutch soils. Soils Found 11:004
4. Hussain M, Sachan A (2019) Dynamic behaviour of Kutch soils under cyclic triaxial and cyclic simple shear testing conditions. Int J Geotech Eng 14(8):1–17
5. Hussain M, Sachan A (2019) Dynamic characteristics of natural Kutch sandy soils. Soil Dyn Earthq Eng 125:105717
6. Hussain M (2019) Static and cyclic liquefaction characteristics of Kutch soils. Ph.D. thesis. Submitted to Indian Institute of Technology Gandhinagar, India
7. Terzaghi K (1944) Theoretical soil mechanics. Chapman and Hall, Wiley, New York
8. Wood DM (1990) Soil behaviour and critical state soil mechanics. Cambridge University Press

Instability of Silty Sands Under Partially Drained Conditions

Sheetal Gujarati, Aparna Shrivastava, Majid Hussain, and Ajanta Sachan

Abstract Instability in the soil element is its inability to sustain the alterations to the current stress-state. The instability line (IL) or critical stress ratio line (CSR) is the maximum stress-state achieved under undrained conditions, and the drained failure envelope (DFE) is the line joining the origin and failure point under drained conditions. The present experimental study involves the effect of effective stress ratio (ESR) on the instability behavior of silty sands under partially drained conditions. Isotropically consolidated compression (CIUC) triaxial tests were conducted on the soil specimens prepared at in-situ dry density and moisture content. Four predefined ESR (T1, T2, T3, T4) were selected such that two of them could depict the stress-state corresponding to a region below IL (T1 and T2) and two of them could depict the region between IL and DFE (T3 and T4). ESR of instability line (η_{IS}) for the silty sand soil specimens was found to be 0.64. During shearing, the partially drained conditions were imposed on the stress-state corresponding to the chosen ESR. It was observed that the maximum effective stress-state in T1 and T2 was achieved after the imposition of partially drained conditions followed by static liquefaction, whereas T3 and T4 showed runaway instability, i.e., the deviatoric stress rapidly reduced indicating the steep fall in stress–strain and $q-p$' curves. Soil specimens with stress-states corresponding to regions of potential instability showed runaway instability under partially drained conditions, which were otherwise stable under completely undrained conditions.

Keywords Instability line · Drained failure envelope · Partially drained

S. Gujarati (✉) · A. Shrivastava · M. Hussain · A. Sachan
Civil Engineering, Indian Institute of Technology Gandhinagar, Gandhinagar, India
e-mail: sheetal.gujrati@alumni.iitgn.ac.in

A. Shrivastava
e-mail: aparna.shrivastava@iitgn.ac.in

M. Hussain
e-mail: majid.hussain@alumni.iitgn.ac.in

A. Sachan
e-mail: ajanta@iitgn.ac

1   Introduction

Instability is the inability of a material to carry load which subsequently results in the failure of a soil mass. Liquefaction is a type of instability, which is expressed as the complete loss of shear strength due to the rapid generation of excess pore water pressure [12]. Several flow failures of slopes and embankments were studied in previous researches, which were a result of static instability in soil masses before liquefaction such as failure in San Fernando Dam and Fort Peck Dam [7, 11]. Pre-failure instability has been investigated experimentally under undrained conditions in studies of static liquefaction of sands by several researchers [2, 10]. Experimental investigations involving triaxial tests [5, 11, 12] and plane-strain tests [4] were performed to explore the onset of static liquefaction from instability line or collapse surface under different boundary conditions. In all the problems, an assumption of completely undrained conditions is made to understand the mechanism and consequences of flow liquefaction or instability. But the instability in soil masses is also a function of stress-state and void ratio at which it is subjected to undrained conditions. The initially induced volumetric strains due to loading events of ephemeral duration followed by static loading lead the soil masses to be subjected to undrained conditions at comparatively lower void ratios. If this current state of soil lies in the zone of potential instability, then rapid runoff instability will be induced which results in consequences more damaging than completely undrained initial state. Hence, the present study aims to evaluate the effect of effective stress ratios on the instability behavior of silty sands under partially drained conditions.

2   Material Properties and Experimental Program

Soil for the current study was collected from the Fatehgarh Dam of Kutch district in Gujarat. The basic geotechnical properties of soil were determined by conducting grain size test, specific gravity, standard proctor test, and direct shear tests. The soil was classified as silty sand (SM), as per Indian Standard Soil Classification System. The specific gravity of soil was determined to be 2.68. The maximum dry density and optimum moisture content were obtained to be 1.99 g/cc and 9.8%, respectively. The grain size distribution results exhibited that soil had 1% gravel, 54% sand, 34% silt and 11% clay. Friction angle (ϕ) of soil was determined to be 35^0 ($c = 0$) by conducting direct shear tests. The specimens were prepared at in-situ moisture content and dry density of 8% and 1.55 g/cc, respectively, by moist tamping technique (Frost and Park, 2003). In the present study, a series of consolidated undrained, drained [1] and partially drained compression tests were performed on Fatehgarh dam soil at 100 kPa of confining pressure. The specimens in all the triaxial tests were sheared at a strain rate of 0.1%/min. Four different effective stress ratios (ESR = q/p') were selected to study the instability behavior under partially drained conditions. The stress-states of first two ESR were chosen below IL and other two were chosen in the

zone between IL and DFE, i.e., the zone of potential instability [8]. The instability line (IL) is the maximum stress-state achieved under undrained conditions and the drained failure envelope (DFE) is the line joining the origin and failure point under drained conditions. The load was determined corresponding to the particular ESR from existing data of drained triaxial test. A series of four partially drained triaxial tests, i.e., (T1, T2, T3, and T4), was then conducted on the specimens prepared at in-situ dry density and moisture content. The specimen was saturated by CO_2 flushing for 45 min followed by water flushing and forced saturation. Shearing stage involved the switching from drained to undrained when the predetermined load (load corresponding to selected ESR from drained test) was achieved during shear deformation of the soil specimen.

3   Results and Discussions

Instability in soil mass is a function of the current stress and material states when the undrained loading conditions are imposed [9]. The line joining the peak of the effective stress path and the stress origin divides the stress space in two regions namely stable zone and potential zone of instability. This bounding envelope is known as instability line (IL). Thus to investigate the instability under completely undrained conditions, a failure envelope or instability line was plotted from the result of undrained compression tests on soil specimens and the effective stress ratio corresponding to the IL was referred to as η_{IS}. Instability line is a function of void ratio (e) and mean effective confining pressure and it is unique for a specimen with same void ratio [7]. The stress–strain response obtained from undrained compression test on Fatehgarh dam soil is shown in Fig. 1a. Specimen exhibited intense strain-softening behavior with a well-defined peak deviatoric stress achieved at very low axial strain. At a very small strain of 0.59%, peak deviatoric stress of 49 kPa was mobilized which reduced to a constant value of 11 kPa with continued axial deformations. The onset of softening just at the peak deviatoric stress in soil specimen was taken as the onset of instability under undrained conditions. Effective stress (p') and deviatoric stress (q) were calculated as per Cambridge model using Eqs. (1) and (2). The ratio of p' to the q at the peak was also referred to as critical stress ratio (CSR) line [11]. To obtain the failure envelope under completely drained conditions, the peak of effective stress paths (ESP) drained compression tests was joined with the stress origin and was referred as drained failure envelope (DFE). This failure envelope represented the maximum effective stress ratio that can be obtained under completely drained conditions. To study the instability under partially drained conditions, the predefined stress paths or stress-states were imposed at conditions that varied from completely undrained to completely drained. The region bounded between IL and DFE was referred to as zone of potential instability by Lade [8]. The imposed effective stress ratios were chosen as per the ESP of drained testing such that two of them below IL and two of them lie in the region of potential instability. To understand the effect of initial stress-states and drainage conditions four ESR's were selected namely T1,
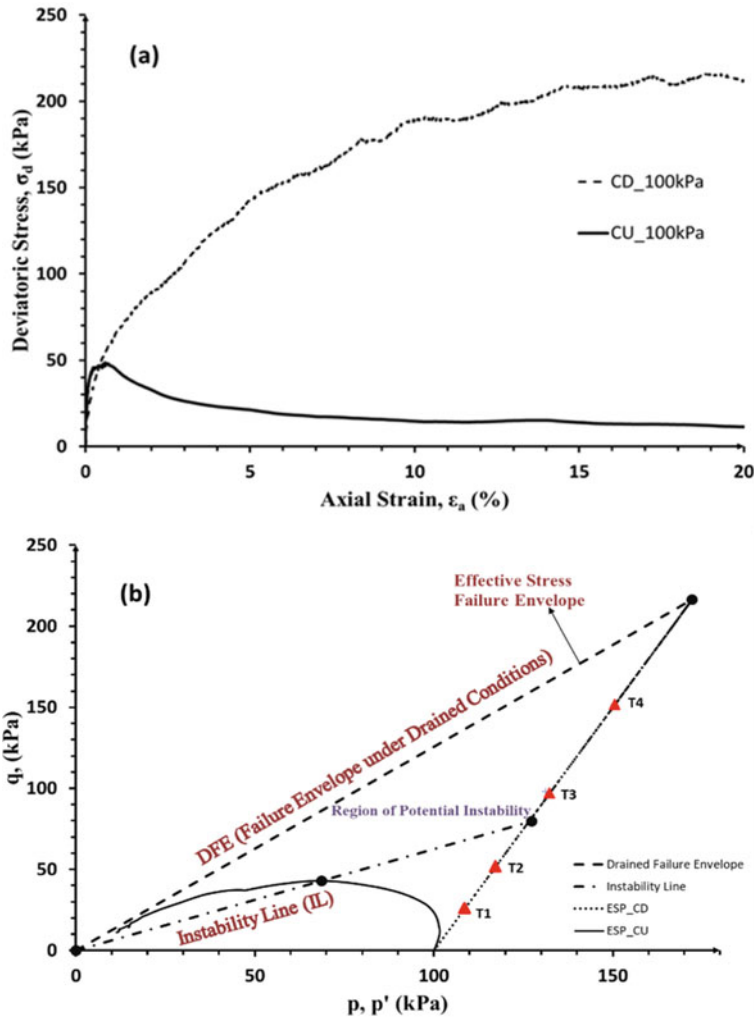
Fig. 1 Shear behavior of Fatehgarh Dam soil.**a** Stress–strain response under drained and undrained conditions. **b** Stress paths under drained and undrained conditions

T2, T3 and T4 with magnitude of (include values), respectively. Figure 1b represents the stress-states of these ESR's corresponding to IL and DFE.

$$p' = \frac{(\sigma_1' + 2\sigma_3')}{3}. \tag{1}$$

$$q = \sigma_1' - \sigma_3' \tag{2}$$

3.1 Stress–Strain Response and Volumetric Response

Material behavior of silty sand was explored under mixed drainage conditions. The isotropically consolidated specimen was subjected to drain shearing up to a predetermined stress ratio. After that undrained conditions were imposed, as shown in Fig. 2a. The load values corresponding to predefined values of ESR were determined from the drained compression tests on the same specimen. The stress–strain response
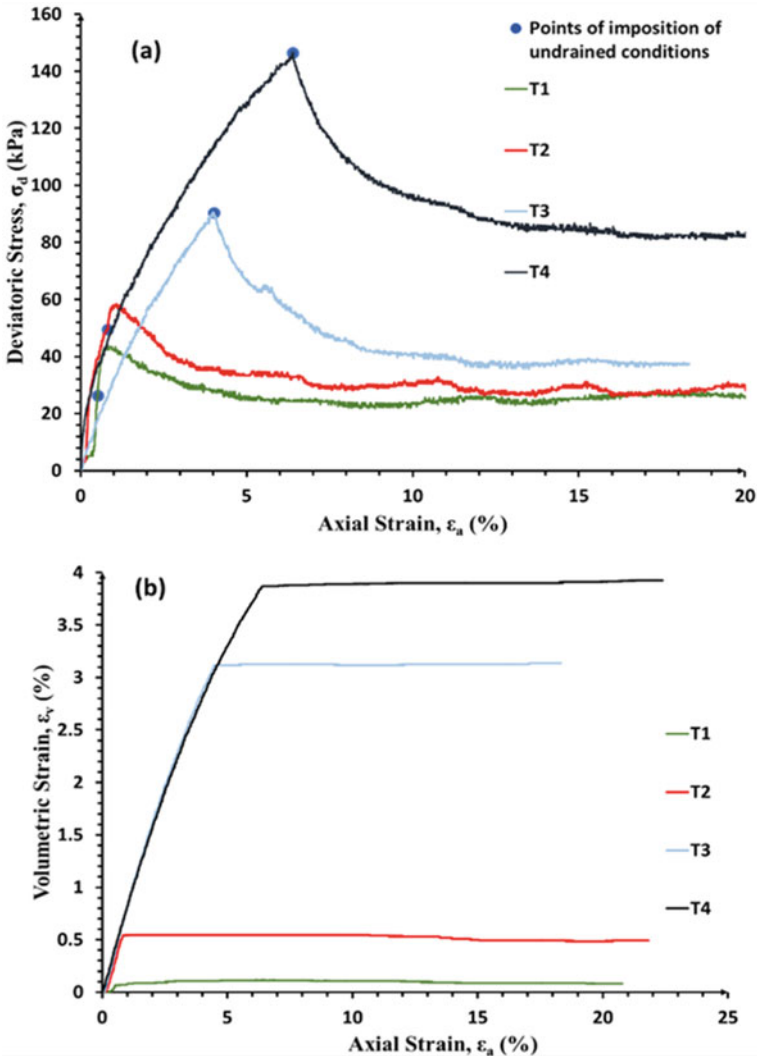
Fig. 2 Shear behavior of Fatehgarh Dam soil under partially drained conditions. **a** Stress–strain response. **b** Volumetric change response

Table 1 Shear behavior of Fatehgarh Dam Soil under partially drained conditions

Test no.	ESR (partially drained conditions imposed)	Strain, "ε_{pd}" (at partially drained condition imposition)	Peak deviatoric (σ_d)	Deviatoric Stress at ε_{pd}	Void ratio at the imposition of undrained conditions (e)
T1	0.24	0.53	44	26	0.68
T2	0.43	0.82	58	50	0.67
T3	0.7	4.02	90	90	0.6
T4	0.99	6.39	146	146	0.59

and volumetric response are shown in Fig. 2a, b, respectively. For the imposed stress ratios T1 and T2 were lying below the instability line or there ESR was less than η_{IS}, stress–strain response ascended and the peak deviatoric stress was achieved after the imposition of undrained conditions for both the imposed stress ratios. The increasing peak deviatoric stress after the imposition of undrained conditions reflects the stable response of the specimen at the existent stress and material states under the applied perturbation (closure of the drainage value). The higher peak deviatoric achieved by specimens in T2 as compared to T1 could be attributed to the lower void ratio of T2 (Table 1). The lower void ratio of specimen at T2 resulted from the higher volumetric strain that was needed to attain the higher stress ratio under the drained conditions (Table 1). The stress–strain response of T1 and T2 depicted a rapid reduction in deviatoric stress with further axial deformations. This is evident from the intense strain-softening response exhibited by the specimens at small strain level of 1% in T1 and T2 as shown in Fig. 2a. After, the imposition of the undrained conditions, rise in deviatoric and subsequent strain-softening the specimens of T1 and T2 attained constant deviatoric stress. The critical state strength of specimen T2 was slightly higher in magnitude than T1 as shown in Fig. 2a. The material state of specimen T2 differs from that of T1 but the stress-states remained in the stable zone when undrained conditions were imposed on it. Therefore, due to lower void ratio of T2, the critical state strength of T2 was observed to be higher as compared to that of T1. This inferred that critical state strength is a function of material state of specimen under undrained conditions.

T3 and T4 represented the higher stress ratios which were lying above the instability line under undrained conditions. The stress–strain response of T3 and T4 depicted sudden drop in deviatoric stress values as soon as the undrained boundary conditions were imposed as shown in Fig. 2a. The sudden drop in deviatoric stress values was accompanied by the large and rapid generation of pore water pressures. The rapid reduction in deviatoric stress led to a reduction in the load-carrying capacity of specimens. The incapability to sustain disturbances to the current stress-states rendered instability within the soil mass of specimens T3 and T4. This revealed that the point of the imposition of undrained conditions in the case of T3 and T4 was also the point corresponding to the onset of instability. The soil specimens exhibited instability since their initial stress-states was lying above the IL in the unstable region and

also because of the inter-particle soil structure. The specimen preparation technique used in the current study resulted in the formation of the metastable inter-particle soil structure. This structure has high compressibility and low load-carrying capacity. Therefore, under undrained conditions at higher stress ratios the silt particles would move into large voids between sand particles which resulted in large excess pore water pressure generation and subsequent instability.

The volumetric response of all tests is presented in Fig. 2b. It was observed that with an increase in ESR the volumetric strain increased with T4 undergoing largest contraction before the undrained condition was imposed. Due to the different volumetric strains, the material state and stress-state for specimens of T3 and T4 were significantly altered from their initial state such that they represented two different configurations when undrained conditions were imposed on them. The void ratio was reduced from 0.682 (void ratio after consolidation) to 0.590 in case of T4 therefore representing densest particle configuration. Also, the void ratio for specimens of T3 and T4 was lower as compared to T1 and T2 when undrained boundary conditions were imposed. Significant contractive volumetric change was observed due to prolonged drainage up to deformation levels of about 4% and 6% in T3 and T4 respectively as depicted in Fig. 2b. These volumetric strains were necessary to achieve the predetermined ESR's. When the undrained conditions were imposed at the existent material state and stress-state, the sudden loss in strength or intense strain-softening was observed due to inability of soil to sustain the changes in its stress-states.

Despite lower initial void ratio, the specimens of T3 and T4 exhibited an intense drop in deviatoric stress suggesting unconditional instability above IL. This reflected the inherent tendency of specimens towards instability in that zone. Thus, IL divides the stress spaces into two zones, i.e., the stable zone which lies below IL and the unstable zone which lies between IL and DFE. The specimens at T3 and T4 depicted diffused mode of failure as no localized deformations were observed in form of shear bands. This mode of failure was captured in the wrinkles formation in the membrane, which were evident during and at the end of shearing stage. The results were in agreement with the results of [8, 12]. These findings concluded that drainage conditions and current stress-state of the specimens were the governing factors for initiation of instability in granular media. These results were in agreement with the past studies conducted by Hussain and Sachan [6].

3.2 Excess Pore Water Pressure Response and Stress Paths

Evolution of pore water pressure under partially drained shearing for all the specimens is illustrated in Fig. 3a. After the imposition of the undrained boundary conditions, excess pore water pressure evolved at a rapid rate for all the applied ESR. The rate and magnitude of excess pore water pressure generated were observed to be strongly influenced by the location of stress-state with respect to the IL. The pore water pressure in specimens of T1 and T2 reached almost 90% of the initial effective confining pressure as depicted in Fig. 3a. The excess pore water pressure developed
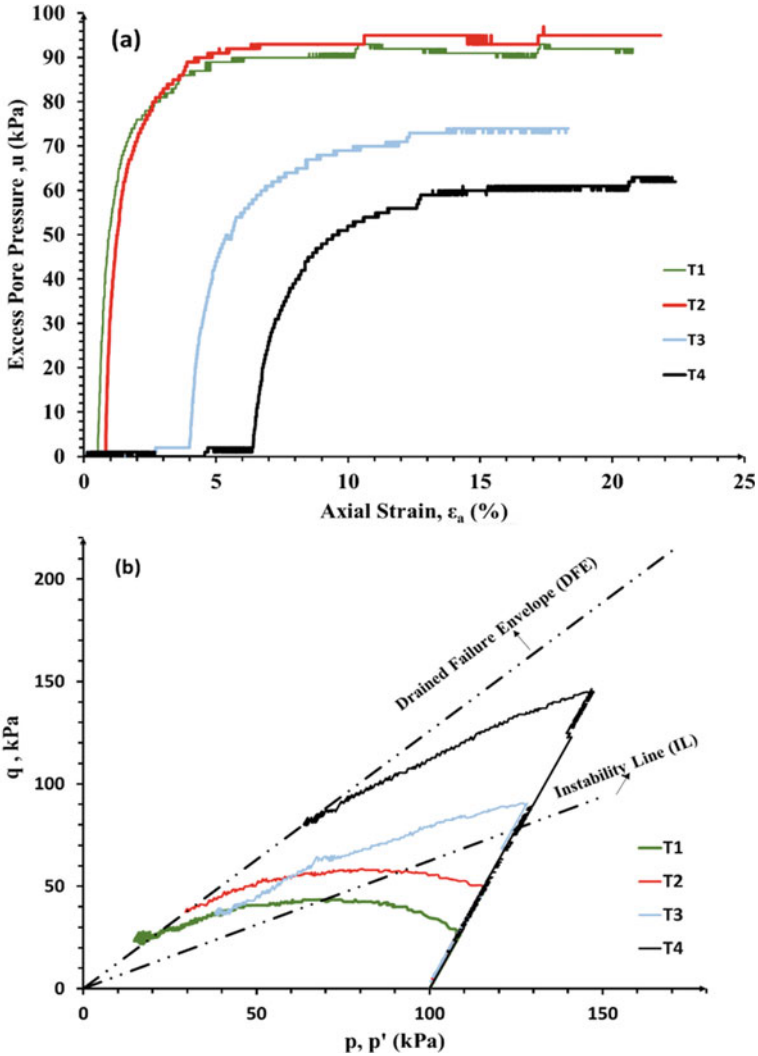
Fig. 3 Shear behavior of Fatehgarh Dam soil under partially drained conditions. **a** Pore water pressure response. **b** Effective stress paths on $p'-q$ diagrams

in the case of T3 and T4 was about 60–70% of effective confining pressure. The reduced pore water pressure generation in case of T3 and T4 could be attributed to the pre-induced volumetric strains (required to achieve that particular stress-state) in the specimens which resulted in dense inter-particle soil structure. The specimens of T3 and T4 achieved almost 50% of the maximum pore water pressure within very small deformations levels after the imposition of undrained boundary conditions. The rapid generation of pore water pressure triggered instability within the soil mass

in T3 and T4. Therefore, specimens with high ESR in unstable region were liable to be followed by static liquefaction after induced instability. The specimens prepared at the same initial void ratio showed different mechanical properties due to location of the stress-states with respect to the IL and drainage conditions. This shows that the stress-state at which undrained conditions were subjected to the specimens plays an important role in the mechanical behavior of soil specimens.

Figure 3b shows the effect of the degree of partially drained conditions on the potential for instability at an otherwise identical initial state. The ESP for all cases were plotted in q-p′ space along with IL and DFE to demarcate the lower and upper bound of unstable zones. The development of positive pore water pressures was responsible for the leftward inclination of the stress paths (Fig. 3b). When undrained conditions were imposed on specimens of T1 and T2, the ESP ascended until it achieved a peak while crossing the IL and then descended asymptotically towards DFE. As the stress path ascended and intercepted the IL, the specimen exhibited large and rapid generation of excess pore water pressure. Further deformation under undrained condition was occurring at reduced effective stress with a subsequent reduction in load-carrying capacity leading to static liquefaction. The specimens of T3 and T4 showed rapid and sudden fall in effective stresses as soon as undrained conditions were imposed on them. The capacity of the soil to resist the applied load at any stage depends on the current mean effective stress. As the effective strength of soil specimens reduced rapidly after the imposition of undrained conditions, therefore, the soil specimens were incapable of sustaining disturbances done to their current stress-states. Thus, soil specimens at T3 and T4 exhibited instability within the soil mass when they were subjected to undrained conditions. The possible cause for this instability was the initial stress-states of soil specimens which were lying in the zone of potential instability. The specimens of T3 and T4 were subjected to more volumetric strains than T1 and T2 and therefore they represented a denser state as compared to T1 and T2. Thus capacity to sustain loads in case of these two (T3 and T4) were expected to be more but the obtained results were in stark contrast. If the conditions were completely undrained, then the ESP would have first ascended to achieve the peak at IL and then it could have either descended to the lower values to achieve steady state or could have dropped to lower value and then increase asymptotically towards DFE. In either case the worst possibility will be static liquefaction due to high pore water pressures at large axial deformations but instability would not be initiated which causes sudden loss of shear strength. Therefore, the soil specimens with same initial conditions having ESR's greater than η_{IS} will undergo instability under undrained conditions. So, initial stress-states are important factors to understand the undrained behavior of silty sands during static loading. Similar stress-path testings were carried out on clean sands by Vaid and Eliadorani [11] and Chu et al. [3] and the results clearly dictated the unconditionally instable behavior of sands in the region of potential instability under imposed undrained conditions. Therefore, it can be concluded that irrespective of the presence of the fines in sands, the soil mass exhibits instability under undrained conditions if its initial stress-states corresponds to the region above instability line.

4 Conclusions

A series of triaxial compression tests were performed under partially drained conditions on silty sand (SM) at different effective stress ratio (ESR) to investigate the effect of initial stress-state on the instability of soil masses. The following conclusions could be drawn from the study:

- The soil specimens with initial stress-states corresponding to the region of stress-space below IL showed high tendencies for static liquefaction at large deformations when undrained conditions were imposed in them. Excess pore water pressures nearly equal to 90% of the effective confining pressure were generated within the specimens which leads to static liquefaction.
- The soil specimens with initial stress-states depicting region present between IL and DFE were prone to instability within soil mass followed by static liquefaction when subjected to undrained boundary conditions. As the soil elements within this region were unstable to sustain the disturbances done to their current stress-state, therefore this region was referred to as zone of potential instability. This region was characterized with the instability failure of soil specimens which leads to loss of shear strength.
- When the initial stress-states of soil specimens were lying below the instability line, the ESP ascended to achieve a peak at IL whereas if the initial stress-states exist in the zone of potential instability than the ESP showed sharp reduction in effective stress values as soon as the undrained conditions were imposed on it. This concludes that the stress-space below IL represents stable zone whereas the stress-space between IL and DFE represents unstable zone when subjected under undrained conditions.
- The critical state strength increased with increase in the ESR values. As more volumetric strains were required to achieve stress-states corresponding to high ESR's, the resulted void ratio of specimens became smaller when undrained conditions were subjected to them. The lower void ratio exhibited denser inter-particle soil structure which was responsible for higher critical state strength.

References

1. ASTM D7181-11 (2018) Standard test method for consolidated drained triaxial compression test for soils
2. Castro G (1969) Liquefaction of sands. Ph.D. thesis. Harvard Soil Mech
3. Chu J, Leroueil S, Leong WK (2003) Unstable behavior of sand and its implication for slope instability. Can Geotech J 40(5):873–885
4. Chu J, Wanatowski D (2008) Instability conditions of loose sand in plane strain. J Geotech Geoenviron Eng 134(1):136–142
5. Daouadji A, AlGali H, Darve F, Zeghloul A (2009) Instability in granular materials: experimental evidence of diffuse mode of failure for loose sands. J Eng Mech 136(5):575–588

6. Hussain M, Sachan A (2019) Volume compressibility and pore pressure response of Kutch soils with varying plastic and non-plastic fines. In: Geotechnics for transportation infrastructure. Springer, Singapore, pp 651–665
7. Hussain M, Bhattacharya D, Sachan A (2019) Static liquefaction response of medium dense silty-sand of Chang Dam. In: 8th international conference on case histories in geotechnical engineering, geo-congress, Philadelphia, USA
8. Lade PV (2002) Instability, shear banding, and failure in granular materials. Int J Solids Struct 39(13–14):3337–3357
9. Rahman MM, Lo SR, Baki MAL (2011) Equivalent granular state parameter and undrained behavior of sand–fines mixtures. Acta Geotech 6(4):183–194
10. Vaid YP, Chern JC (1985) Cyclic and monotonic undrained response of saturated sands. In: Advances in the art of testing soils under cyclic conditions. ASCE, pp 120–147
11. Vaid YP, Eliadorani A (1998) Instability and liquefaction of granular soils under undrained and partially drained states. Can Geotech J 35(6):1053–1062
12. Yamamuro J, Lade PV (1997) Static liquefaction of very loose sands. Can Geotech J 34:905–917. https://doi.org/10.1139/t97-057

Settlement of Saturated Sand Under Horizontal Excitation on Vibration Table for Liquefaction Study

Satyendra Mittal, Tshering Cheki, and Arpit Jain

Abstract Settlements resulting through liquefaction during an earthquake may affect the living conditions of the people and may cause serious fatalities. This paper presents a simplified method for estimating the liquefaction-induced settlements of saturated sand for different relative densities using a shaking table. Sand samples with and without cement grouting were tested for the comparison of liquefaction-induced settlements. Tests were conducted on saturated sand grouting for various relative densities ranging from 35 to 80% using a horizontal vibration table. The significant variations were observed in settlement due to the changes in the acceleration inputs, density and grouting. The settlement resulting from drained behavior of saturated sand specimens after application of varying amplitudes was examined based on its volume decrease characteristics. The performance of the neat cement grout was also examined in this study. It was observed that the settlements of the sand reduced significantly after grouting with cement slurry.

Keywords Liquefaction · Settlement · Grouting · Shake table

1 Introduction

Seismically induced liquefaction of loose saturated soils causes severe damages to the built environment during earthquakes, thus causing serious problems. Some of the major examples of such damages are during the Turkey earthquake (7.6 M_w) in 1999 where hundreds of structures had settled, slide, tilted, deformed laterally and collapsed due to soil liquefaction and ground softening [1]. Similar damages occurred during the Chile earthquake of 2010 [2] with a magnitude of 8.8 (M_w), the Tohoku earthquake (9.0–9.1 M_w) of 2011 [3] and the Bhuj earthquake (7.7 M_w) of 2001 [4]. The 2011 Christchurch earthquake with 6.2 M_w in New Zealand caused

S. Mittal (✉) · T. Cheki · A. Jain
Indian Institute of Technology, Roorkee, India
e-mail: satyendramittal@gmail.com

widespread liquefaction and triggered tremendous damages to buildings and infrastructures. More than 50% of the city of Christchurch was affected due to soil liquefaction causing buildings to settle, tilt or deform whereby most of those structures were made to demolish due to the fact that it was uneconomical to repair [5]. Some of the most common damages caused due to earthquake-induced liquefaction are the failure of pile foundations induced by lateral spreading, settlement and tilt of buildings and houses [5–7]. Many researchers have attempted to develop different types of mitigation techniques to overcome soil liquefaction [8]. But to counter liquefaction, such techniques are usually not employed individually but used in combination of two or more [9]. Around 900 ground improvement projects have been executed out of which 70% of them are for liquefaction countermeasures such as vibratory sand compaction pile method, non-vibratory sand compaction pile method, gravel drain method, lattice-type deep mixing methods. [3]. In addition to technical issues, economic considerations play an important role in proposing the countermeasures against liquefaction-induced settlement of the structures. For example, the available technology for ground improvement under existing structures with the help of chemical grouting by colloidal silica is hardly affordable because it costs about 10 times more than the conventional countermeasures such as the installation of prefabricated vertical drains [10]. Therefore, the countermeasures to be proposed should be economically reasonable and technically effective.

One of the ground improvement techniques called compaction grouting is proposed and examined in this study. Grouting is the process that involves an injection of special liquid or slurry materials called grout into the ground for the purpose of improving the soil. Grouting is the method of stabilizing granular soils. It helps to improve the mechanical properties and reduce the permeability of soils. Various types of grouts such as cementitious and chemical grouts are widely used for foundation treatment of dams, and hydraulic structures and compaction grouting are often used to repair structures that had experienced excessive settlement [11]. This paper presents the results of analysis derived from the shake table tests, where the settlement during liquefaction was observed while testing the saturated sand with and without cement grouting.

2   Experimental Apparatus

The present investigation has been carried out on a vibration table known as the shake table [12]. The shake table comprises of a watertight test tank of 1060 mm long, 600 mm wide and 600 mm high with the sides of tank 5 mm thick steel panels. The test tank is mounted on a horizontal shake table which can be excited in a horizontal direction using steady-state vibrations. The test tank is driven in the horizontal direction with the help of an electric motor through a crank mechanism. The table was set to a desired frequency and amplitude, and then, the predetermined cycles of motion were imparted. A revolution counter is fixed to count the number of cycles, and a hand brake is provided to stop the shake table instantaneously. The

Fig. 1 Shake table test set up used in the study

shake table as shown in Fig. 1 could produce one-dimensional harmonic excitation of varying amplitude (0.1–0.3 g) and frequency up to 12 Hz [13]. Four numbers of glass tube piezometers (5 mm diameter each) were connected to the sides of the test tank through rubber tubes for pore pressure measurements at the height of 430 mm, 350 mm, 250 mm and 100 mm, respectively, measured from the top of the tank. A porous stone duly covered with a 75 µm mesh was fixed at the mouth of every steel pipe joined to rubber tubes so that no soil particle enters into the piezometer. To further reduce the choking and air bubbles, all porous stones were kept in boiled water at 100 °C for about 30 min before fixing at the mouth of the piezometer.

3 Materials Used

Solani river sand has been used for this study. The sand was collected locally from the Solani river bed near Roorkee city which was categorized as poorly graded sand

Table 1 Properties of 43 grade ordinary Portland cement

S. No.	Properties	Description
1	Specific gravity	3.16
2	Setting time	Initial Setting Time:55 min Final Setting Time: 312 min
3	Fineness	5.32%
4	Compressive strength	43 MPa
5	Consistency	33%

(SP) with little fines according to the Unified Soil Classification System. The sand was air-dried and cleaned thoroughly before any experimental work. The sand has a uniform particle size range of $D_{50} = 0.30$ mm and $C_u = 2.53$ which was obtained from the grain size distribution curve. The maximum and minimum void ratios were $e_{max} = 0.89$ and $e_{min} = 0.66$, determined in accordance with the procedure laid in Indian Standard [14]. The specific gravity of sand was 2.53. The neat cement grout which was the mixture of 43 Grade Ordinary Portland Cement (OPC 43) and clean water in the ratio of 1:3 (cement: water) by weight was used as grout during the test. The basic properties of OPC 43 supplied by the manufacturer are given in Table 1.

4 Test Procedures

All the tests on the sand at relative densities of 35, 50, 65 and 80% with and without grout were conducted at an acceleration of 0.1 to 0.3 g under the exciting frequency of 4 Hz. The experimental tests were performed using Shake Table at 4 Hz frequency. These tests were performed on varying relative densities, and their effect has been studied at steady-state vibrations of desired acceleration and frequency loading of 4 Hz [15–17]. This parameter has also been used by several researchers, such as [15, 18–20], Laia (2014), and Komaji (2014) in performing a liquefaction potential study using a shaking table. These values were used since there was no accurate information on the ground motion frequency. However, the strong earthquakes triggering liquefaction had vibration frequencies of 0.5 Hz onwards, and by using 4 Hz frequency, the results are more on conservative side. The duration of shaking adopted in the study was 15 s as per the correlation given by Chauhan [21] for an earthquake of 7.5 magnitudes. Before imparting the shaking, the sample preparation was labeled and the value of static pore water pressures at different depths within the soil samples was first recorded. The electric motor was switched on, and the rise in pore water pressure along with time was recorded. At the end of every test, the water overlying the sample was removed with the help of a sponge and the top surface was labeled to find out the amount of settlement that occurred due to shaking [10–14]. The amount of settlement resulting from liquefaction was calculated based on the volume decrease characteristics of saturated sand samples, and the results were compared with the settlements observed on the grouted samples.

Table 2 Shaking duration by Seed and Idriss [22] correlation used in the study

Magnitude	6	6.5	7	7.5	8	8.5
Time (s)	5	8	11.5	15	21	26

The relative density (D_r) of the sand is defined by the relation:

$$D_r = \frac{e_{max} - e}{e_{max} - e_{min}} \tag{1}$$

$$e = e_{max} - D_r(e_{max} - e_{min}) \tag{2}$$

Using the values of void ratio obtained for all the relative density values, the dry unit weight of sand (γ_d) was calculated from the relation:

$$\gamma_d = \frac{G}{1 + e}\gamma_w \tag{3}$$

where γ_w is the unit weight of water (taken as 10 kN/m^3), G is the specific gravity of sand, taken as 2.53.

The relation between shaking duration and magnitude of earthquake for dynamic studies related to soil liquefaction in the present study was adopted using the correlation given by Seed and Idriss [22] as in Table 2. Seed and Idriss correlation has been preferred by several researchers. Moreover, several other correlations has been developed, but after using the seed and Idriss correlations, significant outcomes were obtained for the soil type used in the current study.

The parameters such as acceleration, frequency and shaking durations were used according to accelerogram data of the 2001 Bhuj earthquake (7.7 magnitudes) according to Chauhan [21]. Therefore, for an earthquake magnitude of 7.5, the shaking duration of 15 s was adopted in the present study.

The neat cement grout was prepared with a simple mix of OPC 43, and clean water in ratio 1:3 (cement: water) by weight. A 25 mm diameter grout pipe of 600 mm length was installed to a required pre-drilled hole in the saturated sample prepared. The grout material is then injected into five stages (100 mm interval) adopting a bottom-up method of compaction grouting in the vertical direction. Total 11 grout holes were thus made, spaced at 255 mm center to center (lengthwise) and 152.5 mm center to center (width-wise) arranged in a triangular pattern shown in Fig. 2. Similarly, for all the relative density of sand, the above procedure was adopted.

5 Results and Discussions

The effects of relative density, acceleration and grouting mechanism on the settlement of the liquefied sand were observed where significant outcomes strengthen the
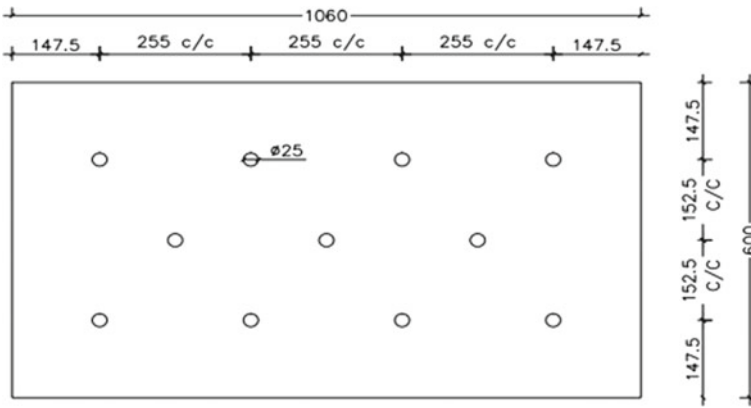
Fig. 2 Arrangement of grout points used in the study

vulnerability of ungrouted sand. The results of the experimental studies were related to the sand tested with and without grouting prepared at relative densities of 35, 50, 65 and 80% as shown in Tables 3 and 4.

Table 3 Settlement and dry unit weight of sand at all density for sand without grouting

D_r (%)	Freq. (Hz)	Acceleration (g)	Weight of sample (Kg)	γ_d before shaking (kN/m^2)	γ_d after shaking (kN/m^2)	Settlement after shaking (mm)
35	4	0.1	472	14.53	15.17	20.10
		0.2		14.53	15.28	23.40
		0.3		14.53	15.33	25.20
50	4	0.1	482	14.83	15.41	17.40
		0.2		14.83	15.54	21.50
		0.3		14.83	15.65	24.80
65	4	0.1	492	15.14	15.71	17.00
		0.2		15.14	15.80	19.60
		0.3		15.14	15.87	21.70
80	4	0.1	503	15.47	15.98	14.50
		0.2		15.47	16.06	17.00
		0.3		15.47	16.16	20.00

Table 4 Settlement and dry unit weight of sand at all density for sand with grouting

D_r (%)	Freq. (Hz)	Acceleration (g)	Weight of sample (Kg)	γ_d before shaking (kN/m^2)	γ_d after shaking (KN/m^2)	Settlement after shaking (mm)
35	4	0.1	472	14.53	15.06	16.50
		0.2		14.53	15.18	20.50
		0.3		14.53	15.26	23.00
50	4	0.1	482	14.83	15.22	11.50
		0.2		14.83	15.33	15.00
		0.3		14.83	15.44	18.50
65	4	0.1	492	15.14	15.47	9.50
		0.2		15.14	15.54	11.50
		0.3		15.14	15.61	14.00
80	4	0.1	503	15.47	15.79	8.50
		0.2		15.47	15.83	10.00
		0.3		15.47	15.91	12.50

5.1 Effect of Relative Density (D_r) and Acceleration on Settlement Behavior

Figure 3a–d illustrates a plot between settlement and relative density with that of the acceleration inputs as 0.1, 0.2 and 0.3 g. This figure shows the variation of settlements with respect to relative density for the sample with and without grouting. It can be observed from Fig. 3 that with an increase in initial relative density the amount of settlement decreases in both the cases. The test result at 35% relative density after shaking at 0.1 g excitation with the frequency of input motion of 4 Hz amounts to 20.10 mm, whereas for 80% relative density after shaking at same excitation level, the settlement was 14.50 mm, indicating a drastic decrease in the settlement at higher relative density. This is because the sand particles got rearranged to form closer packings whereby soil sample densified further, thus decreasing the void ratio which results from the decrease in hydraulic conductivity after shaking. With the inclusion of neat cement grout, the settlement further decreased from 16.50 mm (at 35% D_r) to 8.50 mm (at 80% D_r) tested at 0.1 g amplitude. This is due to the increase in shear strength of the soil when improved with neat cement. The general trend of results is almost similar for all the relative densities for the sand and sand grouted with neat cement as presented in Tables 3 and 4.
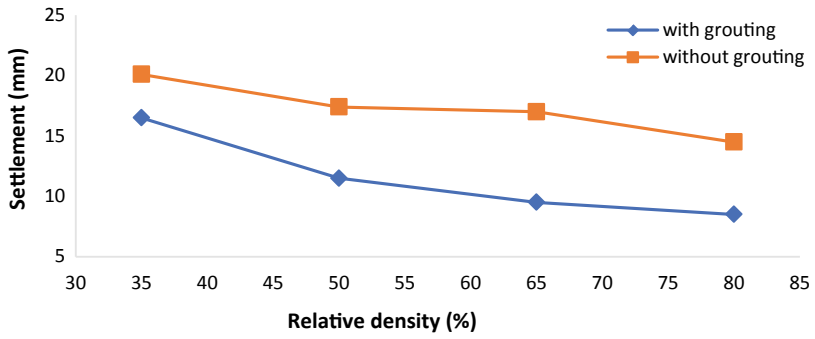
(a) at 0.1g acceleration
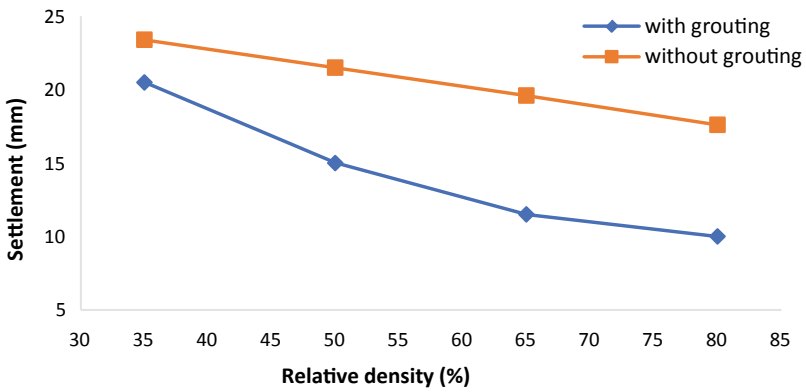
(b) at 0.2g acceleration
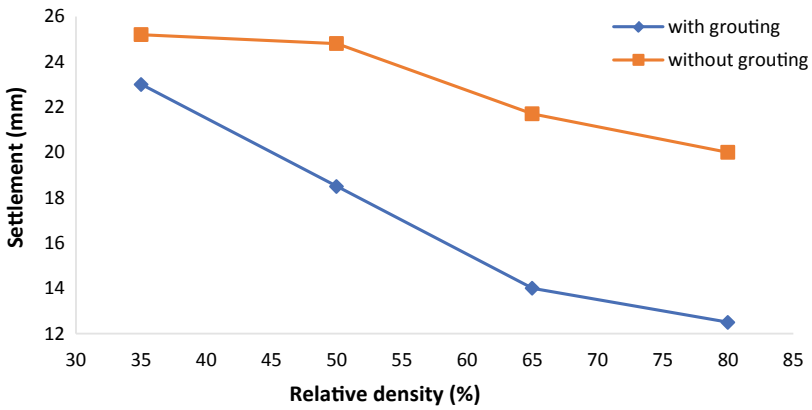
(a) at 0.3g acceleration

Fig. 3 Settlement variation with varying relative density

5.2 Variation of Settlement with Different Acceleration Inputs

Figure 4a, b show the variation of settlement with acceleration for different relative densities. It was observed that for both the samples, the amount of settlement increases with the level of accelerations. For smaller values of acceleration (at 0.1 g), the value of the settlement for all the relative density was observed to be less than that for the sample tested at higher acceleration (at 0.3 g). For example, the values of settlement in the sand without grouting (at 25% D_r) for an acceleration of 0.1 g, 0.2 g

(a) Pure sand

(b) Grouted sand
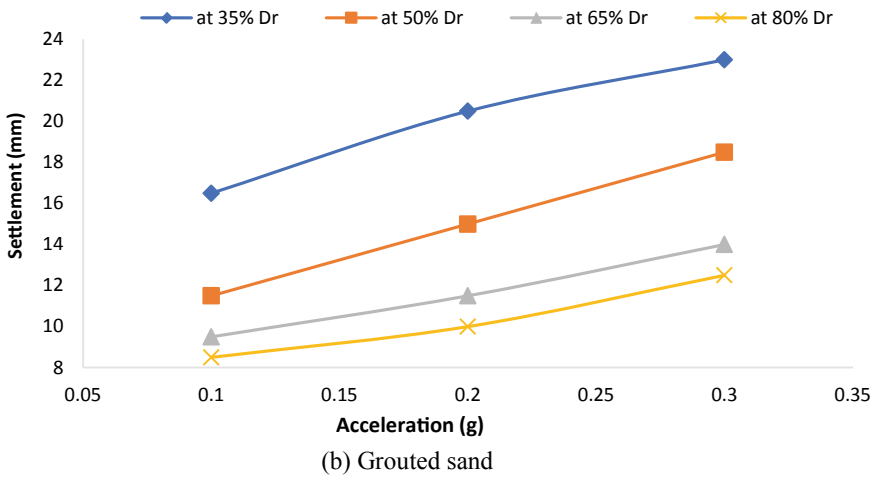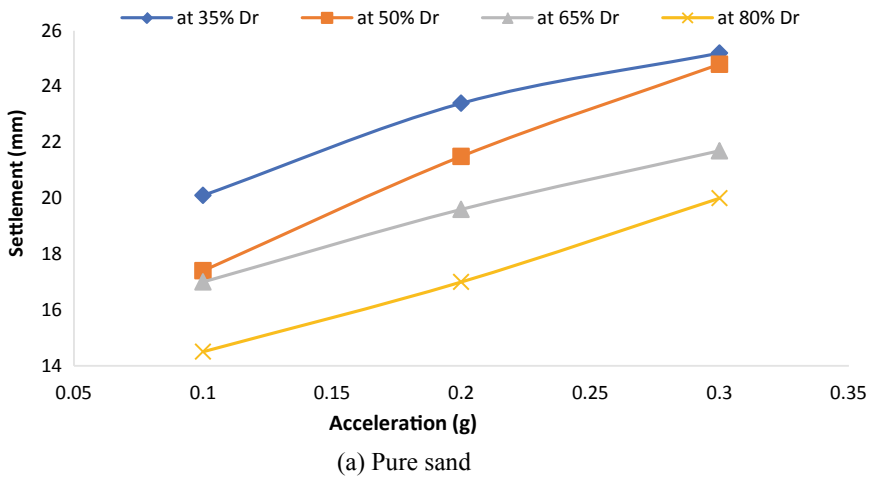
Fig. 4 Settlement versus acceleration at varying relative density

and 0.3 g were 20.10 mm, 23.40 mm and 25.20 mm, respectively. A similar trend was observed for the saturated sand samples prepared at a relative density of 50, 65 and 80%. The second last column of Table 4 shows the settlement measured after shaking duration of 15 s at 4 Hz frequency for the saturated sand sample prepared with the inclusion of neat cement grout tested at different levels of acceleration (at 0.1–0.3 g). It has been observed that by increasing the magnitude of acceleration, the number of settlement increases and the maximum value was 23 mm (at 35% D_r). A similar trend was observed at relative densities of 50, 65 and 80%.

5.3 Effects of Ground Improvement

It can be observed from the test results that the amount of settlement during earthquake shaking at all relative density decreases when the saturated sand is improved with neat cement grout. The test results also indicate that the inclusion of neat cement grout to a saturated sand sample further decreases the amount of settlement prepared at all relative density. This is attributed to the fact that due to the grouting technique the saturated sand is compacted further and the inclusion of grout makes the saturated sand sample a composite material whose strength and stiffness will be much higher than the saturated sand sample prepared without grouting. Thus, the ground improvement on saturated sand decreases the amount of settlement thereby increasing the liquefaction resistance of saturated sand after grouting. It can be further observed from Tables 3 and 4 that there are drastic decreases in the settlement as the relative density increases due to the inclusion of grouts. For 35% relative density, the settlement dropped from 20.10 mm (pure sand) to 16.50 mm (grouted sand) tested at 0.1 g acceleration and for 80% relative density, the settlement dropped from 14.50 mm (pure sand) to 8.50 mm (grouted sand) respectively at 0.1 g acceleration as clearly illustrated in Fig. 4a–d. This may be due to the fact that the compression of sand particles is resisted by the provision of neat cement grouts.

6 Conclusions

In this study, shaking table tests were carried out on saturated Solani river sand, improved with neat cement grout to investigate the settlement effect before and after the dissipation of excess pore water pressure. From an analysis of the results, the following conclusions were drawn:

1. With the increase in relative density, the settlement decreases from 20.10 mm (for 35% D_r of pure sand) to 17.40 mm (for 50% D_r of pure sand) under the vibration of 0.1 g.
2. When the sand was grouted with neat cement and shaking was imparted, the settlement further decreased from 20.10 mm (for 35% D_r of pure sand) to

16.50 mm. The amount of settlement for 80% relative density was reduced to 8.50 mm under the same test conditions.

3. With the inclusion of neat cement grout, the dry unit weight after shaking decreases to 15.06 kN/m^2 and 15.79 kN/m^2, respectively, at 0.1 g for 35% and 80% relative density. At higher levels of excitations, the amount of settlement is high for both samples (pure sand and grouted sand) tested.

4. The grouting technique considered for improving the sand against settlement has been found effective, thereby increasing the liquefaction resistance of loose Solani river sand significantly. Further study can be carried on the application of improvised grouting material to resist the liquefaction of soil.

References

1. Jonathan DB, Rodolfo BS, Durgunoglu T, Onalp A (2004) Subsurface Characterization at ground failure sites in Adapazari. J Geotech Geoenviron Eng ASCE 130(7):673–685
2. Bertalot DD, Brennan AJ, Villalobost FA (2013) Influence of bearing pressure on liquefaction-induced settlement of shallow foundations. Geotechnique 63(5):391–399
3. Yasudaa S, Harada K, Ishikawa K, Kanemaru K (2012) Characteristics of liquefaction in Tokyo Bay area by the 2011 Great East Japan Earthquake. Soils Found 52(5):793–810
4. Suresh R, Dash L, Govindaraju BS (2008) On the probable cause of the failure Kandla port and customs office tower during the 2001 Bhuj earthquake. In: Proceedings of the 14th world conference on earthquake engineering, Beijing, China
5. Cubrinovskia M, Robinsonb K (2016) Lateral spreading: evidence and interpretation from the 2010–2011. Soil Dyn Earthq Eng 187–201
6. Verdugo R, Gonzalez J (2015) Liquefaction-induced ground damages during the 2010 Chile Earthquake. Soil Dyn Earthq Eng 79:280–295
7. Madabhushi GSP, Haigh SK (2010) Liquefaction induced settlement of structures. In: Proceedings of 5th international conference on recent advances in Geotechnical earthquake Engineering and Soil Dynamics, San diego, California
8. Seed RB, Cetin KO, Moss RES, Kammerer AM, Wu J, Pestana JM, Riemer MF (2003) Recent advances in soil liquefaction engineering: A unified and consistent framework. In: Proceedings of the 26th annual ASCE Los Angeles Geotechnical Spring Seminar, Long Beach, California
9. Rasouli R, Towhata I, Rattez H, Vonaesch R (2018) Mitigation of nonuniform settlement of structures due to seismic liquefaction. J Geotech Geoenviron Eng, ASCE 144(11):04018079–04018110
10. Rasouli R, Hayashi K, Zen K (2016) Controlled permeation grouting method for liquefaction mitigation. J Geotech Geoenviron Eng 142(11):04016052
11. Mittal S (2013) An introduction to ground improvement engineering. New Delhi, India
12. Gupta MK (1977) Liquefaction of sand during during earthquake. D Phil Thesis, University of Roorkee, Uttarakhand, India
13. Mittal S, Chauhan R (2013) Liquefaction behavior of reinforced saturated sand under dynamic conditions. Int J Geotech Eng 7(1):109–114
14. IS:2720 (Part-15- 1992) Determination of Density Index (Relative Density) of Cohesionless soils. Bureau of Indian Standards, New Delhi, India
15. Gupta MK (1994) Liquefaction during 1988 earthquakes and a case study. In: Proceedings third international conference on case histories in geotechnical engineering, University of Missouri, Rolla, USA
16. Gupta MK (1977) Liquefaction of sands during earthquakes, Ph.D. thesis, University of Roorkee, Roorkee, India

17. Mittal RK (2007) Behavior of randomly distributed fiber reinforced sand in shallow foundation, Ph.D. thesis, Indian Institute of Technology, Roorkee, India
18. Singh HP, Maheswari BK, Saran S (2008) Liquefaction behavior of the solani sand using small shake table. In: Proceedings of the 12th international conference of the international association for computer method and advances in geomechanics, Goa, 1–6 Oct, India, pp 2797–2804
19. Mase LZ (2013) Analysis of liquefaction potential of Opak Imogiri River (experimental study and empirical analysis), Master's Thesis, Gadjah Mada University, Yogyakarta, Indonesia
20. Mase LZ, Fathani TF, Adi AD (2013) Experimental study of liquefaction potential in Opak River Imogiri, Yogyakarta. In: Proceedings of the 17th annual scientific meeting of the Indonesian geotechnical engineering society, Jakarta, 13–14 Nov, Indonesia, pp 199–205
21. Chauhan R (2012) Study on liquefaction behaviour of reinforced sand. Ph.D. Thesis, University of Roorkee, Uttarakhand, India (2012).
22. Seed HB, Idriss IM (1982) Ground motion and soil liquefaction during earthquakes. Earthquake Engineering Research Institute, Berkeley, CA
23. Kusumawardhani R (2014) Liquefaction variable based on experimental test of very low frequency in clean sand, Ph.D. thesis, Gadjah Mada University, Yogyakarta, Indonesia
24. Mase LZ (2017) Experimental liquefaction study of Southern Yogyakarta using Shaking Table. Teknik Sipil (Jurnal Teoritis dan Terapan Bidang Rekayasa Sipil) ITB 24(1):11–18

Effect of Plasticity Index on Liquefaction Behavior of Silty Clay

Sufyan Ghani and Sunita Kumari

Abstract The fine-grained materials like silt or clay are of non-plastic or plastic in nature, respectively. These properties tend to make an important and consistent difference in the cyclic strength of the soil. Generally, the presence of plastic fines tends to increase the liquefaction resistance of a soil due to dilitative nature of clayey soil. But, there is a contradictive statement for non-plastic fine behavior toward liquefaction resistance. Most of the districts of Bihar falls in Seismic Zones IV and V and are highly populated. These areas have alluvial soil deposits due to existence of numerous number of flood plain. Therefore, evaluation of liquefaction susceptibility based on plasticity index of soil is necessary to provide a guide map for engineers and designers toward safe and economical design of civil engineering structures. The present paper summarizes the effect of plasticity index on liquefaction for River Ganges alluvial soil deposit area. This area is significant in terms of economy and population and falls under seismic Zone IV. Therefore, liquefaction potential analysis has also been carried out to determine the uncertainties in liquefaction resistance considering plasticity index criteria of soil deposits.

Keywords Liquefaction · Plasticity index · Cyclic strength · Silty clay

1 Introduction

Liquefaction is one of the most complex and debated topics in geotechnical engineering associated with the failure of earth structures. Soil deformation caused by monotonic, transient and repeated disturbance of saturated soils under undrained condition leads to the generation of excess pore-water pressure and loss of strength which is major criteria of liquefaction phenomenon. Its devastating effects drew

S. Ghani (✉) · S. Kumari
Department of Civil Engineering, National Institute of Technology Patna, Patna, Bihar 800005, India
e-mail: sufyan04@gmail.com

S. Kumari
e-mail: sunitafce@gmail.com

the attention of geotechnical experts when the Alaska earthquake ($M_w = 9.2$) was followed by the Niigata earthquake ($M_w = 7.5$) in the span of three-month in year 1964 [1]. Both earthquakes produced spectacular examples of liquefaction damages. Failures of slope, foundations of buildings and bridges were noticed. Some of the buried structures were observed floating at ground level after earthquake. There onwards, the liquefaction phenomenon has been studied extensively by numerous researchers in the past few decades. Liquefaction criteria can be divided broadly into two parts, flow liquefaction and cyclic mobility. Flow liquefaction occurs in loose saturated sands and leads to huge instabilities and deformations whereas cyclic mobility is another phenomenon which is observed in medium to dense saturated sands and causes large deformations known as lateral spreading. The shear movements in this type of liquefaction are not as seen in flow liquefaction rather it produces incremental shear movements. Observations made during several earthquakes recently showed evidence of liquefaction in soil with fine content having medium to low plasticity. These types of soil dilate extensively throughout shearing. Fine-grained materials like silt or clay are of non-plastic or plastic in nature respectively. These properties tend to make an important, consistent difference in the cyclic strength of the soil.

2   Review of Literature

Once liquefaction starts, the soil subjected to cyclic loading may undergo a temporary shear strength loss instead of a permanent loss, i.e., cyclic mobility with limited flow deformation Bray and Sancio [2]. Martin and Lew [3] stated that clayey soils are those that have a clay content (particle size < 0.005 mm) greater than 15% and if clayey soil come across during site exploration, then they should be considered as non-liquefiable. However, 1994 Northridge, 1999 Kocaeli, and 1999 Chi-Chi earthquakes showed substantial number of cases where ground failure has caused considerable damage to buildings in silty and clayey soils containing more than 15% clay-size particles. Wang [4] suggested that any clayey soil containing less than 15–20% particles by weight smaller than 0.005 mm and having a water content (w_c) to liquid limit (LL) ratio greater than 0.9 is vulnerable to liquefaction. Re-evaluation of Wang's work provides a number of useful insights regarding the effects of soil sensitivity as expressed through the ratio of w_c/LL, this criterion appears to be a discriminating factor in liquefaction susceptibility. Based on the criteria established by Wang [4], Seed and Idriss [5] suggested that clayey soils could be susceptible to liquefaction only if all three of the following conditions are met, first percent of particles less than 0.005 mm < 15%, second LL < 35% and third w_c/LL > 0.9. This standard came to be known as the Chinese criteria due to its origin. This was initially recommended for seismic design of hydraulic structures which directed that liquefaction can occur during a strong seismic motion in any silty soil which contains less than 15–20% clay particles (smaller than 5 μm size) and has plasticity index of more than 3% and its water content is greater than 90% of its liquid limit (LL). Andrews

and Martin [6] reviewed empirical data and suggested a new assessment index and transformed the conventional Chinese Criteria according to US standards which came to be known as Modified Chinese Criteria. The major differences proposed in this modified criteria as compared to the original Chinese Criteria was that 0.0002 mm particle size was used as the limit between clay and silt particles and Casagrande's Apparatus should be used for obtaining liquid limit. It was also concluded that soils of 2 μm size having percentage finer less than 10% and LL < 32% were susceptible to liquefaction whereas the soils having $\geq$10% finer than 2 μm and LL $\geq$ 32% were not susceptible to liquefaction. Studies undertaken in early 1980s at University of Missouri–Rolla (UMR) (now Missouri University of Science and Technology) also acknowledge the effect of plasticity of soil on the liquefaction of silts based on the results determined from the laboratory test. It was suggested that the cyclic stress ratio (CSR) which is one the governing criteria for causing liquefaction decreases as the plasticity index is increased. Puri [7] concluded that introduction of clay or plasticity to the silt leads to the increase in the resistance of soil mass against liquefaction. Ishihara and Koseki [8] recommended that low plasticity fines (PI < 4) has no influence on the vulnerability of liquefaction. However, it was noted that the effect of the void ratio was not consider in their analysis. Later, Sandoval [9], Prakash and Sandoval [10] demonstrated that silt having plasticity index (PI) in the range of 2–4%, the liquefaction resistance of silt decreases with increasing plasticity. Polito [11] studied various criteria for assessment of liquefaction potential of the soil. In his understanding, soil susceptible to cyclic mobility can be considered as non-liquefiable as compared to the deformation and strain caused under flow liquefaction. Based on series of Cyclic Triaxial Test and considering different geotechnical properties like plasticity, water content, clay content, mean grain size, relative density and void ratio, a clear demarcation line was suggested in between flow liquefaction and cyclic mobility.

Recently Indian standard code [12] is considered as one of the most common and simplified procedure for the evaluation of liquefaction potential of sand deposits. The Indian Standard uses in situ testing such as SPT, CPT and shear wave velocity (V_s) for the assessment of liquefaction potential. By considering the intensity of earthquake for the assessment of liquefaction potential this method does overcome the major shortcomings of all the above-mentioned criteria but despite of being a pioneer in the evaluation of liquefaction susceptibility it remains silent for soil with presence of fine content. Although it does provide a correction for the SPT blow count value (N1)60 based on the percentage of fine content (FC) but no specific equation or relation has been provided considering the plasticity of the soil. Therefore, a reliable and proper method for the assessment of liquefaction susceptibility of soil with fine content is required.

The first step in assessing the possibility of ground failure in silts and clays during earthquakes is to determine the appropriate engineering procedures that would be used in the evaluation. Cyclic strengths can be calculated based on data from in situ testing or laboratory testing and empirical correlations that are similar to the established procedures for evaluating the liquefaction susceptibility of such deposits. The objective of this paper is to evaluate liquefaction susceptibility of the proposed

site using Chinese criteria and Indian standard code and to establish the relationship using plasticity index as a governing criteria.

3 Methodology

Some of the researchers have recommended a relation between plasticity and cyclic strength of soil which has given rise to the use of plasticity index as a key criteria by which liquefaction susceptibility of soil can be determined. These criteria are used to differentiate liquefiable and non-liquefiable soils. Plasticity of the soil can be computed either in terms of the liquid limit or plasticity index.

3.1 Chinese Criteria (1979)

Wang [4] noted the incidence of liquefaction in silty sand to slightly sandy silt soils during the Haicheng earthquake, 1975 and the Tangshan earthquake, 1976, and proposed a criteria which was known as Chinese criteria in 1979 which stated that a fine-grained soil is considered to be susceptible to liquefaction, when all of the following four criteria are satisfied:

Liquid Limit < 35%
Liquidity Index > 0.75
Natural Water Content > 0.9 × Liquid Limit
Percent Passing 0.005 mm Sieve Size < 15%.

The liquid limit of a soil is an indirect measure of the water content or void ratio (density) that corresponds to a specified undrained shear strength of 2–2.5 kPa, while the liquidity index is an indirect measure of the sensitivity of the soil. The first three criteria identify weak sensitive fine-grained soils whereas fourth criterion, which is a measure of the clay content of the soil, eradicates the medium to high plastic soils that will not undergo volume change during the application of cyclic loads. As Chinese criteria are exclusively based on index properties and grain size data it can be concluded that it is independent of the intensity and duration of the applied loads.

3.2 IS Code Method (2016)

Indian standard code [12] "Criteria for Earthquake Resistant Design of Structures" is a considered as one of the most common and simplified practice for the assessment of liquefaction potential of sand deposits in India. This standard primarily focuses on earthquake risk assessment for earthquake resistant design of buildings, liquid

retaining structures, bridges, embankments and retaining walls. The provisions of this standard are also applicable to critical structures like nuclear power plant, petroleum refinery plants and large nuclear dams.

The ratio of CRR (cyclic resistance ratio) to CSR (cyclic strength ratio) is termed as FOS (factor of safety), which indicates the liquefaction susceptibility of the soil deposit. If FOS < 1, soil will liquefy and if FOS ≥ 1, soil will not liquefy.

4 Result and Discussion

The proposed site is situated on the bank of Ganga River of Patna district of Bihar which in an active zone of earthquake classified as seismic Zone IV (high risk zone) of India. This city is highly populated. Also, subsoil in shallow depth is of silty nature with very little cohesion. Hence, a study has been carried out for evaluating liquefaction potential from the available soil data and SPT (N) value. The data obtained from the soil testing has been analyzed using Indian standard code as well as Chinese Criteria recommended by Wang [4].

This paper focuses on calculation of factor of safety for borehole 1 and 2 (BH-1 and BH-2) using the steps mentioned in the IS code. Tables 1 and 2 shows the estimation of effective stress (ES), total stress (TS), cyclic resistance ratio (CRR), cyclic stress ratio (CSR) and factor of safety (FOS), respectively. Figure 1 shows the trend of factor of safety (FOS) verses effective depth (z/z_c) for BH-1 and BH-2, where z is the depth (m) and z_c is the critical depth. The critical depth is taken as z_c = 15 m. Generally, it is found that chances of liquefaction are less beyond 15 m due to existence of overburden pressure.

The factor of safety obtained after the calculation done as per IS 1893 Part I: 2016 code shows that the proposed site is liquefiable. Only a few depths factor of safety was found to be above unity. Therefore, it should be concluded that based on

Table 1 Calculation as per IS code for BH-1

Depth	N60	F.C	CSR	CRR	FOS = CRR/CSR
1.50	3	65.8	0.35	0.15	0.43
3.00	2	65.8	0.34	0.12	0.36
4.50	2	68.0	0.33	0.12	0.37
6.00	3	68.0	0.32	0.13	0.42
7.50	12	68.0	0.31	0.35	1.11
9.00	10	72.6	0.31	0.27	0.86
10.50	10	72.6	0.29	0.25	0.84
12.00	6	96.0	0.28	0.16	0.58
13.50	9	66.2	0.26	0.20	0.77
15.00	10	66.2	0.25	0.21	0.85

Table 2 Calculation as per IS code for BH-2

Depth	N60	F.C	CSR	CRR	FOS = CRR/CSR
1.50	2.00	60.2	0.36	0.12	0.34
3.00	4.00	60.2	0.35	0.18	0.51
4.50	2.00	62.8	0.33	0.12	0.37
6.00	5.00	62.8	0.32	0.18	0.57
7.50	12.00	64.3	0.31	0.34	1.11
9.00	11.00	64.3	0.30	0.29	0.94
10.50	10.00	88.4	0.29	0.24	0.85
12.00	8.00	88.4	0.28	0.19	0.71
13.50	13.00	89.9	0.26	0.27	1.05
15.00	12.00	89.9	0.25	0.24	0.98
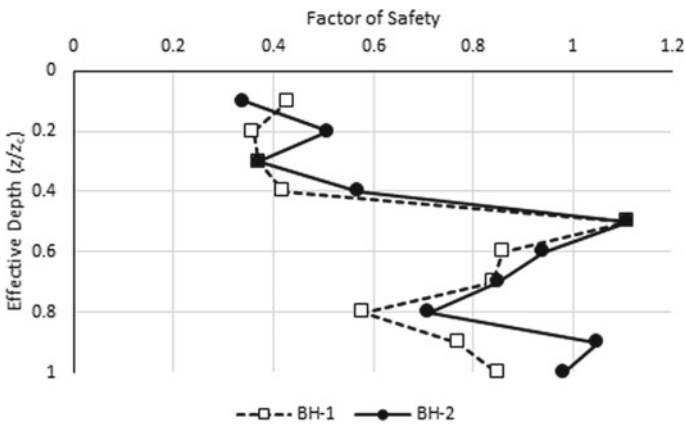
Fig. 1 Effective depth versus factor of safety for BH-1 and BH-2

IS code this site possess the threat of liquefaction and the engineers should select the foundation accordingly on this soil.

The Chinese criteria mainly focus on soils with plasticity, and considering plasticity as one of the governing criteria as observed in the literature. Here, the non-plastic layers are eliminated for further analysis. Liquefaction susceptibility of soil depth with plasticity as per IS 1893 Part I: 2016 code has been provided in Table 3 and it is noted that all of the considered plastic layers are susceptible to liquefaction.

Table 4 shows the basic soil properties of the plastic zones that are present at different depths as well as it depicts various parameters which are used to evaluate liquefaction susceptibility of a soil deposit as per Chinese criteria. The criteria state that soil deposits with $w_C < 0.87 * LL$ or $LL > 33.5$ or $PI > 13$ or clay fraction > 20% are non-liquefiable whereas soil deposits with clay fraction < 20% or $PI < 13\%$

Table 3 Liquefaction susceptibility of plastic layers as per IS Code

Bore Hole No	Depth (m)	FOS	Liquefaction susceptibility as per IS code
1	9.0	0.86	Susceptible
1	12.0	0.58	Susceptible
1	13.5	0.77	Susceptible
2	9.0	0.94	Susceptible
2	12.0	0.71	Susceptible
2	15.0	0.98	Susceptible

Table 4 Soil parameters of plastic layers

Borehole No	Depth (m)	LL	w_C (%)	PI	W_c/LL	FC (%)
1	9.0	36.25	25.13	16	0.69	72.6
1	12.0	37.00	27.34	13.75	0.74	96.0
1	13.5	36.25	22.58	14	0.62	66.2
2	9.0	34.50	25.60	14.25	0.74	64.3
2	12.0	36.25	24.84	13.5	0.68	88.4
2	15	37.25	25.74	13.75	0.69	89.9

are potentially liquefiable. The input parameters such as liquid limit (LL), saturated water content are used to draw a plot to determine liquefaction potential of soil layers.

Figure 2 has been described the estimation of liquefaction based on Chinese criteria Wang [4] and was developed by ASTM (American Standard for Testing
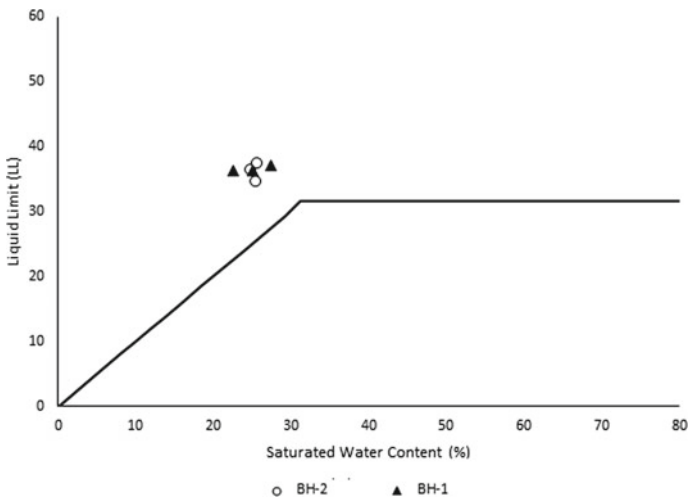
Fig. 2 Assessment of liquefaction using Chinese criteria

Materials). The portion above the plotted line in Fig. 2 represents non-liquefiable zone whereas portion below this line is potentially liquefiable.

Figure 2 demonstrates that the soil layers considered here are non-liquefiable. Considering plasticity and presence of fine content for the analysis has led to such observation. Generally, the presence of plastic fines tend to increase the liquefaction resistance of a soil due to dilitative nature of clayey soil. The presence of fines also influences a soil's ability to develop excess pore pressures. When studying field-based liquefaction there are two effects that should be considered, first and foremost it is the influence of fines on the soil and other is the influence of the fines on the penetration test. Adding fines to a clean sand leads to the filling up of void space to a point where the fines tends to displace the sand grains and dominate the soil matrix and the response to shear stress becomes fines dominated. As fines are added to a sandy soil the penetration resistance decreases up to a great extent. Fines have lower permeability as compared to clean sands which results in increased excess pore pressures on the penetration device thus resulting in lower effective stresses and lower penetration resistance. Both of the above-mentioned effects are blended in a field-based liquefaction assessment and are difficult to separate. Therefore, it has been observed that with an increase in fines there is a systematic decrease in the cyclic stress required to liquefy soil deposit when measured with penetration resistance.

Table 5 clearly embarks that the plastic soil layers became non-susceptible to liquefaction when evaluated using Chinese criteria as per the standards laid down by Wang [4] for a soil to be non-liquefiable. No specific FOS against liquefaction is obtained after using Chinese Criteria because it is based on soils plasticity and fine content. It gives idea of liquefaction susceptibility based on said parameters range. In some cases, it gives significant results as compared to IS code, particularly for soil containing fine content. This directs that consideration of plasticity and fine content may play an important role in evaluation of liquefaction susceptibility of soil deposits having fine content.

Table 6 presents a co-relation between plasticity index (PI) and liquefaction susceptibility of the soil deposits. It can be observed from the table that liquefaction potential of the soil deposits evaluated using IS code are totally contradictory when evaluated using Chinese Criteria. As suggested by Wang [4], soil deposits with PI > 13 will be non-liquefiable which concludes that liquefaction potential decreases

Table 5 Liquefaction susceptibility as per Chinese criteria

Borehole No	Depth (m)	FC (%)	Liquefaction susceptibility as per Chinese criteria
1	9.0	72.6	Non-susceptible
1	12.0	96.0	Non-susceptible
1	13.5	66.2	Non-susceptible
2	9.0	64.3	Non-susceptible
2	12.0	88.4	Non-susceptible
2	15.0	89.9	Non-susceptible

Table 6 Liquefaction susceptibility comparison between the two approaches

PI	Liquefaction susceptibility as per Indian Standard Code	Liquefaction susceptibility as per Chinese criteria
16	Susceptible	Non-susceptible
13.75	Susceptible	Non-susceptible
14	Susceptible	Non-susceptible
14.25	Susceptible	Non-susceptible
13.5	Susceptible	Non-susceptible
13.75	Susceptible	Non-susceptible

as plasticity increases. Plasticity of a soil deposit can either be represented in terms of liquid limit (LL) or plasticity index (PI) and it is a better indicator for evaluating liquefaction susceptibility of soil deposits.

5 Conclusion

The natural variability of the soil conditions on the bank of Ganga River of Patna district of Bihar allows significant study focusing on soil plasticity to figure out liquefiable deposits. It is evaluated that soil with higher level of plasticity is found to undergo different kind of deformation under cyclic loading as compared to those having lower levels of plasticity. Cyclic mobility form of failure was also observed in soils having higher levels of plasticity. On the other hand, soils with lower levels of plasticity exhibit criteria of flow liquefaction. The present analysis clearly indicates that the considered soil deposit is liquefiable as per IS Code whereas as per the Chinese criteria it is non-liquefiable. This signifies that considering plasticity, fine content, water content and liquid limit as the governing criteria makes the soil non-liquefiable. There is no clear demarcation in the IS code for soil having plasticity as well as fine content. Considering plasticity and fine content for evaluating liquefaction susceptibility of the soil has resulted in totally opposite observations. Construction of a structure on liquefiable zone requires a great amount of investment, so if plasticity is believed to be major discriminating criteria in the above-mentioned case it can be inferred that the sites which poses the threat to undergo liquefaction will lie in non-liquefiable zone thus contributing a huge saving in the cost of construction.

References

1. Seed HB (1979) Soil liquefaction and cyclic mobility evaluation for level ground during earthquakes.J Geotech Eng Div ASCE 105(GT2):201–255
2. Bray JD, Sancio RB (2006) Assessment of the liquefaction susceptibility of fine grained soil. J Geotech Eng 132(9):1165–1177

3. Martin GR, Lew M (1999) Recommended procedures for implementation of DMG Special Publication 117—guidelines for analyzing and mitigating liquefaction hazards in California, Southern California Earthquake Centre
4. Wang W (1979) Some findings in soil liquefaction. Report Water Conservancy and Hydro-electric Power Scientific Research Institute, Beijing, China, pp 1–17
5. Seed HB, Idriss IM (1982) Ground motions and soil liquefaction during earthquakes. Earthquake Engineering Research Institute, Berkeley, California
6. Andrews DCA, Martin GR (2000) Criteria for liquefaction of silty soils. In: Proceedings of, 12th world conference on earthquake engineering, Auckland, New Zealand
7. Puri VK (1984) Liquefaction behaviour and dynamic properties of loessial (silty) soils, PhD thesis, University of Missouri–Rolla, Mo
8. Ishihara K, Koseki J (1989) Cyclic shear strength of fines-containing sands. In: Earthquake and Geotechnical and Engineering. Japanese Society of Soil Mechanics and Foundation Engineering, Tokyo, pp 101–106
9. Sandoval J (1989) Liquefaction and settlement characteristics of silt soils, PhD thesis, University of Missouri–Rolla, Mo
10. Prakash S, Sandoval JA (1992) Liquefaction of low plasticity silts. J. Soil Dyn Earthq Engrg 71(7):373–397
11. Polito C (2001) Plasticity based liquefaction criteria. In: Proceedings of the 4th international Conference on recent advances in geotechnical earthquake engineering and soil dynamics. Paper No. 1.33
12. Indian Standard code 1893 Part I (2016) Criteria for earthquake resistant design of structures

Laboratory Investigation on Wave Characteristics Due to Hammer Impact on Different Types of Soil

K. S. Beena, M. Neethu, and Veena Jayakrishnan

Abstract Pile foundations are suitable when the surface soil is fragile, and the load coming from the superstructures is very high. Direct Mud Circulation (DMC) method of piling was considered as the most reliable piling system all over the world. The chiseling action in DMC piling produces stress waves, and these waves may cause problems to the nearby structures. This paper deals with a laboratory model study to investigate the vibration propagation and attenuation characteristics of different types of soil at various test parameters. The responses of soil surface due to impact load were studied, and results showed that the various factors controlling the wave propagation of soil include the distance of impact from the source, relative density of soil, impact hammer energies. The peak vertical acceleration was measured using a triple-axis accelerometer placed at different positions and with the help of SeismoSignal software version 4.3, the corresponding peak particle velocity and displacements were evaluated. The soil dependent parameters k and n were found out from the peak particle velocity, and an attempt is made to develop an equation to predict vibrations on the tested soils.

Keywords Pile driving · Vibrations · Wave propagation · Peak particle acceleration

1 Introduction

Piling methods are essential for building construction and other structures where adequate ground support is not directly available. During the impact of pile installation, waves are generated and at the point of impact, the displacement of an amount

K. S. Beena · M. Neethu · V. Jayakrishnan (✉)
Cochin University of Science and Technology, Kochi, Kerala, India
e-mail: veena.j.90@gmail.com

K. S. Beena
e-mail: beenavg@gmail.com

M. Neethu
e-mail: neethu947@gmail.com

of soil generates both shear waves and compressional waves. When the P-waves and S-waves encounter the ground surface, part of their energy is converted into surface Rayleigh waves and part is reflected into the ground decaying in amplitude in proportion to the square root of distance [1]. The waves generated by human activities propagate in the superficial soil layers, as they move away from their source interact with above ground and in-ground structures. The pile installations create issues-particularly in urban areas such as environmental disturbance, unwanted noise, and a potential hazard for the neighboring properties due to the vibrations. Many of the previous studies presented a numerical model for the prediction of free field vibrations due to impact and vibratory loading [2]. The peak particle velocity of soil depends on the soil constants k and n [3]. Pseudo attenuation model developed by Wiss [1] gives how peak particle velocity varies with respect to distance from source and energy. A reliable prediction model is required in all cases where it is meant to be used [4] as the wave propagates through the soil, attenuation takes place in the form of material and geometrical damping [5].

Many case studies have revealed that ground vibration due to pile driving causes damage to the adjacent structures. The damage due to pile driving occurs either directly or via the settlement of soil beneath the foundations. Ground vibrations caused by pile driving comprise complex radial, transverse and vertical components at the adjacent ground surface [6]. The potential damage to the adjacent structures can be prevented by conducting pre-construction surveys, predicting the anticipated waves before pile driving and monitoring and controlling the vibrations on-site.[7]. It is expected that the vibration level associated with pile driving may vary with distance from the pile driving site since the resulting wave is of periodic nature, which is highly attenuated after a short-range. Also, harmonic frequencies are a low vibration level. Vibrations caused by train loading, blasting, and pile driving can be measured by using 3D geophones [8]. Amick and Gendreau presented several forms of vibration limits applicable to construction vibrations together with the results of a controlled evaluation of construction-related vibrations at a representative site [9].

In the present study, impact load was applied on different soil surfaces and for each drop heights the readings were recorded to get the average values. The peak vertical acceleration was recorded for different soil types at different positions for different hammer energies. MEMS accelerometers can be effectively used in vibration analysis both in the field and laboratory settings [10]. Also, an attempt to develop a vibration prediction model on the tested soil is made.

2 Materials and Methodology

To study the wave propagation characteristics of different types of soil, three types of soil (silty sand, river sand, and lateritic red soil) were selected and collected from three different locations of Kochi, Kerala. Basic geotechnical properties of soil were analyzed according to IS 2720 and are summarized in Table 1.

Table 1 Properties of Soils used in the study

Property	Silty sand	River sand	Lateritic red soil
Specific gravity	2.63	2.59	2.67
Coefficient of friction	35º	37º	30º
Cohesion (kPa)	0.082	0	26
D_{10} (mm)	0.16	0.25	0.4
D_{30} (mm)	0.24	0.5	0.9
D_{50} (mm)	0.31	0.56	1.3
D_{60} (mm)	0.39	0.6	1.6
Gravel (%)	2	0	0
Sand (%)	92.6	98.4	98.5
Silt (%)	5.4	0.6	1.5
Uniformity coefficient, C_u	2.437	2.4	4.2
Coefficient of curvature, C_c	0.923	1.66	1.1
Max dry density (kN/m^3)	18.52	17.2	18.9
Max Void ratio, e_{max}	0.79	0.88	0.87
Min void ratio, e_{min}	0.52	0.508	0.59

2.1 Experimental Setup

A steel tank of length 1.2 m, width 0.70 m, and height 0.90 m was used for the laboratory study. Stiffeners are provided on the sides of tank to prevent bulging of sides during the experiment. Impact load was applied using a hammer which is mounted on a pulley and is properly guided using a MS pipe to ensure that the impact occurs at the same point on the soil surface. The accelerometers and signal analyzers are properly arranged on the test setup. The setup can be fitted in to the tank using bolts in a laboratory while it can be fixed using SPT tripod in a field. The impact load was provided using 10 kg cylindrical weight which was connected to a rope and pulley arrangement. The schematic diagram of the experimental setup is shown in Fig. 1.
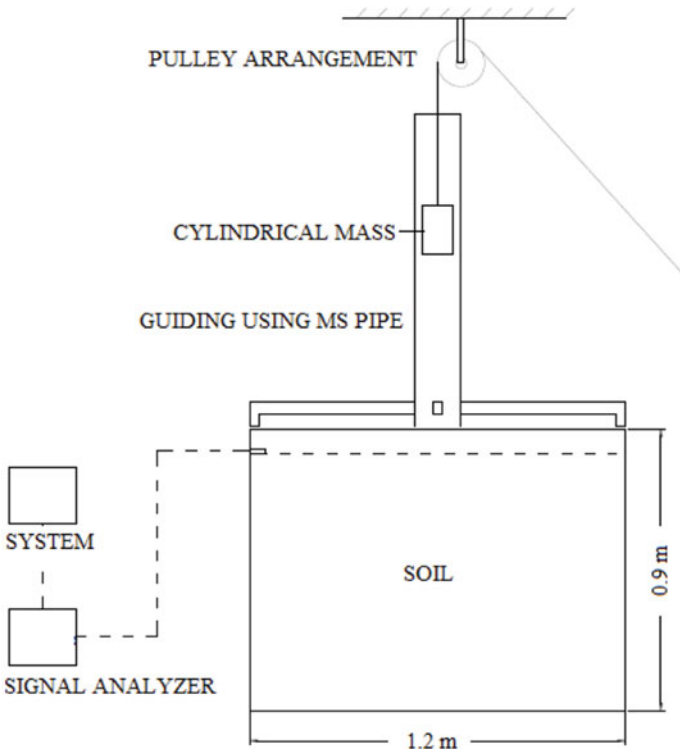
Fig. 1 Schematic diagram of the experimental setup for measuring the vibrations of soil

2.2 Methodology Adopted

Tests were conducted by varying different parameters as follows:

- Type of soil—silty sand, river sand, and lateritic soil
- Relative density—relative density of river sand and silty sand were varied (30 and 60%)

- Impact hammer energy—by varying the height of fall of driving hammer, energy was varied with minimum energy of 50 J and maximum energy of 175 J were used for laboratory investigation
- Distance of measurements from source of impact—0.25 m and 0.45 m from point of impact.

Vertical impact tests were conducted to simulate different impact energy using falling mass of 10 kg with different dropping height (0.5, 1, 1.25, 1.5, and 1.75 m). The energy was varied from 50 to 175 J. The response of the soil during impact was measured by two accelerometers which were connected with an Arduino and which in turn connected with a laptop. Laboratory model study was conducted for finding wave characteristics by varying relative density, type of soil, distance from source, and hammer energy. Two accelerometers (ADXL335) were placed at the soil surface at a distance of 0.25 and 0.45 m from the source of impact to find the peak particle acceleration. The placement of accelerometer sensors at these positions was selected in order to reduce the boundary effects and also large distance between the accelerometers was not possible due to the limitation in the length of the tank. Peak particle velocity and displacements were found out from the recorded acceleration value with the help of SeismoSignal software. To understand the influence of relative density tests were conducted on the two sands at 30 and 60% relative densities.

3 Results and Discussions

To study the wave propagation and attenuation through different types of soil, laboratory model test was conducted by varying the test parameters. This test was helpful to identify how soil type and the impact hammer energies influence the characteristics of waves generated at soil surface. Corresponding peak vertical acceleration, peak particle velocity and displacements were determined in sands at different relative densities and also, in different soils at constant relative density.

3.1 Effect of Hammer Energy and the Distance from Source of Impact

Test was conducted on lateritic red soil at 60% relative density with different hammer energies. Two accelerometers were placed on the soil surface at different position in order to find the effect of distance from source of impact. One accelerometer was placed at distance 0.25 m from the point of impact and the second was at a distance 0.45 m from point of impact. It was observed that acceleration values increase with increasing hammer energy and decrease with increasing distance from the point of impact which may be due to the attenuation of waves through the soil. The peak particle velocity and relative soil movement were measured from the recorded

Table 2 Test results on lateritic soil

Energy(J)	A_1(m/s^2)	V_1(mm/s)	S_1(mm)	A_2(m/s^2)	V_2(mm/s)	S_2(mm)
50	6.31	8.75	0.26	2.71	2.681	0.105
75	8.68	10.258	0.306	3.82	4.73	0.126
100	9.97	13.88	0.41	4.09	6.06	0.16
125	10.12	13.99	0.42	4.96	6.62	0.18
150	13.07	15.822	0.47	4.96	7.19	0.2
175	15.01	17.03	0.49	6.9	7.83	0.23

acceleration values with the help of SeismoSignal tool. Peak particle velocity and displacements also show the same trend that of acceleration. The values obtained are summarized in Table 2. A_1 and A_2 values were given by ADXL335 accelerometers. V_1, V_2, S_1, and S_2 were found out by putting the values of recorded A_1 and A_2 in Seismo Signal.

A_1—Peak vertical acceleration at a distance 0.25 m from the source on the top of soil.

A_2—Peak vertical acceleration at a distance 0.45 m from the source on the top of soil.

V_1—Peak particle velocity at a distance 0.25 m from the source on the top of soil.

V_2—Peak particle velocity at a distance 0.45 m from the source on the top of soil.

S_1—Displacement at a distance 0.25 m from the source on the top of soil.

S_2—Displacement at a distance 0.45 m from the source on the top of soil.

From Fig. 2, it can be observed that as the distance from the source increases and the energy of hammer impact decreases, there is a reduction in the peak particle acceleration values. The acceleration values decrease as expected [11] as the distance increases from the source. Peak particle acceleration, peak particle velocity and displacement showed an average decrease of 57% with the source distance rising from 0.25 to 0.45 m.

The acceleration values obtained from experiments were plotted using SeismoSignal software. The acceleration time history corresponding to lateritic soil is shown in Fig. 3.

3.2 Effect of Relative Density

Impact tests were conducted on river sand and silty sand for two different relative densities, viz., 30 and 60%. Two sensors were used for the measurement of acceleration at a distance of 0.25 m from the source and 0.45 m from the source.

It was observed from all the test results that as the impact hammer energy and the relative density increases, peak vertical acceleration and hence the peak particle velocity increases. As the relative density increases the inter granular solid to solid
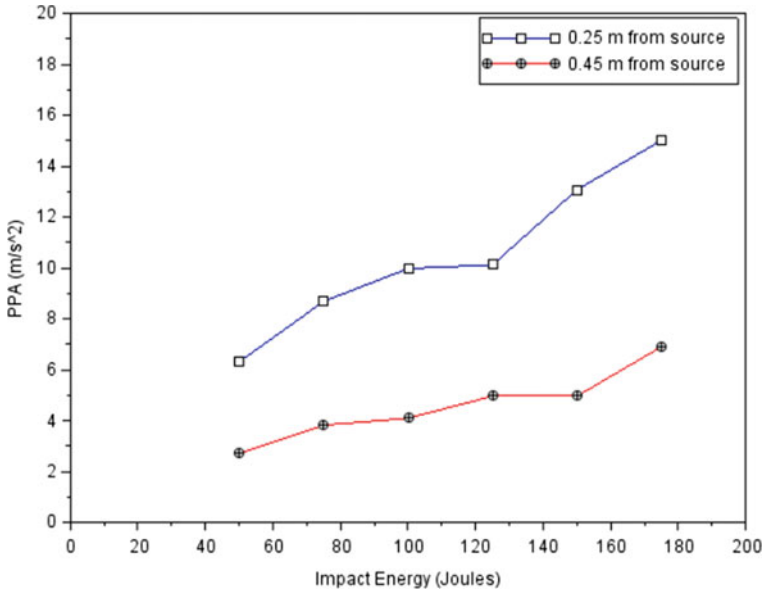
Fig. 2 Variation in peak particle acceleration (PPA) of lateritic soil with respect to distance from source
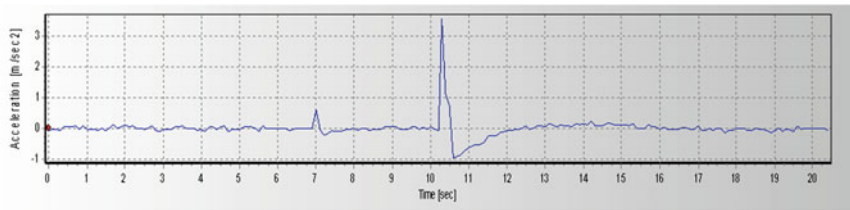
Fig. 3 Acceleration time history of lateritic soil during an impact of 75 J shown by sensor placed at distance of 0.45 m from source

contact between the sand grains may increase resulting in the significant change in the travel path.

The variation of wave propagation parameters for river sand and silty sand with relative density is shown in Figs. 4 and 5, respectively. From the figure, it was also observed that as the distance from the source increases there was a reduction in each test result values.
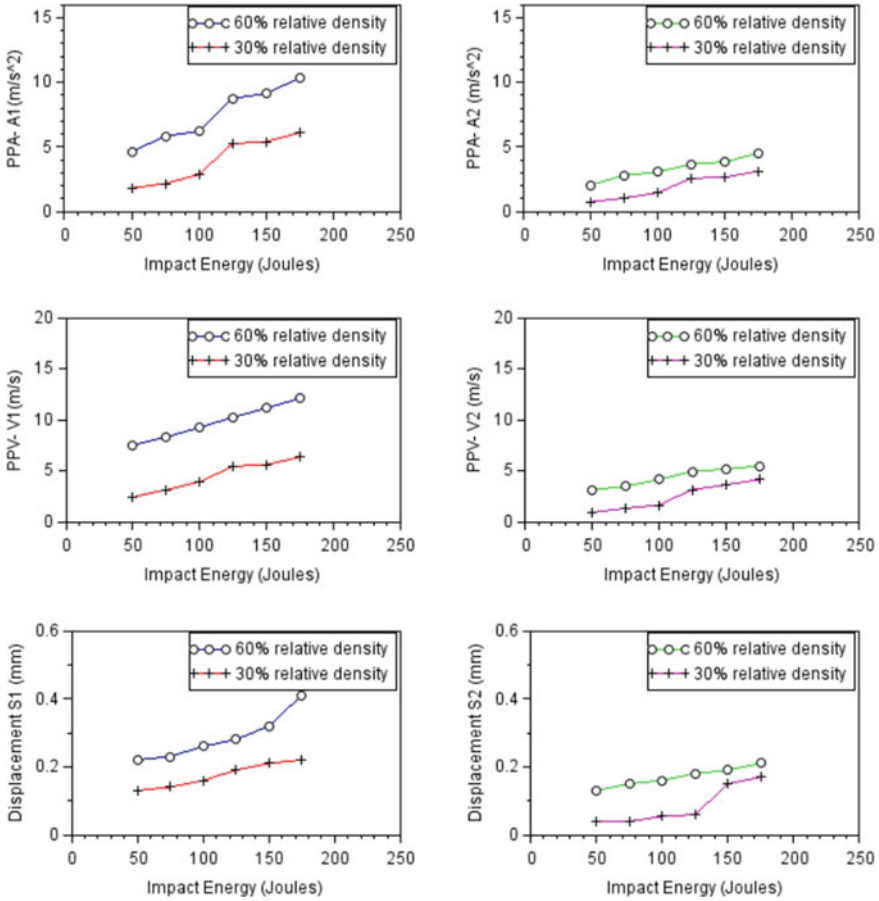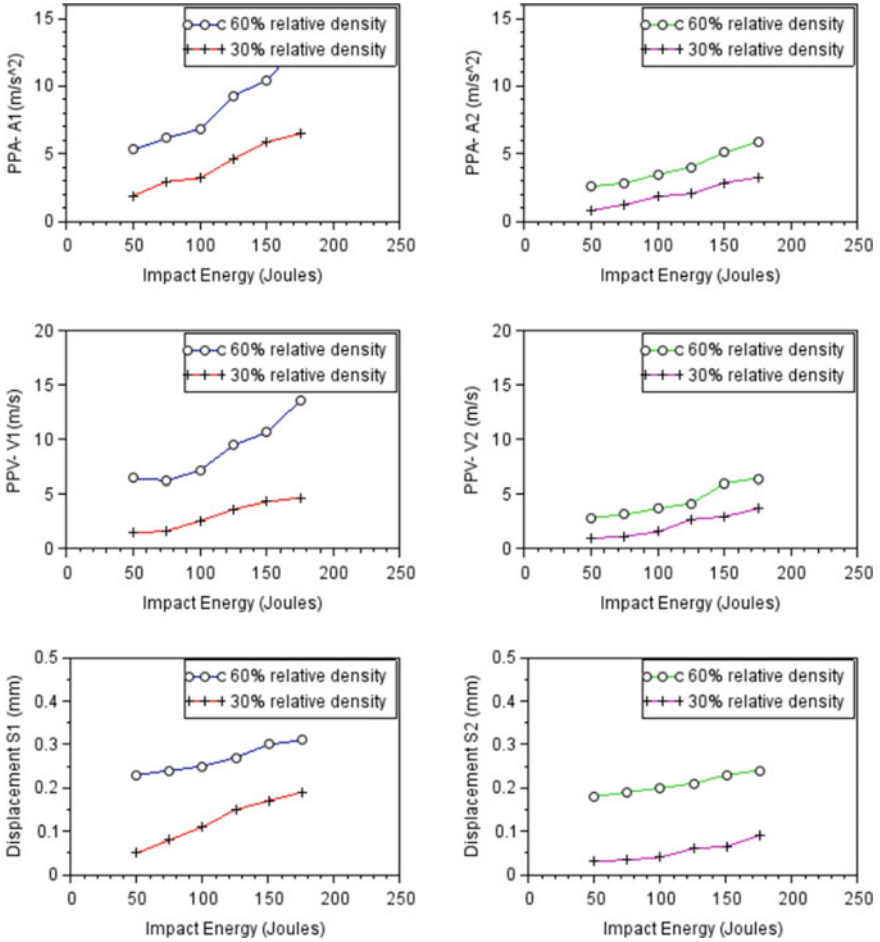
Fig. 4 Variation of wave propagation characteristics of river sand with relative density

3.3 Wave Characteristics Due to Change in Type of Soil

To study the wave propagation characteristics due to the change in type of soil different tests were conducted on three types of soil keeping the relative density constant (60%). It was observed that peak vertical acceleration and peak particle velocity were higher for lateritic soil followed by silty soil and then river sand. The acceleration values showed an increasing trend with increasing hammer energy for all types of soil. The high value of acceleration value obtained by lateritic soil for a particular energy may be due to high cohesion of the soil. Relative densities of all the soils were fixed as 60% for all the test. The maximum dry density of lateritic soil was higher (18.9 kN/m^3) than the silty sand (18.52 kN/m^3), followed by river sand (17.2 kN/m^3). Thus, as the dry density increases an increase in the propagation characteristics was observed. The presence of fine particles can also may influence

Fig. 5 Variation of wave propagation characteristics of silty sand with relative density

the result. The variation in the acceleration value at different types of soil and hammer energies is shown in Fig. 6.

3.4 Determination of Soil Constants

The prediction of vibration generally requires two constants, namely k and n. These constants are entirely dependent on soil condition and impact type. The Peak particle velocity (PPV) is related to impact energy and distance from the impact by the prediction Eq. 1. (Scaled distance relationship as reported in [1] and [7])
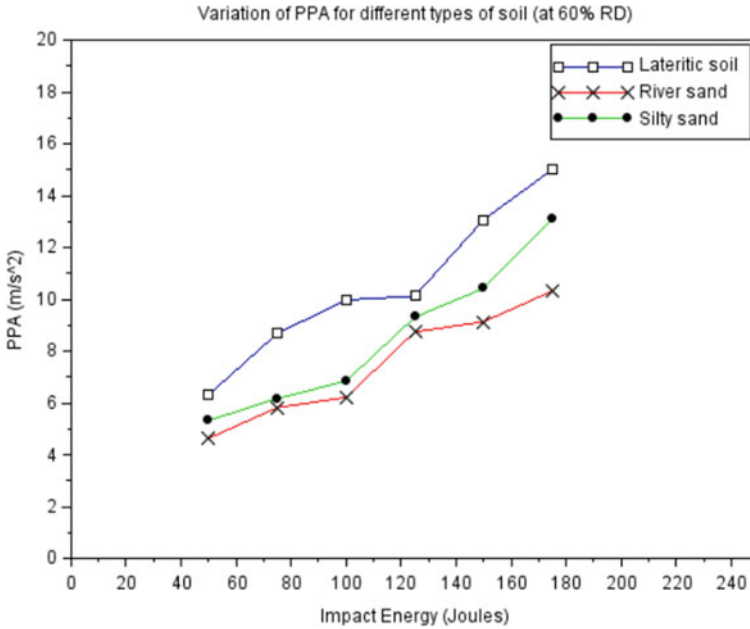
Fig. 6 Variation of peak particle acceleration with type of soil

$$v = k\left[d/\sqrt{E_n}\right]^{-n} \qquad (1)$$

where v is the peak particle velocity,

k is the value of velocity at $d/\sqrt{E} = 1$,
d is the distance from the vibration source,
E_n is the impact energy transferred from the hammer to the soil,
n is the slope or attenuation rate.

Soil constants are determined for each hammer energy for all three types of soil at 60% relative density. The average values of soil constants are determined and are shown in Table 3. The attenuation rate values obtained showed good agreement with the value reported in Balan et al. [12]. The k and n values obtained can be used for finding peak particle velocity of river sand, silty sand and red soil at any hammer

Table 3 Soil dependent constants

Soil type	k	n
Lateritic soil	0.11	1.4
River sand	0.07	1.30
Silty sand	0.10	1.35

energy and at any distance from the source. It is possible to predict the level of vibration is within limit or not using the threshold values set by different countries.

4   Conclusions

Laboratory model studies were conducted by fabricating a model to investigate the wave propagation characteristics and attenuation of waves in different types of soil using an impact hammer. The effect of vibration by varying different parameters (type of soil, relative density, drop height, and distance from source) was studied. The acceleration induced in the soil was measured using ADXL335 accelerometers and data acquisition system placed at different positions. Peak particle velocity and displacements were also found out from the acceleration values with the help of SeismoSignal software.

- The test setup developed in the laboratory can reasonably predict the wave propagation and attenuation in soil.
- The peak vertical acceleration (PVA) observed at 0.25 m from source is more than that of PVA value observed at 0.45 m, this is due to attenuation of waves due to increasing distance from the source.
- Relative density of soil influences wave propagation. PVA recorded shows an increasing trend as the relative density increases.
- PVA recorded in all conditions increases as hammer energy increases.
- Red earth gives highest value for peak vertical acceleration and peak particle velocity compared to river sand and silty sand. This may be due to cohesion and more interparticle attractions.
- Soil dependent constant for three soils was obtained and are found to be in agreement with those existing in literature.

References

1. Wiss JF (1981) Construction vibrations: state of the art. J Geotech Eng Div 107(GT2):167–181
2. Masoumi HR, Degrande G, Lombaert G (2007) Prediction of free field vibrations due to pile driving using a dynamic soil-structure interaction formulation. Soil Dyn Earthquake Eng 27(2):126–143
3. Jaya V, Prajil PT, Balan K (2016) Development of predictive equation for vibration due to DMC piling. Indian Geotech J
4. Deckner F, Viking K, Hintze S (2012) Ground vibrations due to pile and sheet pile driving—prediction models of today. In: Proceedings of the 22nd European young geotechnical engineers conference, Gothenburg, Sweden
5. Ali H, Castellanos J, Hart D, Nukunya B (2003) Real time measurement of the impact of pile driving vibrations on adjacent property during construction. Transportation Research Board Annual meeting (CD-ROM), Washington

6. Selby AR (1991) Ground vibrations caused by pile installation. In: Proceedings of the 4th international conference ion piling and deep foundations, Netherlands
7. Svinkin MR (2006) Mitigation of soil movements from pile driving. Practice periodical ion structural design and construction. ASCE
8. Kim DS, Lee JS (2000) Propagation and attenuation characteristics of various ground vibrations. Soil Dyn Earthquake Eng 19(2):115–201
9. Amick H, Gendreau M (2000) Construction vibrations and their impact on vibration-sensitive facilities. ASCE
10. Ooi GL, Wang YH (2014) Applying MEMS accelerometers to measure ground vibrations and to characterize landslide initiation features in laboratory flume test. Research Gate
11. Svinkin MR (2002) Predicting soil and structure vibrations from impact machines. J Geotech Geoenviron Eng 128(7):602–612
12. Balan K, Jaya V, Arun C (2015) Prediction of ground vibrations produced in DMC type of piling through soft and hard strata. Indian Geotech J

Experimental Estimation of Fabric in Granular Materials Using Shear Wave Velocity Measurements

Mandeep Singh Basson, Jasmine Miller, and Alejandro Martinez

Abstract The arrangement of soil particles and inter-particle contacts constitutes the basis of the soil fabric, which influences the behavior of sandy and clayey soils and can lead to anisotropic soil properties and behavior. Experimental studies have quantified soil fabric using non-destructive methods, such as X-ray computed tomography, which require specialized equipment and complex analysis techniques. Such studies have reported the effect of soil fabric on the small strain shear modulus (G_{max}) and shear strength and dilative behavior of coarse- and fine-grained soils. The purpose of this study is to develop an indirect measure of coarse-grained soil fabric using shear wave velocity (V_s) measurements for coarse-grained materials with different particle shapes. V_s is obtained in different directions using a multi-bender element system consisting of five bender element pairs. The test results are presented as polar distributions of V_s, indicating that particle shape and sample preparation methods influence the stiffness anisotropy. The results highlight the potential of using V_s measurements in different orientations to obtain an indirect estimation of a soil specimen's fabric.

Keywords Granular materials · Fabric anisotropy · Shear wave velocity

1 Introduction

Due to their particulate nature, the behavior of granular materials such as sandy and gravelly soils is affected by the geometrical arrangement of particles, interparticle contacts, and void spaces. Often times, soil fabric is anisotropic, leading to anisotropy in stiffness [1–9], compressibility [2], undrained shear strength [10], and permeability [4]. Anisotropy in soil properties and behavior is a consequence of (i) the inherent fabric which is a result of deposition and post-deposition processes and the gradation and particle shape and (ii) the stress anisotropy resulting from the state of stresses which affects the forces transmitted at interparticle contacts. This

M. S. Basson (✉) · J. Miller · A. Martinez
University of California, Davis, CA 95616, USA
e-mail: mbasson@ucdavis.edu

directional dependence can be directly investigated by measurements of particle and contact orientations or indirectly investigated by measurements of, for instance, skeleton stiffness along different orientations [4].

Shear stiffness at low strains ($<10^{-4}$%, G_{max}) is a fundamental soil property used in analysis of soil behavior and design of geostructures [3, 6, 8, 11–14]. This parameter is related to the soil shear wave velocity (V_s) according to the following relationship:

$$G_{max} = \rho V_s^2 \tag{1}$$

where ρ is the density of the soil. Therefore, a large body of research has been dedicated to the evaluation of V_s either in the laboratory or in the field [7, 11, 12, 15, 16]. The shear stiffness of the soil mass is affected by the interactions between particles, interparticle contact behavior (elastic, brittle, or viscoplastic), and soil fabric. Therefore, anisotropy in stiffness is related to anisotropy in interparticle interactions and fabric [2, 6–8, 15, 17–19]. One advantage of using V_s to estimate G_{max} is that the propagation of shear waves through the soil medium is a low-strain perturbation which does not alter the fabric or cause permanent deformations. Thus, it effectively provides a non-destructive and repeatable measurement.

Various researchers have elaborated on the use of piezoelectric Bender Elements (BEs) as actuators and receivers to measure the shear wave velocity of soil specimens in the laboratory [11, 12, 20–24]. The anisotropy in shear stiffness can be obtained by comparing the V_s measurements from bender elements installed in the vertical and horizontal orientation across a specimen. In addition, the evolution of the shear stiffness can be obtained during sample preparation, consolidation, and shearing [5, 8, 23]. Although these studies provide indirect evidence that the anisotropy in V_s is related to fabric anisotropy, it remains a challenging task to obtain an angular representation of fabric with standard laboratory equipment. This would enable researchers to perform investigations on the effect of fabric on soil behavior and on the evolution of fabric during soil shearing which would inform the development of advanced constitutive models for geotechnical analysis and design.

This paper describes the development of a multi-bender element testing setup for the estimation of fabric anisotropy in laboratory specimens. This testing setup employs several BE pairs that transmit shear waves throughout the specimen in different orientations during isotropic compression. Various granular materials, including glass beads, long grain rice, and natural sand, were tested to highlight the effect of particle shape and sample preparation procedures on the evolution of V_s along different orientations. These results are used to generate polar histograms of V_s which suggest that the proposed system can be used to indirectly estimate fabric anisotropy in the laboratory.

2 Laboratory Experimental Procedure

2.1 Bender Element Configuration

The orientation of the different BEs in the multi-bender element system was selected based on previous fabric studies using the discrete element method (DEM) [1]. Based on the polar histograms of contact normal and normal contact force for granular materials under isotropic compression as shown in Fig. 1a, the BEs were oriented at the angles of 90° (vertical), 75°, 65°, 55°, and 50°, respectively. The bender elements consist of standard piezoelectric actuators, part number T220 from Piezo Systems Inc. The BEs were coated with two layers of epoxy raisin after a parallel connection was made between the two electrodes. Finally, the coated BEs were embedded in polycarbonate end caps diameter and height of 71 mm and 50 mm, respectively. Polycarbonate was chosen for its workability and insulation properties. The BEs were embedded in the end caps with silicone resin such that they had an average free length of 4 mm. Figure 1b shows the holes in the polycarbonate caps and Fig. 1c shows the bottom cap with all the embedded BEs. An external vacuum pump is used to control the effective stress within the specimens; this vacuum was applied through ports on the top and bottom caps that were connected to the specimen through slits. The slits were covered with wire mesh which was used to ground the system and to avoid clogging of the lines with particles.

A waveform generator that produced a square wave with a voltage of 4.5 V was used to drive the BEs, according to recommendations by [21]. The square wave was sent through BEs embedded in the top cap and received through the BEs embedded in the bottom cap. The received signal was first filtered using a butterworth filter and then boosted with a gain of 20. Finally, both the transmitted and the received signals were fed into an oscilloscope (PicoScope) for analysis.
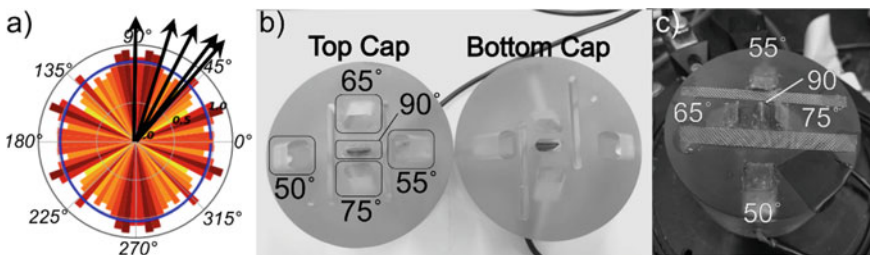
Fig. 1 **a** Polar histogram of contact normal during isotropic compression from DEM simulations from [1] with arrows indicating orientation of BEs in multi-bender element system, **b** machined holes in the polycarbonate caps for the BEs, **c** bottom cap with all the BEs embedded

2.2 Tested Materials and Sample Preparation

Three materials were tested to study the effect of particle shape and fabric on the angular variation shear wave velocities on dry specimens (Fig. 2). Monosized glass beads with a particle diameter of 0.5 mm were used to prepare specimens with small to negligible fabric anisotropy. Long grained rice was used to simulate the prolate particle shape with an aspect ratio of 3.94. Monterey sand, whose particles have an average sphericity of 0.89 and aspect ratio of 1.34, was used as the natural sand material.

Previous studies have highlighted the effect of sample preparation on the fabric of soil specimen which leads to considerable changes in responses such as stiffness and K_o [1, 7], undrained shear strength [10], and accumulation of deformations [7, 19]. Samples of glass beads, long grain rice, and Monterey sand were prepared using the dry deposition (DD) method during which the oven-dried particles were poured into the specimen mold in several layers using a funnel. The funnel was kept slightly above the surface of the material for each layer and gradually raised with a constant velocity to deposit the particles uniformly. Additional samples of Monterey sand were prepared by tamping each layer after dry deposition with the intention of creating a different initial fabric. Dry deposition produces an initial anisotropic fabric with more contacts oriented in the vertical direction, whereas tamping randomizes the orientation of the contacts, thereby decreasing the initial fabric anisotropy [25]. Once a final specimen height of 33 mm was reached, the top cap was inserted, and a vacuum of 10 kPa was applied to the specimen. The isotropic stress was increased from 10 to 60 kPa in 10 kPa increments and then decreased back to 10 kPa. Shear wave velocity measurements were taken for all the five BE pairs for each stress increment/decrement. To determine the density and void ratio of the specimens, their diameter was measured at three different positions and their height was taken at four points for each stress increment/decrement. The void ratios at 60 kPa were 0.52 for glass beads, 0.45 for rice, 0.75 for DD Monterey sand, and 0.66 for tamped Monterey sand. Although there is a difference in void ratio for the tamped and dry deposited samples of Monterey sand, the results from these specimens are used to investigate the effect of sample preparation technique. Figure 3 shows photographs of long grain rice and Monterey sand specimens at 60 kPa. The rice specimen shows that the particles are not clearly arranged in a preferential orientation.
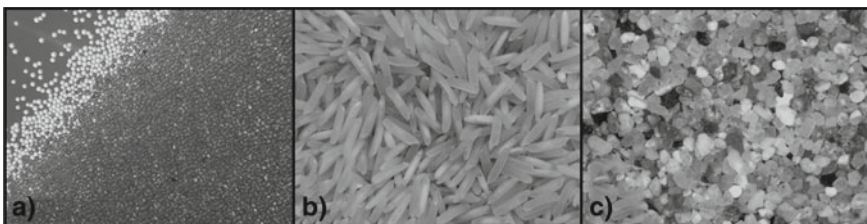

Fig. 2 Different tested materials, **a** glass beads, **b** rice, **c** monterey sand

Fig. 3 Prepared sample at 60 kPa for rice (Left) and monterey sand (Right)

3 Results and Discussion

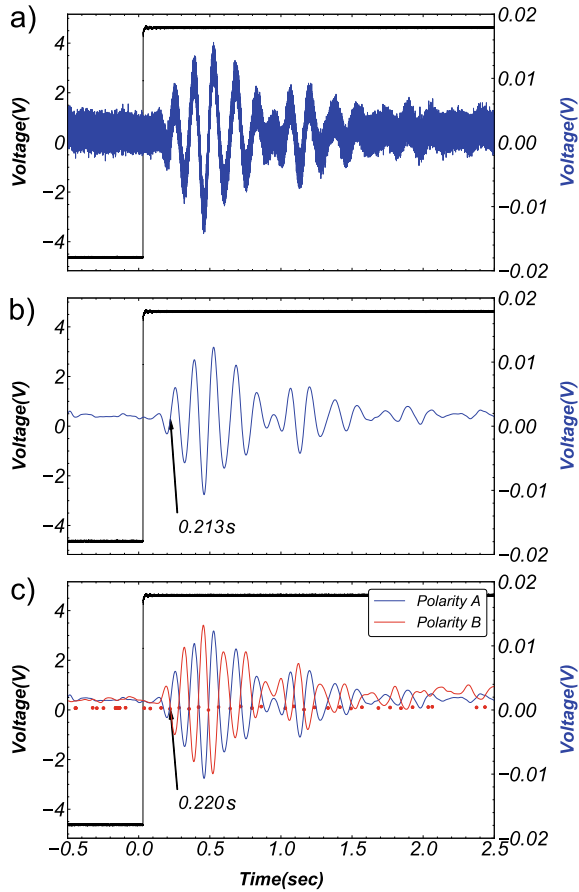### 3.1 Determination of Travel Time

The propagation of shear waves in granular materials is a complex physical phenomenon which produces uncertainty in the signal interpretation, especially in the determination of travel time [12, 20–22, 24, 26, 27]. Furthermore, wave reflections, near field effects, BE directivity, and interference from compression waves add complexity and uncertainty in determination of travel times. Travel times were determined in this investigation based on visual identification of deflection in the received signal [21, 24, 27]. The initial part of the received signal contains small features due to near field and boundary effect. After the first deflection, the received signal reaches the first peak and starts to reverse in direction. The point of intersection of the reversing signal and the zero line is the point of first reversal, which was taken as the point of first arrival in this study. This travel time based on the point of first reversal eliminates the near field effects and matches with the travel time from signal matching techniques [21].

Figure 4a shows the typical raw unfiltered transmitted and received signal in a glass bead specimen confined isotropically at 60 kPa. The transmitted signal is shown in black and the received is shown in blue. After the noise is filtered using a butterworth filter, the time of first arrival is determined as described above. Figure 4b shows the filtered signal along with the black arrow pointing at the point of first reversal.

To verify the accuracy of the determination of the point of the first arrival, additional measurements were taken at different stresses with the polarity of the transmitting BE reversed. The received signals with the original polarity (Polarity A) and the reversed polarity (Polarity B) are plotted in Fig. 4c. The point at which the signals intersect each other was taken as the point of the first arrival. The difference in the time of arrival from visual interpretation (213 ms) and the polarity reversal (220 ms)

is around 3%, indicating the negligible difference between both methods. The wave travel distance was computed using the sample height, the protrusion of each BE outside the end caps, and any tilting of the end caps. The shear wave velocity was computed by dividing the travel distance between each BE pair by the corresponding time of first arrival.

3.2 Influence of Confining Stress on V_s

Different relationships between the shear wave velocity and the effective confining stress have been proposed in the literature [2, 11, 15, 17, 28, 29]. Most relationships take the form of a power law, such as:

$$V_s = \alpha \left(\sigma_m' \right)^{\beta} \qquad (2)$$

where σ_m' is the mean effective stress in the polarization plane, α is the shear wave velocity at an effective confining stress of 1 kPa, and β is an exponent that captures the sensitivity of the skeletal shear stiffness to σ_m'. The β exponent reflect the nature of interparticle contacts and both the α coefficient and β exponent capture changes in fabric during loadings. For an isotropic stress state, σ_m' is the effective confining stress on the specimen. Increases in effective confining stress cause both change in contact stiffness and change in fabric through rearrangement of particles [2, 15, 17].

The V_s measurements from the BE pairs in different orientations follow a power law with mean effective stress as described in Eq. 2 and shown in Fig. 5. The magnitude and evolution of V_s with increasing mean effective stress for the glass bead specimen are nearly identical in the five different orientations. This is due to the negligible fabric anisotropy induced by the spherical particles and the isotropic state of stresses. For the rice specimen, there is a consistently larger V_s for the BE pair oriented at 65°; however, the evolution of V_s is similar for the BE pairs oriented at 50°, 55°, 75°, and 90°. The results from the dry deposited Monterey sand specimens show a decrease in V_s with decreasing angle of the BE pair. This indicates that the specimen is stiffer in the vertical orientation. Since the state of stresses is isotropic, this anisotropy in V_s is produced by anisotropy in fabric. The V_s for the tamped
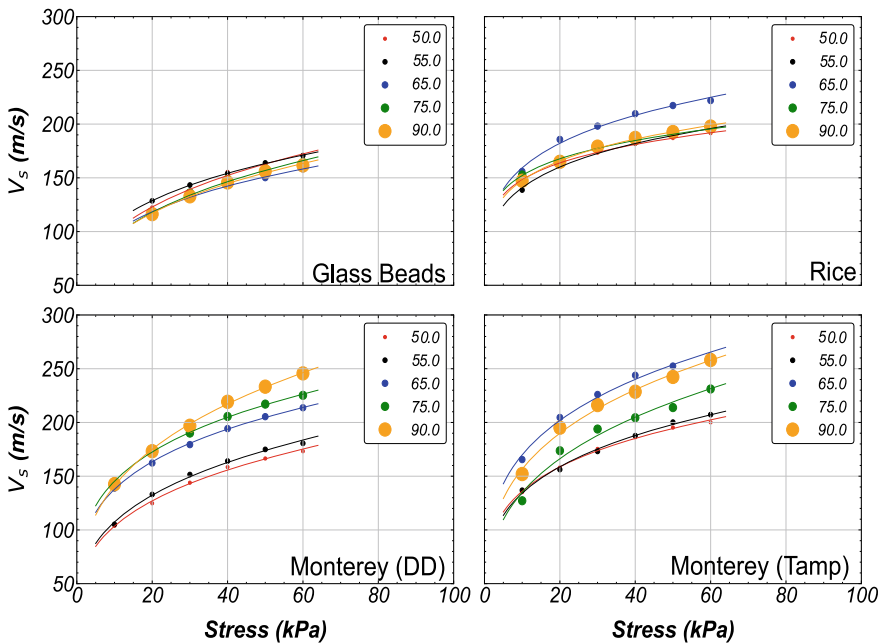
Fig. 5 Increase in the V_s with an increase in confining stress for different bender orientation and different materials

Fig. 6 β exponents and α factors from glass beads, rice, and Monterey sand specimens
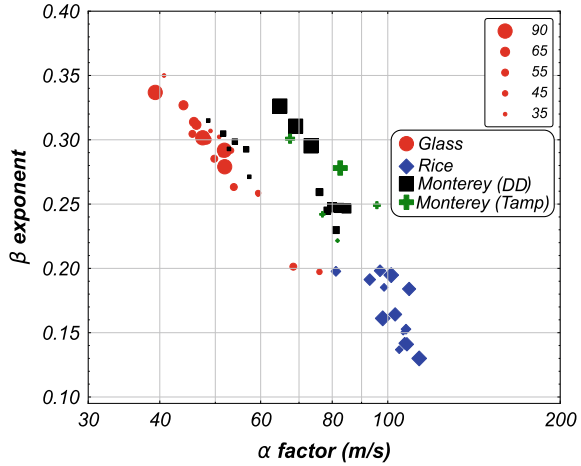
Monterey sand specimen is higher than that of the DD Monterey sand specimen due to the former's greater density. In addition, the V_s is greater at an orientation of 65° for the tamped Monterey sand specimen.

The α coefficient and β exponent, from fits using Eq. 2, were determined for all five BE pairs at all the different mean effective stresses. The results are plotted in Fig. 6, showing an inverse relationship between α and β values. The results and trends are in agreement with observation reported in the literature for soils, sands, clays, and cemented rocks [2]. Analytical solutions and experimental data on interparticle contact deformation at constant fabric justify the following β values: 0 for ideal solid or cemented rocks, 1/6 for elastic Hertzian contact, and 1/4 for rough or angular contact [17].

Results for glass beads show a low α value and a high β value, in agreement with ranges reported in the literature [16, 30]. The relatively high value of β exponent for glass beads can be attributed to their surface roughness, initial fabric induced by the DD preparation technique, and the particle rearrangement (fabric changes) during compression [16, 30]. The results for long grain rice specimen indicate a higher α value and lower β value and are also within the range reported in the literature [26]. This combination usually indicates viscoplastic deformation of contacts upon early loading. This contact deformation, as well as the presence of adsorbed moisture, caused a slight cementation between the rice particles which was observed after the removal of the sample. The results for the Monterey sand specimen lie in between the results for the glass beads and rice specimens. For the dry deposited sample, the response is closer to that of the glass beads sample at lower stresses, gradually moving towards the response of rice as the confining stress is increased. These results indicate two extreme ends in the evolution of V_s with confining stress for granular materials; one end being the results of nearly spherical shape of glass beads and the other end being the results of prolate shape of rice particles, with the results of natural soil particles in between these two extreme ends.

3.3 Angular Variation of V_s for Different Confining Stresses

Vector analysis of contact normal unit vectors, contact normal force vectors, and contact shear force vectors have been used to investigate the anisotropy of soil fabric and its evolution as a response to the applied loading. This anisotropy in fabric is typically represented either in the form of a tensor or in the form of a polar histogram [e.g., 3, 8, 18, 23]. The polar histogram for contact normal and contact normal force is similar and is approximated by the following analytical expression [7]:

$$E(\theta) = E_{avg}(1 + a \cos 2(\theta - \theta_n)) \tag{3}$$

where a is the magnitude of anisotropy, θ_n is the preferential orientation of the angular distribution, and E_{avg} is $1/2\pi$ for contact normal distribution or average contact force (f_{avg}) for contact normal force distribution. An isotopic distribution would be circular with an anisotropy value, a, close of zero, whereas an anisotropic distribution would tend toward a peanut or egg shape with a high anisotropy value. The V_s measurements from the different BE pairs can be used to determine the angular distribution. This distribution can be fitted with an equation that is analogous to Eq. 3, as follows:

$$V_s = V_{s,avg}(1 + a_n \cos 2(\theta - \theta_n)) \tag{4}$$

where a_n is the magnitude of V_s anisotropy, θ_n is the preferential orientation from horizontal of the distribution, and $V_{s,avg}$ is the average V_s for a given mean effective stress. The polar plots for V_s were developed based on the assumption of cross-anisotropy in the specimen for different materials. This assumption is expected to hold true for the imposed isotropic state of stresses [31] and the cylindrical shape of the specimens. The polar plots for different materials are shown in Fig. 7, and the evolution of a_n is shown in Fig. 8.

Due to the similar V_s in all directions for the glass bead specimen, the corresponding polar plots for the different mean effective stresses are concentric circles (Fig. 7). The V_s anisotropy for glass beads is zero for all the stress levels (Fig. 8). For the rice specimen, the V_s at 65° is greater than that at the other orientations. However, the overall distribution is relatively uniform, possibly due to the random orientation of particles, with small anisotropy values between 0.010 and 0.013. The angular distributions for DD Monterey sand specimens are peanut-shaped with a high V_s anisotropy of around 0.25. This anisotropy is the combined effect of particle shape and the initial fabric resulting from the DD preparation. The a_n value for Monterey sand specimen prepared by tamping is small compared to a_n value for DD Monterey sand specimen. The tamping method produces a random orientation of particles which leads to a decrease in the initial fabric anisotropy; however, the elongated shape produces a slight anisotropy.
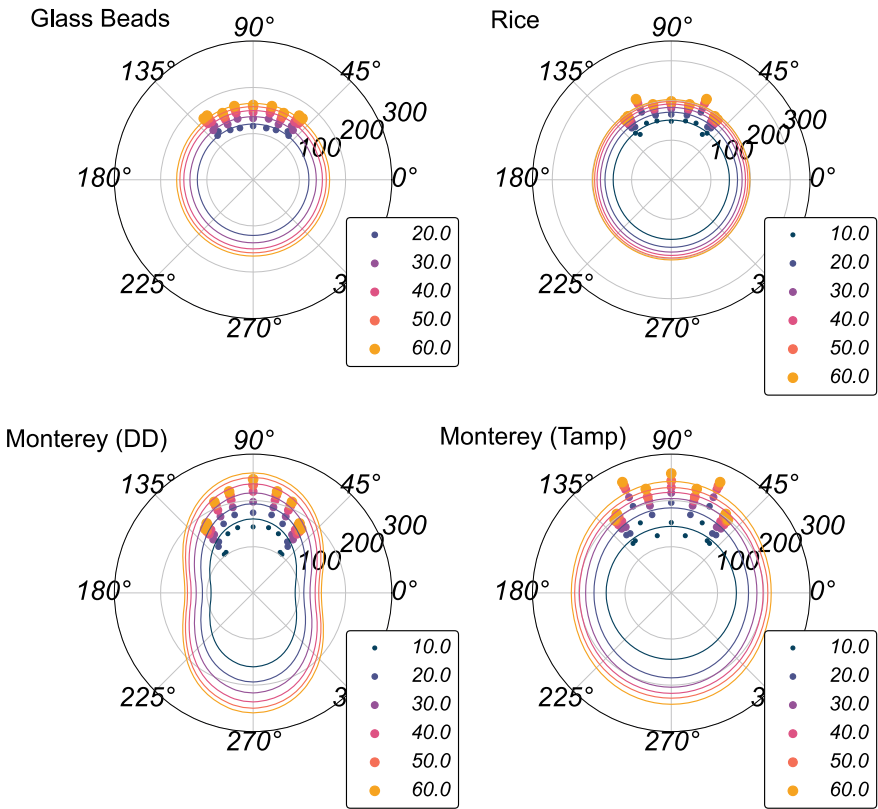
Fig. 7 Polar plots of V_s for different confining stresses for different materials; warmer colors denote higher effective confining stresses

Fig. 8 Evolution of a_n with confining stress for different materials
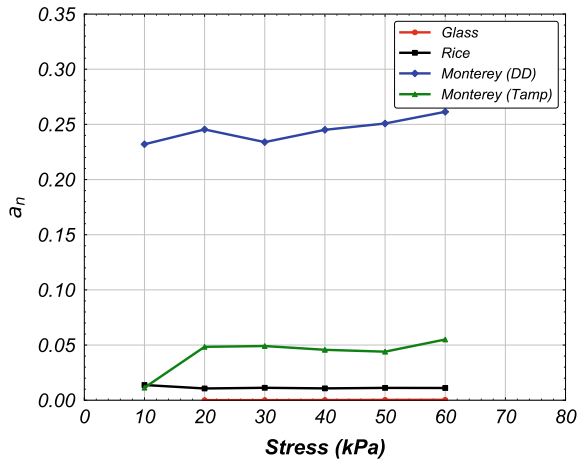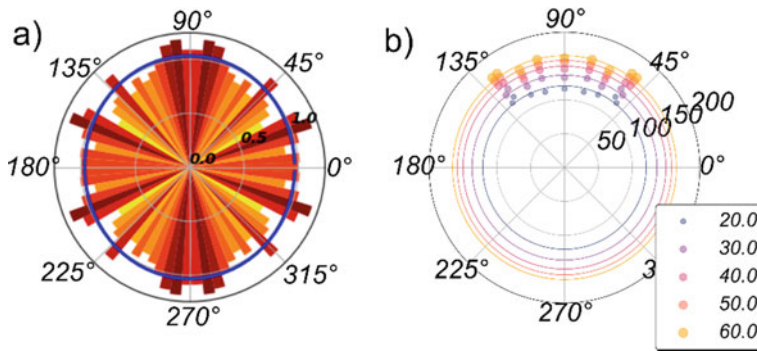
Fig.9 a Contact normal force anisotropy for circular particles under isotopic compression from [1], **b** V_s anisotropy for glass beads under isotropic compression

The polar histogram of contact normals and shear wave velocity follows similar trends. For instance, the histogram for contact normal from simulations on an isotropically consolidated specimen composed of spherical particles is circular, indicating an isotropic distribution (Fig. 9). In a similar manner, the V_s histogram obtained with the multi-bender element system for the specimen of glass beads is also circular, indicating an isotropic distribution (Fig. 9). While the similarity in the polar histograms of various fabric quantities with that of V_s still needs to be verified for different particle shapes, the results presented herein suggest that V_s measurements can provide an indirect measurement of the fabric anisotropy in soil specimens.

4 Conclusion

In this paper, the efficacy of using the anisotropy in shear wave velocity as an indirect measurement of fabric anisotropy is investigated. A novel multi-bender element apparatus, with five pairs of bender elements in different orientations, was developed, and wave propagation experiments were conducted for three different materials under varying magnitudes of isotropic compression. The particle shape, particle arrangement, and contact behavior have an important effect on the anisotropy in shear stiffness, which manifests in the directional variation of V_s. The fabric anisotropy and its direction were estimated by curve fitting of the polar histograms of V_s for different confining effective stresses. Spherical glass beads produced near isotropic V_s distributions, whereas the Monterey sand produced a peanut-shaped, anisotropic V_s distribution. This newly proposed testing setup can provide a complete angular distribution of V_s, may be used as an indirect measurement of a specimen's fabric anisotropy.

References

1. Basson MS, Martinez A (2020) A DEM study of the evolution of fabric of coarse grained materials during oedometric and isotropic compression. In: Proceedings, geo-congress 2020, Minneapolis, Minnesota, USA
2. Cha M, Santamarina JC, Kim H-S, Cho G-C (2014) Small-strain stiffness, shear-wave velocity, and soil compressibility. J Geotech Geoenviron Eng 140:06014011
3. Fu P, Dafalias YF (2015) Relationship between void- and contact normal-based fabric tensors for 2D idealized granular materials. Int J Solids Struct 63:68–81
4. Kuhn MR, Sun W, Wang Q (2015) Stress-induced anisotropy in granular materials: fabric, stiffness, and permeability. Acta Geotech. 10:399–419. https://doi.org/10.1007/s11440-015-0397-5
5. Li B, Zeng X (2014) Effects of fabric anisotropy on elastic shear modulus of granular soils. Earthq Eng Eng Vibr 13:269–278
6. Payan M, Khoshghalb A, Senetakis K, Khalili N (2016) Small-strain stiffness of sand subjected to stress anisotropy. Soil Dyn Earthq Eng 88:143–151
7. Rothenburg L, Bathurst RJ (1989) Analytical study of induced anisotropy in idealized granular materials. Geotechnique 39(4):601–614
8. Wang YH, Mok CM (2008) Mechanisms of small-strain shear-modulus anisotropy in soils. J Geotech Geoenviron Eng 134:1516–1530
9. Yang J, Gu XQ (2013) Shear stiffness of granular material at small strains: does it depend on grain size? Géotechnique 63:165–179
10. Yimsiri S, Soga K (2001) Effects of soil fabric on undrained behavior of sands. In: International conferences on recent advances in geotechnical earthquake engineering and soil dynamics, pp 7
11. Bartake PP, Singh DN (2007) Studies on the determination of shear wave velocity in sands. Geomech Geoeng 2:41–49
12. Blewett J, Blewett IJ, Woodward PK (2000) Phase and amplitude responses associated with the measurement of shear-wave velocity in sand by bender elements. Can Geotech J 37:10
13. Stokoe KH, Santamarina JC (2000) Seismic wave based testing in geotechnical engineering. In: International conference on geotechnical and geological engineering, pp 1490–1536
14. Stokoe KH, Wright SG, Bay JA, Roesset JM (1994) Characterization of geotechical sites by SASW method. Geophys Charact Sites
15. Cho G-C, Dodds J, Santamarina JC (2006) Particle shape effects on packing density, stiffness, and strength: natural and crushed sands. J Geotech Geoenviron Eng 132:591–602
16. Sharifipour M, Dano C, Hicher P-Y (2004) Wave velocities in assemblies of glass beads using bender-extender elements. In: 7th ASCE engineering mechanics conference, Newark, DE, United States
17. Cascante G, Santamarina JC (1996) Interparticle contact behavior and wave propagation. J Geotech Eng 122:831–839
18. Mital U, Kawamoto R, Andrade JE (2019) Effect of fabric on shear wave velocity in granular soils. Acta Geotechnica
19. Roesler SK (1979) Anisotropic shear modulus due to stress anisotropy. J Geotech Eng Div ASCE. https://doi.org/10.1016/0148-9062(79)90065-2
20. Arulnathan R, Boulanger RW, Riemer MF (1998) Analysis of bender element tests. Geotech Test J GTJODJ 21(2):120–131
21. Lee J-S, Santamarina JC (2005) Bender elements: performance and signal interpretation. J Geotech Geoenviron Eng 131:1063–1070
22. Leong EC, Cahyadi J, Rahardjo H (2009) Measuring shear and compression wave velocities of soil using bender–extender elements. Can Geotech J 46:792–812. https://doi.org/10.1139/T09-026
23. O'Donovan J, Ibraim E, O'Sullivan C, Hamlin S, Muir Wood D, Marketos G (2016) Micromechanics of seismic wave propagation in granular materials. Granular Matter 18

24. Viggiani G, Atkinson JH (1995) Interpretation of bender element tests. Geotechnique. https://doi.org/10.1680/geot.1995.45.1.149
25. Yang ZX, Li XS, Yang J (2008) Quantifying and modelling fabric anisotropy of granular soils. Géotechnique 58:237–248. https://doi.org/10.1680/geot.2008.58.4.237
26. Aloufi M, Santamarina JC (1995) Low and high strain macrobehavior of grain masses: the effect of particle eccentricity. Trans ASAE 38:877–887
27. Ogino T, Kawaguchi T, Yamashita S, Kawajiri S (2015) Measurement deviations for shear wave velocity of bender element test using time domain, cross-correlation, and frequency domain approaches. Soils Found 55:329–342
28. Hardin B, Richart F (1963) Elastic wave velocities in granular soils. J Soil Mech Found Div
29. Liu X, Yang J (2018) Shear wave velocity in sand: effect of grain shape. Géotechnique 68:742–748
30. Kang X, Bate B, Ge L (2014) Characterization of shear wave velocity and its anisotropy in uniform granular materials. In: Geo-congress 2014 technical papers. American Society of Civil Engineers, Atlanta, Georgia, pp 2029–2041
31. Kuwano R, Jardine RJ (2002) On the applicability of cross-anisotropic elasticity to granular materials at very small strains. Géotechnique 52:727–749. https://doi.org/10.1680/geot.2002.52.10.727

Shear Behavior and Strain Localization of Kutch Soil

Tanaya Mukati, Rasikh Nazir, and Ajanta Sachan

Abstract The mechanical behavior of soil mass is governed by its mode of deformation. When homogeneous soil mass is subjected to large deformations, it can create concentrated zones of localized deformations within the soil mass. These non-uniformities can be attributed due to the imposed testing conditions or the imperfections inherited within the soil mass. The initiation and propagation of these localized deformations can strongly impact the mechanical behavior of soil. The non-uniformity due to the testing conditions can be minimized by using lubricated end boundary system. The field conditions can be simulated in a more realistic manner by using lubricated end boundary system as it provides free-free boundary conditions as compared to fixed–fixed boundary conditions in conventional frictional end boundary system. The aim of the current study is to evaluate the shear behavior of silty-sand Kutch soil under lubricated end boundary conditions and correlate the response with strain localization patterns of soil. A series of isotopically consolidated undrained compression (CIUC) tests were performed at varying confining pressures under lubricated end boundary conditions. Digital images of the deforming soil specimen were captured during its shearing stage, and digital image analysis (DIA) was performed to obtain the strain localization patterns of soil specimens at different global axial strain levels at chosen confining pressure. The strain localization analysis exhibited an increased tendency to localized deformations as confining pressure was reduced. The Kutch soil specimens reported the diffused mode of failure for all three confining pressures (100, 200 and 300 kPa).

Keywords Strain localization patterns · Shear behavior · Lubricated boundary restraints · Digital image analysis

T. Mukati (✉) · R. Nazir · A. Sachan
Civil Engineering, Indian Institute of Technology Gandhinagar, Gandhinagar, India
e-mail: tanaya.mukati@iitgn.ac.in

R. Nazir
e-mail: rasikh.nazir@iitgn.ac.in

A. Sachan
e-mail: ajanta@iitgn.ac.in

1   Introduction

The mechanical behavior of soil mass is attributed to its mode of deformation. When a soil mass is subjected to loading at high strain levels, it tends to deform non-uniformly leading to the formation of localized zones of deformation within the soil mass. Hence, it becomes essential to study the mechanism of deformation and failure of soil mass in the field of geotechnical engineering. The strain localization in a soil specimen could occur due to the imperfections possessed by it, non-uniform loading or the boundary conditions [1–5]. Rowe and Barden [6] suggested the use of lubricated boundary conditions with specimens having an aspect ratio of 1, in order to minimize the effect of non-uniform straining throughout the height of the specimen. Therefore, the current study was carried out for soil specimens with an aspect ratio of 1 under lubricated end boundary conditions. Over the years, various numerical studies were carried out to understand the concept of strain localization. However, now with the advancement of technology, the initiation and propagation of strain localization can be monitored experimentally and more accurately. Takano et al. [7] used a combination of digital image correlation and CT-tomography technique to study the evolution of strain localization. Previously, digital image analysis (DIA) was also utilized to analyze the strain localization patterns of the deforming soil specimen [8, 9]. Mostly, the studies presented the nature and analysis of strain localization patterns; however, its correlation with the shear behavior was not much discussed. Generally, these studies were carried out using frictional boundary conditions and limited work was done on lubricated boundary conditions with different confining pressures. The present study involves the investigation of strain localization of silty-sands under lubricated end boundary system at different confining pressures. Digital image analysis was used to evaluate the strain localization contours with an assumption that there was no relative displacement between the membrane and the soil specimen. An attempt was made to correlate the shear strength behavior of silty-sand with its strain localization patterns.

2   Material Properties

The current study was carried out on the soil samples collected from Fatehgarh; an earthen dam located in Kutch district of Gujarat. The in-situ density and water content were measured using core-cutter method and were found to be 2.06 g/cc and 6.7%, respectively. The basic geotechnical properties of the soil sample were evaluated in the laboratory of IIT Gandhinagar. The soil sample was classified as SM type, as per Indian Standard Soil Classification System. The soil was found to have 83% sand, 14% silt and 3% clay content. The specific gravity was obtained to be 2.68. The optimum moisture content and maximum dry density of collected soil were determined to be 7.5% and 2.17 g/cc, respectively.

3 Lubricated End Triaxial Setup and Specimen Preparation

The lubricated end triaxial setup was developed to conduct the strain localization analysis of specimen with aspect ratio 1 [6, 10]. Smooth aluminum platens with six radial drainage points at its periphery were fabricated and used to simulate the lubricated end boundary conditions. A thin layer of silicone grease was applied at the surface of the aluminum platen. A circular latex membrane of 100 mm diameter was placed at the top of the grease layer. Two strips of filter paper (30 mm wide and 360 mm long) were placed on the periphery of the platen in such a way that one half of the width was on top platen and the other half was covering the radial drainage. A circular filter paper of 150 mm diameter was placed on the platen in order to cover all the radial drainage points. In order to analyze the strain localization pattern, a dotted latex membrane with mesh size of 7 mm was used (Fig. 1a).

The solid cylindrical soil specimens were prepared at 95% of maximum dry density (MDD). The cylindrical soil specimens of 100 mm height and 100 mm diameter (aspect ratio 1) were prepared using moist tamping technique, as per ASTM D4767-04. This technique involved the use of a three-piece mold made of aluminum with a base plate and a collar at the top. The soil was divided into three equal parts, and an equal amount of compactive effort was imparted to each layer. In order to ensure uniform bond between the layers, each soil layer was scratched with a knife.
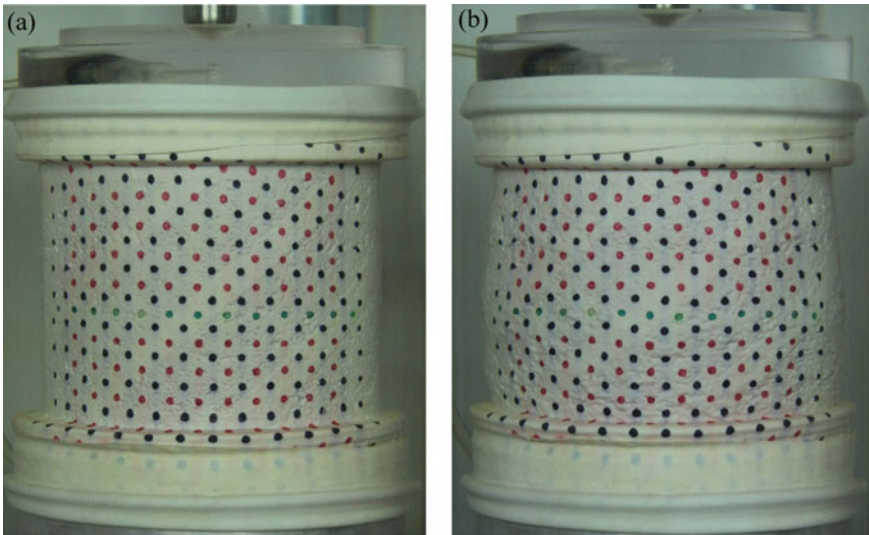
Fig. 1 Images of the soil specimen at **a** 0% global axial strain **b** 16% global axial strain

4   Experimental Program

In the present study, a series of isotropically consolidated undrained compression (CIUC) triaxial tests on lubricated ends were performed at different confining pressures of 100, 200 and 300 kPa [11]. Water flushing and back pressure were used to saturate the specimens. Skempton's pore pressure parameter B was ensured to be above 0.95 before consolidation. All the specimens were sheared at a strain rate of 0.1 mm/min.

To perform digital image analysis (DIA) on deforming specimen, images of the soil specimen were captured during shearing stage with the help of a DSLR camera mounted over a tripod stand. The images were taken for every 0.5 mm deformation, i.e., at an interval of 5 min. These images were processed and strain localization contours were obtained using GeoPIV-RG MATLAB module [12]. In each image about 153 dots, i.e., 17 rows were tracked to analyze strain localization. The surface was assumed to be planar. 8–9 dots were tracked in each row to minimize the effect of curvature. Each image was fed into the module and the centers of the dots were picked manually. The intensity threshold numbers were noted, where the symmetric shaded region was obtained. The lower and upper intensity thresholds were tagged manually to locate the centroid for each dot and an output file containing coordinates was obtained. These coordinate files obtained for all the images, which were utilized to track the relative displacement of the dots. The strain field elements were further determined using Delaunay triangulation. The strain contours were plotted at different global strains to conduct the strain localization analysis.

5   Results and Discussions

5.1   *Shear Strength Behavior of Fatehgarh Soil Under CIUC Triaxial Conditions*

The stress–strain behavior of Fatehgarh soil specimens at different confining pressures of 100, 200 and 300 kPa under CIUC triaxial conditions is shown in Fig. 2a. The peak deviatoric stress was observed to occur around 2% axial strain followed by post-softening response for all the three confining pressures. It was observed that the stiffness of the soil specimen increased with the increase in confining pressure. The effective shear strength parameters c' and ϕ' were obtained to be 0 kPa and 26°, respectively (Fig. 2d). The total shear strength parameters c and ϕ were obtained to be 10 kPa and 19°, respectively (Fig. 2e). All the specimens exhibited bulging at failure during the shearing stage. The strain contours corresponding to small axial strains were also evaluated to evaluate the strain localization initiated before or after the peak stress. The excess pore water pressure response of the soil specimens at different confining pressures was observed to be positive indicating contractive behavior (Fig. 2b). Significant increase in contractive behavior was observed with
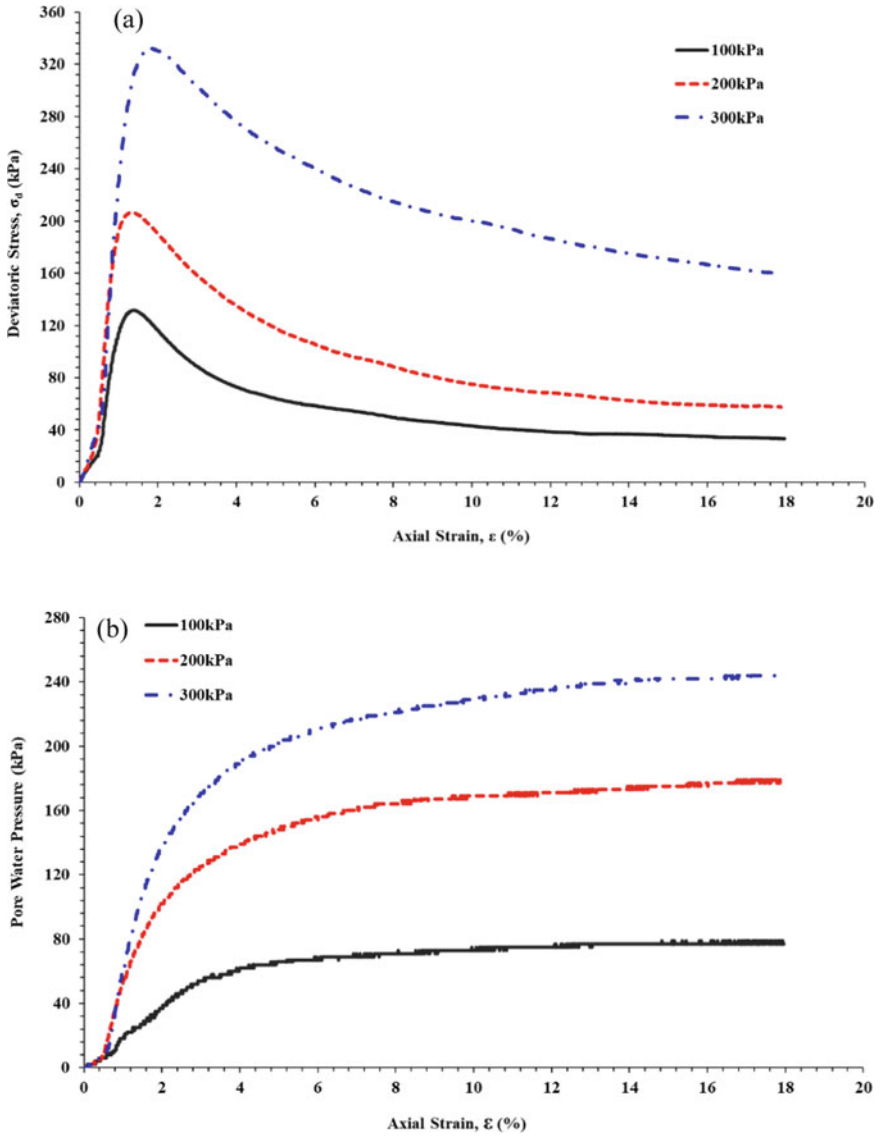
Fig. 2 Shear strength behavior of Fatehgarh soil under CIUC triaxial conditions: **a** deviatoric stress–strain response, **b** pore water pressure response and **c** effective stress paths **d** Modified effective failure envelop (q–p′) **e** Modified failure envelop (q–p)

Fig. 2 (continued)

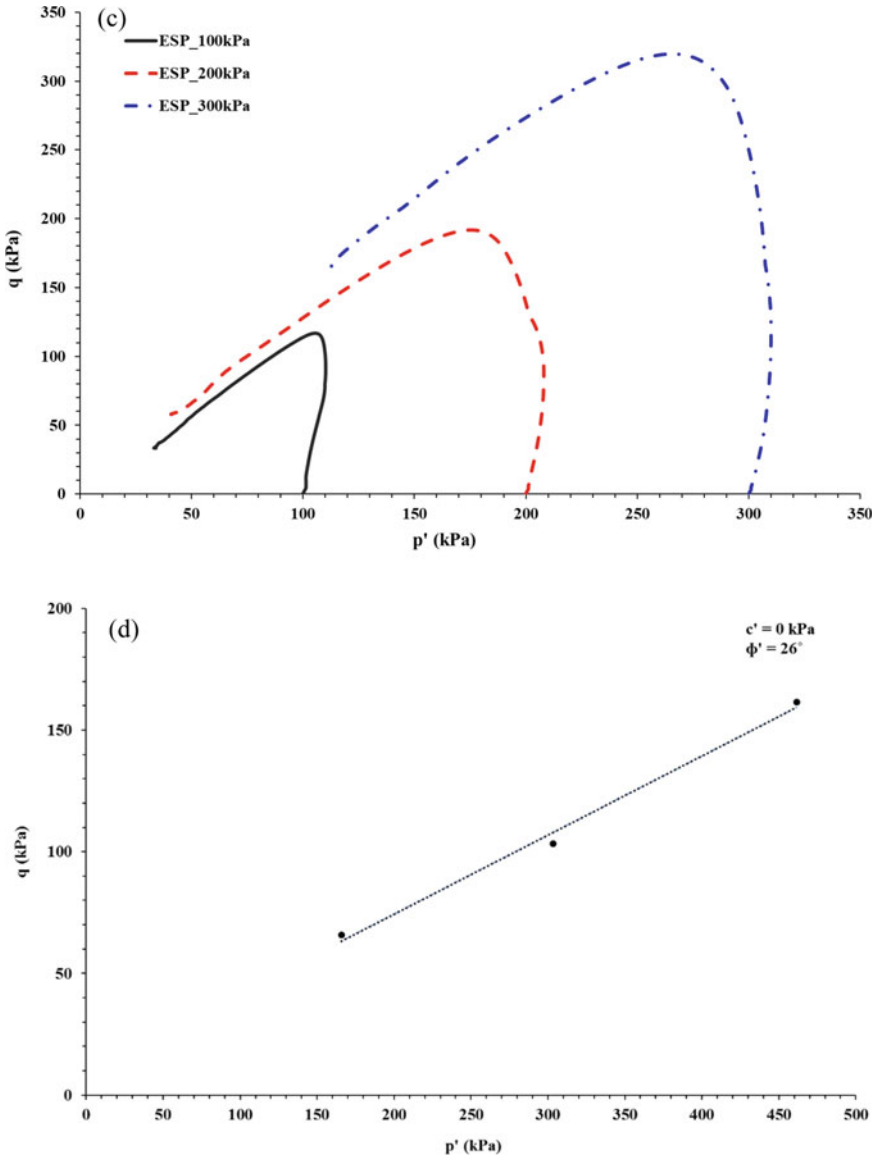the increase in confining pressure. The effective stress paths $(q-p')$ were plotted using MIT model where p' and q were defined using Eqs. 1 and 2, respectively. The effective stress paths moved toward the origin indicating contractive behavior at all three confining pressures, as shown in Fig. 2c. The effective stress paths indicated the tendency of soil specimen to undergo static liquefaction.
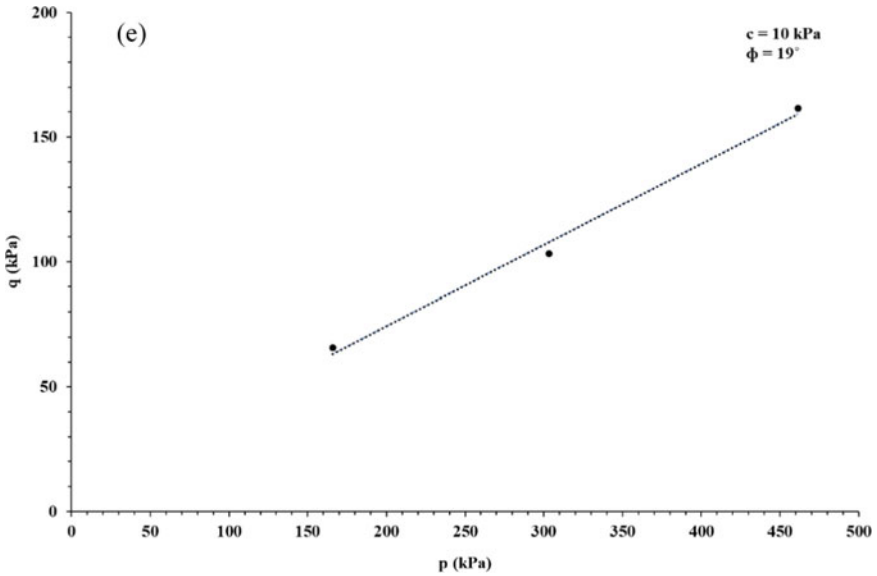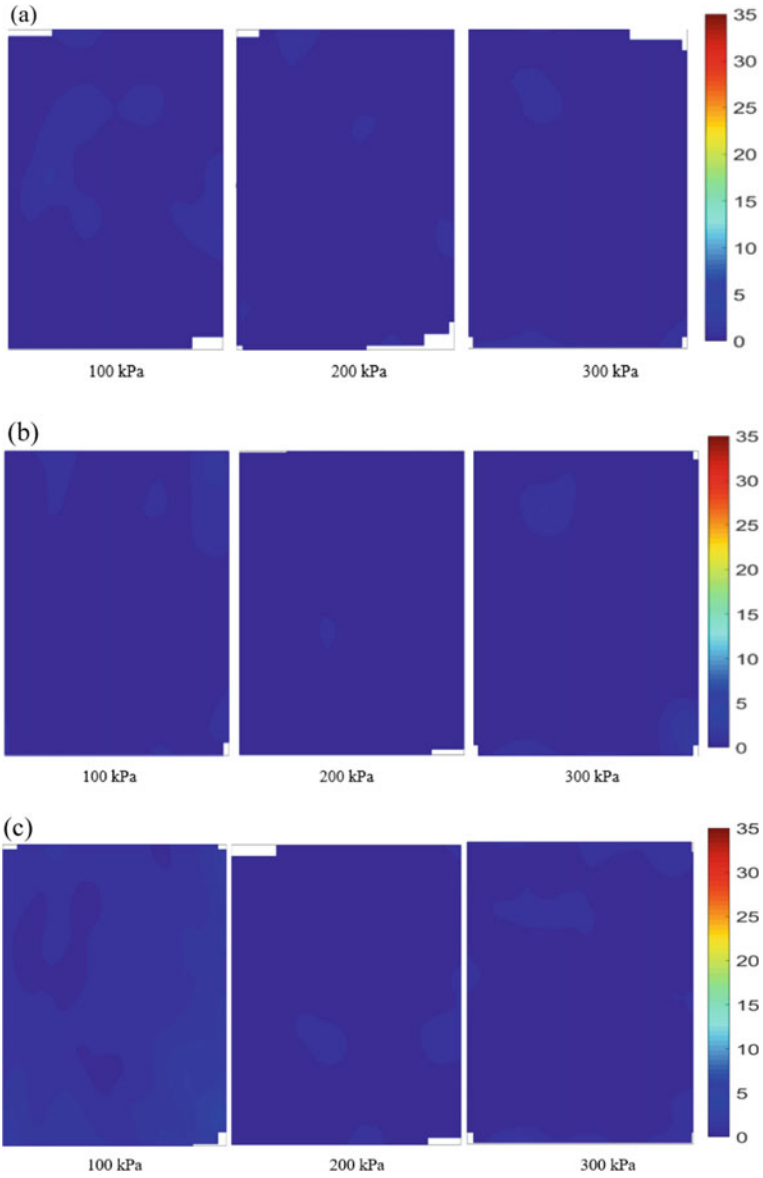
Fig. 2 (continued)

$$p' = \frac{\sigma_1' + \sigma_3'}{2} \tag{1}$$

$$q = \frac{\sigma_1' - \sigma_3'}{2} \tag{2}$$

5.2 Strain Localization Patterns of Fatehgarh Soil Under CIUC Triaxial Conditions

The specimen image captured at 0% global axial strain level was taken as reference to calculate the relative displacement between the dots for the evaluation of strain localization patterns corresponding to different axial global strains, i.e., 0.5, 1, 1.5, 2, 4, 6, 12 and 16%. Figures 3 and 4 depict the strain localization patterns developed at different axial global strain levels corresponding to different confining pressures. For all the three confining pressures (100, 200 and 300 kPa), the maximum local strain of about 35% was observed to develop at a global axial strain of 16%. For 100 kPa confining pressure, the peak deviatoric stress was revealed at an axial global strain of 1.3% (Fig. 2a). However, the variation in the strain localization patterns corresponding to 0.5, 1 and 1.5% global strains was observed to be insignificant (Fig. 3a). The previous strain localization studies reported the initiation of localized deformation before or at the peak deviatoric stress. However, in the present study, the
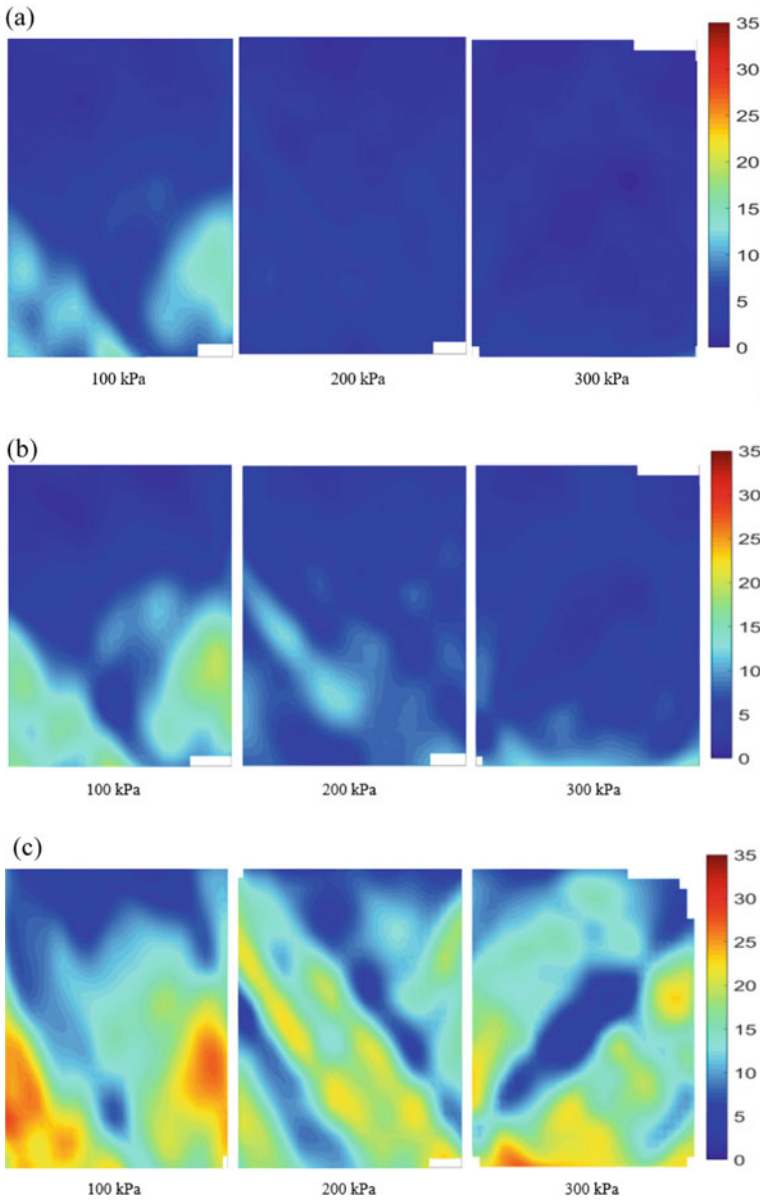
Fig. 3 Strain localization pattern of Fatehgarh soil under CIUC triaxial conditions before failure at **a** 0.5% global strain level, **b** 1% global strain level, **c** 1.5% global strain level and **d** 2% global strain level

(d)

100 kPa   200 kPa   300 kPa
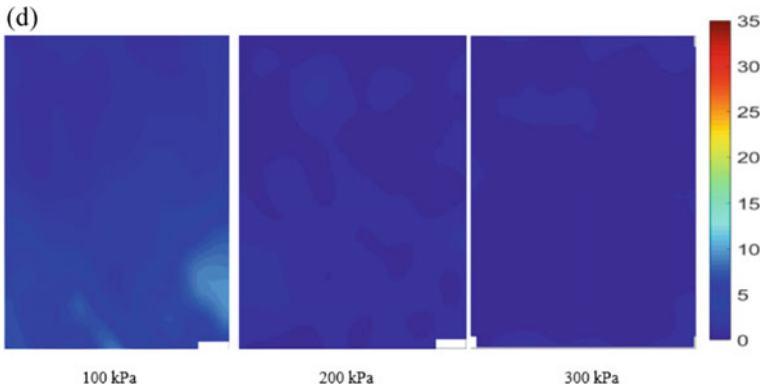
Fig. 3 (continued)

initiation of strain localization was observed to occur after peak deviatoric stress. The onset of localized deformation in specimen subjected to 100 kPa confining pressure was observed at 2% global strain, at which deviatoric stress was 88% of the peak deviatoric stress and maximum local strain was about 10% (Fig. 3d). Beyond 2% of global strain level, the strain localization patterns became more pronounced and intensity of the localized deformations increased throughout the height of the specimen. Similar trend was observed in the soil specimens subjected to 200 and 300 kPa confining pressures. Although the specimens subjected to 200 and 300 kPa exhibited peak deviatoric stress at global axial strain levels of 1.5% and 1.8%, respectively, the initiation of strain localization was not significantly revealed at these strain levels in the strain localization patterns. The localized deformation in specimens subjected to 200 and 300 kPa confining pressure was observed to initiate at a global strain level of 4% and 6%, respectively (Fig. 4a, b). The deviatoric stress at 4% and 6% global strain in specimens subjected to 200 kPa and 300 kPa, respectively, was found to be 65 and 72% of the peak deviatoric stress, respectively. This was due to the specimen subjected to lowest confining pressure acquired higher post-consolidation void ratio as compared to other specimens leading to higher compressibility. Hence, early initiation of local concentrations of strains was observed in the specimens. At 12% global axial strain, the intensity and zones of localized deformation were observed to increase suddenly for all the three confining pressures. There could be a possibility that the localized deformation had already propagated inside the soil specimen; however, the present study is carried out by analyzing the outer surface of the soil specimen only. The strain localization patterns were observed to be more pronounced at higher strains for all the three confining pressures indicating the critical state failure as the dominating failure criterion for this soil. At maximum global axial strain level of 16%, the strain localization patterns for all the three confining pressures exhibited a diffused mode of failure. For all the three confining pressures, the localized deformation was found to initiate from the bottom of the soil specimen and propagate from bottom to top of the specimen's height.

Fig. 4 Strain localization pattern of Fatehgarh soil under CIUC triaxial conditions after failure at **a** 4% global strain level, **b** 6% global strain level, **c** 12% global strain level and **d** 16% global strain level
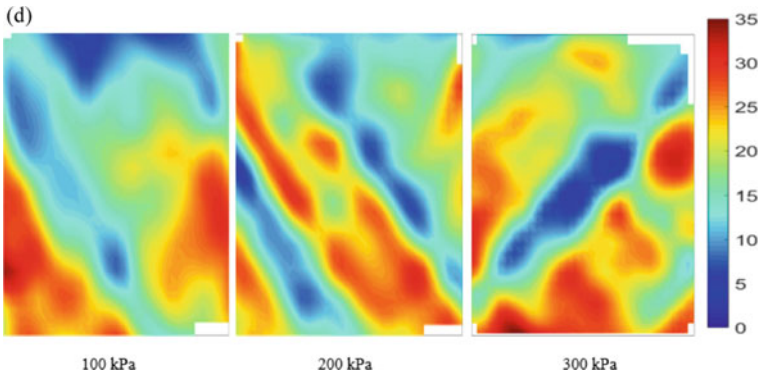
Fig. 4 (continued)

6 Conclusions

Shear behavior and strain localization patterns of Fatehgarh soil were evaluated in the current research by conducting a series of CIUC triaxial tests at different confining pressures of 100, 200 and 300 kPa. Digital image analysis (DIA) technique was used to evaluate the initiation and propagation of non-uniform strains. The key observations of the present study are as follows:

- CIUC triaxial test results indicated the well-defined peak at less than 2% axial strain, followed by the post-peak softening response for all the confining pressures. Bulging was observed in specimens at the time of failure during shear deformation. The excess pore pressure evolution and effective stress path response revealed a contractive behavior of soil at all the three confining pressures.
- Onset of strain localization at 100 kPa confining pressure was observed at 2% global strain. However, the specimens at 200 and 300 kPa confining pressures exhibited the onset of strain localization at 4% and 6% global strain, respectively.
- The zones of localized deformation became more pronounced at higher strain level at all three confining pressures, which indicated the critical state failure as the governing failure criteria for this type of soil.
- For all the confining pressures, the soil specimens exhibited diffused mode of failure.

References

1. Bardet JP (1990) A comprehensive review of strain localization in elastoplastic soils. Comput Geotech 10(3):163–188
2. Desrues J, Lanier J, Stutz P (1985) Localization of the deformation in tests on sand sample. Eng Fract Mech 21(4):909–921

3. Rice JR (1976) Localization of plastic deformation (No. COO-3084/43; CONF-760835-1). Brown Univ., Providence, RI (USA). Div. of Engineering
4. Rudnicki JW, Rice JR (1975) Conditions for the localization of deformation in pressure-sensitive dilatant materials. J Mech Phys Solids 23(6):371–394
5. Wang Q, Lade PV (2001) Shear banding in true triaxial tests and its effect on failure in sand. J Eng Mech 127(8):754–761
6. Rowe PW, Barden L (1964) Importance of free ends in triaxial testing. J Soil Mech Found Div 90(Proc. Paper 3753)
7. Takano D, Lenoir N, Otani J, Hall SA (2015) Localised deformation in a wide-grained sand under triaxial compression revealed by X-ray tomography and digital image correlation. Soils Found 55(4):906–915
8. Lin H, Penumadu D (2006) Strain localization in combined axial-torsional testing on kaolin clay. J Eng Mech 132(5):555–564
9. Sachan A, Penumadu D (2007) Strain localization in solid cylindrical clay specimens using digital image analysis (DIA) technique. Soils Found 47(1):67–78
10. Barden L, McDermott JW (1965) Use of free ends in triaxial testing of clays. J Soil Mech Found Div 91(6):1–24
11. ASTM D4767-11 (2011) Standard test method for consolidated undrained triaxial compression test for cohesive soils. ASTM International, West Conshohocken, PA
12. Stanier SA, Blaber J, Take WA, White DJ (2016) Improved image-based deformation measurement for geotechnical applications. Can Geotech J 53(5):727–739

Evaluation of Wave Propagation Parameters and Attenuation Characteristics of Homogeneous Cohesionless Soil Media

B. Vinoth and Ambarish Ghosh

Abstract A detailed laboratory model study has been carried out to determine wave propagation parameters and attenuation characteristics of homogeneous cohesionless soil media by using shallow surface wave generated due to impact load. Surface waves have been generated due to impact load for varied impact energy levels (4–20 Nm), and motion of soil particles has been measured by using seismic accelerometers on surface of the soil medium for different radial distances (0.4–1.6 m). A simplified analysis procedure has been performed by using correlation of spectral signal of different radial distances to determine wave propagation parameters like Rayleigh wave velocity (V_R, m/s) and Rayleigh wavelength (λ_R, m) and also develop experimental dispersion curve form the different receiver spacing (Δx, m). The attenuation properties of soil like geometric attenuation (γ) and material attenuation (α, m^{-1}) have been evaluated from the characteristics of spectral signal in frequency domain. Finally, the obtained values from the laboratory model test have been compared with the published research work.

Keywords Surface wave · Rayleigh wavelength · Rayleigh wave velocity · Geometric attenuation and material attenuation

1 Introduction

Soil is a natural material and it has a complex behavior. In soil mechanics and soil dynamics, one of the primary tasks is to evaluate the engineering properties of geomaterial by using laboratory or in-situ testing methods for the safe design and analysis of substructure and superstructure. In soil structure interaction, one of the important engineering properties which have been commonly used in design and analysis is the stiffness profile of the soil. To study the behavior of soil under dynamic loading

B. Vinoth (✉) · A. Ghosh
Indian Institute of Engineering Science and Technology, Shibpur 711103, India
e-mail: vino.rs2018@civil.iiests.ac.in

A. Ghosh
e-mail: ambarish@civil.iiests.ac.in

condition has been very much essential, to understand the dynamic forces and deformation characteristics induced in the soil medium that mainly affects the nearby existing structures. Ground motion has been mainly induced due to natural disaster or man-made vibration, which causes the foundation failure, footing failure, settlement problem, structural member failure and soil may lose its shear strengths due to liquefaction, etc. [1, 2]. So, the proper assessment of the engineering properties of soil is required for the safe design of engineered structures, which are very close proximity to earthquake zone or man-made vibrations are required. The various laboratory experiment and field in-situ techniques are available to evaluate the dynamic characterization of soil like shear modulus, damping ratio, surface wave velocity, and shear wave velocity under different shear strain rate. In the 1980s, one of the emerging techniques evolved to determine the dynamic properties of soil by using shallow surface wave. The main objective of this method is to evaluate the stiffness profile of the near-surface geomaterial [3, 4].

Due to ground motion, the seismic waves are generated and propagate in the soil medium; there are mainly two types: (1) surface waves and (2) body waves [1]. The surface wave can propagate far distance and also it has two-third or 67% of its input energy [5]. One of the important surface waves which have been used to determine the properties of the geomaterial is Rayleigh wave velocity, because the Rayleigh wave velocity has been directly influenced by shear wave velocity of the geomaterial. So, surface wave propagation parameters are very much important in order to evaluate the stiffness profile of the soil. The soil is not an elastic material; it had viscous properties or dissipation of energy due to its inherent characteristics of geomaterial. The attenuation characteristics of surface waves are another important parameters often used to assess the damping properties of the soil [6]. During inversion technique, one of the major tasks is to evaluate the dynamic properties of soil which is first to develop the theoretical dispersion curve from the assumed soil parameters (either density, Poisson's ratio, thickness, shear modulus, and shear wave velocity), after development of the theoretical dispersion curve, the next step is to match the theoretical dispersion curve with the obtained experimental dispersion curve, until both curves become good fit with the assumed soil parameters (iterative process). So, in order to construct the stiffness profile (shear wave velocity or shear modulus profile) of soil, first we have to evaluate the experimental dispersion curve for the surface wave.

The present research work mainly focuses on determination of surface wave propagation parameters and attenuation characteristics of homogeneous cohesionless soil from the laboratory model study.

- The attenuation characteristics of soil $\left(\gamma \text{ and } \alpha, \text{m}^{-1}\right)$ have been determined from the varying input energy from 4 to 20 Nm with respect to corresponding radial distance 0.4–1.6 m.
- To evaluate the surface wave propagation parameters (λ_R, m and V_R, $\frac{\text{m}}{\text{s}}$) of the soil medium.
- To develop the experimental dispersion curve for the homogeneous cohesionless soil medium for the various receiver spacings 0.4–0.6 m.

2   Experimental Model Study

Experimental model study has been comprised of testing tank, test material, soil bed preparation techniques, vibration source, and vibration monitoring instrument which has been discussed detail in given below Sects. 2.1–2.3. Figure 1 shows the complete experimental test setup that has been used in the present research work.

2.1   Test Tank and Test Material

The size of the experimental model tank 2 m × 1.5 m × 1 m (inner dimension of the tank) has been used to carry out this research work. The air-dried homogenous cohesionless sandy soil has been used as a test material and the index properties of the soil have been determined from the laboratory test as shown in Table 1. The expanded polystyrene sheet (Thickness is 4.5 cm) has been used to avoid the wave reflection from the boundary of the wall that keeps the surface wave propagates as infinite condition in the soil medium.
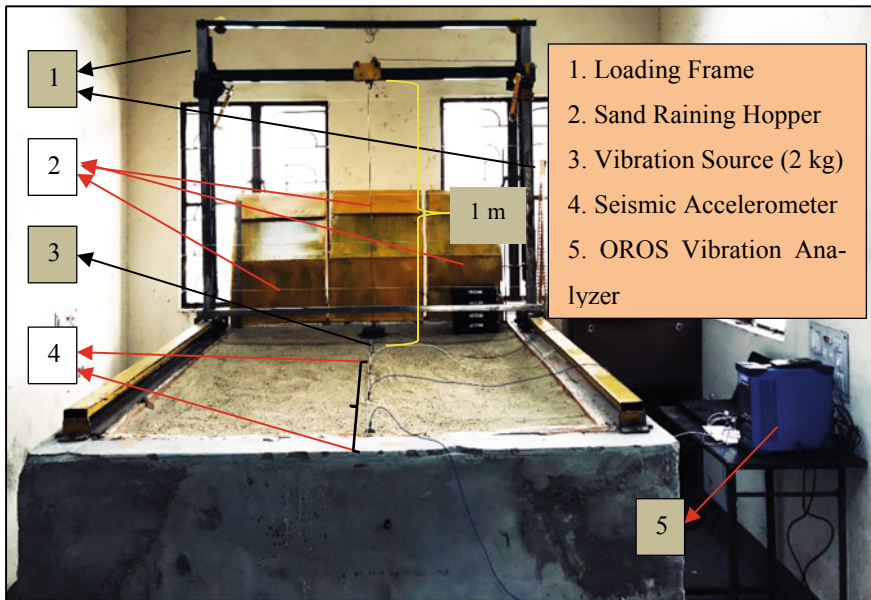

1. Loading Frame
2. Sand Raining Hopper
3. Vibration Source (2 kg)
4. Seismic Accelerometer
5. OROS Vibration Analyzer

Fig. 1 Experimental test setup

Table 1 Properties of soil

Sl. No	Index properties	Values
1	Specific gravity of the soil	2.65
2	Coefficient of curvature (C_c)	1.10
3	Coefficient of uniformity (C_u)	2.05
4	Maximum dry density ($\gamma_{d\mathrm{max}}$, kN/m^3)	16.98
5	Minimum dry density ($\gamma_{d\mathrm{max}}$, kN/m^3)	14.24
6	Density of the soil medium (γ_d, kN/m^3)	15.63
7	Relative density of the soil (R_D, %)	55

2.2 Bed Preparation

The density of the soil bed is 15.63 kN/m^3 and the corresponding relative density of the soil is 55%. The above density has been achieved by using sand raining method and the desired height of fall is 75 cm. The height of fall has been determined from the trial test.

2.3 Vibration Source and Monitoring Instrument

The impact load has been used to generate the surface vibration in soil medium and the mass of 2 kg has been dropped from the height of fall of 0.2–1 m in the circular steel plate that lies in the soil surface, from that vibration force has been transmitted to the soil medium. ICP seismic accelerometers (PCB seismic accelerometers, Model No: TLD394B04) have been used to receive the amplitude of motion of soil particles from different radial distances (0.4 to 1.6 m). The frequency range of seismic accelerometers varies from 0.06 to 450 Hz and has been mounted on soil surface by using 15 cm long spike. The seismic accelerometers have been connected to the OROS spectrum analyzer that records and stores the vibration data in both time domain and frequency domain for the post-processing analysis. The loading arrangement and vibration monitoring instrument setup has been shown in Fig. 1.

3 Test Program

In this section, the methodology or work plan that has been carried out in laboratory model study has been discussed. In laboratory model test, the following parametric variation being carried out to evaluate the surface wave propagation parameters (λ_R, m and V_R m/s), experimental dispersion curve for different receiver spacing, and attenuation characteristics of soil (γ and α, m^{-1}) in Table 2. The layout of the

Table 2 Parametric variation

Sl. No	Properties and parametric variation	Ranges
1	Density of the soil $(\gamma_d, \text{kN/m}^3)$	15.63
2	Relative density (R_D, %)	55
3	Input energy variation (E, Nm)	4, 8, 12, 16 & 20
4	Height of fall (cm)	20, 40, 60, 80 & 100
4	Radial distance (x_1 to x_4, m)	0.4, 0.8, 1.2 & 1.6
5	Receiver spacing (Δx, m)	0.4, 0.5 & 0.6
6	Polystyrene sheet thickness (t, cm)	4.5

test program is shown in Fig. 2. In Fig. 2, the offset distance was including the thickness of the Polystyrene sheet.

- To monitor the motion of the soil particles in both time domain and frequency domain. The amplitude of the motion of soil particles (particle velocity, mm/s) has been measured on surface from their equilibrium position with respect to radial distances from the corresponding input energies as shown in Table 2.
- For the given constant energy (12 Nm), to monitor the amplitude of soil particles, by varying the receiver spacing in the soil medium as shown in Table 2.
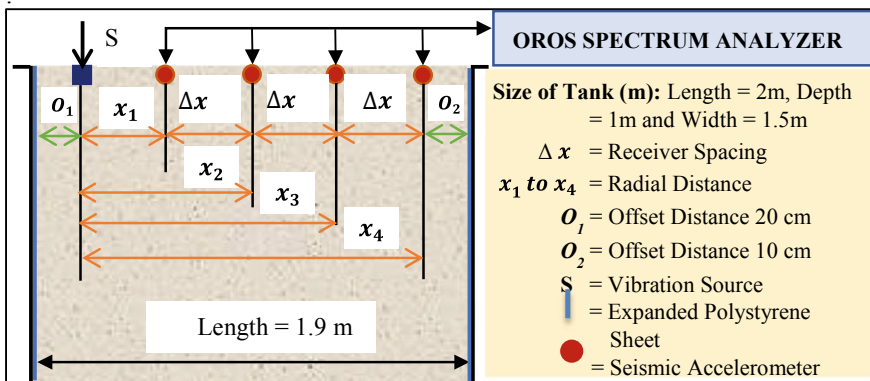
Fig. 2 Layout of the test program

4 Analysis Procedure

This section has briefly explained the analysis procedure being used to evaluate the attenuation characteristic and wave propagation parameters of soil.

4.1 Attenuation Characteristics of Soil

The energy in surface wave amplitude has been attenuated as a function of both distance and the characteristics of material [13]. The surface wave attenuate due to distance mainly depends on geometrical spreading of wavefront and type of wave propagating in the soil medium [5–7] and attenuation due to properties of material mainly depends on hysteretic condition of soil, cohesion, and internal friction between soil particles (i.e., viscous or damping properties).

The geometric attenuation coefficient (γ) has been determined as a function of radial distance has been expressed in Eq. (1).

$$\frac{V_2(t)}{V_1(t)} = \left(\frac{X_1}{X_2}\right)^{\gamma} \tag{1}$$

where γ is geometric attenuation coefficient, $V_1(t)$ and $V_2(t)$ are particle velocities (mm/s) at corresponding distances of X_1 and X_2 from the vibration source. The geometric attenuation mainly varied due to the types of wave generates and propagating in soil medium. From theoretical point of view [8], Rayleigh waves measured on surface the geometric attenuation coefficient (γ) is 0.5 and 2 for body waves [1].

The coefficient of material attenuation (α, m^{-1}) of soil mainly depends on soil type, soil condition, and frequency of seismic wave [1]. The wave attenuation model expressed in Eq. (2) consists of both geometric attenuation (γ) and material attenuation (α, m^{-1}) of the soil [1, 7]. The coefficient of material attenuation (α, m^{-1}) has been expressed as

$$V_2(t) = V_1(t)\left(\frac{r_1}{r_2}\right)^{\gamma}\left(\mathrm{e}^{-\alpha(r_2-r_1)}\right) \tag{2}$$

$$\mathrm{e}^{\alpha(\Delta r)} = \frac{V_1(t)}{V_2(t)}\left(\frac{r_1}{r_2}\right)^{\gamma} \tag{3}$$

$$\alpha = \ln\left(\frac{V_1(t)}{V_2(t)}\left(\frac{r_1}{r_2}\right)^{\gamma}\right) * \left(\frac{1}{\Delta r}\right) \tag{4}$$

where α, m^{-1} is coefficient of material attenuation as a function of $V_1(t)$ and $V_2(t)$ are particle velocities (mm/s) at corresponding distances of r_1 and r_2 from the vibration source.

4.2 Determination of Surface Wave Propagation Parameters of the Homogeneous Cohesionless Soil.

Cross-Correlation Techniques: The correlation techniques can be done in both time and frequency domain signals [14]. In time domain, the surface wave propagation parameters are determined by direct arrival time of seismic signal and the known radial distance between the receivers. In frequency domain, each frequency spectrum consists of both magnitude and phase information. When measuring seismic waves at two or more stations, the spectral properties of signal can be used to determine the surface wave propagation parameters [9]. The cross-power spectrum of the signal can be used to determine the phase lag of the seismic signal. In order to determine the travel time $\Delta t(f)$ of the surface waves (i.e., time lag) between two stations have been expressed in the below Eq. (5).

$$\Delta t(f) = \left[\frac{\Delta\varphi_{xy}}{2\pi f} \right] \tag{5}$$

where $\Delta t(f)$ time lag or travel time between two stations (Δx) and $\Delta\varphi_{xy}$ is phase lag or phase difference (i.e., unwrapped phase angle) between two receivers.

Determination of unwrapped Phase angle $(\Delta\varphi_{xy})$: From experiment, the obtained phase angle has been folded between $\pm 180°$ i.e., wrapped phase, but in Eq. (5) the phase angle which is used to determine the time lag is unwrapped phase angle. The unwrapped phase angle can be determined by adding or unfolding the correct numbers of $360°$ cycles (i.e., $2\pi N$) from wrapped phase angle [10]. During evaluation of unwrapped phase angle, the frequency which contains coherence value less than 95% has been rejected to obtain the better results. The data rejection criteria have been explained in the below section.

Determination of Rayleigh Wave Velocity $(V_R, \text{m/s})$ and Rayleigh Wavelength (λ_R, m): The Rayleigh wave velocity can be determined by using time lag or travel time $\Delta t(f)$ for the different receiver spacing (Δx) of the two stations. The Rayleigh wave velocity (V_R) for a given frequency can be calculated as

$$V_R(f) = \frac{\Delta X}{\Delta t(f)} \tag{6}$$

The corresponding Rayleigh wavelength can be calculated as:

$$\lambda_R = \frac{V_R}{f} \tag{7}$$

where $V_R(\text{m/s})$, Rayleigh wave velocity, and $\lambda_R(\text{m})$, Rayleigh wavelength for each frequency (f, Hz) of the wave propagation in the soil medium. Finally develop

the dispersion curve between Rayleigh wave velocity (V_R, m/s) versus Frequency (Hz) for different receiver spacing (Δx, m).

Experimental Dispersion Curve: The experimental dispersion curve has been constructed by plotting between Rayleigh wave velocity versus frequency or wavelength for the different receiver spacing (Δx). The experimental dispersion curve has been consisting of all modes of propagation of surface wave. During developing the dispersion curve, the following rejection criteria have been used to obtain good results from the acquired data.

Rejection Criteria in Data Analysis: Cross-power spectrum is used to obtain the relative phase shift between signals for different receiver spacing. The frequency response function (FRF) or coherence value can be evaluating by using power spectral density (PSD) of the signal for the different receiver spacing [14]. Both functions are obtained due to cross-correlation of the input and output spectrum for the different receiver spacing between the transducers. Coherence function is a measure of the degree by which input and output signals are linearly correlated. The value close to 1 a good correlation and hence the recorded signals can be unaffected by noise. For the practical purpose, coherence value or frequency response function is above 90–95% is acceptable in data analysis to determine the stiffness profile of the soil [11, 12]. Therefore, data collected in the lab can be conveniently checked, and value close to the 100 or above 95% is considered in the analysis and the values below 95% are eliminated and the corresponding frequency can be omitted during development of experimental dispersion curve. There is another one more rejection criterion which has been used to avoid any near field effects by using obtained Rayleigh wavelength [11].

5 Test Results and Discussion

5.1 Test Results

From the laboratory model study, the typical test results have been formulated in graphical presentation which is shown in Figs. 3, 4 and 5. Figure 3 represents the particle velocity (mm/s) versus time (s) obtained due to variation for input energy (4, 8, 12, 16 & 20 Nm) for the corresponding radial distances of 1.6 m. Figure 4 represents the particle velocity (mm/s) versus frequency (Hz) for the input energy 20 Nm for the corresponding radial distances of 1.6 m. Figure 5 represents (a) time domain signal, (b) frequency domain signal by using FFT, (c) cross-power spectrum or wrapped phase, and (d) coherence function which are obtained from experiment for the 0.4 m receiver spacing (ΔX). A similar kind of data acquisition procedure has been followed to acquire data for 0.4, 0.8, & 1.2 m radial distances and 0.5 & 0.6 m receiver spacing (ΔX). Figure 6 has been plotted between the peak particle velocity
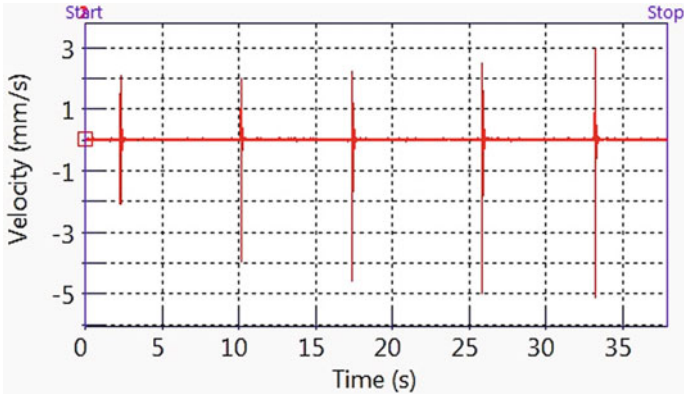
Fig. 3 Represents the particle velocity (mm/s) versus time (s) obtained due to variation for input energy (4, 8, 12, 16, & 20 Nm) for the corresponding radial distances is 1.6 m
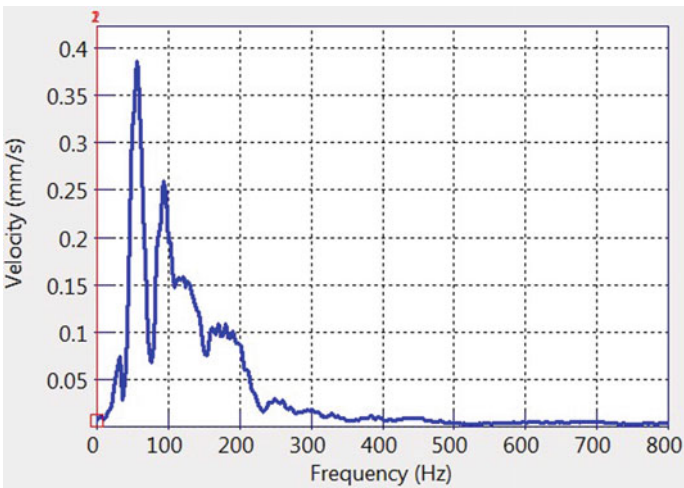
Fig. 4 Represents the particle velocity (mm/s) versus frequency (Hz) for the input energy 20 Nm and the corresponding radial distance is 1.6 m
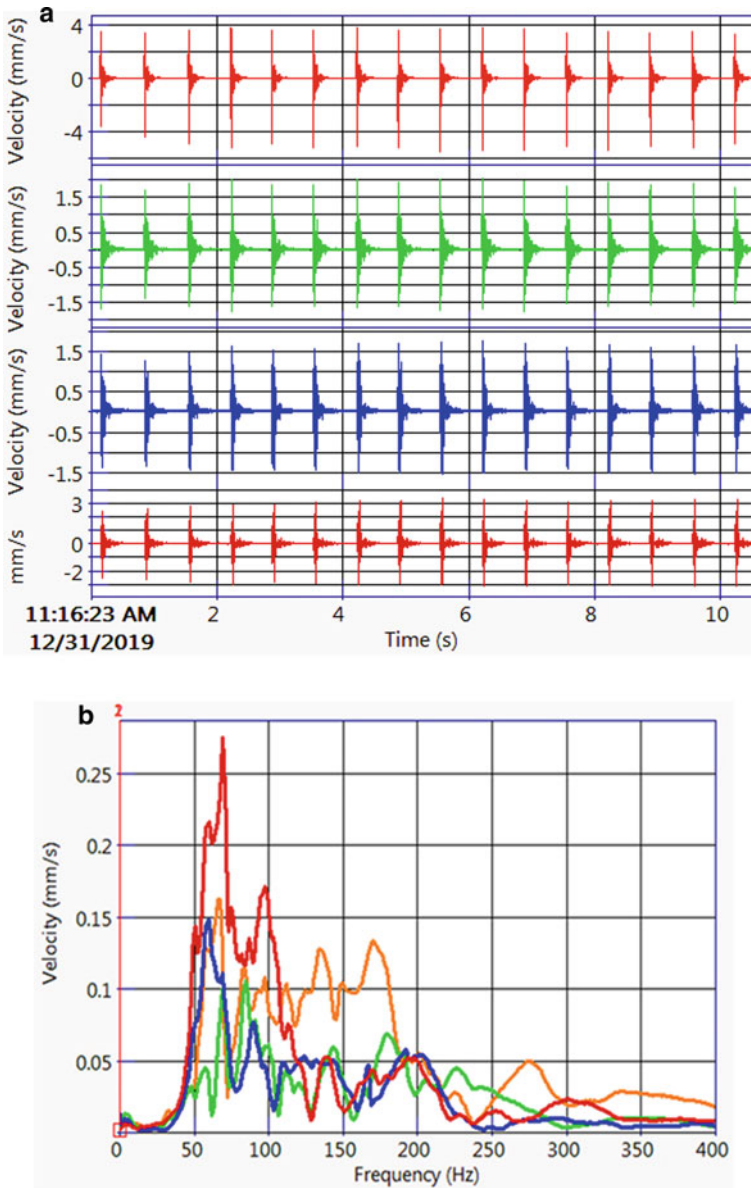
Fig. 5 Represents **a** time domain signal, **b** frequency domain signal by using FFT, **c** cross-power spectrum or wrapped phase, and **d** coherence function are obtained from experiment for the 0.4 m receiver spacing (ΔX)
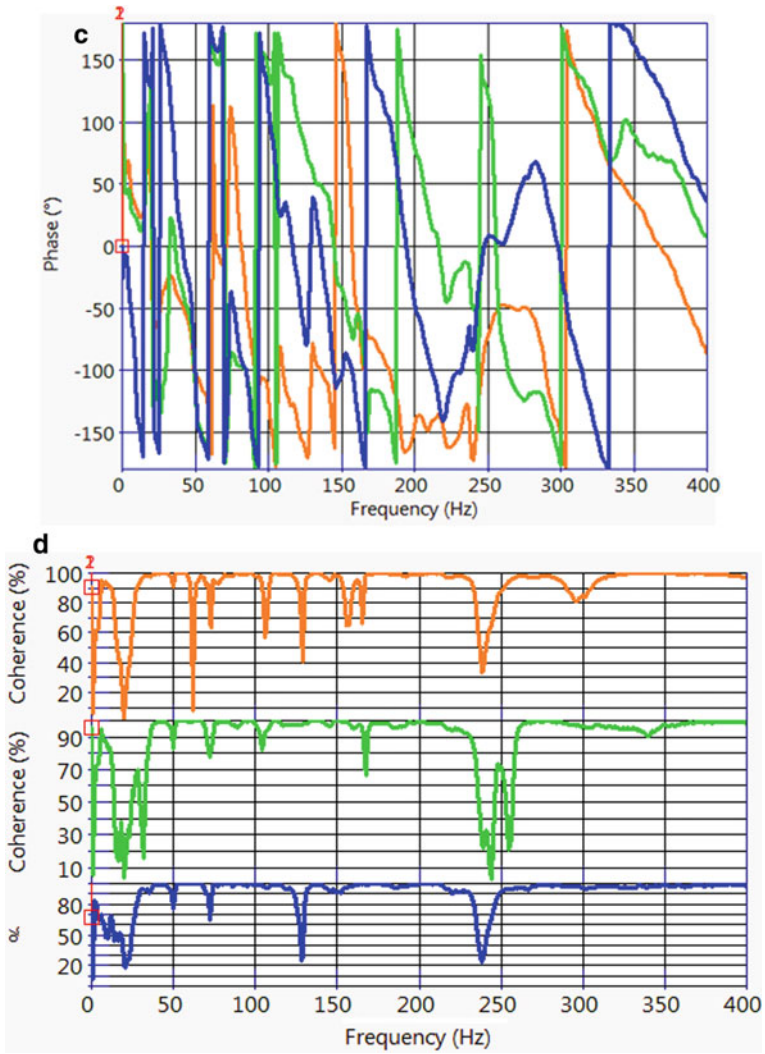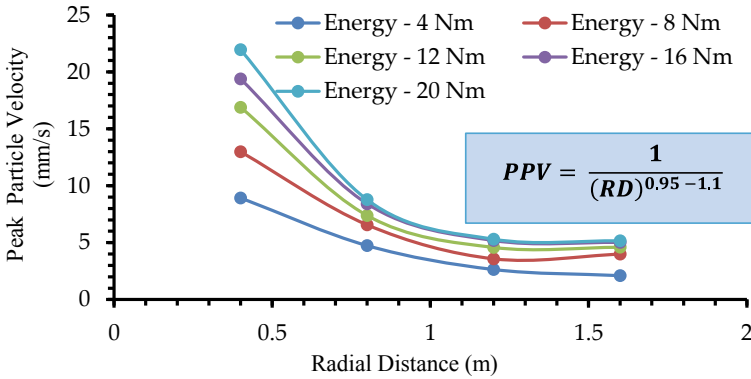
Fig. 5 (continued)

Fig. 6 Plotted between peak particle velocity (PPV, mm/s) and radial distances (m) for the various energies (4–20 Nm)

(mm/s) versus radial distance (m) for the corresponding input energies varying from 4, 8, 12, 16, & 20 Nm.

5.2 Discussion

Determination of geometric attenuation coefficient (γ) and coefficient of material attenuation $(\alpha, \mathrm{m}^{-1})$ of the soil.

The geometric attenuation coefficient has been evaluated by using Eq. (1) and is shown in Fig. 7. Figure 7 plotted between ratio of amplitude of particle velocities (mm/s) versus corresponding ratio of radial distance (m) in logarithmic plot. The geometric attenuation coefficient (γ) mainly indicates how the geometric spreading
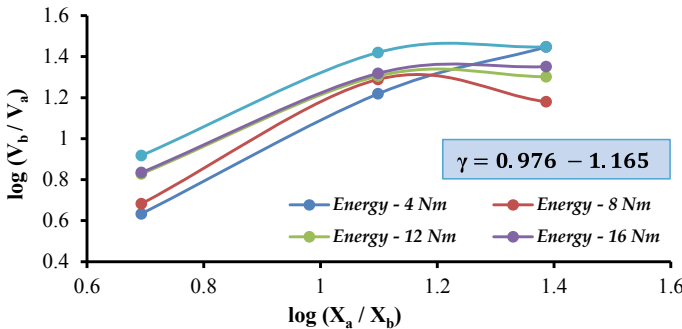
Fig. 7 Plotted between ratio of amplitude of particle velocities $\left(\frac{V_b(t)}{V_a(t)}\right)$ and corresponding ratio of radial distance $\left(\frac{X_a}{X_b}\right)$ in log–log plot
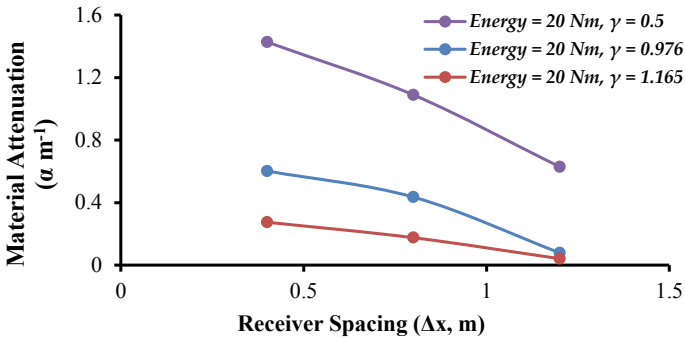
Fig. 8 Plotted between the coefficient of material attenuation (α, m^{-1}) and the coressponding receivers spacing $(\Delta x, m)$ for the input energy of 20 Nm

of wavefront decays with respect to radial distances and it mainly depends on the types of wave and types of wavefront generate in the soil medium. The geometric attenuation coefficient (γ) is independent of the soil properties or vibration source. From the present study, the geometric attenuation coefficient (γ) has been evaluated from the ratio of $\frac{V_b}{V_a}$ with respect to ratio of radial distances $\frac{R_a}{R_b}$. The geometric spreading of surface wave (wavefront coefficient) has been evaluated from fixed position (i.e., $R_a = 0.4$ m from vibration source) to the variation of particle velocity (mm/s) with respect to other radial distances (i.e., $R_b = 0.8$, 1.2, and 1.6 m from vibration source). The geometric attenuation coefficient (γ) has been found from the present study for the given soil condition and varies between 0.976 and 1.165.

The coefficient of material attenuation (α, m^{-1}) of the soil has been determined by using Eq. (4). The geometric attenuation coefficient (γ) value has been substitute in Eq. (4). Based on theoretical study [8], the geometric attenuation coefficient (γ) has been found 0.5 for surface wave propagation due to point source. In Fig. 8 has been shown that coefficient of material attenuation (α, m^{-1}) have been found due to geometric attenuation coefficient (γ) 0.5, 0.976, and 1.165 and the corresponding receiver spacing (ΔX) for 20 Nm energy. The coefficient of material attenuation (α, m^{-1}) mainly depends on the soil condition and frequency of propagation of its surface wave. From the present study, the material attenuation coefficient (α, m^{-1}) has been found between 0.042 and 0.602 (m^{-1}) and it is evaluated from particle velocities and radial distance and its independent on frequency.

Rayleigh Wave Propagation Parameters. The Rayleigh wave velocity and Rayleigh wavelength have been determined by using Eqs. (5) and (6).

Development of Experimental Dispersion Curve. From the present study, two data rejection criteria have been used (1) Wavelength criteria and (2) Coherence value to evaluate the dispersion curve. The wavelength criteria [11] have been proposed between Rayleigh wavelength (λ_R) and receiver spacing (Δx) is $\frac{\lambda_{max}}{3} < \Delta x < 2\lambda_{min}$ and the coherence value 0.95 [11, 12] has been used in present study. During evaluation of experimental dispersion curve for each receiver spacing (Δx), the data
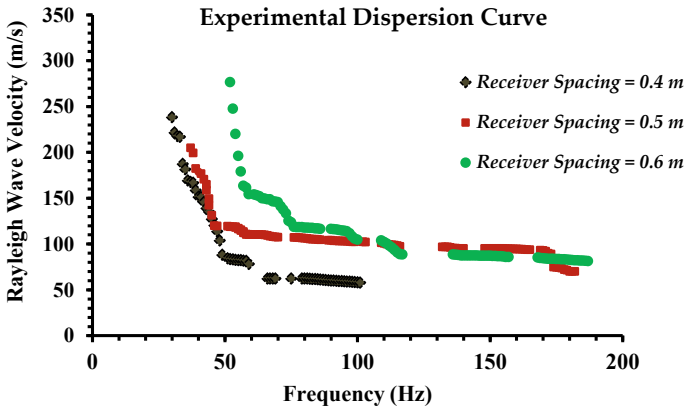
Fig. 9 Experimental dispersion curve, plotted between Rayleigh wave velocity $\left(V_R, \frac{m}{s}\right)$ Versus frequency (Hz) (for the given Input Energy = 12 Nm)

points which did not fulfill the two above criteria have been rejected. The experimental dispersion curve has been developed between Rayleigh wave velocity (m/s) and frequency (Hz) for the receiver spacing 0.4, 0.5, and 0.6 m and developed dispersion curve consists of all modes of surface wave, propagate in soil medium and is shown in Fig. 9

6 Conclusion

The main objective of the present study is to evaluate the attenuation properties (γ and α, m^{-1}) and wave propagation parameters (λ_R, m and V_R, $\frac{m}{s}$) of the homogeneous cohesionless sandy soil by using wave propagation mechanism (shallow surface wave). From the present study, the following conclusion has been drawn based on the laboratory model test and has been presented in below salient points.

- The geometric attenuation coefficient (γ) and coefficient of material attenuation (α, m^{-1}) for the given soil condition have been found between 0.976–1.165 and 0.042–0.602 (m^{-1}).
- The Rayleigh wave velocity (V_R, $\frac{m}{s}$) of the soil varies from 280 to 60 m/s and the corresponding Rayleigh wavelength (λ_R, m) varies from 0.434 to 7.8 m.
- The dominant frequency or frequency bandwidth of the surface wave due to input vibration lies between 36 and 140 Hz for the given soil condition and has been found from the power spectral density (PSD) curve.
- The developed experimental dispersion curve shown in Fig. 9 is comprised of all modes of surface wave (fundamental mode to higher mode).

References

1. Amik H (1999) A frequency—dependent soil propagation model. In: Proceedings of SPIE conference on current developments in vibration control for optomechanical systems, Colorado 3786, pp 72–80
2. Nazarian S, Stokoe II KH (1986a) In situ determination of elastic moduli of pavement system by spectral analysis of surface wave methods (Practical Aspects). Center for Transportation Research, Research Report 1123-1. The University of Texas, Austin
3. Foti S, Parolai S, Albarello D, Picozzi M (2011) Application of surface-wave methods for seismic site characterization. Surveys in Geophysics, vol 32(6). Springer, pp 777–825
4. Richart FE, Hall JR, Woods RD (1970) Vibrations of soils and foundations. Prentice-Hall Upper Saddle River, New Jersy
5. Prakesh S (1981) Soil dynamics. McGraw- Hill Book Companies, U.S.A
6. Kramer SL (1996) Geotechnical earthquake Engineering. Prentice-Hall Upper Saddle River, New Jersy
7. Barkan DD (1962) Dynamics of bases and foundations. McGraw-Hill, New York
8. Gutowski TG, Dym CL (1976) Propagation of ground vibration. J Sound Vib 49(2):179–193
9. Socco LV, Strobbia C (2004) Surface-wave method for near-surface characterization: a tutorial. Near Surf Geophys 2:165–185
10. Al-Hunaidai MO (1992) Difficulties with phase spectrum unwrapping in spectral analysis of surface waves nondestructive testing of pavements. J Canad Geotech 29:506–511
11. Heissey JS, Stokoe KH, Hudson WR, Meyer AH (1982) Determination of in situ shear wave velocity from spectral analysis surface wave methods. Center for transportation research, Research Report 256-2. The University of Texas, Austin
12. Lai CG, Rix GJ, Foti S, Roma V (2002) Simultaneous measurement and inversion of surface wave dispersion and attenuation curves. J Soil Dyn Earthq Eng 22:923–930
13. Kim DS, Lee JS (2000) Propagation and attenuation characteristics of various ground vibrations. J Soil Dyn Earthq Eng 19:115–126
14. Zywicki DJ (1999) Advanced signal processing methods applied to engineering analysis of seismic surface waves. Ph.D. thesis, Georgia Institute of Technology

Parametric Study on Dynamic Properties of Backfill Material and Numerical Modeling of Reinforced Earth Wall for Outward Flow Condition

Seema Kumari , **Pankajkumar Yadav** , **and Arup Bhattacharjee**

Abstract Reinforced soil retaining walls are well known because of their simplicity of field application and cost-viability. When RE walls are executed in earthquake areas, their conduct under the action of seismic loads are needed to be considered to guarantee the safety. It has been observed that most of the failure occurs in the retaining walls under drained condition. As stated by R. M. Koerner among 82 case studies, the failure accompanied by drainage condition is 68%. The failures in reinforced earth wall are generally induced by gravitational force, seepage force, and earthquake force. In this study, two cases are considered, dry condition and drained condition for analysis of failure of reinforced earth walls with tiered configuration (1.2 m offset) and without tiered wall. Studies on tiered configuration walls [1] show that tiered walls are more stable than without tiered walls. At first, modulus properties and dynamic properties of granular backfill material are computed by bender element test (low strain method), and then, properties are incorporated in numerical analysis by finite element method in PLAXIS 2D. The numerical modeling includes plastic analysis, dynamic analysis, and C-Φ strength reduction analysis. It has been observed from the analysis that in dry backfill, the Msf (Factor of safety) obtained by finite element program for RE wall without offset is found to be 2.1 and for two-tiered RE wall factor of safety is 2.3. In drained condition backfill, factor of safety for RE wall without offset after dynamic analysis is found to be 0.41 and for two-tiered RE wall with 1.2 m offset factor of safety is 0.29. The top surface of RE wall must have some impervious layer to avoid percolation of water in backfill to achieve highest order of safety in drained condition.

S. Kumari (✉)
Assam downtown University, Guwahati 781026, Assam, India
e-mail: civil1992seema1@gmail.com

P. Yadav
Department of Civil Engineering, GHRAET, Nagpur, India
e-mail: yadavpankaj1806@gmail.com

A. Bhattacharjee
Department of Civil Engineering, Jorhat Engineering College, Jorhat, Assam, India
e-mail: bhatta_arup@yahoo.com

1 Introduction

Whenever RE walls are built adjacent to, or even near to, standing or flowing water concern over a rising water surface must be considered. Obviously, streams and rivers are the most suspect but other situations are also possible. The definition of flood can be understood as a temporary condition of partial or complete inundation of water. It might include the overflow of inland or tidal waters, rapid accumulation of runoff, mudflow, or the collapse of land along a shore due to water that has exceeded anticipated cyclical levels. Whether the flooding at a wall results from storm surge, riverine flooding, or urban flooding, the physical forces of the flood waters which act on the structure are generally divided into three load cases. These load cases are hydrostatic loads, hydro-dynamic loads, and impact loads. These load cases can often be exacerbated by the effects of water scouring soil from around and below the foundation [2].

Reinforced earth wall is used to describe externally stabilized soil retention system. This system consists of alternating horizontal layers of reinforcement connected to a vertical rigid block. The stability of RE wall depends upon friction between soil and tensile reinforcement but the friction between reinforcement and soil reduced due to the presence of water at the interface [5]. The strength of RE wall decreases under drained condition by four times [6]. During rainy season, backfill becomes completely saturated (Fig. 1) and water percolates outward from RE wall facing (Fig. 2). The presence of water in backfill could decrease the frictional strength of RE wall. This condition of drainage is considered in this research and numerical modeling has been carried out for the same condition. This behavior is not obvious but Figs. 1 and 2 show that it could be possible. The backfill soil remains saturated after complete precipitation of water through it.

Fig. 1 Reinforced earth wall in saturated backfill after rainfall

Fig. 2 Outflow of drained water through RE wall

In this study, two cases are considered, dry condition and drained condition for analysis of failure of RE wall. In the design section and illustration for geosynthetic reinforced walls, the tacit assumption was made that hydrostatic pressures were nonexistent. Stated differently, the usual MSE wall system designs are assumed to contain "free drainage" components such that water will be readily discharged around and/or through the reinforced soil mass and the wall facing. This is indeed to be expected but only if free-draining sands and gravels are used in the reinforced soil zone.

The stresses and displacements in the reinforced earth wall in dry condition and drained condition have been calculated using finite element program (PLAXIS) with 15-nodded elements. The failures in reinforced earth wall are generally induced by gravitational force, seepage force and earthquake force. The plastic analysis is based on Mohr–Coulomb failure criteria and dynamic excitation has been given to the geometry by the prescribed displacement method.

Input parameters like modulus of elasticity, Poisson's ratio, and angle of internal friction will be required in analysis by PLAXIS 2D. Such input parameters are evaluated by bender element test Camacho-Tauta et al. [5]. The backfill material is considered as cohesionless sand. At first, modulus properties of granular backfill material are computed by bender element test and then properties are incorporated in numerical analysis by PLAXIS 2D.

2 Model Parameters

2.1 Properties of Granular Backfill Material

Mohr–Coulomb model is preferred over other soil models as a first approximation of soil behavior in general. This model requires five parameters, which are generally

familiar to most geotechnical engineers and which can be obtained from basic tests on soil samples. These parameters with their standard units are indexed beneath: Young's modulus [E] (kN/m^2), Poisson's ratio [μ], Cohesion [c] (kN/m^2), Internal friction Angle [ϕ]°, and Dilatancy angle [φ]°. For materials with a massive linear elastic variety, it is practical to use E0 (backfill) based on triaxial test or bender element test.

The backfill material is considered as cohesionless sand. The mechanical property of soil sample is computed in laboratory by bender element test [3]. The merits of laboratory tests are ease of measurement and accuracy. This laboratory test is based on wave propagation through soil sample; in this method, the elastic properties of soil are found at very low strain level (10^{-6} to 10^{-5}%). It consists of source element and receiver element arranged in triaxial cell base. When high-frequency electrical pulse is applied to source element, it produces a stress wave that travels through the specimen toward the receiver element, it generates a voltage pulse which is measured by receiver element [4]. Shear waves and primary wave will generate due to high-frequency electrical pulses, which is applied to source element by producing a stress wave. Trace of primary wave velocity and secondary wave velocity by bender element test is shown in Figs. 3, 4, 5, 6, 7, and 8 at different densities. Table 1 gives
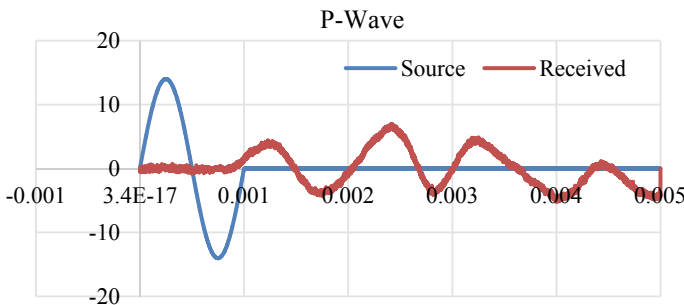
Fig. 3 Density of soil sample-1 is 15.5 kN/m^3
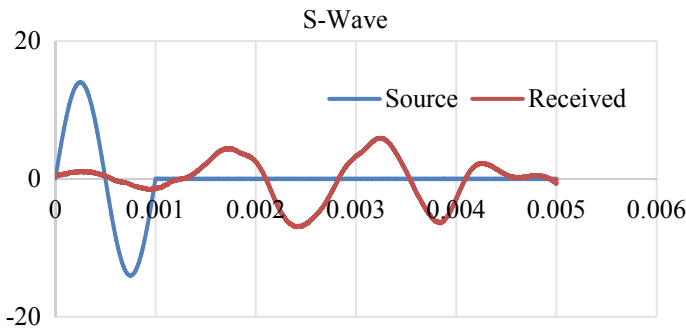
Fig. 4 Density of soil sample-1 is 15.5 kN/m^3

P-Wave
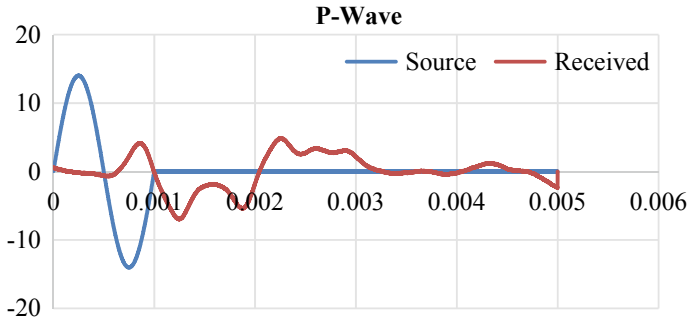
Fig. 5 Density of soil sample-2 is 16.5 kN/m^3
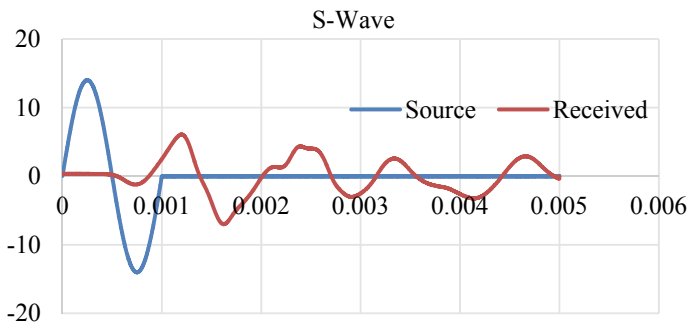
S-Wave

Fig. 6 Density of soil sample-2 is 16.5 kN/m^3
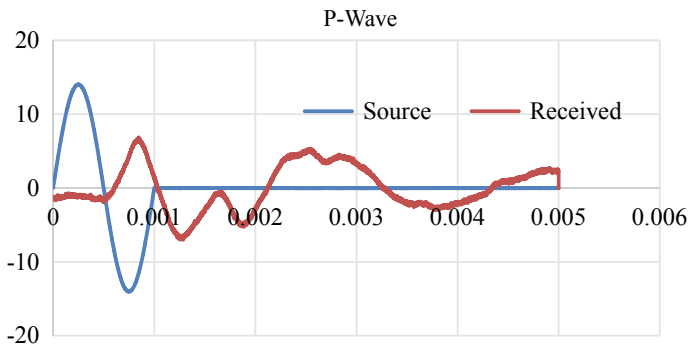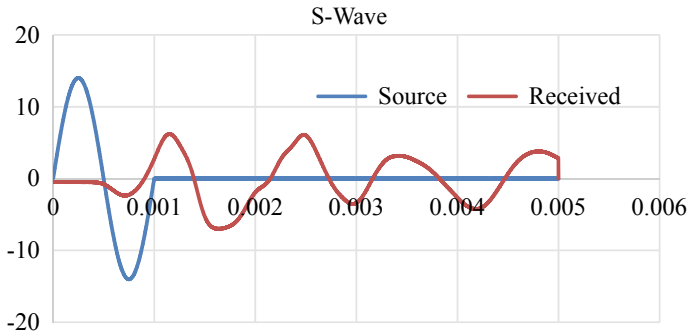
P-Wave

Fig. 7 Density of soil sample-3 is 17.5 kN/m^3

summary of evaluation of primary wave velocity and secondary wave velocity for three samples of sand at different densities of 15.5, 16.5, 17.5 kN/m^3. All modulus

Fig. 8 Density of soil sample-3 is 17.5 kN/m^3

Table 1 Summary of stacking of P-wave and S-wave velocity by bender element test on sand

Density (kN/m^3)	Wave type	Source wave peak t_1 (s)	Received wave peak t_2 (s)	Travel time Δt (s)	Distance (m)	Velocity (m/s)
15.5	P-Wave	0.000248	0.001034	0.000786	0.12	153
	S-Wave	0.000247	0.001697	0.001450	0.12	83
16.5	P-Wave	0.000247	0.001338	0.000671	0.12	179
	S-Wave	0.000244	0.001512	0.001260	0.12	95
17.5	P-Wave	0.000250	0.000868	0.000618	0.12	194
	S-Wave	0.000253	0.003638	0.001157	0.12	104

properties of soil are evaluated by interrelationship between V_s and V_p as shown in Table 2.

Parameters like shear modulus, Poisson's ratio, and young's modulus of the materials are evaluated from Eqs. (1–3), respectively. In Table 2, summary of modulus properties of backfill material is shown. The input parameters of backfill material for PLAXIS 2D is shown in Table 3.

Table 2 Summary of test results of bender element test on sand

Density (kN/m^3)	Wave type	Velocity (m/s)	Poisson's ratio	Young's modulus E, (kPa)	Shear modulus G, (kPa)	Bulk modulus K, (kPa)
15.5	P	153	0.29	27,453	10,623	21,788
	S	83				
16.5	P	179	0.30	38,973	14,966	110,280
	S	95				
17.5	P	194	0.30	48,923	18,812	146,842
	S	104				

Table 3 Properties of backfill material (sand) for PLAXIS 2D

Properties	Unit	Value
Unit weight	kN/m^3	16.5
Young's modulus	kN/m^2	40,000
Poisson's ratio	–	0.3
Cohesion	kN/m^2	1
Friction angle	Degrees	32°

$$G = V_s^2 \rho \tag{1}$$

$$\mu = \frac{\left(\frac{V_p}{V_s}\right)^2 - 2}{2\left(\frac{V_p}{V_s}\right)^2 - 1} \tag{2}$$

$$E = \frac{V_p^2 \rho (1 + \mu)(1 - 2\mu)}{(1 - \mu)} \tag{3}$$

2.2 Facing Wall

The plate element is used to represent facia of wall which is made up of concrete. The modulus of elastic (E) for concrete (cement and aggregates) can be taken up to 50 GPa (ACI 318-08). It can be also calculated according to grade of concrete according to IS-456 2000 ($E = 5000\sqrt{f_{ck}}$), where f_{ck} is characteristic compressive strength. Table 4 represents the modulus and stiffness properties of plate.

Table 4 Material properties of facing wall and geogrid

Properties	Facing wall	Geogrid
Material model	Linear elastic	Elastoplastic
EI (kNm^2/m)	7,467	
Mass-density (kN/m^3)	24	
Poisson's ratio (ν)	0.15	
EA (kN/m)	7E5	2,500

2.3 Geogrid

Geogrids are elastic flexible elements with a normal stiffness and no bending stiffness. Geogrids are represented as soil reinforcements. A geogrid is modeled using elastoplastic constitutive model. EA: Axial/Normal Stiffness.

Material properties of facing wall and geogrid are shown in Table 4.

3 Methodology

3.1 Seismic Analysis of Reinforced Earth Wall

In this study, the response of RE walls in earthquake prone regions after rainfall is studied by the numerical method (FEM) with PLAXIS 2-D software. In a study conducted by Kumari [1], a geosynthetic reinforced soil wall was modeled with the use of Plaxis software. Then, numerical models are calibrated by using experimental model results and the ability of PLAXIS software in prediction of wall displacement, and facing deformation is assessed. Here, one of the models is selected for the analysis of single-tiered (without offset) and two-tiered walls with offset of 1.2 m. The length of the model considered as 20 m beyond the toe of the wall in order to minimize the boundary influence. The models are all fixed at the base and have roller boundaries at the sides.

For dynamic analysis, the wall is excited with sinusoidal wave of maximum horizontal acceleration of 0.4 g by applying prescribed displacement at the base of foundation. The dynamic analysis is carry forwarded by static analysis, and after dynamic analysis, C-Φ strength reduction analysis is carried out, which gives factor of safety. The deformed geometry of wall without offset is shown in Fig. 9 and with tiered configuration (1.2 m offset) is shown in Fig. 10.
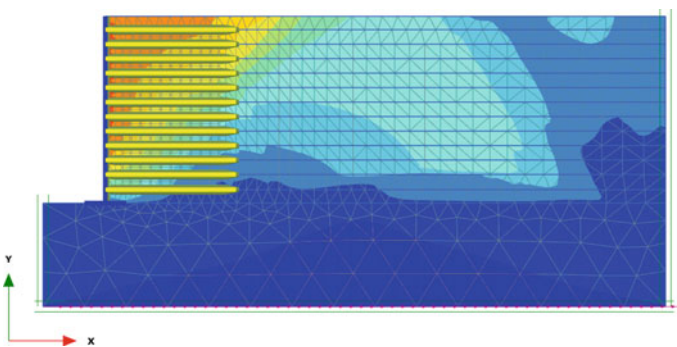

Fig. 9 Reinforced earth wall (without offset)
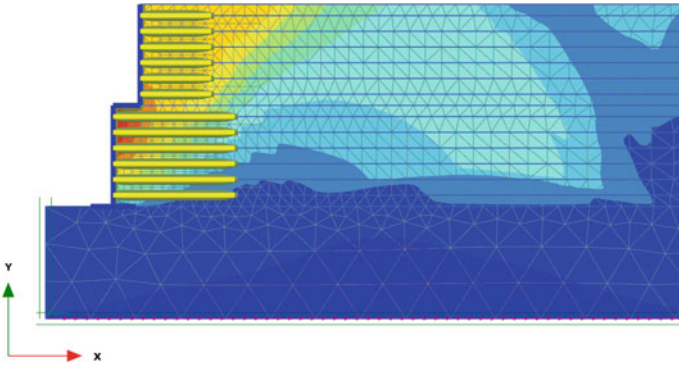
Fig. 10 Two-tiered reinforced earth wall with offset 1.2 m

3.2 Stability Analysis

To ensure the stability of RE wall, factor of safety would be required. The stability analysis of RE wall is performed after static and dynamic analysis which gives the factor of safety by C-Φ strength reduction analysis. During rainy season, the RE wall becomes fully saturated, just after static and dynamic loading the stability in such complex environment will reflect actual failure condition on site.

In dry backfill, the Msf (factor of safety) obtained by finite element program after complete analysis against strength parameters of soil is plotted in Figs. 11 and 12. The factor of safety of RE wall without offset after dynamic analysis is found to be 2.1 and factor of safety of two-tiered RE wall with 1.2 m offset after dynamic analysis is found as 2.3 (Figs. 11 and 12).
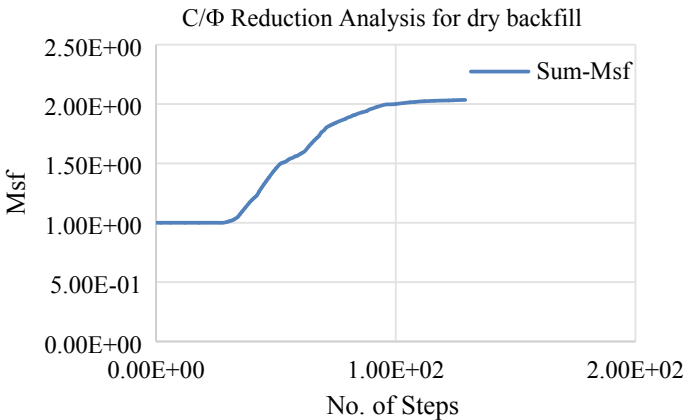
Fig. 11 Msf (factor of safety) of RE wall (without offset)
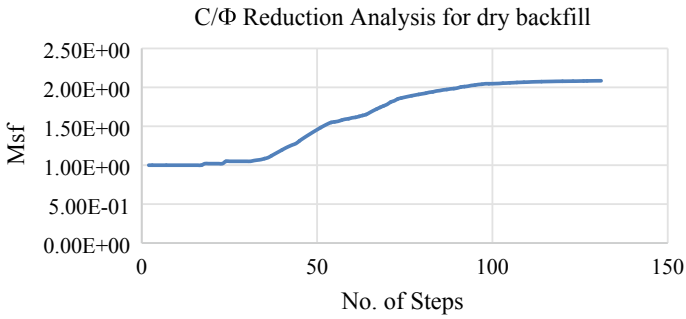
Fig. 12 Msf (factor of safety) of RE wall with 1.2 m offset
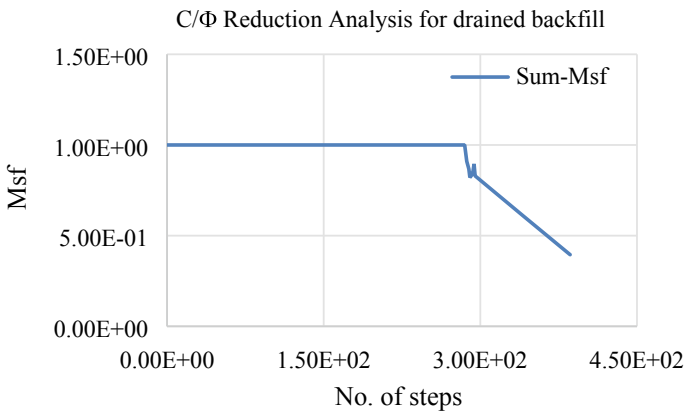
Fig. 13 Msf (factor of safety) of RE wall (without offset)

In drained condition, the reinforced earth wall is analyzed for the factor of safety of RE wall (without offset) after dynamic analysis and for two-tiered RE wall with 1.2 m offset also. Factor of safety for RE wall without offset after dynamic analysis is found to be 0.41, and for two-tiered RE wall with 1.2 m offset, factor of safety found to be 0.29 (Figs. 13 and 14). The reverse case in drained condition may be due to shorter length of geogrid. The factor of safety of RE wall in drained condition can be increased by providing impervious layer in top and bottom of RE wall.

4 Conclusion

This analysis shows that seismic analysis would not sufficient to ensure the safety of reinforced earth wall. The strength reduction analysis under drainage condition would plays important role to ensure safety during service, and it will give a factor
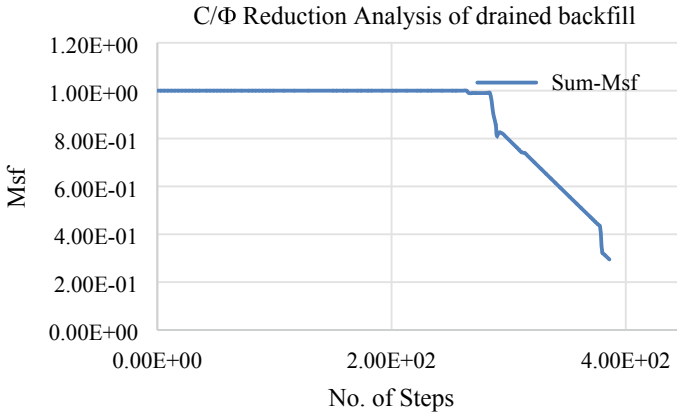
Fig. 14 Msf (factor of safety) of RE wall with 1.2 m offset

of safety. During rainfall, due to improper drainage system the backfill soil remains saturated and outflow of water takes place and this condition is modeled in finite element program.

In dry backfill, the Msf (factor of safety) obtained by finite element program for RE wall (without offset) is found to be 2.1 and for two-tiered RE wall factor of safety is 2.3. In drained condition backfill, factor of safety for RE wall without offset after dynamic analysis is found to be 0.41 and for two-tiered RE wall with 1.2 m offset factor of safety found to be 0.29. This shows that with proper design of RE wall in tiered configuration we can make RE walls more stable in drained conditions also.

In nature, hydrostatic loads are in the form of lateral pressures (horizontal) and buoyant forces (vertical). The lateral forces result from variations in interior and exterior water surface elevations. As the flood water rise, the higher water on the outside of the wall acts inward. Similarly though less common, a rapid drawdown of exterior flood water results in outward pressures on the wall as the retained indoor flood water tried to escape. Sufficient lateral pressures might also cause ever-lasting deflections or collapse of the wall.

As stated by R. M. Koerner among 82 case studies, the failure accompanied by bad drainage condition is 68%. At the top and bottom of RE wall, an impervious layer should be provided to avoid percolation of water in backfill so that highest order of safety could achieved. A layer of damp proofing course should be applied at the base of the RE wall to avoid capillary rise and flooded water from the ground.

References

1. Kumari S (2018) Numerical simulation of tiered reinforced soil retaining wall subjected to dynamic excitations. In: Proceedings of the Indian geotechnical conference-2018. http://www.igs.org.in:8080/portal/igc-proceedings/igc-2018-bengaluru-proceedings/The

me10/TH-10-29.pdf

2. Horvath JS (2010) Lateral pressure reduction on earth-retaining structures using geofoams: correcting some misunderstandings. In: Proceedings of earth retention conference 3, Bellevue, Washington, ASCE GSP-208, pp 862–869. https://doi.org/10.1061/9780784411285

3. Gu X, Yang J, Huang M, Gao G (2015) Bender element tests in dry and saturated sand: signal interpretation and result comparison. Soils Found 55:951–962. https://doi.org/10.1016/j.sandf.2015.09.002

4. Kumar J, Madhusudhan BN (2010) A note on the measurement of travel times using bender and extender elements. Soil Dyn Earthq Eng 30:630–634. https://doi.org/10.1016/j.soildyn.2010.02.003

5. Camacho-Tauta J, Álvarez-Jiménez JD, Reyes-Ortiz OJ (2012) A procedure to calibrate and perform the bender element test. DYNA 79:10–18. Electrónico 2346-2183. ISSN impreso 0012-7353

6. Ashmawy AK, Bourdeau PL (1998) Effect of geotextile reinforcement on the stress-strain and volumetric behavior of Sands. In: Proceedings, 6th international conference on geosynthetics (pp 1079–1082), Atlanta, GA, vol 2

6. Elias V, Christopher BR, Berg RR (2001) Mechanically sta-bilized earth walls and reinforced soil slopes, design and constructionguidelines. FHWA-NHI-00-043, Federal Highway Administration (FHWA), Washington, DC

Experimental and Numerical Study of Shallow Foundation Subjected to Vertical Dynamic Load

N. K. Das, P. Raychowdhury, and S. Ray-Chaudhuri

Abstract Foundation in case of industries and high-rise buildings where turbines, generators, and compressors are installed undergoes vibration. This paper presents the experimental and numerical study on an isolated square shallow foundation under vertical periodic machine vibrations. To excite the foundation with vertical dynamic loading, the eccentric mass shaker is utilized. The eccentric mass shaker essentially consists of two counter-rotating shafts capable of creating vertical periodic loading. A series of block vibration tests are conducted on a square-reinforced cement concrete of size 1 m × 1 m × 0.3 m on field site near western laboratory at IIT Kanpur campus. The shallow foundation is excited with vertical periodic loading of different magnitudes and frequencies. The responses are measured using sensors like accelerometers. The variation in the dynamic responses is recorded, and the same is plotted with varying eccentric force. The resonant amplitude, natural frequency of soil and damping ratio are plotted with frequency. Further, the experimental results are compared with the experimental findings earlier reported in the available literature for the IIT Kanpur campus soil. The numerical simulation of shallow foundation–soil system is done with built-in finite element package ABAQUS and compared to experimental amplitude values.

Keywords Block vibration test · Vertical vibration · Damping · Natural frequency of soil · Resonant amplitude

N. K. Das (✉) · P. Raychowdhury · S. Ray-Chaudhuri
Indian Institute of Technology, Kanpur, Kanpur 208016, India
e-mail: nrjkmr@iitk.ac.in; nrjkmr.das@gmail.com

P. Raychowdhury
e-mail: prishati@iitk.ac.in

S. Ray-Chaudhuri
e-mail: samitrc@iitk.ac.in

1   Introduction

It is a well-established fact that the foundations may experience dynamic load from vibration due to the operation of heavy equipment and movement of vehicles. The seismic response of the structure is significantly affected by soil foundation interaction. Therefore, there is a need to study the soil foundation interaction under vibration from dynamic loading. Large-scale field tests are best suited to study the soil foundation interaction problem. In the past, researchers have considered mainly two approaches for the soil foundation interaction, the first being the spring–mass system and the second being the elastic half-space approach. Reissner [13] had given the theoretical solution for the periodic displacement at the center of circular loaded area. Lysmer [10] had given the expression for spring and damping constants which is frequency independent, and this equation is famously known as Lysmer's analog. Gazetas [6] presented dimensionless charts and formulas for computing the value of dynamic stiffness and dynamic damping of surface and embedded foundation subjected to harmonic excitation. Most of the theories considered assume the foundation as massless and rigid and the soil beneath foundation as uniform viscoelastic half-space with fixed shear modulus and hysteretic damping. These assumptions are not valid in the field due to the uncertainties present in soil properties.

Bhoumik [3] conducted block vibration test on a concrete footing of size 1 m × 0.75 m × 0.7 m at IIT Kanpur under different modes of vibration (uncoupled and coupled vibration both) subjected to harmonic loading. Baidya and Rathi [1] conducted block vibration tests on footing of size 0.4 m × 0.4 m × 0.1 m resting on sand layer to study the effect of layering of soil and rigid layer on the dynamic characteristics. Kumar and Reddy [9] conducted block vibration tests on foundation with spring mounted base. It was noted that due to spring-type cushioning, there is a significant reduction in displacement amplitude and resonant frequency of the foundation. Swain and Ghosh [15] conducted large number of block vibration tests on a pair of shallow foundation (one being the active footing and other being the passive footing) at IIT Kanpur to understand the dynamic interference of footing which aids in the safe design of machine foundation in case of foundation under groups. The transmission ratio is plotted with frequency ratio which predicts the dynamic effect of active footing on the response of passive footing. Das and Raychowdhury [5] studied the performance of reinforced soil bed under the effect of vertical dynamic loading on the machine foundation and found that they performed well in controlling vibration induced deformation. In the present experimental study, the block vibration test is conducted with varying eccentric force level and varying forcing frequency.

1.1   Experimental Program

The block vibration test was conducted through the use of mechanical oscillator on model isolated shallow foundation. The site is first cleaned of leaves, and then,
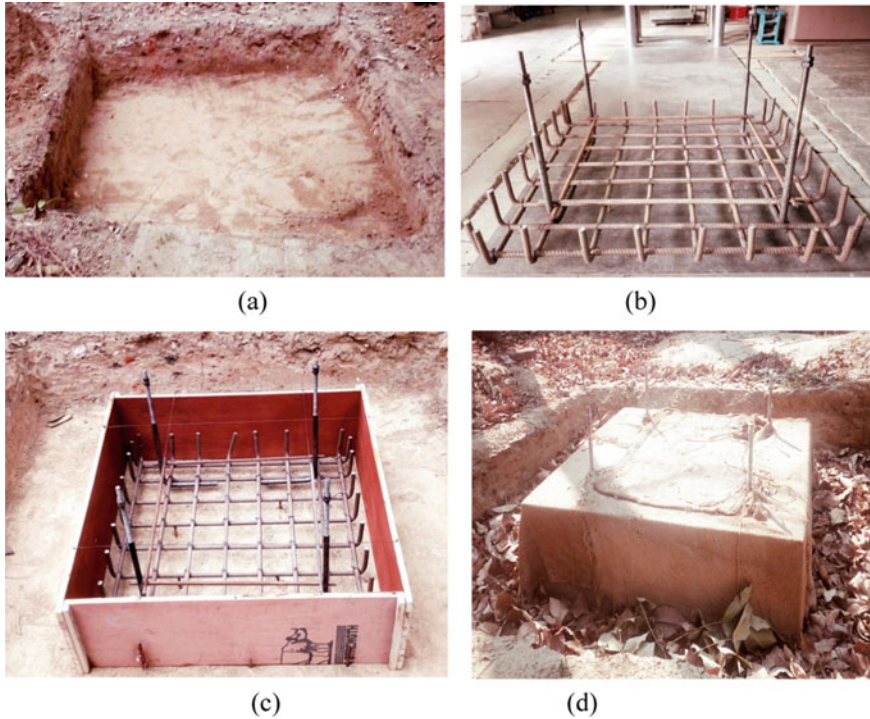
Fig. 1 Different stages of casting of concrete foundation at field site **a** preparation of test pit, **b** reinforcement layout with extruding guide bars, **c** reinforcement placing in test pit with proper formwork, **d** concrete casting at field site

excavation is done to remove the top loose soil as shown in Fig. 1a. The layout of the reinforcement is done by the 16-Φ bar arranged perpendicular to each other as shown in Fig. 1b. The four guide bars are welded to the reinforcement so that later it can be attached to mechanical oscillator. The formwork is placed around reinforcement in the pit with suitable cover as shown in Fig. 1c. A concrete with characteristics strength of 20 MPa was designed for casting of foundation as per IS 456 [8] for 0.3 m^3. The concrete was prepared in four batches. The following ingredients were used for the casting: (i) cement: OPC 33 grade of cement, (ii) fine aggregate: aggregate sieved through 2.36 mm sieve size, (iii) coarse aggregate: aggregate 20 mm size and 10 mm size, (iv) water, (v) admixture: no admixture was used. The concrete casted along with the formwork is as shown in Fig. 1d. To obtain the strength of the concrete, compressive strength tests are done on concrete cube samples after 28 days. The average compressive strength is estimated 31.94 MPa, which is well above the desired strength of 20 MPa.

The block vibration test setup was based on IS 5249 [7] code provision guidelines and the experimental program used by Baidya and Rathi [1], Baidya and Mandal [2],

Swain and Ghosh [15], Das et al. [4] and Das and Raychowdhury [5]. The block vibration test setup is basically consisting of an eccentric mass shaker equipment (MX 100A) from Micron Industries Limited. The eccentric mass shaker is the mechanical oscillator that is capable of producing 10,000 kgf. The principle mechanism of eccentric mass shaker to produce a sinusoidal variation is due to the counterclockwise rotating shafts which can be able to produce periodic vertical force. The eccentricity angle inside mechanical oscillator can be set up to 180 degrees. The shaft of oscillator is driven by the help of 5 HP DC motor, and it can run up to 3000 rpm.

The base plate (MS plate) is connected to the foundation through the help of guide bars over stopper so as to make room for the placing of accelerometer at the center of footing. Then, square-shaped bottom plate is connected to the four guide bars. After the calibration, the mechanical oscillator is placed on the bottom plate of oscillator so that the whole system vibrates as a single entity. The layout of experimental test setup is shown in Fig. 2.

After preparing the cast in situ foundation and proper setup of the mechanical oscillator, the placement of sensors like accelerometer was done. Overall, six accelerometers were connected to the foundation. The four strain gauge-based accelerometer (numbered Accl 1 to Accl 4) is placed on the outer four edges (Accl 1-4 in clockwise direction from southside direction). The accelerometer sensor is connected to the 32-bit data acquisition system (DAQ). The DAQ is further connected to computer having LabVIEW installed in it for recording the raw data. The MEMS-based accelerometer (numbered Accl 5) is placed on the centerline of the foundation. This MEMS-based sensor is further connected to the vibration meter which gives direct reading of acceleration, velocity and displacement. The placement of sensor along with the block vibration test setup is as shown in Fig. 3.
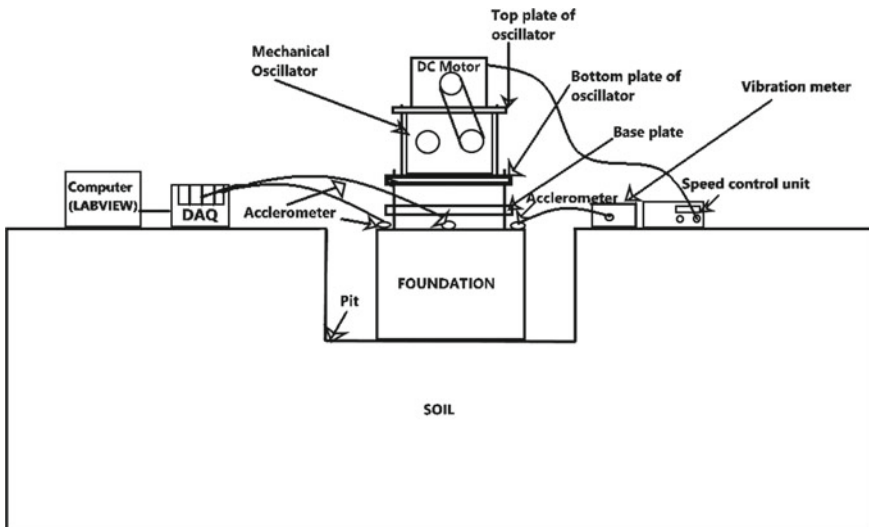
Fig. 2 Layout of block vibration test setup
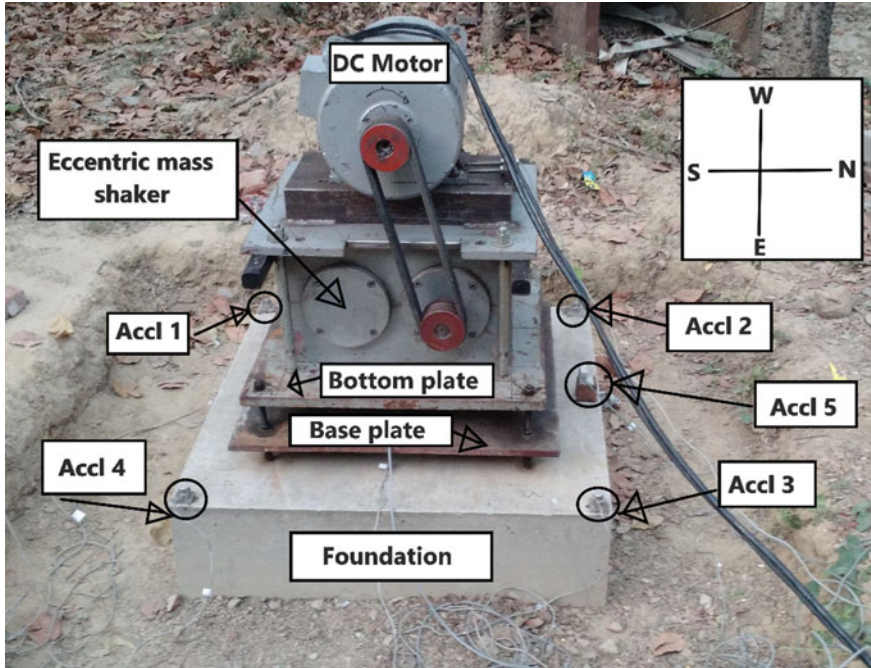
Fig. 3 Photographic view of layout of placement of sensors along with the block vibration test setup

The soil strata at the field site is clayey silt. The top 2 m soil is clayey silt. The water table is 6.5 m below the ground table so that it is well below the zone of influence, i.e., B depth below the base of the footing where B is the width of foundation. The specific gravity of the soil is 2.67. The dry density of the soil is 16.423 kN/m^3. The liquid limit is found to be 26.70%. The plasticity is found to be in the range of low to medium. The cohesion value is 55.7 kN/m^2.

1.2 Experimental Procedure

The block vibration test for the vertical vibration case is conducted on an isolated square foundation of size 1 m × 1 m × 0.3 m for different values of eccentric force and with range of forcing frequencies. The power is fed into AC to DC converter to run the 5 HP DC motor which causes the two shafts of eccentric mass shaker to run in counterclockwise direction, thereby canceling the horizontal forces and addition of forces in the vertical direction. The desired forcing frequency is set by setting the revolution per minute (rpm) by speed control unit. The eccentricity angle range is from 0 to 180 degrees. The speed control unit range is from 300 to 3000 rpm;

thereby, the forcing frequency range is from 5 to 50 Hz. The capacity of mechanical oscillator is 10,000 kgf. The eccentric force depends upon the angle of eccentricity between the unbalanced mass inside the mechanical oscillator and speed of rotation. The eccentric force generated is given by the following Eq. 1

$$F = m_e \times e \times \omega^2 = 0.85624 \times \sin \frac{\theta}{2} \times \omega^2 \tag{1}$$

where F is the force generated in Newton, m_e is the unbalanced mass rotating with radius of e inside the mechanical oscillator in meters, and θ is the angle between the eccentric masses. The eccentric force level is calculated by the following Eq. 2

$$F_e = m_e \times e \times \sin \frac{\theta}{2} = 0.85624 \times \sin \frac{35}{2} \tag{2}$$

The eccentric force corresponds to the 40-degree eccentricity which is 0.25747 N-sec^2. The experiment study was conducted for three eccentricity angles of 15, 35 and 55 degrees. The eccentric force levels corresponding to eccentricity angle of 15, 35 and 55 degrees are 0.11176, 0.25747 and 0.39356 N-sec^2. For each eccentric force level, the forcing frequency range is from 5 to 43 Hz in the increment of every 2 Hz.

First, the calibration of accelerometer sensor was performed before starting the experimentation. While performing the test, responses are recorded (g values) with accelerometer sensors with the help of LabVIEW software using data acquisition system connected with the accelerometer sensor. The micron MEMS accelerometer sensor (Accl 6) connected to the vibration meter which gives the direct value of acceleration, velocity and displacement values. After recording the data in LabVIEW software from different accelerometers (Accl 1 to Accl 5), the recorded data is multiplied with 9.81 so to convert it in m/s^2. Then, the raw data is processed with MATLAB. The samples are recorded at 2000 samples per second so that the Nyquist frequency of the system is 1000 Hz. The baseline correction is made to the acceleration values. The Butterworth filter of fourth order is applied in the selected frequency bandwidth to capture the fundamental mode of the present system. The velocity is calculated by integrating the acceleration values as shown by Eq. 3, and displacement is calculated by integrating the velocity values as shown by Eq. 4 as follows

$$v = \int a \, dt \tag{3}$$

$$s = \int v \, dt \tag{4}$$

where a is the acceleration values recorded in m/s^2, dt is the time taken, v is the velocity in m/s and s is the displacement value in m. The displacement for every forcing frequency is noted and accordingly the graph between displacement and forcing frequency is plotted.

1.3 Experimental Results and Discussion

The block vibration test is conducted on shallow surface foundation of size 1 m ×
1 m × 0.3 m resting on field site near Materials Science Laboratory, IIT Kanpur.
First, establishing the response curve from the data recorded from digital vibration
meter and then finding the resonant frequency and natural frequency of the soil from
the observed response curve [14]. The expression for damping ratio (as shown by
Eq. 5) for the rotating mass excitation is shown below [14]

$$f_{mr} = \frac{f_n}{\sqrt{1 - 2D^2}} \tag{5}$$

where D is the damping ratio, f_n is the natural frequency of the soil considering mass
of vibrating system, f_{mr} is the frequency of rotating mass system at resonance.

After attaining the steady state, the reading from the sensors is recorded. The
displacement values are calculated for each forcing frequency, and the displacement
is plotted with frequency as shown in Fig. 4 for each of three eccentric force levels
in N-sec^2.

When the forcing frequency approaches the natural frequency of the soil, the
rate of increase in the dynamic response, i.e., displacement, velocity or acceleration
amplitudes, is rapid as shown in Fig. 4 (displacement amplitude). This is mainly due
to the propagation of surface waves (Rayleigh wave) which can cause ground defor-
mation. The data points are shown in Fig. 4, and the graph is fitted with spline curve.
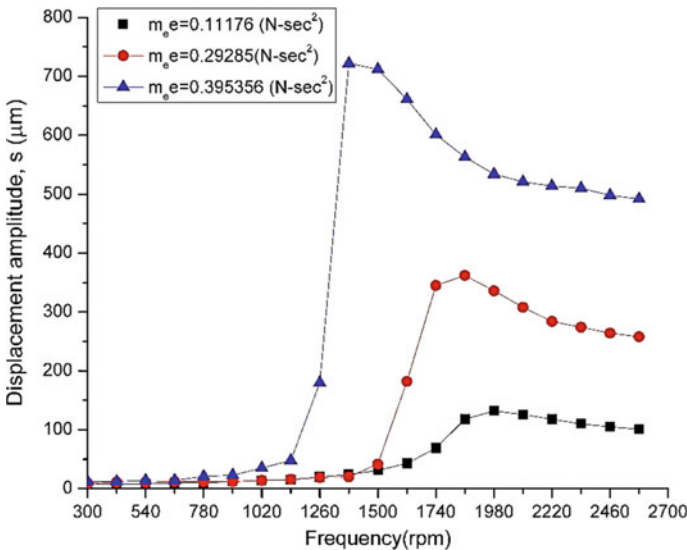After reaching the resonant frequency, the dynamic responses started decreasing. It

Fig. 4 Displacement amplitude variation with forcing frequency at different eccentric force settings

is noted that with increase with eccentric force level, there is decrease in resonant frequency and increase in the resonant displacement amplitude which clearly shows the nonlinearity present in the soil beneath the foundation. This is a well-established fact reported experimentally by Novak [12]. The resonant displacement amplitudes from Fig. 4 are 0.132, 0.362 and 0.722 mm corresponding to eccentric force level of 0.11176, 0.25747 and 0.39536 N-sec^2. The natural frequencies of the soil from Fig. 4 are approximately 33, 29 and 23 Hz corresponding to eccentric force level of 0.11176, 0.25747 and 0.39536 N-sec^2. The results are plotted in the form of graph with eccentric forcing level. With the increase in eccentric force level settings, there is increase in the value of damping (sum of material damping and radiation damping) as shown in Fig. 5. This type of trend is similar with the response obtained for a rotating mass exciter [1, 9, 15].

The test results for the present experimental study on isolated surface foundation of square size with dimension 1 m × 1 m × 0.3 m under vertical oscillation are summarized in Table 1. It is noted from Table 1 that the natural frequency of the soil decreases with the increase in eccentric angle settings.

Bhoumik [3] performed block vibration test on isolated large concrete block at Geotechnical Engineering Laboratory field site, IIT Kanpur, under different modes of oscillation including vertical oscillation case. Swain and Ghosh [15] conducted a large number of block vibration test on interacting footing at Geotechnical Engineering Laboratory field site, IIT Kanpur, including vertical oscillation case of isolated footing. The present study is performed on field site near Materials Science Laboratory, IIT Kanpur; thereby, a comparison can be made between the test results
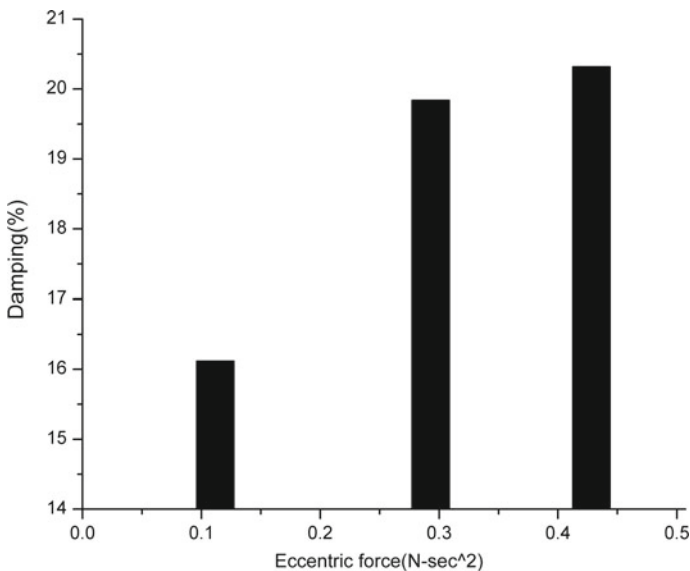
Fig. 5 Damping ratio variation with eccentric force level settings

Table 1 Test results for the present study for vertical vibration case on isolated shallow square foundation under different eccentric force levels

(Present study)	Eccentric force level (N-sec^2)		
System parameters	0.11176	0.29285	0.39536
Resonant displacement amplitude (mm)	0.132	0.362	0.722
Resonant frequency (Hz)	32.90	30.53	23.70
Natural frequency of soil (Hz)	32.03	29.3	22.7
Damping ratio (%)	16.12	19.84	20.32

as the site is nearby. Table 2 enlists the comparison of test parameters and results of the present study with Bhoumik [3], Swain and Ghosh [15] for vertical oscillation case for isolated shallow foundations.

The difference in results can be attributed to the fact that in the present study, the eccentric force level is large in comparison with Bhoumik [3], Swain and Ghosh [15], and also, the foundation size is larger in comparison. The foundation size, type and magnitude of the eccentric load, soil properties significantly affect the response obtained for rotating type excitation [14].

Table 2 Comparison of test parameters and test results for the present study with Bhoumik [3], Swain and Ghosh [15] for vertical oscillation case for isolated foundation at IIT Kanpur

Test parameters	Bhoumik [3]	Swain and Ghosh [15]	Present study
Footing size: RCC(m × m × m)	1 × 0.75 × 0.7	0.55 × 0.55 × 0.20	1 × 1 × 0.3
Soil type (IIT Kanpur)	Silty Clay	Clayey Silt	Clayey Silt
Eccentric force level (N-sec^2)	0.045	0.017, 0.025, 0.033	0.1117, 0.2274, 0.39
Resonant displacement amplitude (mm)	0.127	0.137, 0.210, 0.275	0.152, 0.381, 0.757
Resonant frequency (rpm)	2459	2233, 2081, 1976	1974, 1832, 1422
Natural frequency of soil (rpm)	2404	2156, 2011, 1909	1922, 1758, 1362
Damping ratio (%)	14.47	18.39, 18.23, 18.28	16.12, 19.84, 20.32

2 Numerical Modeling

In the present study, the experimental result was verified with three-dimensional model in ABAQUS, finite element software. The dimension of the shallow foundation is kept same in the numerical simulation of the model foundation–soil system. The sensitivity analysis is performed, and it showed that at a distance of 13B from the edge of footing, the dynamic response is not affected under high frequency. To represent the half-space, the soil base dimension taken is 30 m × 30 m × 20 m so as to reduce the boundary effect as shown in Fig. 6. The pit is modeled as same as that of site with dimension 2 m × 2 m × 0.3 m and foundation with size 1 m × 1 m × 0.3 m. The soil base (30 m x 30 m x 20 m) is modelled with eight node linear brick element (C3D8) to represent the half space. The transition element (tetrahedron) is used to connect the foundation and soil brick element. The four-node linear brick element (C3D4) is used in modeling the soil just beneath the foundation (12 m x 12 m x 4m) and the reinforced cement concrete foundation (1 m x 1 m x 0.3 m). The behavior of soil representing half-space under dynamic loading were modeled as Mohr Coulomb plasticity yield criteria with nonlinear failure envelope [11]. The shear strength of the soil as obtained from direct shear test is having cohesion of 55.7 kN/m^2 and dilation angle of 2/3 of friction angle. The modulus of elasticity of the soil is 12 MPa as obtained from laboratory tests and suitable Poisson ratio of 0.33. The reinforced cement concrete is modeled as elastic material with the modulus of elasticity of 20 GPa and Poisson ratio of 0.2. The displacement is restrained in both lateral and vertical direction along the bottom boundary (U1 = 0, U2 = 0, U3 = 0), and the side boundaries are restrained in the horizontal direction (U1 = 0, U2 = 0, U3#0). The quiet boundaries to control the wave reflections are applied to the vertical sides.
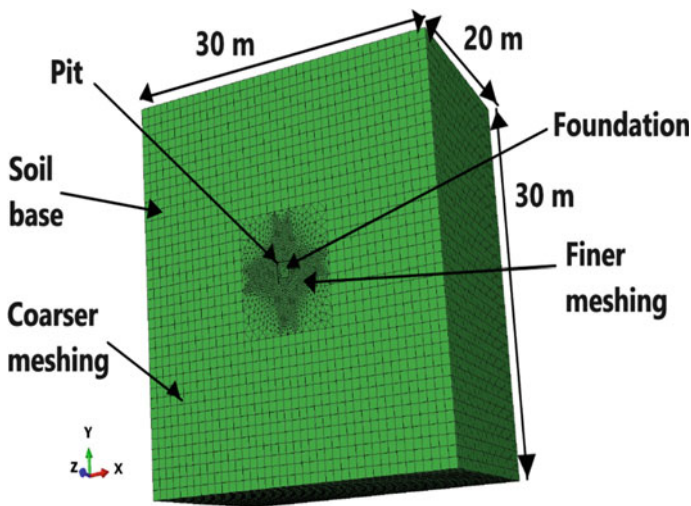

Fig. 6 3D model of the block vibration test setup in ABAQUS software

Table 3 Comparison of experimental and numerical obtained displacement amplitude at resonance condition

| Test parameter	Experimental result			Numerical model result		
Eccentric force (N-sec^2)	0.1117	0.2574	0.3953	0.1117	0.2574	0.3953
Resonant amplitude (mm)	0.132	0.352	0.722	0.217	0.489	0.534

Then fine meshing is done in the brick element near the region of the foundation as the stress concentration is more and for the region away from the foundation coarser meshing is adopted. Multipoint constraints is used to model interaction like as that of laminar soil and constraints type is set to tie type (Hard contact) so to have equal degree of freedom. The material damping was considered as 5%. The dynamic analysis is applied in two stages, first being the uniform geostatic stress which is the stress generated due to concrete foundation and mechanical oscillator parts. In the second stage, the dynamic loading in the vertical direction due to the dynamic force is generated by the oscillator.

The experimental results are verified with the result obtained from the ABAQUS analysis at eccentric force level of 0.11176, 0.25747 and 0.39536 N-sec^2, respectively. The dynamic response at resonance conditions is compared with the ABAQUS results as shown in Table 3. The differences may be due to the non-homogeneity and nonlinearity present in the soil properties at the field site compared to the input parameter used in the numerical analysis.

The dynamic loading is subjected to the foundation–soil which is of the type steady-state dynamics with the frequency range of that applied during experimentation. Therefore, the dynamic loading with the amplitude is applied in the numerical model in the frequency of 5 to 41 Hz. The amplitude under vibration which is the crucial parameter in the design of foundation subjected to strong vibration is noted down from the dynamic analysis. At the eccentricity force of 0.1117 N-sec^2, the displacement contours as obtained are shown in Fig. 7a, b.

3 Conclusion

As modern urbanization and industrial growth progresses, the use of high rising buildings and heavy machines may create strong vibration during its operation at high frequency. This experimental study is an attempt to understand the vertical vibration problem of shallow foundation and that should be duly acknowledged in the design for foundations under vibration. Large-scale field model test was conducted on shallow foundation of square section at field site. The test results are compared well with the previous study made on similar field site at IIT Kanpur. The problem of soil structure interaction is clearly visible from the test results as the value of damping ratio, natural frequency of soil and resonant frequency of the soil changes significantly with the variation of applied eccentric force level and forcing frequency.
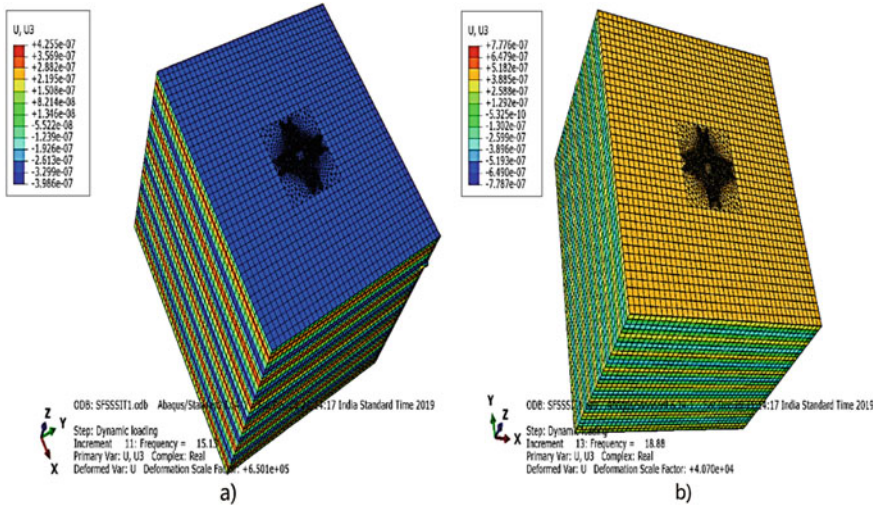
Fig. 7 The displacement contours **a** at 15 Hz and **b** 19 Hz as obtained from the numerical analysis during dynamic loading at eccentricity force of 0.1117 N-sec^2

References

1. Baidya DK, Rathi A (2004) Dynamic response of footings resting on a sand layer of finite thicknes. J Geotech Geoenviron Eng, ASCE 130(6):651–655
2. Baidya, DK, Mandal A (2006) Dynamic response of footing resting on a layered soil system. West Indian J of Eng. 28(2):65–79
3. Bhoumik K (1989) Coupled vibration of footings on elastic half-space. M.Tech. thesis, IIT-Kanpur, Kanpur
4. Das, NK, Raychowdhury P, Chaudhuri SR (2018) A study on dynamic characteristics of shallow foundation from block vibration test. 16th Symposium on Earthquake Engineering, IIT Roorkee, 316, 1–9
5. Das NK, Raychowdhury P (2020) Behavior of machine foundation on reinforced soil. 17th World conference on Earthquake Engineering (17 WCEE), Sept. 27-Oct.2, 2021, Sendai, Japan, pp-1–10, bundle 4c-0042 (proceedings published 2020)
6. Gazetas G (1991) Formulas and charts for impedance of surface and embedded foundations. J Geotech Eng, ASCE 117(9):1363–1381
7. IS (1992) Method of test for determination of in-situ dynamic properties of soils. Indian standard IS:5249. ISI, Manak Bhavan, New Delhi, India
8. IS (2000) Plain and reinforced concrete-code of practice. IS:456, Indian Standards Institution, Manak Bhavan, New Delhi
9. Kumar J, Reddy CO (2006) Dynamic response of footing and machine with spring mounting base. Geotech Geol Eng 24:15–27
10. Lysmer J (1965) Vertical motion of rigid footings. Department of Civil Engineering, University of Michigan. Report to WES Contract Report No. 3-115, 340
11. Navaratnarajah SK, Indraratna B, Ngo NT (2018) Influence of under sleeper pads on ballast behavior under cyclic loading: experimental and numerical studies. J Geotech. Geoenviron Eng 144(9):1–16
12. Novak M (1970) Prediction of footing vibrations. Journal of the Soil Mechanics and Foundations Division, ASCE, vol 96(3), pp 837–861

13. Reissner E (1936) Stationäre, axialsymmetrische Schwingungen eines homogenen elastischen Halbraumes, angeregt durch eine schwingende Masse, Ingenieur-Archiv, vol 7, Teil 6, Dezember, pp 381–396
14. Richart FE, Hall JR, Woods RD (1970) Vibrations of soils and foundations. Prentice-Hall, Englewood Cliffs, NJ
15. Swain A, Ghosh P (2016) Experimental study on dynamic interference effect of two closely spaced machine foundations. Can Geotech J 53(2):196–209

Settlement Analysis of Shallow Foundation on Frictional Soil Under Combined Effect of Static and Cyclic Load

Suvendu Kumar Sasmal and Rabi Narayan Behera

Abstract The settlement of a surface strip footing on dense sand due to long-term repetitive load (1 million cycles) is analyzed with the help of finite element method (FEM). The analysis is performed by applying both static and cyclic load on the center of footing, in the vertical direction and observing the corresponding settlement. The intensity of the static load is determined by dividing the ultimate static load by the factor of safety (*FS*). The static load is calculated for different values of *FS* i.e., 2, 2.5, 3, 3.5. The intensity of the dynamic load ($q_{d(\max)}$) is some percentage of the ultimate bearing capacity (q_u) of the foundation. Three values of ($q_{d(\max)}/q_u$) have been considered in the study, i.e., 5%, 10%, and 13%. Three different frequencies of cyclic load (0.5 Hz, 1 Hz, and 2 Hz) have also been considered. Based on the settlement pattern of the foundation, the critical number of load cycles (n_{cr}) for each case is determined beyond which the increase in settlement becomes insignificant for further load cycles. The study reveals that even a minor change in the frequency of loading can result in major variations in the n_{cr}.

Keywords Dense sand · Strip footing · Repetitive load · Settlement · Critical number of load cycles

1 Introduction

Foundations in the vicinity of industrial areas, generally apart from static loads from the superstructure, are subjected to dynamic forces in the form of machine-induced loads. In cases, such as the foundation beneath the railway track is generally subjected to long-term vertical cyclic loads. Other circumstances include the foundations under vertically oscillating machines. The behavior of these foundations is

---

S. K. Sasmal · R. N. Behera (✉)
Department of Civil Engineering, National Institute of Technology Rourkela, Rourkela, India
e-mail: rnbehera82@gmail.com

S. K. Sasmal
e-mail: suvendukumarsasmal@gmail.com

379

far different from that of the foundations under only static loads. The cyclic settle-
ment response of footing was observed in the late 1970s by Raymond and Komos
[1]. They concluded that the settlement is basically controlled by the cyclic load
intensity and soil condition. A similar methodology was adapted by Das et al. [2]
to study the settlement of square footing. Sawicki et al. [3] observed the response
of circular footing under cyclic load. The response of footing under the incremental
cyclic load was reported by Tafreshi et al. [4]. Apart from experimental models,
various numerical methods are also available to study the actual footing response.
When it comes to the numerical model for shallow foundations, the Winkler model
predicts the foundation response with significant accuracy. With time, this model
has evolved to capture the accurate nonlinear response of footing. The nonlinear
responses were observed with the help of beam on nonlinear Winkler foundation
(BNWF) model by researchers like [5–8].

The numerical analyses discussed mainly the seismic response. Also, the effect
of change in frequency of loading has not been clearly defined in available studies.
Rather than considering dynamic loads of small durations, the present study aims at
studying the long-term response of footing with the help of numerical simulations.
The foundation is modeled using BNWF method to study the response of the foun-
dation. A large number of loading cycles, i.e., 10^6 cycles are applied to the center of
the footing to study the long-term response. This type of loading condition generally
takes place in the case of a railroad foundations. The work is further extended to
observe the influence of possible change in frequency on the settlement response of
footing. The phenomenon of near cessation of settlement after a certain load cycle
is observed which is greatly controlled by the frequency of loading. The numerical
methods and the obtained results are described in the following sections.

2 Numerical Modeling Approach

A finite element model (BNWF model) is adapted to observe the settlement of a strip
footing of dimension 0.5 m × 0.1 m × 0.03 m (Length × Width × Thickness). The
soil parameters used in the analysis are listed in Table 1. A schematic diagram of the
foundation and loading system is shown in Fig. 1. The static load is the allowable
load, determined by dividing the ultimate load by *FS*. The cyclic load is a vertical
rectangular pulse load as shown in Fig. 1. In this study, 1 million cycles are consid-
ered to study the response of footing. The footing is divided into 100 equal parts

Table 1 Soil properties

Relative density (D_r, %)	Angle of internal friction (ϕ, degree)	Unit weight of soil (γ, kN/m^3)	Modulus of elasticity (E, MPa)	Poisson's ratio (υ)
69	40.8	14.36	55	0.35
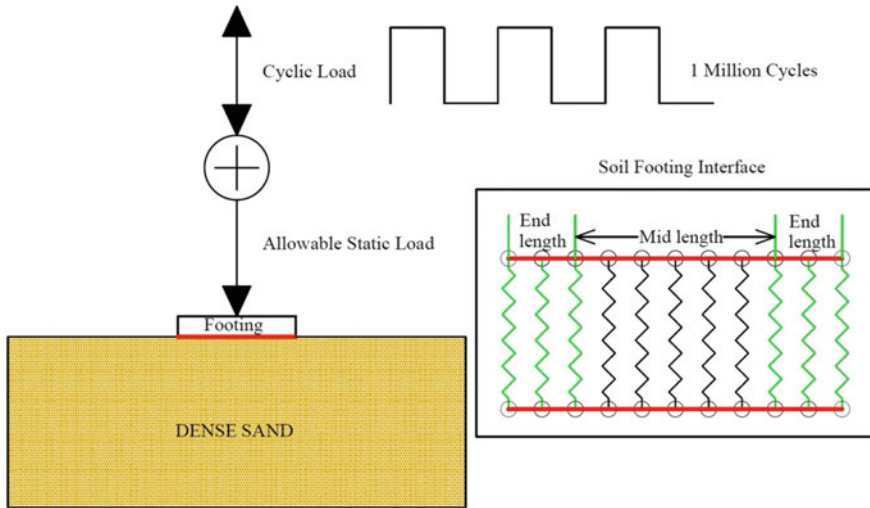
Fig. 1 Schematic diagram of the foundation and loading system

with the help of 101 nodes. The footing nodes having 3 degrees of freedom, DOF (2 translations and 1 rotation) are connected with the soil nodes (fixed, DOF = 0) using springs modeled as zero-length elements. The footing nodes are connected by using one-dimensional elastic beam-column elements defined with the help of area of cross-section, Young's modulus (E), and moment of inertia. Each spring consists of three components, i.e., elastic, plastic, and gap. The role of gap component (drag + closure) is to simulate soil-foundation separation behavior. Radiation damping is provided with the help of a damper parallel to the elastic component. Generally, for soil, a radiation damping value of 5% is applicable. The governing equations for spring behavior can be found in Boulanger [9]. The stiffnesses and capacities of the springs are determined according to Gazetas [10] and Meyerhof [11], respectively. FEMA 356:2000 [12] suggests assigning more stiffness at the end portion of the footing dimension considered (L_{end}). The end length ratio (End length/Total length) and stiffness intensity ratio (End portion stiffness/Mid portion stiffness) for the present model are selected as per Harden et al. [7]. The nonlinear properties for vertical springs are defined by *QzSimple2* material for shallow foundations according to Raychowdhury [13]. The *QzSimple2* springs used for capturing the vertical response have lesser strength in tension to simulate real soil type conditions. Apart from vertical springs, the sliding resistance of footing is considered using additional horizontal spring, defined as *TzSimple* material. The sliding capacity is calculated as

$$t_{\text{ult}} = W \tan \delta \tag{1}$$

Table 2 Details of the
numerical model

FS	$q_{d(\max)}/q_u$, %	f, Hz
2	5	0.5
2.5	10	1
3	13	2
3.5		

where W = weight on footing, δ = soil-concrete interfacial friction angle = 0.66 × ϕ.

The loading applied on the footing consists of 2 phases, application allowable static load followed by the cyclic load. Different amplitudes ($q_{d(\max)}/q_u$ = 5%, 10%, and 13%) and frequencies ($f = 0.5$ Hz, 1 Hz, 2 Hz) of cyclic load are considered to observe the corresponding parametric variation effect on settlement. The parameters and corresponding numeric values used in the study are mentioned in Table 2. The D_r (%), ϕ, and γ are taken as the values considered in Patra et al. [14]. The E and v are determined considering the values listed in EPRI [15]. The entire simulation is performed using numerical tool OpenSEES [16].

2.1 Validation of the Numerical Model

One of the key criterion to evaluate the accuracy of the model is to compare the outcome with that generated from a different constitutive model, for same soil conditions. The suitability from the present model has already been ascertained by comparing the static response of the foundation, for the same footing dimension and soil (dense sand) condition with the results obtained from Plaxis 3D [17]. The details of the validation study can be found in Sasmal and Behera [18] (Fig. 2).

3 Results and Discussions

The long-term settlement responses of footing following simulations of numerical model conditions are illustrated in Figs. 3, 4, 5 and 6 which are discussed in this section.

3.1 Effect of Intensity of Loading

It is obvious that the settlement of footing always increases with the increase in loading intensity (static and cyclic) which can be observed from Figs. 3, 4, 5 and 6. The role of the static load is found to be the major factor that controls the total settlement of footing. A decrease in the settlement is observed with an increase in
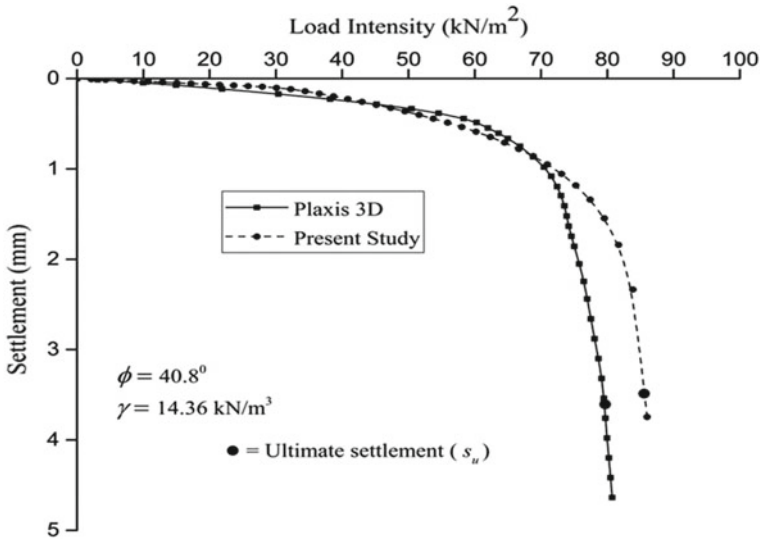
Fig. 2 Verification of accuracy of the present model [18]
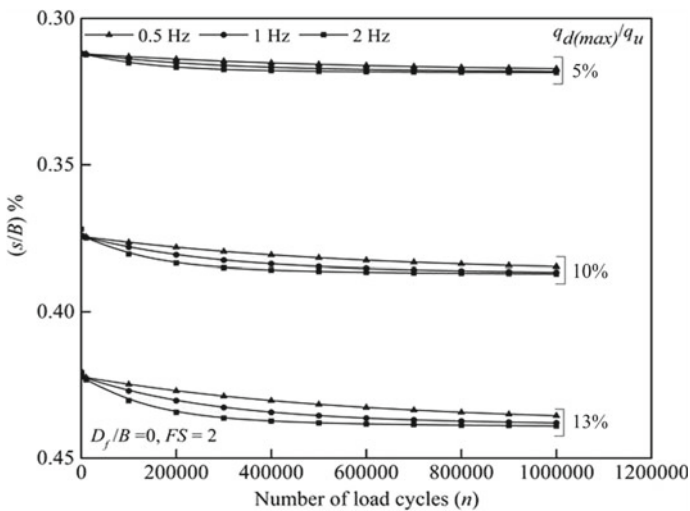
Fig. 3 Long-term settlement of footing under cyclic pulse ($FS = 2$)

the *FS*, keeping the intensity and frequency of cyclic load constant. It is attributed to the fact that the more the *FS*, the less is the amount of static load on the foundation. Hence, it can be inferred that the total settlement is directly proportional to intensity of both cyclic load and static load.

Fig. 4 Long-term settlement of footing under cyclic pulse ($FS = 2.5$)

Fig. 5 Long-term settlement of footing under cyclic pulse ($FS = 3$)
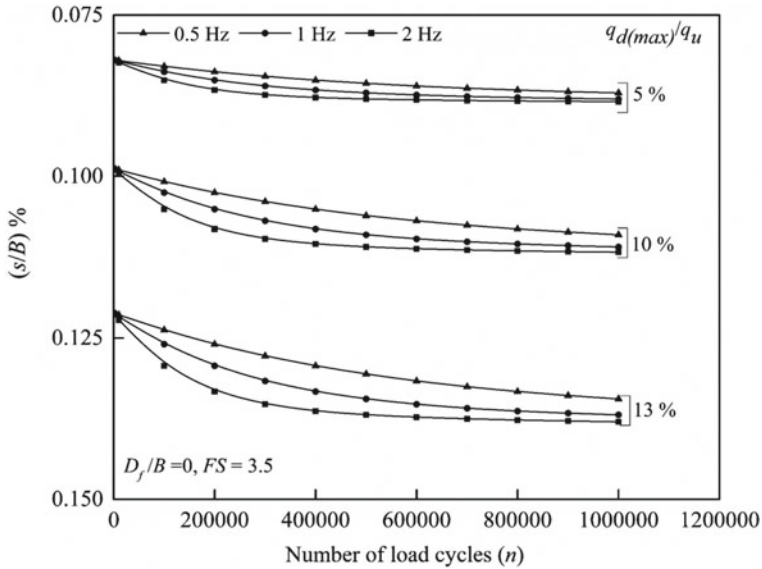
Fig. 6 Long-term settlement of footing under cyclic pulse ($FS = 3.5$)

3.2 Effect of Uncertainty in Loading Frequency

A traditional way of observing the effect of the number of load cycles is to keep the loading frequency constant. However, in real world, the frequency of a certain type of loading is not same always. This is highly dependent on the source of load. In this study, results of the change in the settlement pattern of footi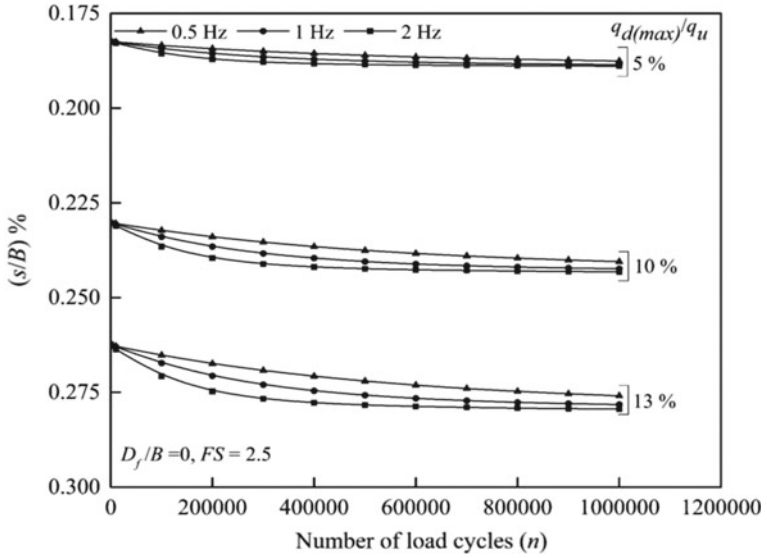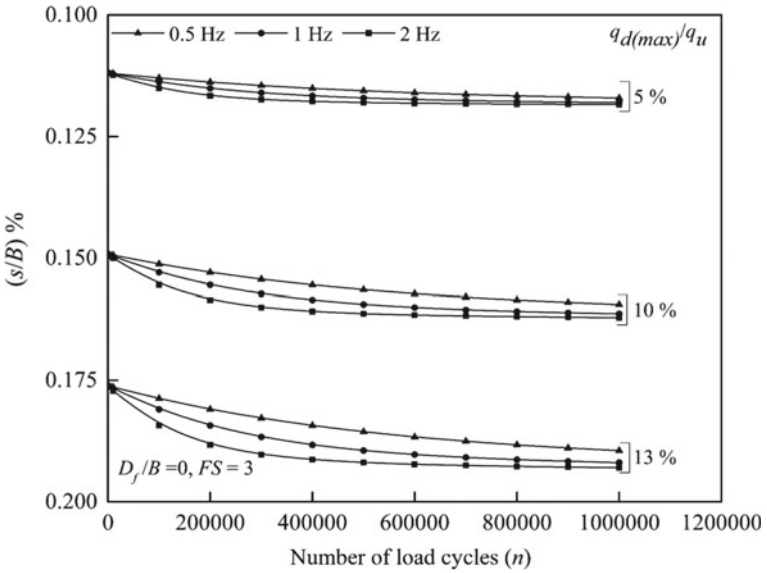ng are presented altering the frequency of loading. It is noted that with a slight increase in the frequency of loading, the settlement of footing increases although not very significantly. The increase in settlement of footing with an increase in frequency is attributed to the fact that the more frequently the load strikes the footing the less time the foundation soil gets to recover from the effect of the previous load cycle. It can be observed from Figs. 3, 4, 5 and 6, as the factor of safety increases, the gap among settlement responses corresponding to three frequencies increases, whereas for a lower factor of safety the settlements for different frequencies have nearly similar values. Hence, the changing frequency of the loading controls the settlement response more for lower values of intensity of static load. It is also observed that, for all the conditions considered in the present study, the footing undergoes more settlement with an increase in the frequency of cyclic load for a higher values of intensity of cyclic load.
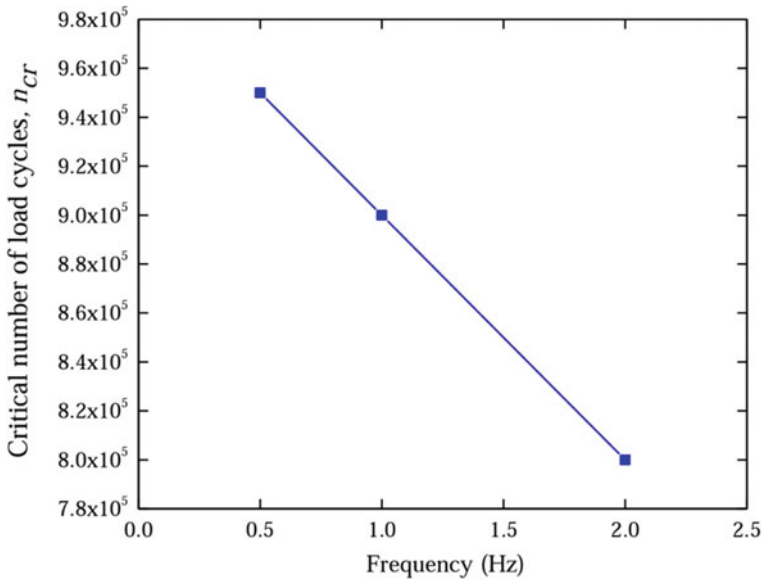
Fig. 7 Critical number of load cycles corresponding to different loading frequencies

3.3 Analysis of the Number of Load Cycles

Upon subjecting the footing to 1 million load cycles, it is observed from Figs. 3, 4, 5 and 6 that the rate of increase in the settlement with further loading cycles becomes very small or negligible after a particular value of the number of load cycles (n_{cr}). This number is dependent on the frequency of loading. This phenomenon takes place due to the increased strength of soil with increasing compression of soil mass with time. Similar outcomes have been presented in Das et al. [2].

Provided the fact that n_{cr} is a time-dependent parameter beneath the footing, its value is bound to be different for different frequencies of loading. n_{cr} takes lower value for higher values of loading frequency, justifying the fact that the more frequently the load compresses the soil mass, the less time is required to achieve sufficient strength so that further loading cannot cause any significant settlement. The n_{cr} values for different frequencies are presented in Fig. 7. It can be observed from Fig. 7 that the n_{cr} is linearly influenced by the frequency of the loading.

4   Conclusions

In the present work, the static-cyclic settlement response of a shallow foundation resting on a homogeneous layer of dense sand is discussed. Emphasis has been given to study the effect of uncertainty in the frequency of loading. Based on the

finite element model and parametric analysis including four different intensities of static load, three intensities of cyclic load, and three frequencies of cyclic load, the following major conclusions are drawn;

- The settlement (*s*) of footing increases with an increase in $q_{d(\max)}/q_u$ (%) and a decrease in *FS*. The settlement becomes negligible after n_{cr}, which is highly influenced by the loading frequency. n_{cr} is lower for higher loading frequency.
- The variation in settlement increases with a change in frequency, for higher values of *FS*.
- Irrespective of the *FS*, the effect of frequency is more felt for higher values of $q_{d(\max)}/q_u$ (%).

References

1. Raymond GP, Komos FE (1978) Repeated load testing of a model plane strain footing. Can Geotech J 15(2):190–201
2. Das BM, Yen SC, Singh G (1995) Settlement of shallow foundation on sand due to cyclic loading. In: International Conference on Recent Advances in Geotechnical Earthquake Engineering and Soil Dynamics, St. Louis, Missouri vol 8, pp 385–388
3. Sawicki A, Swidzinski W, Zadroga B (1998) Settlement of shallow foundation due to cyclic vertical force. Soils Found 38(1):35–43
4. Tafreshi SM, Mehrjardi GT, Ahmadi M (2011) Experimental and numerical investigation on circular footing subjected to incremental cyclic loads. Int J Civil Eng 9(4):265–274
5. Allotey N, El Naggar MH (2003) Analytical moment–rotation curves for rigid foundations based on a Winkler model. Soil Dyn Earthq Eng 23(5):367–381
6. Allotey N, El Naggar MH (2008) An investigation into the Winkler modeling of the cyclic response of rigid footings. Soil Dyn Earthq Eng 28(1):44–57
7. Harden CW, Hutchinson TC, Martin GR, Kutter BL (2005) Numerical modeling of the nonlinear cyclic response of shallow foundations. Rep. No. PEER2005/04, Pacific Earthquake Engineering Research Center (PEER), Berkeley, California
8. Gajan S, Hutchinson TC, Kutter B, Raychowdhury P, Ugalde JA, Stewart JP (2008) Numerical models for the analysis and performance-based design of shallow foundations subjected to seismic loading. Rep. No. 2007/04, Pacific Earthquake Engineering Research Center (PEER), Berkeley, California
9. Boulanger RW (2000) The PySimple1, QzSimple1, and TzSimple1 material documentation. Documentation for the OpenSees platform available at http://opensees.berkeley.edu/
10. Gazetas G (1991) Formulas and charts for impedances of surface and embedded foundations. J Geotech Eng, ASCE 117(9):1363–1381
11. Meyerhof GG (1953) The bearing capacity of foundations under eccentric and inclined loads. In: Proceedings, Third International Conference on Soil Mechanics and Foundation Engineering, pp 440–445
12. FEMA 356 (2000) Prestandard and commentary for the seismic rehabilitation of buildings. American Society of Engineers, Virginia
13. Raychowdhury P (2008) Nonlinear Winkler-based shallow foundation model for performance assessment of seismically loaded structures. Ph. D. dissertation, University of California, San Diego
14. Patra CR, Behera RN, Sivakugan N, Das BM (2012) Ultimate bearing capacity of shallow strip foundation under eccentrically inclined load, Part I. Int J Geotech Eng 6(3):343–352

15. EPRI (1990) Manual on estimating soil properties for foundation design. Electric Power Research Institute, Palo Alto, California
16. OpenSees [Computer Software], University of California, Berkeley
17. Brinkgreve RBJ, Engin E, Swolfs WM (2013) PLAXIS 3D 2013 user manual. Plaxis bv, Delft
18. Sasmal SK, Behera RN (2018) Prediction of combined static and cyclic load-induced settlement of shallow strip footing on granular soil using artificial neural network. Int J Geotech Eng, 1–11. https://doi.org/10.1080/19386362.2018.1557384

Transient Response Prediction of Shallow Foundation Using ANFIS

Suvendu Kumar Sasmal and Rabi Narayan Behera

Abstract The present study focuses on predicting the transient response of a strip footing with the help of adaptive neuro-fuzzy inference system (ANFIS). First, the data set is generated using a numerical model for 108 number of possible conditions varying the soil and loading parameters, using Open System for Earthquake Engineering Simulation (*OpenSEES*). The input parameters are factor of safety (*FS*), embedment ratio (D_f/B), the intensity of cyclic load ($q_{d(\max)}$), and relative density of the soil (D_r, %). The output is (s_f/s_u) %, i.e. the settlement due to the first load cycle (transient settlement, s_f) divided by settlement (s_u) corresponding to the ultimate bearing capacity (q_u) of the foundation. This data set is analyzed using ANFIS. 75% of the entire data was considered for the training and remaining for testing. The study reveals that the transient response of the foundation is significantly affected by the static load on the foundation. The outcomes from the sensitivity analysis of the trained ANFIS model will be helpful in designing foundations in industrial areas.

Keywords Transient response · ANFIS · Settlement · Sensitivity analysis

1 Introduction

Shallow foundations which are generally subjected to static loads are in a steady-state until an additional jerk due to some external loading takes place. The behavior of a foundation under dynamic load consists of two phases or stages: the transient behavior and the steady-state behavior. The transient behavior of the foundation is the response to a sudden change in loading condition, viz. static to dynamic. Under dynamic loading, the behavior of the foundation is highly nonlinear. This nonlinearity in the behavior is a result of nonlinear behavior of soil conditions in addition to the loading parameters. The settlement of footing just after the arrival of dynamic load

S. K. Sasmal · R. N. Behera (✉)
Department of Civil Engineering, National Institute of Technology Rourkela, Rourkela, India
e-mail: rnbehera82@gmail.com

S. K. Sasmal
e-mail: suvendukumarsasmal@gmail.com

can be observed using experimental and numerical procedures. It is important how each of the inputs influences the response of the footing. The importance of the input parameters can be established by performing sensitivity analysis on a model developed with the help of a recent effective technique based on fuzzy algorithms.

Adaptive neuro-fuzzy inference system (ANFIS) is a well-known method for predicting the outputs in terms of supplied inputs. Yilmaz and Kaynar [1] predicted the swelling potential of clayey soil using neural networks and ANFIS. Cabalar et al. [2] presented a review of the application of ANFIS in geotechnical engineering. Trivedi et al. [3] predicted blast-induced fly rock distance using ANN and ANFIS. Asrari et al. [4] predicted the deformation modulus of rock mass using ANFIS. Sethy et al. [5] predicted the ultimate bearing capacity of rectangular footing using ANFIS. Kebria et al. [6] observed the transport of leachate successfully with the help of ANFIS. The axial load carrying capacity of piles was predicted by Ghorbani et al. [7]. Umrao et al. [8] predicted the strength of heterogeneous rock with the help of ANFIS. The bearing capacity of piles was successfully estimated by Harandizadeh et al. [9]. Saadat and Bayat [10] predicted the unconfined compressive strength of soil using ANFIS and nonlinear regression. Moayedi et al. [11] presented a review of the engineering application of neural networks and ANFIS in geotechnical engineering.

A review of the literature of the present decade reflects the suitability of the fuzzy algorithm in the field of geotechnical engineering. However, there is a lack of literature explaining the use of ANFIS in the field of geotechnical earthquake engineering. The present study takes the help of ANFIS to observe the transient response of a strip footing on different types of granular soil. The transient response is the first response of any system to a sudden change in the steady state. In many soil dynamics problems, the steady-state response is only observed neglecting the transient response. In contrast, this paper focuses on the transient response of the foundation. This work also discusses the effect of soil and loading parameters on the transient response of the footing. Lastly, a sensitivity analysis is carried out to ascertain the importance of the input variables.

2 Methodology

The methodology consists of two separate phases: (a) generation of the data set using numerical simulations and (b) analysis of generated data in ANFIS. The details of each part are explained below. The whole methodology is summarized in Fig. 1.

2.1 Numerical Model

The data set is obtained with the help of a numerical model based on beam on nonlinear winkler foundation model carried out using numerical programming tool OpenSEES [12]. This model consists of a footing that is created by using 101 nodes
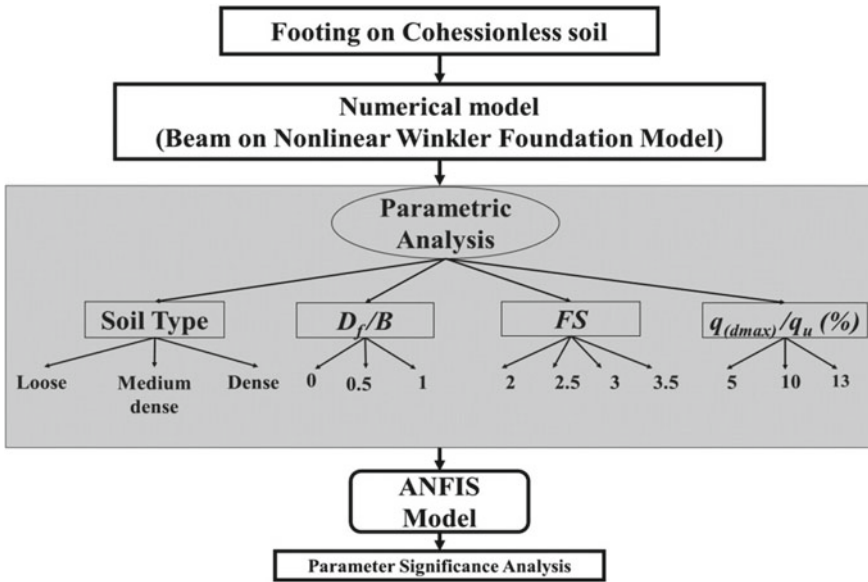
Fig. 1 Flowchart of the methodology

and 100 elastic beam-column elements. Each footing node has three degrees of freedom (two translations and a rotation). The elements are defined by Young's modulus and modulus of inertia. Each footing node is joined to a soil node with the help of nonlinear springs. The soil nodes are fixed, i.e. degree of freedom = 0. The nonlinear springs are defined with the help of soil properties (shear modulus, Poisson's ratio). The details of the soil properties are mentioned in Table 1. Three different types of springs are considered: i.e., *qzsimple2*, *pysimple2*, and *tzsimple2* materials to capture the vertical, passive, and sliding response of the footing, respectively. The finite element mesh is created as per the guidelines mentioned in Harden et al. [13]. The nonlinear springs are modeled following the procedures mentioned in Raychowdhury [14]. The validation study of the model for different sand conditions is presented in Sasmal and Behera [15].

Table 1 Details of the soil parameters

Types of sand	Properties	Source
Loose sand	$D_r = 35\%$, $\phi = 34°$, $\gamma = 13.34$ KN/m^3	Sahu et al. [16]
	$E = 20$ MPa, $v = 0.3$	EPRI [17]
Medium dense sand	$D_r = 51\%$, $\phi = 37.5°$, $\gamma = 13.97$ KN/m^3	Patra et al. [18]
	$E = 36$ MPa, $v = 0.32$	EPRI [17]
Dense sand	$D_r = 69\%$, $\phi = 40.8°$, $\gamma = 14.36$ KN/m^3	Patra et al. [18]
	$E = 55$ MPa, $v = 0.35$	EPRI [17]

The load is applied to the foundation in two stages. First, the allowable static load is applied depending on the factor of safety. Then, a cycle of rectangular pulse is applied on the center of the footing and the total settlement is recorded.

2.2 ANFIS Model

A total of 108 data set as shown in Fig. 1 are generated varying parameters like the relative density of soil (D_r, %), factor of safety (*FS*), the intensity of cyclic load ($q_{d(max)}$), and depth of embedment (D_f) of footing. Out of 108 data sets, 81 are considered for training and the trained model is tested on the remaining 27 data set. The data set for training and testing was selected by using random permutation technique in MATLAB, with the help of the "*randperm*" command.

ANFIS architecture is shown in Fig. 2. The input membership function (*MF*) is taken as "*gbelmf*". The ANFIS model is generated using "*hybrid*" algorithm with 100 *epochs*. Hybrid algorithm is a combination of least square and backpropagation techniques [3].
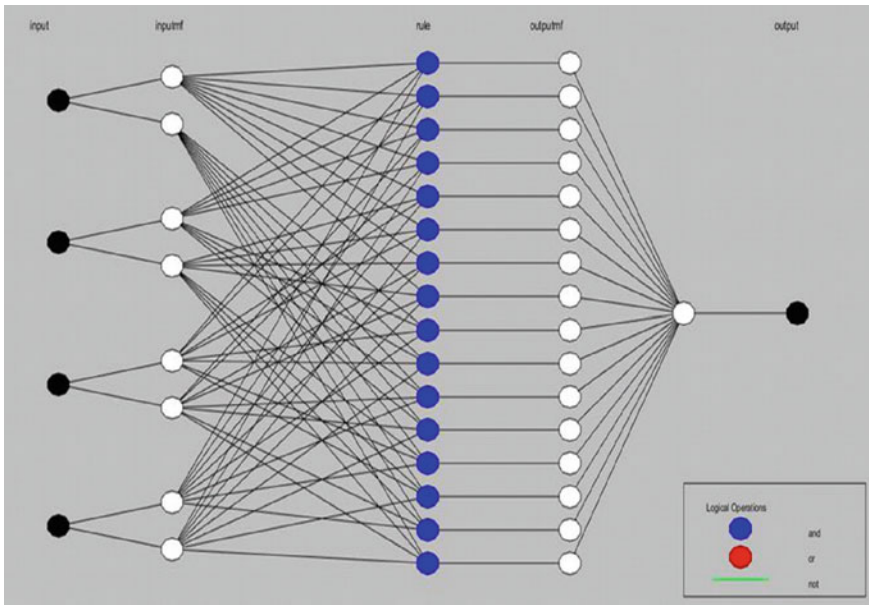
Fig. 2 ANFIS architecture

3   Results and Discussions

The model is tested by predicting the outcomes and comparing these with the observed output from the numerical model. The comparison is shown in Fig. 3. It is observed that the R^2 for both training and testing is found to be 0.98. Hence, it can be interpreted that the present model not only predicts the output accurately but also has very good generalization capability. According to Sethy et al. [5], R^2 can be calculated as;

$$R^2 = \frac{E_1 - E_2}{E_1} \tag{1}$$

$$E_1 = \sum_{i=1}^{n} (O_i - O^*)^2 \tag{2}$$

$$E_2 = \sum_{i=1}^{n} (O_p - O_i)^2 \tag{3}$$
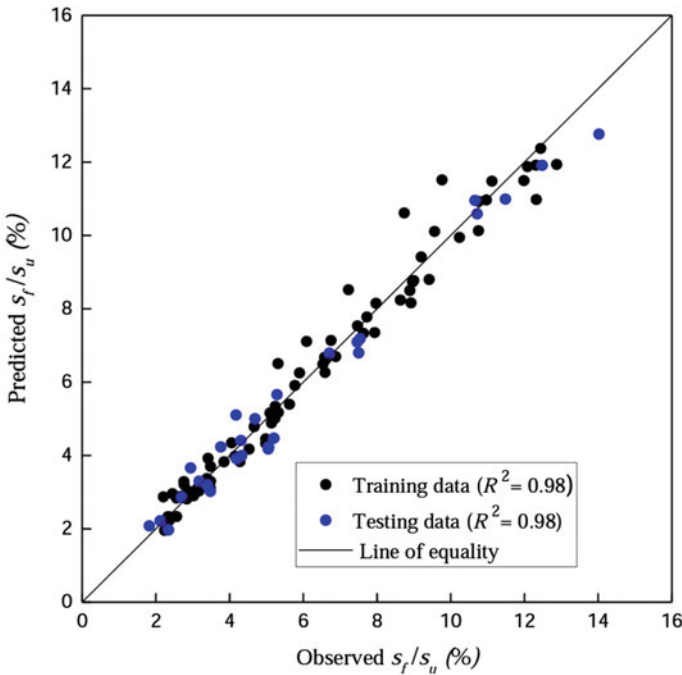
Fig. 3 Comparison of observed and predicted outputs

where, O_i, O^*, and O_p are observed, average observed, and predicted (s_f/s_u) %, respectively.

The variation of the transient settlement with each input parameter is illustrated in Fig. 4. In this figure, input 1, input 2, input 3 and input 4 represent FS, D_f/B, $q_{d(\max)}/q_u$ (%), and D_r (%), respectively. The non-dimensional settlement decreases with an increase in FS, D_f/B, and D_r (%) and increases with an increase in $q_{d(\max)}/q_u$ (%). The combined effect of parameters on the transient settlement is shown in Fig. 5 as surface plots. Apart from FS, where a sharp decrease in output is observed, in case of all the parameters a gradual variation of the output is observed. This phenomenon justifies the importance of static load in controlling the transient behavior of the footing. As the depth of embedment increases, the passive resistance due to the surrounding soil comes into play, thereby creating a more stable footing condition. Due to this, the non-dimensional settlement also decreases with an increase in the depth of embedment. However, it may be observed that the effect of foundation embedment is negligible after a certain value. In the case of the relative density of soil, an increase in the parameter means an increase in the strength of the soil which leads to smaller non-dimensional settlements. It is important to note that, with the increase in the depth of embedment and the relative density the amount of settlement will increase, due to an increased level of ultimate bearing capacity of the foundation, but the non-dimensional parameter (s_f/s_u) % will show the reverse trend.
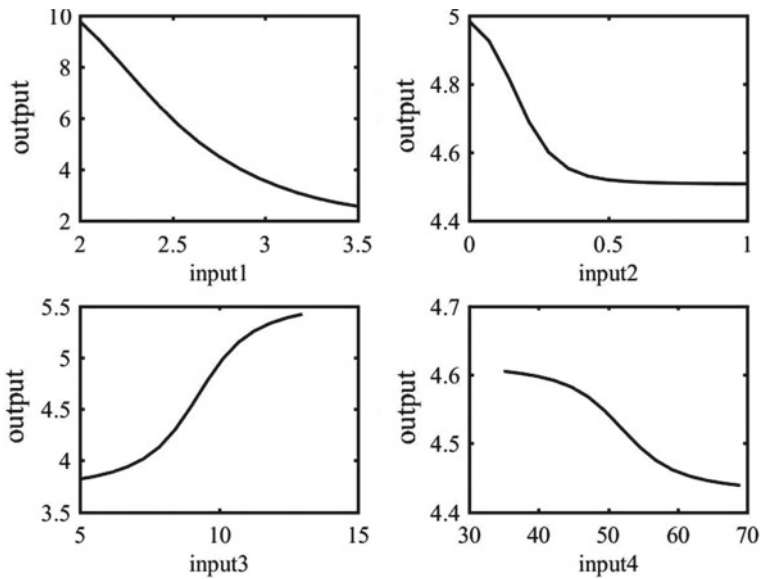
Fig. 4 Variation of output with individual inputs
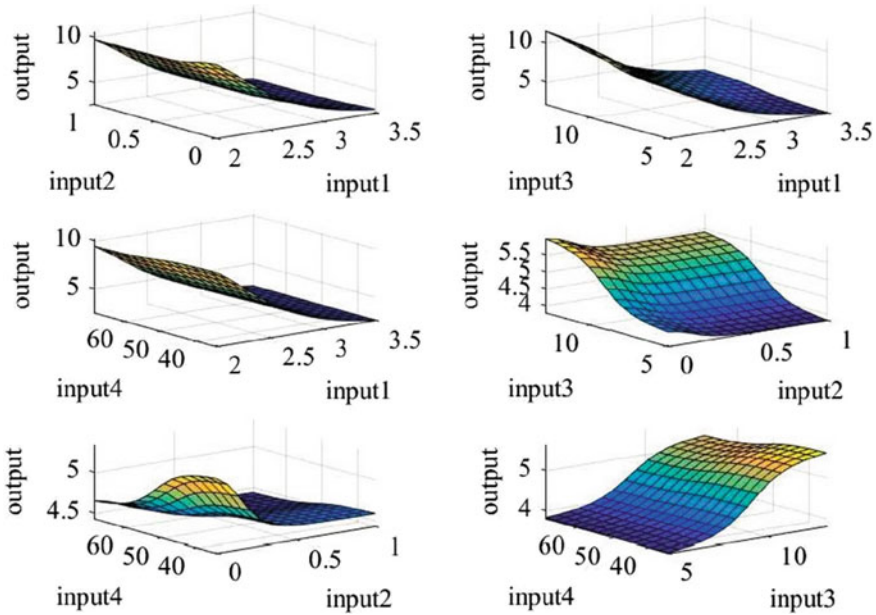
Fig. 5 Surface plots showing input–output relation

4 Sensitivity Analysis

The sensitivity analysis has been carried out using the procedures mentioned in Beura and Bhuyan [19]. The percentage contribution (S_i) of a variable can be calculated as;

$$S_i = \frac{|D_i|}{\sum\limits_{i=1}^{n} |D_i|} \times 100 \tag{4}$$

D_i is calculated by using the procedures mentioned in Beura and Bhuyan [19].

The weight of each parameter is shown in Fig. 6. From Fig. 6, it is revealed that *FS* is the most influencing parameter followed by $q_{d(\max)}/q_u$ (%), D_f/B, and D_r (%). From sensitivity analysis, it is found that the transient response of a foundation is highly dependent on the existing static load on the foundation.

5 Conclusions

A data set generated with the help of Beam on Nonlinear Winkler Model is analyzed using ANFIS. The effect of soil and loading parameters on the non-dimensional
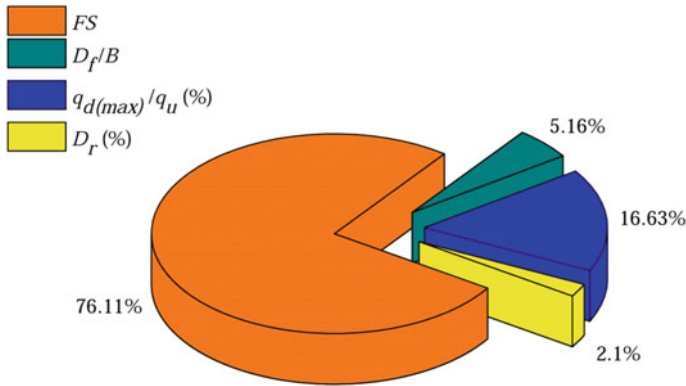
Fig. 6 Significance of input parameters

transient settlement response is described. From the analysis of results obtained from ANFIS and sensitivity analysis the following conclusions are drawn:

(a) ANFIS can be used to predict the transient settlement accurately, with very good generalization.
(b) The non-dimensional transient settlement is directly proportional to the intensity of cyclic load and inversely proportional to the factor of safety, embedment ratio, and relative density of soil.
(c) Sensitivity analysis of trained ANFIS model suggests that the factor of safety and relative density of soil are the most and least influencing parameters, respectively.

References

1. Yilmaz I, Kaynar O (2011) Multiple regression, ANN (RBF, MLP) and ANFIS models for prediction of swell potential of clayey soils. Expert Syst Appl 38(5):5958–5966
2. Cabalar AF, Cevik A, Gokceoglu C (2012) Some applications of adaptive neuro-fuzzy inference system (ANFIS) in geotechnical engineering. Comput Geotech 40:14–33
3. Trivedi R, Singh TN, Gupta N (2015) Prediction of blast-induced flyrock in opencast mines using ANN and ANFIS. Geotech Geol Eng 33(4):875–891
4. Asrari AA, Shahriar K, Ataeepour M (2015) The performance of ANFIS model for prediction of deformation modulus of rock mass. Arab J Geosci 8(1):357–365
5. Sethy BP, Patra CR, Sivakugan N, Das BM (2017) Application of ANN and ANFIS for predicting the ultimate bearing capacity of eccentrically loaded rectangular foundations. Int J Geosynt Ground Eng 3(4):35, 1–14
6. Kebria DY, Ghavami M, Javadi S, Goharimanesh M (2018) Combining an experimental study and ANFIS modeling to predict landfill leachate transport in underlying soil—a case study in north of Iran. Environ Monit Assess 190(1):26, 1–17
7. Ghorbani B, Sadrossadat E, Bazaz JB, Oskooei PR (2018) Numerical ANFIS-based formulation for prediction of the ultimate axial load bearing capacity of piles through CPT data. Geotech Geol Eng 36(4):2057–2076

8. Umrao RK, Sharma LK, Singh R, Singh TN (2018) Determination of strength and modulus of elasticity of heterogenous sedimentary rocks: An ANFIS predictive technique. Measurement 126:194–201
9. Harandizadeh H, Toufigh MM, Toufigh V (2019) Application of improved ANFIS approaches to estimate bearing capacity of piles. Soft Comput 23(19):9537–9549
10. Saadat M, Bayat M (2019) Prediction of the unconfined compressive strength of stabilised soil by Adaptive Neuro Fuzzy Inference System (ANFIS) and Non-linear Regression (NLR). Geomech Geoeng 1–12
11. Moayedi H, Mosallanezhad M, Rashid ASA, Jusoh WAW, Muazu MA (2018) A systematic review and meta-analysis of artificial neural network application in geotechnical engineering: theory and applications. Neural Comput Appl 1–24
12. OpenSEES [Computer Software], University of California, Berkeley
13. Harden C, Hutchinson T, Martin GR, Kutter BL (2005) Numerical modeling of the nonlinear cyclic response of shallow foundations. Rep No 2005/04 Pacific Earthquake Engineering Research Center (PEER) Berkeley California
14. Raychowdhury P (2008) Nonlinear Winkler-based shallow foundation model for performance assessment of seismically loaded structures. Ph.D. dissertation, University of California, San Diego
15. Sasmal SK, Behera RN (2018) Prediction of combined static and cyclic load-induced settlement of shallow strip footing on granular soil using artificial neural network. Int J Geotech Eng 1–11. https://doi.org/10.1080/19386362.2018.1557384
16. Sahu R, Patra CR, Das BM, Sivakugan N (2016) Bearing capacity of shallow strip foundation on geogrid-reinforced sand subjected to inclined load. Int J Geotech Eng 10(2):183–189
17. EPRI (1990) Manual on estimating soil properties for foundation design. Electric Power Research Institute, Palo Alto, California
18. Patra CR, Behara RN, Sivakugan N, Das BM (2012) Ultimate bearing capacity of shallow strip foundation under eccentrically inclined load, Part I. Int J Geotech Eng 6(3):343–352
19. Beura SK, Bhuyan PK (2018) Operational analysis of signalized street segments using multigene genetic programming and functional network techniques. Arab J Sci Eng 43(10):5365–5386

Seismic Bearing Capacity and Elastic Settlement of Footing on Slopes

Sukanta Das and **B. K. Maheshwari**

Abstract The aim of this paper to study the seismic bearing capacity of embedded strip footing on cohesionless soil slopes. In addition, elastic settlement of strip footing on slopes is also examined, which is not yet studied in the literature. Three-dimensional finite element method (3D-FEM)-based numerical analysis in PLAXIS 3D software is carried out for the present investigation. The strip footing located at the horizontal surface is considered first and then the effect of the slope angle is studied. The effect of slope angle, embedment depth and load intensity of footing on slopes are presented in the present study. The results obtained from the present numerical study are compared with available past results in the literature. A strip footing located on the face of the stable granular slopes ($\beta = 20°$ and $30°$) is considered. The seismic bearing capacity in terms of bearing capacity factor is determined. A significant reduction of bearing capacity factor is observed due to the presence of slopes. However, the influence of slope angles on the elastic settlement of strip footing is reported for a constant load and foundation geometry. From the obtained results, as expected the maximum settlement is observed at the center. The elastic settlement of the footing is not significantly dependent on slope angles.

Keywords Bearing capacity · Seismic condition · Elastic settlement · Strip footing · Embedment · Soil slopes · 3D FEM

1 Introduction

In foundation design, the bearing capacity and settlement analysis of a foundations are common in practice. The design of foundation on slopes is still a difficult task for engineers due to less guidelines. The key parameter for designing of foundations on slopes is slope angles which significantly reduce the bearing capacity. Minimum edge distance of foundations from the slope side also influence the bearing capacity of foundation on slopes [1]. Researchers studied the bearing capacity of shallow

S. Das (✉) · B. K. Maheshwari
Department of Earthquake Engineering, Indian Institute of Technology Roorkee, Roorkee, India
e-mail: sukanta1993das@gamil.com

foundation on slopes by either experimentally or theoretically [2–4]. Very few studies on seismic bearing capacity on slopes are available compare to seismic bearing capacity of footing on horizontal surface [5–9].

Meyerhof [1], first considered the effect of embedment depth of footing on slopes. Further, few researchers had considered the effect of embedment of footing on slopes [6, 8, 9]. In the present study, an attempted is made to check, and the embedment of footing on slopes using finite element method (FEM).

Several studies are available for estimation of elastic or immediate settlement of footing on horizontal surface. Many researchers proposed different formulae to determine the elastic settlement based on theory of elasticity [10–12]. In the present study, finite element numerical analysis is carried out to examine the elastic settlement of footing on slopes.

2 Numerical Modeling

In the present study, FEM-based numerical analysis has been considered to examined the bearing capacity and settlement of embedded (D_f) strip footing of width (B) on slopes ($\beta = 20°$, $30°$). In PLAXIS 3D, the FEM model of 200 m width, 30 m deep and extended by 1 m in lateral direction has been considered to adopt the plain strain condition. The height of the slope is taken as 10 m. Figure 1 depicts the nomenclature used for the estimation of bearing capacity and elastic settlement of strip footing on slopes. The soil material has been modeled as ten nodded tetrahedral elements while for the footing six noted triangular plate element has been considered. The Mohr–Coulomb elasto-plastic constitutive has been used for soil and the footing has been assumed as linear elastic. The associated flow rule has been considered in the analysis. A uniformly distributed pressure has been applied on the top of the embedded strip footing on slopes.
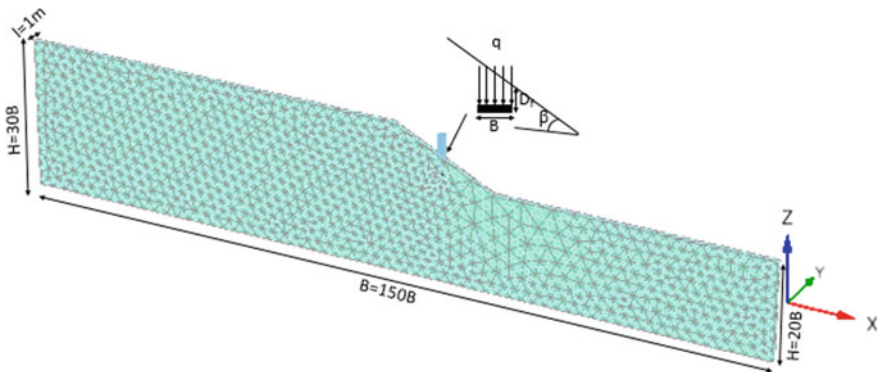
Fig. 1 FEM model used for estimation of seismic bearing capacity of strip footing embedded on slopes

A standard boundary condition has been assigned to FEM model, the bottom edge is fully fixed against any rotation while side edges are free along vertical direction and fixed in lateral direction directions, as shown in Fig. 1. The sloping surface has been kept as free. The medium meshing scheme with required local refinement has been assigned where the results get fully converged and the difference of results is minimum with change of element size.

The equation used in the present study is given by Meyerhof [1] to estimate the bearing capacity, as given in Eq. 1. Where the $N_{\gamma qs}$ is bearing capacity factor.

$$q_u = \frac{1}{2}\gamma BN_{\gamma qs} \tag{1}$$

Elastic settlement occurs in granular soil deposits with in a short time and estimation of elastic settlement is quite common in geotechnical engineering practice. Several studies are available to determine the elastic settlement of footing on horizontal surface. Among all those literatures, Mayne and Poulos [11] proposed an equation based on theory of elasticity which considered all the correction factors, given in Eq. 2. Where ρ_z is settlement, B_e is footing width, ν is Poisson ratio, E_o is Young modulus of soil, I_G is influence factor, I_F is footing stiffness factor, I_E is embedment correction factor, I_R is footing roughness factor. In the present study, linear elastic soil material and perfectly elastic footing have been assumed. The standard FEM model dimension has been considered, as Maney and Poulos [11] stated minimum depth of model has been considered as H/B = 30 m and a trail numerical analysis has been done to fixed the standard lateral dimensions. The standard side distance has been considered at b/B and l/L = 30 where the effect of lateral side is minimum, as shown in Fig. 2a. The footing is discrete into a very small size of elements (no of elements >500) to get accuracy in results. A rectangular flexible footing placed at the crest of the slopes and a uniformly load has been assigned on the footing. The settlement at the center and both corner has been recorded.
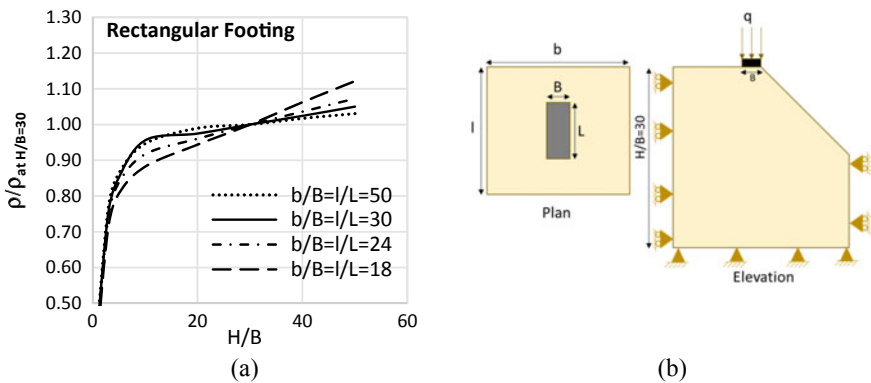

Fig. 2 Nomenclature used to check the elastic settlement of footing on slopes

$$\rho_z = q\,B_e\,\frac{1 - v_s^2}{E_0}\,I_G I_F I_E I_R \tag{2}$$

3 Seismic Bearing Capacity of Strip Footing on Slopes

The seismic bearing capacity of a strip footing on a cohesionless soil has been estimated using FEM analysis. Initially, the seismic bearing capacity of strip footing on horizontal surface has been examined. Further, the effect of slope angle has been considered. The present results have been compared with past results for both footing located on horizontal and sloping surface. From the present numerical analysis, a chart has been proposed to estimate the seismic bearing capacity of strip footing on slopes for different embedment.

3.1 Comparison of Seismic Bearing Capacity

The seismic bearing capacity of strip footing has been determined in terms of seismic bearing capacity factor. The obtained results from the present study have been compared with the past results, as shown in Fig. 3. The comparison of seismic bearing capacity factor of strip footing on horizontal surface has been presented in Fig. 3a, whereas Fig. 3b represents the seismic bearing capacity of strip footing embedded on slopes. The results have been observed as close as reported by Kumar and Rao [7]. The case of $N_{\gamma qs}$ of footing embedded on slopes has been found reasonably closer with that of suggested by Chakraborty and Kumar [13].
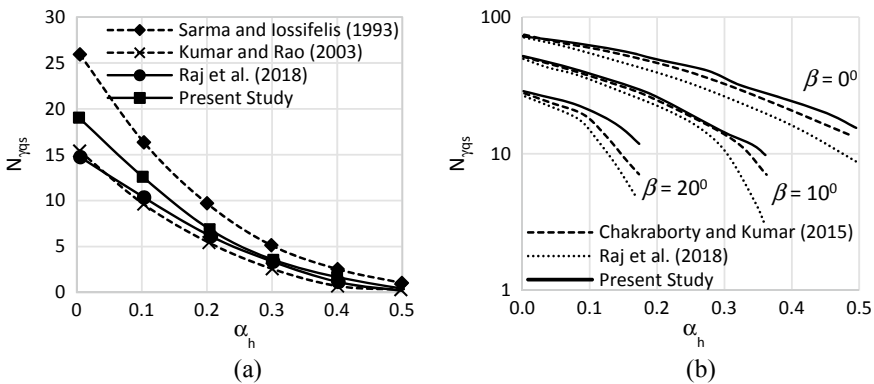
Fig. 3 Comparison of seismic bearing capacity factors $N_{\gamma qs}$ **a** on flat ground ($\beta = 0°$), D/B = 0 and **b** sloping ground, D/B = 1 for $\phi = 30°$

3.2 Effect of Embedment

The influence of embedment on seismic bearing capacity of strip footing on stable slopes has been depicted in Fig. 4. As expected, the bearing capacity increases with the increase of friction angle of soil irrespective of other conditions. For a constant embedment and slope angle, the seismic bearing capacity factor decreases with increase of seismic forces. From Fig. 4a, b, the bearing capacity factor increase with the increase of embedment. The bearing capacity factors decrease with the increases of slope angle. Therefore, the seismic bearing capacity depends on internal friction angle of soil, slope angle and embedment of footing.
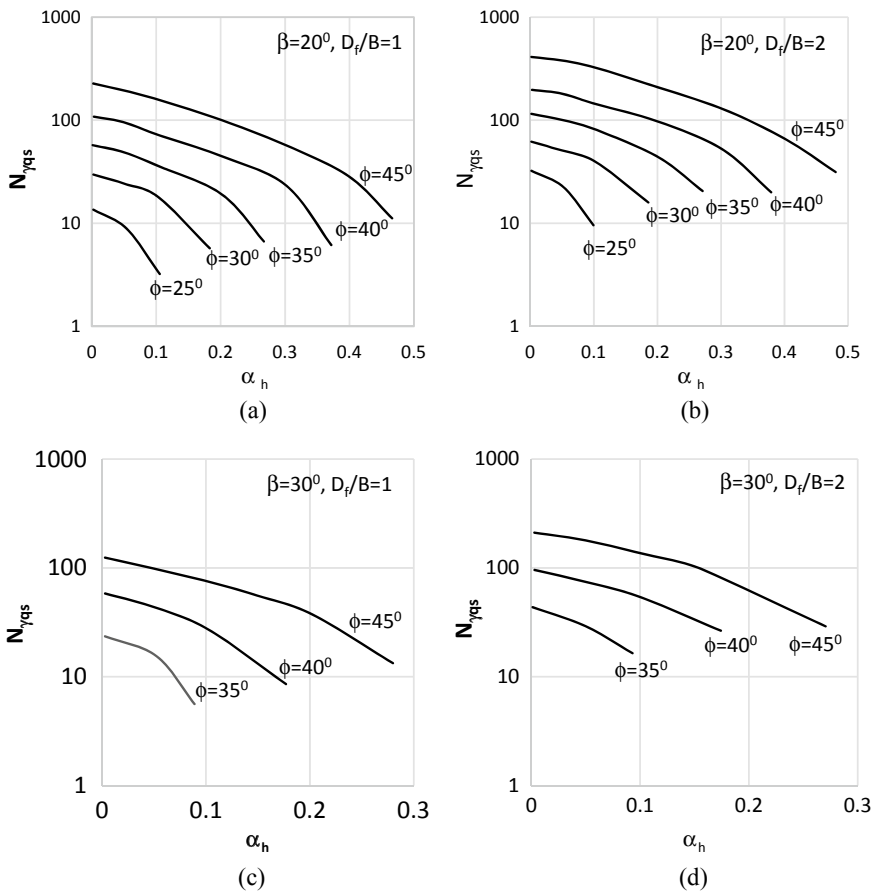
Fig. 4 Seismic bearing capacity factors $N_{\gamma qs}$ **a** D/B $= 1$ for $\beta = 20°$, **b** D/B $= 2$ for $\beta = 20°$, **c** D/B $= 1$ for $\beta = 30°$, **d** D/B $= 2$ for $\beta = 30°$

Table 1 Comparison of settlement influence factor for circular flexible footing

Nishida (1966)						Present study 3D FEM					
I_c			I_e			I_c			I_e		
c/a	Poisson's ratio						Poisson's ratio				
	0.5	0.25	0.00	0.5	0.25	0.00	0.5	0.25	0.00	0.5	0.25	0.00
0	1.5	1.87	2	0.95	1.19	1.27	1.48	1.87	1.98	0.94	1.20	1.27
3.5	0.90	0.99	0.90				0.90	0.99	0.90			
5	0.86	0.94	0.86	0.58	0.60	0.58	0.86	0.94	0.86	0.58	0.60	0.58
100	0.75	0.83	0.75	0.47	0.53	0.47	0.77	0.83	0.76	0.46	0.52	0.47
1000	0.75	0.83	0.75	0.47	0.53	0.47	0.78	0.83	0.77	0.47	0.54	0.48

4   Elastic Settlement of Circular Footing on Slopes

The rectangular footing located at the horizontal and crest of the slopes has been adopted for the estimation of elastic settlement of flexible circular footing. The effect of slope angles on elastic settlement for a constant load and footing geometry has been examining.

4.1   Comparison of Elastic Settlement

The standard FEM model dimension has been considered to check the elastic settlement of footing on horizontal as well as on slopes. Several solutions are available to estimate elastic settlement of footing on slopes. The present numerical results have been compared with past elastic solution. Nishida [14] reported influences factor for determination of elastic settlement of flexible circular footing. In Table 1, the comparison of influence factor has been presented and found good agreement with the present results. Further, the settlement influence factors proposed by Milovic [10] for flexible circular footing and Timoshenko and Goodier [12] for rigid circular footing has been compared with present results, as shown in Fig. 5. Moreover, the obtained FEM results from the present FEM analysis are in good agreement with past studies.

4.2   Effect of Slope Angles

The elastic settlement of footing on slopes has been examined numerically and reported here. The elastic settlement of footing for flexible and rigid footing has been shown in Fig. 6a, b. In case of flexible footing on slopes, the settlement at the center has been observed maximum and minimum at the far corner of the footing

Fig. 5 Comparison of elastic settlement of footing on horizontal surface
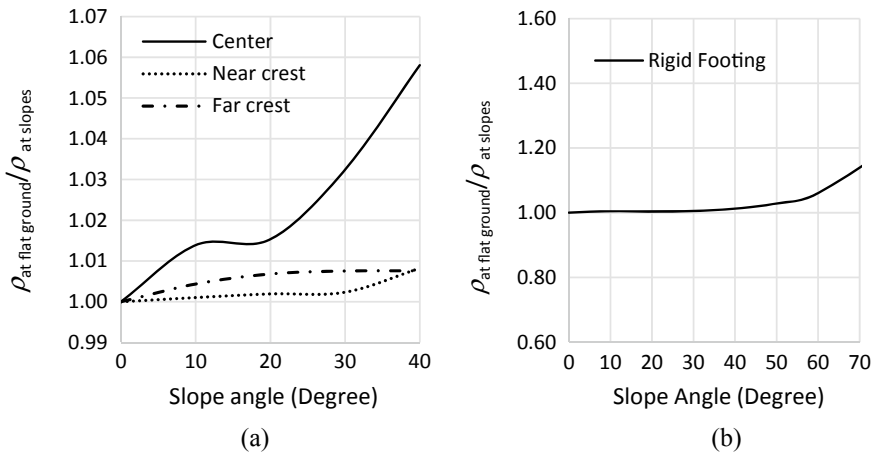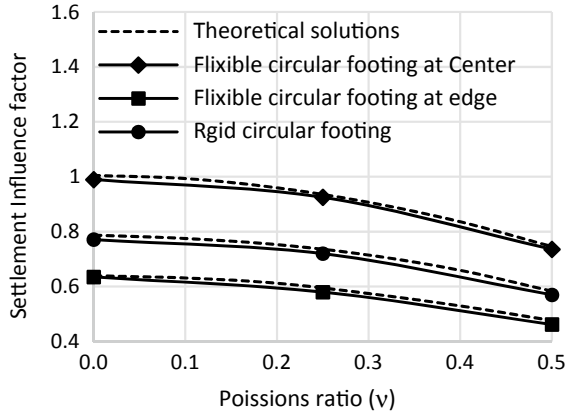
Fig. 6 Elastic settlement of footing on slopes for D/B = 0, E = 10Mpa and ν = 0.25 **a** flexible footing and **b** rigid footing

from slopes. The settlement at the center and near corner of the flexible footing from the slopes has shown an incremental trend. However, the rate of change of increment of settlement has been noted insignificant. Within elastic zone, the effect of slope angle has not found significant on elastic settlement of footing. In rigid footing, the settlement at the center increases after slope angle 45° but in granular soil the slope angle greater than 45° unstable. Moreover, an attempt has been made to check the elastic settlement of footing on slopes and observed insignificant effect of slope angle on elastic settlement of footing.

5   Conclusions

Several numbers of FEM analysis have been carried out for the estimation of seismic bearing capacity and elastic settlement of footing on slopes. Based on the present numerical analysis, the following conclusions can be drawn:

The present results obtained from FEM analysis for both seismic bearing capacity and elastic settlement have been found in good agreement with past studies. However, seismic bearing capacity obtained by limit analysis is quite less than FEM analysis.

The bearing capacity factors decrease with increase of seismic forces in both horizontal and sloping surface. For a constant load and footing geometry, the load carrying capacity is higher for smaller slope angle ($\beta = 20°$) than higher slope angle ($\beta = 30°$).

For a given slope angle, the bearing capacity increases with increases of footing embedment slope that may be due to increase of participating soil volume. The rate of increase of bearing capacity factor is high for larger slope angle. Finally, a chart has been reported for the estimation of seismic bearing capacity of embedded strip footing on slopes.

The effect of slope angle on footing has been examined based on theory of elasticity and no significant effect has been observed. The variation of elastic settlement of flexible footing has been observed within 6–10% at slope angle 0°–40°. However, the same effect has been observed in case of rigid footing.

References

1. Meyerhof GG (1957) The ultimate bearing capacity of foundations on slopes. In: Proceedings of the 4th International Conference on Soil Mechanics and Foundation Engineering, London: International Society for Soil Mechanics and Geotechnical Engineering, pp 384–386
2. Vesic AS (1975) Bearing capacity of shallow foundations. In: Winterkorn HF, Fang HY (eds) Foundation engineering handbook, 1st edn. Van Nostrand Reinhold, New York, pp 121–147
3. Hansen JB (1970) A revised and extended formula for bearing capacity. Danish Geotechnical Institute, Copenhagen, Denmark, pp 5–11
4. Bolton MD, Lau CK (1993) Vertical bearing capacity factors for circular and strip footings on Mohr-Coulomb soil. Can Geotech J 30(6):1024–1033
5. Kumar J, Rao VBKM (2003) Seismic bearing capacity of foundations on slopes. Geotechnique 53(3):347–361
6. Kumar J, Ghosh P (2006) Seismic bearing capacity for embedded footings on sloping ground". Geotechnique 56(2):133–140
7. Choudhury D, Rao K (2006) Seismic bearing capacity of shallow strip footings embedded in slope. Int J Geomech 6(3):176–184
8. Kumar J, Chakraborty D (2013) Seismic bearing capacity of foundations on cohesionless slopes. J Geotec Geoenviron Eng 139(11):1986–1993
9. Raj D, Singh Y, Shukla SK (2018) Seismic bearing capacity of strip foundation embedded in c-φ soil slope. Int J Geomech 18:04018076
10. Milovic SD (1998) A comparison between observed and calculated large settlements of raft foundations. Can Geotech J 35(2):251–263
11. Mayne PW, Poulos HG (1999) Approximate displacement influence factors for elastic shallow foundations. J Geotech Geoenviron Eng, ASCE 125(6):453–460

12. Timoshenko SP, Goodier JN (1970) Theory of elasticity, McGraw-Hill, New York
13. Chakraborty D, Kumar J (2015) Seismic bearing capacity of shallow embedded foundations on a sloping ground surface. Int J Geomech 15(1)
14. Nishida Y (1966) Vertical stress and vertical deformation of ground under a deep circular uniform pressure in the semi-infinite. In: Proceedings of the 1st International Society for Rock Mechanics Congress (ISRM)

Seismic Bearing Capacity of Shallow Foundations on Horizontal and Sloping Grounds: A Comparative Study

Arjun Gaur, Koushik Pandit [ID], and Shantanu Sarkar

Abstract In the present study, different approaches for determining seismic bearing capacity of shallow foundations have been discussed and a comparison has been drawn between seismic bearing capacity of shallow foundations of various widths and foundation depths, resting on both horizontal and sloping grounds. In general, the bearing capacity of foundations for static loading condition has been extensively studied by many researchers in the past. However, limited studies have been found from literatures which highlight the effect of an earthquake event on the bearing capacity of shallow foundations, especially when the foundation is resting on a sloping terrain. In this study, Sarma and Iossifelis (Geotechnique 40(2):265–273, 1990, [1]), Richards et al. (J Geotech Eng, ASCE 119(4):662–674, 1993, [2]), Budhu and Al Karni (Geotechnique 43(1):181–187, 1993, [3]), Soubra (Proceedings of the Institution of Civil Engineers: Geotechnical Engineering, London vol 125(4), pp 230–241, 1997, [4] and 1999), Kumar and Rao (Geotechnique 52(2):79–88, 2002, [5]), and Cascone and Casablanca (Soil Dyn Earthq Eng 84:204–223 2016, [6]) have been studied for computing seismic bearing capacity of shallow foundations of various widths resting on horizontal ground. Similarly, the seismic bearing capacity of shallow foundations of various widths resting on sloping ground has been computed by methods provided by Kumar and Rao (Geotechnique 53(3):347–361, 2003, [7]), and Chaudhary and Rao (Int J Geomech, ASCE 6(3):176–184, 2006, [8]). In the end, the seismic bearing capacity of shallow foundations with varying widths for horizontal and sloping grounds has been compared as obtained from different methods. This study helps in understanding the basic mechanism of load transfer from foundations to the surrounding ground as well as highlights on differences and similarities among different analytical solutions available for determining seismic bearing capacity of shallow foundations.

Keywords Seismic bearing capacity · Sloping ground · Seismic coefficient · Limit analysis · Limit equilibrium method

A. Gaur · K. Pandit (✉) · S. Sarkar
Geotechnical Engineering Group, CSIR—Central Building Research Institute, Roorkee 247667, Uttarakhand, India
e-mail: koushik@cbri.res.in

1   Introduction

For any civil engineering structure, foundations play an important role in transferring the superstructure load to the substrata. Any substrata either made of layered cohesive or cohesionless soil or rock mass should be able to bear the foundation and the load being transferred to it. Hence, neither the substrata nor the foundation itself should fail. For this reason, safe and accurate determination of bearing capacity of foundation is very crucial, especially when the strata location lies in a seismically active zone, such as the hilly states of India, e.g., Himachal Pradesh, Uttarakhand, the seven sister states in the North Eastern part and the newly formed union territory Jammu and Kashmir.

In the present study, different approaches for determining seismic bearing capacity of shallow foundations have been discussed and a comparison has been drawn between seismic bearing capacity of shallow foundations of various widths and foundation depths, resting on both horizontal and sloping grounds. In general, the bearing capacity of foundations for static loading condition has been extensively studied by any researchers in the past. However, limited studies have been found from literatures which highlight the effect of an earthquake event on the bearing capacity of shallow foundations, especially when the foundation is resting on a sloping terrain. Some of the notable and highly cited methods on determining the seismic bearing capacity of foundations have been studied and referred to in this present study. For example, in this study, Sarma and Iossifelis [1], Richards et al. [2], Budhu and Al Karni [3], Soubra [4], Kumar and Rao [5], and Cascone and Casablanca [6] have been studied for computing seismic bearing capacity of shallow foundations of various widths resting on horizontal ground. Similarly, the seismic bearing capacity of shallow foundations of various widths resting on sloping ground has been computed by methods provided by Kumar and Rao [7], and Chaudhary and Rao [8]. The investigation of these seismic bearing capacity computation methods shows that the values of seismic bearing capacity factors examined and modified by different researchers reduce substantially in the earthquake-prone areas and their values depend on many other parameters. In some of these methods, the seismic effect on ground has been incorporated through assigning horizontal and vertical seismic coefficients, where the values of horizontal seismic coefficient were computed from their correlations with internal friction angle of ground material. On the other hand, values of all three seismic bearing capacity factors such as N_{cE}, N_{qE}, and $N_{\gamma E}$ have been computed from their correlations with internal friction angle of slope material and the given slope angle, α (for sloping grounds only). Apart from these, Zhu [9] also discussed about the role of N_γ factor especially for a foundation.

In the present study, the seismic bearing capacity of shallow foundations with varying widths for horizontal and sloping grounds has been compared as obtained from different methods. The present study will help in understanding the basic mechanism of load transfer from foundations to the surrounding ground as well as highlights on differences and similarities among different analytical solutions available for determining seismic bearing capacity of shallow foundations.

Table 1 Parameters considered in the present study

Type	Parameter	Values
Foundation details	Depth (D_f)	1, 1.5 and 2.0
	Width (B) = Length (L)	1, 2 and 3
Soil parameters	Unit weight (γ)	18.33 kN/m^3
	Cohesion (c)	13.4 kN/m^2
	Internal angle of friction (φ)	34.22°
Earthquake parameters	Horizontal earthquake acceleration coefficient (k_h)	0.15
Slope geometry	Slope angle or ground inclination (α)	15 and 20 degree

2 Methodology

For the present study, the seismic bearing capacity factors such as N_{cE}, N_{qE}, and $N_{\gamma E}$ have been computed from their correlations with internal friction angle of slope material for computed horizontal seismic coefficient for a given earthquake zone of study and a slope angle, α selected. These bearing capacity factors were then substituted in the bearing capacity equations given by many researchers to find the seismic bearing capacity of the shallow foundation. In this study, typical soil parameters like the unit weight and shear strength parameters have been evaluated after studying characteristic sample values from different locations in the state of Uttarakhand, especially from the hilly areas. These parameters and their values considered in this study are given as follows:

The ultimate seismic bearing capacity (q_u) is computed from the following equation, given by Terzaghi [10] and suggested by Cascone and Casablanca [6]:

$$q_u = 1.3CN_{cE} + \gamma D_f N_{qE} + 0.4B\gamma N_{\gamma E} \tag{1}$$

By substituting all the necessary values from the given data in Table 1 and the values of seismic bearing capacity factors as calculated from monographs or tables provided by different researchers [1–8] in the above equation, the ultimate seismic bearing capacity (q_u) can be computed.

3 Results

The ultimate seismic bearing capacity of shallow foundations of different widths and foundation depths, resting on both horizontal and sloping grounds, has been determined from various approaches provided by various researchers by adopting the methodology discussed in the earlier section. The obtained results are summarized in the following Tables 2, 3 and 4.

Table 2 Ultimate seismic bearing capacity of shallow foundations on horizontal ground

Researchers	Foundation dimensions		Seismic bearing capacity factors			Computed ultimate seismic
	Width (B),	Depth (D_f),	N_{cE}	N_{qE}	$N_{\gamma E}$	Bearing capacity (q_{ult}), kPa
Sarma and Iossifelis [1]	1	1.0	33.19	23.94	37.31	1290.54
	2	1.0				1564.1
	3	1.0				1837.66
	1	1.5				1509.95
	2	1.5				1783.51
	3	1.5				2057.07
	1	2.0				1729.36
	2	2.0				2002.92
	3	2.0				2276
Richards et al. [2]	1	1.0	28.66	22.52	29.11	1125.48
	2	1.0				1338.91
	3	1.0				1552.35
	1	1.5				1331.87
	2	1.5				1545.31
	3	1.5				1758.74
	1	2.0				1538.27
	2	2.0				1751.7
	3	2.0				1965.14
Budhu AND Al-Karni [3]	1	1.0	32.86	22.95	26.44	1186.95
	2	1.0				1380.81
	3	1.0				1574.66
	1	1.5				1397.28
	2	1.5				1591.14
	3	1.5				1785
	1	2.0				1607.62
	2	2.0				1801.48
	3	2.0				1995.34
Soubra [4]	1	1.0	35.6	24.93	37.21	1349.94
	2	1.0				1622.76
	3	1.0				1895.95
	1	1.5				1578.42
	2	1.5				1851.24
	3	1.5				2124.07
	1	2.0				1806.9

Table 2 (continued)

Researchers	Foundation dimensions		Seismic bearing capacity factors			Computed ultimate seismic
	Width (B),	Depth (D_f),	N_{cE}	N_{qE}	$N_{\gamma E}$	Bearing capacity (q_{ult}), kPa
	2	2.0				2079.73
	3	2.0				2352.55
Kumar and Rao (2002) [5]	1	1.0	35.6	24.93	17.76	1207.33
	2	1.0				1337.55
	3	1.0				1467.76
	1	1.5				1435.81
	2	1.5				1566.03
	3	1.5				1696.25
	1	2.0				1664.3
	2	2.0				1794.51
	3	2.0				1924.73
Cascone and Casablanca [6]	1	1.0	31.97	22.6	20.03	1118.03
	2	1.0				1264.89
	3	1.0				1411.75
	1	1.5				1325.16
	2	1.5				1472.02
	3	1.5				1618.88
	1	2.0				1532.29
	2	2.0				1679.15
	3	2.0				1826.01

The seismic bearing capacity factors have been determined as a function of horizontal earthquake acceleration coefficient (k_h), slope angle or slope inclination (α), and friction angle (φ) of soil. Hence, it is important to develop an easy and simple graph including the effects of all these parameters in the computed values of the ultimate bearing capacities. Hence, in this study, the obtained values of ultimate seismic bearing capacity of the foundations of various widths at different foundation depths have been plotted against a dimensionless number of D_f/B ratios (Figs. 1 and 2).

4 Conclusions

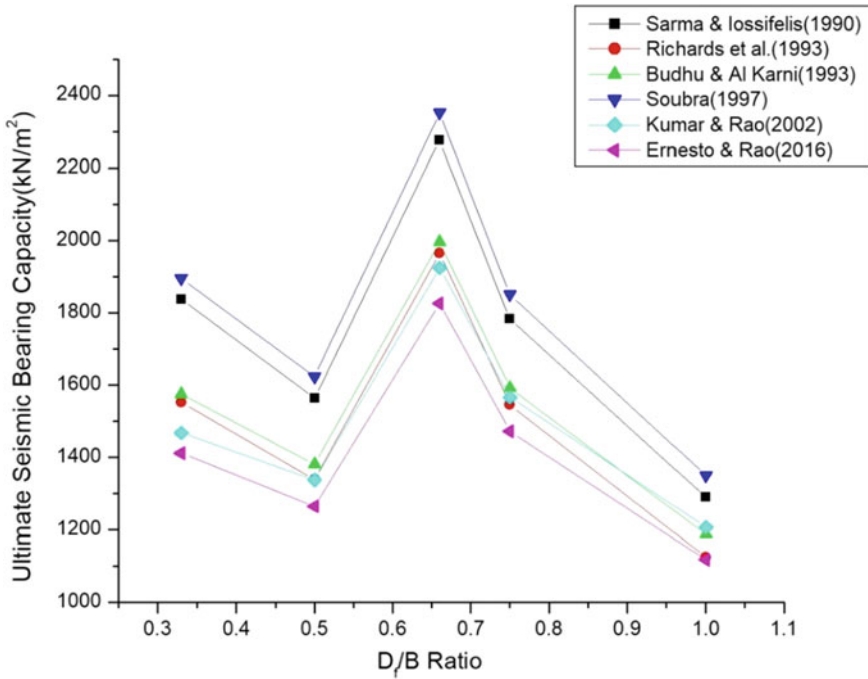Following important conclusions can be drawn from the present study:

- Bearing capacity factors reduce considerably with an increase in the magnitude of horizontal seismic acceleration coefficient (k_h).

Table 3 Ultimate seismic bearing capacity of shallow foundations on sloping ground (slope angle = 15°)

Researchers	Foundation dimensions		Seismic bearing capacity factors			Computed ultimate seismic
	Width (B), m	Depth (D_f), m	N_{cE}	N_{qE}	$N_{\gamma E}$	Bearing capacity (q_{ult}), kPa
Kumar and Rao [7]	1	1.0	15.5	8.97	10.63	512.36
	2	1.0				590.3
	3	1.0				668.24
	1	1.5				594.57
	2	1.5				672.51
	3	1.5				750.45
	1	2.0				676.78
	2	2.0				754.72
	3	2.0				832.66
Choudhury and Rao [8]	1	1.0	11.2	6.04	5.61	346.94
	2	1.0				388.08
	3	1.0				429.21
	1	1.5				402.3
	2	1.5				443.43
	3	1.5				484.57
	1	2.0				457.66
	2	2.0				498.79
	3	2.0				539.92

Table 4 Ultimate seismic bearing capacity of shallow foundations on sloping ground (slope angle = 20°)

Researchers	Foundation dimensions		Seismic bearing capacity factors			Computed ultimate seismic
	Width (B), m	Depth (D_f), m	N_{cE}	N_{qE}	$N_{\gamma E}$	Bearing capacity (q_{ult}), kPa
Kumar and Rao [7]	1	1.0	12.63	5.95	7.21	381.94
	2	1.0				434.8
	3	1.0				487.66
	1	1.5				436.47
	2	1.5				489.33
	3	1.5				542.2
	1	2.0				491
	2	2.0				543.86
	3	2.0				596.73

Fig. 1 Ultimate seismic bearing capacity of the foundations of various widths at different foundation depths for foundations resting on a horizontal ground

- The reduction of $N_{\gamma E}$ factor with an increase in k_h was found to be more sensitive as compared with the reductions in the other bearing capacity factor N_{cE}.
- The magnitudes of all the bearing capacity factors decrease with an increase in slope angle or ground inclination (α).
- The seismic bearing capacity of foundations increases for increasing widths at the same depth for horizontal and sloping grounds, keeping the slope angle constant.
- The seismic bearing capacity of foundations increase for increasing footing depths keeping widths constant for horizontal and sloping grounds, keeping the slope angle constant.
- The seismic bearing capacity of foundations decreases significantly for increasing slope inclinations with respect to the foundation of same widths and depths since the confining pressure on foundation from the soil on the sloping face reduces critically with increasing slope inclination.

Finally, it can be concluded that for the safe design of shallow foundations, one must consider seismicity of the local site and soil conditions as well as the slope geometry.
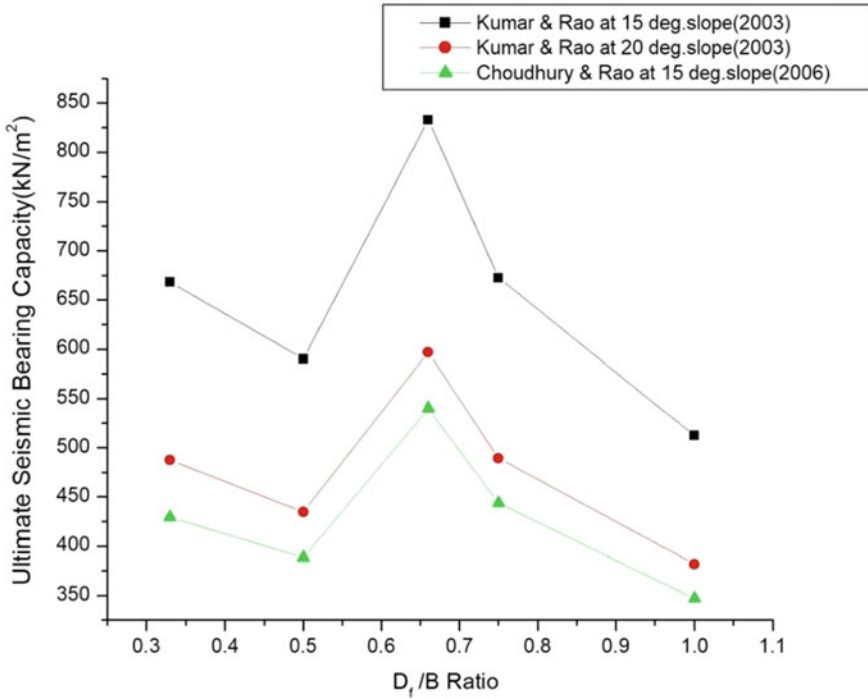
Fig. 2 Ultimate seismic bearing capacity of the foundations of various widths at different foundation depths for foundations resting on a sloping ground

References

1. Sarma SK, Iossifelis IS (1990) Seismic bearing capacity factors of shallow strip footings. Geotechnique, the Institution of Civil Engineers, London 40(2):265–273
2. Richards R, Elms DG, Budhu (1993) Seismic bearing capacity and settlement of foundations. J Geotech Eng, ASCE 119(4):662–674
3. Budhu M, Al-Karni A (1993) Seismic bearing capacity of soils. Geotechnique 43(1):181–187
4. Soubra AH (1997) Seismic bearing capacity of shallow strip footings in seismic conditions. In: Proceedings of the Institution of Civil Engineers: Geotechnical Engineering, London vol 125(4), pp 230–241
5. Kumar J, Rao VBKM (2002) Seismic bearing capacity factors for spread foundations. Geotechnique 52(2):79–88
6. Cascone E, Casablanca O (2016) Static and seismic bearing capacity of shallow strip footings. Soil Dyn Earthq Eng 84:204–223
7. Kumar J, Rao VBKM (2003) Seismic bearing capacity of foundations on slopes. Geotechnique 53(3):347–361
8. Chaudhary D, Rao KS (2006) Seismic bearing capacity of shallow strip footings embedded in slope. Int J Geomech, ASCE 6(3):176–184
9. Zhu D (2000) The least upper-bound solutions for bearing capacity factor Nγ. Soils Found 40(1):123–129
10. Terzaghi K (1943) Theoretical soil mechanics. Wiley, New York

Seismic Response of Buildings Resting on Raft Foundation with EPS Geofoam Buffer

M. V. Sreya, B. R. Jayalekshmi, and Katta Venkataramana

Abstract Seismic isolation is a technique that has been used around the world to protect building structures, non-structural components and content from the damaging effects of earthquake ground shaking. The present study deals with analysing the efficiency of Epoxy Polystyrene (EPS) geofoam buffer as a soil isolation medium to reduce the seismic energy transferred, thereby reducing the dynamic response of building under earthquake loads. The behaviour of an integrated soil isolation-building system has been investigated analytically, by using recorded accelerogram of El Centro earthquake. Finite element simulation of transient response has been carried out on three-dimensional field-scale models of one-storey, two-storey, three-storey and four-storey buildings resting on raft foundation in sand beds of different stiffnesses, with and without soil isolation mechanism. Four sets of three-dimensional buildings of single bay moment resisting concrete frames with 4 m bay length in either directions and 3 m storey height have been considered for the estimation of seismic response. EPS geofoam buffer of thicknesses 0.05, 0.10, 0.15 and 0.20 m and stiffnesses 22, 16, 10 and 5 MPa are placed at a depth of 0.15 m below the raft foundation of dimension 5 m × 5 m × 0.5 m. Different soil stiffnesses are considered to study its effects on the seismic response of building. Size of the soil stratum considered is 55 m × 55 m with a depth of 20 m. Absorbent boundaries have been used to eliminate the problem of reflection of the waves back into the soil from lateral boundaries. The interface between the underneath soil and EPS geofoam is formulated with a coefficient of friction 0.3. The results under field-scale conditions indicate that soil isolation provided by the EPS geofoam buffer substantially reduces the earthquake energy transmission to the superstructure during a strong earthquake.

Keywords Geofoam buffer · Raft foundation · Building-isolated soil system · Finite element modelling

M. V. Sreya (✉) · B. R. Jayalekshmi · K. Venkataramana
Department of Civil Engineering, NITK, Surathkal, Karnataka 575025, India
e-mail: sreya56vellur@gmail.com

1 Introduction

In a seismic isolation system, a flexible or sliding interface positioned between a structure and its foundation is made for the purpose of decoupling the horizontal motions of the ground from the horizontal motions of the structure, thereby reducing earthquake damage to the structure and its contents. Various mechanisms of this type have been invented over the past century, including those using rollers and layers of sand. For example, a building in China has been built with a sand layer between the foundation.

Obtaining high-quality alternative geo-materials is a challenging work in geotechnical engineering. The non-conventional lightweight materials are the solution for such situations.

Apart from the use of geosythetics, there is a new product derived from the geosynthetics, called geofoam, which is available in the market as a lightweight material having density around 1% of the density of soil. Expanded polystyrene (EPS) geofoam is an ultra-lightweight material with a number of geotechnical applications that has been increasing continuously over the last 40 years. It can act as an isolation material due to its main advantages like lightweight and low stiffness. Expanded polystyrene (EPS) geofoam is a closed cellular plastic foam and geosynthetic material, which is used in a wide variety of civil engineering applications including rapid construction of embankment over compressible soils [1, 2], slope stabilization [3], reduction of static and dynamic thrust on retaining walls, bridge abutments and piles [4], as a sub-base fill material [5, 6] and as isolation against dynamic loading [6]. In fact, the application of EPS geofoam can be classified by its function including lightweight fill (density), compressible inclusion, thermal insulation and vibration damper.

Researchers have been working to get a parametric study of the EPS geofoam buffer for its engineering properties. The engineering properties of expanded polystyrene (EPS) have been looked into by Negussey et al. [7, 8]. Stress–strain behaviour and coefficients of lateral earth pressure of soils and EPS were compared in stress-controlled conditions. The results indicated that the engineering properties of EPS can be quantified in a manner similar to that of earth materials. Behaviour of EPS geofoam under static and dynamic loading was studied. Interface of soil and EPS geofoam has also been studied. Average peak friction factor of about 0.88 and the residual friction factor of 0.65 were obtained under both dry and wet conditions for large samples of up to 500 mm × 500 mm in interface area from the direct shear tests [7]. In view of the fact that endeavours have been made over the years to analyse the stress–strain behaviours of sand–EPS mixture, understanding the modulus of elasticity and compressibility coefficient is of special importance in modelling the overall response of a particulate combination, soil density, geofoam block thickness, stiffness of the geofoam material and configuration of specimen.

Stiffness and thickness of the EPS geofoam buffer and stiffness of soil are the parameters considered in the present study for the analysis.

2 Methodology

Finite element simulation of transient response has been carried out on three-dimensional field-scale models of one-storey, two-storey, three-storey and four-storey buildings resting on raft foundation in sand beds of different stiffnesses, with and without soil isolation mechanism. Size of the soil strata considered was of 55mx55m planar area with 20 m depth. One-, two-, three- and four-storey buildings were supported on raft foundation with a size of 5 m × 5 m and of 0.5 m thickness. EPS geofoam was provided for the same planar area of raft, and thickness is varied from 0.05 to 0.20 m. One-bay RC buildings were with 4 m bay length and 3 m height for each storey. Different models were created for buildings with different storey heights, and the thickness and stiffness of the EPS geofoam varied for the models. Areas of cross section of columns and beams taken were 0.3 m × 0.3 m. Figure 1 shows the schematic illustration of building-isolated soil system.

Soil as well as raft was modelled with 8-noded linear brick reduced integration element SOLID 185 and columns and beams with 2-noded linear element BEAM 188. EPS geofoam was discretized with 3D finite strain element SOLSH190. Viscous boundary was given to the lateral sides of the soil stratum, while bottom side was fixed to restrict all kind of movements. Material properties used for the analysis are given in Table 1. Young's modulus of elasticity, Poisson's ratio and density of the material are the properties mainly required for the analysis. All the properties were collected from the parametric studies conducted in the past.

Various thicknesses of EPS considered were 0.05, 0.10, 0.15 and 0.20 m, and stiffnesses considered were 5 MPa, 10 MPa, 16 MPa and 22 MPa, respectively. Effect
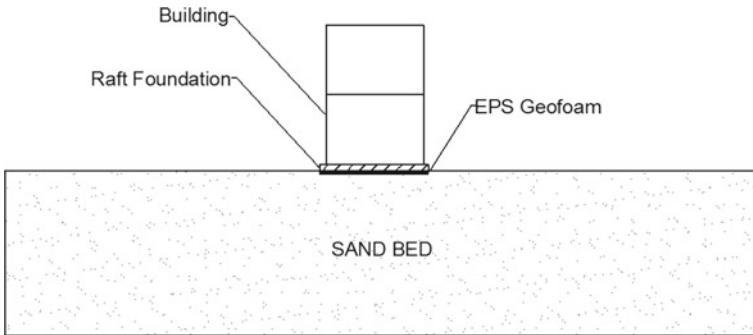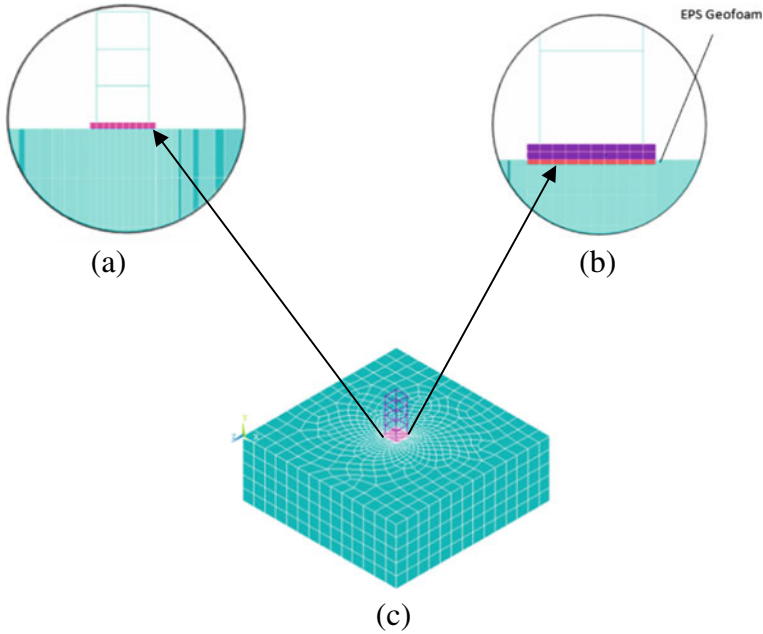

Fig. 1 Schematic illustration of building-isolated soil system

Table 1 Material properties

| Properties	Soil	Concrete	EPS geofoam
Stiffness, E (MPa)	55	22,500	5, 10, 16, 22
Density (kg/m^3)	1840	2500	22
Poisson's ratio	0.3	0.2	0.1

Fig. 2 Finite element models simulated in ANSYS: **a** without EPS geofoam buffer **b** with EPS geofoam buffer **c** isometric view of FEM model

of soil stiffness on the building response was also studied for various stiffnesses of soil such as 1, 20, 55, 100 and 150 MPa, i.e. from loose to very dense sand.

Figure 2 shows the finite element models simulated in ANSYS for cases with and without soil isolation mechanism.

2.1 Seismic Analysis

The building-isolated soil system was subjected to a dynamic seismic load corresponding to the recorded accelerogram of EL Centro earthquake (1940) with scaled down PGA of 0.3 g for the initial 10 s duration (see Fig. 3). Seismic analysis was carried out to study the effect of stiffness and thickness of EPS geofoam material used as soil isolation on the seismic response of buildings. The coefficients of friction between EPS and raft and between soil and EPS were taken as 1.0 and 0.7, respectively [7].
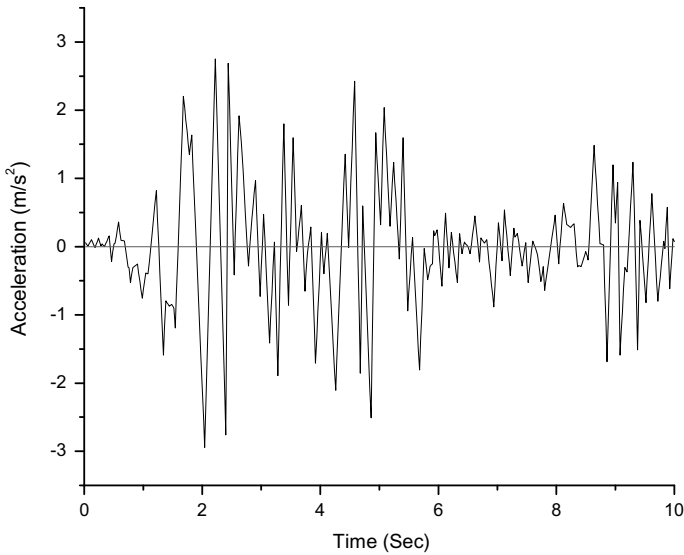
Fig. 3 Time history of input ground acceleration of El Centro earthquake

3   Results and Discussions

Stiffness and thickness effects of EPS geofoam buffer on roof acceleration of the buildings for different storeys were analysed. Analysis was done for buildings resting on soil with different stiffnesses. The results show that the roof acceleration response decreases with the reduction in stiffness and increase in thickness of the EPS geofoam.

3.1   Effect of Stiffness of Soil on Seismic Response of Building

The roof acceleration of building is found to be varying considerably with the soil stiffness. Figure 4 shows the representative sketch of roof acceleration response of three-storey building after time history analysis, which was rested on soil with different stiffnesses of 1, 20, 55, 100 and 150 MPa. Peak values of roof acceleration were noted and plotted in Fig. 5. From the analysis of the building-isolated soil system resting on different soils, it was found that model resting on high and low stiff sand strata shows very good isolation capacity, while those resting on medium stiff soil show less isolation capacity. While stiffness of soil decreased from 55 to 1 MPa, 78% decrease in acceleration was observed. But again, while stiffness increased to 150 MPa from 55 MPa, there was 48% decrease in acceleration.
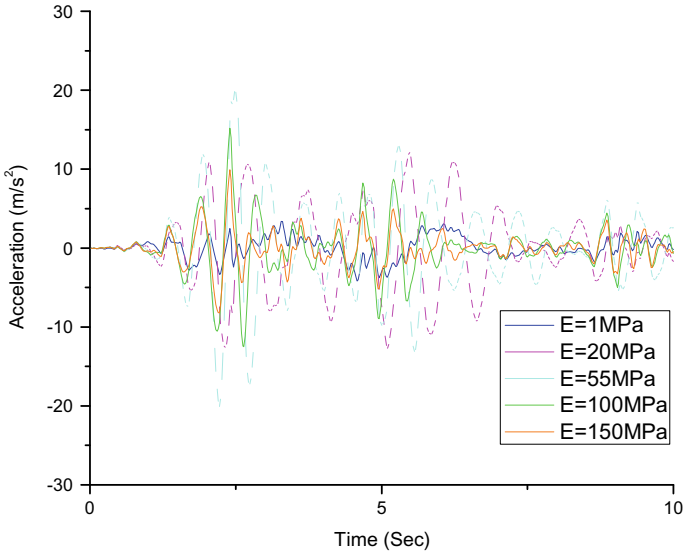
Fig. 4 Roof acceleration response from time history analysis of three-storey building resting on soil with various siffnesses
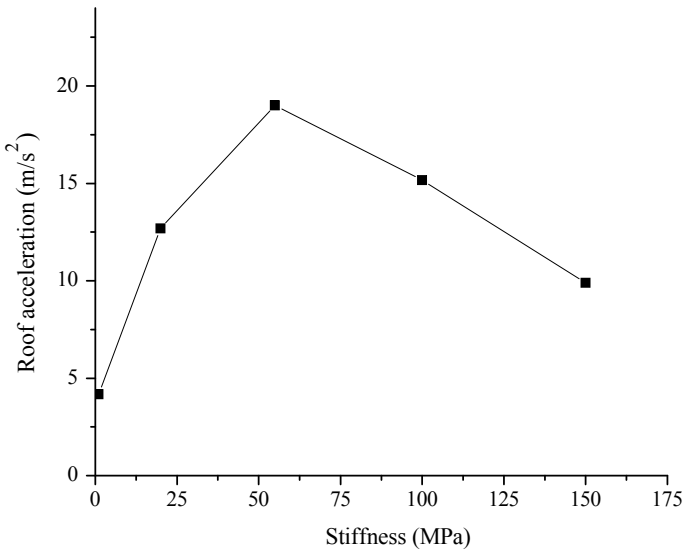
Fig. 5 Roof acceleration of 3 storey building resting on soil with various stiffnesses

3.2 Effect of Stiffness of EPS Geofoam on Seismic Response of Building

The seismic response of building with the variation in the stiffness value of EPS geofoam was analysed by placing the EPS geofoam at 0.15m depth below the raft foundation. Maximum and minimum roof acceleration were observed for two-storey and four-storey building, respectively. The percentage reduction in the acceleration for the one-, two-, three- and four-storey buildings with the change in stiffness of EPS from 5 to 22 MPa was obtained as 5.6%, 7.2%, 5.12% and 6.7%, respectively. Compared to unreinforced soil-building system, around 8% to 30% reduction in acceleration at the roof level was observed for one- to four-storey buildings when the EPS geofoam of stiffness 5 MPa was provided within the soil. The pattern of variation in the roof acceleration which corresponds to the increase in stiffness was found to be the same for all building-isolated soil models which were analysed. Figure 6 shows that less stiff EPS geofoam materials can reduce the acceleration response of the buildings under earthquake loads.
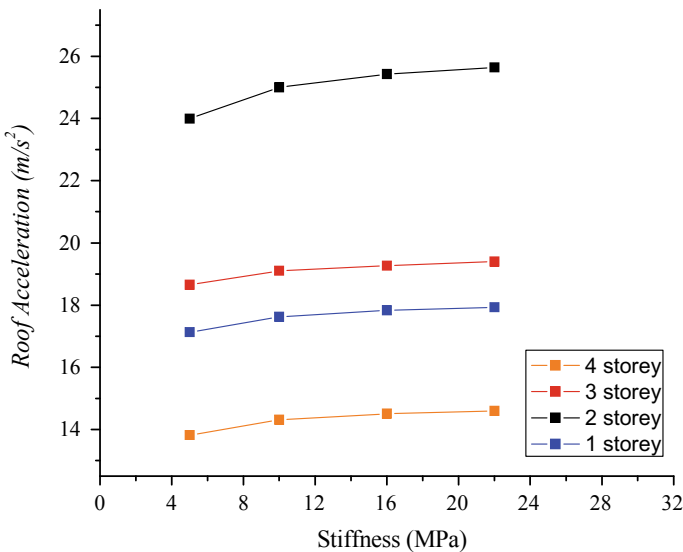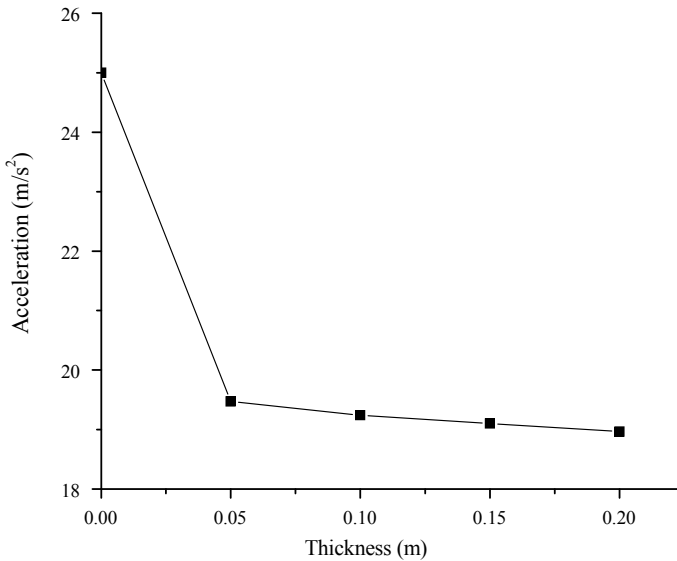

Fig. 6 Variation of roof acceleration with respect to stiffness of EPS geofoam

Fig. 7 Variation of roof acceleration of three-storey building with respect to various thicknesses of EPS geofoam

3.3 Effect of Thickness of EPS Geofoam on Seismic Response of Building

Study on the effect of thickness of EPS geofoam was conducted by providing the EPS geofoam for the entire area of raft foundation. Even though EPS geofoam is available for various thicknesses and dimensions, it is important to fix the thickness approximately as per the requirement.

Compared to the unreinforced conventional building-soil system, there was almost 30% reduction in the acceleration at the roof for the isolated soil-building system when EPS geofoam was provided at a depth of 0.15 m below the raft foundation (Fig. 7). Even though the percentage variation in acceleration which corresponds to stiffnesses considered was within 10%, the results obtained are in conformity with the observations of other researchers from the past studies on the behaviour of EPS geofoam applied for retaining walls [5].

4 Conclusion

Numerical seismic simulation of the integrated building-isolated soil system explores the isolation effect of EPS geofoam buffer, which is placed under raft foundation. A 3D finite element simulation and parametric study in ANSYS software was carried

out to demonstrate the effectiveness of the current method of isolation. The following conclusions are drawn:

1. Soil–EPS interface reduces the seismic energy transferred to the superstructure.
2. Almost 30% reduction in the roof acceleration was obtained for building-isolated soil system when the soil stratum considered was medium dense sand of stiffness 55 MPa.
3. The stiffness and thickness of EPS geofoam material found to be influencing the seismic response of building under earthquake excitations.
4. EPS geofoam material is found to be simple good isolation material for low-rise buildings.

Reference

1. Elragi A (2000) Selected engineering properties and applications of EPS geofoam. State University of New York College of Environmental Science and Forestry, ProQuest Dissertations and Theses
2. Mandal JN, Nimbalkar SS (1999) Reduction of lateral earth pressure by compressible inclusion by centrifuge modeling. In: Proceeding of Indian geotechnical conference, pp 63–67
3. Huang X, Negussey D (2011) EPS geofoam design parameters for pavement structures. GeoFront 2011 Adv Geotech Eng 4544–4554. Ossa A, Romo MP (2011) Dynamic characterization of EPS geofoam. Geotext Geomembr 29(1):40–50
4. Jutkofsky W, Sung J, Negussey D (2000) Stabilization of embankment slope with geofoam. Transp Res Rec J Transp Res Board 1736:94–102
5. Duškov M (1997) Materials research on EPS20 and EPS15 under representative conditions in pavement structures. Geotext Geomembr 15(1):147–181
6. Zarnani S, Bathurst RJ (2009) Influence of constitutive model on numerical simulation of EPS seismic buffer shaking table tests. Geotext Geomembr 27(4):308–312
7. Negussey D, Jahanandish M (1993) Comparison of some engineering properties of expanded polystyrene with those of soils. Transp Res Rec 1418:43–50
8. Negussey D, Anasthas N, Srirajan S (2001) Interface friction properties of EPS geofoam. In: Proceedings of the EPS geofoam, 3rd international conference, Salt Lake City